Quantum engineering of III-nitride nanostructures for infrared optoelectronics

Mark Beeler

▶ To cite this version:

Mark Beeler. Quantum engineering of III-nitride nanostructures for infrared optoelectronics. Quantum Physics [quant-ph]. Université Grenoble Alpes, 2015. English. <NNT : 2015GREAY044>. <tel-01280259>

HAL Id: tel-01280259
https://tel.archives-ouvertes.fr/tel-01280259

Submitted on 29 Feb 2016

HAL is a multi-disciplinary open access archive for the deposit and dissemination of scientific research documents, whether they are published or not. The documents may come from teaching and research institutions in France or abroad, or from public or private research centers.

L'archive ouverte pluridisciplinaire **HAL**, est destinée au dépôt et à la diffusion de documents scientifiques de niveau recherche, publiés ou non, émanant des établissements d'enseignement et de recherche français ou étrangers, des laboratoires publics ou privés.

UNIVERSITÉ DE GRENOBLE

THÈSE

Pour obtenir le grade de

DOCTEUR DE L'UNIVERSITÉ DE GRENOBLE

Spécialité : **Physique / Nanophysique**

Arrêté ministériel : 7 août 2006

Présentée par

Mark BEELER

Thèse dirigée par **Eva MONROY**

préparée au sein du **Laboratoire Nanophysique et Semi-Conducteurs (CEA / INAC / SP2M)**
dans **l'École Doctorale de Physique**

Ingénierie quantique de nanostructures à base de semi-conducteurs III-Nitrures pour l'optoélectronique infrarouge

Thèse soutenue publiquement le **9 juin 2015**
devant le jury composé de :

M Pierre LEFEBVRE
Rapporteur
M Czeslaw SKIERBISZEWSKI
Rapporteur
M Henri MARIETTE
Président
M Raffaele COLOMBELLI
Membre
M Martin EICKHOFF
Membre
Mme Eva MONROY
Membre
M Jean-Luc REVERCHON
Membre

Acknowledgements

This manuscript is an outcome of my research within the group of “Nanophysique et Semiconducteurs” at the “Institut Nanosciences et Cryogénie” at “Commissariat à l’énergie atomique et aux énergies alternatives” in Grenoble, France. For three years I had the opportunity to live and work here in Grenoble, and I could not have done so without the help of so many amazing people.

Firstly, I would like to acknowledge the help of my supervisor Eva Monroy for her constant encouragement and everlifting spirit. Even when the results looked gloomy, you were always there to shed a positive light. You were so patient to teach me everything I wanted to know, and I’ll miss sticking my head around the corner of your office as you drop anything to help me with my problems. Thank you so much for all that you’ve done, and all that you’ve taught me for being a scientist, manager, and friend.

I would also like to thank Henri Mariette (Director of NPSC) and Jean-Michel Gerard (Director of SP2M) for welcoming me into the group and giving me the opportunity to perform my research that was possible thanks to the European project TeraGaN (ERC-StG #278428). I would also like to thank the other administrative staff, Carmelo Castagna and Céline Conche for all their help in navigating the administration of CEA.

I would like to extend my thanks to all the members of the jury for their time and for coming all of this way to Grenoble. To Czeslaw Skierbiszewski and Pierre Lefebvre, the reporters for this manuscript, for their comments and interesting discussions regarding the research. Also to Martin Eickhoff, Raffaele Colombelli, Henri Mariette, and Jean-Luc Reverchon for their interesting questions and discussion after the presentation. Also, I would like to thank Joel E. and Régis for their help in making my presentation the best it could possibly be.

I would also like to thank the group in Giessen (Jörg S., Jörg T., Martin and Pascal) for their assistance both with the characterization of the samples as well as with the growth of the nanowires. I hope this fruitful collaboration continues to bring a multitude of ground-breaking research to both our groups! I would also like to thank our collaborators in Barcelona (Jordi and Maria) for their help on characterizing these nanowire samples and for being so quick to provide beautiful TEM images. I also extend my thanks to our colleagues in Warsaw (Agata and Stanislaw) who were so enthusiastic and eager to work with us, as well as to our colleagues at the Université de Paris-Sud (Maria T., Houssaine, and Francois) for their help on the semipolar samples, and for all of their past help to the previous PhD students.

I am very thankful for all my colleagues here at CEA which helped us produce our results from behind the scenes; Yoann, Yann, Jean, and Didier for their help in always making sure our machines were running, and we had the necessary equipment to do whatever we needed, be it air conditioners or boot covers. I am also thankful for the people who helped train me on the equipment I used throughout this thesis, for Edith and Stephanie for their help with the XRD machines, Catherine for her beautiful TEM images, Martien for her help with the nanowires, Thierry for his help in the cleanroom training, Joel B. for the TRPL training and discussion, Lucien for the AFM training, and Nicolas for the SEM training.

This work would also not be possible if not for the help of Caroline Lim, Akhil Ajay, Jonas Lähnemann, and Manos Trichas. Not only were you a pleasure to work with, you are a great group of scientists to bounce ideas off of, I wish you all the best in the future! I would also like to thank the others who helped me in times of crisis when the paperwork became too much; Thank you Thomas, Caroline and Emanuel for always helping me with my translations and Français pourri. I also have to thank the previous group members that laid the foundation for my work here, Prem, Yulia, Aparna, Sirona, Fernando. SP2M would not have been the same without the amazing atmosphere and innovative personalities in it. Thank you Thibault, Adrien, Luca, David, Lionel, Karine, Pamela, Aurelie, Damien S., Damien M., Anna, Agnès, Buk, Zhihua, Zhang, Toby, and Mattias for making my time here so enjoyable and memorable.

I also have to thank my friends here in Grenoble, Suzana, Martin, Nicole, Fabio, Bhagrav, Hugh, Astri, Rob, Peter, Matt, Alex, Gitte, Jake, Bailey and Graeme for their constant support and constant reminder to search out adventures! Finally, I have to thank my fiancée Lauren for being my rock to lean on and for always putting a smile on my face, and lighting up my life no matter what happens.

Résumé

Ce mémoire de thèse porte sur l'étude de nanostructures semi-conductrices à base de GaN, sous la forme de puits quantiques (PQs) et d'hétérostructures insérées dans des nanofils (NFs). Elles constituent la région active de composants inter-sous-bande (ISB) à base de nitrures pour l'optoélectronique infrarouge. Cette thèse résume des efforts dans la conception de la structure de bande des empilements dans la croissance épitaxiale et la caractérisation structurale et physique des objets réalisés. Le dessin des nanostructures pour ajuster leur longueur d'onde d'absorption/émission a été effectué en utilisant le logiciel Nextnano3 pour la résolution des équations de Schrödinger-Poisson, et les structures ont ensuite été synthétisées par épitaxie par jets moléculaires.

Le manuscrit lui-même est composé d'un texte de 55 pages, d'une bibliographie et neuf articles en annexe dont je suis le premier ou le deuxième auteur. Parmi ces articles, sept sont déjà publiés dans des journaux internationaux à comité de lecture, et deux sont soumis pour publication. Parmi ces documents, il y a un article de revue de l'état de l'art des composants inter-sous-bande (annexe 1), et un chapitre de livre qui donne une image plus complète de la technologie ISB à base de nitrures (annexe 2).

Ce manuscrit est composé de sept chapitres. Un premier chapitre d'introduction générale expose la motivation, les objectifs et l'organisation du mémoire de thèse. Le chapitre 2 rappelle les particularités des matériaux nitrures du groupe III. Le texte commence par une description de la structure cristalline, la polarisation spontanée et les constantes élastiques et piézo-électriques, suivie par la déduction théorique des règles de sélection pour les transitions ISB. Ce chapitre se termine avec une revue de l'état de l'art de la technologie ISB à base de nitrures.

Le chapitre 3 est focalisé sur les techniques expérimentales mises en œuvre durant cette thèse, en commençant par l'épitaxie par jets moléculaires assistée par plasma (PAMBE). On décrit les paramètres de croissance pour les PQs et les NFs à base de GaN. On explique par ailleurs, la méthode de simulation, basé sur le logiciel Nextnano^{3}, et les paramètres physique des matériaux utilisés. Ce chapitre se termine avec une présentation des techniques de caractérisation structurale et optique.

Le cœur de la contribution scientifique de cette thèse est décrit dans les chapitres 4 à 6. Ces chapitres portent respectivement sur les composants THz à base de PQs polaires, les hétérostructures GaN/AlN dans les NF, et les PQs synthétisés sur des plans cristallins d'orientations non-polaires et semi-polaires. Les structures ont été conçues à l'aide du logiciel Nextnano^{3}, et ont été ensuite synthétisées par PAMBE. Pour finir, ces structures ont été caractérisées optiquement et structuralement, avec les résultats présentés dans les chapitres et démontrés dans les annexes.

Le chapitre 4 décrit la conception et la réalisation expérimentale des structures de multi-puits-quantique (MPQ) à base de nitrures polaires avec les transitions ISB dans le domaine spectral THz. Des architectures MPQ à base de 4 couches d'AlGaN sont proposées pour augmenter la stabilité de l'énergie d'absorption ISB compte tenu des incertitudes des paramètres de croissance. Sur ces structures élaborées en PAMBE, nous avons montré expérimentalement une absorption de la lumière polarisée TM à environ 14 THz. Les résultats de ces expériences ont été publiés dans les annexes 3 et 4. Afin d'aller vers des longueurs d'ondes plus longues et vers l'intégration des MPQ dans la région active des composants ISB complexes, il a fallu réduire les champs électriques internes. Cet objectif a été réalisé avec les MPQ de profils pseudo-carrés, avec des barrières plus étroites (monocouches) et des fonctions d'ondes symétriques. La réalisation de ces structures a permis de démontrer une absorption ISB dans la gamme de 53 à 160 µm (publiée dans l'annexe 5). Les deux architectures décrites dans ce chapitre, les MPQs à base de 4 couches et les MPQs pseudo-carrés , ont démontré une énergie d'absorption ISB stable malgré les fluctuations de l'épaisseur de 1-2 monocouches atomiques introduites par la croissance PAMBE, et malgré les fluctuations de la composition des alliages ternaires. Cette robustesse structurelle s'appuie sur des calculs théoriques réalisés au préalable. Enfin, ce chapitre se termine par une proposition de design de structure laser à cascade quantique à base de GaN fonctionnant dans la gamme THz, qui incorpore les architectures MPQ décrites précédemment.

Le chapitre 5 porte principalement sur les propriétés optiques inter-bandes et intra-bandes des hétérostructures à base de nanodisques de GaN/AlN intégrés dans les NFs GaN avec différentes densités de dopage de germanium. Une partie importante de ce chapitre est l'étude des propriétés induites par l'état de contrainte liée à la présence d'une coquille d'AlN. Du point de vue optique, ces nanodisques présentent des temps de vie des porteurs d'environ 5 µs qui ne changent pas beaucoup avec la température. Ce phénomène a été attribué à l'absence de défauts dans la région active de ces NFs et au confinement des porteurs en trois dimensions. Nous avons analysé les résultats des mesures de photoluminescence résolue en temps par comparaison avec des simulations tridimensionnelles de la structure électronique avec le logiciel Nextnano3. Nous avons ainsi démontré théoriquement une séparation des fonctions d'onde de l'électron et du trou le long l'axe de croissance du NF et perpendiculairement à cet axe. L'augmentation de la densité de dopage Ge dans ces structures conduit à une diminution des champs électriques radial et axial qui séparent l'électron et le trou. Cet alignement des fonctions d'ondes induit une diminution du temps de vie des porteurs de presque deux ordres de grandeur (publiés dans l'annexe 6). En utilisant ces structures, nous avons également montré pour la première fois l'absorption ISB dans les hétérostructures NFs, autour des longueurs d'onde télécom. L'énergie des transitions ISB peut être modifiée en changeant

la densité de dopage et l'épaisseur des nanodisques. Nos résultats montrent que les effets à N corps tels que l'effet d'échange ou l´écrantage par des plasmons sont des éléments essentiels à prendre en compte pour expliquer qualitativement les énergies de transition observées dans l'infrarouge (publiés dans l'annexe 7). La différence entre les dopants germanium et silicium est analysée par rapport à leurs effets sur l'absorption ISB dans ces NFs hétérostructurés.

Le chapitre 6 montre la possibilité de synthétiser les hétérostructures GaN/AIN sur les substrats non-polaires et semi-polaires. Nous avons analysé les transitions inter-bande et ISB dans les structures à PQs déposées sur les plans m-(1-100), a-(11-20) et (11-22) du GaN et nous avons comparé les résultats expérimentaux avec des calculs numériques. Par rapport aux plans non-polaires, nous avons observé une supériorité des PQs dits « plans m » par rapport aux structures « plans a » en termes de propriétés optiques et structurales. En nous focalisant sur les structures « plan-m », nous avons montré de l'absorption ISB dans le domaine de 1,5-6,0 µm (publié dans l'annexe 8). De même, des mesures inter-bande et ISB dans les PQs GaN/AlN semi-polaires ont été publiées dans l'annexe 9.

Finalement, le chapitre 7 présente les conclusions de ce travail et apporte plusieurs perspectives en ce qui concerne la fabrication des lasers à cascade quantique et des détecteurs IR à base de NFs.

Table of Contents

Table of Contents 1

Glossary 3

1. General Introduction 4

   1.1. Motivation and targets 4

   1.2. Organization of the manuscript 5

2. Technical introduction 7

   2.1. III-nitrides and their peculiarities 7

   2.2. Quantum confined Stark effect 8

   2.3. Intersubband transitions and the governing principles 9

   2.4. Many body effects 12

   2.5. State of the art for intersubband in nitrides 13

3. Experimental methods 16

   3.1. Material Growth and strain relaxation 16

   3.2. Simulation parameters 18

   3.3. Structural characterization 20

   3.4. Optical characterization 20

4. Results: *c*-plane THz intersubband devices 24

   4.1. Introduction to THz intersubband 24

   4.2. Intersubband absorption in GaN-based quantum wells (Annex 3, 4 and 5) 24

      4.2.1. The step-quantum-well design 24

      4.2.2. The 4-layer quantum well design 26

      4.2.3. The 4-layer pseudo-square quantum well design 27

   4.3. Quantum cascade laser designs 28

   4.4. Quantum cascade laser design constraints 29

   4.5. Conclusions 32

5. Results: Nanowires for intersubband devices 34

   5.1. Introduction to nanowires 34

   5.2. Samples under study 34

5.3. Understanding band-to-band dynamics (Annex 6) ... 35

5.4. Intraband absorption in nanowire heterostructures (Annex 7) ... 40

5.5. Note on silicon vs. germanium for n-type doping. ... 41

5.6. Conclusions ... 41

6. Results: Alternate crystal orientations ... 44

6.1. Introduction to nonpolar and semipolar orientations ... 44

6.1. Optical: *a*- vs *m*- vs *c*-plane substrates ... 44

6.2. Structural: *a*- vs *m*- vs *c*-plane substrates ... 46

6.3. Longer wavelength intersubband transitions in the *m* plane (Annex 8) ... 47

6.4. Growth on semipolar substrates (Annex 9) ... 48

6.5. Conclusions ... 50

7. Conclusions and prospects ... 52

7.1. Conclusions ... 52

7.2. Prospects ... 53

7.2.1. THz quantum cascade laser fabrication ... 53

7.2.2. Nanowire intersubband technology ... 53

7.2.3. Nonpolar Intersubband devices ... 54

Bibliography ... 56

List of publications (annexes) and conference contributions ... 78

Glossary

Abbreviation	Definition
2D	two-dimensional
3D	three-dimensional
ADF	annular dark field
AFM	atomic force microscopy
BEP	beam equivalent pressure
FIR	far-infrared
FTIR	Fourier transform infrared spectroscopy
FWHM	full width at half of the maximum value
HAADF	High angle annular dark field spectroscopy
HRTEM	high resolution transmission electron microscopy
HVPE	hydride vapour phase epitaxy
IR	infrared
ISB	Intersubband
LED	light emitting diode
LO	longitudinal optical
MBE	molecular beam epitaxy
MIR	mid-infrared
ML	monolayers
MOCVD	metalorganic chemical vapor deposition
MOVPE	metal-organic vapor phase epitaxy
MQW	multi-quantum-well
n.i.d.	non-intentionally doped
ND	nanodisk - those inside nanowire heterostructures
NIR	near-infrared
NW	nanowire
PAMBE	plasma-assisted Molecular beam epitaxy
PL	photoluminesence (spectroscopy)
QCD	quantum cascade detector
QCL	quantum cascade laser
QCSE	quantum-confined Starck effect
QD	quantum dot
QW	quantum well
QWIP	quantum well infrared photodetectors
RHEED	reflection high energy electron diffraction
RMS	root of the mean squared
SL	superlattice
STEM	scanning tunneling electron microscopy
TE	transverse electric
TEM	transmission electron microscopy
TM	transverse magnetic
UV	ultraviolet
XRD	X-ray diffraction

1. General Introduction

1.1. Motivation and targets

Group III-nitride semiconductors have made the implementation of full-color optoelectronics possible due to their large direct band gap and doping capabilities; this has led to the development of blue and green light emitting diodes (LEDs). Heterostructures of these materials are found in the marketplace for a variety of applications, such as for blue laser diodes (blue ray players) or LEDs for household lighting. These materials are also currently used in high-power electronics because of their mechanical/thermal robustness [1], high electrical breakdown fields, and high electron motility. Furthermore, III-nitrides are currently the only solid-state alternative to mercury lamps as ultraviolet (UV) emitters [2]. By incorporating aluminum or indium into GaN, the bandgap of the material can be increased or decreased, respectively. The introduction of InGaN in solar cells has also attracted increasing interest because it can be optically active over a large spectral range – from the UV to the near-infrared (NIR) [3]–[7]. Finally, these materials are also becoming interesting due to their large conduction band offset [8], [9], large longitudinal optical (LO) phonon [10], [11] and their applicability to create devices in the IR by using intersubband (ISB) transitions [12].

In ISB devices, proper understanding of the electron and hole distribution and lifetime is crucial for the design of complex devices such as the quantum cascade laser (QCL) [13], [14]. The purpose of this work was to further the understanding of the manipulation of nanoscale systems with the intent of using these systems for ISB optoelectronic devices. An overarching goal for this thesis is to establish the knowledge base necessary and the basic units needed to manipulate III-nitride heterostructures towards the realization of a III-nitride-based QCL. This is done through conduction band engineering to accurately predict the ISB energy of these nanostructures from the NIR to the far-infrared (FIR).

This thesis aims to push the boundaries of GaN-based ISB technologies in a three-pronged approach focusing on *c*-plane GaN, in nanowires (NWs) and finally on nonpolar GaN:

- Using polar *c*-plane technologies, we aim to define the building blocks that will lead to the creation of THz QCLs operating at room-temperature. By analyzing the inherent errors induced from the plasma-assisted molecular beam epitaxy (PAMBE) system, we created conduction band architectures eliciting ISB transitions in the THz spectral region which are insusceptible to these errors. These primary designs were improved upon, by taking into account both the tunability of the transition energy and tunneling transport requirements, in order to move forward towards complete devices. By analyzing the various GaN QCL designs based on GaAs materials, we have proposed a design specifically adapted to GaN.
- Using NW structures, we aim to create ISB devices that can operate at high efficiencies for photodetection and eventually light emission/lasing. Towards this purpose, we have probed the effect of nanodisk (ND) size and doping on the interband and ISB characteristics of GaN/AlN NW heterostructures.

Finally, using alternative crystallographic orientations (nonpolar, semipolar), we aim to create heterostructure designs that can cover the full infrared (IR) spectral region with simplified band engineering through the reduction or cancelation of the polarization-induced electric fields. We have first analyzed various crystallographic orientations to decide which is better in terms of optical and structural performance. In view of the results, we have proceeded to explore the spectral capabilities of *m*-plane superlattices (SLs).

In this thesis, I engineered the conduction band profiles to target certain operating wavelengths from the NIR to FIR by simulating the structures using commercial nextnano^3 software [15]. I was then in charge of the growth of these structures by PAMBE. Polar *c*-plane structures were grown by me, while off-plane structures were grown either by me or by PhD student Caroline Lim. In the case of NW heterostructures, growth was outsourced via collaboration with the group of Prof. Martin Eickhoff at the Justus Liebig University in Giessen (Germany). I optically characterized the *c*-plane samples and the NW heterostructures by photoluminescence (PL) and Fourier transform infrared spectroscopy (FTIR), and the off-plane samples were characterized in collaboration with Caroline Lim and Akhil Ajay. Time-resolved PL measurements were performed under the supervision of Dr. Joël Bleuse. Structural characterization was done in collaboration with Dr. Catherine Bougerol for transmission electron microscopy (TEM) of planar structures and the group of Prof. Jordi Arbiol in the Institut Català de Nanociència i Nanotecnologia, in Barcelona (Spain) for NW heterostructures. X-ray diffraction (XRD) spectroscopy was done with Dr. Edith Bellet-Amalric and Caroline Lim. Atomic force microscopy (AFM) images were procured in collaboration by Arántzazu Núñez Cascajero and Caroline Lim.

1.2. Organization of the manuscript

After this first chapter, which describes the motivation, targets and organization of the thesis, chapter 2 begins with a technical introduction of III-nitride semiconductors and their peculiarities, namely their crystal properties as well as the spontaneous and piezoelectric polarization fields arising from the strain relaxation mechanisms in GaN/Al(Ga)N heterostructures The physics behind ISB transitions are then presented, including the fundamental quantum mechanical equations involved. After this, the state of the art for ISB in III-nitrides is explored and the problems associated with its extension into the FIR are mentioned. Further information on the introduction of these technologies are also found in Annex 1 [16] and Annex 2 [17].

Chapter 3 outlines the experimental techniques used throughout the thesis. It first presents the PAMBE-growth of nanostructures including NWs, and the growth of planar heterostructures on nonpolar, polar and semipolar substrates.. It then outlines the parameters for the simulations performed on the thin film and three-dimensional (3D) heterostructures. Finally, it describes the structural and optical characterisation methods that were used throughout the thesis and how to properly treat the data to reach the conclusions obtained.

The results of the thesis are then introduced in three main chapters, associated with each of the three above-described targets. Chapter 4 covers THz structures grown on *c*-plane substrates. The existing architectures are theoretically analyzed regarding the errors induced within PAMBE growth.

A new design is then proposed and outlined in the two papers (Annex 3 and 4) [18], [19]. Annex 3 describes the inability to reproduce the previous designs, and the proposal for a new 4-layered multi-quantum-well (MQW) design is shown in Annex 4. Because this system was so robust, it was hard to vary the ISB wavelength. By keeping in mind the robustness and the tunneling transport requirements for incorporating these designs into QCL architectures, a pseudo-square design is introduced in Annex 5 [20]. The chapter finishes with a review of existing QCL designs and demonstrates that this pseudo-square design can be used as the building block in LO-phonon-based QCLs.

In chapter 5, NW heterostructures are first explored from an interband approach by using temperature-dependent and time-resolved PL, interpreted by comparison to calculations of the quantum mechanical structure. The main results are presented in Annex 6 [21] and show that the carrier lifetime can be varied over two orders of magnitude by changing the doping level. The ISB properties of these structures are also probed as a function of ND thickness and dopant level. The strain state, eigenfunctions, and ISB properties were simulated, and the results are shown in paper Annex 7 [22].

Chapter 6 starts by comparing the growth of *a*-, *m*-, and *c*-plane GaN/AlN SLs by analyzing their structural and optical properties. In terms of mosaicity, surface roughness, PL linewidth and intensity, and ISB absorption, the *m*-plane SLs were deemed to be the best nonpolar choice. This then led to the design of heterostructures with ISB transitions in the mid infrared (MIR) described in Annex 8. Semipolar planes were also explored for ISB applications, and showed that GaN/AlN MQWs could be fabricated with ISB transitions spanning the NIR as explained in Annex 9 [23].

Finally, chapter 7 contains the conclusions of the thesis and comments on the next steps to be taken for each of the three targets, including the processing of QCLs, NW photodetectors, and nonpolar architectures for quantum well infrared photodetectors (QWIPs), and how to integrate them into existing GaAs device architectures moving towards the FIR.

2. Technical introduction

2.1. III-nitrides and their peculiarities

AlN and GaN were first synthesized in 1907 by crystalline sublimation [24], and in 1931 by reacting ammonia gas with metallic gallium [25], respectively, and were first made by molecular beam epitaxy (MBE) in 1975 for AlN [26] and 1969 for GaN [27]. N-type doping is accomplished primarily through the use of Si [28], and p-type doping, albeit less effectively, is accomplished by using Mg [29].

GaN has been grown heteroepitaxially on a variety of substrates including SiC, Si, and Al_2O_3. Various companies are supplying bulk GaN grown by HVPE [30, p. 196], ammonothermal [31], or other methods, for optical devices such as laser diodes or to sell as substrates (see Table 1).

Company	Product	Growth method
Soraa	GaN	Ammonothermal [32]
Hamamatsu	GaN	HVPE on patterned substrates [33]
Hexatech	AlN	Physical vapor growth [34]
Lumilog	GaN	HVPE [35]
Ammono	GaN	Ammonothermal [36]
Seren Photonics	semi- or nonpolar GaN (templates)	MOCVD [37]
Sumitomo/Soitec	GaN	HVPE [38], [39]
Nanowin	Polar/nonpolar/semipolar GaN	HVPE [40]

Table 1 Various companies producing GaN substrates

In this work we will focus strictly on GaN, AlN and the ternary alloy of AlGaN. (Al,Ga)N can be grown in cubic (β) zincblende phase as well as the hexagonal (α) wurtzite phase. This work deals entirely with the α phase, which is the most thermodynamically stable. The wurtzite crystal structure is described through the use of four miller-Bravais indices (*hkil*). Where *h*,*k*, and *i* are separated by 120° and sit perpendicular to the *c* axis. The *c* plane (0001), the *m* plane (10-10), and the *a* plane (11–20) are indicated in Figure 1.

The [0001] axis is considered positive when the <0001> vector along the bond between the Ga and N points from the metal atom to the nitrogen atom. Conventionally, (0001) crystals are called Ga-polar and are typically preferred over (000–1) N-polar as they are more chemically stable and their surface morphology can be more easily controlled during the growth.

Because of the low symmetry of the crystal, the gravity centres of the positive and negative dipoles do not coincide and there is therefore a spontaneous polarization field along the <0001> axis. Because this has a dependency on the ideality of the crystal, the cation-nitrogen bond length, and the chemical properties of the cation [41], there is a difference in the magnitude of polarization for GaN and AlN. GaN has a spontaneous polarization value (-0.029 C/m^2 [41] or -0.034 C/m^2 [42]) smaller than AlN (-0.081 C/m^2 [41] or -0.090 C/m^2 [42])as a result of the larger crystal non-ideality

i.e. the larger on-axis bond length, and lower aspect ratio unit cell, as well as the larger effective charge and chemical nature of the cation. This spontaneous polarization is a determining factor for the creation of devices and is also the reason that interband devices can function at energies below the bandgap of GaN.

A piezoelectric polarization is also present in a GaN/AlN heterostructures that is linearly dependent on the strain field present within the material. Stress leads to deformations in the lattice according to Hooke's law:

$$\sigma_{ij} = \sum_{kl} C_{ijkl}\varepsilon_{kl}$$

where C_{ijkl} is the elastic tensor, and σ and ε represent the stress and strain respectively. C_{ijkl} is transformed to C_{mn} by replacing m,n = {xx, yy, zz, yz, zx, xy} with m,n = {1, 2, 3, 4, 5, 6}. Due to crystallographic symmetry, many of the tensors within C_{ijkl} are 0, and the matrix can be represented by 5 independent tensors such that $C_{11}=C_{22}$, $C_{12}=C_{21}$, $C_{13}=C_{31}=C_{23}=C_{32}$, C_{33}, $C_{44}=C_{55}$, $C_{66}=0.5(C_{11}-C_{21})$ [43], [44], [45, p. 199], [46]–[50] and the values can be seen in Table 3.

In the case of biaxial stress of a material grown along the [0001] direction ($\sigma_z = 0$ and $\sigma_x = \sigma_y$), the strain-induced piezoelectric polarization (P_{pz}) can be expressed as:

$$P_{pz} = 2\varepsilon_x\left(e_{31} - e_{33}\frac{C_{13}}{C_{33}}\right) = 2\frac{a - a_0}{a_0}\left(e_{31} - e_{33}\frac{C_{13}}{C_{33}}\right)$$

where a and a_0 represents the out-of-plane lattice parameters of the strained and bulk materials, and e_{31} and e_{33} represent the piezoelectric constants from the piezoelectric tensor. The values for these can be seen in Table 3.

Calculations for strain distribution in 3D structures are more complex in contrast to planar structures. For instance, in the case of NW heterostructures, the strain distribution is numerically calculated by assuming relaxation to the minimum total elastic energy and zero-stress boundary conditions at the surface.

2.2. Quantum confined Stark effect

The most common orientation for growing GaN is along the [0001] direction. This is because it has uniform atomic composition in that layer; the top is either Ga or N. This growth direction is aligned with the spontaneous polarization in the material, which, in heterostructures generates internal electric fields and phenomena such as the quantum confined Stark effect (QCSE). When electrons and holes are confined in a QW, the internal electric field shifts the electron states to lower energies, while the hole states are shifted to higher energies, reducing the permitted light absorption and emission frequencies. Additionally, the external electric field within the quantum well (QW) shifts electrons and holes to opposite sides of the well, decreasing the overlap integral, which in turn reduces the recombination efficiency of the system.

Growth of GaN in nonpolar (perpendicular to the spontaneous polarization vector) and semipolar (inclined with respect to the spontaneous polarization vector) orientations has been mainly motivated by the reduction of the QCSE, and started in 1987 [51]. By growing on nonpolar planes,

the internal electric field is null along the growth axis, while for semipolar planes, it is greatly decreased.

Figure 1 (a) shows a schematic of the growth planes of the wurtzite crystal and the associated band structure and wavefunctions for heterostructures of GaN/AlN grown along the (b) *c* and (c) nonpolar crystal orientations.

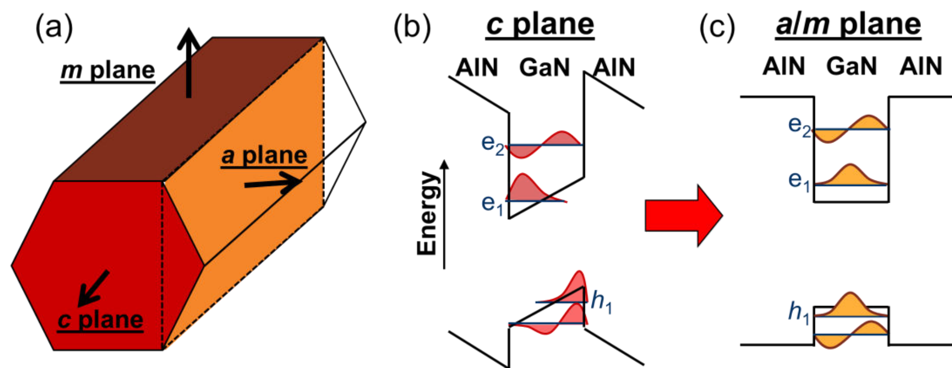

Figure 1 (a) Schematic diagram of various planes within a hexagonal unit cell: m plane (1-100) , *a* plane (11-20) and *c* plane (0001). (b) Band diagram schematics for *c*-plane AlN/GaN/AlN QWs. The internal electric field within *c*-plane GaN causes asymmetry in the wavefunctions. (c) Band diagram for a/m-plane AlN/GaN/AlN QWs. This asymmetry is not present in the *a*/*m*-plane QW due to the absence of the internal electric field.

Nonpolar GaN has been used in devices since 2000, with the first demonstration of a laser diode using nonpolar *m*-plane [52] and *a*-plane GaN [53] in 2003. Research has since expanded to a number of avenues including quantum dots (QDs) [54], [55], AlGaN/GaN MQWs [56], InGaN/GaN [57], [58], thicker films of GaN [59]–[61] or AlN [62], as well as to devices such as LEDs [63], lasers [64] and transistors [65]. However, for nonpolar growth, there is strong anisotropy of the surface properties resulting in layers with high defect densities. A compromise to this is seen with semipolar planes [66].

Initial research on the growth of semipolar GaN was driven by the need for longer wavelength laser diodes in the green [67], [68] and violet, as well as longer wavelength LEDs reaching the red and amber [69]–[71]. It has since shown promise in its ability to more easily incorporate indium [72]–[75], and has led to the creation of various start-ups like Soraa and Kaai [76], [77].

Substrates for epitaxial growth have been the main challenge for these systems and the best performing devices have been obtained using substrates acquired by slicing HVPE GaN boules along the nonpolar and semipolar planes. Research has also been done to create semipolar GaN using preconditioned templates [78]–[84].

2.3. Intersubband transitions and the governing principles

Semiconductors can be made optically active at IR wavelengths by engineering the quantized confinement of the electronic levels in QWs, NWs or QDs. QCLs or QWIPs are well-known illustrations of quantum-engineered devices. These controlled-by-design devices rely on optical ISB transitions between quantum-confined states, either within the conduction band or within the

valence band. The desired wavelength of operation can be obtained by a proper choice of the layer thicknesses and compositions.

The first ISB transitions were seen in an n-doped Si system in 1974[85]. Since then, ISB absorption has moved to other materials, including GaAs [86], [87], and the III-nitrides[88].

ISB transitions are governed by selection rules: to interact, incoming light needs to have an electric field in parallel to that of the heterostructure (perpendicular to the semiconductor layers). This imposes the use of TM polarized light, and necessitates the use of waveguides or surface gratings to couple light into the active region. Furthermore, due to the inversion symmetry, only transitions between wavefunctions of opposite parity are allowed.

A comprehensive introduction to ISB physics in QWs can be found in the works of Bastard [89] or Liu and Capasso [14]. In this section, we briefly introduce the polarization selection rule characteristic of ISB transitions. For this purpose, we consider a QW with two confined states in a single-particle approach. Transition rates *W* from states *i* to *f* are described by Fermi's golden rule as follows:

$$W_{if} = \frac{2\pi}{\hbar} \left|\langle \Psi_f | H' | \Psi_i \rangle\right|^2 \partial\left(E_f - E_i - \hbar\omega\right) \tag{1}$$

where H' is the interaction Hamiltonian, E_i and E_f and Ψ_i and Ψ_f are the energies of confinement levels and wavefunctions of the initial and final states respectively, and $\hbar\omega$ is the influencing radiation energy. As the radiation wavelength is much larger than the QW width in the case of IR radiation, a dipole approximation can be applied to the Hamiltonian.

$$H' = \frac{q^2 F_o^2}{4 m^{*2} \omega^2} (\boldsymbol{e} \cdot \boldsymbol{p}) \tag{2}$$

where *q* the elementary charge; F_o is the amplitude of the electric field; m^* the effective mass; ω the wavelength of light, and $\boldsymbol{e}$, and $\boldsymbol{p}$ the polarization and momentum operators respectively.

$$W_{if} = \frac{\pi}{\hbar} \frac{q^2 F_o^2}{2 m^{*2} \omega^2} \left|\langle \Psi_f | \boldsymbol{e} \cdot \boldsymbol{p} | \Psi_i \rangle\right|^2 \partial\left(E_f - E_i - \hbar\omega\right) \tag{3}$$

By expressing the wavefunctions as products of periodic Bloch functions, *u*, and a slowly-varying envelope functions, *f*, the transition rate can be shown:

$$W_{if} = \frac{\pi}{\hbar} \frac{q^2 F_o^2}{2 m^{*2} \omega^2} \left|\langle u_b f_s | \boldsymbol{e} \cdot \boldsymbol{p} | u_{b'} f_{s'} \rangle\right|^2 \delta\left(E_f - E_i - \hbar\omega\right) \tag{4}$$

where b and b', and s and s' are the band and subband indices of the initial and final states, respectively. This can be expanded to give:

$$\langle u_b f_s | \boldsymbol{e} \cdot \boldsymbol{p} | u_{b'} f_{s'} \rangle = \boldsymbol{e} \cdot \langle u_b | \boldsymbol{p} | u_{b'} \rangle \langle f_s | f_{s'} \rangle + \boldsymbol{e} \cdot \langle u_b | u_{b'} \rangle \langle f_s | \boldsymbol{p} | f_{s'} \rangle \tag{5}$$

The first term describes interband transitions (if b≠b' then $\langle u_b|u_{b'}\rangle$≈0). The second term describes the ISB transitions (if b=b' then the first term vanishes and $\langle u_b|u_{b'}\rangle$=1). This leaves ISB transitions to be governed by $\langle f_s|\boldsymbol{p}|f_{s'}\rangle$.

The motion of electrons in x and y inside thin film structures grown along the z axis by assuming a Bloch wavefunction for both the well and barrier and assuming $\frac{\partial H'}{\partial t} = 0$:

$$f_s(\vec{r}) = \frac{1}{\sqrt{A}} e^{i\vec{k}_{2D}\vec{r}} \chi_s(z) \tag{6}$$

where $\vec{k}_{2D}$ and $\vec{r}$ are the two-dimensional (2D) wave vector and the position vector respectively; A is the sample area and χ_s is the envelope function component along z. This follows to a substitution to obtain the ISB dipole matrix element:

$$\left\langle f_{s\vec{k}_{2D}} \middle| \boldsymbol{e} \cdot \boldsymbol{p} \middle| f_{s'\vec{k'}_{2D}} \right\rangle = \frac{1}{A} \int d^3r \, e^{-i\vec{k}_{2D}\vec{r}} \chi_s^*(z) \left[\boldsymbol{e_x p_x} + \boldsymbol{e_y p_y} + \boldsymbol{e_z p_z} \right] e^{i\vec{k'}_{2D}\vec{r}} \chi_{s'}(z) \tag{7}$$

upon substitution into Equation 3, taking into account that $\vec{p}_{s\,s'} = im \times \omega \vec{r}_{s\,s'}$ we can rewrite the transition rate as follows:

$$W_{if} = \delta\left(\vec{k}_{2D} - \vec{k'}_{2D}\right) \frac{\pi q^2 F_o^2}{2\hbar} |e_z|^2 |\langle \chi_s^*(z) \, |z| \, \chi_{s'}(z) \rangle|^2 \, \delta\left(E_f - E_i - \hbar\omega\right) \tag{8}$$

From equation 7; terms containing $\boldsymbol{e_x}$ or $\boldsymbol{e_y}$ vanish unless *s=s'* and $\vec{k}_{2D} = \vec{k'}_{2D}$ (identical states). Equation 8 contains the first delta function to conserve these momentum requirements. Also, because of the presence of e_z, only electric fields in the z direction couple to discrete energy levels of the QW. This is the basis for the polarization selection rule which leads to the use of waveguides and surface gratings, and why only transverse magnetic (TM) polarized light interacts with the energy levels. Furthermore, transitions between states with the same wavefunction parity are not allowed – this is only the case for symmetric QWs.

Under the assumption that the lattice periodic function is the same in all constituent materials, a Schrödinger equation only for the envelope function can be derived with the goal to isolate the eigenenergies.

$$\frac{-\hbar}{2m^*} \nabla^2 \cdot f_s(\vec{r}) + V(\vec{r}) f_s(\vec{r}) = E_n f_s(\vec{r}) \tag{9}$$

Substituting the values for $f_s(\vec{r})$ from Equation 6, and solving the differential equation leads to the energy eigenvalues of the form

$$E_n(\vec{k}) = E_{n0} + \frac{\hbar^2 \, \vec{k}_{2D}^{\,2}}{2m^*} \tag{10}$$

where E_{n0} depends on the potential profile $V(z)$. For symmetric QWs with infinite barriers, the following eigenvalues are obtained:

$$\chi_n(z) = \sqrt{\frac{2}{L}}\sin\left(\frac{n\pi z}{L}\right) \quad and \quad E_n(\vec{k}_{2D}) = \frac{n^2\hbar^2\pi^2}{2m^*L^2} + \frac{\hbar^2\vec{k}_{2D}^{\,2}}{2m^*} \tag{11}$$

where L is the QW thickness. Due to the large effective mass of GaN ($m^*/m_0 \approx 0.2$) [90], versus GaAs($m^*/m_0 \approx 0.067$) [91], or InAs ($m^*/m_0 \approx 0.023$) [92], very thin QWs are required in the for large ISB energies

2.4. Many body effects

The transition between quantum-confined states relies on the fact that one of the states must be populated. In the case of absorption this requires the use of doping to occupy the ground state of the QWs [93] and this elicits many-body effects such as the depolarization shift, the exchange interaction, or the screening of the internal electric field.

The depolarization shift (also known as plasmon screening) and the exciton shift introduce a correction to the ISB energy that can be expressed by:

$$\breve{E}_{s's} = E_{s's}\sqrt{1+\alpha-\beta} \tag{12}$$

where α and β correspond to the depolarization and exciton shifts, respectively, and $E_{s's}$ to the ISB energy between states s' and s.

The ***depolarization shift*** is due to the external radiation interacting with the electron plasma, which leads to a modulation of the carrier density and an increase of the transition energy, which can be estimated as [13]

$$\alpha = \frac{2\sigma_s}{E_{s's}}\frac{-q^2}{2\pi\epsilon\epsilon_0}\int dz\left[\int_{-\infty}^{z} dz'\Psi_{s'}(z')\Psi_s(z')\right]^2 \tag{13}$$

where σ_s is the sheet carrier density, ϵ the dielectric constant, ϵ_0 the permitivity of vacuum. The second half of the expression represents the ISB coulomb integral for laterally homogeneous systems.

Additionally, the ***exciton shift*** arises from the interaction between the excited electron and the ground-state hole [94].

$$\beta = \frac{-2\sigma_s}{E_{s's}}\int dz\,\Psi_{s'}(z)^2\Psi_s(z)^2\frac{\partial}{\partial\sigma(z)}\left(\left(\frac{9\pi}{4}\right)^{\frac{1}{3}}\frac{-e^2m^*}{4\pi^2 r_s\epsilon^2\epsilon_0 a_B}\left[1+B\frac{r_s}{A}\ln\left(1+\frac{A}{r_s}\right)\right]\right) \tag{14}$$

where A=21, B=0.7734 [13], [94], m* is the effective mass, $r_s = \left[\frac{4\pi}{3}\left(\frac{\epsilon a_B}{m}\right)^3 \sigma(z)\right]^{-\frac{1}{3}}$, $\sigma(z)$ is the 3D electron density such that $\int \sigma(z) = \sigma_s$ and a_B is the Bohr radius.

The ***exchange interaction*** accounts for the electron repulsion between electrons with parallel spin as a result of the Pauli principle. This acts to lower the energy of the highly-populated ground state and red shifts the interband, but blue-shifts the ISB. This effect is directly proportional to the dopant concentration in the level, and via a Taylor series expansion can be represented as [95], [96]:

$$E_{exch}(k) = -\frac{e^2 k_f}{4\pi\epsilon\epsilon_0}\left[\frac{2}{\pi}\boldsymbol{E}\left(\frac{k}{k_f}\right) - 0.32\left(\frac{k_f}{k_L}\right)\right] \tag{15}$$

where k_L is equivalent to $\frac{\pi}{L}$, L is the QW's thickness, **E** is the elliptic integral, and $k_f = \sqrt{2\pi\sigma_s}$.

The ***direct Coulomb interaction*** is as a direct result of Coulomb-Coulomb interactions and tends to screen the internal electric field. It is given as follows [95], [97]:

$$E_{dir} = \frac{3\sigma q^2}{8\epsilon\epsilon_0 k_L^2} \tag{16}$$

Taking into account the summation of the above-described many-body effects, the ISB transition energy can be estimated as:

$$E_{s's_{eff}} = E_{s's}\left(\sqrt{1+\alpha-\beta}\right) - E_{exch} - E_{dir} \tag{17}$$

2.5. State of the art for intersubband in nitrides

III-nitride semiconductors (GaN, AlN, InN and their alloys), with their wide band gap and a large conduction band offset (~ 1.8 eV for GaN/AlN [98]–[100]), have been attracting much interest for ISB devices operating from the NIR to FIR spectral range. GaN is transparent in a large spectral region, notably for wavelengths longer than 360 nm (band gap), except for the Reststrahlen band (from 9.6 µm to 19 µm). Absorption in the range of 7.3 µm to 9 µm has been observed in bulk GaN substrates with carrier concentrations <10^{16} cm^{-3} [101]–[103], and was attributed to the second harmonic of the Reststrahlen band. Although this absorption might hinder the fabrication of waveguided devices in this spectral region, its effect in planar devices with µm-sized active regions is negligible, since the absorption coefficient related to two-phonon processes is much smaller than the one associated with ISB transitions [104], [105]. Conversely, III-nitrides do not present problems of inter-valley scattering, since the L and X points are much higher in energy (>2 eV) than the Γ point.

Various review articles have been written following the evolution of the GaN-based ISB technology [16], [17], [106], [107, p. -], [108]–[110]. The first observation of ISB absorption in GaN/AlGaN QWs was published at wavelengths above 2.8 µm [88] in 1999. The wavelength was then

tuned down to 1.75 µm [111] and finally ISB was seen around the telecommunication wavelength of 1.55 µm [112] in 2000. Since them, ISB transitions have been observed at room temperature in nitride-based QWs and QDs by a number of groups (University of Paris-Sud, Bell Labs, Nothwestern Univ., Univ. of Boston, Cornell Univ., Univ. of Tokyo, Sophia Univ., Toshiba Corp., CHREA-CNRS, EPFL, Chalmers Univ. of Technology, Univ. of Magdeburg, and CEA-INAC).

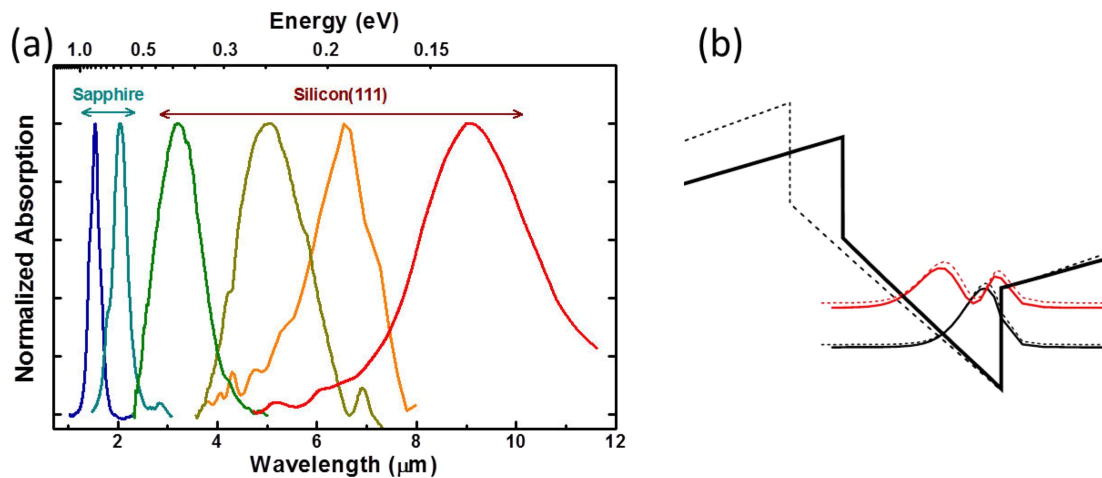

Figure 2 **(a)** Normalized absorption spectra for various samples showing that ISB transitions can span from the NIR to the MIR. The substrates used for these samples are also noted above the respective wavelength ranges. **(b)** An illustration of the QCSE where the well width of a GaN well is changed by 30%. With an increase in the well width by 30%, a decrease in the ISB energy of less than 3% is seen.

Besides the telecommunications range, there has also been interest to create devices towards longer wavelengths. Using GaN/AlN QWs, the e_2-e_1 ISB transition can be tuned in the 1.0 to 3.5 µm wavelength range by changing the QW thickness from 1 nm to 7 nm [100], [113]–[120]. By using AlGaN instead of AlN in the barriers, the wavelength range can be extended further into the MIR up to 10 µm [93], [121]–[126] as seen in Figure 2 (a). However, for larger QWs (>5 nm), the first two confined electron levels get trapped in the triangular section of the QW, which results in a saturation of the e_2-e_1 value by the QCSE, as seen in Figure 2 (b).

To further reduce the ISB transition energy, Machhadani et al. [127] proposed an alternative strategy to approach a flat potential in the QW layers by engineering the internal electric field. The investigated structures contain a stack of step-QWs, each period consisting of a GaN well, an $Al_{0.05}Ga_{0.95}N$ step barrier and an $Al_{0.1}Ga_{0.9}N$ barrier. Transmission measurements performed at 4 K reveal TM-polarized ISB absorption at 70 and 150 µm.

The first prototypes of nitride-based ISB devices were room-temperature multi-Tbit/s all-optical switches operating at 1.5 µm [128]. Meanwhile, the first demonstrations of III-nitride photovoltaic and photoconductive QWIPs and QD IR photodetectors were demonstrated in 2003 [129], [130] and 2006 [131]–[133] respectively for NIR frequencies, and in 2010 in the FIR [134]. Ultrafast all-optical switches have also been demonstrated [128], [135]–[138]. The first evidence of strong electron coupling in GaN/AlN double QWs [139] led to the demonstration of the first charge-transfer GaN-based ISB electro-optical modulators [140]. Finally, NIR ISB luminescence from GaN/AlN QWs [141]–[143] and QDs [144] was detected. The concept of quantum cascading in III-nitrides has also been

demonstrated through the development of QD-based quantum cascade photodetectors (QCD)s operating in the 1.5-2.0 μm spectral range [145], [146], which opens prospects for QCLs.

3. Experimental methods

3.1. Material Growth and strain relaxation

The growth of III-nitrides has occurred in a variety of instruments, each with their own particular benefits and drawbacks. Table 2 lists the typical machines used to grow GaN and AlN, including metalorganic vapor phase epitaxy (MOVPE) / chemical vapor deposition (MOCVD), hydride vapor phase epitaxy (HVPE)[30], MBE and reactive sputtering.

MOVPE/ MOCVD	– Precursors: Mixtures of trimethylindium, -gallium, or –aluminium ($(CH_3)_3M$), and NH_3 [147] – Growth temperature: 1000-1100°C [148]–[150] – Results: High growth rate (1-3 µm/h) and excellent material quality and control over layer thickness and doping.
HVPE	– Precursors: GaCl, NH_3 [151] – Growth temperature: 1000-1050°C [148], [152]–[154] – Results: Very high growth rate (up to 100 µm/h). Possibility to synthesize mm-thick GaN crystal boules to slice free-standing wafers [155].
MBE	– Precursors: High purity metals and N_2 or NH_3 – Growth temperature: 700-800 [156] – Results: very low growth rate, excellent control over layer composition. Can start and stop the growth of layers with atomic precision as well as the flux of a specific atom giving layer-by –layer control over the alloy concentration and thickness. Furthermore, in-situ reflection high-energy electron diffraction (RHEED) characterization greatly helps to characterize the growth. Gas-MBE also exists, which uses ammonia or hydrazine for the N-precursor.
Sputtering	– Precursors: High purity metals or III-nitride blanks and N_2 – Growth temperature: 300-750°C – Results: lower crystal quality but deposition is possible in any substrate and in large surfaces. [157]

Table 2 List of methodologies used to grow GaN and AlN.

The samples studied in this thesis are grown strictly using PAMBE. Substrates for *m*-plane and *a*-plane exploration consisted of free-standing GaN sliced along nonpolar surfaces from (0001)-oriented GaN boules synthesized by HVPE by Nanowin (Suzhou Nanowin Science and Technology Co., Ltd). The semipolar substrates consisted of 2-µm-thick (11-22)-oriented GaN layers deposited on m-sapphire by MOVPE by Dr. Ph. de Mierry and Dr. G. Nataf at CRHEA-CNRS [75]. In the case of *c*-plane GaN/Al(Ga)N heterostructures, growth was performed on 1-µm-think AlN-on-sapphire templates (for NIR structures) or on 4-µm-thick GaN-on-Si(111) templates (for MIR structures), both deposited by MOVPE by Dowa Electronics Materials Co., Ltd. For the fabrication of devices operating in the NIR (1.3-3 µm), the use of AlN-on-sapphire templates is preferred to maintain the structure under compressive strain and thus prevent crack propagation. For devices operating beyond 3 µm, GaN-on-Si(111) substrates are preferred to guarantee IR transparency of the substrate [125].

The RHEED was the main in-situ measurement tool used to calibrate and ensure epitaxial quality of all the samples grown in this thesis. By analyzing the diffraction pattern, the surface roughness, in-plane lattice constants, and the surface morphology could be established. Measuring RHEED intensity oscillations, the growth rate can be deciphered. Furthermore, by timing the desorption time of the Ga excess on the GaN(0001) surface, the substrate temperature could be estimated.

This thesis focuses on GaN, AlN and the ternary alloy AlGaN. It is also possible to grow InGaN and InN heterostructures, which would be theoretically preferred to develop an ISB technology due to the much lower electron effective mass of InN. However, In-containing technologies are penalized by the large lattice mismatch between GaN and InN, severe alloy inhomogeneities and interdiffusion/segregation at the InGaN/GaN interfaces [158], [159]. Therefore, the GaN/Al(Ga)N system is a more feasible solution for ISB devices.

The growth of (0001)-oriented GaN, AlN and AlGaN by PAMBE is extensively discussed in the literature [160]–[166]. For the growth of GaN using PAMBE, the Ga/N ratio is a critical parameter that directly influences the surface morphology. Too low of ratio result in a rough, facetted surface morphology [162], too high and Ga accumulates on the surface. Thin films of GaN in this thesis are always grown under slightly Ga-rich conditions, where the Ga flux was set to a value slightly below the limit of accumulation. In this mode two monolayers (ML) of Ga form on the surface of the sample in a dynamic equilibrium [160], [161], [168]–[170], and is stable for growth temperatures above 700°C [167]. These growth conditions have been theoretically explained through the creation of an efficient diffusion channel underneath a thin metal layer on top of the growing surface [161], [168], and have been proven to improve the surface morphology and decrease the defect density [167], [171]. The substrate temperature was around 720°C as deduced from the Ga desorption time[160], and the growth rate was determined by the flux of nitrogen and was in the range of 0.3 to 0.5 ML/s.

In the case of AlN, the deposition of layers with atomically flat surface morphology also requires metal-rich conditions [165]. However, Al does not desorb from the surface at the standard growth temperature for GaN. Therefore, to eliminate the Al excess at the surface, it is necessary to perform periodic growth interruptions under nitrogen. Due to the preferential incorporation of Al into the crystal over Ga [125], [163], [172], alloys of AlGaN can be created without having to remove the Ga-bilayer. By opening the Al shutter, a flux of Al is incorporated into the GaN growth that displaces the Ga atoms. For example, when growing $Al_{0.05}Ga_{0.95}N$, a flux of Al at 5% of the flux of N is used.

The PAMBE growth of NWs was initially demonstrated on sapphire [173], [174], then on Si[175].The NWs from this thesis were grown by PAMBE on Si(111) substrates at a temperature around 790°C [176]–[180] using a Ga/N ratio of 0.25 [181]. They are grown catalyst-free in the <000-1> direction (N-polar) [182]. These NWs are hexagonal prims with *m*-plane facets [183], [184]. NW growth proceeds from two angles, either by direct material deposition, or through the diffusion of atoms along the wire sidewalls to the apex [180], [185]–[187]. The marker technique showed that growth occurs under different circumstances than with 2D layers due to the negligible diffusion of N atoms [171], the Ga diffusion from the sidewalls and 3D nature of the growth [188], [189] which

contribute to the faster axial growth rate over 2D layers. For growing heterostructures using AlN, the diffusion of Al was found to be insignificant [186], [188], and this contributed to the natural formation of an AlN shell. GaN/AlN heterostructures have been demonstrated axially [174], [190]–[193], and radially [186], [188], but growing radial heterostructures has the drawback of a shadowing effect [194], [195] that is difficult to overcome [196].

Nonpolar Growth began in 2000, with the growth of *m*-plane (10-10) GaN on γ-$LiAlO_2$ [52]. Since then, the growth of nonpolar GaN has been well studied. *a*-plane GaN has been grown on *r*-plane sapphire [53], [197]–[201], and *a*-plane SiC [202], whereas *m*-plane GaN has been grown on *m*-plane SiC [203]. However, in 2006 efforts to grow these materials refocused towards substrates cut from HVPE-grown boules [204], [205]. This thesis focuses on these free-standing *m*- and *a*-plane GaN substrates. For on-axis *m*-plane substrates, the problem of hillocks plagued the growth [206], and was drastically reduced by incorporating a miscut in the *c* direction above 0.45° [207], above 0.7°[208], or 1°[209]. Due to the anisotropy in nonpolar crystal orientations, there is a higher risk of generating basal plane stacking faults [59], [198], [210].

Semipolar GaN can be grown in numerous crystal orientations, such as (10-11), (10-1-3) (11-22) on substrates such as (100) and (110) spinel [211] or on *m*-plane sapphire [66], [211]. In the case of (11-22)-oriented GaN grown by PAMBE, a Ga coverage independent of exposure time is only observed for a Ga coverage below 1 ML [212]–[214], and smooth GaN is theoretically predicted to grow in N-rich conditions [214]. However, optimized surface morphology is seen when there is a Ga-excess of 1 ML [215]. By growing directly on *m*-plane sapphire, the structures should be grown under Ga-rich conditions for streaky RHEED patterns, as III/V ratios smaller than unity lead to 3D growth [215]. This direct growth also results in metal-polar [210] samples containing two crystalline orientations [215]–[217]. However, by growing on an AlN buffer, a reduction in the secondary crystalline orientation is seen [215]. The growth of AlN on *m*-sapphire is either (11-22) or (10-10) depending on the III/V ratio [66] where, higher III/V ratios lead to larger inclusion of (10-10) crystals [66]. Rougher surfaces are seen when the III/V ratio strays from unity, and (10-12) AlN is optimally grown at a III/V ratio of about 0.85 [66]. In this thesis, the GaN was grown in the (11-22) direction on top of 2-μm-thick (11-22)-oriented GaN layers deposited on *m*-sapphire by MOVPE [75]. The growth rate of the PAMBE setup was set to 0.3 ML/s at a growth temperature of 715°C [215].

3.2. Simulation parameters

The simulations of the strain state, band diagram and electronic levels were performed using nextnano^3 [15], taking the spontaneous and piezoelectric polarization into account. For thin films, the 8x8kp Schrödinger-Poisson solver was used self-consistently. The k·p theory model overcomes the assumption of parabolic band structures that are usually considered for convenience at the bottom of the conduction band and the top of the valence band. By incorporating this non-parabolicity, differences in ISB energy of up to 25% can be seen [218].

As GaN/AlN is a lattice mismatched system with an in-plane lattice mismatch of 2.5%, the effect of strain and lattice relaxation plays a defining role in both the device functionality as well as the band structure. Additionally, GaN/AlGaN heterostructures are very sensitive to the piezoelectric

fields, which make the calculation of the strain state of GaN/Al(Ga)N heterostructures crucial for understanding the electric fields and therefore the band profiles. The effect of the strain state has two main effects on the band diagram: Firstly it changes the band gaps of the materials, and secondly it changes the piezoelectric polarization within the materials. This induces changes in both the interband and ISB energies.

Parameters		**GaN**	**AlN**
Lattice constants, nm [109, p. 200]	a	0.31892	0.3112
	c	0.51850	0.4982
Spontaneous polarization, Cm^{-2} [41]		-0.029	-0.081
Piezoelectric constants, Cm^{-2} [41]	e_{13}	-0.49	-0.60
	e_{33}	0.73	1.46
Elastic constants, GPa [45], [47]	C_{11}	390	396
	C_{12}	145	140
	C_{13}	106	108
	C_{33}	398	373
Dielectric constant[219]		10	8.5
Luttinger parameters[220]	A_1	-5.947	-3.991
	A_2	-0.528	-0.311
	A_3	5.414	3.671
	A_4	-2.512	-1.147
	A_5	-2.510	-1.329
	A_6	-3.202	-1.952
	A_7	0	0
	$E_P^{//}$ [eV]	14	17.3
	$E_P^{\perp}$ [eV]	14	16.3
Deformation potentials, eV [219]	a_{c1}	-4.6	-4.5
	a_{c2}	-4.6	-4.5
	D_1	-1.70	-2.89
	D_2	6.30	4.89
	D_3	8.00	7.78
	D_4	-4.00	-3.89
	D_5	-4.00	-3.34
	D_6	-5.66	-3.94
Band offset, eV [218]		1.8	

Table 3 The material parameters used in the theoretical calculations in nextnano[3]. The sources for each parameter are shown beside the parameter name.

In the case of 3D calculations, the effective mass approximation was used so that the simulations would converge at useful spatial resolutions. Simulations were done step-wise: The 3D strain distribution was first calculated by minimizing the elastic energy and applying zero-stress boundary

conditions at the surface. With this input, the nonlinear Poisson equation was classically solved to obtain the 3D band structure of the complete wire. After the Poisson equation was solved in equilibrium, the eigenfunctions were calculated by solving the Schrödinger equation in a quantum region that covered one ND in the center of the NW, including the AlN barriers on the top and bottom. nextnano^3 does not completely incorporate many-body effects, and for calculations at high dopant levels, only the screening of the internal electric field is taken into account.

3.3. Structural characterization

The structural characterisation of the samples was done employing various methods to show the macro- and microscopic properties of the materials:

- The periodicity of the samples was analyzed by XRD under the supervision of Dr. Edith Bellet-Amalric, using a Seifert XRD 3003 PTS-HR system. Typical samples had θ-2θ scans of the (0002) reflections done to determine the SL periods. The experimental measurements were then juxtaposed to simulated curves obtained from X'Pert Epitaxy software from Panalytical and a SL misfit strain relaxation could be calculated. Additional information of the strain state was extracted via reciprocal space maps.
- The surface roughness of the layers was measured by AFM in the tapping mode with a Veeco Dimension 3100 microscope. Data visualization and processing were carried out using the WSxM software [221].
- For planar structures, TEM studies were realized by Dr. Catherine Bougerol using the microscopy facilities of CEA/INAC. For NW heterostructures, TEM images were provided by the group of Prof. Jordi Arbiol in the Institut Català de Nanociència i Nanotecnologia, in Barcelona (Spain).

3.4. Optical characterization

Optical characterization of the samples was mostly used to identify ISB transitions via FTIR spectroscopy, and band-to-band transitions via PL techniques.

FTIR was used to probe the ISB absorption using a variety of lamps and photodetectors incorporated into a Bruker V70v spectrometer. The source, beam-splitter and detector for each spectral range (NIR, MIR and FIR) are summarized in Table 4.

	NIR	MIR	FIR
Source	Tungsten	Globar	Hg-Arc
Beam-splitter	CaF_2	KBr	Si
Detector	MCT	MCT	Bolometer
Temperature of sample	Room (300 K)	Room (300 K)	Liquid He (5 K)
Temperature of detector	Liquid Nitrogen (77 K)	Liquid Nitrogen (77 K)	Liquid He (5 K)

Table 4 Source, beam-splitter and detector used to measure ISB absorption in the NIR, MIR and FIR. The temperatures of the samples and detectors are also noted.

For their characterization, all samples grown on silicon-based templates were polished into multi-pass waveguides with 30° facets. The angle was chosen so that the light impinging the waveguide perpendicular to the facet had numerous interactions with the GaN, even in the case of a small deviation of the incidence angle. Figure 3 (a) shows the schematic of the waveguide where and the light is incident on the GaN from the Si. Focusing at the Si/GaN interface, light incidence angles below 49° (red) result in total reflection at this interface, i.e., the light does not transmit into the GaN layer. Incidence angles between 49° and 73° (green) lead to transmission into the GaN and total reflection at the GaN/air interface. Finally, incidence angles larger than 73° (orange) lead to transmission through the GaN into the air. Therefore, nominal incidence at 60° is chosen (i.e. normal incidence to a 30° facet). If we consider now the deflection of the light at the Si/air interface, the analysis is depicted in Figure 3 (b). For incidence angles below 18°, there is total reflection at the GaN/Si interface, whereas for incidence angles larger than 18°, light transmits into GaN and there is total reflection at the GaN/air interface. Transmission to air does not happen at any angle. Therefore, our choice of 30° facet allows light incidence in a large range of angles (18° to 180° as described in Figure 3 (b)). These calculations were made according to Snell's law assuming the refractive index of air to be 1, Si to be 3.48, and GaN to be 2.316 (1.55 µm). Following a similar reasoning, samples grown on sapphire-based templates or bulk GaN were polished at 45°.

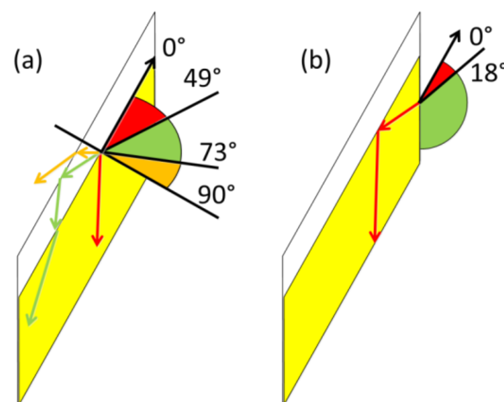

Figure 3 Schematic of the interaction of light with the multi-pass waveguide where the Si is depicted in yellow and the GaN-based active layer is depicted in white. **(a)** Reflection/transmission behavior at the silicon/GaN interface as a function of the angle of incidence. The orange region (90°>θ>73°) depicts the angles where light enters the GaN is transmitted to the air. The green region (73°>θ>49°) depicts the angles where there is total internal reflection at the GaN/air interface. The red region (49°>θ>0°) depicts angles where there is total reflection at the Si/GaN interface (no interaction with the active layer). **(b)** Schematic of the light transmission at the air/Si interface (30° facet). Angles <18° lead to total reflection at the GaN/Si interface.

The samples were tested in transmission mode using a polarizer to discern between the transverse-electric (TE) and TM polarized light. By taking the selection rules into account, the ISB absorption should appear as a dip in the TM transmission spectrum. In the case of FIR characterization, two sample pieces were placed back-to-back to double the amount of surface perpendicular to the incoming beam, and to increase the detected signal.

For samples exhibiting ISB activity in the FIR, a trade-off between the absorption intensity and the FTIR signal intensity is observed. At low angles of incidence (20°<θ<35°) there are fewer interactions

between the light and the active layers which leads to larger amounts of light reaching the bolometer. A larger absorption is seen at high angles of incidence, but it is associated with a poor signal-to-noise ratio. An easy approach to identify the ISB absorption was to monitor the TE/TM transmission ratio over several angles, as seen in Figure 4. When increasing from 32° to 65° an increase in the absorption is seen around 120 cm^{-1}.

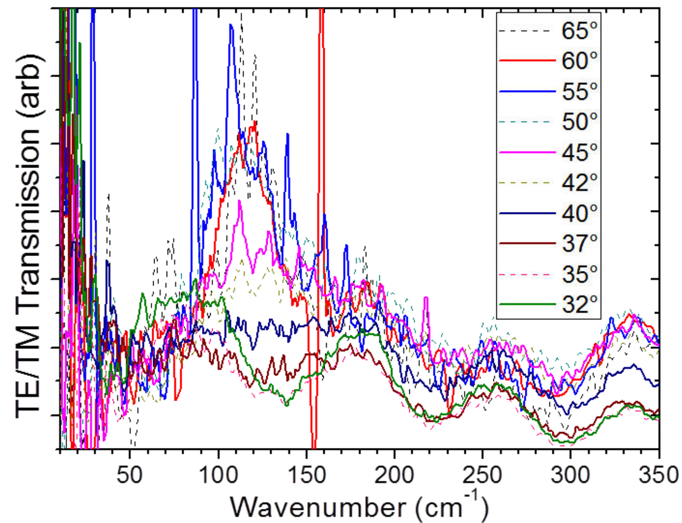

Figure 4 The division of TE light by TM light through a sample for various angles of incidence on the sample as a function of wavenumber. An interference pattern is seen in all the samples, and is most visible at angles below 37°. After this angle, there is increased interaction with the sample. Decreased TM transmission through the sample is seen at larger angles; which is attributed to the ISB absorption from e_1 to e_2. The noise level of the signal also increases with increasing angle of incidence.

- PL spectroscopy was used to probe the interband transition energy. A continuous-wave frequency-doubled Ar^+ laser (λ = 244 nm) was used as an excitation source. The emission was collected by a Jobin-Yvon monochromator and was detected by a UV-enhanced charge coupled device.
- Time-resolved PL was measured by exciting with a pulsed Ti-sapphire laser source (λ = 270 nm, pulse width = 200 fs). The time between pulses was 2 to 5 µs as decided by a cavity damper, and the excitation power was about 0.5-1 mW. The PL emission was acquired by a Jobin-Yvon Triax320 monochromator and a Hamamatsu C–5680 streak camera.

4. Results: *c*-plane THz intersubband devices

4.1. Introduction to THz intersubband

A compact, continuous-wave solid-state source to bridge the gap between the MIR lasers and the oscillating transistors for gigahertz electronics is greatly sought after for many applications, for instance in fields such as astronomy or analytical science. “Technological innovation is also allowing THz applications into fields such as information and communications technology; biology and medical sciences; non-destructive evaluation; homeland security; quality control of food and agricultural products; global environmental monitoring; and ultrafast computing among others” [222]. A significant breakthrough took place in 2001 with the first demonstration of a GaAs-based QCL operating at ~4.4 THz [223]. Since then, rapid progress has been made in terms of device performance. To date, THz QCLs have been demonstrated in the 0.85-12 THz range [224]–[227], with pulsed operation up to 199 K at 3.2 THz [228], [229] or 186K at 3.9 THz [230]. These lasers have shown output powers of 1W at 3.4 THz [231] and slightly higher by using MIR-to-THz conversion techniques [232]. Despite advances, devices keep on working at cryogenic temperatures because of the thermal degradation of the population inversion caused by thermal backfilling and thermally-activated phonon scattering. The low LO phonon energy in arsenide compounds (36 meV) constitutes a major bottleneck for operation room temperature operation. Furthermore, As-based technologies have a Reststrahlen band reaching from 30 to 40 µm [233], which hinders the production of THz radiation at these wavelengths. GaN-based technologies, with an LO phonon at 90 meV, have become a promising alternative to create room temperature sources for THz radiation, and cover the forbidden band of GaAs.

4.2. Intersubband absorption in GaN-based quantum wells (Annex 3, 4 and 5)

4.2.1. The step-quantum-well design

Research on III-nitrides in the THz spectral region has proceeded over the last five years with the introduction of the first structure to show FIR-ISB absorption in a controlled manner [134]. This first design used a “step-quantum-well” setup to reduce the internal electric field in the QW, and to approach the quantized states to THz levels. Figure 5(a) shows the conduction band diagram of a step-QW design consisting of $Al_{0.1}Ga_{0.9}N$/GaN/ $Al_{0.05}Ga_{0.95}N$ (3 nm / 3 nm / 13 nm), and indicates the first and second electronic levels with their respective squared wavefunctions (Ψ^2). This 3-layer structure is designed around the principle of polarization equivalency. The design can be separated effectively into two portions; the first is the “barrier”, which comprises of the high-Al-content $Al_xGa_{1-x}N$ layer and the GaN layer. The second portion is the “well”, which is the low-Al-content $Al_xGa_{1-x}N$ layer. The design creates a semi-flat band in the “well” by having the “barrier” balanced at the same average Al percentage, i.e. the average polarization in the “barrier” is approximately equal to the average polarization in the “well”. This allows the structure to have variations in conduction band edge, and therefore electron confinement, but it ensures a negligible internal electric field in the “well”. However, the asymmetry of the design leads to the confinement of $\Psi^2(e_1)$ close to the GaN layer, while the bimodality of $\Psi^2(e_2)$ has the largest electron density within the middle of the “well”

lowering the overall oscillator strength. Devices that focused on this principle were fabricated at Boston University, and showed similar ISB absorption and photodetection [234].

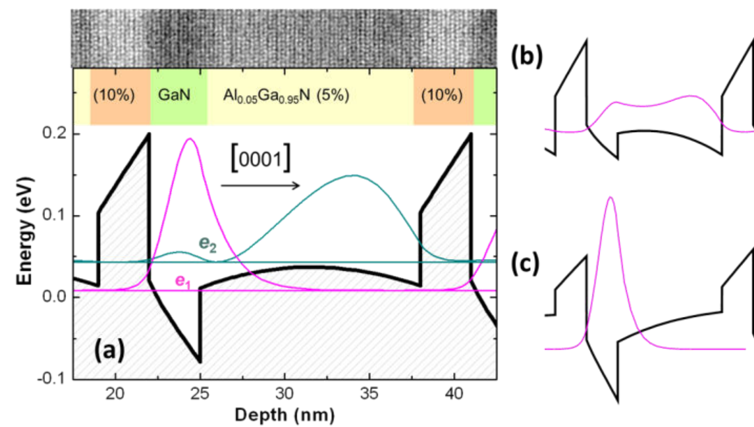

Figure 5 **(a)** Conduction band profile, and first (e1) and second (e2) electronic levels with their associated squared wavefunctions for an $Al_{0.1}Ga_{0.9}N/GaN/Al_{0.05}Ga_{0.95}N/GaN$ (3 nm / 3 nm / 13 nm) step QW. On top, high-angle annular dark field (HAADF)-scanning tunneling electron microscope (STEM) image of one period of the grown structure. **(b)** Shift of the wavefunction of the first electronic level [Ψ^2(e1)] associated with a decrease of the Al concentration in the "well" layer. A lower "well" Al concentration creates a secondary confinement area at the opposite side of the well. **(c)** A higher "well" Al concentration creates a more triangular well and increases confinement towards the GaN layer. (From Annex 3)

In this thesis, the original design from Machhadani et al. [134] was structurally reproduced. Samples with very similar structures, showed ISB absorption that was not at the same energy as reported (Annex 3). Therefore, the robustness of the step-QW system was explored as by defining the experimental conditions that could lead to changes in the ISB wavelength. The primary reason for the variation of the ISB wavelength was deemed to be the uncertainties associated with the growth method, either in terms of layer thickness or in terms of alloy compositions. For instance, changing the aluminum concentration within the layers breaks the polarization balance, and causes a shift in the location of the electron density function, and in the ISB transitional energy. A decrease in the Al content of the "well" results in the formation of a secondary point of low conduction band energy at the interface between the high-Al-content barrier layer and the "well", as illustrated in Figure 5(b). This low point competes for Ψ^2 and turns e_1 into a bimodal distribution. Conversely, with an increase in the "well" Al content, the electric field in the "well" pushes Ψ^2 towards the GaN layer and increases the confinement, as shown in Figure 5(c).

In order to explore the effect of variation in the growth, TEM images and XRD spectra were analyzed to see the extent of variation within a range of samples. By analyzing several series of samples through XRD characterization, the variation of the SL period was lower than 10%. The errors in the Al concentration are mostly associated with errors in the growth rate calibration, and, to a minor degree, errors in the measurement of the Al flux. We estimate these accumulated errors to be less than 10%, and this was taken as the normal variation for measuring the robustness of the system.

4.2.2. The 4-layer quantum well design

In this thesis, to surmount the limitations of the step-QW geometry, a robust alternative to this design is presented, which includes the insertion of an additional AlGaN layer to separate the GaN layer from the “well” (Annex 3 and 4). This “separation layer” is designed so that there is no confined state in the GaN layer. In this architecture, the polarization is not fully compensated, which results in a triangular profile in the active well, but greatly increases the robustness of the system and the oscillator strength of the first ISB transition. The design, consisting on a 4-layer sequence, can be seen in Figure 6(a).

Figure 6(b) shows the theoretical value of the ISB wavelength as the five vertices of a regular pentagon. Each vertex has a structural parameter associated with it that was varied considering realistic deviations in the epitaxial growth: ±2 ML (~ 0.5 nm) as the error bar for thicknesses and ±10% as the error bar for the aluminum content in $Al_xGa_{1-x}N$. The colored area represents the minimum and maximum values of the ISB transition wavelength associated with the indicated variation of structural parameters. The smaller area associated with the 4-layer QW in the Figure demonstrates that this design is much more robust than the step-QW structure. The ISB dependence on the thickness and composition of the “separation layer” was also analyzed, and was shown to exhibit the same robustness as the rest of the system (Annex 3 and 4).

This modified geometry was synthesized with various doping concentrations in the GaN layer. It showed TM-polarized ISB absorption at 14 THz whose intensity and linewidth increased with doping (Annex 3 and 4). Consistently, ISB absorption was not observed in an undoped reference.

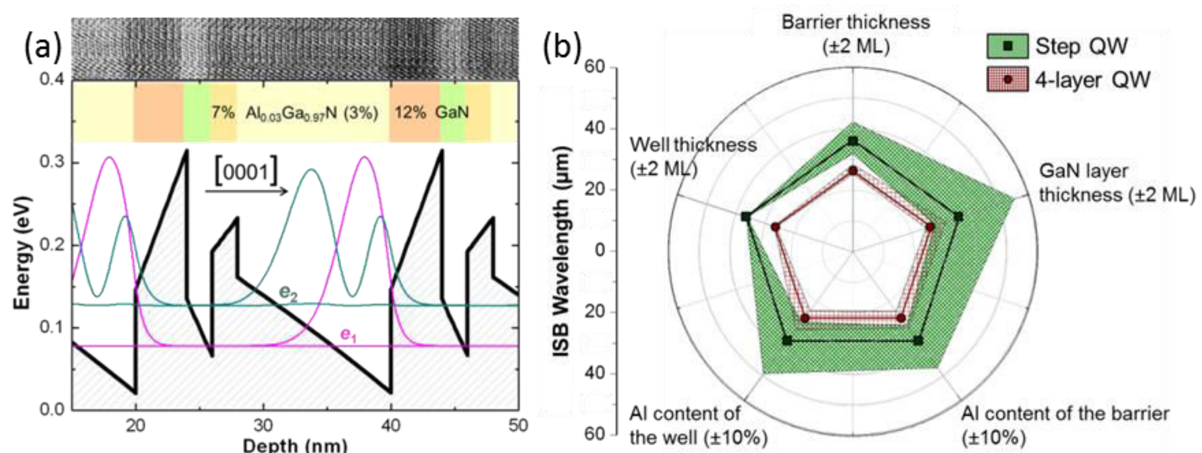

Figure 6 **(a)** Conduction band profile for an Al0.1Ga0.9N/GaN/ Al0.07Ga0.93N/Al0.03Ga0.97N (4 nm / 2 nm / 2 nm / 12 nm) 4-layer-QW design. On top, HAADF-STEM image of one period of the grown structure. **(b)** Illustration of the robustness of the 4-layer-QW system compared with the step-QW design. In each case, the dots indicate the nominal ISB transitional wavelength. The colored area represents the variation between the minimum and maximum values of the ISB transition wavelength associated with the variation of the indicated structural parameters on each vertex. The “barrier” refers to the Al0.1Ga0.9N layer, while the “well” is the Al0.03Ga0.97N (Al0.05Ga0.95N) for the 4-layer (step-QW design).

4.2.3. The 4-layer pseudo-square quantum well design

The information gained from the above-described studies (Annex 3 and 4) confirmed the ability of the simulations to accurately predict the band structure and ISB spacing for complex *c*-plane MQW architectures. However, the 4-layer design sacrifices tunability, and does not completely compensate the internal electric field. Furthermore, the width of the complex barrier inhibits electron tunneling transport, which complicates the incorporation of such QWs in an electrically driven device structure. By thinning the barriers to 1 nm as well as the GaN well, this architecture could potentially be used for photodetectors. However, due to the confinement of the first level (e_1) to a triangular well that is defined almost entirely by the internal electric field, the device would not be able extract/inject electrons from/to the lowest electronic state by resonant tunneling transport, as required in quantum cascade structures. For these reasons, an alternative design is desired which acts as a compromise between the extreme robustness of the 4-layer MQW and the tunability of the 3-layered step-QW design.

The pseudo-square design presented in Figure 7 demonstrates a trade-off between robustness and the ability to incorporate into device architectures. The proposed geometry achieves THz ISB absorption by compensating the polarization-induced internal electric fields, and uses potential barriers that are thin enough to facilitate tunneling at low bias. The proposed band structure in Figure 7(a) consists of four AlGaN layers with nominal Al concentrations of 12, 0, 5 and 7%. The highest Al concentration (the concentration of the barrier) is chosen as the sum of the other two, so that the structure can be realized by PAMBE using two Al effusion cells. In this pseudo-square QW, the electric field is compensated by creating a gradual increase in polarization field throughout the quantum "trough" formed by the 3 low-Al-content layers. Because of this gradual increase, the electron density function is delocalized from a single layer, and is quantum-confined across all three layers by the thickness of the trough, and not by the polarization field. Simulations show that the oscillator strength of the pseudo-square QW is the same as the 4-layered MQW system, and an order of magnitude greater than that of the step-QW configuration. The ISB energy of the design in Figure 7(a) is nominally targeted at 25 meV, and can be tuned by changing the width of the trough. At zero bias, the second electronic level, e_2, is localized in the QW, but the tunneling probability of electrons in e_2 increases by biasing in the <0001> direction.

The ISB transition deviations in the pseudo-square design are generally smaller than those induced within the step-QW, and larger than those of the 4-layer QW (see robustness analysis in Figure 7(b)). For a fair comparison of the structures, it is important to consider that they are engineered to operate at different wavelengths. Defining the relative errors as $\Delta\lambda/\lambda$, the average wavelength variation that can be induced by growth uncertainties is 10%, 8.8% and 25%, for pseudo-square QWs, 4-layer QWs and step-QWs, respectively.

Pseudo-square QWs fabricated by PAMBE present ISB absorption at 160 µm, which blue shifts to 50 µm with increasing doping level, and can be tuned from 100 to 75 µm by changing the width of the quantum trough (see Annex 5).

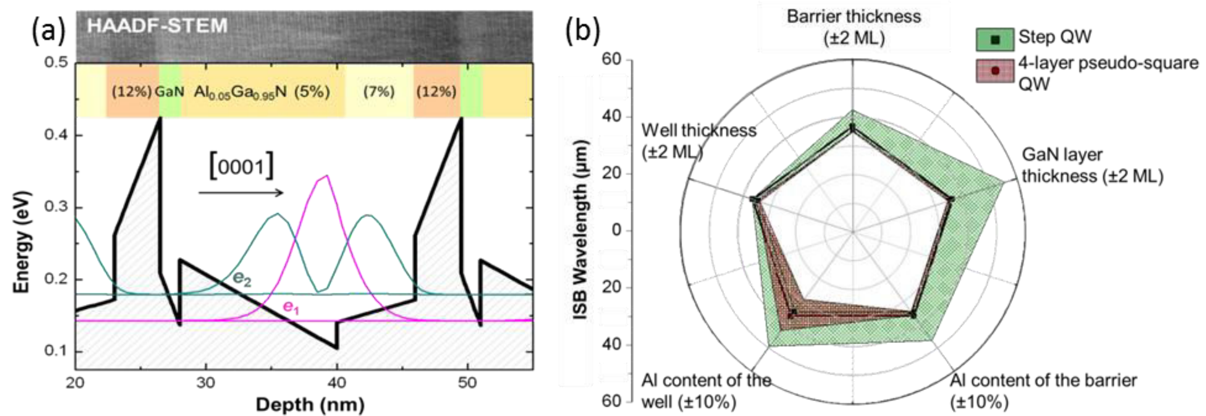

Figure 7 **(a)** Conduction band profile for an $Al_{0.12}Ga_{0.88}N$/GaN/ $Al_{0.05}Ga_{0.95}N$/$Al_{0.07}Ga_{0.93}N$ (3.5 nm / 3.5 nm / 12 nm / 6 nm) 4-layer pseudo-square QW design. On top, HAADF-STEM image of one period of the grown structure. **(b)** Illustration of the robustness of the 4-layer pseudo-square QW system compared with the step-QW design. In each case, the dots indicate the nominal ISB transitional wavelength. The colored area represents the variation between the minimum and maximum values of the ISB transition wavelength associated with the variation of the indicated structural parameters on each vertex. The "barrier" refers to the $Al_{0.12}Ga_{0.88}N$ layer, while the "well" is the $Al_{0.05}Ga_{0.95}N$ in each case.

4.3. Quantum cascade laser designs

QCLs are unipolar (electrons only) devices that operate on the principle of electron recycling. Electrons cascade through a series of levels to create a population inversion in an active QW, which leads to the emission of light at a designed wavelength. Figure 8 is a schematic of the types of GaAs-based QCL structures that have been proposed for the THz spectral region. These include (a) the chirped SL, and (b) the resonant phonon. The figures were taken from Williams et al. [235].

QCLs function on the principle that electrons are electrically injected into the system to level *2.* They then emit THz radiation and drop down to level *1*. Electrons then tunnel from level *1* to the proceeding level 2 via an extraction mechanism; this is the basic repeating unit of the QCL.

In a chirped SL configuration (Figure 8(a)), electrons are extracted from level *1* by tunnelling along a SL of QWs where the quantized electronic levels are finely spaced to form a pseudo-miniband of energies. Population inversion is obtained because electrons tend to relax to the lowest energetic level in a miniband. A variation on this is the bound-to-continuum design where that the upper state *2* is a "bound defect state within the gap" [236], [237]. These bound-to-continuum designs typically have lower oscillator strength, and better temperature and power performance than basic chirped SL designs.

Resonant-phonon designs (Figure 8 (b)) have high oscillator strengths, and rely on the LO phonon to create population inversion [238]–[240]. Electrons tunnel from the lower state *1* to a coupled extractor state, and emit an LO phonon to then occupy the upper lasing state. This type of design has large problems within the GaAs system where the LO phonon energy is 36 meV, and can depopulate the lower laser state, but also the upper laser state [241], [242]. These designs have smaller oscillator strengths than chirped SL designs, but compensate for that fact by having repeating units that are half the thickness (can have twice as many repeating units) [243].

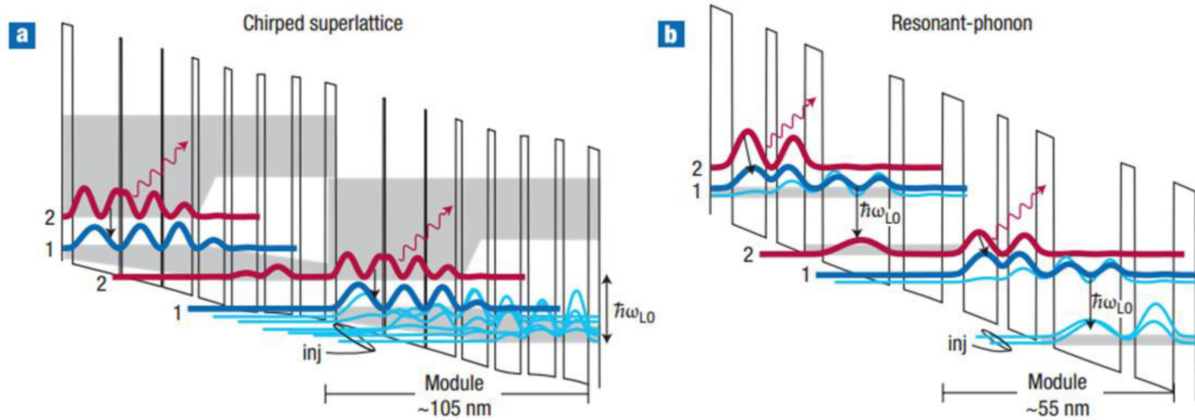

Figure 8 Schematic band diagrams of the **(a)** chirped SL and **(b)** resonant phonon designs for GaAs-based QCLs. In each case the wavefunctions are shown in red (noted 2), navy (noted 1) and light blue. Red wavefunctions denote the location of the population inversion; navy wavefunctions denote the lower laser state, and are designed to be several meV (5-100 meV) from the upper laser state. The light blue wavefunctions are for the depopulation/extraction from the lower laser state and repopulation of the proceeding upper laser state.

GaN-based QCLs have been theorized to work up to room temperature by a variety of researchers from the University of Leeds [244], [245], Boston University [1], [246], RIKEN (Japan) [247]–[249], the University of Tabriz [250], [251], the University of Connecticut [252], [253], and the National Institute of Information and Communications Technology in Japan [254], [255]. All of these designs focus on the resonant-phonon architecture and predict functionality at high temperatures.

RIKEN in particular presented THz QCL designs based on four-well resonant-phonon GaN/AlGaN structures [256]–[258]. The structures have been synthesized by PAMBE using a “droplet elimination by thermal annealing” technique [259], and they have been processed in a single-metal plasmon waveguide geometry [256], [257], [260]. Electroluminescence at 1.37 THz has been reported in a first structure [257] grown both on a GaN-on-sapphire template and on bulk GaN. Polarization-dependent electroluminescence was also reported at 2.82 THz that was slightly tunable by changing the driving voltage in the 20-21 V range, using a second design grown on an AlN-on-sapphire template [260]. More recently, this group has reported electroluminescence at 6.97 THz in a double-QW structure. The signal was integrated over 10 minutes with a signal-to noise ratio near 5. The active region consisted of 200 repeats of 1.5nm $Al_{0.15}Ga_{0.85}N$/ 4nm GaN/ 1.5 nm $Al_{0.15}Ga_{0.85}N$/ 6 nm GaN grown on an AlN-on-sapphire template. This device has been subject to much criticism in the ISB community, due to the scarcity of characterization data, and the fact that no other lab has been able to repeat or verify the results.

4.4. Quantum cascade laser design constraints

The design constraints for QCL architectures are listed as restrictions in order to ensure laser functionality and evade pitfalls for inefficiencies. These restrictions focus on the effective extraction of the electrons to depopulate the lower laser state, a high injection rate for the repopulation of the upper laser state, and ensuring population inversion. In this thesis, using a resonant-phonon configuration; GaN-based QCL designs are proposed. These designs use a pseudo-square QW as the

lasing QW, and a step-QW to act as the extractor/injector. Figure 9 shows a schematic for the eigenenergies and wavefunctions of an ideal QCL.

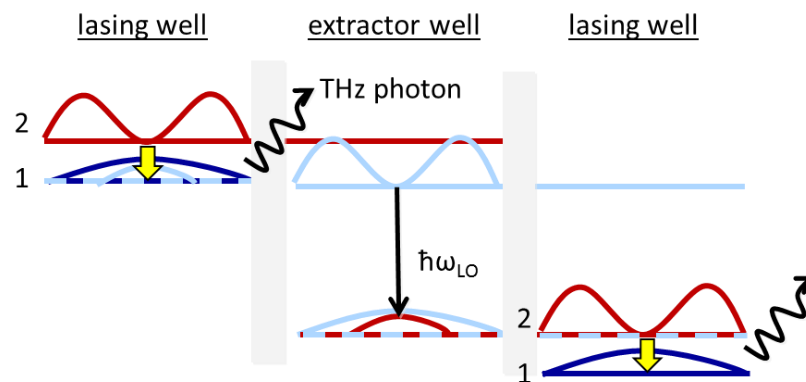

Figure 9 Schematic diagram for resonant phonon QCL design. Red wavefunctions depict the upper laser state, *2*, navy wavefunctions depict the lower laser state, *1*, and light blue wavefunctions depict the extraction mechanism. Yellow arrows indicate the ISB transitions and emission of THz radiation. The LO-phonon-assisted transition is indicated within the extractor from the upper state to the injecting state. The transition between the upper and lower laser states (*2*→*1*) emits a photon at THz frequencies. The flow of electrons goes from top left to bottom right.

The basic design restrictions for QCLs include:

i. *The ISB energy between the upper and lower lasing levels is at the desired THz frequency*
ii. *The lower lasing eigenenergy (1) is equivalent to the upper extractor level eigenenergy*
iii. *The upper extractor level has wavefunction in the lasing well at the eigenenergy of (1)*
iv. *The upper extractor eigenenergy is 1 × LO phonon energy above the injector state eigenenergy*
v. *The upper laser level (2) is at an eigenenergy equivalent to the injector state eigenenergy*
vi. *The lower laser state has wavefunction in the proceeding extractor well*

Figure 10 shows a GaN/AlGaN QCL design simulated by nextnano[3] which uses a resonant phonon design following the above design constraints. It is engineered using four AlGaN concentrations, (A, B, 0, and A+B) so that it can be fabricated using a PAMBE setup with two Al-effusion cells. The barriers are very thin (1 nm) and will easily facilitate tunnelling to the proceeding active trough. In this design, the extractor (step QW) acts only to align the lower lasing state to the higher energetic levels in the proceeding trough. Because of the thickness of the barriers and the alignment of the upper lasing level to a level within the proceeding trough, population inversion will not occur because there is not much incentive for the electrons to emit versus just tunnelling through the barriers into the continuum.

Therefore, in order to create a device that reaches high level of population inversion it is necessary to implement another two restrictions:

vii. *The upper lasing state does not have wavefunction in the proceeding well (extractor)*
viii. *The LO-phonon-assisted transition occurs in the extractor and not in the lasing well*

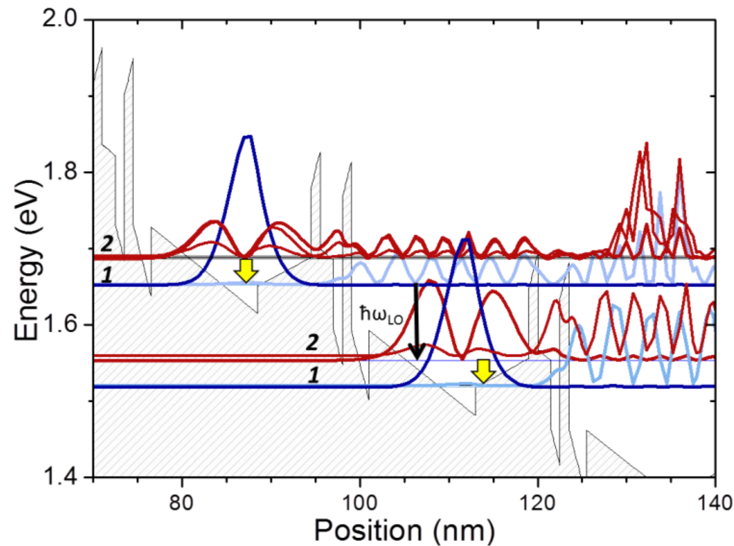

Figure 10 Simulated nexnano[3] architecture for a GaN-based resonant-phonon QCL. The colors and labels match those in Figure 9. The flow of electrons goes from top left to bottom right. The design for the repeating unit is as follows for material parameters and thickness: 1 nm $Al_{0.12}Ga_{0.088}N$ /2nm GaN /12nm $Al_{0.05}Ga_{0.095}N$ /6 nm $Al_{0.07}Ga_{0.093}N$ /1 nm $Al_{0.12}Ga_{0.088}N$ /1.5 nm $Al_{0.05}Ga_{0.095}N$ /1 nm GaN

Restriction *vii* means that the upper lasing state will have the majority of the wavefunction in the lasing well, but will have a portion upstream of the lasing QW. Conversely, the lower laser state will have a portion downstream of the lasing QW. The downstream potential-barrier will inherently be larger (or equal) for e_1 as it is for e_2. This can be overcome by properly aligning the upper lasing state so that it is energetically placed between two discretely quantized states of the extractor; preferably between the first and the second excited levels of the extractor (this is because of the decreasing spacing between higher quantized states). This will keep the electrons from tunneling to the extractor, and will ensure population inversion.

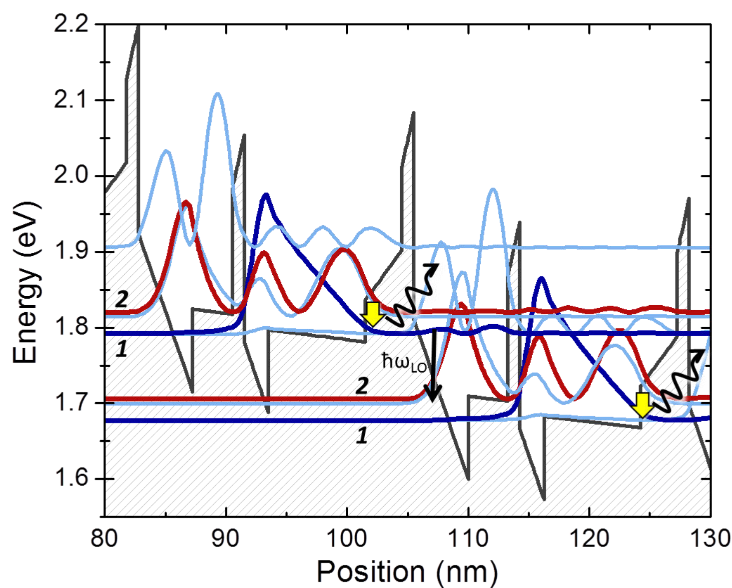

Figure 11 Simulated nextnano[3] GaN/AlGaN QCL design meeting the design restrictions mentioned above. The colors and labels match those in Figure 9. The flow of electrons goes from top left to bottom right. The design

for the repeating unit is as follows for material parameters and thickness: 1 nm $Al_{0.15}Ga_{0.085}N$ /2 nm GaN /8 nm $Al_{0.06}Ga_{0.094}N$ /3 nm $Al_{0.09}Ga_{0.091}N$ /1 nm $Al_{0.15}Ga_{0.085}N$ /4.5 nm GaN /3.25 nm $Al_{0.06}Ga_{0.094}N$

Extraction of the electron from the lower laser state should occur by coupling this level with the first excited level of the extractor, which should be separated from the ground extractor level (injector level) by 1×LO phonon energy. The injector level should be coupled with the upper lasing state of the proceeding laser QW.

Taking these rules into respect, a design is proposed in Figure 11 which constitutes a three level system over four quantized states, where the ISB energy between two of the states is 27.3 meV (11 THz) and the other is the LO phonon.

Due to the applied electric field of 12.75 MV, this design has significant wavefunction overlap from the injector state to the upper laser state. It also has the upper laser state aligned between the e_2 and e_3 of the extractor and as such; has very little wavefunction downstream. This should contribute to a strong population inversion. The part of this design which needs improvement is the wavefunction overlap from the lower laser state to the upper extractor state, but it should not impede the lasing properties of this device.

4.5. Conclusions

Various polar *c*-plane GaN/AlGaN MQWs with ISB transitions in the THz spectral region are proposed and experimentally demonstrated. By analysing the ISB energy’s robustness against fluctuations in the growth process and the architecture’s feasibility of resonant tunneling transport (incorporability into real devices), a “pseudo-square” MQW architecture was chosen as the best approach for the lasing well in QCL designs. This architecture consists of four layers of AlGaN with different Al compositions, and can exhibit ISB absorption from 6 to 2 THz in agreement with theoretical calculations. Using this “pseudo-square” structure, polar-GaN-based QCL structures were conceived, and the design restrictions for the creation of these structures are explained.

5. Results: Nanowires for intersubband devices

5.1. Introduction to nanowires

As optoelectronic devices push towards higher efficiencies, the control of carrier relaxation becomes a key aspect for device engineering, which is particularly relevant in the case of ISB optoelectronics such as QWIPs, QCDs, and QCLs. Longer intraband lifetimes have been proven to exist in laterally confined systems, including QDs [133], [261]–[263] and NWs [264], [265]. In the case of NWs, their large surface-to-volume ratio allows misfit strain to be elastically released, extending the viable active region size and composition beyond the limits of planar systems or QDs. For these reasons, NWs are under study to improve the performance of THz QCLs [266], [267], whose operating temperatures are currently limited by nonradiative scattering processes that quickly depopulate the upper laser level.

Semiconductor NWs have already become a powerful kind of nano-material with promising applications in electronics[268], optoelectronics [269], [270], energy conversion [271], [272], and sensorics [273], [274]. Research on NWs has also stemmed out towards the creating of single photon emitters [275], and THz emitters [276]. By using NWs in these instances, the emission of a single photon can be controlled [277]–[280]and high correlation can be observed. NWs have also been theorized to induce effects that show quantum entanglement [281] and show evidence of majorana fermions [282]–[284].

From the experimental-ISB viewpoint, IR absorption associated with ISB transitions between laterally confined states have been observed in bismuth NWs [285]–[287], and their properties have proven relevant to understand the operation of Si-NW field effect transistors [288]. However, ISB absorption has not been demonstrated in as-grown NWs due to the presence of stacking faults and polytypisms in GaAs [289]–[292]. Conversely, ISB electroluminescence was recently obtained from nanopilars that were lithographically defined on a standard GaAs/AlGaAs QCL structure (top-down approach) [293].

GaN is a model material for the study of ISB transitions in NW heterostructures, because the presence of stacking faults or extended defects can be limited to the first hundred nanometers close to the substrate. At the beginning of this thesis, the only experimental result for ISB absorption had been reported by Tanaka et al. [294] in a sample containing GaN/AlN (1 nm/2.7 nm) NW heterostructures. In order to fully understand the NW heterostructures and how the strain and material characteristics influence the 3D confinement and the positioning of the electronic levels in these systems, their ISB and interband characteristics were explored.

5.2. Samples under study

In this thesis, a theoretical and experimental study of the electronic structure of GaN/AlN NW heterostructures is presented. The samples consisted of N-polar AlN/GaN NW heterostructures synthesized by PAMBE on Si(111) substrates. These heterostructures consist of a non-intentionally doped (n.i.d.) GaN NW base with a length of 600 nm and a radius ranging from 25 to 40 nm. This base is followed by 40 periods of GaN:Ge/AlN NDs, and a 20-nm-thick n.i.d. GaN cap layer. Ge was

used as a dopant instead of Si as it introduces less strain in GaN being similar in size to Ga [295], [296], and it induces negligible change in the NW aspect ratio, even for high Ge doping levels (3.3×10^{20} cm^3) [176]. Additionally, Si was proven to migrate to the surface of the NWs [297] decreasing the doping efficiency. The thickness of the GaN NDs was varied between 3 nm and 8 nm, while the thickness of the AlN sections (barriers) was kept constant at 4 nm. The Ge concentration in the NDs was varied in the 5×10^{17} to 3×10^{20} cm^{-3} range.

Figure 12 shows annular dark field (ADF) and high-resolution transmission electron microscopy (HRTEM) images of two of the samples, which confirm the growth of the wires along the <0001> direction for both the GaN and AlN, with a perfect epitaxy consecutively achieved between both materials. The GaN/AlN heterostructures are enveloped by a thin (2-5 nm) AlN layer, starting from the top-most AlN barrier extending along the GaN stem. In the HRTEM images, the AlN sections often present {1-102} facets close to the sidewalls.

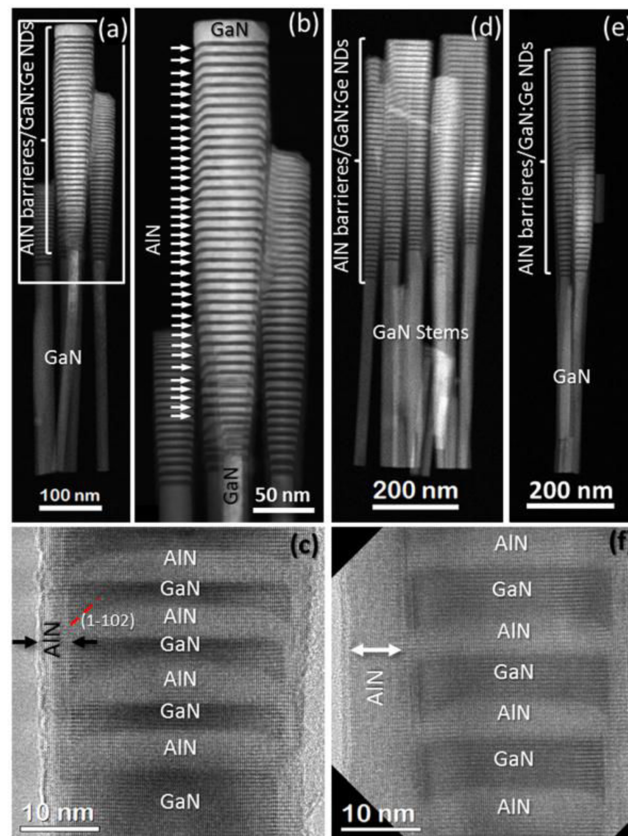

Figure 12 **(a)** ADF image of a set of GaN NWs from sample S6, containing 40 periods of AlN/GaN NDs. **(b)** Zoom-in of the squared area in (a). **(c)** HRTEM image of several GaN NDs and AlN barriers. **(d,e)** ADF images of sets of wires from sample S9. **(f)** HRTEM image of several GaN NDs, separated by AlN barriers.

5.3. Understanding band-to-band dynamics (Annex 6)

In order to probe the band-to-band characteristics of these NWs, they were characterized by PL (see Annex 6). The low-temperature (T = 5 K) PL emission of the structures red shifts for increasing ND thickness, and blue shifts and broadens for increasing doping levels, which can be assigned to the screening of the internal electric field by the free carriers. For all the samples the PL intensities

remain almost constant up to about 100 K, after which they drop to 60 to 80% of their maximum values, at room temperature. This behavior is characteristic of GaN/AlN nanostructures with 3D confinement, in contrast to planar structures which generally exhibit a PL quenching of several orders of magnitude at room temperature [298].

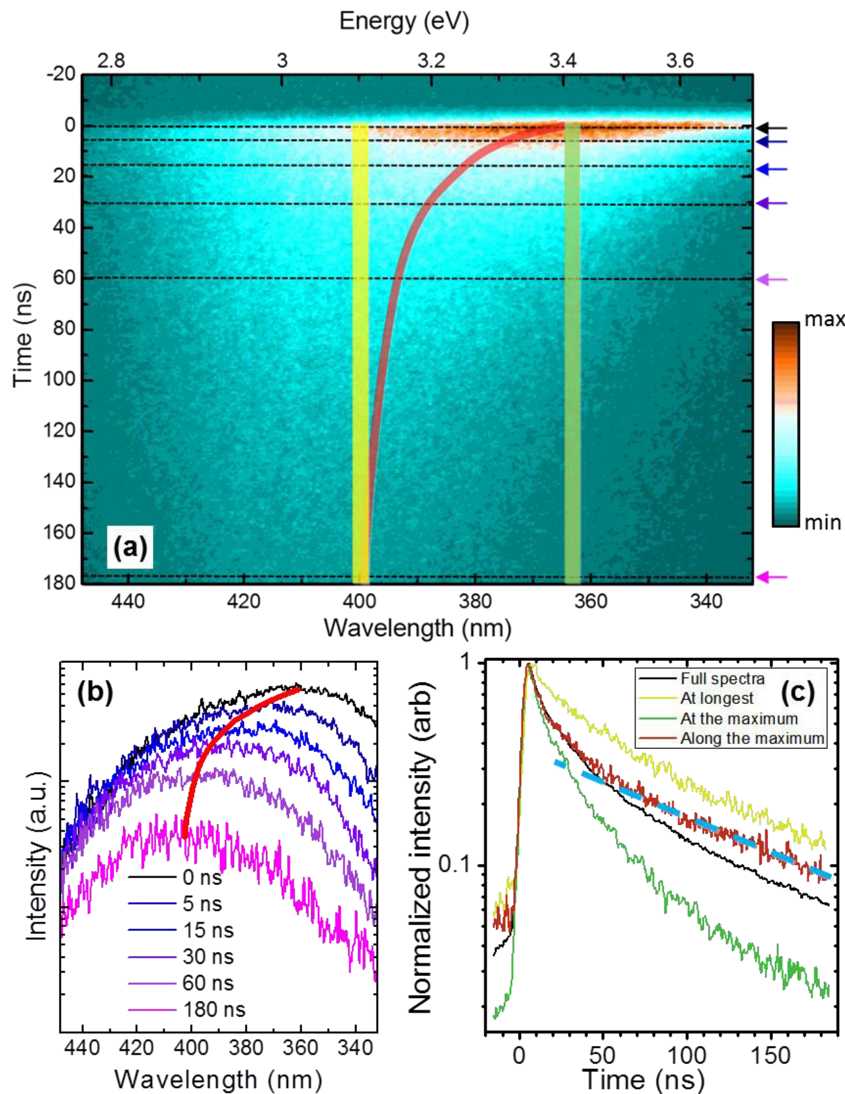

Figure 13 **(a)** Time resolved PL measurement of sample N3 from Annex 6. The green stripe depicts the relaxation scheme at the wavelength of maximum peak intensity. The yellow line depicts the wavelength intensity profile at the relaxed peak wavelength. of maximum intensity after the laser-induced screening has subsided. The red stripe follows the maximum intensity by varying the wavelength with time. **(b)** Evolution of the PL spectra as a function of time. The time of maximum intensity is taken as t = 0. The spectra were acquired at the times indicated with arrows on the right hand side of Figure 13(a), with a time integration window of 0.4 ns. **(c)** Evolution of the PL peak intensity as a function of time for each of the schemes shown in Figure 13(a). The black line represents the integration of the full spectrum over all 116 nm. The integration linewidths are 116 nm, 5 nm, 5 nm, and 0.1 nm for the black, yellow, green and red lines respectively. The blue dashed line is an exponential fit to the PL decay for times longer than 60 ns from the relaxation scheme that incorporates the red-shift from the descreening.

To confirm the screening of the internal electric field with doping, the samples were further analyzed by time-resolved PL. As a typical example, Figure 13(a) shows a time-resolved PL measurement of one of the samples (N3 in Annex 6) at low temperature (T = 5 K). The PL spectra at

different times are seen in Figure 13(b). The emission presents a red shift of 45 nm during the first ~60 ns before a steady-state is obtained. This spectral shift is systematic through all the investigated samples and ranges from 0.1 to 0.3 eV, and decreases with increasing doping levels. Figure 13(c) depicts different analyses of the normalized intensity decay profile: integrating the whole spectra, a stripe at the wavelength of maximum peak intensity, a stripe at the relaxed peak wavelength (peak wavelength at 180 ns), and finally a stripe which follows the maximum intensity by varying the wavelength with time. The intensity profiles are drastically different and present 1/e relaxation times that vary by a factor of 5. It is therefore important to follow the correct analysis procedure.

In the samples under study, the initial red shift and non-exponential behavior are attributed to the perturbation of the band structure induced by the excitation (screening of the polarization fields), and to band filling, as previously observed in GaN/AlGaN QWs [218]. Therefore, in our analysis, only the time constants extracted during the exponential decay regimes (dashed line in Figure 13(c)) were considered. This regime reflects the carrier dynamics of the original band structure, once the photo-induced perturbation from the laser is dissipated.

The evolution of the characteristic PL decay time was analyzed as a function of temperature with the results plotted in Figure 14. In all cases, the PL decay times remain constant (±10%) from 10 K to 300 K, as previously observed in the case of Stransky-Krastanov GaN/AlN QDs [299]. This demonstrates that the 3D confinement in the NDs efficiently suppresses thermally-activated non-radiative recombination channels up to room temperature. The thermally stable PL decay time led us to attribute the thermal quenching of the integrated PL intensity to carrier losses during the relaxation of the hot photoexcited carriers towards the exciton ground states.

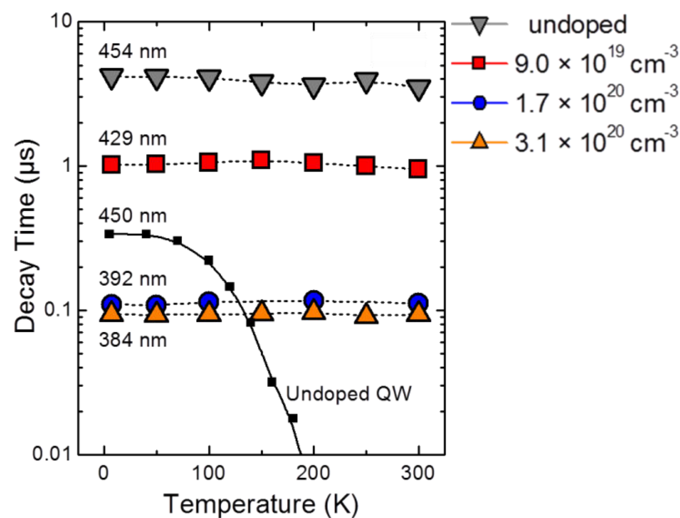

Figure 14 The characteristic PL decay times extracted from the exponential part of the PL decays (similar to Figure 13(c)), plotted as a function of temperature and Ge-dopant level. The macroscopic PL emission wavelengths are indicated in the figure. The PL decay times of an n.i.d. GaN/AlN QW (labeled n.i.d. QW) emitting at approximately the same wavelength that N1 are superimposed. (After Annex 6)

In addition to this stability, the low- and high-temperature PL lifetimes of the dots varied by nearly two orders of magnitude when changing the dopant concentration. At high dopant

concentrations the lifetimes were as low as several ns, while at low dopant concentrations they were on the µs scale. These results are juxtaposed to a QW with the same e_1-h_1 energetic spacing as the lowest doped wire. Even at 5K, the lifetime within the wire is an order of magnitude longer and the QW has a drastically shorter lifetime at higher temperatures.

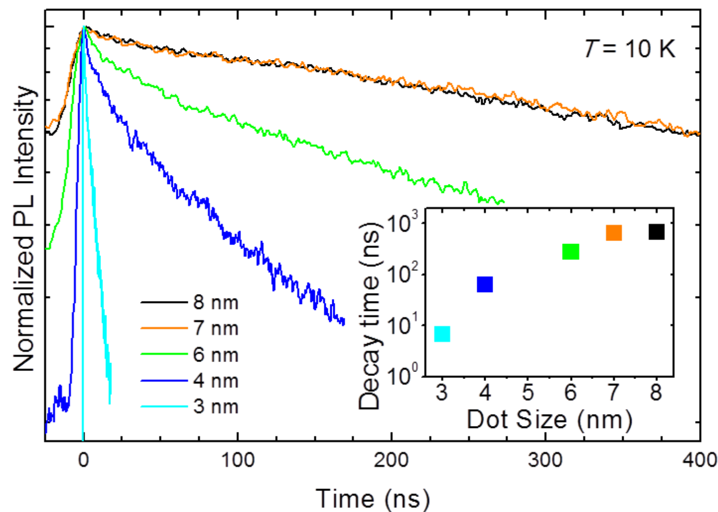

Figure 15 Normalized PL intensity as a function of time at T=10K for samples with ND thicknesses from 3 to 8 nm. The decay times are extracted and plotted in the inset as a function of the ND thickness. The decay times range from several nanoseconds to nearly 1 µs for the largest NDs.

In addition to the screening of the internal electric field via doping, the carrier relaxation rate as a function of the ND size was also monitored. Figure 15 shows the decay profiles as a function of time and the 1/e times as a function of the ND size has been inset. These NDs were doped to an intermediate level ([Ge] = 9 × 10^{20} cm^{-3}). A drastic increase in the relaxation time is seen as a function of the dot thickness.

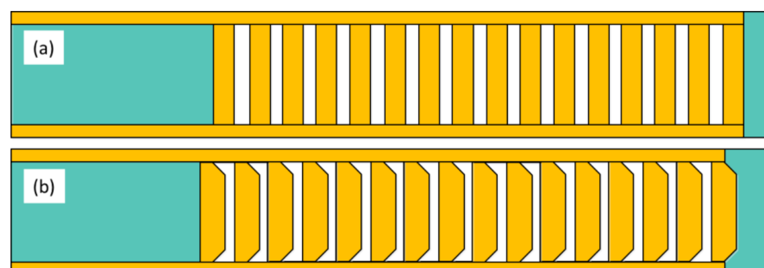

Figure 16 Schematic for the NW heterostructures. The GaN cap and stem are shown in green while the AlN barriers and shells are shown in yellow. The white portions are the GaN NDs which were doped to the appropriate concentrations. The figures are shown for the **(a)** flat AlN barriers and **(b)** truncated hexagonal pyramid AlN barriers.

To understand the above-described results, the NW heterostructures were simulated in 3D using nextnano[3]. The NWs are represented as hexagonal prisms set on a GaN substrate, to provide a reference in-plane lattice parameter. The NDs were first simulated as flat disks of GaN inserted into an AlN prism, which acted as both the shell and the barriers (Figure 16(a)). However, as described above, the NDs were not actually flat hexagonal disks; they exhibited {1-102} facets at the interface between the NDs and the shell. The model was therefore changed to more correctly incorporate

these facets. The material model of the NWs was redefined by a series of hexagonal prisms and truncated hexagonal pyramids to fully create the schematic of the NW as shown in figure 16 (b). The quantum mechanical states of these NW heterostructures were then simulated, and the ISB and interband properties were studied in addition to the shapes of the wavefunctions. The presence of the {1-102} facets leads to 10% lower interband energy and 6% higher ISB energy in comparison to rectangular-section NDs.

In the case of NW heterostructures, the strain distribution is paramount to understand the band-to-band dynamics. The surface strain relaxation results in non-zero ε_{xz} and ε_{yz} shear strain components, which in turn lead to radial piezoelectric polarization associated with the non-zero e_{15} piezoelectric constant in the wurtzite lattice. At low dopant concentrations, these phenomena create a radial band bending which separates the electron and hole wavefunctions in the radial direction (see Figure 17), with holes located axially on top of the ND and radially close to the surface, and electrons located axially at the bottom of the ND and radially centered. However, the relatively weak radial electric field can be rapidly screened by doping, which leads to both a radial and axial centralization of the hole underneath the electron. This results in an increase in the overlap integral between the electron and hole, and consequently a decrease in the radiative lifetime, in addition to the luminescence blue shift.

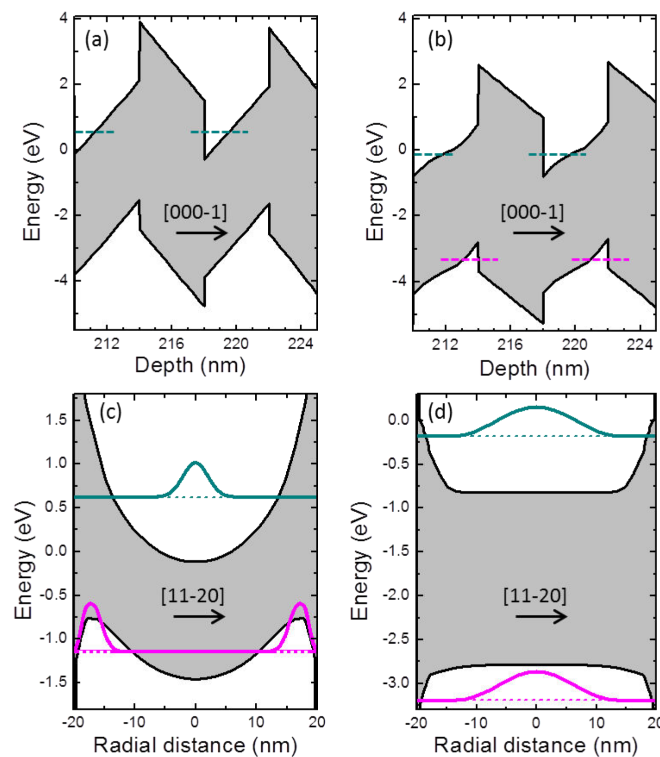

Figure 17 Calculations of the conduction and valence band profiles and first electronic levels of electrons (green) and holes (pink). **(a, b)** Conduction and valence band profiles along [000–1] taken at the center of the NW, for (a) undoped NDs and (b) Ge-doped NDs (sample N3). The ground electron and hole levels are indicated by dashed lines. In (a), the ground hole level is not indicated because the value of the squared wavefunction along the center of the NW is zero. **(c, d)** Radial conduction and valence band profiles for the (c) undoped and (d) Ge-doped ND in the center of the stack. Note that the conduction band was taken at the

bottom of the disk, while the valence band was taken at the top of the ND. The squared wavefunctions of the ground electron and hole states are indicated in the figures. (After Annex 6)

5.4. Intraband absorption in nanowire heterostructures (Annex 7)

By simulating the electronic structure and extracting several hundred quantized levels within the NW heterostructures, the secondary quantized states (p_z, p_x, p_y) can be extracted. Because the NDs are quite large (quantum mechanically speaking) in the radial direction, the energy levels that are separated in the radial sense are energetically very close. For instance, the p_x and p_y orbitals show energy levels that are 27-29 meV away from the first excited state *s*, but are several hundred meV from p_z.

The ISB properties of NW heterostructures with differing doping levels and ND thicknesses were probed using FTIR spectroscopy. In Annex 7, the observation of TM-polarized IR absorption lines assigned to the s-p_z intraband transition is reported. The s-p_x and s-p_y intraband transitions were not observed, most likely due to fluctuations of the NW radius and to the preferential coupling of TM light to the NW geometry. Doping induces a blue shift of the s-p_z absorption line attributed to many-body effects, namely the exchange interaction and depolarization shift, which overpower the red shift induced the screening of the internal electric field. Conversely, the s-p_z transition red shifts with increasing ND thickness as theoretically expected. Figure 18(a) shows the intraband transition wavelength along with the calculations of the ISB wavelength by including various many-body effects for various doping levels.

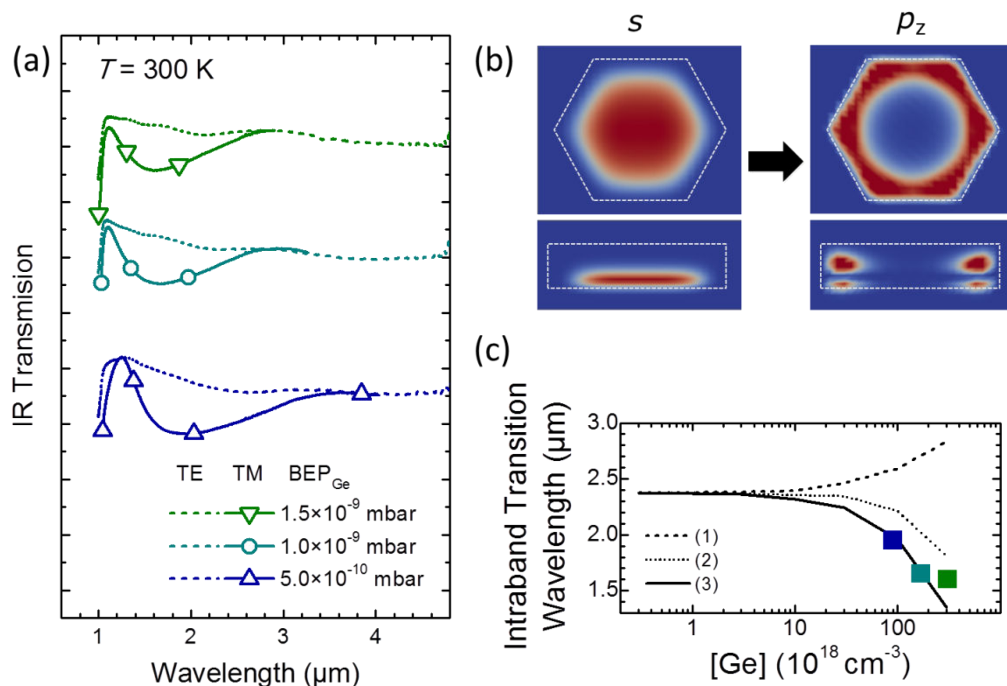

Figure 18 **(a)** shows the IR transmission curves for NDs with differing dopant concentrations. Absorption is seen in the TM-polarized light attributed to the e_1-e_2 (or s-p_z) transition. **(b)** the simulated shape of the wavefunctions for the first (*s*) and second (p_z) excited states levels inside the NDs including their axial and radial positions within the NDs. **(c)** The experimental values for the ISB transition plotted as a function of dopant concentration. The simulations of ISB energy are overlayed and show that with the inclusion of the (1) screening of the internal electric field (2) exchange interaction, and (3) depolarization shift that they can predict the ISB energy within the NW heterostructure. (After Annex 7)

5.5. Note on silicon vs. germanium for n-type doping.

As a first approach to study intraband phenomena in GaN/AlN NW heterostructures, Si was used as a dopant because of its well-known properties as an n-type dopant of GaN. Upon experiencing difficulties for the observation of intraband absorption, germanium was explored as an alternative dopant for both PAMBE [300] and MOCVD growth [301], [302]. This was because its size is more similar to Ga. Additionally, In the case of NWs, Ge was used as a dopant over Si due to the fact that Si migrates to the surface of GaN NWs [297], Ge introduces less strain in GaN being similar in size to Ga [295], [296] and the change of the NW aspect ratio is negligible even for high Ge doping levels (3.3×10^{20} cm^3) [176].

In terms of optical properties of the NW heterostructures, a shift in the ISB wavelength was seen in GaN/AlN NW heterostructures doped with Si and Ge at the same beam equivalent pressure (BEP), as illustrated in Figure 19. The red shift observed in the Si-doped NDs was associated with an inferior incorporation of the dopants into the heterostructure.

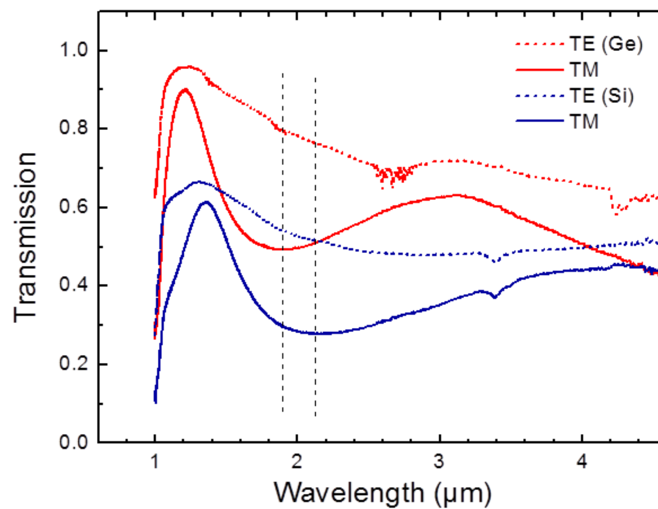

Figure 19 The transmission of TE (dashed) and TM (solid) light for Ge- (red) and Si-doped (blue) NW heterostructures. The dashed lines indicate the local minima for the TM-polarized light. The difference between the TM and TEM polarized light is attributed to the e_1-e_2 ISB transition. The structures were doped to a similar BEP and exhibited ISB transitions at 1.9 and 2.15 µm for the Ge- and Si-doped structures respectively.

5.6. Conclusions

We have studied the optical properties (interband and intersubband) of GaN/AlN NW heterostructures doped with germanium. In terms of interband properties, we report GaN/AlN NW heterostructures displaying PL decay times on the order of microseconds that persist up to room temperature. Doping the GaN ND insertions with Ge can reduce these PL decay times by up to two orders of magnitude. These phenomena are explained by the 3D electric field distribution within the GaN NDs, which has an axial component in the range of a few MV/cm associated with the spontaneous and piezoelectric polarization, and a radial piezoelectric contribution associated with the shear components of the lattice strain (several hundred KV/cm). At low dopant concentrations, a large electron-hole separation in both the axial and radial directions is present. By increasing the Ge-dopant concentration within the NDs, the electric field creating this separation is screened, and the

electron and hole wavefunction can be aligned in space, which consequently decreases the PL lifetime.

These GaN/AlN NW heterostructures display TM-polarized infrared absorption in the NIR assigned to the s-p_z ISB transition in the NDs. The ISB energy of these s-p_z transitions within the NDs can be shifted either by changing the thickness of the NDs, or the dopant concentration within the NDs. From a theoretical analysis, we conclude that the AlN shell generated during the heterostructure growth applies a uniaxial compressive strain which blue shifts the interband optical transitions, but has little influence on the ISB transitions. The presence of surface states at the density levels expected for *m*-plane GaN leads to the depletion of the GaN base of the NWs, but is insufficient to screen the polarization-induced internal electric field in the heterostructures. With the addition of dopants, the ISB transitions are blue shifted due to many-body effects, namely the exchange interaction and depolarization shift, which exceed the red shift induced by carrier screening.

6. Results: Alternate crystal orientations

6.1. Introduction to nonpolar and semipolar orientations

In nonpolar samples, the lack of the internal electric field and high conduction band offset theoretically allows for ISB devices to be designed in the same fashion as GaAs devices. By eliminating the effect of the internal electric fields, the ISB energy can be straightforwardly decreased to unprecedentedly low levels. In spite of these advantages, ISB activity in GaN has mainly focused on the *c* plane because of the inability to obtain high quality SL structures along other crystal orientations. The availability of high quality substrates and the challenge to control 2D growth on the highly anisotropic nonpolar surfaces have been the limiting factors for these technologies.

Until relatively recently, ISB absorption had not been shown from non- or semipolar crystal planes. Nonpolar cubic GaN was the first to show ISB activity [303], [304] in 2007. In 2008, ISB transitions at 2.5 and 3.75 µm were observed using semipolar (11-22) GaN/AlN heterostructures [305]. Nowadays, *m*-plane growth of SLs has been well studied [306]–[308], and MIR absorption has been shown in samples grown by MOCVD from 4.2 to 5 µm [126]. QWIPs in the MIR on *m*-plane substrates have been demonstrated at 9 and 7.5 µm [309]. Furthermore, *m*-plane samples have shown FIR-ISB absorption [310], and resonant tunneling capabilities [311], which confirm their applicability for THz applications. Oddly enough, *m*-plane ISB absorption has not been shown in the NIR, and the relaxation mechanisms within these SL structures have not been fully explored.

6.1. Optical: *a*- vs *m*- vs *c*-plane substrates

By placing all three substrates (*a*-, *m*-, and *c*-plane) on the same molyblock, the morphology of the samples can be determined from identical growth conditions and samples with identical QW thicknesses can be compared. Heterostructures containing 40 repeats of 4 nm of AlN and GaN:Si QW thicknesses of 1.5, 2.5 and 3.5 nm were grown under the optimum growth conditions for *c*-plane growth (Ga bilayer, 720°C). The samples were grown simultaneously on bulk *m*- and *a*-plane substrates, as well as on *c*-plane AlN-on-sapphire templates. All samples were capped with 30-40nm of AlN. The samples were rigorously tested using FTIR, PL, AFM and XRD and the results are shown against simulated values from nextnano^3.

Figure 20(a) shows the experimental low-temperature (5 K) PL data for samples. Using nextnano^3, the electronic structure of *m*- and *c*-plane heterostructures were simulated, and can be seen in Figure 20(b). Figure 20(a) shows that *m*-plane samples have PL intensities systematically twice as high as *a*-plane samples, and 20 times higher than the *c*-plane samples, in agreement with literature [312]. This occurred for samples over all QW widths, and is due to the internal electric field in the *c* plane that separates the electron and hole in space and reduces the overlap integral. Furthermore, *c*-plane samples show interband energies that are systematically lower than the bandgap energy of GaN except for very small wells. This is because of the onset of the QCSE after a thickness of 1.5-1.75 nm. It can also be noted that samples grown on the *a* and *m* planes show asymptotic behaviour when approaching the GaN bandgap for larger well widths; demonstrating the lack of an internal electric field within these systems.

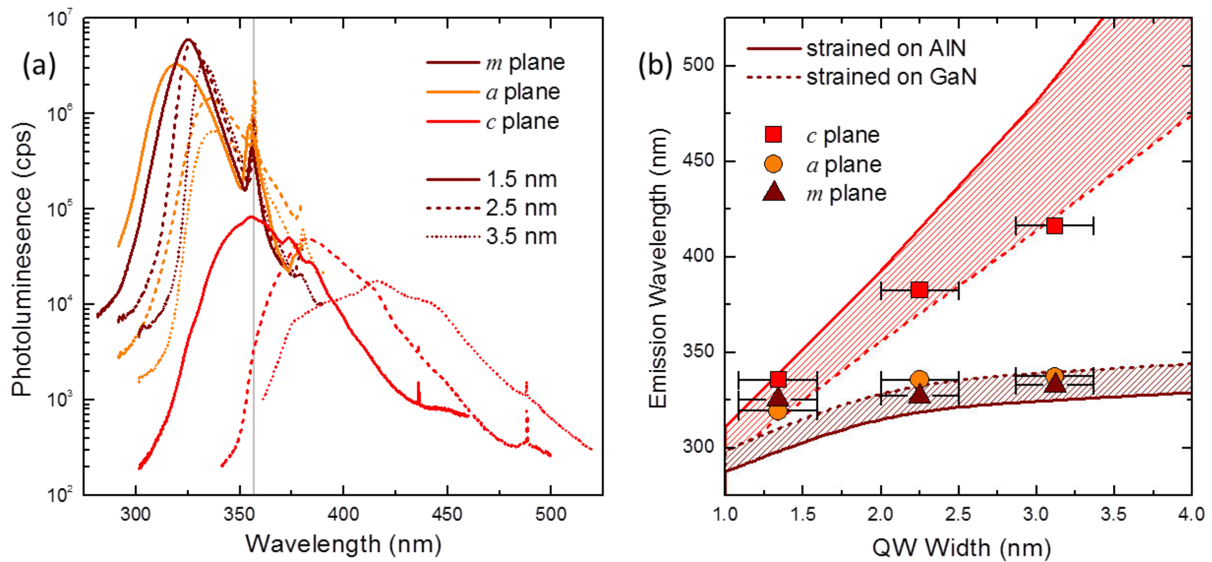

Figure 20 **(a)** PL spectra of samples grown on various substrates (indicated by color), and with various QW widths (indicated by solid, dashed or dotted lines). The grey line marks the GaN bandgap. **(b)** The extracted peak PL wavelength as a function of the QW width. Simulations are shown as lines for polar (red) and nonpolar (brown) crystal orientations. The strain state was either strained on AlN (solid) or on GaN (dashed), and the experimental points are shown as a function of well width for each crystal orientation. The error bars for the experimental data comes from variations in the QW width due to growth.

The ISB energies of these samples were also simulated with nextnano[3] and measured using FTIR. Samples exhibited TM-polarized ISB absorption in agreement with the simulated values (Figure 21).

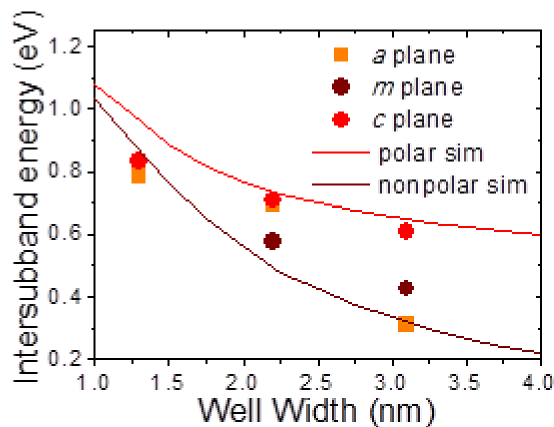

Figure 21 ISB energy of the e_1-e_2 transition as a function of the well width for polar and nonpolar crystal orientations. Simulations are shown as lines for polar (red) and nonpolar (brown) crystal orientations. The dots represent experimental data for samples grown on the *a*, *m*, and *c* planes.

Optically, *m*-plane samples are shown to be superior to *a*-plane samples. This is concluded from the higher and narrower PL intensities and similar performance for ISB transitions.

6.2. Structural: *a*- vs *m*- vs *c*-plane substrates

Figure 22 shows the AFM images of each of the samples grown on *a*- and *m*- plane substrates. They can be compared to the *c*-plane image showing step-like growth. Note that samples grown on *a*-plane substrates are systematically rougher than for *m*-plane samples.

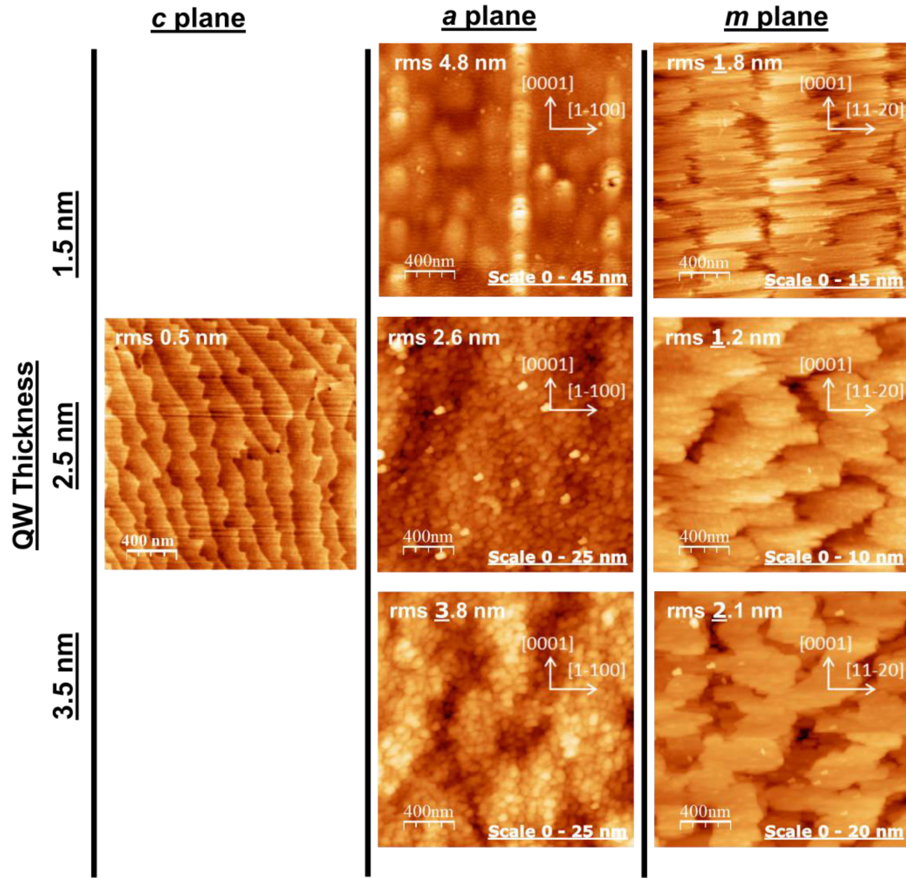

Figure 22 The 2x2 µm AFM images extracted for the samples grown on the *a*, *m*, and *c* planes for various QW widths. Samples grown on the *c* plane all showed root-mean-square (RMS) roughness values near 0.5 nm and step-like growth.

The mosaicity of the samples was analyzed by XRD. Data for the samples with a QW thickness of 2.3 nm is summarized in Table 5. The full width at half maximum (FWHM) of the rocking curves were measured for the substrate and the MQW along the (3-300) and (11-20) reflections for *m*-plane and *a*-plane samples, respectively. Scans with ϕ = 0° and ϕ = 90° were performed ($\Delta\omega$c and $\Delta\omega$a, respectively for the *m*-oriented samples, and $\Delta\omega$c and $\Delta\omega$m, respectively for the *a*-oriented sample), which provide information on the sample mosaicity in the *c* and *a* directions for the *m*-plane sample, and in the *c* and *m* directions for the *a*-plane sample. Comparing these values in Table 5, it appears that, even though the crystalline quality of *a*-plane substrates in terms of mosaicity was better than for the *m*-plane substrates, all the *m*-plane MQWs present better quality than the *a*-plane MQWs.

Substrate plane	t_{QW} (nm)	t_B (nm)	Average Al content (%)	XRD Period (nm)	XRD FWHM MQW (°)	XRD FWHM GaN (°)
m	2.3	3.5	60	5.8	$\Delta\omega_c = 0.44$	$\Delta\omega_c = 0.037$

					$\Delta\omega_a = 0.30$	$\Delta\omega_a = 0.040$
a	2.3	3.5	60	5.8	$\Delta\omega_c = 0.53$	$\Delta\omega_c = 0.019$
					$\Delta\omega_m = 0.40$	$\Delta\omega_m = 0.023$

Table 5 Structural data for the sample with QW thickness of 2.3 nm and barriers nominally at 4 nm. The crystallographic orientation (substrate), QW thickness (t_{QW}), barrier thickness(t_B), average Al concentration throughout the heterostructure, RMS roughness, period extracted from XRD, FWHM of the (3-300) reflection of the MQW and the substrate, as well as the extracted strain relaxation characteristics are shown.

Upon comparison of the PL data to the AFM images, the discrepancy in the optical performance between the *a*- and *m*-plane samples seems to be due to a higher structural defect density.

6.3. Longer wavelength intersubband transitions in the *m* plane (Annex 8)

Based on these results, a series of *m*-plane GaN/AlGaN MQWs were designed to determine the accessible spectral range in the MIR. The QWs were enlarged to achieve the desired spectral shift, and the AlN barriers were replaced by AlGaN to reduce the lattice mismatch and keep the highest quantized electronic level just below the conduction band edge to potentially act as QWIPs. The barriers were chosen to be 22.6 nm thick, in order to prevent coupling between QWs. The well widths were varied from 2 to 3.1 nm with barrier-Al concentrations ranging from 44 to 26%. These samples were simultaneously grown on bulk *m*-plane substrates and *c*-plane GaN-on-Si templates. The structural and optical properties of these samples were studied using PL, FTIR, XRD, and are summarized in Table 6.

t_{QW} (nm)	t_B (nm) [Al Content (%)]	Measured PL emission (eV) [theory (eV)]	Theoretical ISB e_2-e_1 energy (meV)	Measured ISB e_2-e_1 energy (meV)
3.11	22.6 [26]	3.60 [3.59]	186	253
2.83	22.6 [31]	3.61 [3.62]	223	229
2.54	22.6 [35]	3.64 [3.65]	260	264
1.98	22.6 [44]	3.68 [3.74]	356	337

Table 6 Structural and optical properties of samples grown to exhibit ISB transitions spanning the MIR spectral range. The measured QW thickness (t_{QW}), barrier thickness (t_B), barrier-Al content as well as optical properties for the PL and ISB characteristics are shown, with their respective simulated values from nextnano^3.

Figure 23(a) shows the ISB absorption of the GaN/AlGaN with various QW thicknesses. Figure 23(b) compares the experimental ISB energies with their simulated values from nextnano^3. ISB absorption is demonstrated in the 350-200 meV range (3.5 to 6 µm), the limit being set by the GaN substrate absorption associated with the second-order harmonic of the Reststrahlen band.

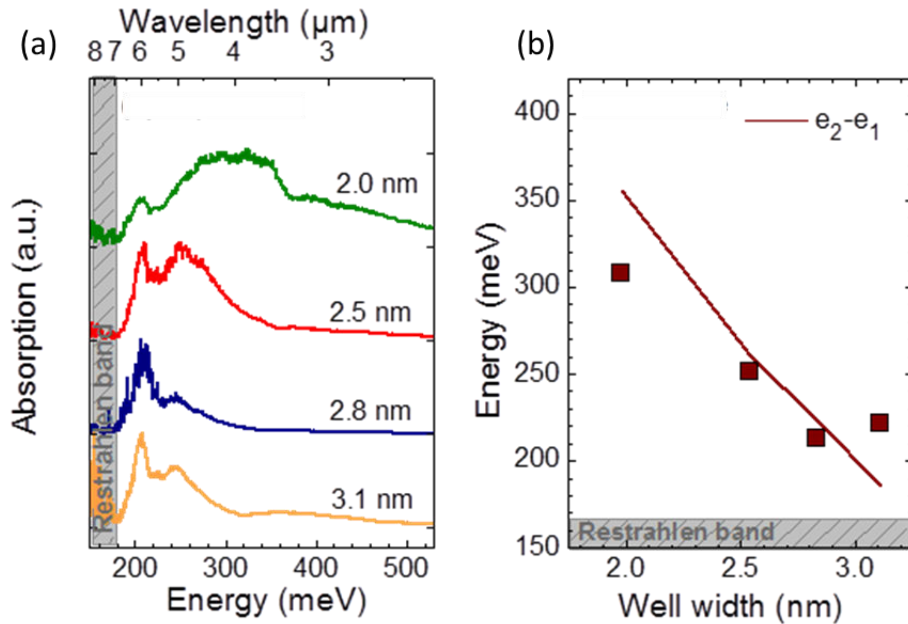

Figure 23 **(a)** ISB plotted absorption as a function of energy for samples with varying well widths grown on the *m* plane. The ISB absorbance varies from 250 to 350 meV with decreasing well width. **(b)** The extracted peak ISB wavelength values and plotted as a function of well width. The experimental values are shown as dots, while the lines represent the values extracted from nextnano[3] simulations assuming a relaxation to the average-Al-content of the MQWs.

6.4. Growth on semipolar substrates (Annex 9)

Due to the strong anisotropy of growth on the a and *m* planes, semipolar planes have been an alternative to reduce the electric field within thin-film structures [313] while still avoiding this anisotropy [66]. By growing GaN/AlN MQW samples with various well thicknesses, the band-to-band and ISB properties of *c*- and semipolar architectures can be directly compared [23]. Samples were grown by PAMBE with well thicknesses varying from 1.2 to 3 nm. The band-to-band properties of these samples were probed by PL and showed a decrease in the internal electric field similar to that shown for nonpolar samples. Figure 24(a) shows the ISB absorption as a function of the QW width for the polar and semipolar samples, while Figure 24(b) shows their ISB properties compared to the values extracted from nextnano[3] simulations strained on AlN and GaN substrates. The ISB absorptions of semipolar samples show a significant red shift with respect to the polar ones due to the reduction of the internal electric field in the QWs.

In view of these promising results, we tried to extend the ISB further into the MIR. Semipolar samples were designed and grown with AlGaN barriers and thicker QWs. However, these samples did not demonstrate ISB absorption. The samples were analyzed using HAADF-STEM in collaboration with Prof. P. Ruterana (CIMAP, CNRS-ENSICAEN, Caen, France) and the results are shown in Figure 25. Strong alloy inhomogeneities are observed in the AlGaN barriers. Similar features were observed in thick AlGaN layers grown at various substrate temperatures. Due to these fluctuations, we decided to focus our efforts on the *m* plane as the best crystallographic plane to reduce the internal electric field in the QWs.

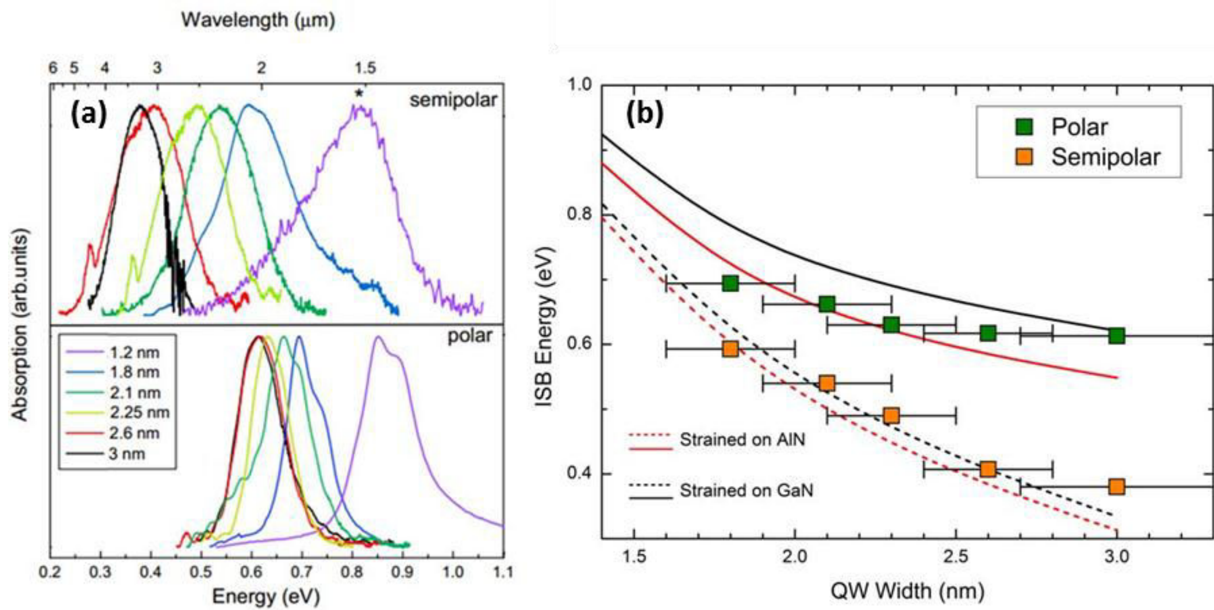

Figure 24 **(a)** the ISB absorption found in the TM polarization for samples with various well thicknesses for (top) semipolar, and (bottom) polar crystallographic growth conditions. The well width is varied from 1.2 to 3 nm and ISB absorption spans from 1.5 to 3.4 µm. **(b)** The extracted peak absorption values plotted as a function of the well width for polar (green) and semipolar (orange) orientations. Simulated values are shown as lines for polar (dashed) and semipolar (solid) crystal orientations. The strain state was either strained on AlN (red) or on GaN (black). The error bars for the experimental data comes from variations in the QW width due to growth.

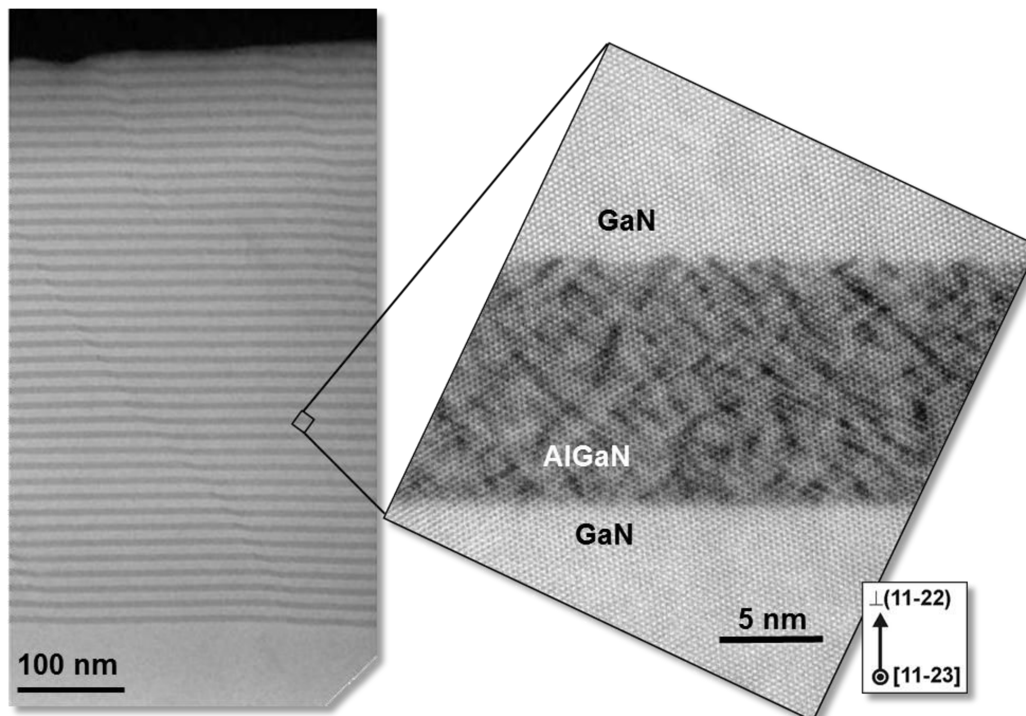

Figure 25 Left: HAADF-STEM images of GaN/AlGaN heterostructures grown with 40 repeats of 12 nm $Al_{0.2}Ga_{0.8}N$ and 16 nm GaN. Right: Zoom showing alloy inhomogeneities in the AlGaN barriers.

6.5. Conclusions

The feasibility of using alternate crystallographic planes for ISB applications was explored, including nonpolar (1-100) *m* and (11-20) *a* planes, and the semipolar (11-22) plane. Regarding nonpolar structures, through studies of GaN/AlN MQWs in the NIR we demonstrate that growth on *m*-plane substrates is optically and structurally superior to the growth on *a*-plane substrates. Focusing on *m*-plane growth and extending the study to ternary alloys (GaN/AlGaN MQWs), we demonstrate ISB absorption in the 1.5 to 6 μm range, where the limit was set by the substrate absorption associated with the second order of the Reststrahlen band. In the case of the (11-22) semipolar plane, it showed promise for GaN/AlN heterostructures, but the ISB spectral range could not be extended to the MIR or FIR, due to strong alloy fluctuations within the AlGaN ternary alloy.

7. Conclusions and prospects

7.1. Conclusions

This thesis pushes the boundaries of GaN-based ISB technologies in a three-pronged approach focusing on extending the viable region for ISB transitions in *c*-plane GaN QWs into the THz spectral region, exploring the feasibility of NW-based ISB technologies, and assessing the capabilities of nonpolar/semipolar GaN MQWs for ISB optoelectronics.

Extending the viable ISB transition energy into the FIR using GaN/AlGaN MQWs with single barriers and single QWs is not easily accomplished due to the QCSE. By analyzing the sources of error associated with the growth of MQW structures and the feasibility of tunneling transport through the barriers (incorporability into real devices), a “pseudo-square” MQW architecture consisting of four layers of AlGaN with different Al compositions was proposed as the best approach for the lasing well in QCL designs. These MQWs were fabricated by PAMBE and exhibited tunable ISB transitions from 6 to 2 THz by changing the QW thickness and dopant concentration. Using this pseudo-square structure, the design restrictions for the creation of LO-phonon–based QCLs were explained, and a final design for a *c*-plane GaN QCL was proposed.

Motivated by demonstrations of long lifetimes, and essentially-defect-free active regions in laterally-confined systems such as QDs and NWs, GaN/AlN NW heterostructures were explored as an alternative active media for ISB devices. In terms of interband properties, GaN/AlN NW heterostructures were found to display PL decay times on the order of microseconds that persist up to room temperature. This phenomenon is explained by the 3D electric field distribution within the GaN NDs, which has an axial component in the range of a few MV/cm associated with the spontaneous and piezoelectric polarization, and a radial piezoelectric contribution associated with the shear components of the lattice strain (hundreds of kV/cm). It was demonstrated that this radial electric field leads to a spatial separation of the electron and hole that can be screened by increasing the Ge-dopant concentration within the NDs; aligning the electron and hole wavefunctions in space. This alignment was demonstrated to reduce the PL lifetime of these NW heterostructures by two orders of magnitude. The ISB properties of these NWs were also probed with respect to ND thickness and dopant level. It was shown that with increasing dot thickness, the ISB energy red-shifts from 1.5 to 1.8 µm, and with increasing dopant concentration, the ISB transition is strongly blue shifted. This blue shift is attributed to many-body effects, namely the exchange interaction and depolarization shift, which exceed the red shift induced by carrier screening.

The feasibility of using alternate crystallographic planes for ISB applications has also been explored, including the nonpolar (1-100) *m* and (11-20) *a* planes, and the semipolar (11-22) plane. Regarding nonpolar structures, GaN/AlN MQWs for NIR applications were grown simultaneously on *m-, a-*, and *c*-plane substrates. Samples grown on *m*-plane substrates were superior to those grown on *a*-plane substrates in terms of surface roughness, mosaicity, PL linewidth and intensity, as well as ISB absorption in the 1.5 to 3 µm range. Focusing on *m*-plane growth and extending the study to ternary alloys (GaN/AlGaN MQWs), ISB absorption is demonstrated in the 1.5 to 6 µm range, the long-wavelength limit being set by the substrate absorption associated with the second order of the

Reststrahlen band, starting around 7 µm. Along the lines of reducing the internal electric field while reducing the in-plane anisotropy, GaN/AlN MQWs were grown on the (11-22) semipolar plane. These structures demonstrated tunable ISB energies spanning the NIR from 1.5 to 3.3 µm. However, semipolar GaN/AlGaN MQWs targeting the MIR and FIR did not show ISB absorption due to strong alloy fluctuations within the AlGaN ternary alloy.

7.2. Prospects

7.2.1. THz quantum cascade laser fabrication

Because GaAs QCL technologies have been constantly improving over the last 12 years, there is a wealth of knowledge in terms of wavefunction engineering that can be applied to GaN technologies. Through the implementation of hybrid designs (between chirped superlattice and LO-phonon) GaAs QCLs have improved in both their temperature and power performance. Because existing GaN designs consist only of two basic wells (the extractor and the lasing well), the addition of other wells (such as an injector) could increase the lasing efficiency and lead to higher-temperature and higher-power lasers. By growing these structures on bulk substrates, this will drastically lower the defect densities, and therefore the threshold currents. If these substrates are doped with Si or Ge, it will also allow for back contacts to be created on the devices.

Besides the design of the active region, THz QCLs also rely on waveguiding to properly direct the emission of light. Metal-metal waveguides are typically used in the GaAs system [314], but due to the challenge of creating an etch-stop layer in GaN-based structures, it is very difficult to create this type of back-etched structures in a reliable way. Surface plasmon waveguides seem to be the easiest way to accomplish this waveguiding [238][247], [248]. Spoof surface plasmon waveguides have also been theorized to decrease waveguide losses by a factor of 10, but require many more lithographic steps [315], [316].

Upon the creation of solid state THz sources and detectors operating at room temperature, there are many opportunities to use these devices for applications ranging from ultrafast wireless data transfer to portable characterization tools. Eventually, these devices could replace existing technologies for characterizing materials in the industry and at home. Additionally, these lasers could be used in the diagnosis of epidermal diseases such as melanoma, and with increased laser power would come the ability to probe deeper tissues and materials. Diagnostics could be extended to complete 3D body scans to search for cancer, bone diseases, or at higher resolutions could come the tracking of chemical flow on a micron scale. These high-power sources could also be used for non-destructive defect analysis, or security screenings, and could also be used to verify the authenticity of high quality wines or archeological artifacts.

7.2.2. Nanowire intersubband technology

NWs are seated to improve the performance of ISB devices, particularly QCLs, whose operating temperatures are limited by nonradiative scattering processes, and photodetectors, by increasing the collection efficiency of photoexcited carriers. Critical steps in this direction involve the

assessment of the accessible spectral range, and the evaluation of NW heterostructures in terms of light emission/lasing and detection. In order to move the response of these NW heterostructures to longer wavelengths, the ISB energy should be decreased by increasing the thickness of the NDs, and decreasing the Al content of the barriers. It will be particularly challenging to get into the FIR because of the expected alloy inhomogeneities, which could be a major hurdle for creating homogeneous barriers. Additionally, processing technologies need to be developed to increase the waveguiding properties of NW ensembles, due to the fact that that ISB transitions occur perpendicular to the NW growth axis.

7.2.3. Nonpolar Intersubband devices

Nonpolar ISB absorption has been shown to cover nearly the entire IR spectrum and simulations have successfully been able to predict the ISB wavelength. By emulating the designs of GaAs QCLs, the research that has occurred in this material system can be used. Such designs have already been theorized [316]–[318], but have not yet been experimentally demonstrated.

If QCL structures are to be fabricated, it would also be beneficial to pursue more methods of creating large nonpolar substrates, either by increasing the growth rate and crystal quality of HVPE-grown boules or by improving the quality of nonpolar ammonothermal substrates. An alternative approach would be the use of patterned substrates and facetted growth surfaces.

Bibliography

[1] E. Bellotti, K. Driscoll, T. D. Moustakas, and R. Paiella, “Monte Carlo study of GaN versus GaAs terahertz quantum cascade structures,” *Appl. Phys. Lett.*, vol. 92, no. 10, p. 101112, Mar. 2008.

[2] C. Himwas, R. Songmuang, Le Si Dang, J. Bleuse, L. Rapenne, E. Sarigiannidou, and E. Monroy, “Thermal stability of the deep ultraviolet emission from AlGaN/AlN Stranski-Krastanov quantum dots,” *Appl. Phys. Lett.*, vol. 101, no. 24, p. 241914, 2012.

[3] A. Mukhtarova, S. Valdueza-Felip, C. Durand, Q. Pan, L. Grenet, D. Peyrade, C. Bougerol, W. Chikhaoui, E. Monroy, and J. Eymery, “InGaN/GaN multiple-quantum well heterostructures for solar cells grown by MOVPE: case studies,” *Phys. Status Solidi C*, vol. 10, no. 3, pp. 350–354, 2013.

[4] S. Valdueza-Felip, A. Mukhtarova, L. Grenet, C. Bougerol, C. Durand, J. Eymery, and E. Monroy, “Improved conversion efficiency of as-grown InGaN/GaN quantum-well solar cells for hybrid integration,” *Appl. Phys. Express*, vol. 7, no. 3, p. 032301, Mar. 2014.

[5] L. Redaelli, A. Mukhtarova, S. Valdueza-Felip, A. Ajay, C. Bougerol, C. Himwas, J. Faure-Vincent, C. Durand, J. Eymery, and E. Monroy, “Effect of the quantum well thickness on the performance of InGaN photovoltaic cells,” *Appl. Phys. Lett.*, vol. 105, no. 13, p. 131105, Sep. 2014.

[6] S. Valdueza-Felip, A. Mukhtarova, Q. Pan, G. Altamura, L. Grenet, C. Durand, C. Bougerol, D. Peyrade, F. González-Posada, J. Eymery, and E. Monroy, “Photovoltaic Response of InGaN/GaN Multiple-Quantum Well Solar Cells,” *Jpn. J. Appl. Phys.*, vol. 52, no. 8S, p. 08JH05, Aug. 2013.

[7] J. Wu, “When group-III nitrides go infrared: New properties and perspectives,” *J. Appl. Phys.*, vol. 106, no. 1, p. 011101, Jul. 2009.

[8] J. Baur, K. Maier, M. Kunzer, U. Kaufmann, and J. Schneider, “Determination of the GaN/AlN band offset via the (-/0) acceptor level of iron,” *Appl. Phys. Lett.*, vol. 65, no. 17, pp. 2211–2213, Oct. 1994.

[9] S.-H. Wei and A. Zunger, “Valence band splittings and band offsets of AlN, GaN, and InN,” *Appl. Phys. Lett.*, vol. 69, no. 18, pp. 2719–2721, Oct. 1996.

[10] R. Dingle, D. D. Sell, S. E. Stokowski, and M. Ilegems, “Absorption, Reflectance, and Luminescence of GaN Epitaxial Layers,” *Phys. Rev. B*, vol. 4, no. 4, pp. 1211–1218, Aug. 1971.

[11] A. S. Barker and M. Ilegems, “Infrared Lattice Vibrations and Free-Electron Dispersion in GaN,” *Phys. Rev. B*, vol. 7, no. 2, pp. 743–750, Jan. 1973.

[12] N. Suzuki and N. Iizuka, “Feasibility Study on Ultrafast Nonlinear Optical Properties of 1.55-µm Intersubband Transition in AlGaN/GaN Quantum Wells,” *Jpn. J. Appl. Phys.*, vol. 36, no. Part 2, No. 8A, pp. L1006–L1008, Aug. 1997.

[13] M. Helm, “The Basic Physics of Intersubband Transitions,” in *in “Intersubband Transitions in Quantum Wells: Physics and Device Applications I”, Ed. H. C. Liu, and F. Capasso*, San Diego: Acad. Press, 2000.

[14] H. C. Liu and F. Capasso, *Intersubband transitions in quantum wells : Physics and device applications I*. San Diego, CA: Academic Press, 2000.

[15] S. Birner, T. Zibold, T. Andlauer, T. Kubis, M. Sabathil, A. Trellakis, and P. Vogl, “nextnano: General Purpose 3-D Simulations,” *IEEE Trans. Electron Devices*, vol. 54, no. 9, pp. 2137–2142, Sep. 2007.

[16] M. Beeler, E. Trichas, and E. Monroy, "III-nitride semiconductors for intersubband optoelectronics: a review," *Semicond. Sci. Technol.*, vol. 28, no. 7, p. 074022, Jul. 2013.

[17] M. Beeler, E. Monroy, "*III-nitride semiconductors: new infrared intersubband technologies*" in "*Gallium Nitride (GaN): Physics, Devices, and Technology*", edited by F. Medjdoub and K. Iniewski (Taylor & Francis, New York, Aug. 2015). ISBN: 9781482220032

[18] M. Beeler, C. Bougerol, E. Bellet-Amalric, and E. Monroy, "Terahertz absorbing AlGaN/GaN multi-quantum-wells: Demonstration of a robust 4-layer design," *Appl. Phys. Lett.*, vol. 103, no. 9, p. 091108, 2013.

[19] M. Beeler, C. Bougerol, E. Bellet-Amalaric, and E. Monroy, "THz intersubband transitions in AlGaN/GaN multi-quantum-wells," *Phys. Status Solidi A*, vol. 211, no. 4, pp. 761–764, Apr. 2014.

[20] M. Beeler, C. Bougerol, E. Bellet-Amalric, and E. Monroy, "Pseudo-square AlGaN/GaN quantum wells for terahertz absorption," *Appl. Phys. Lett.*, vol. 105, no. 13, p. 131106, Sep. 2014.

[21] M. Beeler, C. B. Lim, P. Hille, J. Bleuse, J. Schörmann, M. de la Mata, J. Arbiol, M. Eickhoff, and E. Monroy, "Long-lived excitons in GaN/AlN nanowire heterostructures," *ArXiv14127720 Cond-Mat*, Dec. 2014.

[22] M. Beeler, P. Hille, J. Schörmann, J. Teubert, M. de la Mata, J. Arbiol, M. Eickhoff, and E. Monroy, "Intraband Absorption in Self-Assembled Ge-Doped GaN/AlN Nanowire Heterostructures," *Nano Lett.*, vol. 14, no. 3, pp. 1665–1673, Mar. 2014.

[23] H. Machhadani, M. Beeler, S. Sakr, E. Warde, Y. Kotsar, M. Tchernycheva, M. P. Chauvat, P. Ruterana, G. Nataf, P. De Mierry, E. Monroy, and F. H. Julien, "Systematic study of near-infrared intersubband absorption of polar and semipolar GaN/AlN quantum wells," *J. Appl. Phys.*, vol. 113, no. 14, p. 143109, 2013.

[24] F. Fichter, "Über Aluminiumnitrid," *Z. Für Anorg. Chem.*, vol. 54, no. 1, pp. 322–327, 1907.

[25] W. C. Johnson, J. B. Parson, and M. C. Crew, "Nitrogen Compounds of Gallium. III," *J. Phys. Chem.*, vol. 36, no. 10, pp. 2651–2654, 1931.

[26] S. Yoshida, S. Misawa, and A. Itoh, "Epitaxial growth of aluminum nitride films on sapphire by reactive evaporation," *Appl. Phys. Lett.*, vol. 26, no. 8, pp. 461–462, Apr. 1975.

[27] B. B. Kosicki and D. Kahng, "Preparation and Structural Properties of GaN Thin Films," *J. Vac. Sci. Technol.*, vol. 6, no. 4, pp. 593–596, Jul. 1969.

[28] A. L. Rosa, J. Neugebauer, J. E. Northrup, C.-D. Lee, and R. M. Feenstra, "Adsorption and incorporation of silicon at GaN(0001) surfaces," *Appl. Phys. Lett.*, vol. 80, no. 11, pp. 2008–2010, Mar. 2002.

[29] H. Amano, M. Kito, K. Hiramatsu, and I. Akasaki, "P-Type Conduction in Mg-Doped GaN Treated with Low-Energy Electron Beam Irradiation (LEEBI)," *Jpn. J. Appl. Phys.*, vol. 28, no. 12A, p. L2112, Dec. 1989.

[30] H. P. Maruska and J. J. Tietjen, "The preparation and properties of vapor-deposited single-crystal-line GaN," *Appl. Phys. Lett.*, vol. 15, no. 10, pp. 327–329, Nov. 1969.

[31] T. Hashimoto, F. Wu, J. S. Speck, and S. Nakamura, "A GaN bulk crystal with improved structural quality grown by the ammonothermal method," *Nat. Mater.*, vol. 6, no. 8, pp. 568–571, Aug. 2007.

[32] D. Ehrentraut, R. T. Pakalapati, D. S. Kamber, W. Jiang, D. W. Pocius, B. C. Downey, M. McLaurin, and M. P. D'Evelyn, "High Quality, Low Cost Ammonothermal Bulk GaN Substrates," *Jpn. J. Appl. Phys.*, vol. 52, no. 8S, p. 08JA01, Aug. 2013.

[33] H. Yoshida, Y. Takagi, and M. Kuwabara, "Nitride semiconductor substrate," US Patent # 8759837 B2, 24-Jun-2014.

[34] P. Lu, R. Collazo, R. F. Dalmau, G. Durkaya, N. Dietz, B. Raghothamachar, M. Dudley, and Z. Sitar, "Seeded growth of AlN bulk crystals in m- and c-orientation," *J. Cryst. Growth*, vol. 312, no. 1, pp. 58–63, Dec. 2009.

[35] B. Beaumont, P. Gibart, J.-C. Guillaume, G. Nataf, M. Vaille, and S. Haffouz, "Process for producing an epitaxial layer of gallium nitride," US Patent # 6802902 B2, 12-Oct-2004.

[36] R. Dwiliński, R. Doradziński, J. Garczyński, L. Sierzputowski, J. M. Baranowski, and M. Kamińska, "Exciton photo-luminescence of GaN bulk crystals grown by the AMMONO method," *Mater. Sci. Eng. B*, vol. 50, no. 1–3, pp. 46–49, Dec. 1997.

[37] T. Wang, "Semiconductor devices and fabrication methods," US Patent # 20140299968 A1, 09-Oct-2014.

[38] T. Okahisa, "Method of manufacturing GaN crystal substrate," US Patent # 7481881 B2, 27-Jan-2009.

[39] T. Nakamura and K. Motoki, "GaN Substrate Technologies for Optical Devices," *Proc. IEEE*, vol. 101, no. 10, pp. 2221–2228, Oct. 2013.

[40] X. J. Su, K. Xu, G. Q. Ren, J. F. Wang, Y. Xu, X. H. Zeng, J. C. Zhang, D. M. Cai, T. F. Zhou, Z. H. Liu, and H. Yang, "Electrical and optical inhomogeneity in N-face GaN grown by hydride vapor phase epitaxy," *J. Cryst. Growth*, vol. 372, pp. 43–48, Jun. 2013.

[41] F. Bernardini, V. Fiorentini, and D. Vanderbilt, "Spontaneous polarization and piezoelectric constants of III-V nitrides," *Phys. Rev. B*, vol. 56, no. 16, pp. R10024–R10027, Oct. 1997.

[42] A. Zoroddu, F. Bernardini, P. Ruggerone, and V. Fiorentini, "First-principles prediction of structure, energetics, formation enthalpy, elastic constants, polarization, and piezoelectric constants of AlN, GaN, and InN: Comparison of local and gradient-corrected density-functional theory," *Phys. Rev. B*, vol. 64, no. 4, p. 045208, Jul. 2001.

[43] K. Kim, W. R. L. Lambrecht, and B. Segall, "Erratum: Elastic constants and related properties of tetrahedrally bonded BN, AlN, GaN, and InN [Phys. Rev. B 53, 16310 (1996)]," *Phys. Rev. B*, vol. 56, no. 11, pp. 7018–7018, Sep. 1997.

[44] K. Kim, W. R. L. Lambrecht, and B. Segall, "Elastic constants and related properties of tetrahedrally bonded BN, AlN, GaN, and InN," *Phys. Rev. B*, vol. 53, no. 24, pp. 16310–16326, Jun. 1996.

[45] A. F. Wright, "Elastic properties of zinc-blende and wurtzite AlN, GaN, and InN," *J. Appl. Phys.*, vol. 82, no. 6, pp. 2833–2839, 1997.

[46] Y. Takagi, M. Ahart, T. Azuhata, T. Sota, K. Suzuki, and S. Nakamura, "Brillouin scattering study in the GaN epitaxial layer," *Phys. B Condens. Matter*, vol. 219–220, pp. 547–549, Apr. 1996.

[47] A. Polian, M. Grimsditch, and I. Grzegory, "Elastic constants of gallium nitride," *J. Appl. Phys.*, vol. 79, no. 6, pp. 3343–3344, Mar. 1996.

[48] M. Yamaguchi, T. Yagi, T. Azuhata, T. Sota, K. Suzuki, S. Chichibu, and S. Nakamura, "Brillouin scattering study of gallium nitride: elastic stiffness constants," *J. Phys. Condens. Matter*, vol. 9, no. 1, p. 241, Jan. 1997.

[49] C. Deger, E. Born, H. Angerer, O. Ambacher, M. Stutzmann, J. Hornsteiner, E. Riha, and G. Fischerauer, “Sound velocity of AlxGa1−xN thin films obtained by surface acoustic-wave measurements,” *Appl. Phys. Lett.*, vol. 72, no. 19, pp. 2400–2402, May 1998.

[50] L. E. McNeil, M. Grimsditch, and R. H. French, “Vibrational Spectroscopy of Aluminum Nitride,” *J. Am. Ceram. Soc.*, vol. 76, no. 5, pp. 1132–1136, 1993.

[51] T. Sasaki and S. Zembutsu, “Substrate-orientation dependence of GaN single-crystal films grown by metalorganic vapor-phase epitaxy,” *J. Appl. Phys.*, vol. 61, no. 7, pp. 2533–2540, Apr. 1987.

[52] P. Waltereit, O. Brandt, A. Trampert, H. T. Grahn, J. Menniger, M. Ramsteiner, M. Reiche, and K. H. Ploog, “Nitride semiconductors free of electrostatic fields for efficient white light-emitting diodes,” *Nature*, vol. 406, no. 6798, pp. 865–868, Aug. 2000.

[53] M. D. Craven, P. Waltereit, F. Wu, J. S. Speck, and S. P. DenBaars, “Characterization of a-Plane GaN/(Al,Ga)N Multiple Quantum Wells Grown via Metalorganic Chemical Vapor Deposition,” *Jpn. J. Appl. Phys.*, vol. 42, no. 3A, p. L235, Mar. 2003.

[54] S. Founta, F. Rol, T. Andreev, B. Gayral, E. Bellet-Amalric, C. Moisson, H. Mariette, and B. Daudin, “GaN quantum dots grown on non-polar a-plane SiC by plasma-assisted molecular beam epitaxy,” *Phys. Status Solidi C*, vol. 2, no. 7, pp. 2341–2344, 2005.

[55] N. Garro, A. Cros, J. A. Budagosky, A. Cantarero, A. Vinattieri, M. Gurioli, S. Founta, H. Mariette, and B. Daudin, “Reduction of the internal electric field in GaN/AlN quantum dots grown on the a-plane of SiC substrates,” *Phys. Status Solidi C*, vol. 2, no. 11, pp. 3851–3855, 2005.

[56] W. H. Sun, E. Kuokstis, M. Gaevski, J. P. Zhang, C. Q. Chen, H. M. Wang, J. W. Yang, G. Simin, M. Asif Khan, R. Gaska, and M. S. Shur, “Strong ultraviolet emission from non-polar AlGaN/GaN quantum wells grown over r-plane sapphire substrates,” *Phys. Status Solidi A*, vol. 200, no. 1, pp. 48–51, 2003.

[57] Y. J. Sun, O. Brandt, S. Cronenberg, S. Dhar, H. T. Grahn, K. H. Ploog, P. Waltereit, and J. S. Speck, “Nonpolar $In_xGa_{1-x}N$/GaN (1-100) multiple quantum wells grown on γ-$LiAlO_2$(100) by plasma-assisted molecular-beam epitaxy,” *Phys. Rev. B*, vol. 67, no. 4, p. 041306, Jan. 2003.

[58] Y. J. Sun, O. Brandt, M. Ramsteiner, H. T. Grahn, and K. H. Ploog, “Polarization anisotropy of the photoluminescence of M-plane (In,Ga)N/GaN multiple quantum wells,” *Appl. Phys. Lett.*, vol. 82, no. 22, pp. 3850–3852, Jun. 2003.

[59] Y. J. Sun, O. Brandt, U. Jahn, T. Y. Liu, A. Trampert, S. Cronenberg, S. Dhar, and K. H. Ploog, “Impact of nucleation conditions on the structural and optical properties of M-plane GaN(1-100) grown on γ-$LiAlO_2$,” *J. Appl. Phys.*, vol. 92, no. 10, pp. 5714–5719, Nov. 2002.

[60] R. Armitage, M. Horita, J. Suda, and T. Kimoto, “m-plane GaN layers grown by rf-plasma assisted molecular beam epitaxy with varying Ga∕N flux ratios on m-plane 4H-SiC substrates,” *J. Appl. Phys.*, vol. 101, no. 3, p. 033534, Feb. 2007.

[61] C. Q. Chen, M. E. Gaevski, W. H. Sun, E. Kuokstis, J. P. Zhang, R. S. Q. Fareed, H. M. Wang, J. W. Yang, G. Simin, M. A. Khan, H.-P. Maruska, D. W. Hill, M. M. C. Chou, and B. Chai, “GaN homoepitaxy on freestanding (1-100) oriented GaN substrates,” *Appl. Phys. Lett.*, vol. 81, no. 17, pp. 3194–3196, Oct. 2002.

[62] R. Armitage, J. Suda, and T. Kimoto, “Epitaxy of nonpolar AlN on 4H-SiC (1-100) substrates,” *Appl. Phys. Lett.*, vol. 88, no. 1, p. 011908, Jan. 2006.

[63] K. C. Kim, M. C. Schmidt, H. Sato, F. Wu, N. Fellows, M. Saito, K. Fujito, J. S. Speck, S. Nakamura, and S. P. DenBaars, “Improved electroluminescence on nonpolar m -plane InGaN/GaN quantum wells LEDs,” *Phys. Status Solidi RRL – Rapid Res. Lett.*, vol. 1, no. 3, pp. 125–127, May 2007.

[64] J. W. Raring, M. C. Schmidt, C. Poblenz, Y.-C. Chang, M. J. Mondry, B. Li, J. Iveland, B. Walters, M. R. Krames, R. Craig, P. Rudy, J. S. Speck, S. P. DenBaars, and S. Nakamura, “High-Efficiency Blue and True-Green-Emitting Laser Diodes Based on Non-c-Plane Oriented GaN Substrates,” *Appl. Phys. Express*, vol. 3, no. 11, p. 112101, Nov. 2010.

[65] T. Fujiwara, S. Rajan, S. Keller, M. Higashiwaki, J. S. Speck, S. P. DenBaars, and U. K. Mishra, “Enhancement-Mode m-plane AlGaN/GaN Heterojunction Field-Effect Transistors,” *Appl. Phys. Express*, vol. 2, no. 1, p. 011001, Jan. 2009.

[66] L. Lahourcade, E. Bellet-Amalric, E. Monroy, M. Abouzaid, and P. Ruterana, “Plasma-assisted molecular-beam epitaxy of AlN(11-22) on m sapphire,” *Appl. Phys. Lett.*, vol. 90, no. 13, p. 131909, 2007.

[67] Y. Enya, Y. Yoshizumi, T. Kyono, K. Akita, M. Ueno, M. Adachi, T. Sumitomo, S. Tokuyama, T. Ikegami, K. Katayama, and T. Nakamura, “531 nm Green Lasing of InGaN Based Laser Diodes on Semi-Polar {2021} Free-Standing GaN Substrates,” *Appl. Phys. Express*, vol. 2, no. 8, p. 082101, Aug. 2009.

[68] Y. Yoshizumi, M. Adachi, Y. Enya, T. Kyono, S. Tokuyama, T. Sumitomo, K. Akita, T. Ikegami, M. Ueno, K. Katayama, and T. Nakamura, “Continuous-Wave Operation of 520 nm Green InGaN-Based Laser Diodes on Semi-Polar {2021} GaN Substrates,” *Appl. Phys. Express*, vol. 2, no. 9, p. 092101, Sep. 2009.

[69] M. Funato, M. Ueda, Y. Kawakami, Y. Narukawa, T. Kosugi, M. Takahashi, and T. Mukai, “Blue, Green, and Amber InGaN/GaN Light-Emitting Diodes on Semipolar {11-22} GaN Bulk Substrates,” *Jpn. J. Appl. Phys.*, vol. 45, no. 7L, p. L659, Jul. 2006.

[70] H. Sato, R. B. Chung, H. Hirasawa, N. Fellows, H. Masui, F. Wu, M. Saito, K. Fujito, J. S. Speck, S. P. DenBaars, and S. Nakamura, “Optical properties of yellow light-emitting diodes grown on semipolar (11-22) bulk GaN substrates,” *Appl. Phys. Lett.*, vol. 92, no. 22, p. 221110, Jun. 2008.

[71] R. Sharma, P. M. Pattison, H. Masui, R. M. Farrell, T. J. Baker, B. A. Haskell, F. Wu, S. P. DenBaars, J. S. Speck, and S. Nakamura, “Demonstration of a semipolar (10-1-3) InGaN∕GaN green light emitting diode,” *Appl. Phys. Lett.*, vol. 87, no. 23, p. 231110, Dec. 2005.

[72] D. A. Browne, E. C. Young, J. R. Lang, C. A. Hurni, and J. S. Speck, “Indium and impurity incorporation in InGaN films on polar, nonpolar, and semipolar GaN orientations grown by ammonia molecular beam epitaxy,” *J. Vac. Sci. Technol. A*, vol. 30, no. 4, p. 041513, Jul. 2012.

[73] D. F. Feezell, J. S. Speck, S. P. DenBaars, and S. Nakamura, “Semipolar (20-2-1) InGaN/GaN Light-Emitting Diodes for High-Efficiency Solid-State Lighting,” *J. Disp. Technol.*, vol. 9, no. 4, pp. 190–198, Apr. 2013.

[74] A. Das, S. Magalhães, Y. Kotsar, P. K. Kandaswamy, B. Gayral, K. Lorenz, E. Alves, P. Ruterana, and E. Monroy, “Indium kinetics during the plasma-assisted molecular beam epitaxy of semipolar (11−22) InGaN layers,” *Appl. Phys. Lett.*, vol. 96, no. 18, p. 181907, May 2010.

[75] P. De Mierry, T. Guehne, M. Nemoz, S. Chenot, E. Beraudo, and G. Nataf, “Comparison between Polar (0001) and Semipolar (11-22) Nitride Blue–Green Light-Emitting Diodes Grown on *c* - and *m* -Plane Sapphire Substrates,” *Jpn. J. Appl. Phys.*, vol. 48, no. 3, p. 031002, Mar. 2009.

[76] R. Sharma, E. M. Hall, C. Poblenz, and M. P. D'Evelyn, "Solid state laser device using a selected crystal orientation in non-polar or semi-polar GaN containing materials and methods," US Patent # 8284810 B1, 09-Oct-2012.

[77] J. W. Raring, E. M. Hall, and M. P. D'Evelyn, "White light devices using non-polar or semipolar gallium containing materials and phosphors," US Patent # 20100025656 A1, 04-Feb-2010.

[78] F. Tendille, P. De Mierry, P. Vennéguès, S. Chenot, and M. Teisseire, "Defect reduction method in (11-22) semipolar GaN grown on patterned sapphire substrate by MOCVD: Toward heteroepitaxial semipolar GaN free of basal stacking faults," *J. Cryst. Growth*, vol. 404, pp. 177–183, Oct. 2014.

[79] F. Scholz, T. Meisch, M. Caliebe, S. Schörner, K. Thonke, L. Kirste, S. Bauer, S. Lazarev, and T. Baumbach, "Growth and doping of semipolar GaN grown on patterned sapphire substrates," *J. Cryst. Growth*, vol. 405, pp. 97–101, Nov. 2014.

[80] Y. Honda, N. Kameshiro, M. Yamaguchi, and N. Sawaki, "Growth of (1-101) GaN on a 7-degree off-oriented (0 0 1) Si substrate by selective MOVPE," *J. Cryst. Growth*, vol. 242, no. 1–2, pp. 82–86, Jul. 2002.

[81] N. Okada, A. Kurisu, K. Murakami, and K. Tadatomo, "Growth of Semipolar (11-22) GaN Layer by Controlling Anisotropic Growth Rates in r-Plane Patterned Sapphire Substrate," *Appl. Phys. Express*, vol. 2, no. 9, p. 091001, Sep. 2009.

[82] H.-G. Chen, T.-S. Ko, S.-C. Ling, T.-C. Lu, H.-C. Kuo, S.-C. Wang, Y.-H. Wu, and L. Chang, "Dislocation reduction in GaN grown on stripe patterned r-plane sapphire substrates," *Appl. Phys. Lett.*, vol. 91, no. 2, p. 021914, Jul. 2007.

[83] P. de Mierry, N. Kriouche, M. Nemoz, S. Chenot, and G. Nataf, "Semipolar GaN films on patterned r-plane sapphire obtained by wet chemical etching," *Appl. Phys. Lett.*, vol. 96, no. 23, p. 231918, Jun. 2010.

[84] B. Leung, Q. Sun, C. Yerino, Y. Zhang, J. Han, B. Hyun Kong, H. Koun Cho, K.-Y. Liao, and Y.-L. Li, "Growth evolution and microstructural characterization of semipolar (11-22) GaN selectively grown on etched r-plane sapphire," *J. Cryst. Growth*, vol. 341, no. 1, pp. 27–33, Feb. 2012.

[85] A. Kamgar, P. Kneschaurek, G. Dorda, and J. Koch, "Resonance Spectroscopy of Electronic Levels in a Surface Accumulation Layer," *Phys. Rev. Lett.*, vol. 32, no. 22, pp. 1251–1254, Jun. 1974.

[86] L. Esaki and H. Sakaki, "New Photoconductor," *IBM Tech. Discl. Bull.* vol. 20, pp. 2456–2457, 1977.

[87] L. C. West and S. J. Eglash, "First observation of an extremely large-dipole infrared transition within the conduction band of a GaAs quantum well," *Appl. Phys. Lett.*, vol. 46, no. 12, pp. 1156–1158, 1985.

[88] N. Suzuki and N. Iizuka, "Effect of Polarization Field on Intersubband Transition in AlGaN/GaN Quantum Wells," *Jpn. J. Appl. Phys.*, vol. 38, no. Part 2, No. 4A, pp. L363–L365, Apr. 1999.

[89] G. Bastard, *Wave mechanics applied to semiconductor heterostructures,* Halsted Press, 1988.

[90] A. M. Witowski, K. Pakuła, J. M. Baranowski, M. L. Sadowski, and P. Wyder, "Electron effective mass in hexagonal GaN," *Appl. Phys. Lett.*, vol. 75, no. 26, pp. 4154–4155, Dec. 1999.

[91] A. Raymond, J. L. Robert, and C. Bernard, "The electron effective mass in heavily doped GaAs," *J. Phys. C Solid State Phys.*, vol. 12, no. 12, p. 2289, Jun. 1979.

[92] R. A. Stradling and R. A. Wood, “The temperature dependence of the band-edge effective masses of InSb, InAs and GaAs as deduced from magnetophonon magnetoresistance measurements,” *J. Phys. C Solid State Phys.*, vol. 3, no. 5, p. L94, May 1970.

[93] P. K. Kandaswamy, H. Machhadani, Y. Kotsar, S. Sakr, A. Das, M. Tchernycheva, L. Rapenne, E. Sarigiannidou, F. H. Julien, and E. Monroy, “Effect of doping on the mid-infrared intersubband absorption in GaN/AlGaN superlattices grown on Si(111) templates,” *Appl. Phys. Lett.*, vol. 96, no. 14, p. 141903, 2010.

[94] W. L. Bloss, “Effects of Hartree, exchange, and correlation energy on intersubband transitions,” *J. Appl. Phys.*, vol. 66, no. 8, p. 3639, 1989.

[95] K. M. S. V. Bandara, D. D. Coon, B. O, Y. F. Lin, and M. H. Francombe, “Exchange interactions in quantum well subbands,” *Appl. Phys. Lett.*, vol. 53, no. 20, p. 1931, 1988.

[96] K. M. S. V. Bandara, D. D. Coon, B. O, Y. F. Lin, and M. H. Francombe, “Erratum: Exchange interactions in quantum well subbands [Appl. Phys. Lett. 53, 1931 (1988)],” *Appl. Phys. Lett.*, vol. 55, no. 2, p. 206, 1989.

[97] M. O. Manasreh, F. Szmulowicz, T. Vaughan, K. R. Evans, C. E. Stutz, and D. W. Fischer, “Origin of the blueshift in the intersubband infrared absorption in GaAs/$Al_{0.3}Ga_{0.7}As$ multiple quantum wells,” *Phys. Rev. B*, vol. 43, no. 12, pp. 9996–9999, Apr. 1991.

[98] N. Binggeli, P. Ferrara, and A. Baldereschi, “Band-offset trends in nitride heterojunctions,” *Phys. Rev. B*, vol. 63, no. 24, p. 245306, May 2001.

[99] D. Cociorva, W. G. Aulbur, and J. W. Wilkins, “Quasiparticle calculations of band offsets at AlN–GaN interfaces,” *Solid State Commun.*, vol. 124, no. 1–2, pp. 63–66, Sep. 2002.

[100] M. Tchernycheva, L. Nevou, L. Doyennette, F. Julien, E. Warde, F. Guillot, E. Monroy, E. Bellet-Amalric, T. Remmele, and M. Albrecht, “Systematic experimental and theoretical investigation of intersubband absorption in GaN∕AlN quantum wells,” *Phys. Rev. B*, vol. 73, no. 12, p. 125347, Mar. 2006.

[101] M. Hao, S. Mahanty, R. S. Qhalid Fareed, S. Tottori, K. Nishino, and S. Sakai, “Infrared properties of bulk GaN,” *Appl. Phys. Lett.*, vol. 74, no. 19, pp. 2788–2790, 1999.

[102] J. Yang, G. J. Brown, M. Dutta, and M. A. Stroscio, “Photon absorption in the Restrahlen band of thin films of GaN and AlN: Two phonon effects,” *J. Appl. Phys.*, vol. 98, no. 4, p. 043517, 2005.

[103] M. Welna, R. Kudrawiec, M. Motyka, R. Kucharski, M. Zając, M. Rudziński, J. Misiewicz, R. Doradziński, and R. Dwiliński, “Transparency of GaN substrates in the mid-infrared spectral range,” *Cryst. Res. Technol.*, vol. 47, no. 3, pp. 347–350, Mar. 2012.

[104] P. K. Kandaswamy, H. Machhadani, C. Bougerol, S. Sakr, M. Tchernycheva, F. H. Julien, and E. Monroy, “Midinfrared intersubband absorption in GaN/AlGaN superlattices on Si(111) templates,” *Appl. Phys. Lett.*, vol. 95, no. 14, p. 141911, 2009.

[105] P. K. Kandaswamy, H. Machhadani, Y. Kotsar, S. Sakr, A. Das, M. Tchernycheva, L. Rapenne, E. Sarigiannidou, F. H. Julien, and E. Monroy, “Effect of doping on the mid-infrared intersubband absorption in GaN/AlGaN superlattices grown on Si(111) templates,” *Appl. Phys. Lett.*, vol. 96, no. 14, p. 141903, 2010.

[106] F. H. Julien, M. Tchernycheva, L. Nevou, L. Doyennette, R. Colombelli, E. Warde, F. Guillot, and E. Monroy, “Nitride intersubband devices: prospects and recent developments,” *Phys. Status Solidi A*, vol. 204, no. 6, pp. 1987–1995, Jun. 2007.

[107] M. Razeghi, “III-Nitride Optoelectronic Devices: From Ultraviolet Toward Terahertz,” *IEEE Photonics J.*, vol. 3, no. 2, pp. 263–267, Apr. 2011.

[108] H. Machhadani, P. Kandaswamy, S. Sakr, A. Vardi, A. Wirtmüller, L. Nevou, F. Guillot, G. Pozzovivo, M. Tchernycheva, A. Lupu, L. Vivien, P. Crozat, E. Warde, C. Bougerol, S. Schacham, G. Strasser, G. Bahir, E. Monroy, and F. H. Julien, "GaN/AlGaN intersubband optoelectronic devices," *New J. Phys.*, vol. 11, no. 12, p. 125023, Dec. 2009.

[109] B. Gil, *III-Nitride Semiconductors and Their Modern Devices*, Oxford University Press, 2013.

[110] M. Tchernycheva, F. H. Julien, and E. Monroy, "Review of nitride infrared intersubband devices," 2010, vol. 7602, p. 76021A–76021A–12.

[111] C. Gmachl, H. M. Ng, and A. Y. Cho, "Intersubband absorption in GaN/AlGaN multiple quantum wells in the wavelength range λ∼1.75–4.2 μm," *Appl. Phys. Lett.*, vol. 77, no. 3, pp. 334–336, Jul. 2000.

[112] C. Gmachl, H. M. Ng, S.-N. George Chu, and A. Y. Cho, "Intersubband absorption at λ∼1.55 μm in well- and modulation-doped GaN/AlGaN multiple quantum wells with superlattice barriers," *Appl. Phys. Lett.*, vol. 77, no. 23, pp. 3722–3724, 2000.

[113] N. Iizuka, K. Kaneko, and N. Suzuki, "Near-infrared intersubband absorption in GaN/AlN quantum wells grown by molecular beam epitaxy," *Appl. Phys. Lett.*, vol. 81, no. 10, pp. 1803–1805, 2002.

[114] K. Kishino, A. Kikuchi, H. Kanazawa, and T. Tachibana, "Intersubband transition in $(GaN)_m/(AlN)_n$ superlattices in the wavelength range from 1.08 to 1.61 μm," *Appl. Phys. Lett.*, vol. 81, no. 7, pp. 1234–1236, 2002.

[115] A. Helman, M. Tchernycheva, A. Lusson, E. Warde, F. H. Julien, K. Moumanis, G. Fishman, E. Monroy, B. Daudin, D. Le Si Dang, E. Bellet-Amalric, and D. Jalabert, "Intersubband spectroscopy of doped and undoped GaN/AlN quantum wells grown by molecular-beam epitaxy," *Appl. Phys. Lett.*, vol. 83, no. 25, pp. 5196–5198, 2003.

[116] P. K. Kandaswamy, F. Guillot, E. Bellet-Amalric, E. Monroy, L. Nevou, M. Tchernycheva, A. Michon, F. H. Julien, E. Baumann, F. R. Giorgetta, D. Hofstetter, T. Remmele, M. Albrecht, S. Birner, and L. S. Dang, "GaN/AlN short-period superlattices for intersubband optoelectronics: A systematic study of their epitaxial growth, design, and performance," *J. Appl. Phys.*, vol. 104, no. 9, p. 093501, 2008.

[117] C. Bayram, N. Péré-laperne, and M. Razeghi, "Effects of well width and growth temperature on optical and structural characteristics of AlN/GaN superlattices grown by metal-organic chemical vapor deposition," *Appl. Phys. Lett.*, vol. 95, no. 20, p. 201906, 2009.

[118] T. G. Andersson, X. Y. Liu, T. Aggerstam, P. Holmström, S. Lourdudoss, L. Thylen, Y. L. Chen, C. H. Hsieh, and I. Lo, "Macroscopic defects in GaN/AlN multiple quantum well structures grown by MBE on GaN templates," *Microelectron. J.*, vol. 40, no. 2, pp. 360–362, Feb. 2009.

[119] X. Y. Liu, P. Holmström, P. Jänes, L. Thylén, and T. G. Andersson, "Intersubband absorption at 1.5–3.5 μm in GaN/AlN multiple quantum wells grown by molecular beam epitaxy on sapphire," *Phys. Status Solidi B*, vol. 244, no. 8, pp. 2892–2905, Aug. 2007.

[120] K. Berland, M. Stattin, R. Farivar, D. M. S. Sultan, P. Hyldgaard, A. Larsson, S. M. Wang, and T. G. Andersson, "Temperature stability of intersubband transitions in AlN/GaN quantum wells," *Appl. Phys. Lett.*, vol. 97, no. 4, p. 043507, 2010.

[121] B. Sherliker, M. Halsall, I. Kasalynas, D. Seliuta, G. Valusis, M. Vengris, M. Barkauskas, V. Sirutkaitis, P. Harrison, V. D. Jovanovic, D. Indjin, Z. Ikonic, P. J. Parbrook, T. Wang, and P. D. Buckle, "Room temperature operation of AlGaN/GaN quantum well infrared photodetectors at a 3–4 μm wavelength range," *Semicond. Sci. Technol.*, vol. 22, no. 11, pp. 1240–1244, Nov. 2007.

[122] N. Péré-Laperne, C. Bayram, L. Nguyen-The, R. McClintock, and M. Razeghi, “Tunability of intersubband absorption from 4.5 to 5.3 μm in a GaN/$Al_{0.2}Ga_{0.8}N$ superlattices grown by metalorganic chemical vapor deposition,” *Appl. Phys. Lett.*, vol. 95, no. 13, p. 131109, 2009.

[123] C. Bayram, “High-quality AlGaN/GaN superlattices for near- and mid-infrared intersubband transitions,” *J. Appl. Phys.*, vol. 111, no. 1, p. 013514, 2012.

[124] C. C. Huang, F. J. Xu, X. D. Yan, J. Song, Z. Y. Xu, L. B. Cen, Y. Wang, J. H. Pan, X. Q. Wang, Z. J. Yang, B. Shen, B. S. Zhang, X. S. Chen, and W. Lu, “Intersubband transitions at atmospheric window in $Al_xGa_{1-x}N$/GaN multiple quantum wells grown on GaN/sapphire templates adopting AlN/GaN superlattices interlayer,” *Appl. Phys. Lett.*, vol. 98, no. 13, p. 132105, 2011.

[125] P. K. Kandaswamy, H. Machhadani, C. Bougerol, S. Sakr, M. Tchernycheva, F. H. Julien, and E. Monroy, “Midinfrared intersubband absorption in GaN/AlGaN superlattices on Si(111) templates,” *Appl. Phys. Lett.*, vol. 95, no. 14, p. 141911, 2009.

[126] T. Kotani, M. Arita, and Y. Arakawa, “Observation of mid-infrared intersubband absorption in non-polar m-plane AlGaN/GaN multiple quantum wells,” *Appl. Phys. Lett.*, vol. 105, no. 26, p. 261108, Dec. 2014.

[127] H. Machhadani, Y. Kotsar, S. Sakr, M. Tchernycheva, R. Colombelli, J. Mangeney, E. Bellet-Amalric, E. Sarigiannidou, E. Monroy, and F. H. Julien, “Terahertz intersubband absorption in GaN/AlGaN step quantum wells,” *Appl. Phys. Lett.*, vol. 97, no. 19, p. 191101, 2010.

[128] N. Iizuka, K. Kaneko, and N. Suzuki, “All-Optical Switch Utilizing Intersubband Transition in GaN Quantum Wells,” *IEEE J. Quantum Electron.*, vol. 42, no. 8, pp. 765–771, Aug. 2006.

[129] D. Hofstetter, S.-S. Schad, H. Wu, W. J. Schaff, and L. F. Eastman, “GaN/AlN-based quantum-well infrared photodetector for 1.55 μm,” *Appl. Phys. Lett.*, vol. 83, no. 3, pp. 572–574, Jul. 2003.

[130] E. Baumann, F. R. Giorgetta, D. Hofstetter, H. Lu, X. Chen, W. J. Schaff, L. F. Eastman, S. Golka, W. Schrenk, and G. Strasser, “Intersubband photoconductivity at 1.6 μm using a strain-compensated AlN∕GaN superlattice,” *Appl. Phys. Lett.*, vol. 87, no. 19, p. 191102, 2005.

[131] L. Doyennette, L. Nevou, M. Tchernycheva, A. Lupu, F. Guillot, E. Monroy, R. Colombelli, and F. H. Julien, “GaN-based quantum dot infrared photodetector operating at 1.38 μm,” *Electron. Lett.*, vol. 41, no. 19, pp. 1077 – 1078, Sep. 2005.

[132] A. Vardi, N. Akopian, G. Bahir, L. Doyennette, M. Tchernycheva, L. Nevou, F. H. Julien, F. Guillot, and E. Monroy, “Room temperature demonstration of GaN/AlN quantum dot intraband infrared photodetector at fiber-optics communication wavelength,” *Appl. Phys. Lett.*, vol. 88, no. 14, p. 143101, Apr. 2006.

[133] A. Vardi, G. Bahir, S. E. Schacham, P. K. Kandaswamy, and E. Monroy, “Photocurrent spectroscopy of bound-to-bound intraband transitions in GaN/AlN quantum dots,” *Phys. Rev. B*, vol. 80, no. 15, p. 155439, Oct. 2009.

[134] H. Machhadani, Y. Kotsar, S. Sakr, M. Tchernycheva, R. Colombelli, J. Mangeney, E. Bellet-Amalric, E. Sarigiannidou, E. Monroy, and F. H. Julien, “Terahertz intersubband absorption in GaN/AlGaN step quantum wells,” *Appl. Phys. Lett.*, vol. 97, no. 19, pp. 191101–191101–3, Nov. 2010.

[135] Y. Li, A. Bhattacharyya, C. Thomidis, T. D. Moustakas, and R. Paiella, “Ultrafast all-optical switching with low saturation energy via intersubband transitions in GaN/AlN quantum-well waveguides,” *Opt. Express*, vol. 15, no. 26, pp. 17922–17927, 2007.

[136] L. Monteagudo-Lerma, S. Valdueza-Felip, F. B. Naranjo, P. Corredera, L. Rapenne, E. Sarigiannidou, G. Strasser, E. Monroy, and M. González-Herráez, “Waveguide saturable

absorbers at 155 µm based on intraband transitions in GaN/AlN QDs," *Opt. Express*, vol. 21, no. 23, p. 27578, Nov. 2013.

[137] N. Iizuka, H. Yoshida, N. Managaki, T. Shimizu, S. Hassanet, C. Cumtornkittikul, M. Sugiyama, and Y. Nakano, "Integration of GaN/AlN all-optical switch with SiN/AlN waveguide utilizing spot-size conversion," *Opt. Express*, vol. 17, no. 25, pp. 23247–23253, Dec. 2009.

[138] L. Nevou, J. Mangeney, M. Tchernycheva, F. H. Julien, F. Guillot, and E. Monroy, "Ultrafast relaxation and optical saturation of intraband absorption of GaN/AlN quantum dots," *Appl. Phys. Lett.*, vol. 94, no. 13, p. 132104, 2009.

[139] M. Tchernycheva, L. Nevou, L. Doyennette, F. H. Julien, F. Guillot, E. Monroy, T. Remmele, and M. Albrecht, "Electron confinement in strongly coupled GaN∕AlN quantum wells," *Appl. Phys. Lett.*, vol. 88, no. 15, p. 153113, 2006.

[140] N. Kheirodin, L. Nevou, H. Machhadani, P. Crozat, L. Vivien, M. Tchernycheva, A. Lupu, F. H. Julien, G. Pozzovivo, S. Golka, G. Strasser, F. Guillot, and E. Monroy, "Electrooptical Modulator at Telecommunication Wavelengths Based on GaN/AlN Coupled Quantum Wells," *IEEE Photonics Technol. Lett.*, vol. 20, no. 9, pp. 724–726, May 2008.

[141] L. Nevou, F. H. Julien, R. Colombelli, F. Guillot, and E. Monroy, "Room-temperature intersubband emission of GaN/AlN quantum wells at λ=2.3 µm," *Electron. Lett.*, vol. 42, no. 22, pp. 1308–1309, 2006.

[142] L. Nevou, M. Tchernycheva, F. H. Julien, F. Guillot, and E. Monroy, "Short wavelength (λ=2.13 µm) intersubband luminescence from GaN∕AlN quantum wells at room temperature," *Appl. Phys. Lett.*, vol. 90, no. 12, p. 121106, 2007.

[143] K. Driscoll, Y. Liao, A. Bhattacharyya, L. Zhou, D. J. Smith, T. D. Moustakas, and R. Paiella, "Optically pumped intersubband emission of short-wave infrared radiation with GaN/AlN quantum wells," *Appl. Phys. Lett.*, vol. 94, no. 8, p. 081120, 2009.

[144] L. Nevou, F. H. Julien, M. Tchernycheva, F. Guillot, E. Monroy, and E. Sarigiannidou, "Intraband emission at λ≈1.48 µm from GaN∕AlN quantum dots at room temperature," *Appl. Phys. Lett.*, vol. 92, no. 16, p. 161105, 2008.

[145] A. Vardi, G. Bahir, F. Guillot, C. Bougerol, E. Monroy, S. E. Schacham, M. Tchernycheva, and F. H. Julien, "Near infrared quantum cascade detector in GaN/AlGaN/AlN heterostructures," *Appl. Phys. Lett.*, vol. 92, no. 1, p. 011112, Jan. 2008.

[146] A. Vardi, N. Kheirodin, L. Nevou, H. Machhadani, L. Vivien, P. Crozat, M. Tchernycheva, R. Colombelli, F. H. Julien, F. Guillot, C. Bougerol, E. Monroy, S. Schacham, and G. Bahir, "High-speed operation of GaN/AlGaN quantum cascade detectors at λ ≈ 1.55 µm," *Appl. Phys. Lett.*, vol. 93, no. 19, p. 193509, Nov. 2008.

[147] M. J. Almond, C. E. Jenkins, D. A. Rice, and K. Hagen, "Organometallic precursors to the formation of GaN by MOCVD: structural characterisation of $Me_3Ga \cdot NH_3$ by gas-phase electron diffraction," *J. Organomet. Chem.*, vol. 439, no. 3, pp. 251–261, Nov. 1992.

[148] E. V. Etzkorn and D. R. Clarke, "Cracking of GaN films," *J. Appl. Phys.*, vol. 89, no. 2, pp. 1025–1034, Jan. 2001.

[149] D. Kapolnek, X. H. Wu, B. Heying, S. Keller, B. P. Keller, U. K. Mishra, S. P. DenBaars, and J. S. Speck, "Structural evolution in epitaxial metalorganic chemical vapor deposition grown GaN films on sapphire," *Appl. Phys. Lett.*, vol. 67, no. 11, pp. 1541–1543, Sep. 1995.

[150] G. Martinez-Criado, M. Kuball, M. Benyoucef, A. Sarua, E. Frayssinet, B. Beaumont, P. Gibart, C. R. Miskys, and M. Stutzmann, “Free-standing GaN grown on epitaxial lateral overgrown GaN substrates,” *J. Cryst. Growth*, vol. 255, no. 3–4, pp. 277–281, Aug. 2003.

[151] R. J. Molnar, W. Götz, L. T. Romano, and N. M. Johnson, “Growth of gallium nitride by hydride vapor-phase epitaxy,” *J. Cryst. Growth*, vol. 178, no. 1–2, pp. 147–156, Jun. 1997.

[152] E. Richter, C. Hennig, M. Weyers, F. Habel, J.-D. Tsay, W.-Y. Liu, P. Brückner, F. Scholz, Y. Makarov, A. Segal, and J. Kaeppeler, “Reactor and growth process optimization for growth of thick GaN layers on sapphire substrates by HVPE,” *J. Cryst. Growth*, vol. 277, no. 1–4, pp. 6–12, Apr. 2005.

[153] M. K. Kelly, R. P. Vaudo, V. M. Phanse, L. Görgens, O. Ambacher, and M. Stutzmann, “Large Free-Standing GaN Substrates by Hydride Vapor Phase Epitaxy and Laser-Induced Liftoff,” *Jpn. J. Appl. Phys.*, vol. 38, no. 3A, p. L217, Mar. 1999.

[154] K. Motoki, T. Okahisa, N. Matsumoto, M. Matsushima, H. Kimura, H. Kasai, K. Takemoto, K. Uematsu, T. Hirano, M. Nakayama, S. Nakahata, M. Ueno, D. Hara, Y. Kumagai, A. Koukitu, and H. Seki, “Preparation of Large Freestanding GaN Substrates by Hydride Vapor Phase Epitaxy Using GaAs as a Starting Substrate,” *Jpn. J. Appl. Phys.*, vol. 40, no. 2B, p. L140, Feb. 2001.

[155] X. Xu, R. . Vaudo, C. Loria, A. Salant, G. . Brandes, and J. Chaudhuri, “Growth and characterization of low defect GaN by hydride vapor phase epitaxy,” *J. Cryst. Growth*, vol. 246, no. 3–4, pp. 223–229, Dec. 2002.

[156] R. Held, D. E. Crawford, A. M. Johnston, A. M. Dabiran, and P. I. Cohen, “In situ control of GaN growth by molecular beam epitaxy,” *J. Electron. Mater.*, vol. 26, no. 3, pp. 272–280, Mar. 1997.

[157] J. W. Shon, J. Ohta, K. Ueno, A. Kobayashi, and H. Fujioka, “Fabrication of full-color InGaN-based light-emitting diodes on amorphous substrates by pulsed sputtering,” *Sci. Rep.*, vol. 4, Jun. 2014.

[158] A. Dussaigne, B. Damilano, N. Grandjean, and J. Massies, “Indium surface segregation in InGaN/GaN quantum wells,” in *2002 International Conference on Molecular Beam Epitaxy*, 2002, pp. 151–152.

[159] Y. Nanishi, Y. Saito, and T. Yamaguchi, “RF-Molecular Beam Epitaxy Growth and Properties of InN and Related Alloys,” *Jpn. J. Appl. Phys.*, vol. 42, no. 5R, p. 2549, May 2003.

[160] C. Adelmann, J. Brault, G. Mula, B. Daudin, L. Lymperakis, and J. Neugebauer, “Gallium adsorption on (0001) GaN surfaces,” *Phys. Rev. B*, vol. 67, no. 16, p. 165419, Apr. 2003.

[161] J. Neugebauer, T. Zywietz, M. Scheffler, J. Northrup, H. Chen, and R. Feenstra, “Adatom Kinetics On and Below the Surface: The Existence of a New Diffusion Channel,” *Phys. Rev. Lett.*, vol. 90, no. 5, p. 056101, Feb. 2003.

[162] B. Heying, R. Averbeck, L. F. Chen, E. Haus, H. Riechert, and J. S. Speck, “Control of GaN surface morphologies using plasma-assisted molecular beam epitaxy,” *J. Appl. Phys.*, vol. 88, no. 4, pp. 1855–1860, 2000.

[163] E. Iliopoulos and T. D. Moustakas, “Growth kinetics of AlGaN films by plasma-assisted molecular-beam epitaxy,” *Appl. Phys. Lett.*, vol. 81, no. 2, pp. 295–297, 2002.

[164] E. Monroy, B. Daudin, E. Bellet-Amalric, N. Gogneau, D. Jalabert, F. Enjalbert, J. Brault, J. Barjon, and L. S. Dang, “Surfactant effect of In for AlGaN growth by plasma-assisted molecular beam epitaxy,” *J. Appl. Phys.*, vol. 93, no. 3, pp. 1550–1556, 2003.

[165] G. Koblmueller, R. Averbeck, L. Geelhaar, H. Riechert, W. Hösler, and P. Pongratz, “Growth diagram and morphologies of AlN thin films grown by molecular beam epitaxy,” *J. Appl. Phys.*, vol. 93, no. 12, pp. 9591–9597, 2003.

[166] G. Mula, C. Adelmann, S. Moehl, J. Oullier, and B. Daudin, “Surfactant effect of gallium during molecular-beam epitaxy of GaN on AlN (0001),” *Phys. Rev. B*, vol. 64, no. 19, p. 195406, Oct. 2001.

[167] P. K. Kandaswamy, F. Guillot, E. Bellet-Amalric, E. Monroy, L. Nevou, M. Tchernycheva, A. Michon, F. H. Julien, E. Baumann, F. R. Giorgetta, D. Hofstetter, T. Remmele, M. Albrecht, S. Birner, and L. S. Dang, “GaN/AlN short-period superlattices for intersubband optoelectronics: A systematic study of their epitaxial growth, design, and performance,” *J. Appl. Phys.*, vol. 104, no. 9, p. 093501, 2008.

[168] J. Northrup, J. Neugebauer, R. Feenstra, and A. Smith, “Structure of GaN(0001): The laterally contracted Ga bilayer model,” *Phys. Rev. B*, vol. 61, no. 15, pp. 9932–9935, Apr. 2000.

[169] A. R. Smith, R. M. Feenstra, D. W. Greve, M. S. Shin, M. Skowronski, J. Neugebauer, and J. E. Northrup, “Reconstructions of GaN(0001) and $(000\bar{1})$ surfaces: Ga-rich metallic structures,” *J. Vac. Sci. Technol. B*, vol. 16, no. 4, pp. 2242–2249, Jul. 1998.

[170] A. R. Smith, V. Ramachandran, R. M. Feenstra, D. W. Greve, A. Ptak, T. Myers, W. Sarney, L. Salamanca-Riba, M. Shin, and M. Skowronski, “Surface Reconstruction during Molecular Beam Epitaxial Growth of GaN (0001),” *MRS Internet J. Nitride Semicond. Res.*, vol. 3, Jan. 1998.

[171] T. Zywietz, J. Neugebauer, and M. Scheffler, “Adatom diffusion at GaN (0001) and $(000\bar{1})$ surfaces,” *Appl. Phys. Lett.*, vol. 73, no. 4, pp. 487–489, Jul. 1998.

[172] E. Monroy, B. Daudin, E. Bellet-Amalric, N. Gogneau, D. Jalabert, F. Enjalbert, J. Brault, J. Barjon, and L. S. Dang, “Surfactant effect of In for AlGaN growth by plasma-assisted molecular beam epitaxy,” *J. Appl. Phys.*, vol. 93, no. 3, pp. 1550–1556, 2003.

[173] M. Yoshizawa, A. Kikuchi, M. Mori, N. Fujita, and K. Kishino, “Growth of Self-Organized GaN Nanostructures on Al_2O_3(0001) by RF-Radical Source Molecular Beam Epitaxy,” *Jpn. J. Appl. Phys.*, vol. 36, no. 4B, p. L459, Apr. 1997.

[174] M. Yoshizawa, A. Kikuchi, N. Fujita, K. Kushi, H. Sasamoto, and K. Kishino, “Self-organization of GaN/$Al_{0.18}Ga_{0.82}N$ multi-layer nano-columns on (0001) Al_2O_3 by RF molecular beam epitaxy for fabricating GaN quantum disks,” *J. Cryst. Growth*, vol. 189–190, pp. 138–141, Jun. 1998.

[175] M. A. Sánchez-García, F. J. Sánchez, F. B. Naranjo, F. Calle, E. Calleja, E. Muñoz, U. Jahn, and K. H. Ploog, “Crystal Morphology and Optical Emissions of GaN layers grown on Si(111) substrates by Molecular Beam Epitaxy,” *MRS Internet J. Nitride Semicond. Res.*, vol. 3, Jan. 1998.

[176] J. Schörmann, P. Hille, M. Schäfer, J. Müßener, P. Becker, P. J. Klar, M. Kleine-Boymann, M. Rohnke, M. de la Mata, J. Arbiol, D. M. Hofmann, J. Teubert, and M. Eickhoff, “Germanium doping of self-assembled GaN nanowires grown by plasma-assisted molecular beam epitaxy,” *J. Appl. Phys.*, vol. 114, no. 10, p. 103505, 2013.

[177] F. Furtmayr, M. Vielemeyer, M. Stutzmann, J. Arbiol, S. Estradé, F. Peirò, J. R. Morante, and M. Eickhoff, “Nucleation and growth of GaN nanorods on Si (111) surfaces by plasma-assisted molecular beam epitaxy - The influence of Si- and Mg-doping,” *J. Appl. Phys.*, vol. 104, no. 3, p. 034309, Aug. 2008.

[178] F. Furtmayr, J. Teubert, P. Becker, S. Conesa-Boj, J. R. Morante, A. Chernikov, S. Schäfer, S. Chatterjee, J. Arbiol, and M. Eickhoff, “Carrier confinement in GaN/$Al_xGa_{1-x}N$ nanowire heterostructures ($0<x\leq1$),” *Phys. Rev. B*, vol. 84, no. 20, p. 205303, Nov. 2011.

[179] S. Fernández-Garrido, J. Grandal, E. Calleja, M. A. Sánchez-García, and D. López-Romero, "A growth diagram for plasma-assisted molecular beam epitaxy of GaN nanocolumns on Si(111)," *J. Appl. Phys.*, vol. 106, p. 6102, Dec. 2009.

[180] R. Songmuang, O. Landré, and B. Daudin, "From nucleation to growth of catalyst-free GaN nanowires on thin AlN buffer layer," *Appl. Phys. Lett.*, vol. 91, no. 25, p. 251902, Dec. 2007.

[181] E. Calleja, M. A. Sánchez-García, F. J. Sánchez, F. Calle, F. B. Naranjo, E. Muñoz, U. Jahn, and K. Ploog, "Luminescence properties and defects in GaN nanocolumns grown by molecular beam epitaxy," *Phys. Rev. B*, vol. 62, no. 24, pp. 16826–16834, Dec. 2000.

[182] S. Fernández-Garrido, X. Kong, T. Gotschke, R. Calarco, L. Geelhaar, A. Trampert, and O. Brandt, "Spontaneous Nucleation and Growth of GaN Nanowires: The Fundamental Role of Crystal Polarity," *Nano Lett.*, vol. 12, no. 12, pp. 6119–6125, Dec. 2012.

[183] M. Korytov, M. Benaissa, J. Brault, T. Huault, T. Neisius, and P. Vennéguès, "Effects of capping on GaN quantum dots deposited on $Al_{0.5}Ga_{0.5}N$ by molecular beam epitaxy," *Appl. Phys. Lett.*, vol. 94, no. 14, p. 143105, Apr. 2009.

[184] M. Arlery, J. L. Rouvière, F. Widmann, B. Daudin, G. Feuillet, and H. Mariette, "Quantitative characterization of GaN quantum-dot structures in AlN by high-resolution transmission electron microscopy," *Appl. Phys. Lett.*, vol. 74, no. 22, pp. 3287–3289, May 1999.

[185] R. K. Debnath, R. Meijers, T. Richter, T. Stoica, R. Calarco, and H. Lüth, "Mechanism of molecular beam epitaxy growth of GaN nanowires on Si(111)," *Appl. Phys. Lett.*, vol. 90, no. 12, p. 123117, Mar. 2007.

[186] R. Calarco, R. J. Meijers, R. K. Debnath, T. Stoica, E. Sutter, and H. Lüth, "Nucleation and Growth of GaN Nanowires on Si(111) Performed by Molecular Beam Epitaxy," *Nano Lett.*, vol. 7, no. 8, pp. 2248–2251, Aug. 2007.

[187] J. Ristić, E. Calleja, S. Fernández-Garrido, L. Cerutti, A. Trampert, U. Jahn, and K. H. Ploog, "On the mechanisms of spontaneous growth of III-nitride nanocolumns by plasma-assisted molecular beam epitaxy," *J. Cryst. Growth*, vol. 310, no. 18, pp. 4035–4045, Aug. 2008.

[188] R. Songmuang, T. Ben, B. Daudin, D. González, and E. Monroy, "Identification of III–N nanowire growth kinetics via a marker technique," *Nanotechnology*, vol. 21, no. 29, p. 295605, Jul. 2010.

[189] L. Lymperakis and J. Neugebauer, "Large anisotropic adatom kinetics on nonpolar GaN surfaces: Consequences for surface morphologies and nanowire growth," *Phys. Rev. B*, vol. 79, no. 24, p. 241308, Jun. 2009.

[190] J. Ristić, E. Calleja, M. Sánchez-García, J. Ulloa, J. Sánchez-Páramo, J. Calleja, U. Jahn, A. Trampert, and K. Ploog, "Characterization of GaN quantum discs embedded in $Al_xGa_{1-x}N$ nanocolumns grown by molecular beam epitaxy," *Phys. Rev. B*, vol. 68, no. 12, Sep. 2003.

[191] J. Ristić, E. Calleja, A. Trampert, S. Fernández-Garrido, C. Rivera, U. Jahn, and K. H. Ploog, "Columnar AlGaN/GaN Nanocavities with AlN/GaN Bragg Reflectors Grown by Molecular Beam Epitaxy on Si(111)," *Phys. Rev. Lett.*, vol. 94, no. 14, p. 146102, Apr. 2005.

[192] J. Ristić, E. Calleja, S. Fernández-Garrido, A. Trampert, U. Jahn, K. H. Ploog, M. Povoloskyi, and A. D. Carlo, "GaN/AlGaN nanocavities with AlN/GaN Bragg reflectors grown in AlGaN nanocolumns by plasma assisted MBE," *Phys. Status Solidi A*, vol. 202, no. 3, pp. 367–371, Feb. 2005.

[193] R. Songmuang, G. Katsaros, E. Monroy, P. Spathis, C. Bougerol, M. Mongillo, and S. De Franceschi, "Quantum Transport in GaN/AlN Double-Barrier Heterostructure Nanowires," *Nano Lett.*, vol. 10, no. 9, pp. 3545–3550, Sep. 2010.

[194] N. Grandjean, J. Massies, F. Semond, S. Y. Karpov, and R. A. Talalaev, “GaN evaporation in molecular-beam epitaxy environment,” *Appl. Phys. Lett.*, vol. 74, no. 13, pp. 1854–1856, Mar. 1999.

[195] A. J. Ptak, M. R. Millecchia, T. H. Myers, K. S. Ziemer, and C. D. Stinespring, “The relation of active nitrogen species to high-temperature limitations for $(000\bar{1})$ GaN growth by radio-frequency-plasma-assisted molecular beam epitaxy,” *Appl. Phys. Lett.*, vol. 74, no. 25, pp. 3836–3838, Jun. 1999.

[196] S. D. Carnevale, J. Yang, P. J. Phillips, M. J. Mills, and R. C. Myers, “Three-Dimensional GaN/AlN Nanowire Heterostructures by Separating Nucleation and Growth Processes,” *Nano Lett.*, vol. 11, no. 2, pp. 866–871, Feb. 2011.

[197] H. M. Ng, “Molecular-beam epitaxy of GaN/$Al_xGa_{1-x}N$ multiple quantum wells on R-plane $(10\bar{1}2)$ sapphire substrates,” *Appl. Phys. Lett.*, vol. 80, no. 23, pp. 4369–4371, Jun. 2002.

[198] M. D. Craven, S. H. Lim, F. Wu, J. S. Speck, and S. P. DenBaars, “Structural characterization of nonpolar (1120) a-plane GaN thin films grown on $(1\bar{1}02)$ r-plane sapphire,” *Appl. Phys. Lett.*, vol. 81, no. 3, pp. 469–471, Jul. 2002.

[199] M. D. Craven, S. H. Lim, F. Wu, J. S. Speck, and S. P. DenBaars, “Threading dislocation reduction via laterally overgrown nonpolar (11-20) a-plane GaN,” *Appl. Phys. Lett.*, vol. 81, no. 7, pp. 1201–1203, Aug. 2002.

[200] B. A. Haskell, F. Wu, M. D. Craven, S. Matsuda, P. T. Fini, T. Fujii, K. Fujito, S. P. DenBaars, J. S. Speck, and S. Nakamura, “Defect reduction in (11-20) a-plane gallium nitride via lateral epitaxial overgrowth by hydride vapor-phase epitaxy,” *Appl. Phys. Lett.*, vol. 83, no. 4, pp. 644–646, Jul. 2003.

[201] B. A. Haskell, F. Wu, S. Matsuda, M. D. Craven, P. T. Fini, S. P. DenBaars, J. S. Speck, and S. Nakamura, “Structural and morphological characteristics of planar (1120) a-plane gallium nitride grown by hydride vapor phase epitaxy,” *Appl. Phys. Lett.*, vol. 83, no. 8, pp. 1554–1556, Aug. 2003.

[202] M. D. Craven, F. Wu, A. Chakraborty, B. Imer, U. K. Mishra, S. P. DenBaars, and J. S. Speck, “Microstructural evolution of a-plane GaN grown on a-plane SiC by metalorganic chemical vapor deposition,” *Appl. Phys. Lett.*, vol. 84, no. 8, pp. 1281–1283, Feb. 2004.

[203] N. F. Gardner, J. C. Kim, J. J. Wierer, Y. C. Shen, and M. R. Krames, “Polarization anisotropy in the electroluminescence of m-plane InGaN–GaN multiple-quantum-well light-emitting diodes,” *Appl. Phys. Lett.*, vol. 86, no. 11, p. 111101, Mar. 2005.

[204] K. Fujito, S. Kubo, H. Nagaoka, T. Mochizuki, H. Namita, and S. Nagao, “Bulk GaN crystals grown by HVPE,” *J. Cryst. Growth*, vol. 311, no. 10, pp. 3011–3014, May 2009.

[205] R. M. Farrell, E. C. Young, F. Wu, S. P. DenBaars, and J. S. Speck, “Materials and growth issues for high-performance nonpolar and semipolar light-emitting devices,” *Semicond. Sci. Technol.*, vol. 27, no. 2, p. 024001, Feb. 2012.

[206] R. M. Farrell, D. A. Haeger, X. Chen, C. S. Gallinat, R. W. Davis, M. Cornish, K. Fujito, S. Keller, S. P. DenBaars, S. Nakamura, and J. S. Speck, “Origin of pyramidal hillocks on GaN thin films grown on free-standing m-plane GaN substrates,” *Appl. Phys. Lett.*, vol. 96, no. 23, p. 231907, Jun. 2010.

[207] A. Hirai, Z. Jia, M. C. Schmidt, R. M. Farrell, S. P. DenBaars, S. Nakamura, J. S. Speck, and K. Fujito, “Formation and reduction of pyramidal hillocks on m-plane {1-100} GaN,” *Appl. Phys. Lett.*, vol. 91, no. 19, p. 191906, Nov. 2007.

[208] R. M. Farrell, D. A. Haeger, X. Chen, M. Iza, A. Hirai, K. M. Kelchner, K. Fujito, A. Chakraborty, S. Keller, S. P. DenBaars, J. S. Speck, and S. Nakamura, “Effect of carrier gas and substrate misorientation on the structural and optical properties of m-plane InGaN/GaN light-emitting diodes,” *J. Cryst. Growth*, vol. 313, no. 1, pp. 1–7, Dec. 2010.

[209] Y.-D. Lin, M. T. Hardy, P. S. Hsu, K. M. Kelchner, C.-Y. Huang, D. A. Haeger, R. M. Farrell, K. Fujito, A. Chakraborty, H. Ohta, J. S. Speck, S. P. DenBaars, and S. Nakamura, “Blue-Green InGaN/GaN Laser Diodes on Miscut m-Plane GaN Substrate,” *Appl. Phys. Express*, vol. 2, no. 8, p. 082102, Aug. 2009.

[210] R. Liu, A. Bell, F. A. Ponce, C. Q. Chen, J. W. Yang, and M. A. Khan, “Luminescence from stacking faults in gallium nitride,” *Appl. Phys. Lett.*, vol. 86, no. 2, p. 021908, Jan. 2005.

[211] T. J. Baker, B. A. Haskell, F. Wu, P. T. Fini, J. S. Speck, and S. Nakamura, “Characterization of Planar Semipolar Gallium Nitride Films on Spinel Substrates,” *Jpn. J. Appl. Phys.*, vol. 44, no. 7L, p. L920, Jul. 2005.

[212] S. Founta, F. Rol, E. Bellet-Amalric, J. Bleuse, B. Daudin, B. Gayral, H. Mariette, and C. Moisson, “Optical properties of GaN quantum dots grown on nonpolar (11-20) SiC by molecular-beam epitaxy,” *Appl. Phys. Lett.*, vol. 86, no. 17, p. 171901, Apr. 2005.

[213] M. McLaurin, B. Haskell, S. Nakamura, and J. S. Speck, “Gallium adsorption onto (11-20) gallium nitride surfaces,” *J. Appl. Phys.*, vol. 96, no. 1, pp. 327–334, Jul. 2004.

[214] J. E. Northrup and J. Neugebauer, “Theory of GaN (10-10) and (11-20) surfaces,” *Phys. Rev. B*, vol. 53, no. 16, pp. R10477–R10480, Apr. 1996.

[215] L. Lahourcade, J. Renard, B. Gayral, E. Monroy, M. P. Chauvat, and P. Ruterana, “Ga kinetics in plasma-assisted molecular-beam epitaxy of GaN(11-22): Effect on the structural and optical properties,” *J. Appl. Phys.*, vol. 103, no. 9, p. 093514, 2008.

[216] T. J. Baker, B. A. Haskell, F. Wu, J. S. Speck, and S. Nakamura, “Characterization of Planar Semipolar Gallium Nitride Films on Sapphire Substrates,” *Jpn. J. Appl. Phys.*, vol. 45, no. 2L, p. L154, Feb. 2006.

[217] A. Chakraborty, T. J. Baker, B. A. Haskell, F. Wu, J. S. Speck, S. P. Denbaars, S. Nakamura, and U. K. Mishra, “Milliwatt Power Blue InGaN/GaN Light-Emitting Diodes on Semipolar GaN Templates,” *Jpn. J. Appl. Phys.*, vol. 44, no. 7L, p. L945, Jul. 2005.

[218] M. Tchernycheva, L. Nevou, L. Doyennette, F. Julien, E. Warde, F. Guillot, E. Monroy, E. Bellet-Amalric, T. Remmele, and M. Albrecht, “Systematic experimental and theoretical investigation of intersubband absorption in GaN∕AlN quantum wells,” *Phys. Rev. B*, vol. 73, no. 12, p. 125347, Mar. 2006.

[219] S.-H. Park, “Crystal Orientation Effects on Electronic Properties of Wurtzite GaN/AlGaN Quantum Wells with Spontaneous and Piezoelectric Polarization,” *Jpn. J. Appl. Phys.*, vol. 39, no. Part 1, No. 6A, pp. 3478–3482, Jun. 2000.

[220] P. Rinke, M. Winkelnkemper, A. Qteish, D. Bimberg, J. Neugebauer, and M. Scheffler, “Consistent set of band parameters for the group-III nitrides AlN, GaN, and InN,” *Phys. Rev. B*, vol. 77, no. 7, p. 075202, Feb. 2008.

[221] I. Horcas, R. Fernández, J. M. Gómez-Rodríguez, J. Colchero, J. Gómez-Herrero, and A. M. Baro, “WSXM: A software for scanning probe microscopy and a tool for nanotechnology,” *Rev. Sci. Instrum.*, vol. 78, no. 1, p. 013705, Jan. 2007.

[222] M. Tonouchi, “Cutting-edge terahertz technology,” *Nat. Photonics*, vol. 1, no. 2, pp. 97–105, Feb. 2007.

[223] R. Köhler, A. Tredicucci, F. Beltram, H. E. Beere, E. H. Linfield, A. G. Davies, D. A. Ritchie, R. C. Iotti, and F. Rossi, "Terahertz semiconductor-heterostructure laser," *Nature*, vol. 417, no. 6885, pp. 156–159, May 2002.

[224] G. Scalari, C. Walther, J. Faist, H. Beere, and D. Ritchie, "Electrically switchable, two-color quantum cascade laser emitting at 1.39 and 2.3THz," *Appl. Phys. Lett.*, vol. 88, no. 14, p. 141102, Apr. 2006.

[225] A. W. M. Lee, Q. Qin, S. Kumar, B. S. Williams, Q. Hu, and J. L. Reno, "Real-time terahertz imaging over a standoff distance (>25meters)," *Appl. Phys. Lett.*, vol. 89, no. 14, p. 141125, Oct. 2006.

[226] G. Scalari, C. Walther, M. Fischer, M. I. Amanti, R. Terazzi, and N. Hoyler, "Recent progress on long wavelength quantum cascade lasers between 1-2 THz," in *The 20th Annual Meeting of the IEEE Lasers and Electro-Optics Society, 2007. LEOS 2007*, pp. 755–756, 2007.

[227] K. Ohtani, M. Beck, and J. Faist, "Double metal waveguide InGaAs/AlInAs quantum cascade lasers emitting at 24 µm," *Appl. Phys. Lett.*, vol. 105, no. 12, p. 121115, Sep. 2014.

[228] S. Fathololoumi, E. Dupont, C. W. I. Chan, Z. R. Wasilewski, S. R. Laframboise, D. Ban, A. Mátyás, C. Jirauschek, Q. Hu, and H. C. Liu, "Terahertz quantum cascade lasers operating up to $\sim$ 200 K with optimized oscillator strength and improved injection tunneling," *Opt. Express*, vol. 20, no. 4, pp. 3866–3876, Feb. 2012.

[229] N. Horiuchi, "Quantum cascade lasers: Chasing room temperature," *Nat. Photonics*, vol. 6, no. 4, pp. 213–213, Apr. 2012.

[230] S. Kumar, Q. Hu, and J. L. Reno, "186 K operation of terahertz quantum-cascade lasers based on a diagonal design," *Appl. Phys. Lett.*, vol. 94, no. 13, p. 131105, Mar. 2009.

[231] L. Li, L. Chen, J. Zhu, J. Freeman, P. Dean, A. Valavanis, A. G. Davies, and E. H. Linfield, "Terahertz quantum cascade lasers with >1 W output powers," *Electron. Lett.*, vol. 50, no. 4, pp. 309–311, Feb. 2014.

[232] M. Razeghi, Q. Y. Lu, N. Bandyopadhyay, S. Slivken, and Y. Bai, "Room temperature continuous wave THz quantum cascade laser source with high power operation," 2014, vol. 9199, pp. 919902–919902–7.

[233] S. Adachi, "GaAs and related materials: bulk semiconduction and superlattice properties," *Singapore: World Scientific*, 1994.

[234] F. F. Sudradjat, W. Zhang, J. Woodward, H. Durmaz, T. D. Moustakas, and R. Paiella, "Far-infrared intersubband photodetectors based on double-step III-nitride quantum wells," *Appl. Phys. Lett.*, vol. 100, no. 24, p. 241113, Jun. 2012.

[235] B. S. Williams, "Terahertz quantum-cascade lasers," *Nat. Photonics*, vol. 1, no. 9, pp. 517–525, 2007.

[236] G. Scalari, N. Hoyler, M. Giovannini, and J. Faist, "Terahertz bound-to-continuum quantum-cascade lasers based on optical-phonon scattering extraction," *Appl. Phys. Lett.*, vol. 86, no. 18, p. 181101, May 2005.

[237] M. Rochat, D. Hofstetter, M. Beck, and J. Faist, "Long-wavelength (λ≈16 µm), room-temperature, single-frequency quantum-cascade lasers based on a bound-to-continuum transition," *Appl. Phys. Lett.*, vol. 79, no. 26, pp. 4271–4273, Dec. 2001.

[238] B. S. Williams, S. Kumar, H. Callebaut, Q. Hu, and J. L. Reno, "Terahertz quantum-cascade laser at λ≈100 µm using metal waveguide for mode confinement," *Appl. Phys. Lett.*, vol. 83, no. 11, pp. 2124–2126, Sep. 2003.

[239] Q. Hu, B. S. Williams, S. Kumar, H. Callebaut, S. Kohen, and J. L. Reno, "Resonant-phonon-assisted THz quantum-cascade lasers with metal–metal waveguides," *Semicond. Sci. Technol.*, vol. 20, no. 7, pp. S228–S236, Jul. 2005.

[240] M. A. Stroscio, M. Kisin, G. Belenky, and S. Luryi, "Phonon enhanced inverse population in asymmetric double quantum wells," *Appl. Phys. Lett.*, vol. 75, no. 21, pp. 3258–3260, Nov. 1999.

[241] B. S. Williams, B. Xu, Q. Hu, and M. R. Melloch, "Narrow-linewidth terahertz intersubband emission from three-level systems," *Appl. Phys. Lett.*, vol. 75, no. 19, pp. 2927–2929, Nov. 1999.

[242] B. S. Williams, H. Callebaut, Q. Hu, and J. L. Reno, "Magnetotunneling spectroscopy of resonant anticrossing in terahertz intersubband emitters," *Appl. Phys. Lett.*, vol. 79, no. 26, pp. 4444–4446, Dec. 2001.

[243] H. C. Liu and F. Capasso, *Intersubband transitions in quantum wells : Physics and device applications II*. San Diego, CA: Academic Press, 2000.

[244] V. D. Jovanović, D. Indjin, Z. Ikonić, and P. Harrison, "Simulation and design of GaN/AlGaN far-infrared ($\lambda \sim 34$ μm) quantum-cascade laser," *Appl. Phys. Lett.*, vol. 84, no. 16, pp. 2995–2997, Apr. 2004.

[245] P. Harrison, D. Indjin, V. D. Jovanović, A. Mirčetić, Z. Ikonić, R. W. Kelsall, J. McTavish, I. Savić, N. Vukmirović, and V. Milanović, "A physical model of quantum cascade lasers: Application to GaAs, GaN and SiGe devices," *Phys. Status Solidi A*, vol. 202, no. 6, pp. 980–986, 2005.

[246] E. Bellotti, K. Driscoll, T. D. Moustakas, and R. Paiella, "Monte Carlo simulation of terahertz quantum cascade laser structures based on wide-bandgap semiconductors," *J. Appl. Phys.*, vol. 105, no. 11, p. 113103, 2009.

[247] W. Terashima and H. Hirayama, "Design and fabrication of terahertz quantum cascade laser structure based on III-nitride semiconductors," *Phys. Status Solidi C*, vol. 6, no. S2, pp. S615–S618, 2009.

[248] W. Terashima and H. Hirayama, "Terahertz intersubband electroluminescence from GaN/AlGaN quantum cascade laser structure on AlGaN template," Proceedings in *2011 36th International Conference on Infrared, Millimeter and Terahertz Waves (IRMMW-THz)*, 2011.

[249] W. Terashima and H. Hirayama, "Molecular beam epitaxy growth of GaN/AlGaN quantum cascade structure using droplet elimination by thermal annealing technique," *Phys. Status Solidi A*, vol. 208, no. 5, pp. 1187–1190, 2011.

[250] B. Mirzaei, A. Rostami, and H. Baghban, "Terahertz dual-wavelength quantum cascade laser based on GaN active region," *Opt. Laser Technol.*, vol. 44, no. 2, pp. 378–383, Mar. 2012.

[251] A. Rostami, B. Mirzaei, and H. Baghban, "Two-wavelength THz quantum cascade laser with highly enhanced temperature characteristics," Proceedings in *Communications and Photonics Conference and Exhibition (ACP), 2009 Asia*, vol. 2009-Supplement, pp. 1 –8, 2009.

[252] H. Chou, M. Anwar, and T. Manzur, "Active layer design and power calculation of nitride-based THz quantum cascade lasers," *Proc. SPIE*, vol. 8268, p. 82680O, Jan. 2012.

[253] H. Chou, T. Manzur, and M. Anwar, "Active layer design of THz GaN quantum cascade lasers," *Proc. SPIE*, vol. 8023, p. 802309, May 2011.

[254] H. Yasuda, I. Hosako, and K. Hirakawa, "Designs of GaN-based terahertz quantum cascade lasers for higher temperature operations," in *2012 Conference on Lasers and Electro-Optics (CLEO)*, 2012.

[255] H. Yasuda, T. Kubis, and K. Hirakawa, “Non-equilibrium Green’s function calculation for GaN-based terahertz quantum cascade laser structures,” Proceedings in *2011 36th International Conference on Infrared, Millimeter and Terahertz Waves (IRMMW-THz)*, 2011.

[256] W. Terashima and H. Hirayama, “Design and fabrication of terahertz quantum cascade laser structure based on III-nitride semiconductors,” *Phys. Status Solidi C*, vol. 6, no. S2, pp. S615–S618, 2009.

[257] W. Terashima and H. Hirayama, “Spontaneous emission from GaN/AlGaN terahertz quantum cascade laser grown on GaN substrate,” *Phys. Status Solidi C*, vol. 8, no. 7–8, pp. 2302–2304, 2011.

[258] W. Terashima and H. Hirayama, “Terahertz intersubband electroluminescence from GaN/AlGaN quantum cascade laser structure on AlGaN template,” in *2011 36th International Conference on Infrared, Millimeter and Terahertz Waves (IRMMW-THz)*, p.1-2, 2011.

[259] W. Terashima and H. Hirayama, “The Utility of Droplet Elimination by Thermal Annealing Technique for Fabrication of GaN/AlGaN Terahertz Quantum Cascade Structure by Radio Frequency Molecular Beam Epitaxy,” *Appl. Phys. Express*, vol. 3, no. 12, p. 125501, 2010.

[260] H. Hirayama and W. Terashima, “Recent progress toward realizing GaN-based THz quantum cascade laser,” *Proc. SPIE*, vol. 8993, p. 89930G–89930G–9, 2013.

[261] K. Moumanis, A. Helman, F. Fossard, M. Tchernycheva, A. Lusson, F. H. Julien, B. Damilano, N. Grandjean, and J. Massies, “Intraband absorptions in GaN/AlN quantum dots in the wavelength range of 1.27–2.4 μm,” *Appl. Phys. Lett.*, vol. 82, no. 6, pp. 868–870, 2003.

[262] M. Tchernycheva, L. Nevou, L. Doyennette, A. Helman, R. Colombelli, F. H. Julien, F. Guillot, E. Monroy, T. Shibata, and M. Tanaka, “Intraband absorption of doped GaN∕AlN quantum dots at telecommunication wavelengths,” *Appl. Phys. Lett.*, vol. 87, no. 10, p. 101912, 2005.

[263] F. Guillot, E. Bellet-Amalric, E. Monroy, M. Tchernycheva, L. Nevou, L. Doyennette, F. H. Julien, L. S. Dang, T. Remmele, M. Albrecht, T. Shibata, and M. Tanaka, “Si-doped GaN∕AlN quantum dot superlattices for optoelectronics at telecommunication wavelengths,” *J. Appl. Phys.*, vol. 100, no. 4, p. 044326, 2006.

[264] Chia-Fu Hsu, Jeong-Seok O, P. Zory, and D. Botez, “Intersubband quantum-box semiconductor lasers,” *IEEE J. Sel. Top. Quantum Electron.*, vol. 6, no. 3, pp. 491–503, May 2000.

[265] E. A. Zibik, T. Grange, B. A. Carpenter, N. E. Porter, R. Ferreira, G. Bastard, D. Stehr, S. Winnerl, M. Helm, H. Y. Liu, M. S. Skolnick, and L. R. Wilson, “Long lifetimes of quantum-dot intersublevel transitions in the terahertz range,” *Nat. Mater.*, vol. 8, no. 10, pp. 803–807, Aug. 2009.

[266] M. Krall, M. Brandstetter, C. Deutsch, H. Detz, T. Zederbauer, A. M. Andrews, W. Schrenk, G. Strasser, and K. Unterrainer, “Towards nanowire-based terahertz quantum cascade lasers: prospects and technological challenges,” *Proc. SPIE*, vol. 8640, p. 864018-6, 2013.

[267] T. Grange, “Nanowire terahertz quantum cascade lasers,” *arXiv:1301.1258*, 2013.

[268] W. Lu and C. M. Lieber, “Nanoelectronics from the bottom up,” *Nat. Mater.*, vol. 6, no. 11, pp. 841–850, Nov. 2007.

[269] S. Deshpande, J. Heo, A. Das, and P. Bhattacharya, “Electrically driven polarized single-photon emission from an InGaN quantum dot in a GaN nanowire,” *Nat. Commun.*, vol. 4, p. 1675, Apr. 2013.

[270] Y. Nakayama, P. J. Pauzauskie, A. Radenovic, R. M. Onorato, R. J. Saykally, J. Liphardt, and P. Yang, “Tunable nanowire nonlinear optical probe,” *Nature*, vol. 447, no. 7148, pp. 1098–1101, Jun. 2007.

[271] W. Wu, X. Wen, and Z. L. Wang, “Taxel-Addressable Matrix of Vertical-Nanowire Piezotronic Transistors for Active and Adaptive Tactile Imaging,” *Science*, vol. 340, no. 6135, pp. 952–957, Apr. 2013.

[272] J. Wallentin, N. Anttu, D. Asoli, M. Huffman, I. Aberg, M. H. Magnusson, G. Siefer, P. Fuss-Kailuweit, F. Dimroth, B. Witzigmann, H. Q. Xu, L. Samuelson, K. Deppert, and M. T. Borgstrom, “InP Nanowire Array Solar Cells Achieving 13.8% Efficiency by Exceeding the Ray Optics Limit,” *Science*, vol. 339, no. 6123, pp. 1057–1060, Jan. 2013.

[273] Y. Cui, “Nanowire Nanosensors for Highly Sensitive and Selective Detection of Biological and Chemical Species,” *Science*, vol. 293, no. 5533, pp. 1289–1292, Aug. 2001.

[274] J. Wallys, J. Teubert, F. Furtmayr, D. M. Hofmann, and M. Eickhoff, “Bias-Enhanced Optical pH Response of Group III–Nitride Nanowires,” *Nano Lett.*, vol. 12, no. 12, pp. 6180–6186, Dec. 2012.

[275] J. Claudon, J. Bleuse, N. S. Malik, M. Bazin, P. Jaffrennou, N. Gregersen, C. Sauvan, P. Lalanne, and J.-M. Gérard, “A highly efficient single-photon source based on a quantum dot in a photonic nanowire,” *Nat. Photonics*, vol. 4, no. 3, pp. 174–177, Mar. 2010.

[276] G. Sun, R. Chen, Y. J. Ding, H. P. T. Nguyen, and Z. Mi, “InGaN/GaN dot-in-a-wire: ultimate terahertz nanostructure,” *Laser Photonics Rev.*, vol. 9, no. 1, pp. 105–113, 2015.

[277] M. J. Holmes, K. Choi, S. Kako, M. Arita, and Y. Arakawa, “Room-Temperature Triggered Single Photon Emission from a III-Nitride Site-Controlled Nanowire Quantum Dot,” *Nano Lett.*, vol. 14, no. 2, pp. 982–986, 2014.

[278] M. E. Reimer, G. Bulgarini, N. Akopian, M. Hocevar, M. B. Bavinck, M. A. Verheijen, E. P. A. M. Bakkers, L. P. Kouwenhoven, and V. Zwiller, “Bright single-photon sources in bottom-up tailored nanowires,” *Nat. Commun.*, vol. 3, p. 737, Mar. 2012.

[279] T. M. Babinec, B. J. M. Hausmann, M. Khan, Y. Zhang, J. R. Maze, P. R. Hemmer, and M. Lončar, “A diamond nanowire single-photon source,” *Nat. Nanotechnol.*, vol. 5, no. 3, pp. 195–199, Mar. 2010.

[280] J. Bleuse, J. Claudon, M. Creasey, N. S. Malik, J.-M. Gérard, I. Maksymov, J.-P. Hugonin, and P. Lalanne, “Inhibition, Enhancement, and Control of Spontaneous Emission in Photonic Nanowires,” *Phys. Rev. Lett.*, vol. 106, no. 10, p. 103601, Mar. 2011.

[281] R. Singh and G. Bester, “Nanowire Quantum Dots as an Ideal Source of Entangled Photon Pairs,” *Phys. Rev. Lett.*, vol. 103, no. 6, p. 063601, Aug. 2009.

[282] T. D. Stanescu and S. Tewari, “Majorana Fermions in Semiconductor Nanowires: Fundamentals, Modeling, and Experiment,” *J. Phys. Condens. Matter*, vol. 25, no. 23, p. 233201, Jun. 2013.

[283] R. M. Lutchyn, J. D. Sau, and S. Das Sarma, “Majorana Fermions and a Topological Phase Transition in Semiconductor-Superconductor Heterostructures,” *Phys. Rev. Lett.*, vol. 105, no. 7, p. 077001, Aug. 2010.

[284] Y. Oreg, G. Refael, and F. von Oppen, “Helical Liquids and Majorana Bound States in Quantum Wires,” *Phys. Rev. Lett.*, vol. 105, no. 17, p. 177002, Oct. 2010.

[285] M. R. Black, M. Padi, S. B. Cronin, Y.-M. Lin, O. Rabin, T. McClure, G. Dresselhaus, P. L. Hagelstein, and M. S. Dresselhaus, “Intersubband transitions in bismuth nanowires,” *Appl. Phys. Lett.*, vol. 77, no. 25, pp. 4142–4144, Dec. 2000.

[286] M. Black, Y.-M. Lin, S. Cronin, O. Rabin, and M. Dresselhaus, "Infrared absorption in bismuth nanowires resulting from quantum confinement," *Phys. Rev. B*, vol. 65, no. 19, May 2002.

[287] M. R. Black, K. R. Maskaly, O. Rabin, Y. M. Lin, S. B. Cronin, M. Padi, Y. Fink, and M. S. Dresselhaus, "Studies of Intersubband Transitions in Arrays of Bi Nanowire Samples Using Optical Transmission," in *Symposia U/V – Nanophase and Nanocomposite Materials IV*, 2001, vol. 703.

[288] S. C. Rustagi, N. Singh, Y. F. Lim, G. Zhang, S. Wang, G. Q. Lo, N. Balasubramanian, and D.-L. Kwong, "Low-Temperature Transport Characteristics and Quantum-Confinement Effects in Gate-All-Around Si-Nanowire N-MOSFET," *IEEE Electron Device Lett.*, vol. 28, no. 10, pp. 909–912, Oct. 2007.

[289] T. Akiyama, T. Yamashita, K. Nakamura, and T. Ito, "Band Alignment Tuning in Twin-Plane Superlattices of Semiconductor Nanowires," *Nano Lett.*, vol. 10, no. 11, pp. 4614–4618, Nov. 2010.

[290] C. Thelander, P. Caroff, S. Plissard, A. W. Dey, and K. A. Dick, "Effects of Crystal Phase Mixing on the Electrical Properties of InAs Nanowires," *Nano Lett.*, vol. 11, no. 6, pp. 2424–2429, Jun. 2011.

[291] M. I. Amanti, A. Bismuto, M. Beck, L. Isa, K. Kumar, E. Reimhult, and J. Faist, "Electrically driven nanopillars for THz quantum cascade lasers," *Opt. Express*, vol. 21, no. 9, p. 10917, Apr. 2013.

[292] V. G. Dubrovskii and N. V. Sibirev, "Growth thermodynamics of nanowires and its application to polytypism of zinc blende III-V nanowires," *Phys. Rev. B*, vol. 77, no. 3, Jan. 2008.

[293] M. I. Amanti, A. Bismuto, M. Beck, L. Isa, K. Kumar, E. Reimhult, and J. Faist, "Electrically driven nanopillars for THz quantum cascade lasers," *Opt. Express*, vol. 21, no. 9, p. 10917, Apr. 2013.

[294] K. Tanaka, K. Ikuno, Y. Kasai, K. Fukunaga, H. Kunugita, K. Ema, A. Kikuchi, and K. Kishino, "Ultrafast intersubband relaxation dynamics at 1.55µm in GaN/AlN multiple quantum disk nanocolumns," *J. Lumin.*, vol. 128, no. 5–6, pp. 1084–1086, May 2008.

[295] A. Dadgar, J. Bläsing, A. Diez, and A. Krost, "Crack-Free, Highly Conducting GaN Layers on Si Substrates by Ge Doping," *Appl. Phys. Express*, vol. 4, no. 1, p. 011001, Jan. 2011.

[296] S. Fritze, A. Dadgar, H. Witte, M. Bügler, A. Rohrbeck, J. Bläsing, A. Hoffmann, and A. Krost, "High Si and Ge n-type doping of GaN doping - Limits and impact on stress," *Appl. Phys. Lett.*, vol. 100, no. 12, p. 122104, 2012.

[297] F. Schuster, A. Winnerl, S. Weiszer, M. Hetzl, J. A. Garrido, and M. Stutzmann, "Doped GaN nanowires on diamond: Structural properties and charge carrier distribution," *J. Appl. Phys.*, vol. 117, no. 4, p. 044307, Jan. 2015.

[298] Ž. Gačević, A. Das, J. Teubert, Y. Kotsar, P. K. Kandaswamy, T. Kehagias, T. Koukoula, P. Komninou, and E. Monroy, "Internal quantum efficiency of III-nitride quantum dot superlattices grown by plasma-assisted molecular-beam epitaxy," *J. Appl. Phys.*, vol. 109, no. 10, p. 103501, May 2011.

[299] J. Simon, N. T. Pelekanos, C. Adelmann, E. Martinez-Guerrero, R. André, B. Daudin, L. S. Dang, and H. Mariette, "Direct comparison of recombination dynamics in cubic and hexagonal GaN/AlN quantum dots," *Phys. Rev. B*, vol. 68, no. 3, p. 035312, Jul. 2003.

[300] P. R. Hageman, W. J. Schaff, J. Janinski, and Z. Liliental-Weber, "n-type doping of wurtzite GaN with germanium grown with plasma-assisted molecular beam epitaxy," *J. Cryst. Growth*, vol. 267, no. 1–2, pp. 123–128, Jun. 2004.

[301] S. Nakamura, T. Mukai, and M. Senoh, “Si- and Ge-Doped GaN Films Grown with GaN Buffer Layers,” *Jpn. J. Appl. Phys.*, vol. 31, no. 9R, p. 2883, Sep. 1992.

[302] J. K. Sheu and G. C. Chi, “The doping process and dopant characteristics of GaN,” *J. Phys. Condens. Matter*, vol. 14, no. 22, p. R657, Jun. 2002.

[303] E. A. DeCuir, E. Fred, M. O. Manasreh, J. Schörmann, D. J. As, and K. Lischka, “Near-infrared intersubband absorption in nonpolar cubic GaN∕AlN superlattices,” *Appl. Phys. Lett.*, vol. 91, no. 4, p. 041911, 2007.

[304] E. A. DeCuir, M. O. Manasreh, E. Tschumak, J. Schörmann, D. J. As, and K. Lischka, “Cubic GaN/AlN multiple quantum well photodetector,” *Appl. Phys. Lett.*, vol. 92, no. 20, p. 201910, May 2008.

[305] L. Lahourcade, P. K. Kandaswamy, J. Renard, P. Ruterana, H. Machhadani, M. Tchernycheva, F. H. Julien, B. Gayral, and E. Monroy, “Interband and intersubband optical characterization of semipolar (11-22)-oriented GaN/AlN multiple-quantum-well structures,” *Appl. Phys. Lett.*, vol. 93, no. 11, p. 111906, 2008.

[306] J. Shao, D. N. Zakharov, C. Edmunds, O. Malis, and M. J. Manfra, “Homogeneous AlGaN/GaN superlattices grown on free-standing (1-100) GaN substrates by plasma-assisted molecular beam epitaxy,” *Appl. Phys. Lett.*, vol. 103, no. 23, p. 232103, Dec. 2013.

[307] J. Shao, L. Tang, C. Edmunds, G. Gardner, O. Malis, and M. Manfra, “Surface morphology evolution of m-plane (1-100) GaN during molecular beam epitaxy growth: Impact of Ga/N ratio, miscut direction, and growth temperature,” *J. Appl. Phys.*, vol. 114, no. 2, p. 023508, Jul. 2013.

[308] A. M. Armstrong, K. Kelchner, S. Nakamura, S. P. DenBaars, and J. S. Speck, “Influence of growth temperature and temperature ramps on deep level defect incorporation in m-plane GaN,” *Appl. Phys. Lett.*, vol. 103, no. 23, p. 232108, Dec. 2013.

[309] A. Pesach, E. Gross, C.-Y. Huang, Y.-D. Lin, A. Vardi, S. E. Schacham, S. Nakamura, and G. Bahir, “Non-polar m-plane intersubband based InGaN/(Al)GaN quantum well infrared photodetectors,” *Appl. Phys. Lett.*, vol. 103, no. 2, p. 022110, 2013.

[310] C. Edmunds, J. Shao, M. Shirazi-HD, M. J. Manfra, and O. Malis, “Terahertz intersubband absorption in non-polar m-plane AlGaN/GaN quantum wells,” *Appl. Phys. Lett.*, vol. 105, no. 2, p. 021109, Jul. 2014.

[311] C. Bayram, Z. Vashaei, and M. Razeghi, “Reliability in room-temperature negative differential resistance characteristics of low-aluminum content AlGaN/GaN double-barrier resonant tunneling diodes,” *Appl. Phys. Lett.*, vol. 97, no. 18, p. 181109, Nov. 2010.

[312] Z. Vashaei, C. Bayram, P. Lavenus, and M. Razeghi, “Photoluminescence characteristics of polar and nonpolar AlGaN/GaN superlattices,” *Appl. Phys. Lett.*, vol. 97, no. 12, p. 121918, Sep. 2010.

[313] A. E. Romanov, T. J. Baker, S. Nakamura, J. S. Speck, and ERATO/JST UCSB Group, “Strain-induced polarization in wurtzite III-nitride semipolar layers,” *J. Appl. Phys.*, vol. 100, no. 2, p. 023522, 2006.

[314] M. A. Belkin, J. A. Fan, S. Hormoz, F. Capasso, S. P. Khanna, M. Lachab, A. G. Davies, and E. H. Linfield, “Terahertz quantum cascade lasers with copper metal-metal waveguides operating up to 178 K,” *Opt. Express*, vol. 16, no. 5, pp. 3242–3248, Mar. 2008.

[315] G. Sun, J. B. Khurgin, and D. P. Tsai, “Spoof plasmon waveguide enabled ultrathin room temperature THz GaN quantum cascade laser: a feasibility study,” *Opt. Express*, vol. 21, no. 23, p. 28054, Nov. 2013.

[316] G. Sun, J. B. Khurgin, and D. P. Tsai, “Feasibility of spoof surface plasmon waveguide enabled ultrathin room temperature THz GaN quantum cascade laser,” *Proc. SPIE*. in *Symposium UU – Phonon-Interaction-Based Materials Design—Theory, Experiments and Applications*, vol. 8984, 2014.

[317] F. Ai-Bing, H. Ming-Rui, Y. Yao, S. Wen-Zhong, and L. Hui-Chun, “An optically pumped GaN/AlGaN quantum well intersubband terahertz laser,” *Chin. Phys. B*, vol. 22, no. 2, p. 026803, Feb. 2013.

[318] H. C. Chou, A. Mazady, J. Zeller, T. Manzur, and M. Anwar, “Room-Temperature Quantum Cascade Laser: ZnO/$Zn_{1-x}Mg_xO$ Versus GaN/$Al_xGa_{1-x}N$,” *J. Electron. Mater.*, vol. 42, no. 5, pp. 882–888, Apr. 2013.

List of publications (annexes) and conference contributions

Annex 1

M. Beeler, E. Trichas, and E. Monroy, "III-nitride semiconductors for intersubband optoelectronics: a review," *Semicond. Sci. Technol.*, vol. 28, no. 7, p. 074022, Jul. 2013.

Annex 2

M. Beeler, E. Monroy, "*III-nitride semiconductors: new infrared intersubband technologies*" in "*Gallium Nitride (GaN): Physics, Devices, and Technology*", edited by F. Medjdoub and K. Iniewski (Taylor & Francis, New York, Aug. 2015). ISBN: 9781482220032

Annex 3

M. Beeler, C. Bougerol, E. Bellet-Amalaric, and E. Monroy, "THz intersubband transitions in AlGaN/GaN multi-quantum-wells," *Phys. Status Solidi A*, vol. 211, no. 4, pp. 761–764, Apr. 2014.

Annex 4

M. Beeler, C. Bougerol, E. Bellet-Amalric, and E. Monroy, "Terahertz absorbing AlGaN/GaN multi-quantum-wells: Demonstration of a robust 4-layer design," *Appl. Phys. Lett.*, vol. 103, no. 9, p. 091108, 2013.

Annex 5

M. Beeler, C. Bougerol, E. Bellet-Amalric, and E. Monroy, "Pseudo-square AlGaN/GaN quantum wells for terahertz absorption," *Appl. Phys. Lett.*, vol. 105, no. 13, p. 131106, Sep. 2014.

Annex 6

M. Beeler, C. B. Lim, P. Hille, J. Bleuse, J. Schörmann, M. de la Mata, J. Arbiol, M. Eickhoff, and E. Monroy, "Long-lived excitons in GaN/AlN nanowire heterostructures," *Phys. Rev. B.*, 91, 205440, May 2015.

Annex 7

M. Beeler, P. Hille, J. Schörmann, J. Teubert, M. de la Mata, J. Arbiol, M. Eickhoff, and E. Monroy, "Intraband Absorption in Self-Assembled Ge-Doped GaN/AlN Nanowire Heterostructures," *Nano Lett.*, vol. 14, no. 3, pp. 1665–1673, Mar. 2014.

Annex 8

C. B. Lim, M. Beeler, A. Ajay, J. Lähnemann, E. Bellet-Amalric, C. Bougerol, and E. Monroy, "*Intersubband transitions in nonpolar GaN/Al(Ga)N heterostructures in the short and mid-wavelength infrared regions*," Submitted to *J. Appl. Phys.* in 2015.

Annex 9

H. Machhadani, M. Beeler, S. Sakr, E. Warde, Y. Kotsar, M. Tchernycheva, M. P. Chauvat, P. Ruterana, G. Nataf, P. De Mierry, E. Monroy, and F. H. Julien, "Systematic study of near-infrared intersubband absorption of polar and semipolar GaN/AlN quantum wells," *J. Appl. Phys.*, vol. 113, no. 14, p. 143109, 2013.

[1] **III-N heterostructures for infrared optoelectronics: present and perspectives**
E. Monroy, M. Beeler, Y. Kotsar, S. Valdueza-Felip, R. Songmuang, S. Sakr, M. Tchernycheva, and F. H. Julien, E. Gross, A. Pesach, G. Bahir, M.-P. Chauvat, and P. Ruterana, *21st European Workshop on Heterostructure Technology (HETECH 2012), Barcelone, Spain. Nov. 2012*

[2] **Progress and perspectives of GaN-based intersubband optoelectronics**
E. Monroy, M. Beeler, Y. Kotsar, S. Valdueza-Felip, E. Trichas, R. Songmuang, S. Sakr, M. Tchernycheva, F. H. Julien, E. Gross, A. Pesach, G. Bahir, M.-P. Chauvat, and P. Ruterana, *E-MRS Spring Meeting 2013 Strasbourg, France. May 2013*

[3] **(Oral) Design of robust AlGaN/GaN quantum-well heterostructures with intersubband transitions in the THz spectral region**
M. Beeler, C. Bougerol, E. Bellet-Amalric, Q. Pan, and E. Monroy, *E-MRS Spring Meeting 2013 Strasbourg, France. May 2013*

[4] **(Poster) Design of robust AlGaN/GaN quantum-well heterostructures with intersubband transitions in the THz spectral region**
M. Beeler, C. Bougerol, E. Bellet-Amalric, K. Lorenz, E. Alves, and E. Monroy, *10th International Conference on Nitride Semiconductors (ICNS10), Washington, US. Aug. 2013*

[5] **III-N quantum cascade structures**
E. Monroy, M. Beeler, E. Trichas, S. Valdueza-Felip, E.Bellet-Amalric, C. Bougerol, S. Sakr, M. Tchernycheva, F. H. Julien, E. Gross, A. Pesach, and G. Bahir, *10th International Conference on Nitride Seminconductors (ICNS-9), Washington, US, Aug. 2013*

[6] **GaN/AlN Heterostructured Nanowires for Photodetection and Sensing**
E. Monroy, M. den Hertog, R. Songmuang, M. Beeler, F. Gonzalez-Posada, P. Hille, J. Schörmann, and M. Eickhoff, *TUM-IAS Focus Workshop on Nanowires, Munich, Germany. Oct. 2013*

[7] **Progress on III-nitride materials for intersubband optoelectronics**
M. Beeler, E. Bellet-Amalric, C. Bougerol, and E. Monroy, *Photonics West (SPIE), San Francisco, U.S.A. Jan. 2014*

[8] **GaN/Al(Ga)N nanostructures for intersubband optoelectronics**
E. Monroy, M. Beeler, Bellet-Amalric, C. Bougerol, P. Hille, J. Schörmann, M. Eickhoff, M. Tchernycheva, F. H. Julien, A. Vardi, and G. Bahir, *E-MRS Spring Meeting 2014, Lille, France. May 2014*

[9] **(Invited) Demonstration of Intersubband transitions in Ge-doped GaN/AlN heterstructured nanowires**
M. Beeler, P. Hille, J. Schörmann, M. de la Mata, J. Arbiol, M. Eickhoff, and E. Monroy, *5th Int. Symposium on the Growth of III-Nitrides (ISGN5). Atlanta, US. May 2014*

[10] **(Oral) Pseudo-square AlGaN/GaN quantum-well heterostructures with THz intersubband transitions**
M. Beeler, C. Bougerol, E. Bellet-Amalric, and E. Monroy, *5th Int. Symposium on the Growth of III-Nitrides (ISGN5). Atlanta, US. May 2014*

[11] **Intersubband optoelectronics using nitride semiconductors: A new infrared technology**
E. Monroy, M. Beeler, E. Bellet-Amalric, C. Bougerol, P. Hille, J. Schörmann, M. Eickhoff, M. Tchernycheva, F. H. Julien, and G. Bahir, *CMOS Emerging Technologies Research, Grenoble, France. July 2014*

[12] **(Oral) Pseudo-Square AlGaN/GaN Quantum Well Heterostructures for THz Intersubband Optoelectronics**
M. Beeler, C. Bougerol, E. Bellet-Amalric, and E. Monroy, *International Workshop on Nitride Semiconductors (IWN-2014), Wroclaw, Poland. August 2014*

[13] **(Poster) Intersubband Transitions in GaN/AlN Nanowires: Theoretical and Experimental Study**
M. Beeler, P. Hille, J. Schörmann, M. de la Mata, J. Arbiol, M. Eickhoff, and E. Monroy, *International Workshop on Nitride Semiconductors (IWN-2014), Wroclaw, Poland. August 2014*

[14] **(Poster) Exploring nonpolar crystal orientations bulk substrates for intersubband optoelectronics**
M. Beeler, A. Núñez-Cascajero, E. Bellet-Almaric, C. Bougerol, and E. Monroy, *International Workshop on Nitride Semiconductors (IWN-2014), Wroclaw, Poland. August 2014*

Conference Poster Award

[15] **Multi-technic approach for nanoscale structural analysis of nitride-based nanostructures**
C. Bougerol, T. Auzelle, M. Beeler, B. Daudin, C. Durand, J. Eymery, M. Lopez-Haro, E. Monroy, A. Mukhtarova, and E. Robin, *International Workshop on Nitride Semiconductors (IWN-2014), Wroclaw, Poland. August 2014*

[16] **III-Nitrides for Infrared Optoelectronics**
M. Beeler, C. B. Lim, E. Bellet-Amalric, C. Bougerol, and E. Monroy, *10th International Symposium on Semiconductor Light Emitting Devices (ISSLED 2014), Kaohsiung, Taiwan. Dec. 2014*

[17] **Nonpolar GaN/Al(Ga)N Superlattices for Intersubband Optoelectronics**
C. B. Lim, M. Beeler, E. Bellet-Amalric, C. Bougerol, and E. Monroy, *10th International Symposium on Semiconductor Light Emitting Devices (ISSLED 2014), Kaohsiung, Taiwan. Dec. 2014*

[18] **(Oral) Interband carrier dynamics in Ge-doped GaN/AlN nanowire heterostructures**
M. Beeler, C. B. Lim, P. Hille, J. Schörmann, M. de la Mata, J. Arbiol, M. Eickhoff, J. Bleuse, and E. Monroy, *10th International Symposium on Semiconductor Light Emitting Devices (ISSLED 2014), Kaohsiung, Taiwan. Dec. 2014*

Award for the best student oral presentation

[19] **Nanoscale structural analysis of nitride-based nanostructures: a multi-technic approach**
C. Bougerol, J.P. Barnes, M. Beeler, E. Bellet-Amalric, B. Bonef, A. Grenier, P.H. Jouneau, M. Lopez-Haro, E. Monroy, and E. Robin, *Photonics West (SPIE), San Francisco, U.S.A. January 2015*

[20] **New approaches to intersubband transitions in III-nitride heterostructures**
E. Monroy , C. B. Lim, M. Beeler, A. Ajay, J. Lähnemann, E. Bellet-Amalric, J. Bleuse, and C. Bougerol, *2015 Compound Semiconductor Week, Santa Barbara, CA, USA. June 2015*

[21] **(Submitted) Determination of internal electric fields in binary GaN/AlN multi-quantum wells: experimental and ab initio comparative study**
A. Kaminska, P. Strak, J. Borysiuk, J. Z. Domagala, E. Grzanka, M. Beeler, K. Sakowski, E. Monroy and S. Krukowski, *44th "Jaszowiec" International School and Conference on the Physics of Semiconductors, Wisla, Poland. June 2015*

[22] **(Submitted) Nanoscale strain and quantitative chemical analysis of nitride heterostructures: A multitechnique approach**
C. Bougerol, B. Bonef, B. Hass, M. Beeler, M. Lopez-Haro, E. Robin, P. H. Jouneau, A. Grenier, E. Bellet-Amalric, and E. Monroy, *11th International Conference on Nitride Semiconductors (ICNS11),Beijing, China. Aug. 2015*

[23] **(Submitted) Pressure influence on the optical properties of GaN/AlN multi-quantum wells - experimental investigations**
A. Kaminskaa, P. Strak, J. Borysiuk, J. Domagała, M. Beeler, E. Monroy , and Stanislaw Krukowski, *Joint AIRAPT-25th & EHPRG-53rd International Conference on High Pressure Science and Technology, Madrid, Spain. Aug. 2015*

Annex 1

IOP PUBLISHING SEMICONDUCTOR SCIENCE AND TECHNOLOGY

Semicond. Sci. Technol. **28** (2013) 074022 (26pp) doi:10.1088/0268-1242/28/7/074022

INVITED REVIEW

III-nitride semiconductors for intersubband optoelectronics: a review

M Beeler, E Trichas and E Monroy

CEA-Grenoble, INAC/SP2M/NPSC, 17 rue des Martyrs, 38054 Grenoble, France

E-mail: eva.monroy@cea.fr

Received 3 December 2012, in final form 19 January 2013
Published 21 June 2013
Online at stacks.iop.org/SST/28/074022

Abstract

III-nitride nanostructures have recently emerged as promising materials for new intersubband (ISB) devices in a wide variety of applications. These ISB technologies rely on infrared optical transitions between quantum-confined electronic states in the conduction band of GaN/Al(Ga)N nanostructures, namely quantum wells or quantum dots. The large conduction band offset (about 1.8 eV for GaN/AlN) and sub-picosecond ISB relaxation of III-nitrides render them appealing materials for ultrafast photonic devices in near-infrared telecommunication networks. Furthermore, the large energy of GaN longitudinal-optical phonons (92 meV) opens prospects for high-temperature THz quantum cascade lasers and ISB devices covering the 5–10 THz band, inaccessible to As-based technologies due to phonon absorption. In this paper, we describe the basic features of ISB transitions in III-nitride quantum wells and quantum dots, in terms of theoretical calculations, material growth, spectroscopy, resonant transport phenomena, and device implementation. The latest results in the fabrication of control-by-design devices such as all-optical switches, electro-optical modulators, photodetectors, and lasers are also presented.

(Some figures may appear in colour only in the online journal)

1. Introduction

1.1. Historical introduction

Semiconductor materials can be made optically active at infrared (IR) wavelengths regardless of their band gap by engineering the electron quantum confinement in thin layers. Such controlled-by-design devices rely on optical intersubband (ISB) transitions between electronic confined states, and the desired transitional wavelength can be obtained through engineering of the layer thicknesses. The first studies of ISB absorption date back to 1974, when Kamgar *et al* [1] recorded optical transitions between bound electronic levels in an accumulation layer on *n*-type Si(1 0 0) under far-IR illumination. Since then, a number of works on Si space-charge regions and III–V surface layers have contributed to a more detailed understanding of quantum confinement in thin-film structures, many-body effects, ISB absorption selection rules, oscillator strengths and line shapes [2]. The extrapolation of these principles to GaAs/AlGaAs quantum wells (QWs) to shift the transition wavelength to the mid-IR was first suggested by Esaki and Sakaki [3], and subsequent experimental [4, 5] and theoretical studies [6, 7] led to the first experimental measurement of strong ISB absorption in a series of multiple QWs (MQWs), performed by West and Eglash [8]. These results set the basis for the fabrication of the first QW infrared photodetector (QWIP), by Levine *et al* [9, 10]. In 1994, Faist *et al* [11] presented a major breakthrough in the ISB technology: an alternative to the conventional laser diode, with a novel operating principle—the quantum cascade laser (QCL). This was the beginning of tremendous development of the ISB technology which resulted in commercially available devices operating in the mid- and far-IR.

Nowadays, ISB optoelectronic devices (photodetectors and emitters) based on the III-As material system (GaAs/AlGaAs, InGaAs/AlInAs, or GaInAs/AlAsSb) can be tuned from the mid-IR to the THz spectral range. Operation at shorter wavelengths (<3 μm) is limited by the

 © 2013 IOP Publishing Ltd Printed in the UK & the USA

available conduction band offset and by material transparency. III-nitride semiconductors (GaN, AlN, InN and their alloys), with their wide band gap and a large conduction band offset (∼1.8 eV for GaN/AlN [12–14]), are attracting much interest for ISB devices operating in the near-IR spectral range, particularly in the 1.3–1.55 μm wavelength window used for fiber-optic communications [15–17]. GaN is transparent in a large spectral region, notably for wavelengths longer than 360 nm (band gap), except for the Rehstrahlen band (from 9.6 to 19 μm). Absorption in the range of 7.3 to 9 μm has been observed in bulk GaN substrates with carrier concentrations $<10^{16}$ cm^{-3} [18–20], and was attributed to the second harmonic of the Restrahlen band. Although this second band might hinder the fabrication of waveguided devices in this spectral region, its effect in planar devices with μm-sized active regions (for instance, QWIPs) is negligible. This is because the absorption coefficient related to two-phonon processes is much smaller than the one associated with ISB transitions. This has been experimentally demonstrated by the identification of ISB absorption in AlGaN/GaN QWs within such a band [21, 22]. On the other hand, III-nitrides do not present problems of inter-valley scattering, since the L and X points are much higher in energy (>2 eV) than the Γ point.

The feasibility of a GaN-based ISB technology in the telecommunication spectral range was early predicted by Suzuki *et al* [15, 23], who additionally estimated an ISB relaxation time around 80 fs at 1.55 μm, i.e. about 30 times shorter than that in InGaAs QWs, and high third-order nonlinear susceptibility (around 1.6×10^{-15} m^2 V^{-2} for a carrier concentration $n = 1 \times 10^{18}$ cm^{-3}). These characteristics led them to propose GaN/AlGaN QWs as the active media for multi-terabit/s ISB all-optical switches. In the next decade, their prediction proved valid and the first prototypes of GaN-based ISB devices operating at 1.55 μm have closely fulfilled their expectations.

On the other hand, there is an interest to push the III-nitride ISB technology toward longer wavelengths, particularly to the THz frequency range. The potential of this spectral region in applications like security screening, quality control and medical diagnostics has driven extensive development of optoelectronic components. Due to the large LO-phonon energy of GaN (about three times that of GaAs), room temperature operation becomes feasible for ISB devices covering the IR band that was typically inaccessible to As-based semiconductors due to phonon absorption.

1.2. Physics of intersubband transitions: polarization selection rule

For a comprehensive introduction to ISB physics in QWs, we refer the readers to the work of Bastard [24] or Liu and Capasso [25]. In this section, we briefly introduce the polarization selection rule characteristic of ISB transitions in QWs and we derive an expression for the ISB absorption coefficient. For this purpose, we consider a QW with two confined states in a single-particle approach. Any transition from a state i to a state f, interband or ISB, can be described with Fermi's golden rule:

$$W_{fi} = \frac{2\pi}{\hbar}|\langle\psi_f|H'|\psi_i\rangle|^2\delta(E_f - E_i - \hbar\omega), \qquad (1)$$

where H' is the interaction Hamiltonian, $\hbar\omega$ is the radiation energy, and ψ and E are the wave functions and energies of the confinement levels for the initial (i) and final (f) states. As the radiation wavelength is much larger than the lattice periodicity in the case of interband transitions, and larger than the QW width in the case of ISB transitions, it is possible to apply the dipole approximation:

$$H' = \frac{q^2F_0^2}{4m*^2\,\omega^2}\,(\vec{\varepsilon}\cdot\vec{p}), \qquad (2)$$

where q denotes elementary charge, F_0 is the electric field amplitude, $m*$ is effective mass, and $\vec{\varepsilon}$ and $\vec{p}$ are the polarization vector and the momentum operator, respectively. Substituting equation (2) in equation (1) we obtain

$$W_{fi} = \frac{2\pi}{\hbar}\frac{q^2F_0^2}{4m*^2\,\omega^2}\left|\langle\psi_f\right|\vec{\varepsilon}\cdot\vec{p}\left|\psi_i\rangle\right|^2\delta(E_f - E_i - \hbar\omega). \qquad (3)$$

Applying the envelop function formalism, the wavefunction of an electron $\psi_i(\vec{r})$ can be expressed as a product of a periodic Bloch function, $u_\nu(\vec{r})$, and a slowly varying envelope function, $f_n(\vec{r})$, where n denotes the quantum numbers of the problem. Under the assumption that the lattice-periodic function is the same in all constituent materials a Schrödinger equation only for the envelope function can be derived:

$$\frac{-\hbar}{2m*}\nabla^2 f_n(\vec{r}) + V(\vec{r})f_n(\vec{r}) = E_n f_n(\vec{r}), \qquad (4)$$

where $V(\vec{r})$ is the potential profile and E_n are the energy eigenvalues. Introducing the envelop function expression in a QW:

$$f_n(\vec{r}) = \frac{1}{\sqrt{S}}\exp(i\vec{k}_\perp\cdot\vec{r}_\perp)\chi(z), \qquad (5)$$

where S is the sample area, $\chi(z)$ is the envelop function component along the growth axis, and $\vec{k}_\perp$ and $\vec{r}_\perp$ denote the two-dimensional (2D) vectors (k_x, k_y) and (x, y), the solution of equation (4) leads to energy eigenvalues of the form

$$E_n(k_\perp) = E_{n0} + \frac{\hbar^2k_\perp^2}{2m^*}, \qquad (6)$$

where the subband energies E_{n0} depend on the potential profile $V(z)$. For a symmetric QW with infinite barriers, the following eigenvalues are obtained:

$$E_n(k_\perp) = \frac{n^2\hbar^2k_\perp^2}{2m*L^2} + \frac{\hbar^2k_\perp^2}{2m^*}, \qquad (7)$$

where L is the QW thickness. Note that, due to the relatively large electron effective mass of GaN (m^*/m_0∼0.2) compared to GaAs (m^*/m_0∼0.067) or InAs (m^*/m_0∼0.023), very thin GaN QWs are required to attain large ISB transition energies.

Coming back to equation (3), the matrix element $\langle\psi_f|\vec{\varepsilon}\cdot\vec{p}|\psi_i\rangle$ splits into

$$\langle\psi_f|\vec{\varepsilon}\cdot\vec{p}|\psi_i\rangle = \vec{\varepsilon}\cdot\langle u_\nu|\vec{p}|u_{\nu'}\rangle\langle f_n|f_{n'}\rangle + \vec{\varepsilon}\cdot\langle u_\nu|u_{\nu'}\rangle\langle f_n|\vec{p}|f_{n'}\rangle, \qquad (8)$$

where ν and ν' and n and n' are the band and subband indices of final and initial states, respectively. The first term describes the interband transitions and it vanishes in the case of transitions within the same band. It consists of a dipole matrix element of Bloch functions, which dictates the

interband polarization selection rules, and an overlap integral of the envelope functions, which gives rise to selection rules concerning the electron and hole subband quantum numbers. The second term represents the ISB processes, and it consists of an overlap integral of Bloch functions, which is nonzero when two envelope states are taken from the same band, and a dipole matrix element of the envelope functions, which defines the *polarization selection rule*:

$$\langle f_n|\,\vec{\varepsilon}\cdot\vec{p}\,|f_{n'}\rangle = \frac{1}{S}\varepsilon_z\delta\left(k_\perp^i - k_\perp^f\right)\int \mathrm{d}z\chi_n^*(z)p_z\chi_{n'}(z). \quad (9)$$

Thus, only the z-component of the electric field couples to the ISB transition, i.e. structures respond only to transverse-magnetic (TM) polarized light, which imposes the use of surface gratings or waveguide configurations to couple the light into the active region.

Inserting equation (9) in equation (3) and taking into account that the momentum can be described as $\vec{p}_{nn'} = im * \omega\vec{r}_{nn'}$, the ISB transition rate can be rewritten as

$$W_{fi} = \frac{2\pi}{\hbar}\frac{q^2F_0^2}{4}\varepsilon_z^2|\langle\chi_f(z)|z|\chi_i(z)\rangle|^2 \times \delta\left(k_\perp^i - k_\perp^f\right)\delta(E_f - E_i - \hbar\omega). \quad (10)$$

The ISB absorption coefficient between states i and f is usually defined through the ratio of the absorbed electromagnetic energy per unit time and volume, $\hbar\omega W_{fi}/V$, and the intensity of the incident radiation, $I = \frac{1}{2}nc\varepsilon_0F_0^2$: where ε_0 is the vacuum permittivity, n is the refractive index of the material and c is the speed of light:

$$\alpha(\omega) = \frac{\pi q^2(E_f - E_i)}{nc\varepsilon_0\hbar V} \times \varepsilon_z^2\sum_{i,f}2|\langle\chi_f(z)|z|\chi_i(z)\rangle|^2[f(E_i) - f(E_f)]\delta(E_f - E_i - \hbar\omega), \quad (11)$$

with $f(E)$ being the Fermi function. The sum can be expressed as the difference of carrier surface density of the two subbands, $n_i^S - n_f^S$:

$$\sum_{i,f}2[f(E_i) - f(E_f)] = S\left(n_i^S - n_f^S\right), \quad (12)$$

where S is the crystal surface. Therefore, the ISB absorption coefficient between two subbands can be written as

$$\alpha(\omega) = \frac{\pi(E_f - E_i)}{nc\varepsilon_0\hbar L}\left(n_i^S - n_f^S\right)\varepsilon_z^2\mu_{if}^2\delta(E_f - E_i - \hbar\omega), \quad (13)$$

where $\mu_{if} = q\left\langle\chi_f(z)\right|z\left|\chi_i(z)\right\rangle$ is the ISB dipole matrix element.

The dipole matrix element only involves the envelop wavefunctions for the initial and final subbands. Thus, as z is odd, *only transitions between subbands with opposite parity of the envelope wavefunctions are allowed in symmetric QWs*. This selection rule does not apply for asymmetric potential profiles.

The coupling efficiency between the two subbands is given by the oscillator strength, which is shown as

$$F_{if} = \frac{2m_0(E_f - E_i)}{q^2\hbar^2}\mu_{if}^2. \quad (14)$$

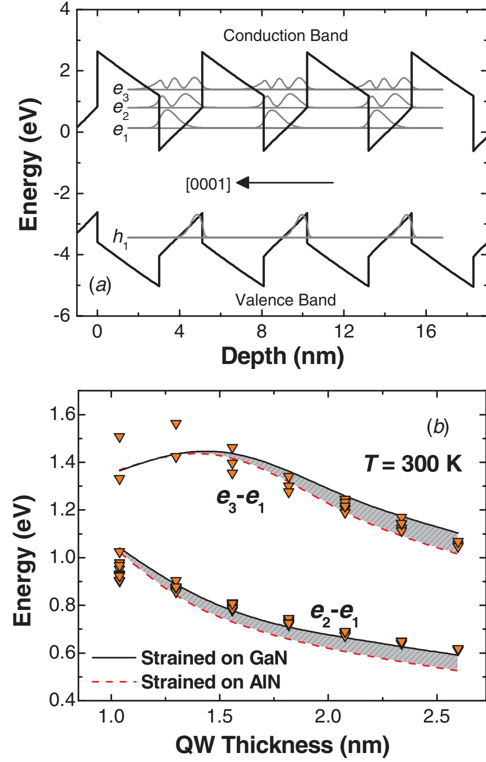

Figure 1. (*a*) Band diagram of GaN/AlN QWs in an infinite superlattice with 3 nm thick AlN barriers and 2 nm thick GaN QWs. The structure is considered strained on an AlN substrate. The electron wavefunctions of the ground hole state, h_1, the ground electron state, e_1, and the excited electron states, e_2 and e_3, are presented. (*b*) Variation of the e_2–e_1 and e_3–e_1 ISB transition energy as a function of the QW thickness in GaN/AlN MQW structures with 3 nm thick barriers. Triangles indicate experimental data and solid and dashed lines correspond to theoretical calculations assuming the structure fully strained on AlN and on GaN substrates, respectively. Reprinted with permission from [28]. Copyright 2008, American Institute of Physics.

2. Intersubband absorption in III-nitride nanostructures

2.1. GaN/AlGaN polar quantum wells

2.1.1. Modeling. The optical properties of (0 0 0 1)-oriented nitride QWs are strongly affected by the presence of an internal electric field arising from the piezoelectric and spontaneous polarization discontinuity between the well and barrier materials [26]. This is one of the most influential characteristics of III-nitride semiconductors, and plays a major role in determining the band structure. Figure 1(*a*) presents the band diagram of a GaN/AlN (2 nm/3 nm) superlattice calculated using the nextnano3 8-band k.p Schrödinger–Poisson solver [27] with the material parameters described in [28]. The structures were considered strained on the AlN substrate. The electronic potential takes on a characteristic saw-tooth profile due to the internal electric field. The electron wavefunctions of the ground hole state h_1, the ground electron state e_1 and the excited electron states e_2 and e_3 are presented in the figure. Due to the built-in electric field, the electron

wavefunctions are shifted toward the [0 0 0 1] direction and the hole wavefunctions toward the [0 0 0 1] direction (quantum-confined Stark effect, QCSE). In narrow QWs (∼1 nm) the energy difference between e_1 and e_2 is mostly determined by the confinement in the QW, whereas for larger QWs (>2 nm) this difference is mostly determined by the QCSE, since both electronic levels lie in the triangular part of the QW potential profile. A detailed description of the evolution of the ISB transitions e_2–e_1 and e_3–e_1 with the QW thickness and strain state is presented in figure 1(*b*) and compared with experimental data from GaN/AlN MQWs. The increase in the e_2–e_1 ISB energy difference in the calculations for the MQW strained on GaN is related to the enhanced electric field, due to the larger piezoelectric coefficients of the AlN barrier in comparison to the GaN QW [28].

The band structure simulations show that certain QW thicknesses can result in a configuration where the $e_1 \rightarrow e_2$ transition has approximately the same energy as the $e_2 \rightarrow e_3$ (or for very thick barrier layers the $e_2 \rightarrow e_4$) transition. This is an interesting experimental situation because it can result in the enhancement of second-order and third-order nonlinear effects such as two-photon absorption [29], second-harmonic generation [30] or saturable absorption [31].

In nitride heterostructures, the charge distribution depends not only on the Si doping level in the QWs, but also on the presence of non-intentional dopants and on the carrier redistribution due to the internal electric field. The polarization discontinuity between heterostructure layers leads to strong band bendings, which typically result in the formation of a depletion layer on one side of the active region and an accumulation layer on the other side (see figure 2(*a*)). Therefore, a realistic view of the charge distribution in a device is only achieved by extending the electronic modeling to the complete structure. As an illustration of this phenomena, Kandaswamy *et al* have studied the contribution of the internal electric field induced by a 50 nm thick $Al_xGa_{1-x}N$ cap layer to the ISB absorption of 40-period non-intentionally doped GaN/AlN (1.5/1.5 nm) MQWs grown on AlN [28]. The Al mole fraction of the cap layer was $x = 0$, 0.25, 0.5 and 1 for the samples under study. Measurements of ISB absorption in these samples, presented in figure 2(*c*), confirm a monotonic increase and broadening of the absorption when increasing the Al mole fraction of the cap layer. These results are consistent with the simulations of the electronic structure in figures 2(*a*) and (*b*), where we observe that the use of AlN as a cap layer lowers the conduction band of the first GaN QWs below the Fermi level (dash-dotted line at 0 eV in the figures), whereas the use of GaN as a cap layer results in the depletion of the MQW active region. Therefore, we conclude that the internal electric field induced by the cap layer can result in a significant (even dominant) contribution to the infrared absorption in GaN/AlN MQW structures.

2.1.2. Growth and defect analysis. A main requirement for the growth of the III-nitride nanostructures required for ISB devices is a precise control of the thickness and interfaces. Molecular-beam epitaxy (MBE) seems to be the most suitable technique for this application thanks to its low growth temperature that hinders GaN-AlN interdiffusion [32]. Plasma-assisted MBE (PAMBE) was the first method to produce III-nitride nanostructures displaying ISB transitions at telecommunication wavelengths (1.3, 1.55 μm) [33–39]. The growth of (0 0 0 1)-oriented GaN, AlN and AlGaN by PAMBE is extensively discussed in the literature [40–45]. Deposition of III-nitride 2D layers requires a precise control of the III/V flux ratio during the growth; particularly, it demands slightly metal-rich conditions, and hence growth optimization requires the determination of stoichiometric flux conditions

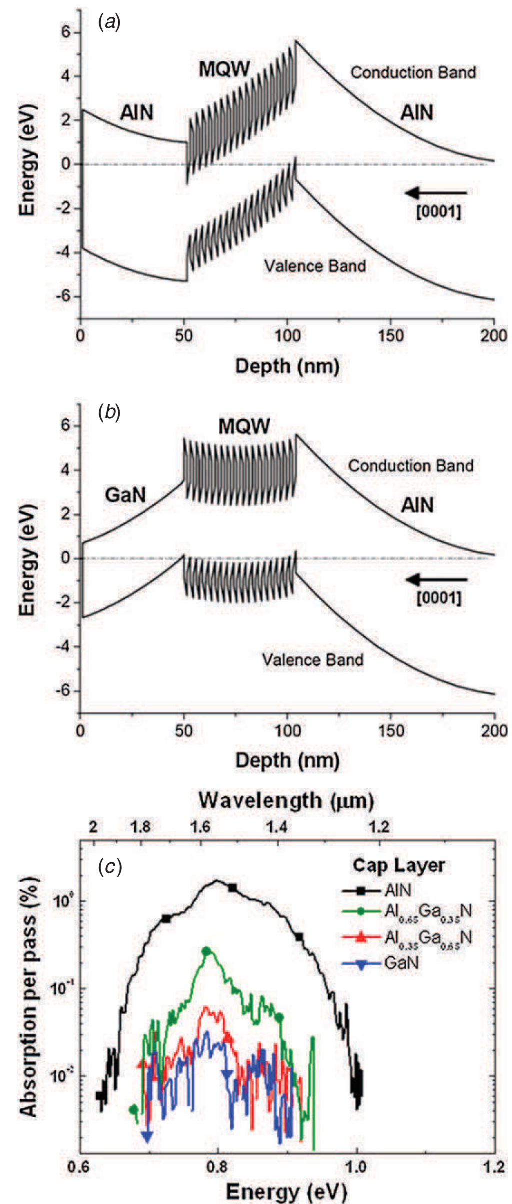

Figure 2. Band diagram of nonintentionally doped GaN/AlN (1.5/1.5 nm) MQW structures with (*a*) AlN cap layer and (*b*) GaN cap layer. (*c*) Room-temperature TM-polarized ISB absorption spectra of nonintentionally doped GaN/AlN (1.5/1.5 nm) MQW structures finished with a 50 nm thick $Al_xGa_{1-x}N$ cap layer with different Al mole fractions. Reprinted with permission from [28]. Copyright 2008, American Institute of Physics.

and precise control of the growth temperature. In the case of GaN, at a substrate temperature higher than 700 °C, there is a certain range of Ga fluxes for which the Ga excess remains in a situation of dynamic equilibrium on the growing front, i.e. the Ga coverage is independent of the Ga exposure time. Smooth surfaces are generally achieved under a moderate Ga excess [40, 42, 46, 47], when the Ga excess arranges into a so-called laterally-contracted Ga bilayer, which consists of two Ga layers adsorbed on the Ga-terminated (0 0 0 1) GaN surface [40, 41, 47–49]. Some groups prefer growing under higher Ga fluxes, in the droplet formation regime. They periodically consume the Ga excess by shuttering the Ga cell and exposing the surface to active nitrogen [50, 51]. This method provides high-quality layers, but it is important to predict the additional GaN thickness from consuming the excess, which depends on the impinging Ga flux, the active nitrogen flux and the substrate temperature. Finally, it has also been reported that smooth surface morphologies can be achieved via stoichiometric growth at high temperature (∼780–790 °C), when GaN decomposition is already active [52]. However, this growth method has not been applied to ISB devices or GaN/AlGaN QWs, and problems associated with material interdiffusion are expected [53].

An alternative to the above-described GaN growth conditions is the use of a surfactant to promote 2D growth [54]. Indium has been reported to behave as a surfactant for the PAMBE growth of (Al,G)aN, since it favors 2D growth under slightly N-rich conditions [41, 44, 55–57]. The utility of this growth method to synthesize GaN/AlN QWs displaying ISB absorption has been demonstrated [28].

In the case of AlN, the deposition of layers with atomically flat surface morphology also requires metal-rich conditions [45]. However, Al does not desorb from the surface at the standard growth temperature for GaN. Therefore, to eliminate the Al excess at the surface, it is necessary to perform periodic growth interruptions under nitrogen. An alternative approach to achieve 2D growth of AlN and low Al content (<50%) Al(Ga)N layers is to use Ga (or In) as a surfactant, with the Al flux corresponding to the required Al mole fraction [28, 43, 58].

GaN/AlN QWs displaying ISB transitions in the near-IR can also be synthesized by metalorganic vapor phase epitaxy (MOVPE) [59–61]. In this case, a critical parameter to attain devices in the telecommunication spectral range (1.3 μm, 1.55 μm) is the reduction of the growth temperature from the 1050–1100 °C optimum range for GaN growth down to 900–950 °C (or even to 770 °C [62]), in order to minimize the GaN-AlN interdiffusion. Furthermore, deposition under compressive strain (e.g. using AlN substrates) is recommended at these growth temperatures to prevent the red shift of the ISB transition due to instabilities of the GaN/AlN interface [63].

Since GaN/AlN is a lattice mismatched system (2.5% in-plane lattice mismatch), it is important to understand the effects of strain and misfit relaxation at the contact layer/active region interface, as well as the strain generated by layer alternation within the active region of the ISB device. The mechanisms of strain relaxation can be elastic, i.e. undulation of the surface, or plastic, i.e. by introduction of extended defects, which can affect the device properties causing nonradiative recombination, carrier scattering, or enhanced diffusion of dopants and impurities. There are several types of plastic relaxation: crack propagation (commonly observed in III-nitrides under tensile stress), decohesion of the layer, introduction of misfit dislocations (MDs) or glide of pre-existing threading dislocations (TDs). The density of edge-type TDs should be kept to a minimum since they cause losses in the transmission of TM polarized light, which adversely affects the performance of ISB devices [64]. These TDs propagate from the heteroepitaxial substrates (typical TD densities in commercial GaN-on-sapphire or AlN-on-sapphire templates are in the 10^8 cm^{-2} and 10^9 cm^{-2} range, respectively), but they are also generated during the growth due to the plastic strain relaxation, since MDs often fold toward the growth direction, giving rise to the edge-type TDs [65].

Plastic relaxation in semiconductors with cubic symmetry, such as silicon and GaAs, usually takes place along the ⟨1 1 0⟩ {1 1 1} main slip system, either by nucleation of dislocation half loops at the growth surface or by bowing of pre-existing threading dislocations into the heterointerface [66]. However, it is not clear how semiconductors with hexagonal symmetry, such as III nitrides, relax the misfit stress. In the case of nitride heterostructures grown along the [0 0 0 1] axis, the formation of regular networks of MDs is hindered since the most crystallographically favorable slip system, the (0 0 0 1) basal plane with ⟨11–20⟩ {0 0 0 2} slip directions, lies parallel to the heterointerfaces. This means that the resolved misfit stress on the main slip plane is zero [67]. Thus, only secondary slip systems that are oblique to the basal plane can have a resolved misfit stress and may contribute to plastic relaxation. It has been observed that MDs following the secondary ⟨11–23⟩ {11–22} slip system can be generated at heterointerfaces when shear stress is intentionally or unintentionally induced by three-dimensional (3D) growth [68, 69], by crack formation [65, 70], or in close proximity to V-defects [71]. Therefore, the relaxation mechanism depends not only on the structure itself, but also on the growth conditions. In general, GaN/AlGaN heterostructures grown under tensile stress on GaN substrates tend to crack along the ⟨11–20⟩ crystallographic direction at a certain critical thickness [70, 72, 73]. In the case of crack-free GaN/AlGaN superlattices deposited under compressive strain, the main relaxation mechanism is the tilt of the *a*-type TDs towards ⟨1–100⟩, the inclination angle depending on the lattice misfit between the MQWs and the underlayer [74]. It has been proposed that the diagonal movement is due to a staircase-like movement of the dislocations through the stack, with a misfit segment at each well. Strain relaxation via TD inclination has also been observed in AlGaN layers deposited on mismatched AlGaN [75].

In PAMBE growth, the metal-to-N ratio and the growth temperature are key parameters that define the strain relaxation rate during growth [76]. Ga-rich conditions delay crack propagation and minimize strain relaxation [58]. They also allow good control of the layer thickness and Al incorporation in AlGaN alloys. In the case of GaN/AlN MQWs and in addition to the relaxation mechanisms described above, the periodic misfit relaxation appears associated with

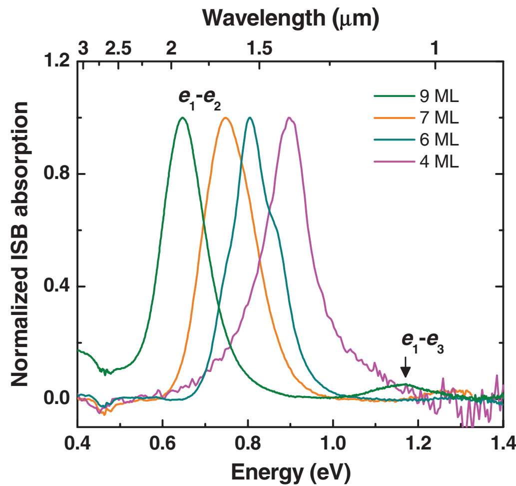

Figure 3. Room-temperature TM-polarized ISB absorption spectra from 20-period Si-doped GaN/AlN MQW structures with 3 nm thick AlN barriers and different GaN QW thickness. All the samples were grown on 1 μm thick AlN-on-sapphire templates without cap layer. The absorption peaks labeled e_1–e_2 and e_1–e_3 are assigned to the corresponding intra-conduction-band transitions as described in figure 1(*a*). Reprinted with permission from [28]. Copyright 2008, American Institute of Physics.

the formation of stacking fault loops that initiate at the beginning of the AlN barrier deposition, propagate through the barrier and close within the following QW [58]. In contrast, transmission electron microscopy (TEM) images from GaN/AlGaN superlattices (ternary alloy barriers) do not reveal stacking faults or other periodic defects [77].

2.1.3. Intersubband optical characterization. Figure 3 shows the ISB absorption of Si-doped AlN/GaN MQWs with 3 nm thick AlN barriers and QW thickness of 5, 6, 7 and 9 ML [14, 28]. The samples show a pronounced TM-polarized absorption, attributed to the transition from the first to the second electronic levels in the QW ($e_1 \rightarrow e_2$), while no absorption was observed for TE-polarized light within experimental sensitivity. For large QWs ($\geqslant$8 ML), the $e_1 \rightarrow e_3$ transition is observed, as indicated in figure 3; this transition is forbidden in symmetric QWs [78], but is allowed in nitride QWs because the internal electric field in the well breaks the symmetry of the potential. The experimental values of e_2–e_1 and e_3–e_1 as a function of the QW width are presented in figure 1, showing a good fit with theoretical calculations.

The line width of the absorption remains in the 70–100 meV range for QWs doped at 5×10^{19} cm^{-2}, and the ISB absorption efficiency per reflection attains 3–5%. A record small line width of ~40 meV has been achieved in non-intentionally doped structures [79]. The spectra present either Lorentzian shape or are structured with two or three well-defined Loretzial-shaped peaks [14]. These multiple peaks correspond to the expected values of the e_1–h_1 line in QWs whose thickness is equal to an integer number of GaN monolayers. For very narrow QWs, a variation in the thickness by 1 ML implies an important shift in the ISB transitions (about 100 meV for QWs of 4–5 ML). This value is comparable to the full width at half maximum (FWHM) of the absorption lines, and hence results in well resolved PL peaks instead of broadening the emission lines. Thickness fluctuations might originate from a drift of the growth rate with time, resulting in a variation in the QW thickness. However, *in situ* measurements of the growth rate and TEM studies confirmed that structured absorption spectra appear in samples where no growth rate drift is detected. In these samples, cathodoluminscence studies confirmed the presence of in-plane thickness fluctuations which appear associated with dislocations or extended defects [28].

Regarding the thermal stability of the ISB transition in GaN/AlN MQWs, it has been found that the ISB absorption energy decreases only by ~ 6 meV at 400 °C relative to its room temperature value [80].

Using GaN/AlN QWs, the e_2–e_1 ISB transition can be tuned in the 1.0–3.5 μm wavelength range by changing the QW thickness from 1 to 7 nm [14, 28, 35, 36, 38, 60, 73, 80, 81] with AlN barriers thicknesses in the 1.5–5.1 nm range. For larger QWs (>5 nm), the first two electron-confined levels get trapped in the triangular section of the QW, which results in a saturation of the e_2–e_1 value. Therefore, to shift the absorption toward longer wavelengths, it is necessary to reduce the effect of the internal electric field in the QWs. A first approach consisted of using GaN/AlGaN MQWs, thereby reducing the Al mole fraction in the barriers. By changing the geometry and composition, the ISB absorption can be tailored to cover the near-IR range above 1.0 μm and mid-IR region up to 5.3 μm [33, 34, 82–90]. To attain longer wavelengths, the requirement of substrate transparency imposes the replacement of sapphire-based templates by semi-insulating Si(1 1 1) as a substrate [21]. Using GaN-on-Si(1 1 1) templates, Kandaswamy *et al* have demonstrated the extension of the ISB absorption range of GaN/AlGaN QWs up to 10 μm [21], as illustrated in figure 4(*a*). A slight red shift of the ISB transition is observed when increasing the compressive strain in the QWs, as theoretically predicted [87].

To further reduce the ISB transition energy, Machhadani *et al* [91] propose an alternative strategy to approach a flat potential in the QW layers by engineering the internal electric field. The investigated structures contain a stack of step-QWs, each period consisting of a GaN well, an $Al_{0.05}Ga_{0.95}N$ step barrier and an $Al_{0.1}Ga_{0.9}N$ barrier. Transmission measurements performed at 4 K reveal TM-polarized ISB absorption at ~2 THz, in good agreement with simulations, as shown in figure 5.

2.1.4. Effect of doping. In order to observe ISB absorption, it is necessary to control the carrier concentration in the QWs to guarantee that the first electronic level is populated. High doping levels also have an effect on the targeted operating wavelength. The ISB absorption energy can blue shift markedly due to many-body effects [22, 38], mostly due to exchange interaction and depolarization shift, as illustrated in figures 4(*b*) and (*c*). On the other hand, studies of the effect of the dopant location have shown a dramatic reduction of the ISB absorption line width by using a δ-doping technique with Si donors placed at the end of the QW [92]. This line width

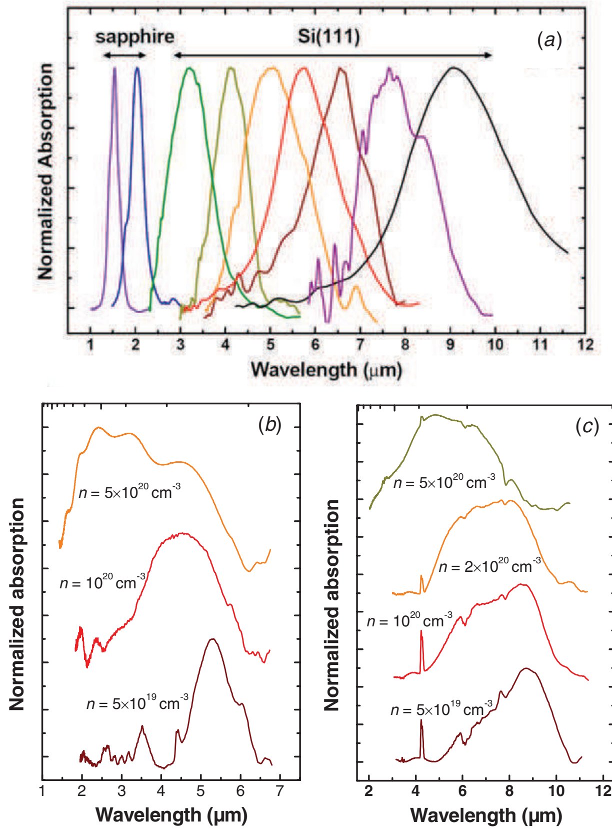

Figure 4. (*a*) Room-temperature TM-polarized IR photo-induced absorption spectra measured in GaN/AlGaN MQW structures with different barrier Al contents and QW width, grown either on sapphire or on Si(1 1 1) templates. Reprinted with permission from [21]. Copyright 2009, American Institute of Physics. (*b*) Infrared absorption spectra for TM-polarized light measured from $GaN/Al_{0.2}Ga_{0.8}N$ (3 nm/3 nm) MQWs with different doping levels. Spectra are vertically shifted for clarity. Reprinted with permission from [22]. Copyright 2010, American Institute of Physics. (*c*) IR absorption spectra for TM-polarized light measured from $GaN/Al_{0.1}Ga_{0.9}N$ (7 nm/4 nm) MQWs with different doping levels. Spectra are vertically shifted for clarity. (After [22].)

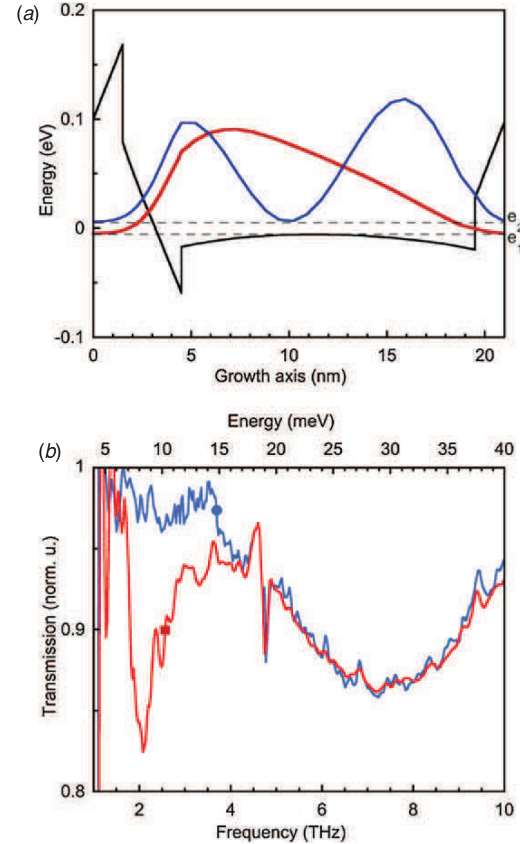

Figure 5. (*a*) Conduction band profile and squared envelope functions of the first two electronic levels (e_1, e_2) for a step-QW sample with 15 nm thick step barrier. (*b*) Transmission spectra for TM- (square) and TE- (circle) polarized light at $T = 4.7$ K. Reprinted with permission from [91]. Copyright 2010, American Institute of Physics.

reduction is attributed to an improvement of the interfacial roughness.

When integrating III-nitride nanostructures in a complete device, it is necessary to keep in mind that the magnitude of the carrier distribution depends not only on the Si doping level in the QWs, but also on the presence of non-intentional dopants, and on the carrier redistribution due to the internal electric field. The large polarization discontinuities in the III-N material system can result in a significant (even dominant) contribution to the IR absorption in GaN/AlN superlattices [28].

2.2. Coupled quantum wells

The design of advanced ISB devices, like optically or electrically pumped ISB lasers, requires the exploitation of multi-level system with finely tuned oscillator strengths and lifetimes. Coupled QWs are the basic element for such systems. In III-nitrides, the realization of coupled QWs is complicated by the relatively heavy electron effective mass and the large conduction band offset. As a result, very thin barriers (1–3 ML) are required to achieve strong interwell coupling in the GaN/AlN material system [93].

Coupling between GaN QWs was first experimentally investigated by Gmachl *et al* [34, 37] by using double GaN QWs coupled by AlGaN barriers with large (0.65 or 0.9) Al mole fractions. The coupling barrier thicknesses varied from 0.7 to 6 nm. Degenerate doping of the QWs (10^{20} cm^{-3}) was used to establish a common reference energy at the Fermi level, which decreases the uncertainties related to intrinsic internal electric fields. The broadening and structuration of the ISB absorption peaks were attributed to transitions toward excited states exhibiting anticrossing.

Coupled GaN/AlN QWs were first demonstrated by Tchernycheva *et al* [94] using 0.5 nm thick AlN coupling barriers. The intersubband absorption spectra present two distinct peaks attributed to the transition, firstly between the ground states of the two coupled wells, and secondly between the ground state and the delocalized excited state between the two wells. As an alternative approach, Driscoll *et al* have opted to decrease the Al content of the coupling barrier to 39–53%, so that strong coupling is achieved with thicker barriers (∼5 ML). In this fashion, the barrier's Al content

can be used as a tunable parameter to control the coupling strength [95].

The influence of polarization-induced electric fields on the ISB absorption and the associated variation of the refractive index in AlN/GaN coupled QWs has been theoretically analyzed by Cen *et al* [96, 97] using a self-consistent Schrödinger–Poisson solver. The results are used to discuss the application of these structures in ultrafast two-color optoelectronic devices and electro-optical modulators operating within the optical communication wavelength range.

2.3. In containing superlattices: AlInN/GaN, AlInN/GaInN and GaN/GaInN

As described above, the lattice mismatch between GaN and AlN can lead to high defect densities and risk of cracking in GaN/AlN superlattices. An alternative material approach to overcome this problem is the use of AlInN alloys. AlInN with an In composition around 17–18% is lattice matched to GaN and presents a refractive index contrast equivalent to AlGaN with 46% Al content (6% contrast with GaN at 1.55 μm wavelength). Therefore, AlInN is a promising material to form distributed Bragg reflectors and thick waveguide layers [98]. However, lattice-matched AlInN/GaN heterostructures still exhibit an electric field as large as 3 MV cm^{-1}, solely generated by the spontaneous polarization discontinuity.

The potential of AlInN/GaN lattice-matched systems for application in ISB technology has been explored [99, 100]. However, this material system is not adapted to serve as active region for telecommunication devices since the conduction band offset is in the range of ~1 eV [101]. Nevertheless, ISB absorption in the near-IR spectral region has been reported at 2.3–2.9 μm in lattice-matched GaN/AlInN superlattices grown by MOVPE [99] and by MBE [102].

An alternative approach to manage the strain in the structure while retaining access to shorter wavelengths is possible by adding small concentrations of In (below 10%) both in the barrier and in the QW, forming an AlInN/GaInN superlattice [103, 104]. This material combination reduces the probability of crack propagation in comparison to GaN/AlN, although it maintains a certain degree of strain. Room-temperature ISB absorption in the 1.52–2.45 μm wavelength range has been demonstrated in AlInN/GaInN MQWs [103]. Efforts to simulate the electronic structure of these superlattices have been recently reported [105]; however, it remains challenging to control precisely the In mole fraction during the superlattice growth.

Regarding the GaN/GaInN system, only theoretical calculations of the ISB transition energy have been published so far [106].

2.4. Quantum dots

An alternative approach to QW structures for the fabrication of devices is based on optical transitions between bound states in the conduction band of quantum dot (QD) superlattices [107, 108]. Quantum dot IR photodetectors (QDIPs) are expected to ultimately outperform QWIPs in terms of low dark current, high photoelectric gain and sensitivity [109]. Furthermore, under certain conditions, intraband bound-to-continuum transitions in QDs can be nearly independent of the polarization of excitation [110–112].

In the case of III-nitrides, GaN/AlN QD structures can be synthesized by PAMBE through GaN deposition under compressive strain and under N-rich conditions [79, 113]. In this situation, 2D growth proceeds normally to create a 2-ML-thick wetting layer. Due to the lattice mismatch between AlN and GaN, further GaN deposition leads to the formation of 3D islands above this 2D wetting layer (Stranski–Krastanov growth mode). These GaN QDs are well-defined hexagonal truncated pyramids with {1–103} facets [114], and no Ga–Al interdiffusion has been observed [115]. The QD size can be tuned by modifying the amount of GaN in the QDs, the growth temperature or the growth interruption time after deposition of the QDs (Ostwald ripening). By adjusting the growth conditions, QDs with height (diameter) in the range of 1–1.5 nm (10–40 nm), and density between 10^{11} cm^{-2} and 10^{12} cm^{-2} can be synthesized (see atomic force microscopy image in figure 6(*a*) as an example) [116]. To populate the first electronic level, silicon can be incorporated into the QDs without significant perturbation of the QD morphology.

Similar GaN/AlN QDs can be synthesized by ammonia-MBE by performing a growth interruption after deposition of a GaN thickness larger than 3 ML (~0.8 nm), which instantaneously leads to the formation of 3D islands [117]. Regarding MOVPE, the formation of 3D GaN islands has been first demonstrated using Si as an antisurfactant [118]. With this method, the shape and the density of GaN QDs can be controlled by the Si dose, the growth temperature, the growth time and the Al content of the AlGaN layer below the islands [119]. GaN/AlN QDs have also been synthesized by low-pressure MOVPE using very low V/III ratios [120]. Depositing over a critical thickness of 4 ML of GaN results in a spontaneous transition from the 2D to the 3D growth mode. The density of the QDs can be tuned between 10^9 and 10^{10} cm^{-2}, keeping typical QD diameter and height around 20 and 2 nm, respectively. The size of the QDs can be controlled to a considerable extent by changing the growth temperature and V/III ratio.

Andreev *et al* have calculated the electronic structure of GaN/AlN QDs using the $k \times p$ model and taking the internal electric field into account [121–123]. These calculations have been complemented by Ranjan *et al* [124] through the use of the tight-binding theory and a self-consistent treatment to account for carrier screening of the electric field. The models show that the polarization-related internal electric field localizes the electrons at the pyramid apex, whereas the holes are located close to the wetting layer. In addition to the carrier separation along the growth axis, the electric field can provide a strong additional lateral confinement for carriers localized in the dot, which greatly modifies their electronic structure and optical properties [123].

From the experimental viewpoint, early studies of intraband phenomena in GaN QDs showed photoinduced IR absorption in the 1.27–2.4 μm spectral range in undoped nanostructures synthesized by ammonia-MBE [125]. Later on, PAMBE-grown Si-doped QD superlattices have been reported

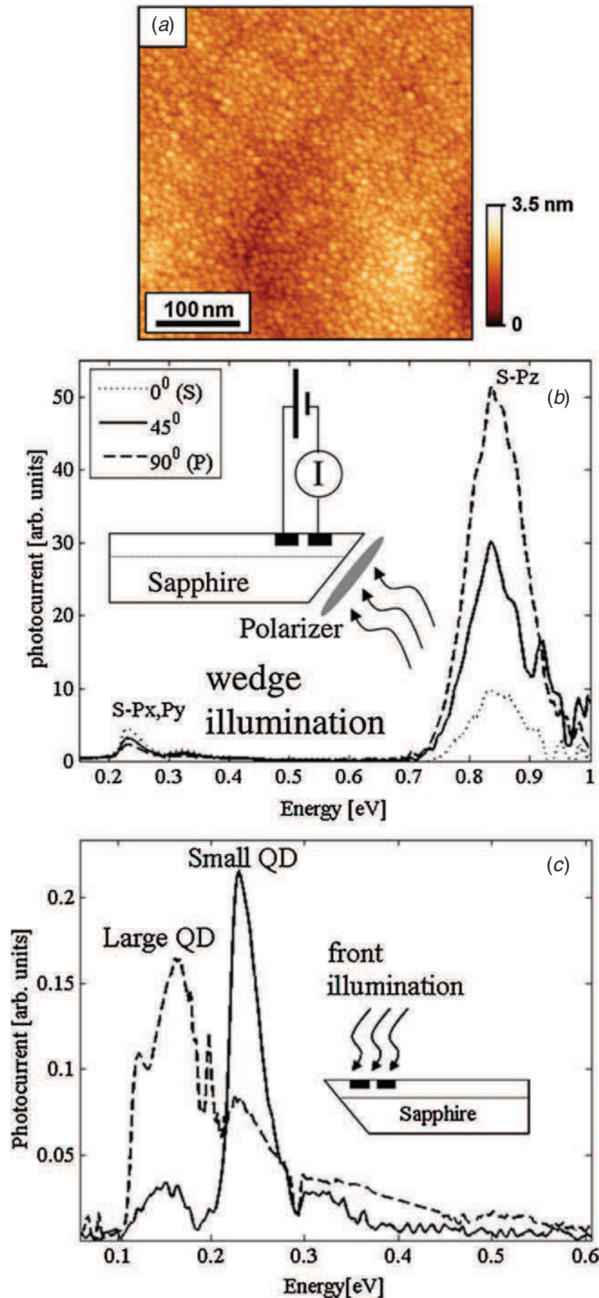

Figure 6. (*a*) Atomic force microscopy image of a GaN QD layer synthesized on AlN by PAMBE, showing a high density ($\sim 10^{12}$ cm^{-3}) of small (height ∼1.3 nm; base diameter ∼11 nm) QDs. (*b*) Polarization-dependent spectral response (photocurrent) of a GaN/AlN QD stack measured in wedge illumination. The normalized response of both s–p_z in the near IR and s–$p_{x,y}$ in the mid-IR; the s–p_z peak is about ten times larger than the s–$p_{x,y}$ peak. (*c*) Mid-IR spectral response of two GaN/AlN QD stacks with smaller (full line) and larger (dash line) QDs measured at $T = 12$ K under front illumination and 10 V bias. Sapphire cutoff is at 0.22 eV. Reprinted with permission from [127]. Copyright 2009, American Physical Society.

to exhibit strong TM-polarized intraband absorption at room temperature, which can be tuned from 0.74 eV (1.68 μm) to 0.90 eV (1.38 μm) as a function of the QD size [116, 126]. The broadening of the absorption peak can be as small as ∼80 meV for the most homogeneous samples. This absorption line is attributed to transitions from the ground state of the conduction band, s, to the first excited electronic state confined along the growth axis, p_z. The lateral confinement in the QDs should give rise to additional transitions under TE-polarized excitation. However, taking into account the lateral dimension of the QDs ∼7 nm, the s–$p_{x,y}$ transitions should be masked by the sapphire absorption for $\lambda > 5$ μm. The optical signature associated with s–$p_{x,y}$ was first observed by Vardi *et al* who studied mid-IR intraband transitions in GaN/AlN QDs using in-plane electronic transport at low temperatures [127], as illustrated in figures 6(*b*), (*c*). The measured s–$p_{x,y}$ energy separation (0.1–0.3 eV) presented in figure 6(*c*) was significantly larger than the equivalent transition energy in InGaAs\GaAs QDs. Their analysis shows that the appearance of large energy s–$p_{x,y}$ in GaN\AlN QDs is due to the strong internal electric field in the QDs which results in stronger confinement of the electrons at the QD top facet.

The homogeneous line width of the s–p_z intraband transition at 1.55 μm in GaN/AlN QDs was assessed by means of nonlinear spectral hole-burning experiments [128]. These measurements demonstrated that electron–electron scattering plays a minor role in the coherence relaxation dynamics, since the homogeneous line width of 15 meV at 5 K does not depend on the incident pump power. This suggests the predominance of other dephasing mechanisms such as spectral diffusion.

TM-polarized IR absorption in the 1.6–2 μm wavelength range, attributed to s–p_z intraband transitions, has also been reported in ternary AlGaN/AlN QDs measured at room temperature. The s–p_z transition red shifts for increasing Al mole fraction in the QDs as a result of the reduction of the band offset, in good agreement with theoretical calculations [129].

2.5. Alternative crystallographic orientations

The already high design complexity of ISB devices further increases in materials with internal electric field like polar III-nitrides. A simple solution to this problem consists in using non-polar crystallographic orientations like the *m*-plane {1–100} or the *a*-plane {11–20} [130]. However, epitaxy for these orientations is an arduous task, due to strong anisotropy of the surface properties, resulting in a high density of crystalline defects. An alternative approach is the growth on semipolar planes [130], which are those (*hkil*) planes with at least two non-zero *h*, *k* or *i* Miller indices and a nonzero *l* Miller index. Semipolar planes allow a considerable reduction in the internal electric field [131] while presenting a lower in-plane anisotropy than non-polar surfaces [132, 133].

Regarding nonpolar materials, ISB optical absorption at $\lambda \sim 2.1$ μm with a FWHM = 120 meV has been reported in Si-doped 1.75 nm thick GaN QWs with 5.1 nm thick AlN barriers grown by PAMBE on *r*-plane sapphire and displaying pure *a*-plane orientation [134].

Near-IR ISB absorption has also been reported on semipolar (11–22)-oriented GaN/AlN MQWs grown by PAMBE [133]. The band structure of these semipolar

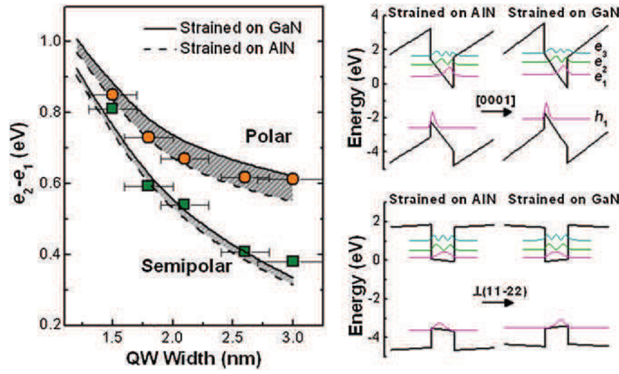

Figure 7. Left: Variation of e_2–e_1 energy as a function of well width in polar and semipolar GaN/AlN MQWs with 5 nm thick AlN barriers, strained on GaN and AlN. Right: band diagram of (0 0 0 1)- and (11–22)-oriented GaN/AlN (2.5 nm/5 nm) MQWs, assuming the structure fully strained on AlN and on GaN. Adapted with permission from [133]. Copyright 2008, American Institute of Physics.

GaN/AlN QWs strained on GaN and on AlN is represented in figure 7. In comparison to polar QWs, semipolar structures exhibit quasi-square potential band profiles with symmetric wavefunctions, due to the reduced electric field in the range of 0.5–0.6 MV cm^{-1} in the QWs. The evolution of the e_2–e_1 ISB transition energy with the QW thickness is represented in figure 7, where symbols correspond to experimental measurements obtained from identical polar and semipolar samples consisting of 40 periods of GaN/AlN with 3 nm thick AlN barriers. The absorption FWHM (∼80–110 meV [133]) is comparable to the one measured in polar structures [14, 28]. However, in semipolar structures, the reduction in the internal electric field results in a red shift of the ISB energy. Also the spectral shape of semipolar absorption is Gaussian, in contrast to the Lorentzian shape described for polar GaN/AlN QWs. This is due to the spectral dispersion generated by thickness fluctuations and by the presence of stacking faults in semipolar material, both inducing carrier localization in the range of a few meV, much smaller than the FWHM of the ISB absorption line.

Another approach to eliminate the internal electrical field in III-nitride heterostructures is the use of III-nitride semiconductors crystallized in the zinc-blend crystallographic phase. The LO phonon energy in cubic GaN is almost the same as in wurtzite GaN (92.7 meV [135]), but the effective mass is significantly smaller ($m^* = 0.11$–$0.17m_0$ [136, 137]) than in wurtzite GaN ($m^* = 0.2m_0$), which should result in higher gain and lower threshold current in QCLs. The cubic orientation can be selected by PAMBE using 3C-SiC substrates. However, due to their thermodynamically unstable nature, cubic films present low structural quality with a high density of stacking faults. ISB absorption in the 1.40–4.0 μm spectral range has been reported in cubic GaN/AlN MQWs [138, 139], in agreement with theoretical calculations assuming a conduction band offset of 1.2 eV and an effective mass $m^* = 0.11m_0$ (see figure 8). ISB THz absorption at 4.7 THz has also been observed in cubic GaN/Al$_{0.05}$Ga$_{0.95}$N (12 nm/15 nm) QWs [139].

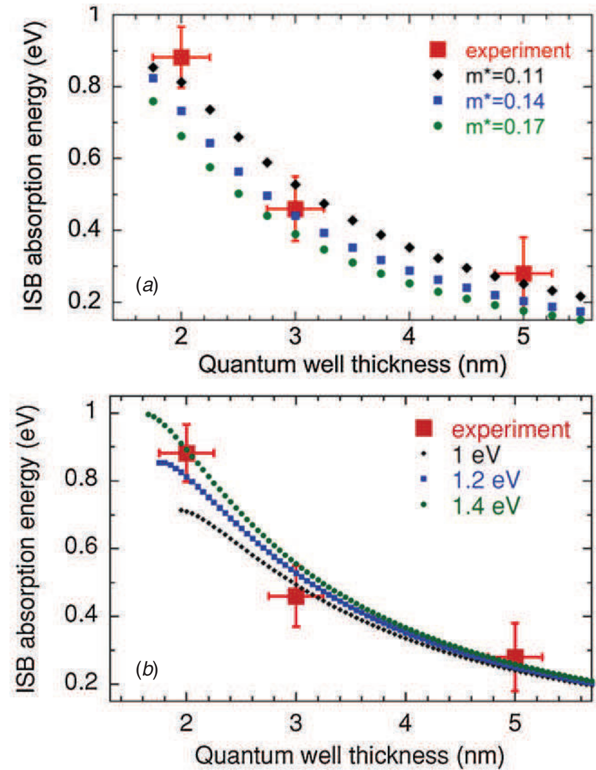

Figure 8. (*a*) ISB transition energy in cubic GaN/AlN MQWs calculated within effective mass approximation compared to the experimental data (red squares). The following parameters are used in the calculations: conduction band offset = 1.2 eV for all curves; black diamonds: $m^*_{e\mathrm{GaN}} = 0.11m_0$, $m^*_{hh\ \mathrm{GaN}} = 0.8m_0$, $m^*_{e\ \mathrm{AlN}} = 0.19m_0$, $m^*_{hh\ \mathrm{AlN}} = 1.2m_0$; blue squares: $m^*_{e\mathrm{GaN}} = 0.14m_0$, $m^*_{hh\ \mathrm{GaN}} = 0.86m_0$, $m^*_{e\ \mathrm{AlN}} = 0.28m_0$, $m^*_{hh\ \mathrm{AlN}} = 1.44m_0$; green circles: $m^*_{e\mathrm{GaN}} = 0.17m_0$, $m^*_{hh\ \mathrm{GaN}} = 0.85m_0$, $m^*_{e\ \mathrm{AlN}} = 0.3m_0$, $m^*_{hh\ \mathrm{AlN}} = 1.39m_0$. (*b*) ISB absorption energies calculated for different conduction band offset values, compared to the experimental data (red squares). The following effective masses are used: $m^*_{e\mathrm{GaN}} = 0.11m_0$, $m^*_{hh\ \mathrm{GaN}} = 0.8m_0$, $m^*_{e\ \mathrm{AlN}} = 0.19m_0$, and $m^*_{hh\ \mathrm{AlN}} = 1.2m_0$. In both plots, the error bars correspond to ± 1 ML thickness fluctuation for the abscissa and to the FWHM of the transition for the ordinate. Reprinted with permission from [139]. Copyright 2009, American Physical Society.

3. All-optical switches

The development of multi-terabit optical time division multiplexing (OTDM) networks depends on the implementation of all-optical switches and wavelength converters operating at room temperature. In these devices, the switching is based on ISB absorption bleaching by an intense control pulse, as originally demonstrated at long IR wavelengths using GaAs/AlGaAs [140]. These devices should demonstrate an ultrafast response capable of sustaining high repetition rates with low switching energy and high contrast ratio. Attempts to realize these features lead to the consideration of resonant nonlinearities in semiconductor nanostructures [141]. Thanks to the ultrafast ISB recovery time (in the 140–400 fs range [37, 142–146]) associated with the strong interaction of electrons with LO phonons, GaN/AlN QWs or QDs have been proposed as the active medium for

all-optical switches (saturable absorbers) operating at Tbit/s data rates and at telecommunication wavelengths.

The use of GaN/AlGaN QWs for all-optical modulators at telecommunication wavelengths was first proposed by Suzuki *et al* [15, 147]. Since then, all-optical switching at $\sim$1.55 μm with sub-picosecond commutation time has been demonstrated by several groups [31, 64, 144, 145, 148–151]. In general, these devices consist of GaN/AlN MQWs embedded in a ridge waveguide. In such structures, a critical parameter to reduce transmission losses is the reduction of edge-type dislocations. These defects introduce acceptor centers where electrons can be captured, and therefore can effectively act as a wire-grid polarizer which leads to selective attenuation of the TM-polarized signal [152]. Control switching energies as low as 38 pJ for 10 dB modulation depth [149] and 25 pJ for 5 dB contrast [151] have been demonstrated using a waveguide with an AlN cladding below the active GaN/AlN QWs, and GaN or Si_xN_y as the upper cladding layer, respectively. Theoretical calculations predict a reduction of the switching energy by a factor of 30 by replacing the GaN/AlN QWs with properly designed AlN/GaN/AlGaN coupled QWs [153, 154].

From the material viewpoint, the parameter responsible for absorption saturation is the optical third-order susceptibility, $\chi^{(3)}$. Comparative studies using the forward degenerate four-wave mixing technique in a boxcars configuration point to an increase of $\chi^{(3)}$ by a factor of 5 in QDs compared to QWs [155]. From the experimental viewpoint, the intraband absorption saturation of GaN/AlN QDs has been probed by Nevou *et al* [31], obtaining values in the range of 15–137 MW cm^{-2} (0.03–0.27 pJ μm^{-2}). In spite of the large signal variation (a consequence of the focusing uncertainty in the sample), even the upper estimate of the saturation intensity for QDs is smaller than the corresponding value for GaN/AlN QWs (9.46 W μm^{-2} [149]).

4. Resonant tunneling transport

4.1. Mesa-structured resonant tunneling diodes

Understanding electron resonant transport is of critical importance for the fabrication of electrically driven ISB devices. Furthermore, resonant tunneling diodes (RTDs) are attractive for terahertz frequency applications, since oscillators based on RTDs have recently shown operation frequencies up to 1.1 THz [156, 157]. III-N heterostructures in particular are expected to provide a larger peak-to-valley ratio (PVR) in the resonant tunneling current due to their large and adjustable band offsets compared to other materials.

Studies of electron transport through single GaN/AlN/GaN barriers indicate that bias induces a re-distribution of charges in the GaN layers, but does not significantly modify the polarization-induced electric field in the barrier [158, 159]. For 0.5 and 1 nm thick AlN barriers, electron tunneling is confirmed by optical characterization. For AlN barriers in the 1–3 nm range, conductive AFM measurements reveal efficient current blockage, with pure screw dislocations being the main source of leakage current [159, 160]. Finally, leakage due to AlN relaxation and interband tunneling was observed for 5 nm thick barriers [159, 161].

The first theoretical investigation into resonant tunneling in GaN/AlGaN double-barrier heterostructures was presented in 2001 by Grinyaev and Ruzzhuvalov [162]. Since then, the development of a nitride-based RTD became a hot topic. First reports of resonant tunneling in Al(Ga)N/GaN double barriers [163–166] were highly controversial because of the scarcity and irreproducibility of the published data. In 2002, Kikuchi *et al* reported the first measurements of resonant tunneling in PAMBE-grown AlN/GaN heterostructures consisting of 40 μm square encapsulated mesa-diodes [163]. A negative differential resistance (NDR) was recorded at 2.4 V bias, with a peak current density of 180 A cm^{-2} and PVR of 32. However, the NDR was only observed in forward bias[1] and only when scanning from negative toward positive bias. Theoretical calculations accounting for polarization effects [167–171] can explain some of the features observed by Kikuchi, namely the asymmetric current–voltage characteristics, but not the current hysteresis. Since then, many other groups have faced similar problems of hysteresis and instabilities [159, 172–178].

The development of III-N RTDs still remains a challenging task due to the presence of trap-like defects and impurities in the heterostructures. These traps are thermally activated, and therefore their effect on the tunneling current is minimized when the temperature decreases [179], resulting in a larger PVR at lower temperatures. Improved reproducibility of the NDR is achieved by decreasing the substrate dislocation density [173, 175, 176], decreasing the device mesa size [159, 180], or using low-aluminum-content AlGaN/GaN double-barriers [178]. The NDR reproducibility is also drastically improved when scanning the voltage from a sufficiently negative starting bias due to the detrapping of charges via the Poole–Frenkel effect [159, 180].

Resonant electron transport through MQWs, namely a seven-period GaN/AlN stack, has also been reported [181]. The devices show asymmetric current–voltage characteristics displaying NDR features at room temperature under forward bias. These features, which persist for multiple scans and are reproducible for both upward and downward sweeping voltage, are interpreted as a consequence of the resonant tunneling between the fundamental and excited states of adjacent QWs.

4.2. Resonant tunneling transport in nanowires

III-Nitride nanowire (NW) heterostructures offer an alternative approach by minimizing the effects of strain relaxation, which not only provides dislocation-free material, but also attenuates the piezoelectric effects. Nano-scale RTDs based on NW heterostructures were first demonstrated using InP/InAs [182]. Recently, electron resonant tunneling transport was presented in single defect-free *n-i-n* GaN NWs containing closely spaced (4 nm) AlN double barriers grown by PAMBE [183], as illustrated by the TEM image in figure 9(*a*). The devices were fabricated with a back-gate NW-field effect transistor geometry, placing the double-barrier structure in between the source and drain contacts. The transistor's low-temperature

[1] It is conventionally considered that the positive electrode is the top contact in samples grown along the [0 0 0 1] axis.

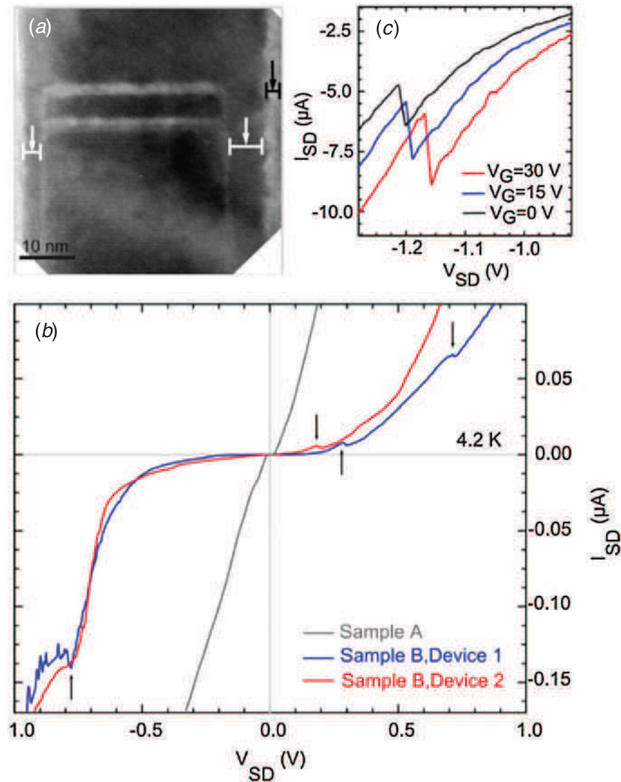

Figure 9. (*a*) High-resolution TEM image a GaN NW section containing a double-barrier heterostructure, i.e. a pair 2 nm thick AlN barriers (bright contrast) separated by a 6 nm thick GaN section. The GaN lateral growth around the AlN barriers is resolved in the image (white arrows). The sharp contrast observed at the right facet of the NW (black arrow) corresponds to native gallium oxide. (*b*). Source-drain current–voltage ($I_{SD} - V_{SD}$) characteristics at 4.2 K of GaN NWs with two closely-spaced AlN tunnel barriers in comparison with that of *n-i-n* GaN NWs. (*c*) $I_{SD}-V_{SD}$ characteristics showing the evolution of the NDR appearing at negative V_{SD} for different values of gate voltage V_G. Adapted with permission from [183]. Copyright 2010, American Chemical Society.

current–voltage characteristics (figure 9(*b*)) exhibit NDR features, attributed to the onset of tunneling via the confined levels between the AlN barriers. The bias value displaying NDR features can be tuned by adjusting the electrostatic potential via the back-gate bias (figure 9(*c*)). The NDR features in these NW-RTDs are reproducible for both bias sweeping directions and no degradation of the device characteristics are found after repeated measurements.

Rigutti *et al* studied the electrical transport through GaN NWs containing multiple GaN/AlN nano-disks [184]. They found that the presence of a spontaneously formed GaN shell surrounding GaN/AlN nano-disks significantly influences the device characteristics. When the GaN shell does not exist, the current mainly flows though the multiple nano-disks and reproducible NDR is observed, which is attributed to the electron tunneling through the electronic states available in those nano-disks. In contrast, the NDR feature disappears when the GaN shell is present, as the current mainly flows through the shell close to the NW sidewalls.

Finally, there has been an attempt to take advantage of the suppressed internal electric field in AlN/GaN heterostructures grown in the non-polar orientation by growing the AlN/GaN double barriers on the *m*-plane sidewall of a GaN NW [185]. The electron transport was measured using an SEM equipped with nano-manipulators, capable of contacting individual NWs. NDR characteristics were found in the ensemble and individual AlN/GaN core shell NWs, and are explained by the resonant tunneling through the AlN/GaN double barrier. Individual NW measurements show NDR at room temperature with a peak current density of 5×10^5 A cm^{-2}.

5. Electro-optical modulators

Electro-optical modulators are essential components for fiber-optic communication at $\lambda = 1.55$ μm, since they aid to overcome the inherent speed limitations and positive chirp of conventionally used interband semiconductor lasers. Electro-optical amplitude and phase modulators allow for control of the amplitude, phase and/or polarization state of an optical beam as a function of a bias voltage. State-of-the-art technologies in this field include modulators based on the QCSE of interband transitions in InGaAsP QWs [186], and others based on the electro-optic effect in materials like $LiNbO_3$ within a Mach–Zehnder configuration [187]. These devices present several drawbacks, such as low saturation power and positive chirp in the former case, and the need for high driving voltage and larger size in the latter case. Achieving a significant improvement in device performance requires a change of technological approach. Exploiting ISB transitions in QWs has been proposed as a means to reduce the driving voltage and increase the bandwidth [188–190]. Moreover, the higher ISB transitional oscillator strength in comparison to interband transitions, should allow for further miniaturization of the devices.

The first electro-absorption ISB modulation experiments on AlN/GaN QWs were based on the electrical depletion of a five-period AlN/GaN (1.5 nm/1.5 nm) MQW structure grown on a thick GaN buffer [191]. The absorption spectrum of such a sample presents two distinct peaks related to ISB transitions in both the QWs and in the 2D electron gas located at the interface of the lowest AlN barrier and the underlying GaN buffer. The ratio of these two absorption peaks can be adjusted by applying an external field, which influences the overall band structure and, more specifically, the free carrier density in the QWs. To increase the modulation depth, the interaction of light with the active medium should be enhanced, which can be achieved with a waveguide geometry [17]. Through the use of a 1-μm-thick $Al_{0.5}Ga_{0.5}N$ waveguiding layer on AlN, and with three active GaN/AlN QWs operating at $\lambda = 1.55$ μm, a modulation depth of 13.5 dB was observed for a −9V/+7V voltage swing (10 dB for 5 V voltage swing).

The intrinsic speed limit can be greatly improved by emptying active QWs into a local reservoir, instead of transferring carriers over the whole active region. This is the principle of the coupled-QW modulator: The electro-modulation originates from electron tunneling between a wide well (reservoir) and a narrow well separated by an

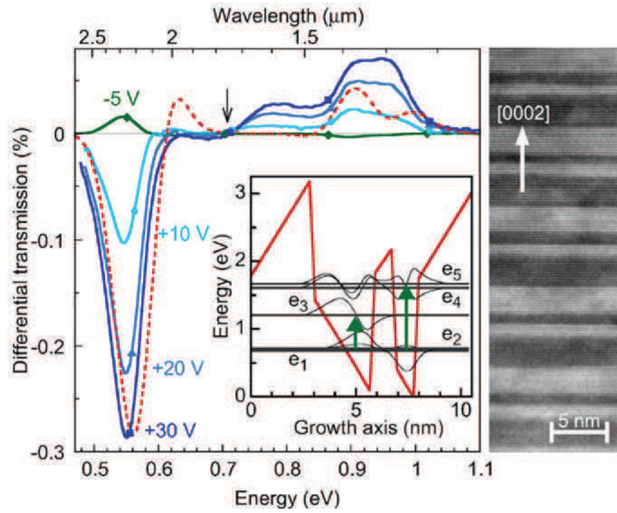

Figure 10. Differential transmission ΔT/T for applied bias pulses of +30 V (squares), +20 V (triangles), +10 V (circles), and −5 V (diamonds). The arrow ponts the energy at which a discontinuity of the derivative of the FTIR spectrum occurs. The dashed line shows the calculated transmission change for 0.8 V bias across the active region. The inset shows the conduction band profile and energy levels for one period of coupled QWs. Right panel: high-resolution TEM image showing five periods of coupled QWs in the active region. Adapted with permission from [192]. Copyright 2007, American Institute of Physics.

ultrathin (∼1 nm) AlN barrier (see the inset of figure 10). Experiments on GaN QW coupling via AlN [94] or AlGaN [95] barriers have set the basis for the demonstration of room-temperature ISB electro-modulated absorption at telecommunication wavelengths in GaN/AlN coupled QWs with AlGaN contact layers [192–194]. Figure 10 illustrates the design and performance of a modulator with 1 nm thick AlN coupling barriers [192, 193]. Positive bias favors electron transfer from the reservoir well to the active well, which increases the ISB absorption at 1.3–1.6 μm. Under reverse bias, the electrons tunnel back to the reservoir well and the structure becomes transparent at telecommunication wavelengths. The $BW_{\text{-3dB}}$ cut-off frequency is limited by the resistance × capacitance (RC) time constant and is as high as 3 GHz for 15 × 15 μm^2 mesas. This frequency could be further improved by reducing the access resistance of the AlGaN contact layers. According to Hölmstrom, the high-speed performance of such modulators will ultimately be determined by the ISB absorption line width Γ, since their capacitance depends on the line width as $C{\sim}\Gamma^3$ [188, 189].

All the above-described electro-optical modulators rely on light amplitude modulation via ISB absorption. Based on Kramers–Kronig relations, the ISB absorption should also translate into a variation of the refractive index at wavelengths close to the transition, which can be used for phase modulation. This concept was verified experimentally at mid-IR (∼10 μm) wavelengths using the stark shift of ISB transitions in GaAs/AlGaAs step QWs [195]. The strongly nonlinear susceptibility observed in GaN/AlN QWs [155, 196] has led to the first theoretical proposals of all-optical cross-phase modulators [96].

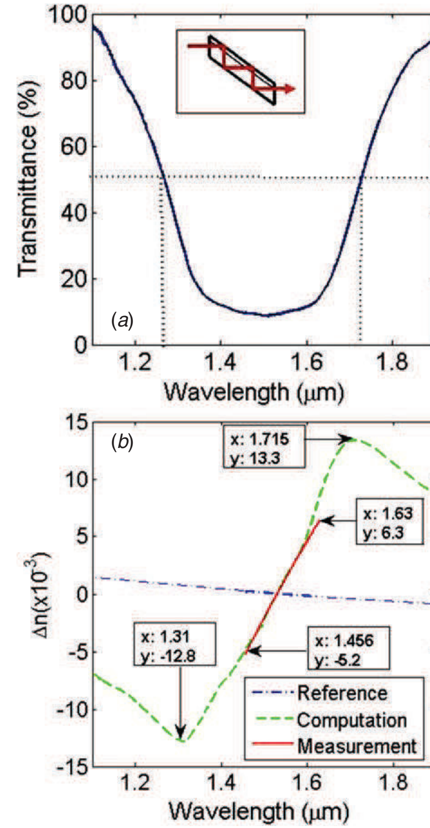

Figure 11. (a) Normalized transmittance of 100 periods of GaN/AlN QWs measured in multi-pass waveguide configuration as described in the inset. (b) Measured refractive index dispersion due to ISB absorption in the GaN/AlN MQWs interaction layer (solid red line). Kramers–Kronig computation of the FTIR measured absorption shown on the left (green dashed line). The measured reference sample refractive index dispersion (blue dotted-dashed line) is of the order of 10^{-4}. (Adapted from [198].)

Using a depletion modulator consisting of 3 GaN/AlN QWs inserted in an $Al_{0.5}Ga_{0.5}N$/AlN ridge waveguide on sapphire, Lupu *et al* [197] reported a variation of the refractive index around ∼1.5 μm deduced from the shift of the beating interference maxima for different order modes. The change in the refractive index was derived to be $\Delta n = -5 \times 10^{-3}$ as the population was changed from complete depletion to full population of the QWs. This result is in close agreement with the observation of a refractive index dispersion between -5×10^{-3} to 6×10^{-3} in a 100-period Si-doped GaN/AlN (1.5 nm/3 nm) MQWs using a free-space Mach–Zehnder interferometer configuration [198]. Figure 11 illustrates the ISB absorption and variation of refractive index measured in such samples. The values of Δn are comparable to those obtained at the same wavelength in phase modulators based on interband transitions in InGaAsP/InP QWs using the quantum confined Stark effect [199], and they are one order of magnitude higher than the index variation obtained in silicon [200]. These results open the way for the realization of ISB Mach–Zehnder interferometer phase modulators in the optical communication wavelength range.

6. Infrared photodetectors

6.1. Quantum well/quantum dot infrared photodetectors

Quantum well infrared photodetectors (QWIPs) have found widespread application for thermal imaging, using mature materials such as GaAs. In nitrides, however, with the possibility of tuning ISB transitions in the 1.3–1.55 μm range, and with rapid carrier relaxation (∼140 fs), the main motivation for QWIPs is high-speed detectors for optical communications. Photoconductive GaN/AlN QWIPs operating at 1.6–1.76 μm have been demonstrated [201, 202]. The responsivity was estimated to be 0.1 mA W^{-1} at 10 K; however, the photocurrent signal could only be observed up to 120–170 K, even though the optical absorption remained unchanged up to room temperature. Later, Uchida *et al* demonstrated GaN/AlN QWIPs operating at 1.55 μm at room temperature with a responsivity of 0.11 mA W^{-1} under 15 V bias. Finally, photoconductive IR photodetectors based on cubic GaN/AlN QW superlattices have also been reported [203]. These devices exhibit a photovoltaic effect that is overtaken by the dark current for temperatures above 215 K. This photoresponse is consistent with ISB transition phenomena, but the mechanism behind the photovoltaic behavior remains unknown.

Lateral QDIPs have also been fabricated by depositing planar contacts on samples consisting of 20 periods of Si-doped GaN/AlN QDs, first operating at liquid nitrogen temperature [204] and then at room temperature [127, 205]. The devices exhibit photocurrent for TM-polarized excitation in the 1.4–1.9 μm spectral range, following the intraband s-p_z selections rules. At low temperature ($T = 10$ K), mid-IR photoresponse to TE-polarized light is also observed and attributed to s–$p_{x,y}$ transitions. The appearance of photocurrent due to these bound-to-bound transitions is attributed to conductivity via lateral hopping [127]. Further studies have shown that deep levels in the AlN barriers may also contribute to the photocurrent, giving rise to negative photoconductivity effects [206].

In spite of these early demonstrations, photoconductive devices keep presenting a low yield due to the large dark current originating from the high density of dislocations in heteroepitaxial III-nitrides (∼10^9 cm^{-2}), particularly in GaN/AlN devices targeting near-IR wavelengths. An alternative to bypass the leakage problem consists of exploiting the device's photovoltaic response, where zero-bias operation guarantees a minimum dark current. Photoconductive QWIPs already displayed a photovoltaic response [207], which was less sensitive to defects [202], particularly to those associated with the yellow band in GaN [208], in agreement with observations in photovoltaic versus photoconductive interband detectors [209].

The photovoltaic operation of GaN/AlN QWIPs at telecommunication wavelengths and at room temperature was first studied in detail by Hofstetter *et al* [29, 59, 210–212]. The working principle of photovoltaic ISB detectors is based on resonant optical rectification processes in asymmetric QWs [29], as described by Rosencher and Bois in asymmetric GaAs/AlGaAs QWs [213]. In a GaN/AlN superlattice, due to the QW asymmetric potential profile, the excitation of an electron into the upper quantized level is accompanied by a small displacement in the growth direction, and an electrical dipole moment is created. For a high electron density and many QWs, these microscopic dipole moments add up to a macroscopic polarization of the crystal, which can be detected as an external photovoltage. A strong performance enhancement (responsivity increase by a factor of 60) of these detectors has been achieved by using QDs instead of QWs in the active region [214]. The improvement is attributed to the longer electron lifetime in the upper QD states and the increased lateral electron displacement.

An interesting application of photovoltaic ISB photodetectors is the so-called multi-spectral detectors, operating in various wavelength ranges, with potential applications in surveillance, failure analysis and meteorology. Hofstetter *et al* [215, 216] have combined optical interband and ISB transitions with a monolithic integration of a photoconductive UV interband (solar-blind) detector based on an AlGaN thin film and a photovoltaic near-IR ISB detector based on an AlN/GaN superlattice, as illustrated in figure 12. The two detectors exhibit spectrally narrow responsivity curves, thus enlarging the UV-to-visible rejection ratio in the case of the UV device, and improving the noise behavior in the case of the IR detector at room temperature.

6.2. Quantum cascade detectors

Quantum cascade detectors (QCDs) are photovoltaic devices consisting of several periods of an active QW coupled to a short-period superlattice which serves as an extractor [217, 218]. Under illumination, electrons from the ground state, e_1, are excited to the upper state of the active QW, e_2, and then transferred to the extractor region where they experience multiple relaxations toward the next active QW. This results in a macroscopic photovoltage in an open circuit configuration. As major advantage, their dark current is extremely low and the capacitance can be reduced by increasing the number of periods, which enables high frequency response.

GaN/AlGaN QCDs operating in the near-IR have been reported [219, 220], with their structure illustrated in figure 13. These devices take advantage of the polarization-induced internal electric field to design an efficient AlGaN/AlN electron extractor where the energy levels are separated by approximately the LO-phonon energy (∼90 meV), forming a phonon ladder. The peak responsivity of these GaN/AlGaN QCDs at room temperature was ∼10 mA W^{-1} (∼1000 V W^{-1}) [219]. Detectors containing 40 periods of active region with the size 17 × 17 μm^2 exhibit the BW_{-3dB} cut-off frequency at 19.7 GHz [221]. However, the speed of these quantum cascade detectors is governed by their *RC* constant, and not by an intrinsic mechanism. Pump and probe measurements of these devices pointed to an ISB scattering time in the active QW of 0.1 ps and a transit time through the extractor of 1 ps [222]. With these data, the intrinsic frequency bandwidth is expected to be above 160 GHz, significantly higher than theoretical predictions by Gryshchenko *et al* [223].

Sakr *et al* [224] have shown a significant improvement of a GaN/AlGaN QCD in terms of responsivity and bandwidth,

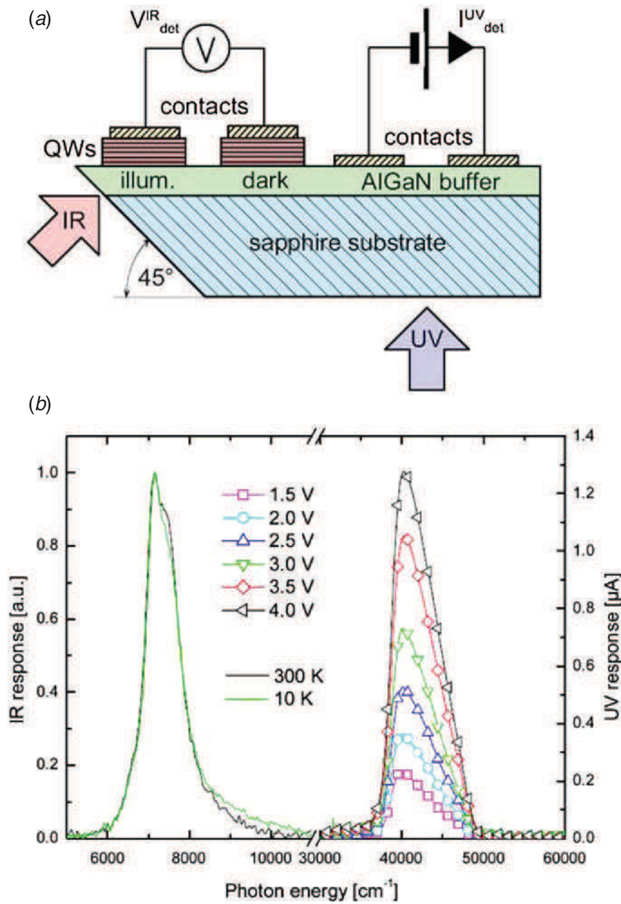

Figure 12. (*a*) Schematic cross section through the sample showing the relative positions of the UV and the IR detector. The QWs are used as the detection layer for the IR, while the AlGaN buffer is the detection layer for the UV radiation. (*b*) Measured spectral responsivity curves for the UV (1.5 to 4.0 V in steps of 0.5 V at 300 K) and the IR detector (10 and 300 K) (after [216]).

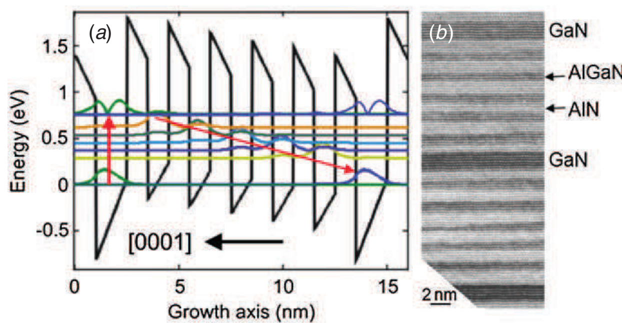

Figure 13. (*a*) Band diagram and energy levels in one stage of the structure. (*b*) HRTEM image of a period of the structure (active GaN QW followed by five-period AlGaN/AlN extractor), viewed along the ⟨11–20⟩ axis. Reprinted with permission from [219]. Copyright 2008, American Institute of Physics.

reaching at least 9.5 ± 2 mA W^{-1} for 10 × 10 μm^2 devices at 1.5 μm peak detection wavelength at room temperature, with a $BW_{-3\text{dB}}$ frequency response of ∼40 GHz. The enhanced responsivity is achieved by illuminating the side facet of the QCDs (illumination perpendicular to the growth axis), as a result of the good coupling between TM-polarized waveguide-propagated light and ISB transitions. The frequency bandwidth is improved by reducing the top contact resistance and the contact layer resistivity, as well as the device capacitance through increasing the number of periods.

Based on the presence of the internal field in III-nitride QWs, symmetry breaking of the potential permits ISB transitions not only between the ground electronic state and the first excited state, $e_1 \rightarrow e_2$, but also between e_1 and the second excited state, e_3, a transition forbidden in symmetric QWs [14]. This feature was exploited for the fabrication of a two-color GaN-based QCD operating at 1.7 and 1 μm at room temperature absorption wavelengths associated to the e_1–e_2 and e_2–e_3 transitions, respectively [225]. It should be noted that although the oscillator strength associated with $e_1 \rightarrow e_3$ is 21 times smaller than that of $e_1 \rightarrow e_2$, the responsivity at 1 μm is only 12 times smaller than that at 1.7 μm. This is a consequence of the increased transfer efficiency into the extractor for electrons in the e_3 subband due to the lower effective barrier and of the multiple relaxation paths to the extractor stage.

Finally, a simplified QCD design where the extractor superlattice has been replaced by an AlGaN layer has been proposed [226]. The thickness and composition of the extractor alloy is chosen so that the energy separation between the ground state of the extractor and the ground state of the active QW is close to the LO-phonon energy. An alloy-extractor device presenting peak photovoltaic response at 1.9 μm has been demonstrated [226].

6.3. THz intersubband photodetectors

The first demonstration of a nitride-based THz ISB photodetector has been reported by Sudradjat *et al* [227]. In the far-IR spectral region, a reduction of the dislocation density allows for the fabrication of photoconductive QWIPs. A key design element for these devices is the optimization between two conflicting requirements: (i) the need for large oscillator strength of the absorbing transitions, which is favored by the use of well-confined upper subbands, and (ii) the efficient escape of the photoexcited electron out of the QW, which is favored by absorbing from a bound level directly into the continuum. A good compromise is attained with QWs whose first excited state is nearly resonant with the conduction band edge in the barriers, leading to what are commonly referred to as *bound-to-quasi-bound absorbing transitions* [10]. This was achieved in nitride-based THz ISB photodetectors by creating a nearly flat potential profile using the step-QW design [91], so that the first excited subband can be positioned at any desired energy relative to the top of the barriers by changing the QW thickness (see figure 14(*a*)), imitating the design of As-based structures. The fabricated devices present a photocurrent spectrum centered at 23 μm wavelength (=13 THz frequency), well resolved from low temperature ($T = 20$ K in figure 14(*b*)) up to $T = 50$ K, with a responsivity of approximately 7 mA W^{-1} [227].

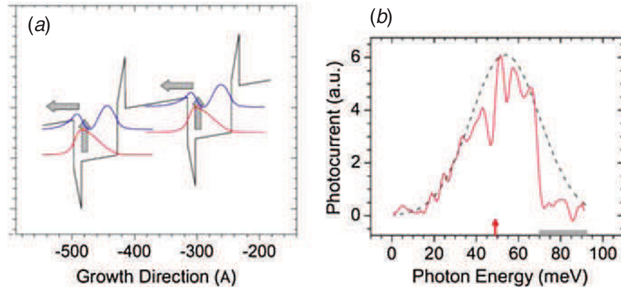

Figure 14. (*a*) Conduction band profile of an AlGaN far-IR QWIP structure under bias, where each repeat unit consists of an $Al_{0.16}Ga_{0.84}N$ barrier and a $GaN/Al_{0.08}Ga_{0.92}N$ step-QW. The squared envelope functions of the ground-state and first excited state of each QW are also shown, referenced to their respective energy levels. The vertical and horizontal arrows indicate, respectively, photon absorption and photoelectron escape into the continuum of unbound states over the barriers. (*b*) Photocurrent spectrum of a double-step-QW AlGaN THz QWIP measured at $T = 20$ K under 0.8 V bias (solid line), and Gaussian fit (dashed line). The grey band near the horizontal axis indicates the Restrahlen band of GaN. The vertical arrow marks the calculated transition energy. Reprinted with permission from [227]. Copyright 2012, American Institute of Physics.

7. Toward the quantum cascade laser

7.1. Light emission in superlattices

ISB luminescence is an inefficient process due to competition with nonradiative electron relaxation via interactions with LO phonons (sub-picosecond), or electron–electron interactions and impurity scattering (tens of picoseconds). However, this does not hinder the realization of QCLs: in the population inversion regime, short radiative lifetime and high stimulated gain can be achieved thanks to the strong ISB transitional oscillator strength.

Despite of the inefficiency of the process, room-temperature ISB luminescence in the 2–2.3 μm spectral range has been observed in GaN/AlN MQWs under optical pumping [228–230]. The QWs were designed to exhibit three bound states in the conduction band. The emission arises from the e_3–e_2 ISB transition. Photoluminescence excitation spectroscopy shows that the emission is only observed for TM-polarized excitation at wavelengths corresponding to the e_1–e_3 ISB transition.

Room-temperature intraband emission has also been observed in optically pumped GaN/AlN quantum dots [231]. The p_z-s intraband luminescence was observed at $\lambda = 1.48$ μm under optical excitation at $\lambda = 1.34$ μm perpendicular to the [0 0 0 1] growth axis. The population of the p_z state arises from Raman scattering by GaN A_1 longitudinal optical phonons. Based on the emission spectral shape, we estimate that the homogeneous linewidth of the s-p_z intraband transition is less than 4 meV.

In spite of these observations, further work is required in terms of growth optimization, processing and dedicated laser active region and cavity design in order to develop quantum fountain lasers.

7.2. Quantum cascade laser structures

QCLs rely on transitions between quantized conduction band states of a suitably designed semiconductor MQW structure [11]. Due to the polarization selection rules associated with ISB transitions, these devices are in-plane emitters, with their electric-field vector perpendicular to the plane of the layers. An electron injected into the *active QWs* first undergoes an ISB lasing transition, and is rapidly extracted by a fast non-radiative transition, which maintains the population inversion. Then, the electron tunnels through the *injector region* toward the upper level of the next active QWs. By using several tens or even hundreds of periods of active region + injector in a series (a cascade), higher optical gains and multiple photons per electron are obtained. The emitting wavelength can be tuned in the range of a few microns to well above 10 μm, by changing the design parameters, such as the quantum well (QW) thickness and barrier height.

Typical QCLs have been engineered and fabricated using arsenide-based systems such as AlGaAs and InGaAs and AlInAs/GaInAs/InP. These complex GaAs-based structures require precise structure control and excellent homogeneity of the material, both in plane and along the multiple periods that compose the active region. Due to the large lattice mismatch and defect structure of the GaN/AlN system, the fabrication of GaN-based QCLs operating in the near-IR does not appear feasible, despite several theoretical proposals [16, 232, 233] and promising results in terms of waveguide fabrication [234]. However, there is an increasing interest and research effort for the fabrication of the first GaN QCL in the far-IR, particularly in the so-called THz domain, spectral region where the lattice mismatch of the structure is reduced, and where it should be possible to exploit the large LO phonon of III-nitrides in order to realize devices operating at room temperature.

Since the first demonstration of a THz QCL in 2001 [235] rapid progress has been made in terms of device performance. To date, QCL has been demonstrated in the 0.85–5 THz range [236], with pulsed operation up to 186 K [237, 238], and pulsed output powers of up to 250 mW [239]. The devices have evolved through different designs including the resonant-phonon, the chirped superlattice, bound-to-continuum and hybrid designs [237, 240]. There are two major processes that cause the degradation of population inversion (and thus gain) in THz QCLs at high temperature: thermal backfilling and thermally activated phonon scattering. Backfilling of the lower radiative state with electrons from the heavily populated injector occurs either by thermal excitation (according to the Boltzmann distribution), or by reabsorption of non-equilibrium LO-phonons (the hot-phonon effect) [241]. The other main degradation mechanism is the onset of thermally activated LO-phonon scattering, as electrons in the upper radiative state acquire sufficient in-plane kinetic energy to emit an LO-phonon and relax nonradiatively to the lower radiative state. This causes the upper-state lifetime τ_{21} to decrease exponentially according to

$$\tau_{12} \propto \exp\left[-\left(E_{\mathrm{LO}} - h\nu\right)/k_{\mathrm{B}}T_{\mathrm{e}}\right], \qquad (15)$$

where $h\nu$ is the THz photon energy, and k_{B} is the Boltzmann constant. Both of these mechanisms greatly depend on the

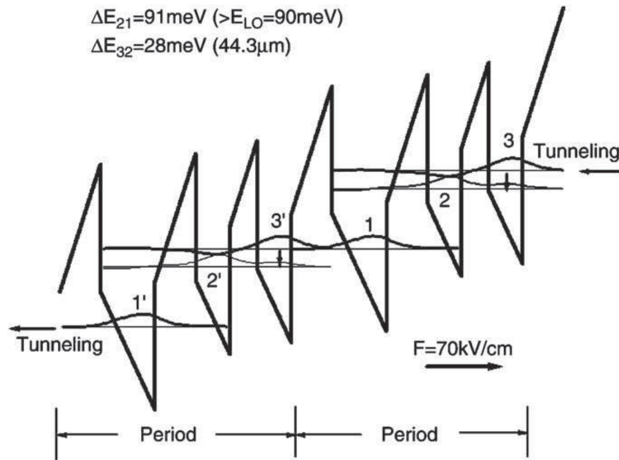

Figure 15. Band structure, subband energy separations and envelope wave functions of the active region of the proposed AlGaN THz QCL structure. Two periods are shown, each with 3 QWs with layer thicknesses as (nm): 3, 4, 3, 2.5, 2 and 2.5. Wells underlined and barriers plain. The transition from 3–2 is engineered through a coupled QW to be 28 meV, while the 2–1 transition is engineering to be on the order of the longitudinal optical phonon (90 meV). With an applied bias of 70 kV cm^{-1}, tunneling between states 1 and 3 occurs in for the cascade effect and carrier recycling. Reprinted from [243], with permission from Elsevier.

electron gas temperature T_e, which is 50–100 K higher than the lattice temperature during device operation.

In general, resonant-phonon QCL designs show the best temperature performance. In this scheme, injector states are designed so that the lower radiative state is resonantly coupled into the upper injector level, which is separated by approximately the LO-phonon energy from the second injector level, providing efficient depopulation of the lower lasing state and a fast relaxation path toward the upper radiative state. The explicit inclusion of an LO-phonon scattering event for depopulation means that resonant-phonon designs present a relatively large energetic barrier (about one LO phonon) to thermal backfilling. However, the low LO-phonon energy in arsenide compounds constitutes a major bottleneck for operation at higher temperatures. Furthermore, the LO phonon of GaAs systems causes an unobtainable emission gap in lasing systems (Restrahlen band at 8–9 THz), which is an intrinsic property of the material system.

Nitride semiconductors, namely GaN, have an LO phonon energy of 92 meV, much higher than the ambient thermal energy. A number of designs for a GaN THz QCL have been proposed [214, 242–249], all focusing on the resonant-phonon architecture first theorized in 2003 [240]. Figure 15 presents the basic device structure for polar III-nitrides. Below we summarize the efforts of various groups working on this topic, who have introduced design improvements but keep the same underlying concept.

Researchers from the University of Leeds (UK) have engineered one of the first designs for GaN-based QCLs using a fully consistent scattering rate equation model [242], and an energy balance method [250]. Both electron–LO-phonon and electron–electron scattering mechanisms are taken into account. They have created a contour plot outlining the wavelengths of emission theorized with different well and barrier thickness within a superlattice, after appropriate strain balancing [232]. They have also proposed a 34 μm wavelength QCL design in both the *a* and *c* planes [242]. Population inversions in active laser states up to 19% for the *a*-plane, and up to 40% for the *c*-plane design, are predicted and, based on estimated modal gain and waveguide/mirror losses, they conclude that the observation of laser action in GaN/AlGaN cascades should be feasible in both planes.

Terashima and Hirayama (RIKEN, Japan) have presented THz QCL designs based on four-well resonant-phonon GaN/AlGaN structures [246, 251, 252]. The structures have been synthesized by PAMBE using a 'droplet elimination by thermal annealing' technique [51], and they have been processed in a single-metal plasmon waveguide geometry [246, 252]. Electronluminescence at 1.37 THz has been reported in a first structure [251], and polarization-dependent electroluminescence at 2.82 THz, slightly tunable by changing the driving voltage in the 20–21 V range, has been reported using a second design [252].

The group of Paiella and Moustakas at Boston University has proposed a QCL design emitting at 2 THz, designed using a Schrödinger-equation solver based on the effective-mass approximation, with the characteristic built-in electric fields of nitride heterostructures included explicitly [245]. They have also performed a rigorous comparison between a GaAs/AlGaAs and the GaN/AlGaN THz QCLs emitting at the same wavelength using a microscopic model of carrier dynamics in QCL gain media based on a set of Boltzmann-like equations solved with a Monte Carlo technique [245, 253]. Results show that the population inversion within GaN lasers is much less dependent on temperature than conventional GaAs designs, as presented in figure 16. From the experimental viewpoint, they have explored tunneling effects in cascade-like superlattices, their temperature dependence and the effect of bias for multiple device architectures [254].

Mirzaei *et al* have proposed a dual-wavelength QCL to emit at both 33 and 52 μm with similar behavior of the output optical power for both wavelengths [249]. The design uses the LO-phonon resonance to extract electrons from the lower radiative levels, and incorporates a miniband injector, theorized via rate equation analysis to operate properly up to 265 K.

Chou *et al* have modeled GaN-based resonant-phonon THz lasers using a transfer matrix method, paying particular attention to the effect of the strain state [248]. They predict higher THz power in GaN/AlGaN heterostructures as compared to heterostructures incorporating In [255].

Finally, Yasuda *et al* have used the non-equilibrium Green's function to model GaN THz QCL devices, namely a four-well resonant-phonon InAlGaN/GaN structure on (0 0 0 1)-oriented GaN [247], and a two-well non-polar GaN/AlGaN structure [256].

Overall, many different designs from various simulation models have been presented. They all focus on the resonant-phonon architecture and predict functionality at high temperatures. Some devices have been fabricated, but

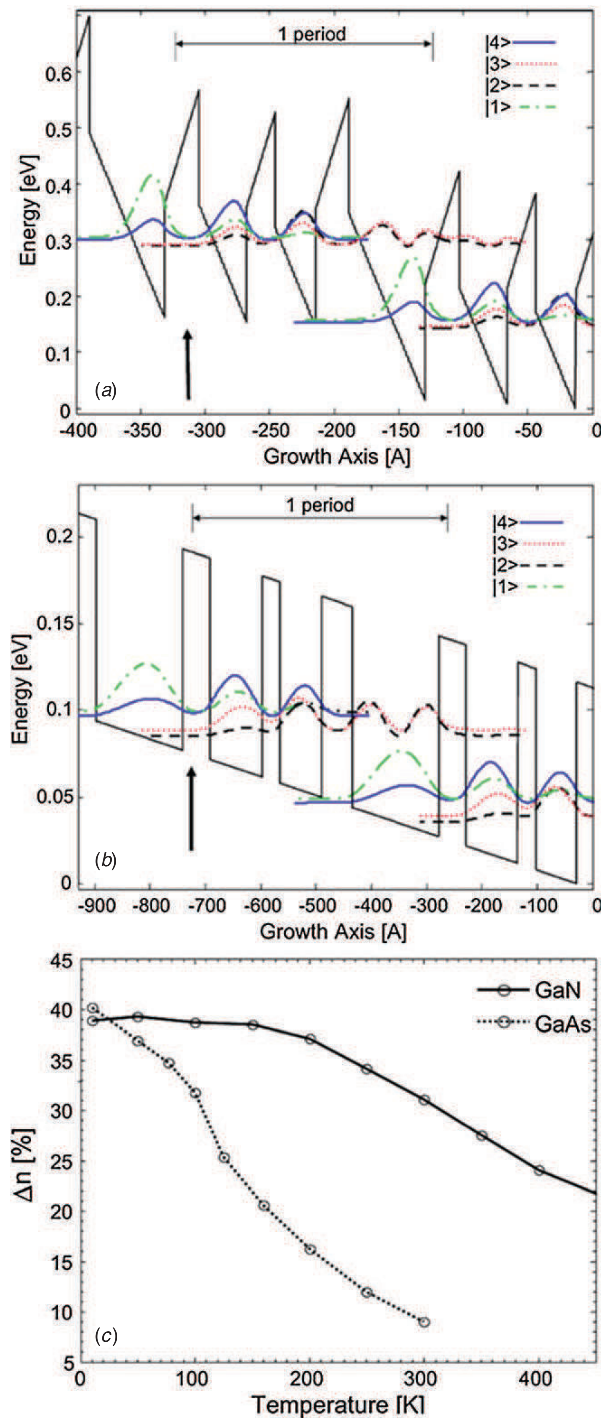

Figure 16. Conduction-band profile and squared envelope functions of (*a*) a GaN/$Al_{0.15}Ga_{0.85}N$ and (*b*) a GaAs/$Al_{0.15}Ga_{0.85}As$ QCL gain media both for emision at 2 THz. The two structures are plotted in the presence of an external field of (*a*) 73 kV cm^{-1} and (*b*) 11 kV cm^{-1}. The layer thicknesses of a single stage, starting from the injection barrier (indicated by the arrow) and moving downstream, are **26**/37/**22**/31/**26**/59 Å for the GaN structure and **49**/94/**33**/74/**56**/156 Å for the GaAs structure (the boldfaced numbers refer to the barrier layers). (*c*) Calculated fractional population inversion of the THz QCL structures in (*a*), indicated by the solid line, and (*b*), indicated by the dotted line. Reprinted with permission from [245]. Copyright 2008, American Institute of Physics.

none have shown lasing properties. All the current research suggests that THz QCL devices are feasible, but there are still numerous problems for device engineering including the unavailability of substrates, difficult band engineering, weak current transport as well as the problems from lattice mismatch [232], doping [234] and waveguide construction [233]. The above-summarized papers have provided solutions toward managing the optical/electronic design, the lattice mismatch and fabrication methodology, but the fabrication of a functioning laser device remains a challenge.

8. Conclusions and perspectives

In this paper, we have reviewed recent research on III-nitride ISB optoelectronics. III-nitride heterostructures are excellent candidates for high-speed ISB devices in the near-IR thanks to their large conduction band offset (∼1.8 eV for the GaN/AlN system) and subpicosecond ISB scattering rates. However, bandgap engineering requires exquisite control of material growth and modeling that are notoriously difficult in GaN/AlGaN. First prototypes of nitride-based ISB devices are room-temperature multi-Tbit/s all-optical switches operating at 1.5 μm, photovoltaic and photoconductive QWIPs, QDIPs and ISB electro-optical modulators. Near-IR ISB luminescence from GaN/AlN QWs and QDs has been reported. The concept of quantum cascade applied to III-nitrides has been demonstrated by the development of QCDs operating in the 1.0–4.5 μm spectral range.

An emerging field for GaN-based ISB devices is the extension toward the far-IR spectral range, with several theoretical designs of GaN QCLs recently reported. At far-IR wavelengths, the large GaN LO-phonon energy (92 meV) becomes a valuable property to achieve ISB operation at relatively high temperatures, and also to cover IR wavelengths that are not accessible by other III–V semiconductors due to Restrahlen absorption. However, the extension of this ISB technology toward longer wavelengths requires a reduction of the polarization-induced internal electric field, which sets new material challenges.

Acknowledgment

This work is supported by the EU ERC-StG 'TeraGaN' (#278428) project.

References

[1] Kamgar A, Kneschaurek P, Dorda G and Koch J 1974 Resonance spectroscopy of electronic levels in a surface accumulation layer *Phys. Rev. Lett.* **32** 1251–4

[2] Ando T, Fowler A B and Stern F 1982 Electronic properties of two-dimensional systems *Rev. Mod. Phys.* **54** 437–672

[3] Esaki L and Sakaki H 1977 New photoconductor *IBM Tech. Discl. Bull.* **20** 2456–7

[4] Chiu L C, Smith J S, Margalit S, Yariv A and Cho A Y 1983 Application of internal photoemission from quantum-well and heterojunction superlattices to infrared photodetectors *Infrared Phys.* **23** 93–7

[5] Smith J S, Chiu L C, Margalit S, Yariv A and Cho A Y 1983 A new infrared detector using electron emission from multiple quantum wells *J. Vac. Sci. Technol.* B **1** 376–8

[6] Coon D D and Karunasiri R P G 1984 New mode of IR detection using quantum wells *Appl. Phys. Lett.* **45** 649–51

[7] Coon D D, Karunasiri R P G and Liu H C 1986 Fast response quantum well photodetectors *J. Appl. Phys.* **60** 2636–8

[8] West L C and Eglash S J 1985 First observation of an extremely large-dipole infrared transition within the conduction band of a GaAs quantum well *Appl. Phys. Lett.* **46** 1156–8

[9] Levine B F, Choi K K, Bethea C G, Walker J and Malik R J 1987 New 10 μm infrared detector using intersubband absorption in resonant tunneling GaAlAs superlattices *Appl. Phys. Lett.* **50** 1092–4

[10] Levine B F 1993 Quantum-well infrared photodetectors *J. Appl. Phys.* **74** R1–81

[11] Faist J, Capasso F, Sivco D L, Sirtori C, Hutchinson A L and Cho A Y 1994 Quantum cascade laser *Science* **264** 553–6

[12] Binggeli N, Ferrara P and Baldereschi A 2001 Band-offset trends in nitride heterojunctions *Phys. Rev.* B **63** 245306

[13] Cociorva D, Aulbur W G and Wilkins J W 2002 Quasiparticle calculations of band offsets at AlN–GaN interfaces *Solid State Commun.* **124** 63–66

[14] Tchernycheva M, Nevou L, Doyennette L, Julien F, Warde E, Guillot F, Monroy E, Bellet-Amalric E, Remmele T and Albrecht M 2006 Systematic experimental and theoretical investigation of intersubband absorption in GaN/AlN quantum wells *Phys. Rev.* B **73** 125347

[15] Suzuki N and Iizuka N 1997 Feasibility study on ultrafast nonlinear optical properties of 1.55-μm intersubband transition in AlGaN/GaN quantum wells *Japan. J. Appl. Phys.* **36** L1006–8

[16] Hofstetter D *et al* 2010 Intersubband transition-based processes and devices in AlN/GaN-based heterostructures *Proc. IEEE* **98** 1234–48

[17] Machhadani H *et al* 2009 GaN/AlGaN intersubband optoelectronic devices *New J. Phys.* **11** 125023

[18] Hao M, Mahanty S, Qhalid Fareed R S, Tottori S, Nishino K and Sakai S 1999 Infrared properties of bulk GaN *Appl. Phys. Lett.* **74** 2788–90

[19] Yang J, Brown G J, Dutta M and Stroscio M A 2005 Photon absorption in the restrahlen band of thin films of GaN and AlN: Two phonon effects *J. Appl. Phys.* **98** 043517

[20] Welna M, Kudrawiec R, Motyka M, Kucharski R, Zając M, Rudziński M, Misiewicz J, Doradziński R and Dwiliński R 2012 Transparency of GaN substrates in the mid-infrared spectral range *Cryst. Res. Technol.* **47** 347–50

[21] Kandaswamy P K, Machhadani H, Bougerol C, Sakr S, Tchernycheva M, Julien F H and Monroy E 2009 Midinfrared intersubband absorption in GaN/AlGaN superlattices on Si(1 1 1) templates *Appl. Phys. Lett.* **95** 141911

[22] Kandaswamy P K, Machhadani H, Kotsar Y, Sakr S, Das A, Tchernycheva M, Rapenne L, Sarigiannidou E, Julien F H and Monroy E 2010 Effect of doping on the mid-infrared intersubband absorption in GaN/AlGaN superlattices grown on Si(1 1 1) templates *Appl. Phys. Lett.* **96** 141903

[23] Suzuki N and Iizuka N 1998 Electron scattering rates in AlGaN/GaN quantum wells for 1.55-μm inter-subband transition *Japan. J. Appl. Phys.* **37** L369–71

[24] Bastard G 1988 Les Editions de Physique *Wave mechanics applied to semiconductor heterostructures* (Les Ulis Cedex: Halsted Press)

[25] Liu H C and Capasso F 2000 Physics and Device Applications I *Intersubband transitions in quantum wells* (San Diego, CA: Academic)

[26] Bernardini F, Fiorentini V and Vanderbilt D 1997 Spontaneous polarization and piezoelectric constants of III–V nitrides *Phys. Rev.* B **56** R10024–7

[27] Birner S, Zibold T, Andlauer T, Kubis T, Sabathil M, Trellakis A and Vogl P 2007 Nextnano: general purpose 3D simulations *IEEE Trans. Electron Devices* **54** 2137–42

[28] Kandaswamy P K *et al* 2008 GaN/AlN short-period superlattices for intersubband optoelectronics: a systematic study of their epitaxial growth, design, and performance *J. Appl. Phys.* **104** 093501

[29] Hofstetter D, Baumann E, Giorgetta F R, Guillot F, Leconte S and Monroy E 2007 Optically nonlinear effects in intersubband transitions of GaN/AlN-based superlattice structures *Appl. Phys. Lett.* **91** 131115

[30] Nevou L, Tchernycheva M, Julien F, Raybaut M, Godard A, Rosencher E, Guillot F and Monroy E 2006 Intersubband resonant enhancement of second-harmonic generation in GaN/AlN quantum wells *Appl. Phys. Lett.* **89** 151101

[31] Nevou L, Mangeney J, Tchernycheva M, Julien F H, Guillot F and Monroy E 2009 Ultrafast relaxation and optical saturation of intraband absorption of GaN/AlN quantum dots *Appl. Phys. Lett.* **94** 132104

[32] Sarigiannidou E, Monroy E, Gogneau N, Radtke G, Bayle-Guillemaud P, Bellet-Amalric E, Daudin B and Rouvière J L 2006 Comparison of the structural quality in Ga-face and N-face polarity GaN/AlN multiple-quantum-well structures *Semicond. Sci. Technol.* **21** 612–8

[33] Gmachl C, Ng H M, George Chu S-N and Cho A Y 2000 Intersubband absorption at $\lambda\sim$1.55 μm in well- and modulation-doped GaN/AlGaN multiple quantum wells with superlattice barriers *Appl. Phys. Lett.* **77** 3722–4

[34] Gmachl C, Ng H M and Cho A Y 2001 Intersubband absorption in degenerately doped GaN/$Al_xGa_{1-x}N$ coupled double quantum wells *Appl. Phys. Lett.* **79** 1590–2

[35] Kishino K, Kikuchi A, Kanazawa H and Tachibana T 2002 Intersubband transition in $(GaN)_m/(AlN)_n$ superlattices in the wavelength range from 1.08 to 1.61 μm *Appl. Phys. Lett.* **81** 1234–6

[36] Iizuka N, Kaneko K and Suzuki N 2002 Near-infrared intersubband absorption in GaN/AlN quantum wells grown by molecular beam epitaxy *Appl. Phys. Lett.* **81** 1803–5

[37] Heber J D, Gmachl C, Ng H M and Cho A Y 2002 Comparative study of ultrafast intersubband electron scattering times at $\sim$1.55 μm wavelength in GaN/AlGaN heterostructures *Appl. Phys. Lett.* **81** 1237–9

[38] Helman A *et al* 2003 Intersubband spectroscopy of doped and undoped GaN/AlN quantum wells grown by molecular-beam epitaxy *Appl. Phys. Lett.* **83** 5196–8

[39] Zhou Q, Chen J, Pattada B, Manasreh M O, Xiu F, Puntigan S, He L, Ramaiah K S and Morkoç H 2003 Infrared optical absorbance of intersubband transitions in GaN/AlGaN multiple quantum well structures *J. Appl. Phys.* **93** 10140–2

[40] Adelmann C, Brault J, Mula G, Daudin B, Lymperakis L and Neugebauer J 2003 Gallium adsorption on (0 0 0 1) GaN surfaces *Phys. Rev.* B **67** 165419

[41] Neugebauer J, Zywietz T, Scheffler M, Northrup J, Chen H and Feenstra R 2003 Adatom kinetics on and below the surface: the existence of a new diffusion channel *Phys. Rev. Lett.* **90** 056101

[42] Heying B, Averbeck R, Chen L F, Haus E, Riechert H and Speck J S 2000 Control of GaN surface morphologies using plasma-assisted molecular beam epitaxy *J. Appl. Phys.* **88** 1855–60

[43] Iliopoulos E and Moustakas T D 2002 Growth kinetics of AlGaN films by plasma-assisted molecular-beam epitaxy *Appl. Phys. Lett.* **81** 295–7

[44] Monroy E, Daudin B, Bellet-Amalric E, Gogneau N, Jalabert D, Enjalbert F, Brault J, Barjon J and Dang L S 2003 Surfactant effect of In for AlGaN growth by plasma-assisted molecular beam epitaxy *J. Appl. Phys.* **93** 1550–6

[45] Koblmueller G, Averbeck R, Geelhaar L, Riechert H, Hösler W and Pongratz P 2003 Growth diagram and morphologies of AlN thin films grown by molecular beam epitaxy *J. Appl. Phys.* **93** 9591–7

[46] Mula G, Adelmann C, Moehl S, Oullier J and Daudin B 2001 Surfactant effect of gallium during molecular-beam epitaxy of GaN on AlN (0 0 0 1) *Phys. Rev.* B **64** 195406

[47] Brown J S, Koblmülller G, Wu F, Averbeck R, Riechert H and Speck J S 2006 Ga adsorbate on (0 0 0 1) GaN: *In situ* characterization with quadrupole mass spectrometry and reflection high-energy electron diffraction *J. Appl. Phys.* **99** 074902

[48] Northrup J, Neugebauer J, Feenstra R and Smith A 2000 Structure of GaN(0 0 0 1): the laterally contracted Ga bilayer model *Phys. Rev.* B **61** 9932–5

[49] Koblmüller G, Brown J, Averbeck R, Riechert H, Pongratz P and Speck J S 2005 Continuous evolution of Ga adlayer coverages during plasma-assisted molecular-beam epitaxy of (0 0 0 1) GaN *Appl. Phys. Lett.* **86** 041908

[50] Moseley M, Billingsley D, Henderson W, Trybus E and Doolittle W A 2009 Transient atomic behavior and surface kinetics of GaN *J. Appl. Phys.* **106** 014905

[51] Terashima W and Hirayama H 2010 The utility of droplet elimination by thermal annealing technique for fabrication of GaN/AlGaN terahertz quantum cascade structure by radio frequency molecular beam epitaxy *Appl. Phys. Express* **3** 125501

[52] Koblmüller G, Reurings F, Tuomisto F and Speck J S 2010 Influence of Ga/N ratio on morphology, vacancies, and electrical transport in GaN grown by molecular beam epitaxy at high temperature *Appl. Phys. Lett.* **97** 191915

[53] Gogneau N, Jalabert D, Monroy E, Sarigiannidou E, Rouvière J L, Shibata T, Tanaka M, Gerard J M and Daudin B 2004 Influence of AlN overgrowth on structural properties of GaN quantum wells and quantum dots grown by plasma-assisted molecular beam epitaxy *J. Appl. Phys.* **96** 1104–10

[54] Grandjean N and Massies J 1996 Kinetics of surfactant-mediated epitaxy of III–V semiconductors *Phys. Rev.* B **53** R13231–4

[55] Widmann F, Daudin B, Feuillet G, Pelekanos N and Rouvière J L 1998 Improved quality GaN grown by molecular beam epitaxy using In as a surfactant *Appl. Phys. Lett.* **73** 2642–4

[56] Kruse C, Einfeldt S, Böttcher T and Hommel D 2001 In as a surfactant for the growth of GaN (0 0 0 1) by plasma-assisted molecular-beam epitaxy *Appl. Phys. Lett.* **79** 3425–7

[57] Monroy E, Guillot F, Gayral B, Bellet-Amalric E, Jalabert D, Gérard J-M, Si Dang L, Tchernycheva M and Julien F H 2006 Observation of hot luminescence and slow inter-sub-band relaxation in Si-doped GaN/$Al_xGa_{1-x}N$ ($x = 0.11, 0.25$) multi-quantum-well structures *J. Appl. Phys.* **99** 093513

[58] Kandaswamy P K, Bougerol C, Jalabert D, Ruterana P and Monroy E 2009 Strain relaxation in short-period polar GaN/AlN superlattices *J. Appl. Phys.* **106** 013526

[59] Baumann E *et al* 2006 Near infrared absorption and room temperature photovoltaic response in AlN/GaN superlattices grown by metal-organic vapor-phase epitaxy *Appl. Phys. Lett.* **89** 041106

[60] Bayram C, Péré-laperne N and Razeghi M 2009 Effects of well width and growth temperature on optical and structural characteristics of AlN/GaN superlattices grown by metal-organic chemical vapor deposition *Appl. Phys. Lett.* **95** 201906

[61] Sodabanlu H, Yang J-S, Sugiyama M, Shimogaki Y and Nakano Y 2009 Strain effects on the intersubband transitions in GaN/AlN multiple quantum wells grown by low-temperature metal organic vapor phase epitaxy with AlGaN interlayer *Appl. Phys. Lett.* **95** 161908

[62] Yang J-S, Sodabanlu H, Sugiyama M, Nakano Y and Shimogaki Y 2009 Blueshift of intersubband transition wavelength in AlN/GaN multiple quantum wells by low temperature metal organic vapor phase epitaxy using pulse injection method *Appl. Phys. Lett.* **95** 162111

[63] Nicolay S, Feltin E, Carlin J-F, Grandjean N, Nevou L, Julien F H, Schmidbauer M, Remmele T and Albrecht M 2007 Strain-induced interface instability in GaN/AlN multiple quantum wells *Appl. Phys. Lett.* **91** 061927

[64] Iizuka N, Kaneko K and Suzuki N 2006 All-optical switch utilizing intersubband transition in GaN quantum wells *IEEE J. Quantum Electron.* **42** 765–71

[65] Floro J A, Follstaedt D M, Provencio P, Hearne S J and Lee S R 2004 Misfit dislocation formation in the AlGaN/GaN heterointerface *J. Appl. Phys.* **96** 7087–94

[66] Matthews J W and Blakeslee A E 1974 Defects in epitaxial multilayers *J. Cryst. Growth* **27** 118–25

[67] Ponce F A 1997 Detects and interfaces in GaN epitaxy *MRS Bull.* **22** 51–57

[68] Moran B, Wu F, Romanov A E, Mishra U K, Denbaars S P and Speck J S 2004 Structural and morphological evolution of GaN grown by metalorganic chemical vapor deposition on SiC substrates using an AlN initial layer *J. Cryst. Growth* **273** 38–47

[69] Kehagias T, Delimitis A, Komninou P, Iliopoulos E, Dimakis E, Georgakilas A and Nouet G 2005 Misfit accommodation of compact and columnar InN epilayers grown on Ga-face GaN (0 0 0 1) by molecular-beam epitaxy *Appl. Phys. Lett.* **86** 151905

[70] Hearne S J, Han J, Lee S R, Floro J A, Follstaedt D M, Chason E and Tsong I S T 2000 Brittle-ductile relaxation kinetics of strained AlGaN/GaN heterostructures *Appl. Phys. Lett.* **76** 1534–6

[71] Liu R, Mei J, Srinivasan S, Ponce F A, Omiya H, Narukawa Y and Mukai T 2006 Generation of misfit dislocations by basal-plane slip in InGaN/GaN heterostructures *Appl. Phys. Lett.* **89** 201911

[72] Einfeldt S, Heinke H, Kirchner V and Hommel D 2001 Strain relaxation in AlGaN/GaN superlattices grown on GaN *J. Appl. Phys.* **89** 2160–7

[73] Andersson T G, Liu X Y, Aggerstam T, Holmström P, Lourdudoss S, Thylen L, Chen Y L, Hsieh C H and Lo I 2009 Macroscopic defects in GaN/AlN multiple quantum well structures grown by MBE on GaN templates *Microelectron. J.* **40** 360–2

[74] Cherns P D, McAleese C, Kappers M J and Humphreys C J 2007 Microscopy of Semiconducting Materials *Strain relaxation in an AlGaN/GaN quantum well system* ed A G Cullis and P A Midgley (Dordrecht: Springer) pp 25–28

[75] Cantu P, Wu F, Waltereit P, Keller S, Romanov A E, DenBaars S P and Speck J S 2005 Role of inclined threading dislocations in stress relaxation in mismatched layers *J. Appl. Phys.* **97** 103534

[76] Bellet-Amalric E, Adelmann C, Sarigiannidou E, Rouvière J L, Feuillet G, Monroy E and Daudin B 2004 Plastic strain relaxation of nitride heterostructures *J. Appl. Phys.* **95** 1127–33

[77] Kotsar Y, Doisneau B, Bellet-Amalric E, Das A, Sarigiannidou E and Monroy E 2011 Strain relaxation in GaN/AlxGa1-xN superlattices grown by plasma-assisted molecular-beam epitaxy *J. Appl. Phys.* **110** 033501

[78] Yang R, Xu J and Sweeny M 1994 Selection rules of intersubband transitions in conduction-band quantum wells *Phys. Rev.* B **50** 7474–82

[79] Guillot F, Amstatt B, Bellet-Amalric E, Monroy E, Nevou L, Doyennette L, Julien F H and Dang L S 2006 Effect of Si doping on GaN/AlN multiple-quantum-well structures for intersubband optoelectronics at telecommunication wavelengths *Superlatt. Microstruct.* **40** 306–12

[80] Berland K, Stattin M, Farivar R, Sultan D M S, Hyldgaard P, Larsson A, Wang S M and Andersson T G 2010 Temperature stability of intersubband transitions in AlN/GaN quantum wells *Appl. Phys. Lett.* **97** 043507

[81] Liu X Y, Holmström P, Jänes P, Thylén L and Andersson T G 2007 Intersubband absorption at 1.5–3.5 μm in GaN/AlN multiple quantum wells grown by molecular beam epitaxy on sapphire *Phys. Status Solidi* B **244** 2892–905

[82] Suzuki N and Iizuka N 1999 Effect of polarization field on intersubband transition in AlGaN/GaN quantum wells *Japan. J. Appl. Phys.* **38** L363–5

[83] Ng H M, Gmachl C, Siegrist T, Chu S N G and Cho A Y 2001 Growth and characterization of GaN/AlGaN superlattices for near-infrared intersubband transitions *Phys. Status Solidi* a **188** 825–31

[84] Ng H M, Gmachl C, Heber J D, Hsu J W P, Chu S N G and Cho A Y 2002 Recent progress in GaN-based superlattices for near-infrared intersubband transitions *Phys. Status Solidi* b **234** 817–21

[85] Sherliker B *et al* 2007 Room temperature operation of AlGaN/GaN quantum well infrared photodetectors at a 3–4 μm wavelength range *Semicond. Sci. Technol.* **22** 1240–4

[86] Péré-Laperne N, Bayram C, Nguyen-The L, McClintock R and Razeghi M 2009 Tunability of intersubband absorption from 4.5 to 5.3 μm in a GaN/$Al_{0.2}Ga_{0.8}N$ superlattices grown by metalorganic chemical vapor deposition *Appl. Phys. Lett.* **95** 131109

[87] Tian W *et al* 2012 Tunability of intersubband transition wavelength in the atmospheric window in AlGaN/GaN multi-quantum wells grown on different AlGaN templates by metalorganic chemical vapor deposition *J. Appl. Phys.* **112** 063526

[88] Bayram C 2012 High-quality AlGaN/GaN superlattices for near- and mid-infrared intersubband transitions *J. Appl. Phys.* **111** 013514

[89] Huang C C *et al* 2011 Intersubband transitions at atmospheric window in $Al_xGa_{1-x}N$/GaN multiple quantum wells grown on GaN/sapphire templates adopting AlN/GaN superlattices interlayer *Appl. Phys. Lett.* **98** 132105

[90] Edmunds C, Tang L, Li D, Cervantes M, Gardner G, Paskova T, Manfra M J and Malis O 2012 Near-infrared absorption in lattice-matched AlInN/GaN and strained AlGaN/GaN heterostructures grown by MBE on low-defect GaN substrates *J. Electron. Mater.* **41** 881–6

[91] Machhadani H, Kotsar Y, Sakr S, Tchernycheva M, Colombelli R, Mangeney J, Bellet-Amalric E, Sarigiannidou E, Monroy E and Julien F H 2010 Terahertz intersubband absorption in GaN/AlGaN step quantum wells *Appl. Phys. Lett.* **97** 191101

[92] Edmunds C, Tang L, Shao J, Li D, Cervantes M, Gardner G, Zakharov D N, Manfra M J and Malis O 2012 Improvement of near-infrared absorption linewidth in AlGaN/GaN superlattices by optimization of delta-doping location *Appl. Phys. Lett.* **101** 102104

[93] Suzuki N, Iizuka N and Kaneko K 2003 Calculation of near-infrared intersubband absorption spectra in GaN/AlN quantum wells *Japan. J. Appl. Phys.* **42** 132–9

[94] Tchernycheva M, Nevou L, Doyennette L, Julien F H, Guillot F, Monroy E, Remmele T and Albrecht M 2006 Electron confinement in strongly coupled GaN/AlN quantum wells *Appl. Phys. Lett.* **88** 153113

[95] Driscoll K, Bhattacharyya A, Moustakas T D, Paiella R, Zhou L and Smith D J 2007 Intersubband absorption in AlN/GaN/AlGaN coupled quantum wells *Appl. Phys. Lett.* **91** 141104

[96] Cen L B, Shen B, Qin Z X and Zhang G Y 2009 Influence of polarization induced electric fields on the wavelength and the refractive index of intersubband transitions in AlN/GaN coupled double quantum wells *J. Appl. Phys.* **105** 093109

[97] Cen L B, Shen B, Qin Z X and Zhang G Y 2009 Near-infrared two-color intersubband transitions in AlN/GaN coupled double quantum wells *J. Appl. Phys.* **105** 053106

[98] Lupu A *et al* 2008 Lattice-matched GaN-InAlN waveguides at $\lambda = 1.55$ μm grown by metal-organic vapor phase epitaxy *IEEE Photon. Technol. Lett.* **20** 102–4

[99] Nicolay S, Carlin J-F, Feltin E, Butté R, Mosca M, Grandjean N, Ilegems M, Tchernycheva M, Nevou L and Julien F H 2005 Midinfrared intersubband absorption in lattice-matched AlInN/GaN multiple quantum wells *Appl. Phys. Lett.* **87** 111106

[100] Nicolay S, Feltin E, Carlin J-F, Mosca M, Nevou L, Tchernycheva M, Julien F H, Ilegems M and Grandjean N 2006 Indium surfactant effect on AlN/GaN heterostructures grown by metal-organic vapor-phase epitaxy: applications to intersubband transitions *Appl. Phys. Lett.* **88** 151902

[101] Gonschorek M, Carlin J-F, Feltin E, Py M A, Grandjean N, Darakchieva V, Monemar B, Lorenz M and Ramm G 2008 Two-dimensional electron gas density in $Al_{1-x}In_xN$/AlN/GaN heterostructures ($0.03 \leqslant x < 0.23$) *J. Appl. Phys.* **103** 093714

[102] Malis O, Edmunds C, Manfra M J and Sivco D L 2009 Near-infrared intersubband absorption in molecular-beam epitaxy-grown lattice-matched InAlN/GaN superlattices *Appl. Phys. Lett.* **94** 161111

[103] Cywiński G *et al* 2006 Growth of thin AlInN/GaInN quantum wells for applications to high-speed intersubband devices at telecommunication wavelengths *J. Vac. Sci. Technol.* B **24** 1505–9

[104] Kudrawiec R, Motyka M, Cywin'ski G, Siekacz M, Skierbiszewski C, Nevou L, Doyennette L, Tchernycheva M, Julien F H and Misiewicz J 2008 Contactless electroreflectance spectroscopy of inter- and intersub-band transitions in AlInN/GaInN quantum wells *Phys. Status Solidi* c **5** 503–7

[105] Akabli H, Almaggoussi A, Abounadi A, Rajira A, Berland K and Andersson T G 2012 Intersubband energies in $Al_{1-y}In_yN/Ga_{1-x}In_xN$ heterostructures with lattice constant close to aGaN *Superlatt. Microstruct.* **52** 70–77

[106] Zhu J, Ban S-L and Ha S-H 2012 Phonon-assisted intersubband transitions in wurtzite GaN/$In_xGa_{1-x}N$ quantum wells *Chin. Phys.* B **21** 097301

[107] Berryman K W, Lyon S A and Segev M 1997 Mid-infrared photoconductivity in InAs quantum dots *Appl. Phys. Lett.* **70** 1861–3

[108] Phillips J, Kamath K and Bhattacharya P 1998 Far-infrared photoconductivity in self-organized InAs quantum dots *Appl. Phys. Lett.* **72** 2020–2

[109] Ryzhii V 1996 The theory of quantum-dot infrared phototransistors *Semicond. Sci. Technol.* **11** 759–65

[110] Pan D, Towe E and Kennerly S 1998 Normal-incidence intersubband (In, Ga)As/GaAs quantum dot infrared photodetectors *Appl. Phys. Lett.* **73** 1937–9

[111] Chen Z, Baklenov O, Kim E T, Mukhametzhanov I, Tie J, Madhukar A, Ye Z and Campbell J C 2001 Normal incidence InAs/Al_xGa_{1-x}As quantum dot infrared

photodetectors with undoped active region *J. Appl. Phys.* **89** 4558–63

[112] Chu L, Zrenner A, Bichler M and Abstreiter G 2001 Quantum-dot infrared photodetector with lateral carrier transport *Appl. Phys. Lett.* **79** 2249–51

[113] Daudin B, Widmann F, Feuillet G, Samson Y, Arlery M and Rouvière J 1997 Stranski–Krastanov growth mode during the molecular beam epitaxy of highly strained GaN *Phys. Rev.* B **56** R7069–72

[114] Chamard V, Schülli T, Sztucki M, Metzger T, Sarigiannidou E, Rouvière J-L, Tolan M and Adelmann C 2004 Strain distribution in nitride quantum dot multilayers *Phys. Rev.* B **69** 125327

[115] Sarigiannidou E, Monroy E, Daudin B, Rouvière J L and Andreev A D 2005 Strain distribution in GaN/AlN quantum-dot superlattices *Appl. Phys. Lett.* **87** 203112

[116] Guillot F *et al* 2006 Si-doped GaN/AlN quantum dot superlattices for optoelectronics at telecommunication wavelengths *Phys. Status Solidi* a **203** 1754–8

[117] Damilano B, Grandjean N, Semond F, Massies J and Leroux M 1999 From visible to white light emission by GaN quantum dots on Si(1 1 1) substrate *Appl. Phys. Lett.* **75** 962–4

[118] Tanaka S, Iwai S and Aoyagi Y 1996 Self-assembling GaN quantum dots on $AlxGa_{1-x}N$ surfaces using a surfactant *Appl. Phys. Lett.* **69** 4096–8

[119] Ramvall P, Riblet P, Nomura S, Aoyagi Y and Tanaka S 2000 Optical properties of GaN quantum dots *J. Appl. Phys.* **87** 3883–90

[120] Miyamura M, Tachibana K and Arakawa Y 2002 High-density and size-controlled GaN self-assembled quantum dots grown by metalorganic chemical vapor deposition *Appl. Phys. Lett.* **80** 3937–9

[121] Andreev A and O'Reilly E 2000 Theory of the electronic structure of GaN/AlN hexagonal quantum dots *Phys. Rev.* B **62** 15851–70

[122] Andreev A D and O'Reilly E P 2001 Optical transitions and radiative lifetime in GaN/AlN self-organized quantum dots *Appl. Phys. Lett.* **79** 521–3

[123] Williams D, Andreev A, O'Reilly E and Faux D 2005 Derivation of built-in polarization potentials in nitride-based semiconductor quantum dots *Phys. Rev.* B **72** 235318

[124] Ranjan V, Allan G, Priester C and Delerue C 2003 Self-consistent calculations of the optical properties of GaN quantum dots *Phys. Rev.* B **68** 115303

[125] Moumanis K, Helman A, Fossard F, Tchernycheva M, Lusson A, Julien F H, Damilano B, Grandjean N and Massies J 2003 Intraband absorptions in GaN/AlN quantum dots in the wavelength range of 1.27–2.4 μm *Appl. Phys. Lett.* **82** 868–70

[126] Tchernycheva M, Nevou L, Doyennette L, Helman A, Colombelli R, Julien F H, Guillot F, Monroy E, Shibata T and Tanaka M 2005 Intraband absorption of doped GaN/AlN quantum dots at telecommunication wavelengths *Appl. Phys. Lett.* **87** 101912

[127] Vardi A, Bahir G, Schacham S E, Kandaswamy P K and Monroy E 2009 Photocurrent spectroscopy of bound-to-bound intraband transitions in GaN/AlN quantum dots *Phys. Rev.* B **80** 155439

[128] Nguyen D T, Wüster W, Roussignol P, Voisin C, Cassabois G, Tchernycheva M, Julien F H, Guillot F and Monroy E 2010 Homogeneous linewidth of the intraband transition at 1.55 μm in GaN/AlN quantum dots *Appl. Phys. Lett.* **97** 061903

[129] Himwas C, Songmuang R, Dang L S, Bleuse J, Rapenne L, Sarigiannidou E and Monroy E 2012 Thermal stability of the deep ultraviolet emission from AlGaN/AlN Stranski–Krastanov quantum dots *Appl. Phys. Lett.* **101** 241914

[130] Speck J S and Chichibu S F 2011 Nonpolar and semipolar group III nitride-based materials *MRS Bull.* **34** 304–12

[131] Romanov A E, Baker T J, Nakamura S, Speck J S and ERATO/JST UCSB Group 2006 Strain-induced polarization in wurtzite III-nitride semipolar layers *J. Appl. Phys.* **100** 023522

[132] Lahourcade L, Bellet-Amalric E, Monroy E, Abouzaid M and Ruterana P 2007 Plasma-assisted molecular-beam epitaxy of AlN(11–22) on m sapphire *Appl. Phys. Lett.* **90** 131909

[133] Lahourcade L, Kandaswamy P K, Renard J, Ruterana P, Machhadani H, Tchernycheva M, Julien F H, Gayral B and Monroy E 2008 Interband and intersubband optical characterization of semipolar (1122)-oriented GaN/AlN multiple-quantum-well structures *Appl. Phys. Lett.* **93** 111906

[134] Gmachl C and Ng H M 2003 Intersubband absorption at ~2.1 μm in A-plane GaN/AlN multiple quantum wells *Electron. Lett.* **39** 567–9

[135] Brazis R and Raguotis R 2006 Monte Carlo modeling of phonon-assisted carrier transport in cubic and hexagonal gallium nitride *Opt. Quantum Electron.* **38** 339–47

[136] Pugh S K, Dugdale D J, Brand S and Abram R A 1999 Electronic structure calculations on nitride semiconductors *Semicond. Sci. Technol.* **14** 23–31

[137] Suzuki M and Uenoyama T 1996 Optical gain and crystal symmetry in III–V nitride lasers *Appl. Phys. Lett.* **69** 3378–80

[138] DeCuir E A, Fred E, Manasreh M O, Schörmann J, As D J and Lischka K 2007 Near-infrared intersubband absorption in nonpolar cubic GaN/AlN superlattices *Appl. Phys. Lett.* **91** 041911

[139] Machhadani H, Tchernycheva M, Sakr S, Rigutti L, Colombelli R, Warde E, Mietze C, As D J and Julien F H 2011 Intersubband absorption of cubic GaN/Al(Ga)N quantum wells in the near-infrared to terahertz spectral range *Phys. Rev.* B **83** 075313

[140] Noda S, Yamashita T, Ohya M, Muromoto Y and Sasaki A 1993 All-optical modulation for semiconductor lasers by using three energy levels in n-doped quantum wells *IEEE J. Quantum Electron.* **29** 1640–7

[141] Wada O 2004 Femtosecond all-optical devices for ultrafast communication and signal processing *New J. Phys.* **6** 183

[142] Iizuka N, Kaneko K, Suzuki N, Asano T, Noda S and Wada O 2000 Ultrafast intersubband relaxation ($\leqslant$150 fs) in AlGaN/GaN multiple quantum wells *Appl. Phys. Lett.* **77** 648–50

[143] Gmachl C, Frolov S V, Ng H M, Chu S-N G and Cho A Y 2001 Sub-picosecond electron scattering time for λ = 1.55 μm intersubband transitions in GaN/AlGaN multiple quantum wells *Electron. Lett.* **37** 378

[144] Rapaport R, Chen G, Mitrofanov O, Gmachl C, Ng H M and Chu S N G 2003 Resonant optical nonlinearities from intersubband transitions in GaN/AlN quantum wells *Appl. Phys. Lett.* **83** 263

[145] Iizuka N, Kaneko K and Suzuki N 2005 Sub-picosecond all-optical gate utilizing GaN intersubband transition *Opt. Express* **13** 3835–40

[146] Hamazaki J, Kunugita H, Ema K, Kikuchi A and Kishino K 2005 Intersubband relaxation dynamics in GaN/AlN multiple quantum wells studied by two-color pump-probe experiments *Phys. Rev.* B **71** 165334

[147] Suzuki N, Iizuka N and Kaneko K 2000 Intersubband transition in AlGaN–GaN quantum wells for ultrafast all-optical switching at communication wavelength *Proc. SPIE* **3940** 127–38

[148] Iizuka N, Kaneko K and Suzuki N 2004 Sub-picosecond modulation by intersubband transition in ridge waveguide with GaN/AlN quantum wells *Electron. Lett.* **40** 962963

[149] Li Y, Bhattacharyya A, Thomidis C, Moustakas T D and Paiella R 2007 Ultrafast all-optical switching with low saturation energy via intersubband transitions in GaN/AlN quantum-well waveguides *Opt. Express* **15** 17922–7

[150] Sodabanlu H, Yang J-S, Tanemura T, Sugiyama M, Shimogaki Y and Nakano Y 2011 Intersubband absorption saturation in AlN-based waveguide with GaN/AlN multiple quantum wells grown by metalorganic vapor phase epitaxy *Appl. Phys. Lett.* **99** 151102

[151] Iizuka N, Yoshida H, Managaki N, Shimizu T, Hassanet S, Cumtornkittikul C, Sugiyama M and Nakano Y 2009 Integration of GaN/AlN all-optical switch with SiN/AlN waveguide utilizing spot-size conversion *Opt. Express* **17** 23247–53

[152] Iizuka N, Kaneko K and Suzuki N 2006 Polarization dependent loss in III-nitride optical waveguides for telecommunication devices *J. Appl. Phys.* **99** 093107

[153] Sun G, Khurgin J B and Soref R A 2005 Nonlinear all-optical GaN/AlGaN multi-quantum-well devices for 100 Gb/s applications at $\lambda = 1.55\ \mu$m *Appl. Phys. Lett.* **87** 201108

[154] Li Y and Paiella R 2006 Intersubband all-optical switching based on Coulomb-induced optical nonlinearities in GaN/AlGaN coupled quantum wells *Semicond. Sci. Technol.* **21** 1105–10

[155] Valdueza-Felip S, Naranjo F B, Gonzalez-Herraez M, Fernandez H, Solis J, Guillot F, Monroy E, Nevou L, Tchernycheva M and Julien F H 2008 Characterization of the resonant third-order nonlinear susceptibility of Si-Doped GaN–AlN quantum wells and quantum dots at 1.5 μm *IEEE Photon. Technol. Lett.* **20** 1366–8

[156] Suzuki S, Asada M, Teranishi A, Sugiyama H and Yokoyama H 2010 Fundamental oscillation of resonant tunneling diodes above 1 THz at room temperature *Appl. Phys. Lett.* **97** 242102

[157] Feiginov M, Sydlo C, Cojocari O and Meissner P 2011 Resonant-tunnelling-diode oscillators operating at frequencies above 1.1 THz *Appl. Phys. Lett.* **99** 233506

[158] Leconte S, Guillot F, Sarigiannidou E and Monroy E 2007 Charge distribution and vertical electron transport through GaN/AlN/GaN single-barrier structures *Semicond. Sci. Technol.* **22** 107–12

[159] Leconte S, Gerrer L and Monroy E 2009 Electronic transport through GaN/AlN single barriers: effect of polarisation and dislocations *Microelectron. J.* **40** 339–41

[160] Simpkins B S, Yu E T, Waltereit P and Speck J S 2003 Correlated scanning kelvin probe and conductive atomic force microscopy studies of dislocations in gallium nitride *J. Appl. Phys.* **94** 1448–53

[161] Simon J, Zhang Z, Goodman K, Xing H, Kosel T, Fay P and Jena D 2009 Polarization-induced zener tunnel junctions in wide-band-gap heterostructures *Phys. Rev. Lett.* **103** 026801

[162] Grinyaev S N and Razzhuvalov A N 2001 Resonant electron tunneling in GaN/$Ga_{1-x}Al_xN$(0 0 0 1) strained structures with spontaneous polarization and piezoeffect *Phys. Solid State* **43** 549–55

[163] Kikuchi A, Bannai R, Kishino K, Lee C-M and Chyi J-I 2002 AlN/GaN double-barrier resonant tunneling diodes grown by rf-plasma-assisted molecular-beam epitaxy *Appl. Phys. Lett.* **81** 1729–31

[164] Foxon C T *et al* 2003 Current–voltage instabilities in GaN/AlGaN resonant tunnelling structures *Phys. Status Solidi* c **0** 2389–92

[165] Belyaev A E, Foxon C T, Novikov S V, Makarovsky O, Eaves L, Kappers M J and Humphreys C J 2003 Comment on 'AlN/GaN double-barrier resonant tunneling diodes grown by rf-plasma-assisted molecular-beam epitaxy' *Appl. Phys. Lett.* **83** 3626

[166] Kikuchi A, Bannai R, Kishino K, Lee C-M and Chyi J-I 2003 Response to 'Comment on "AlN/GaN double-barrier resonant tunneling diodes grown by rf-plasma-assisted molecular-beam epitaxy"' *Appl. Phys. Lett.* **83** 3628

[167] Indlekofer K M, Donà E, Malindretos J, Bertelli M, Kocan M, Rizzi A and Lüth H 2002 Modelling of polarization charge-induced asymmetry of I–V characteristics of AlN/GaN-based resonant tunnelling structures *Phys. Status Solidi* b **234** 769–72

[168] Sacconi F, Di Carlo A and Lugli P 2002 Modeling of GaN-based resonant tunneling diodes: influence of polarization fields *Phys. Status Solidi* a **190** 295–9

[169] Sakr S, Warde E, Tchernycheva M and Julien F H 2011 Ballistic transport in GaN/AlGaN resonant tunneling diodes *J. Appl. Phys.* **109** 023717

[170] Berland K, Andersson T and Hyldgaard P 2011 Polarization-balanced design of heterostructures: application to AlN/GaN double-barrier structures *Phys. Rev.* B **84** 245313

[171] Warde E, Sakr S, Tchernycheva M and Julien F H 2012 Vertical transport in GaN/AlGaN resonant tunneling diodes and superlattices *J. Electron. Mater.* **41** 965–70

[172] Hermann M, Monroy E, Helman A, Baur B, Albrecht M, Daudin B, Ambacher O, Stutzmann M and Eickhoff M 2004 Vertical transport in group III-nitride heterostructures and application in AlN/GaN resonant tunneling diodes *Phys. Status Solidi* c **1** 2210–27

[173] Golka S, Pflügl C, Schrenk W, Strasser G, Skierbiszewski C, Siekacz M, Grzegory I and Porowski S 2006 Negative differential resistance in dislocation-free GaN/AlGaN double-barrier diodes grown on bulk GaN *Appl. Phys. Lett.* **88** 172106

[174] Kurakin A M, Vitusevich S A, Danylyuk S V, Naumov A V, Foxon C T, Novikov S V, Klein N, Lüth H and Belyaev A E 2006 Capacitance characterization of AlN/GaN double-barrier resonant tunnelling diodes *Phys. Status Solidi* c **3** 2265–9

[175] Vashaei Z, Bayram C and Razeghi M 2010 Demonstration of negative differential resistance in GaN/AlN resonant tunneling diodes at room temperature *J. Appl. Phys.* **107** 083505

[176] Bayram C, Vashaei Z and Razeghi M 2010 Room temperature negative differential resistance characteristics of polar III-nitride resonant tunneling diodes *Appl. Phys. Lett.* **97** 092104

[177] Bayram C, Vashaei Z and Razeghi M 2010 AlN/GaN double-barrier resonant tunneling diodes grown by metal-organic chemical vapor deposition *Appl. Phys. Lett.* **96** 042103

[178] Bayram C, Vashaei Z and Razeghi M 2010 Reliability in room-temperature negative differential resistance characteristics of low-aluminum content AlGaN/GaN double-barrier resonant tunneling diodes *Appl. Phys. Lett.* **97** 181109

[179] Petrychuk M V, Belyaev A E, Kurakin A M, Danylyuk S V, Klein N and Vitusevich S A 2007 Mechanisms of current formation in resonant tunneling AlN/GaN heterostructures *Appl. Phys. Lett.* **91** 222112

[180] Boucherit M, Soltani A, Monroy E, Rousseau M, Deresmes D, Berthe M, Durand C and De Jaeger J-C 2011 Investigation of the negative differential resistance reproducibility in AlN/GaN double-barrier resonant tunnelling diodes *Appl. Phys. Lett.* **99** 182109

[181] Sakr S, Kotsar Y, Tchernycheva M, Warde E, Isac N, Monroy E and Julien F H 2012 Resonant tunneling transport in a GaN/AlN multiple-quantum-well structure *Appl. Phys. Express* **5** 052203

[182] Björk M T, Ohlsson B J, Thelander C, Persson A I, Deppert K, Wallenberg L R and Samuelson L 2002 Nanowire resonant tunneling diodes *Appl. Phys. Lett.* **81** 4458–60

[183] Songmuang R, Katsaros G, Monroy E, Spathis P, Bougerol C, Mongillo M and De Franceschi S 2010 Quantum transport in GaN/AlN double-barrier heterostructure nanowires *Nano Lett.* **10** 3545–50

[184] Rigutti L, Jacopin G, Bugallo A D L, Tchernycheva M, Warde E, Julien F H, Songmuang R, Galopin E, Largeau L and Harmand J-C 2010 Investigation of the electronic transport in GaN nanowires containing GaN/AlN quantum discs *Nanotechnology* **21** 425206

[185] Carnevale S D, Marginean C, Phillips P J, Kent T F, Sarwar A T M G, Mills M J and Myers R C 2012 Coaxial nanowire resonant tunneling diodes from non-polar AlN/GaN on silicon *Appl. Phys. Lett.* **100** 142115

[186] Lewen R, Irmscher S, Westergren U, Thylen L and Eriksson U 2004 Segmented transmission-line electroabsorption modulators *J. Lightwave Technol.* **22** 172–9

[187] Kondo J *et al* 2005 High-speed and low-driving-voltage thin-sheet X-cut $LiNbO_3$ modulator with laminated low-dielectric-constant adhesive *IEEE Photon. Technol. Lett.* **17** 2077–9

[188] Holmstrom P 2001 High-speed mid-IR modulator using stark shift in step quantum wells *IEEE J. Quantum Electron.* **37** 1273–82

[189] Holmstrom P 2006 Electroabsorption modulator using intersubband transitions in GaN–AlGaN–AlN step quantum wells *IEEE J. Quantum Electron.* **42** 810–9

[190] Holmström P, Liu X Y, Uchida H, Aggerstam T, Kikuchi A, Kishino K, Lourdudoss S, Andersson T G and Thylén L 2007 Intersubband photonic devices by group-III nitrides *Proc. SPIE* **6782** 67821N

[191] Baumann E, Giorgetta F R, Hofstetter D, Leconte S, Guillot F, Bellet-Amalric E and Monroy E 2006 Electrically adjustable intersubband absorption of a GaN/AlN superlattice grown on a transistorlike structure *Appl. Phys. Lett.* **89** 101121

[192] Nevou L *et al* 2007 Short-wavelength intersubband electroabsorption modulation based on electron tunneling between GaN/AlN coupled quantum wells *Appl. Phys. Lett.* **90** 223511

[193] Kheirodin N *et al* 2008 Electrooptical modulator at telecommunication wavelengths based on GaN/AlN coupled quantum wells *IEEE Photon. Technol. Lett.* **20** 724–6

[194] Dussaigne A *et al* 2010 Growth of intersubband GaN/AlGaN heterostructures *Proc. SPIE* **7608** 76080H

[195] Dupont E B, Delacourt D and Papuchon M 1993 Mid-infrared phase modulation via Stark effect on intersubband transitions in GaAs/GaAlAs quantum wells *IEEE J. Quantum Electron.* **29** 2313–8

[196] Li Y, Bhattacharyya A, Thomidis C, Liao Y, Moustakas T D and Paiella R 2008 Refractive-index nonlinearities of intersubband transitions in GaN/AlN quantum-well waveguides *J. Appl. Phys.* **104** 083101

[197] Lupu A, Tchernycheva M, Kotsar Y, Monroy E and Julien F H 2012 Electroabsorption and refractive index modulation induced by intersubband transitions in GaN/AlN multiple quantum wells *Opt. Express* **20** 12541

[198] Gross E, Pesach A, Monroy E, Schacham S E and Bahir G 2013 Direct measurement of refractive index change around intersubband transition resonance using free-space Mach–Zehnder interferometer *Opt. Express* **21** 3800–8

[199] Zucker J E, Bar-Joseph I, Miller B I, Koren U and Chemla D S 1989 Quaternary quantum wells for electro-optic intensity and phase modulation at 1.3 and 1.55 μm *Appl. Phys. Lett.* **54** 10–2

[200] Soref R and Bennett B 1987 Electrooptical effects in silicon *IEEE J. Quantum Electron.* **23** 123–9

[201] Hofstetter D, Schad S-S, Wu H, Schaff W J and Eastman L F 2003 GaN/AlN-based quantum-well infrared photodetector for 1.55 μm *Appl. Phys. Lett.* **83** 572–4

[202] Baumann E, Giorgetta F R, Hofstetter D, Lu H, Chen X, Schaff W J, Eastman L F, Golka S, Schrenk W and Strasser G 2005 Intersubband photoconductivity at 1.6 μm using strain-compensated AlN/GaN superlattice *Appl. Phys. Lett.* **87** 191102

[203] DeCuir E A, Manasreh M O, Tschumak E, Schörmann J, As D J and Lischka K 2008 Cubic GaN/AlN multiple quantum well photodetector *Appl. Phys. Lett.* **92** 201910

[204] Doyennette L, Nevou L, Tchernycheva M, Lupu A, Guillot F, Monroy E, Colombelli R and Julien F H 2005 GaN-based quantum dot infrared photodetector operating at 1.38 μm *Electron. Lett.* **41** 1077–8

[205] Vardi A, Akopian N, Bahir G, Doyennette L, Tchernycheva M, Nevou L, Julien F H, Guillot F and Monroy E 2006 Room temperature demonstration of GaN/AlN quantum dot intraband infrared photodetector at fiber-optics communication wavelength *Appl. Phys. Lett.* **88** 143101

[206] Vardi A, Bahir G, Schacham S E, Kandaswamy P K and Monroy E 2010 Negative photoconductivity due to intraband transitions in GaN/AlN quantum dots *J. Appl. Phys.* **108** 104512

[207] Baumann E, Giorgetta F R, Hofstetter D, Wu H, Schaff W J, Eastman L F and Kirste L 2005 Tunneling effects and intersubband absorption in AlN/GaN superlattices *Appl. Phys. Lett.* **86** 032110

[208] Reshchikov M A and Morkoç H 2005 Luminescence properties of defects in GaN *J. Appl. Phys.* **97** 061301

[209] Monroy E, Omn s F and Calle F 2003 Wide-bandgap semiconductor ultraviolet photodetectors *Semicond. Sci. Technol.* **18** R33–51

[210] Hofstetter D, Baumann E, Giorgetta F R, Graf M, Maier M, Guillot F, Bellet-Amalric E and Monroy E 2006 High-quality AlN/GaN-superlattice structures for the fabrication of narrow-band 1.4 μm photovoltaic intersubband detectors *Appl. Phys. Lett.* **88** 121112

[211] Giorgetta F R, Baumann E, Guillot F, Monroy E and Hofstetter D 2007 High frequency ($f = 2.37$ GHz) room temperature operation of 1.55 μm AlN/GaN-based intersubband detector *Electron. Lett.* **43** 185–7

[212] Hofstetter D *et al* 2009 Photodetectors based on intersubband transitions using III-nitride superlattice structures *J. Phys.: Condens. Matter* **21** 174208

[213] Rosencher E and Bois P 1991 Model system for optical nonlinearities: asymmetric quantum wells *Phys. Rev.* B **44** 11315–27

[214] Hofstetter D, Di Francesco J, Kandaswamy P K, Das A, Valdueza-Felip S and Monroy E 2010 Performance improvement of AlN/GaN-based intersubband detectors by using quantum dots *IEEE Photon. Technol. Lett.* **22** 1087–9

[215] Hofstetter D, Theron R, Baumann E, Giorgetta F R, Golka S, Strasser G, Guillot F and Monroy E 2008 Monolithically integrated AlGaN/GaN/AlN-based solar-blind ultraviolet and near-infrared detectors *Electron. Lett.* **44** 986

[216] Hofstetter D, Baumann E, Giorgetta F R, Théron R, Guillot F, Monroy E, Golka S and Strasser G 2009 Monolithically integrated UV/IR-photodetectors based on an AlN/GaN-based superlattice grown on an AlGaN buffer layer *Phys. Status Solidi* c **6** S818–21

[217] Gendron L, Carras M, Huynh A, Ortiz V, Koeniguer C and Berger V 2004 Quantum cascade photodetector *Appl. Phys. Lett.* **85** 2824

[218] Giorgetta F R *et al* 2009 Quantum cascade detectors *IEEE J. Quantum Electron.* **45** 1039–52

[219] Vardi A, Bahir G, Guillot F, Bougerol C, Monroy E, Schacham S E, Tchernycheva M and Julien F H 2008 Near infrared quantum cascade detector in GaN/AlGaN/AlN heterostructures *Appl. Phys. Lett.* **92** 011112

[220] Sakr S, Kotsar Y, Haddadi S, Tchernycheva M, Vivien L, Sarigiannidou I, Isac N, Monroy E and Julien F H 2010 GaN-based quantum cascade photodetector with 1.5 μm peak detection wavelength *Electron. Lett.* **46** 1685–6

[221] Vardi A *et al* 2008 High-speed operation of GaN/AlGaN quantum cascade detectors at $\lambda \approx 1.55$ μm *Appl. Phys. Lett.* **93** 193509

[222] Vardi A, Sakr S, Mangeney J, Kandaswamy P K, Monroy E, Tchernycheva M, Schacham S E, Julien F H and Bahir G 2011 Femto-second electron transit time characterization in GaN/AlGaN quantum cascade detector at 1.5 μm *Appl. Phys. Lett.* **99** 202111

[223] Gryshchenko S V, Klymenko M V, Shulika O V, Sukhoivanov I A and Lysak V V 2012 Temperature dependence of electron transport in GaN/AlGaN quantum cascade detectors *Superlatt. Microstruct.* **52** 894–900

[224] Sakr S *et al* 2013 GaN/AlGaN waveguide quantum cascade photodetectors at $\lambda \approx 1.55$ μm with enhanced responsivity and ~40 GHz frequency bandwidth *Appl. Phys. Lett.* **102** 011135

[225] Sakr S, Giraud E, Dussaigne A, Tchernycheva M, Grandjean N and Julien F H 2012 Two-color GaN/AlGaN quantum cascade detector at short infrared wavelengths of 1 and 1.7 μm *Appl. Phys. Lett.* **100** 181103

[226] Sakr S, Giraud E, Tchernycheva M, Isac N, Quach P, Warde E, Grandjean N and Julien F H 2012 A simplified GaN/AlGaN quantum cascade detector with an alloy extractor *Appl. Phys. Lett.* **101** 251101

[227] Sudradjat F F, Zhang W, Woodward J, Durmaz H, Moustakas T D and Paiella R 2012 Far-infrared intersubband photodetectors based on double-step III-nitride quantum wells *Appl. Phys. Lett.* **100** 241113

[228] Nevou L, Julien F H, Colombelli R, Guillot F and Monroy E 2006 Room-temperature intersubband emission of GaN/AlN quantum wells at $\lambda = 2.3$ μm *Electron. Lett.* **42** 1308–9

[229] Nevou L, Tchernycheva M, Julien F H, Guillot F and Monroy E 2007 Short wavelength ($\lambda = 2.13$ μm) intersubband luminescence from GaN/AlN quantum wells at room temperature *Appl. Phys. Lett.* **90** 121106

[230] Driscoll K, Liao Y, Bhattacharyya A, Zhou L, Smith D J, Moustakas T D and Paiella R 2009 Optically pumped intersubband emission of short-wave infrared radiation with GaN/AlN quantum wells *Appl. Phys. Lett.* **94** 081120

[231] Nevou L, Julien F H, Tchernycheva M, Guillot F, Monroy E and Sarigiannidou E 2008 Intraband emission at $\lambda \approx 1.48$ μm from GaN/AlN quantum dots at room temperature *Appl. Phys. Lett.* **92** 161105

[232] Jovanović V D, Ikonić Z, Indjin D, Harrison P, Milanović V and Soref R A 2003 Designing strain-balanced GaN/AlGaN quantum well structures: application to intersubband devices at 1.3 and 1.55 μm wavelengths *J. Appl. Phys.* **93** 3194–7

[233] Stattin M, Berland K, Hyldgaard P, Larsson A and Andersson T G 2011 Waveguides for nitride based quantum cascade lasers *Phys. Status Solidi* c **8** 2357–9

[234] Ive T, Berland K, Stattin M, Fälth F, Hyldgaard P, Larsson A and Andersson T G 2012 Design and fabrication of AlN/GaN heterostructures for intersubband technology *Japan. J. Appl. Phys.* **51** 01AG07

[235] Köhler R, Tredicucci A, Beltram F, Beere H E, Linfield E H, Davies A G, Ritchie D A., Iotti R C and Rossi F 2002 Terahertz semiconductor-heterostructure laser *Nature* **417** 156–9

[236] Scalari G, Walther C, Fischer M, Terazzi R, Beere H, Ritchie D and Faist J 2009 THz and sub-THz quantum cascade lasers *Laser Photon. Rev.* **3** 45–66

[237] Williams B S 2007 Terahertz quantum-cascade lasers *Nature Photon.* **1** 517–25

[238] Kumar S, Hu Q and Reno J L 2009 186 K operation of terahertz quantum-cascade lasers based on a diagonal design *Appl. Phys. Lett.* **94** 131105

[239] Williams B S, Callebaut H, Hu Q and Reno J L 2001 Magnetotunneling spectroscopy of resonant anticrossing in terahertz intersubband emitters *Appl. Phys. Lett.* **79** 4444

[240] Williams B S, Callebaut H, Kumar S, Hu Q and Reno J L 2003 3.4-THz quantum cascade laser based on longitudinal-optical-phonon scattering for depopulation *Appl. Phys. Lett.* **82** 1015–7

[241] Lü J T and Cao J C 2006 Monte Carlo simulation of hot phonon effects in resonant-phonon-assisted terahertz quantum-cascade lasers *Appl. Phys. Lett.* **88** 061119

[242] Jovanović V D, Indjin D, Ikonić Z and Harrison P 2004 Simulation and design of GaN/AlGaN far-infrared ($\lambda \sim 34$ μm) quantum-cascade laser *Appl. Phys. Lett.* **84** 2995–7

[243] Sun G, Soref R A and Khurgin J B 2005 Active region design of a terahertz GaN/$Al_{0.15}Ga_{0.85}N$ quantum cascade laser *Superlatt. Microstruct.* **37** 107–13

[244] Vukmirović N, Jovanović V D, Indjin D, Ikonić Z, Harrison P and Milanović V 2005 Optically pumped terahertz laser based on intersubband transitions in a GaN/AlGaN double quantum well *J. Appl. Phys.* **97** 103106

[245] Bellotti E, Driscoll K, Moustakas T D and Paiella R 2008 Monte Carlo study of GaN versus GaAs terahertz quantum cascade structures *Appl. Phys. Lett.* **92** 101112

[246] Terashima W and Hirayama H 2009 Design and fabrication of terahertz quantum cascade laser structure based on III-nitride semiconductors *Phys. Status Solidi* c **6** S615–8

[247] Yasuda H, Kubis T and Hirakawa K 2011 Non-equilibrium Green's function calculation for GaN-based terahertz quantum cascade laser structures *IRMMW-THz: 36th Int. Conf. on Infrared, Millimeter and Terahertz Waves* 1–2

[248] Chou H, Manzur T and Anwar M 2011 Active layer design of THz GaN quantum cascade lasers *Proc. SPIE* **8023** 802309

[249] Mirzaei B, Rostami A and Baghban H 2012 Terahertz dual-wavelength quantum cascade laser based on GaN active region *Opt. Laser Technol.* **44** 378–83

[250] Harrison P, Indjin D, Jovanović V D, Mirčetić A, Ikonić Z, Kelsall R W, McTavish J, Savić I, Vukmirović N and Milanović V 2005 A physical model of quantum cascade lasers: application to GaAs, GaN and SiGe devices *Phys. Status Solidi* a **202** 980–6

[251] Terashima W and Hirayama H 2011 Spontaneous emission from GaN/AlGaN terahertz quantum cascade laser grown on GaN substrate *Phys. Status Solidi* c **8** 2302–4

[252] Terashima W and Hirayama H 2011 Terahertz intersubband electroluminescence from GaN/AlGaN quantum cascade laser structure on AlGaN template *IRMMW-THz: 36th Int. Conf. on Infrared, Millimeter and Terahertz Waves* 1–2

[253] Bellotti E, Driscoll K, Moustakas T D and Paiella R 2009 Monte Carlo simulation of terahertz quantum cascade

laser structures based on wide-bandgap semiconductors *J. Appl. Phys.* **105** 113103

[254] Sudradjat F, Zhang W, Driscoll K, Liao Y, Bhattacharyya A, Thomidis C, Zhou L, Smith D J, Moustakas T D and Paiella R 2010 Sequential tunneling transport characteristics of GaN/AlGaN coupled-quantum-well structures *J. Appl. Phys.* **108** 103704

[255] Chou H, Anwar M and Manzur T 2012 Active layer design and power calculation of nitride-based THz quantum cascade lasers *Proc. SPIE* **8268** 82680O

[256] Yasuda H, Hosako I and Hirakawa K 2012 Designs of GaN-based terahertz quantum cascade lasers for higher temperature operations *CLEO: Conf. on Lasers and Electro-Optics* 1–2

Annex 2

8 III-Nitride Semiconductors: New Infrared Intersubband Technologies

AU: Please provide first names for M. Beeler and E. Monroy.

M. Beeler and E. Monroy

CONTENTS

8.1 Introduction 244
8.2 Intersubband Absorption in III-Nitride Nanostructures 245
8.2.1 GaN/AlGaN Polar Quantum Wells 245
8.2.1.1 Modeling 245
8.2.1.2 Growth and Defect Analysis 246
8.2.1.3 Intersubband Optical Characterization 249
8.2.1.4 Effect of Doping 250
8.2.2 Far-Infrared Multilayer Architectures 252
8.2.3 Coupled Quantum Wells 255
8.2.4 In-Containing Superlattices: AlInN/GaN, AlInN/GaInN, and GaN/GaInN 256
8.2.5 Quantum Dots 257
8.2.6 Nanowire Heterostructures 259
8.2.7 Alternative Crystallographic Orientations 259
8.2.8 Cubic III-Nitrides 261
8.3 All-Optical Switches 262
8.4 Electro-Optical Modulators 263
8.5 Infrared Photodetectors 264
8.5.1 Quantum Well/Quantum Dot Infrared Photodetectors 264
8.5.2 Quantum Cascade Detectors 266
8.6 Toward the Quantum Cascade Laser 269
8.6.1 Light Emission in Superlattices 269
8.6.2 Quantum Cascade Laser Structures 270
8.7 Conclusions and Prospects 273
Acknowledgments 274
References 274

K22181_C008.indd 243 6/3/15 10:53 AM

GaN/Al(Ga)N semiconductors have emerged within the last decade as promising materials for founding new intersubband (ISB) technologies relying on infrared (IR) optical transitions between quantum-confined electronic states in the conduction band of nanostructures (quantum wells [QWs], quantum dots [QDs], and nanowires). The large conduction-band offset (about 1.8 eV for GaN/AlN) and the sub-picosecond ISB relaxation time render III-nitrides suitable for the fabrication of ultrafast photonic devices for optical telecommunication networks in the near-IR range. Furthermore, the high energy of GaN longitudinal optical phonons (92 meV) opens prospects for high-temperature THz quantum cascade lasers (QCLs) and ISB devices covering the 5- to 10-THz band, inaccessible to As-based technologies due to phonon absorption.

Key words: nitride, infrared, intersubband, quantum well.

8.1 INTRODUCTION

The term “intersubband” is used to describe electronic transitions between confined states in either the conduction band or the valence band of semiconductor nanostructures. In such systems, ISB optical transitions at a desired operation wavelength can be obtained by the adequate choice of layer thicknesses, which is the base of the “band-structure engineering” concept. The first studies of ISB absorption date back to the 1970s [1,2] and refer to electronic transitions between confined levels in an accumulation layer on *n*-type Si (100), observed under far-IR illumination. The extrapolation of these principles to GaAs/AlGaAs QWs to shift the transition wavelength to mid-IR was first suggested by Esaki and Sakaki [3], and subsequent experimental [4,5] and theoretical studies [6,7] led to the first experimental measurement of strong ISB absorption in a series of multiple quantum wells (MQWs) performed by West and Eglash [8]. These results lead to the fabrication of the first quantum well infrared photodetector (QWIP), by Levine et al. [9,10]. In 1994, Faist et al. [11] presented a major breakthrough in ISB technology: the QCL. This was the beginning of tremendous development of the ISB technology, which resulted in commercially available devices operating in the mid- and far-IR. For a comprehensive introduction to ISB physics in QWs, we refer the readers to the work by Bastard [12] or Liu and Capasso [13].

Nowadays, ISB optoelectronic devices based on the III-As material system (GaAs/AlGaAs, InGaAs/AlInAs, or GaInAs/AlAsSb) can be tuned from the mid-IR to the THz spectral range. Operation at shorter wavelengths (<3 μm) is limited by the available conduction-band offset and by material transparency. III-Nitride semiconductors (GaN, AlN, InN, and their alloys), with their wide bandgap and large conduction-band offset (~1.8 eV for GaN/AlN [14–16]), are attracting much interest for ISB devices operating in the near-IR spectral range, particularly in the 1.3- to 1.55-μm wavelength window used for fiber-optic communications [17–20]. GaN is transparent in a large spectral region, notably for wavelengths longer than 360 nm (bandgap), except for the Restrahlen band (from 9.6 to 19 μm). Absorption in the range of 7.3–9 μm has been observed in bulk GaN substrates with carrier concentrations < 10^{16} cm^{-3} [21–23] and was attributed to the second harmonic of the Restrahlen band. Although this second band might hinder the fabrication of waveguided devices in this spectral

K22181_C008.indd 244 6/3/15 10:53 AM

region, its effect in planar devices with micrometer-sized active regions is negligible, since the absorption coefficient related to two-phonon processes is much smaller than the one associated with ISB transitions [24,25]. On the other hand, III-nitrides do not present problems of inter-valley scattering, since the L and X points are much higher in energy (>2 eV) than the Γ point.

There is also an interest to push the III-nitride ISB technology toward longer wavelengths, particularly to the THz frequency range [20]. The potential of this spectral region in applications like security screening, quality control, and medical diagnostics has driven extensive development of optoelectronic components. Because of the large LO-phonon energy of GaN (about three times that of GaAs), room temperature operation becomes feasible for ISB devices covering the IR band that was typically inaccessible to As-based semiconductors due to phonon absorption.

8.2 INTERSUBBAND ABSORPTION IN III-NITRIDE NANOSTRUCTURES

8.2.1 GaN/AlGaN Polar Quantum Wells

8.2.1.1 Modeling

The optical properties of (0001)-oriented nitride QWs are strongly affected by the presence of internal electric fields arising from the piezoelectric and spontaneous polarization discontinuity between the various nitride compounds [26]. Figure 8.1a presents the band diagram of a GaN/AlN (2 nm/3 nm) superlattice calculated using the nextnano^3 8-band k.p Schrödinger–Poisson solver [27] with the material parameters described by Kandaswamy et al. [28]. The electronic potential takes on a characteristic saw-tooth profile due to the internal electric field. The electron wave functions of the ground hole state h_1, ground electron state e_1, and excited electron states e_2 and e_3 are presented in Figure 8.1. In narrow QWs (~1 nm) the energy difference between e_1 and e_2 is mostly determined by the confinement in the QW, whereas for larger QWs (>2 nm) this difference is ruled by the internal electric field, since both electronic levels lie in the triangular part of the QW potential profile. The evolution of the e_2–e_1 and e_3–e_1 energy differences with the QW thickness and strain state is presented in Figure 8.1b and compared with experimental data from GaN/AlN MQWs. The increase in the e_2–e_1 ISB energy calculated when considering the MQW strained on GaN is related to the enhancement of the electric field in the QW, due to the larger piezoelectric coefficients of the AlN barrier in comparison with the GaN QW [28]. On the other hand, the band structure simulations show that certain QW thicknesses can result in a configuration where the $e_1 \rightarrow e_2$ transition has approximately the same energy as $e_2 \rightarrow e_3$ (or as $e_2 \rightarrow e_4$ for very thick barrier layers), which can result in the enhancement of second-order and third-order nonlinear effects such as two-photon absorption [29], second-harmonic generation [30], or saturable absorption [31].

In nitride heterostructures, charge distribution depends not only on the Si doping level in the QWs but also on the presence of non-intentional dopants and on the carrier redistribution due to the internal electric field. The polarization discontinuity between heterostructure layers leads to strong band bending, which typically results in the formation of a depletion layer on one side of the active region and an accumulation layer

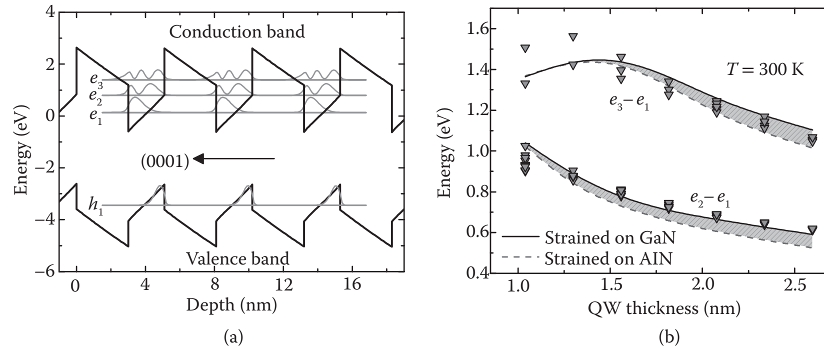

FIGURE 8.1 (a) Band diagram of GaN/AlN quantum wells (QWs) in an infinite superlattice with 3-nm-thick AlN barriers and 2-nm-thick GaN QWs. The structure is considered strained on an AlN substrate. The electron wave functions of the ground hole state, h_1, ground electron state, e_1; and excited electron states, e_2 and e_3, are presented. (b) Variation of the e_2–e_1 and e_3–e_1 intersubband (ISB) transition energy as a function of the QW thickness in GaN/AlN multiple quantum well structures with 3-nm-thick barriers. Triangles indicate experimental data, and solid and dashed lines correspond to theoretical calculations, assuming that the structure fully strained on AlN and on GaN substrates, respectively. (From Kandaswamy et al., *J. Appl. Phys.*, 104(9), 093501, 2008 [28].)

on the other side (Figure 8.2a). Therefore, a realistic view of the charge distribution in a device is only achieved by extending the electronic modeling to the complete structure. As an illustration of this phenomena, Kandaswamy et al. [28] have studied the contribution of the internal electric field induced by a 50-nm-thick $Al_xGa_{1-x}N$ ($x = 0$, 0.25, 0.5, and 1) cap layer to the ISB absorption of 40-period non-intentionally doped GaN/AlN (1.5/1.5 nm) MQWs grown on AlN [28]. Measurements of ISB absorption in these samples confirm a monotonous increase and broadening of the absorption when increasing the Al mole fraction of the cap layer. This trend is consistent with the simulations of the electronic structure in Figure 8.2a and b, where the use of AlN as a cap layer lowers the conduction band of the first GaN QWs below the Fermi level (dash-dotted line at 0 eV in the figures), whereas the use of GaN as a cap layer results in the depletion of the MQW active region.

8.2.1.2 Growth and Defect Analysis

AU: Please check if “III-nitride two-dimensional layers” should be changed to “two-dimensional III-nitride layers.”

A main requirement for the growth of III-nitride nanostructures for ISB devices is the precise control of thickness and interfaces. Molecular beam epitaxy (MBE) seems to be the most suitable technique for this application thanks to its low growth temperature, which hinders GaN–AlN interdiffusion [32]. Plasma-assisted molecular beam epitaxy (PAMBE) was the first method to produce III-nitride nanostructures displaying ISB transitions at telecommunication wavelengths (1.3, 1.55 μm) [33–39]. The growth of (0001)-oriented GaN, AlN, and AlGaN by PAMBE is extensively discussed in the literature [40–45]. Deposition of III-nitride two-dimensional (2D) layers requires a precise control of the III/V flux ratio during the growth; it demands

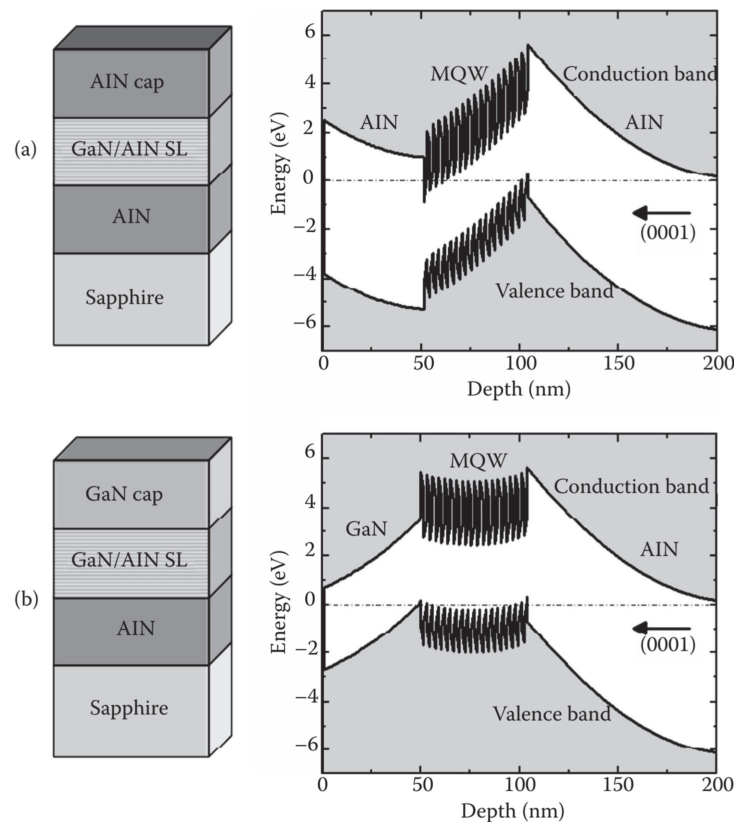

FIGURE 8.2 Band diagram of non-intentionally doped GaN/AlN (1.5/1.5 nm) multiple quantum well structures with (a) GaN cap layer and (b) AlN cap layer. (From Kandaswamy et al., *J. Appl. Phys.*, 104(9), 093501, 2008 [28].)

AU: Please specify what SL refers to in Figure 8.2.

slightly metal-rich conditions, and hence growth optimization requires the determination of stoichiometric flux conditions and precise control of the growth temperature. In the case of GaN, at a substrate temperature higher than 700°C there is a certain range of Ga fluxes for which the Ga excess remains in a situation of dynamic equilibrium on the growing front, that is, the Ga coverage is independent of the Ga exposure time. Smooth surfaces are generally achieved under moderate Ga-rich conditions [40,42,46,47], when the Ga excess arranges into a so-called laterally contracted Ga bilayer, which consists of two Ga layers adsorbed on the Ga-terminated (0001) GaN surface [40,41,47–49].

In the case of AlN, the deposition of layers with atomically flat surface morphology also requires metal-rich conditions [45]. However, Al does not desorb from the surface at the standard growth temperature for GaN. Therefore, to eliminate the Al excess at the surface it is necessary to perform periodic growth interruptions under nitrogen. An alternative approach to achieve 2D growth of AlN and low Al content (<50%) of Al(Ga)N layers is to use Ga as a surfactant, with the Al flux corresponding to the required Al mole fraction [28,43,50].

GaN/AlN QWs displaying ISB transitions in the near-IR can also be synthesized by metalorganic vapor phase epitaxy (MOVPE) [51–53]. In this case, a critical parameter to attain devices in the telecommunication spectral range (1.3 μm, 1.55 μm) is the reduction in growth temperature from the 1050°C–1100°C optimum range for GaN growth down to 900°C–950°C (or even to 770°C [54]), to minimize the GaN–AlN interdiffusion. Furthermore, deposition under compressive strain (e.g., using AlN substrates) is recommended at these growth temperatures to prevent the red shift of the ISB transition due to instabilities of the GaN/AlN interface [55].

Since GaN/AlN is a lattice-mismatched system (2.5% in-plane lattice mismatch), it is important to understand the effects of strain and misfit relaxation. The density of edge-type threading dislocations (TDs) should be kept to a minimum since they cause losses in the transmission of transverse-magnetic (TM)-polarized light, which adversely affects the performance of ISB devices [56]. These TDs propagate from the heteroepitaxial substrates (typical TD densities in commercial GaN-on-sapphire or AlN-on-sapphire templates are in the 10^8 cm^{-2} and 10^9 cm^{-2} range, respectively), but they are also generated during the growth due to the plastic strain relaxation, since misfit dislocations (MDs) often fold toward the growth direction, giving rise to edge-type TDs [57].

AU: Please confirm if the expansion of TM and TE to transverse-magnetic and transverse-electric, respectively, is correct.

It is not clear how semiconductors with hexagonal symmetry, such as III-nitrides, relax the misfit stress. In the case of nitride heterostructures grown along the [0001] axis, the formation of regular networks of MDs is hindered since the most crystallographically favorable slip system, (0001) basal plane with <11-20> {0002} slip directions, lies parallel to the heterointerfaces. This means that the resolved misfit stress on the main slip plane is zero [58]. Thus, only secondary slip systems that are oblique to the basal plane can have a resolved misfit stress and may contribute to plastic relaxation. It has been observed that MDs following the secondary <11-23> {11-22} slip system can be generated at heterointerfaces when shear stress is intentionally or unintentionally induced by three-dimensional (3D) growth [59,60], by crack formation [57,61], or in close proximity to V-defects [62]. Therefore, the relaxation mechanism depends not only on the structure itself but also on the growth conditions. In general, GaN/AlGaN heterostructures grown under tensile stress on GaN substrates tend to crack along the <11-20> crystallographic direction at a certain critical thickness [61,63,64]. In the case of crack-free GaN/AlGaN superlattices deposited under compressive strain, the main relaxation mechanism is the tilt of the *a*-type TDs toward <1-100>, the inclination angle depending on the lattice misfit between the MQWs and the underlayer [65]. It has been proposed that the diagonal movement is due to a staircase-like movement of the dislocations through the stack, with a misfit segment at each well. Strain relaxation via TD inclination has also been observed in AlGaN layers deposited on mismatched AlGaN [66].

AU: Please confirm that numbers appearing inside angle brackets and curly braces in this chapter refer to crystallographic orientations.

In PAMBE growth, the metal to N ratio and the growth temperature are key parameters that define the strain relaxation rate during growth [67]. Ga-rich conditions delay crack propagation and minimize strain relaxation [50]. They also allow good control of the layer thickness and Al incorporation in AlGaN alloys. In the case of GaN/AlN MQWs and in addition to the relaxation mechanisms described earlier, the periodic misfit relaxation appears to be associated with the formation of stacking fault loops that initiate at the beginning of the AlN barrier deposition, propagate

through the barrier, and close within the following QW [50]. In contrast, transmission electron microscopy (TEM) images from GaN/AlGaN superlattices (ternary alloy barriers) do not reveal stacking faults or other periodic defects [68].

8.2.1.3 Intersubband Optical Characterization

Figure 8.3 shows the ISB absorption of Si-doped AlN/GaN MQWs with 3-nm-thick AlN barriers and QW thicknesses of 5, 6, 7, and 9 ML [16,28]. The samples show a pronounced TM-polarized absorption, attributed to the transition from the first to the second electronic levels in the QW ($e_1 \rightarrow e_2$), whereas no absorption was observed for transvers-electric (TE)-polarized light within experimental sensitivity. For large QWs (≥8 ML), the $e_1 \rightarrow e_3$ transition is observed, as indicated in Figure 8.3; this transition is forbidden in symmetric QWs [69] but is allowed in nitride QWs because the internal electric field in the well breaks the symmetry of the potential. The experimental values of $e_2 – e_1$ and $e_3 – e_1$ as a function of QW width are presented in Figure 8.1, showing a good fit with theoretical calculations.

AU: Please specify what ML refers to.

The line width of the absorption remains in the 70- to 100-meV range for QWs doped at 5×10^{19} cm^{-2}, and the ISB absorption efficiency per reflection attains 3%–5%. A record small line width of ~40 meV has been achieved in non-intentionally doped structures [70]. The spectra either present Lorentzian shape or is structured with two or three well-defined peaks in Lorentzian shape [16]. These multiple peaks correspond to the expected values of the $e_1 \rightarrow e_2$ line in QWs whose thickness is equal to an integer number of GaN monolayers. For very narrow QWs, a variation

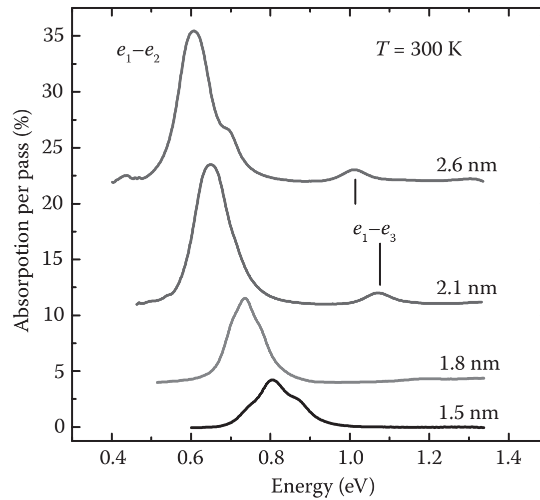

FIGURE 8.3 Room-temperature transverse-magnetic-polarized intersubband absorption spectra from 20-period Si-doped GaN/AlN multiple quantum well structures with 3-nm-thick AlN barriers and different GaN quantum well thickness. All the samples were grown on 1-μm-thick AlN-on-sapphire templates without cap layer. The absorption peaks labeled $e_1 – e_2$ and $e_1 – e_3$ are assigned to the corresponding intra-conduction-band transitions as described in Figure 8.1a. The spectra are vertically shifted for clarity. (From Kandaswamy et al., *J. Appl. Phys.*, 104(9), 093501, 2008 [28].)

in the thickness by 1 ML implies an important shift in the ISB transitions (about 100 meV for QWs of 4 to 5 ML). This value is comparable to the full width at half maximum (FWHM) of the absorption lines and hence results in well-resolved absorption peaks. Thickness fluctuations might originate from a drift of the growth rate with time, resulting in a variation in the QW thickness. However, in situ measurements of the growth rate and TEM studies confirmed that structured absorption spectra appear in samples where no growth rate drift is detected. In these samples, cathodoluminescence studies confirmed the presence of in-plane thickness fluctuations, which appear to be associated with dislocations or extended defects [28]. Regarding the thermal stability of the ISB transition in GaN/AlN MQWs, it has been found that the ISB absorption energy decreases only by ~6 meV at 400°C relative to its room temperature value [71].

Using GaN/AlN QWs, the $e_1 \rightarrow e_2$ ISB transition can be tuned in the 1.0- to 3.5-μm wavelength range by changing the QW thickness from 1 to 7 nm [16,28,35,36,38,52,64,71,72] with AlN barrier thicknesses in the 1.5- to 5.1-nm range. For larger QWs (>5 nm), the first two electron-confined levels get trapped in the triangular section of the QW, which results in a saturation of the e_2–e_1 value. Therefore, to shift the absorption toward longer wavelengths it is necessary to reduce the effect of the internal electric field in the QWs. A first approach consisted of using GaN/AlGaN MQWs, thereby reducing the Al mole fraction in the barriers. By changing the geometry and composition, the ISB absorption can be tailored to cover the near-IR range above 1.0 μm and the mid-IR region up to 5.3 μm [33,34,73–82]. To attain longer wavelengths, the requirement of substrate transparency imposes the replacement of sapphire-based templates by semi-insulating Si (111) as a substrate [24]. Using GaN-on-Si (111) templates, Kandaswamy et al. [24] have demonstrated the extension of the ISB absorption range of GaN/AlGaN QWs up to 10 μm, as illustrated in Figure 8.4a. A slight red shift of the ISB transition is observed when increasing the compressive strain in the QWs, as theoretically predicted [78].

8.2.1.4 Effect of Doping

To observe ISB absorption, it is necessary to control the carrier concentration in QWs to guarantee that the first electronic level is populated. High doping levels also have an effect on the targeted operating wavelength. The ISB absorption energy can blue shift markedly due to many-body effects [25,38,83], mostly due to exchange interaction and depolarization shift, as illustrated in Figure 8.4b and (c). On the other hand, studies of the effect of dopant location have shown a dramatic reduction of the ISB absorption line width by using a δ-doping technique with Si donors placed at the end of the QW [84]. This line width reduction is attributed to an improvement of interfacial roughness. It has also been theorized that doping in the wells should provide red-shifted [85] and stronger [86] ISB absorptions versus doping in the barriers.

When integrating III-nitride nanostructures into complete devices, it is necessary to keep in mind that the magnitude of the carrier distribution depends not only on the Si doping level in the QWs but also on the presence of non-intentional dopants and on the carrier redistribution due to the internal electric field. The large polarization discontinuities in the III-N material system can result in a significant (even dominant) contribution to the IR absorption in GaN/AlN superlattices [28].

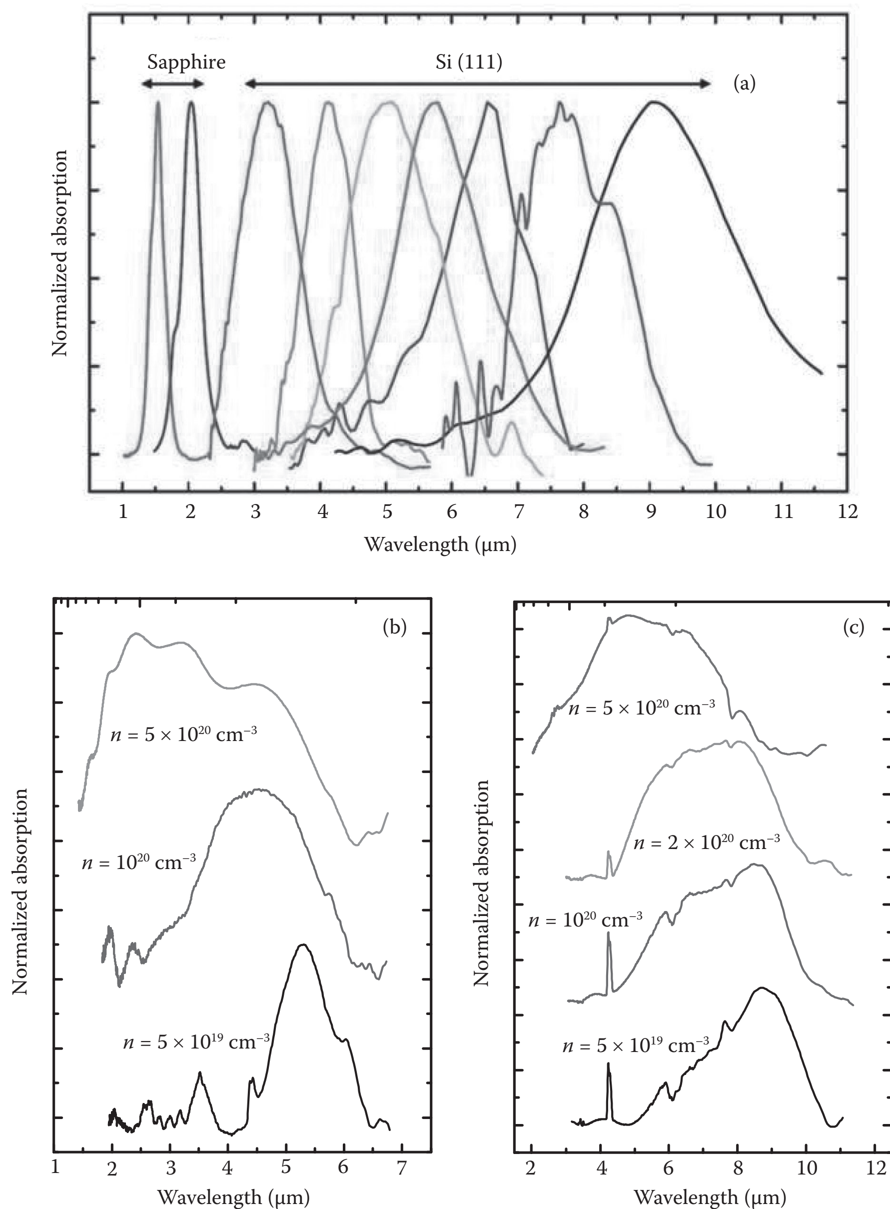

FIGURE 8.4 (a) Room-temperature transverse-magnetic (TM)-polarized infrared (IR) photo-induced absorption spectra measured in GaN/AlGaN multiple quantum well (MQW) structures with different barrier Al contents and quantum well (QW) width, grown either on sapphire or on Si (111) templates [24]. (b) Infrared absorption spectra for TM-polarized light measured from GaN/$Al_{0.2}Ga_{0.8}N$ (3 nm/3 nm) MQWs with different doping levels. Spectra are vertically shifted for clarity [25]. (c) IR absorption spectra for TM-polarized light measured from GaN/$Al_{0.1}Ga_{0.9}N$ (7 nm/4 nm) MQWs with different doping levels. Spectra are vertically shifted for clarity. (From Kandaswamy et al., *Appl. Phys. Lett.*, 96(14), 141903, 2010 [25].)

8.2.2 Far-Infrared Multilayer Architectures

AlGaN/GaN QWs displaying ISB transitions at 9.08 μm (136 meV) have been demonstrated [24]. However, in large QWs the internal electric field associated with the spontaneous and piezoelectric polarization discontinuities in the GaN/AlGaN system becomes the dominating characteristic for determining energy levels, which are no longer sensitive to changes in QW thickness. To further reduce the ISB transition energy, the first proposed architecture consisted of a three-layer well (step QW) with a virtually flat potential profile [87–89]. Figure 8.5a shows

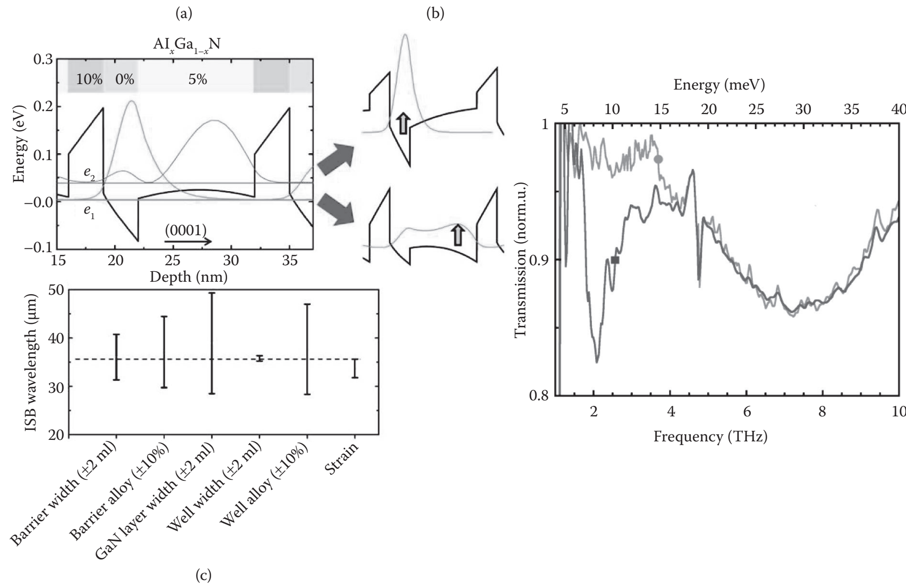

FIGURE 8.5 (a) Conduction-band profile, and first (e_1) and second (e_2) electronic levels with their associated wave functions for an $Al_{0.05}Ga_{0.95}N/Al_{0.1}Ga_{0.9}N/GaN$ (10 nm/3 nm/3 nm) step quantum well (QW) [88]. (b) Shift of the wave function of the first electronic level associated with a variation of the Al concentration in the well layer. A higher step-well Al concentration (top) creates a more triangular well and increases confinement toward the GaN layer. A lower step-well Al concentration (down) creates a secondary confinement area at the opposite side of the well. To illustrate the effect clearly, the band profiles correspond to Al0.07Ga0.93N/$Al_{0.1}Ga_{0.9}N/GaN$ (10 nm/3 nm/3 nm) (top) and $Al_{0.03}Ga_{0.97}N/Al_{0.1}Ga_{0.9}N/GaN$ (10 nm/3 nm/3 nm) (bottom) [88]. (c) Illustration of the robustness of the step-QW system. The dashed line indicates the nominal transition wavelength for an $Al_{0.05}Ga_{0.95}N/Al_{0.1}Ga_{0.9}N/GaN$ (10 nm/3 nm/3 nm) step QW. The error bars represent the minimum and maximum values attributed to the uncertainties associated to growth. The barrier and GaN well thicknesses were changed from 3 nm to 2.5 nm and 3.5 nm. The barrier Al content was changed from 10% to 11% and 9%. The step-well alloy was changed from 5% to 4.5% and 5.5% (±10%). The step-well thickness was changed from 10 nm to 12 nm and 8 nm. The strain error bar illustrates the variation of the intersubband transition when evolving from a structure fully strained on GaN to a structure fully strained on $Al_{0.1}Ga_{0.9}N$ [88]. (d) Transmission spectra for transverse-magnetic- (square) and transverse-electric- (circle) polarized light at T = 4.7 K. (From Machhadani et al., *Appl. Phys. Lett.*, 97(19), 191101, 2010 [87].)

K22181_C008.indd 252 6/3/15 10:53 AM

the conduction-band diagram of a step-QW design, in this example consisting of $Al_{0.1}Ga_{0.9}N/GaN/Al_{0.05}Ga0.95N$ (3 nm/3 nm/10 nm). This three-layer structure is designed around the principle of polarization equivalency. The design can be broken effectively into two portions: The first is the "barrier," which comprises the high-Al-content $Al_xGa_{1-x}N$ layer and the GaN layer. The second portion is the "well," which is the low-Al-content $Al_xGa_{1-x}N$ layer. The design creates a semi-flat band in the well by having the barrier balanced at the same average Al percentage, that is, the average polarization in the barrier is approximately equal to the average polarization in the well. This configuration is associated with the minimum energy spacing between the ground electronic state and the first excited state, as described by Wu et al. [90]. Samples following the step-QW design in Figure 8.5a have been synthesized by PAMBE on GaN templates on float-zone Si (111) to evade problems of substrate transparency [24], and ISB absorption at ~2 THz (~70 μm) (illustrated in Figure 8.5d) and at ~13 THz (~22 μm) has been reported [87,89].

The weakness of the step-QW design lies in the fact that any deviation from this balance results in an internal electric field in the well, which shifts the wave function associated with the first electronic level toward the GaN layer (Figure 8.5b top, for higher Al content in the well) or toward the high-Al-content layer (Figure 8.5b down, for lower average Al content in the well). Thus, any imbalance in the structure has a drastic effect on ISB wavelength. The limitations of the step-QW configuration can be surmounted by the insertion of an additional AlGaN layer to separate the GaN layer from the low-Al-content $Al_xGa_{1-x}N$ well [88]. The "separation layer" is designed so that there is no confined state in the GaN layer. This architecture, described in Figure 8.6a, does not evade the quantum-confined Stark effect, but the GaN layer contributes to reduce the average spontaneous polarization of the complex barrier structure ($Al_{0.1}Ga_{0.9}N/GaN/Al_{0.07}Ga_{0.93}N$), which results in a lower electric field in the QW. The robustness of this design is analyzed in Figure 8.6c and shows much less variation of the ISB transition energy than the step-QW architecture with respect to the growth uncertainties.

The incorporation of separation layer results in a geometry where the internal electric field is not fully compensated, that is, the QW keeps a triangular potential profile. As a consequence, the four-layer MQW system is more sensitive to changes in strain state versus the step-QW design. The strain error bar in Figure 8.6c illustrates the variation of the ISB transition when evolving from a structure fully strained on GaN to a structure fully strained on $Al_{0.1}Ga_{0.9}N$. These error bars are comparable to those generated by uncertainties in the structural parameters. However, the MQWs are expected to evolve toward a minimum elastic energy configuration independently of the substrate [68], so that the uncertainty in the strain state of the structure (neglecting the initial relaxation) is much smaller ($<\pm0.025\%$ variation of the in-plane lattice parameter) than the values simulated in Figure 8.5c (±0.12%).

AlGaN/GaN 40-period MQW structures following the four-layer MQW design in Figure 8.6b were deposited by PAMBE. Figure 8.6d shows the low-temperature (T = 5–10 K) far-IR transmission spectra of samples with different doping concentrations. In the sample with a lower doping level ([Si] = 1.5×10^{19} cm^{-3}), a TM-polarized absorption dip centered around 27–29 μm (~14 THz), which gets

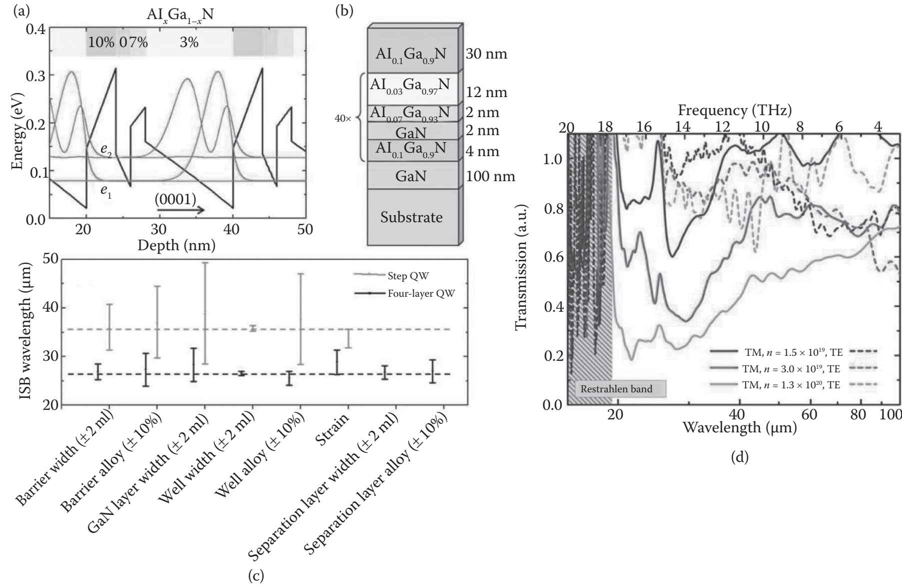

FIGURE 8.6 (a) Conduction band profile, and first (e_1) and second (e_2) electronic levels with their associated wave functions for an $Al_{0.1}Ga_{0.9}N/GaN/Al_{0.07}Ga_{0.93}N/Al_{0.03}Ga_{0.097}N$ (4 nm/2 nm/2 nm/12 nm) four-layer quantum well (QW) design. (b) Schematic drawing of the structure synthesized by plasma-assisted molecular beam epitaxy (PAMBE). (c) Illustration of the robustness of the four-layer QW system (black) compared with the step QW (gray). The dashed lines indicate the nominal transition wavelengths for an $Al_{0.05}Ga_{0.95}N/Al_{0.1}Ga_{0.9}N/GaN$ (10 nm/3 nm/3 nm) step QW and an $Al_{0.1}Ga_{0.9}N/GaN/Al_{0.07}Ga_{0.93}N/Al_{0.03}Ga_{0.97}N$ (4 nm/2 nm/2 nm/12 nm) four-layer QW. The error bar represents the minimum and maximum values attributed to the uncertainties associated with growth. In the four-layer QW, the barrier thickness was changed from 2 nm to 1.5 nm and 2.5 nm. The barrier Al content was changed from 10% to 11% and 9%. The GaN layer thickness was changed from 2 nm to 1.5 nm and 2.5 nm. The well thickness was changed from 12 nm to 11.5 nm and 12.5 nm, and its Al content was changed from 3% to 2.7% and 3.3% (±10%). The separation layer thickness was changed from 2 nm to 1.5 nm and 2.5 nm, and its Al content was changed from 7% to 6.3% and 7.7%. The strain error bar illustrates the variation of the ISB transition when evolving from a structure fully strained on GaN to a structure fully strained on $Al_{0.1}Ga_{0.9}N$. (d) Far-IR transmission measurement of four-layer multiple quantum wells with different doping levels for transverse-electric- and transverse-magnetic (TM)-polarized light. The spectra have been normalized by the response of a similar undoped superlattice, which exhibits no intersubband activity. The noise observed for wavelengths < 10 μm is due to the GaN Restrahlen absorption. The dip in TM-polarized transmission at 27–30 μm is assigned to the transition between the first and the second electronic levels in the QWs. (From Beeler et al., *Appl. Phys. Lett.*, 103(9), 091108, 2013 [88].)

AU: This is not a color book. Please check and change all references to color in figures and figure captions.

deeper and broader with increasing doping level, is observed. This absorption line is attributed to the transition from the first to the second electronic level in the QW, in good agreement with theoretical calculations.

The normalized absorption line width for the sample with a doping level [Si] = 1.5×10^{19} cm^{-3} is $\Delta f/f \sim 0.25$ [88], which is a significant improvement in comparison to results in step QWs ($\Delta f/f \sim 0.5$ in the study by Machhadani et al. [87]).

From progress on the four-layer design, robustness was deemed a key attribute to create these devices. However, the four-layer design used complex barrier systems to achieve this desired robustness. Such complex barrier structures inhibited tunneling transport, and therefore the incorporation of the architecture into ISB devices using the quantum cascade principle. This led Beeler et al. [91] to propose a pseudo-square QW, a four-layer architecture where the compensation of the polarization-induced internal electric field is obtained by creating a gradual increase in polarization field throughout the quantum "trough" generated by three low-Al-content layers (see schematic description in Figure 8.7). This design has single-layer barriers that can permit tunneling transport under bias. Experimentally, it is shown that the ISB wavelength can be varied from 150 to 75 μm by changing the size of the quantum trough, and from 100 to 50 μm by changing the doping level, as illustrated in Figure 8.7d.

8.2.3 Coupled Quantum Wells

The design of advanced ISB devices, like optically or electrically pumped ISB lasers, requires the exploitation of multilevel systems with finely tuned oscillator

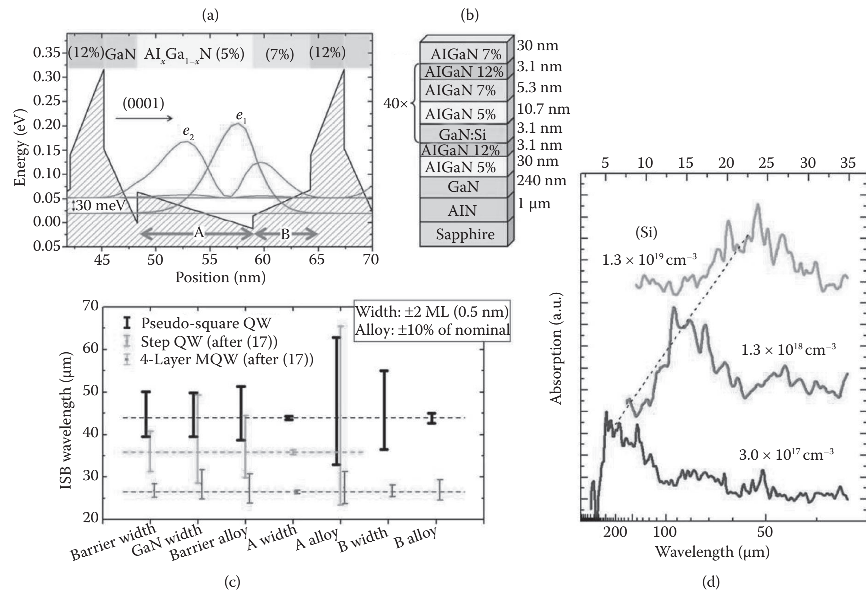

FIGURE 8.7 (a) Band profile of a pseudo-square quantum well (QW) where the first and second confined electronic levels are indicated as e_1 and e_2, respectively. The nominal compositions of the layers are indicated earlier. (b) Schematic description of the structure that was grown on an AlN-on-sapphire substrate. (c) Illustration of the robustness of the pseudo-square QWs. The dashed lined indicates the nominal transition wavelengths. The error bars represent the minimum and maximum values attributed to the uncertainties associated with growth (geometries changed by ±0.5 nm and alloys changed by ±10%). Similar data for step QWs and four-layer QWs are included for comparison [17]. (d) Spectral absorption of transverse-magnetic (TM)-polarized light in samples with different doping levels. Spectra are found from dividing transverse-electric (TE)- by TM-polarized light, then normalizing this division against reference spectra not showing absorption. (From Beeler et al., *Appl. Phys. Lett.* [91].)

AU: Please check if "after" can be deleted in the reference callouts "(after [17])" in Figure 8.7.

AU: Please specify section number.

AU: For this source line, please update publishing year, volume number, and page range.

K22181_C008.indd 255 6/3/15 10:53 AM

strengths and lifetimes. Coupled QWs are the basic element for such systems. In III-nitrides, the realization of coupled QWs is complicated by the relatively heavy electron effective mass and the large conduction-band offset. As a result, very thin barriers (1–3 ML) are required to achieve strong interwell coupling in the GaN/AlN material system [92].

Coupling between GaN QWs was first experimentally investigated by Gmachl et al. [34,37] by using double GaN QWs coupled by AlGaN barriers with large (0.65 or 0.9) Al mole fractions. The coupling barrier thicknesses varied from 0.7 to 6 nm. Degenerate doping of the QWs (10^{20} cm^{-3}) was used to establish a common reference energy at the Fermi level, which decreases the uncertainties related to intrinsic internal electric fields. The broadening and structuration of ISB absorption peaks were attributed to transitions toward excited states exhibiting anticrossing.

Coupled GaN/AlN QWs were first demonstrated by Tchernycheva et al. [93] using 0.5-nm-thick AlN coupling barriers. The ISB absorption spectra present two distinct peaks attributed to the transition: first, between the ground states of the two coupled wells and, second, between the ground state and the delocalized excited state between the two wells. As an alternative approach, Driscoll et al. have opted to decrease the Al content of the coupling barrier to 39%–53%, so that strong coupling is achieved with thicker barriers (~5 ML). In this fashion, the barrier's Al content can be used as a tunable parameter to control the coupling strength [94].

The influence of polarization-induced electric fields on ISB absorption and the associated variation of refractive index in AlN/GaN-coupled QWs has been theoretically analyzed by Cen et al. [95,96] for their application in ultrafast two-color optoelectronic devices and electro-optical modulators operating within the optical communication wavelength range.

8.2.4 In-Containing Superlattices: AlInN/GaN, AlInN/GaInN, and GaN/GaInN

The lattice mismatch between GaN and AlN can lead to high defect densities and the risk of cracking in GaN/AlN superlattices. An alternative material approach to overcome this problem is the use of AlInN alloys. AlInN with an In composition around 17%–18% is lattice matched to GaN and presents a refractive index contrast equivalent to AlGaN with 46% Al content (6% contrast with GaN at 1.55-μm wavelength). Therefore, AlInN is a promising material to form distributed Bragg reflectors and thick waveguide layers [97]. However, lattice-matched AlInN/GaN heterostructures still exhibit an electric field as large as 3 MV/cm, solely generated by the spontaneous polarization discontinuity.

The potential of AlInN/GaN lattice-matched systems for application in ISB technology has been explored [98,99]. However, this material system is not adapted to serve as the active region for telecommunication devices since the conduction-band offset is in the range of ~1 eV [100]. Nevertheless, ISB absorption in the near-IR spectral region has been reported at 2.3–2.9 μm in lattice-matched GaN/AlInN superlattices grown by MOVPE [98] and by MBE [101].

An alternative approach to manage the strain in the structure while retaining access to shorter wavelengths is possible by adding small concentrations of In (below 10%) both in the barrier and in the QW, forming an AlInN/GaInN superlattice [102,103]. This material combination reduces the probability of crack propagation in comparison with GaN/AlN, although it maintains a certain degree of strain. Despite the challenges to precisely control the In mole fraction, room-temperature ISB absorption in the 1.52- to 2.45-μm wavelength range has been theorized [104,105] and was demonstrated in AlInN/GaInN MQWs [102].

Regarding the polar GaN/GaInN system, only theoretical calculations of ISB transition energy have been published so far [106,107].

8.2.5 Quantum Dots

An alternative approach to QW structures for the fabrication of devices is based on optical transitions between bound states in the conduction band of QD superlattices [108,109]. Quantum dot infrared photodetectors (QDIPs) are expected to ultimately outperform QWIPs in terms of low dark current, high photoelectric gain, and sensitivity [110]. Furthermore, under certain conditions intraband bound to continuum transitions in QDs can be nearly independent of the polarization of excitation [111–113].

In the case of III-nitrides, GaN/AlN QD structures can be synthesized by PAMBE through GaN deposition under compressive strain and under N-rich conditions [70,114]. In this situation, 2D growth proceeds normally to create a 2-ML-thick wetting layer. Due to the lattice mismatch between AlN and GaN, further GaN deposition leads to the formation of 3D islands above this 2D wetting layer (Stranski–Krastanov growth mode). These GaN QDs are well-defined hexagonal truncated pyramids with {1-103} facets [115]. The QD size can be tuned by modifying the amount of GaN in the QDs, growth temperature, or growth interruption time after deposition of the QDs (Ostwald ripening). By adjusting the growth conditions, QDs with height (diameter) in the range of 1–1.5 nm (10–40 nm) and density between 10^{11} cm^{-2} and 10^{12} cm^{-2} can be synthesized (see atomic force microscopy image in Figure 8.8a as an example) [116]. To populate the first electronic level, silicon can be incorporated into the QDs without significant perturbation of the QD morphology.

AU: Please specify what k and p refer to.

Andreev et al. [117–119] have calculated the electronic structure of GaN/AlN QDs using the $k \times p$ model and taking the internal electric field into account. These calculations have been complemented by Ranjan et al. [120] through the use of the tight-binding theory and a self-consistent treatment to account for carrier screening of the electric field.

The models show that the polarization-related internal electric field localizes the electrons at the pyramid apex, whereas holes are rather located close to the wetting layer. In addition to the carrier separation along the growth axis, the electric field can provide a strong additional lateral confinement for carriers localized in the dot, which strongly modifies their electronic structure and optical properties [119].

From the experimental viewpoint, Si-doped QD superlattices have been reported to exhibit strong TM-polarized intraband absorption at room temperature, which can be tuned from 0.74 eV (1.68 μm) to 0.90 eV (1.38 μm) as a function of the QD size

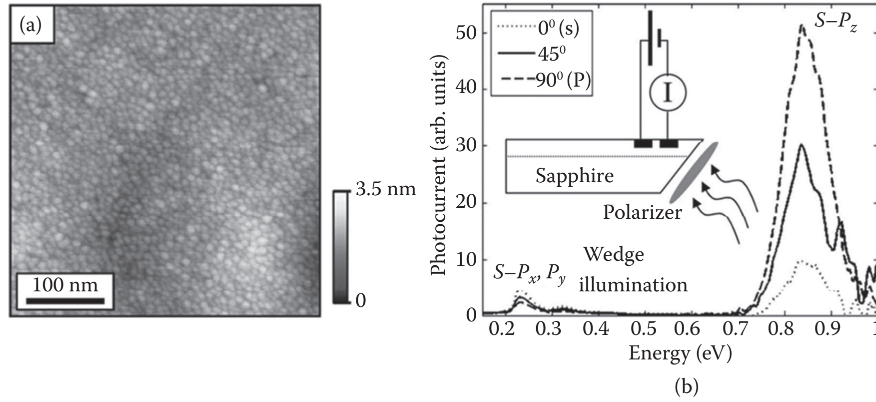

FIGURE 8.8 (a) Atomic force microscopy image of a GaN quantum dot (QD) layer synthesized on AlN by plasma-assisted molecular beam epitaxy (PAMBE), showing a high density (~10^{12} cm^{-3}) of small (height, ~1.3 nm; base diameter, ~11 nm) QDs. (b) Polarization-dependent spectral response (photocurrent) of a GaN/AlN QD stack measured in wedge illumination. The normalized response of both s–p_z in the near infrared (IR) and s–$p_{x,y}$ in the mid-IR; the s–p_z peak is about 10 times larger than the s–$p_{x,y}$ peak. (From Vardi et al., *Phys. Rev. B*, 80(15), 155439, 2009 [122].)

[116,121]. The broadening of the absorption peak can be as small as ~80 meV for the most homogeneous samples. This absorption line is attributed to transitions from the ground state of the conduction band, *s*, to the first excited electronic state confined along the growth axis, p_z. The lateral confinement in the QDs should give rise to additional transitions under TE-polarized excitation. However, taking into account the lateral dimension of the QDs, ~7 nm, the s–$p_{x,y}$ transitions should be masked by the sapphire absorption for $\lambda > 5$ μm. The optical signature associated with s–$p_{x,y}$ was first observed by Vardi et al., who studied near-IR and mid-IR intraband transitions in GaN/AlN QDs using in-plane electronic transport at low temperatures [122], as illustrated in Figure 8.8b. The measured s–$p_{x,y}$ energy separation (0.1–0.3 eV) was significantly larger than the equivalent transition energy in InGaAs\GaAs QDs. Their analysis shows that the appearance of large-energy s–$p_{x,y}$ in GaN\AlN QDs is due to the strong internal electric field in the QDs, which results in stronger confinement of the electrons at the QD top facet.

The homogeneous line width of the s–p_z intraband transition at 1.55 μm in GaN/AlN QDs was assessed by means of nonlinear spectral hole-burning experiments [123]. These measurements demonstrated that electron–electron scattering plays a minor role in the coherence relaxation dynamics, since the homogeneous line width of 15 meV at 5 K does not depend on the incident pump power. This suggests the predominance of other dephasing mechanisms such as spectral diffusion.

TM-polarized IR absorption in the 1.6- to 2-μm wavelength range, attributed to s–p_z intraband transitions, has also been reported in ternary $Al_xGa_{1-x}N$/AlN QDs (x = 0–0.42) measured at room temperature. The s–p_z transition red shifts for increasing Al mole fraction in the QDs as a result of the reduction in band offset, in good agreement with theoretical calculations [124,125].

8.2.6 Nanowire Heterostructures

Using the enhanced quantum-confined properties of QDs, a variety of structures can be created. However, QDs can only be grown under specific strain situations, limiting the degree to which these QD devices can be engineered. Nanowires do not have these limitations and due to the unique strain relaxation mechanisms can provide a much larger array of material pairings, beyond the limitations of planar and QD systems. Nanowire heterostructures in particular offer a unique situation for a variety of devices requiring low-defect-density active regions and large lattice-mismatched materials.

Following these benefits, nanowire heterostructures of Ge-doped GaN/AlN have been grown by PAMBE, with the result illustrated in the TEM images in Figure 8.9a and b [126]. The nanowire disk sizes were varied in the 2- to 8-nm range, and the doping level was varied over two orders of magnitude. The ISB energies were measured via Fourier transform infrared (FTIR), and Figure 8.9c displays the results in a series of samples with different doping levels. The TM-polarized absorption is assigned to the s–p_z intraband transition in the Ge-doped GaN/AlN nanodisks. The s–p_z absorption line experiences a blue shift with increasing Ge concentration and a red shift with increasing nanodisk thickness. Theoretical calculations in Figure 8.9d show that the intraband transitions are strongly blue shifted due to many-body effects, that is, the exchange interaction and depolarization shift.

8.2.7 Alternative Crystallographic Orientations

The presence of internal electric field in polar materials increases the design complexity of ISB devices. A simple approach to circumvent this problem consists of using nonpolar crystallographic orientations like *m*-plane {1-100} or *a*-plane {11-20} [127]. However, epitaxy for these orientations is an arduous task, due to strong anisotropy of surface properties, resulting in a high density of crystalline defects. An alternative approach is the growth on semipolar planes [127], which are those (*hkil*) planes with at least two nonzero *h*, *k*, or *i* Miller indices and a nonzero *l* Miller index. Semipolar planes allow considerable reduction in the internal electric field [128] while presenting a lower in-plane anisotropy than nonpolar surfaces [129,130].

Regarding nonpolar materials, ISB optical absorption at $\lambda \sim 2.1$ μm with FWHM = 120 meV has been reported in Si-doped 1.75-nm-thick GaN QWs with 5.1-nm-thick AlN barriers grown by PAMBE on *r*-plane sapphire and displaying pure *a*-plane orientation [131]. Furthermore, ISB absorption has been shown at THz frequencies in *m*-plane GaN/AlGaN MQW structures [132]. The ISB energy was tuned in the 15.6- to 26.1-meV range by changing the well sizes and alloy compositions of the barriers.

Near-IR ISB absorption has also been reported on semipolar (11-22)-oriented GaN/AlN MQWs grown by PAMBE [130,133], as illustrated in Figure 8.10a. In comparison with polar QWs, semipolar structures exhibit quasi-square potential band profiles with symmetric wave functions, due to the reduced electric field in the range of 0.5–0.6

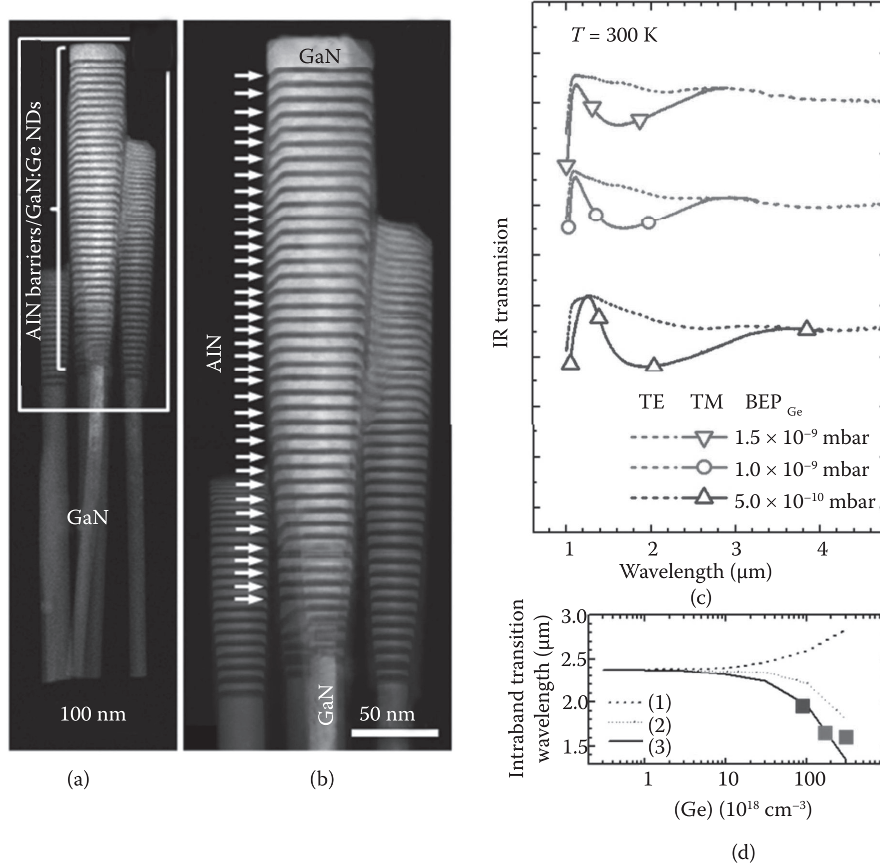

FIGURE 8.9 (a) Annular dark field transmission electron microscopy image of a set of GaN nanowires from a sample containing 40 periods of AlN/GaN nanodisks. (b) Zoom-in of the squared area in (a). (c) Room-temperature infrared transmission spectra for transverse-electric (TE)- (dashed) and transverse-magnetic (TM)-polarized (solid) light measured for Ge-doped GaN/AlN (4 nm/4 nm) heterostructured nanowires with different doping levels in the GaN nanodisks (NDs). The spectra are vertically shifted for clarity. (d) Variation of the intraband transition wavelength as a function of the estimated Ge concentration. Dots are experimental values from (c); the dashed line labeled (1) is a one-dimensional calculation of the intraband transition accounting for the screening of the internal electric field; the dotted line (2) incorporates corrections associated with both screening and exchange interaction; the solid line (3) accounts for screening, exchange interaction, and depolarization shift. (From Beeler et al., *Nano Lett.*, 14(3), 1665–1673, 2014 [126].)

MV/cm in the QWs. The evolution of e_2–e_1 ISB transition energy with QW thickness is represented in Figure 8.10b, where symbols correspond to experimental measurements obtained from identical polar and semipolar samples consisting of 40 periods of GaN/AlN with 3-nm-thick AlN barriers. The absorption FWHM (~ 80–110 meV [130,133]) is comparable to the one measured in polar structures [16,28]. However, in

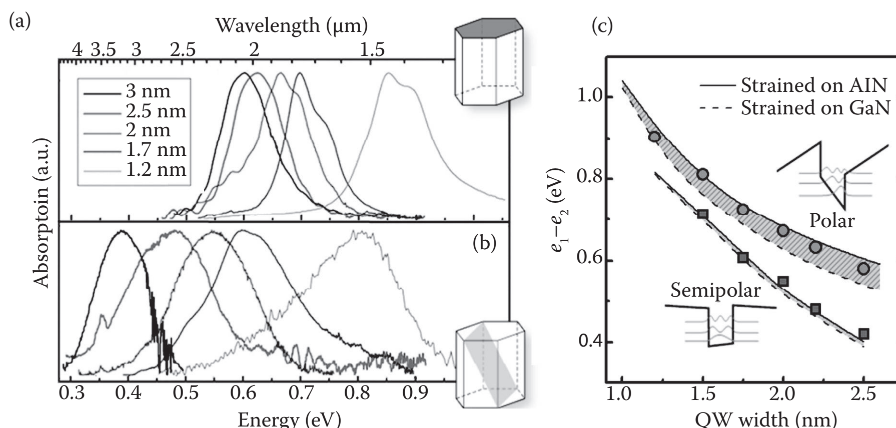

FIGURE 8.10 Intersubband (ISB) absorption spectra for (a) polar and (b) semipolar GaN/AlN quantum wells (QWs) with different well thicknesses. (c) Calculated and measured ISB absorption energy versus well thickness. (From Machhadani et al., *J. Appl. Phys.*, 113(14), 143109, 2013 [133].)

semipolar structures the reduction in internal electric field results in a red shift of the ISB energy. Also, the spectral shape of semipolar absorption is Gaussian, in contrast to the Lorentzian shape described for polar GaN/AlN QWs. This is due to the spectral dispersion generated by thickness fluctuations and presence of stacking faults in semipolar material, both inducing carrier localization in the range of a few millielectron volts, much smaller than the FWHM of the ISB absorption line.

8.2.8 Cubic III-Nitrides

Another approach to eliminate the internal electrical field in III-nitride heterostructures is the use of III-nitride semiconductors crystallized in the zinc-blend crystallographic phase. The LO-phonon energy in cubic GaN is almost the same as in wurtzite GaN (92.7 meV [134]), but the effective mass is significantly smaller (m^* = 0.11–0.17 [135,136]) than in wurtzite GaN (m^* = 0.2), which should result in higher gain and lower threshold current in QCLs. It has also been theorized that these systems could be used to create QD photodetectors with high gain and sensitivity [137].

The cubic orientation can be selected by PAMBE using 3C–SiC substrates. However, due to their thermodynamically unstable nature cubic films present low structural quality with a high density of stacking faults. ISB absorption in the 1.40- to 4.0-μm spectral range has been reported in cubic GaN/AlN MQWs [138–140], in agreement with theoretical calculations assuming a conduction-band offset of 1.2 eV and an effective mass of m^* = 0.11. ISB THz absorption at 4.7 THz has also been observed in cubic GaN/$Al_{0.05}Ga_{0.95}N$ (12 nm/15 nm) QWs [139,140]. Using slightly different material properties (a conduction-band offset of 1.6 eV and an effective mass m^* = 0.11), Radosavljevic et al. have theorized that MIR ISB absorption could be tuned by applying a bias perpendicular to the layers [141].

AU: Please specify what MIR refers to.

8.3 ALL-OPTICAL SWITCHES

The increasing bandwidth demand in optical communication networks impels the development of all-optical devices, particularly targeting the 1.55-μm transmission band of optical fibers. In particular, there is a need for all-optical switches capable of sustaining high repetition rates (sub-picosecond response time) with low switching energy and high modulations depths. These specifications led researchers to consider the use of resonant nonlinearities [142], to exploit phenomena like nonlinear absorption, self- and cross-phase modulation, self- and cross-gain modulation, and four-wave mixing. In this case, switching can be achieved through absorption saturation by an intense control pulse, as originally demonstrated in GaAs-based structures [143]. Using GaN/AlGaN, the switching is achieved by ISB absorption bleaching. Thanks to the ultrafast ISB recovery time (in the 140- to 400-fs range [37,144–148]) associated with the strong interaction of electrons with LO phonons, GaN/AlN QWs or QDs have been proposed as the active medium for all-optical switches (saturable absorbers) operating at terabit-per-second data rates and at telecommunication wavelengths.

The use of GaN/AlGaN QWs for all-optical modulators at telecommunication wavelengths was first proposed by Suzuki et al. [17,149]. Since then, all-optical switches at ~1.55 μm with sub-picosecond commutation times have been demonstrated by several groups [31,56,146,147,150–153]. In general, these devices consist of GaN/AlN MQWs embedded in a ridge waveguide. In such structures, a critical parameter to reduce transmission losses is the reduction of edge-type dislocations. These defects introduce acceptor centers where electrons can be captured and therefore can effectively act as a wire-grid polarizer, which leads to selective attenuation of the TM-polarized signal [154]. Control switching energies of 38 pJ for 10-dB modulation depth [151] and 25 pJ for 5-dB contrast [153] have been demonstrated using a waveguide with an AlN cladding below the active GaN/AlN QWs and GaN or Si_xN_y as the upper cladding layer, respectively. Theoretical calculations predict a reduction of the switching energy by a factor of 30 by replacing the GaN/AlN QWs with properly designed AlN/GaN/AlGaN-coupled QWs [155].

From the material viewpoint, the parameter responsible for absorption saturation is the optical third-order susceptibility, $\chi^{(3)}$. Comparative studies using the forward degenerate four-wave mixing technique in a boxcars configuration point to an increase of $\chi^{(3)}$ by a factor of five in QDs compared to QWs [156]. From the experimental viewpoint, the intraband absorption saturation of GaN/AlN QDs was probed by Nevou et al. [31], obtaining values in the range of 15–137 MW/cm^2 (0.03–0.27 pJ/μm^2). In spite of the large signal variation (a consequence of the focusing uncertainty in the sample), even the upper estimate of the saturation intensity for QDs is smaller than the corresponding value for GaN/AlN QWs (9.46 W/μm^2 [151]). Based on these results, Monteagudo-Lerma et al. made a comparison of the performance as saturable absorbers of 3 periods of GaN/AlN QWs and QDs inserted in a GaN-on-AlN waveguide structure [157]. In the case of 5-μm-wide QW-based waveguides, a 10-dB change in transmittance was achieved for input energies of ~24 pJ with 150-fs pulses. This value was improved by almost a factor of two by the replacement of QW by QDs as active elements. The reduction of the waveguide width to 2 μm (monomode waveguide) resulted in a further decrease in the required control pulse energy to ~8 pJ for 10-dB modulation (Figure 8.11).

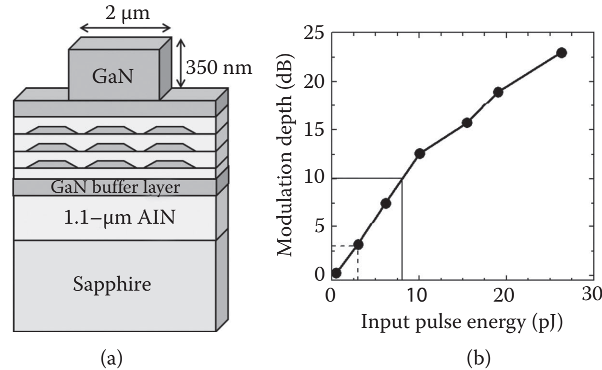

FIGURE 8.11 Schematic description of a quantum dot (QD)-based AlN/GaN all-optical switch in a ridge-waveguide configuration. Transmittance increase versus control pulse energy for transverse-magnetic (TM)-polarized light measured in a 1.5-mm-long 2-μm-wide QD-based waveguide. (Data from Monteagudo-Lerma et al., *Opt. Express*, 21(23), 27578, 2013 [157])

8.4 ELECTRO-OPTICAL MODULATORS

Electro-optical amplitude and phase modulators allow tuning the amplitude, phase, and/or polarization state of an optical beam as a function of the control voltage. State-of-the-art technologies in this field include modulators based on the quantum-confined Stark effect of interband transitions in InGaAsP QWs [158] and on the electro-optical effect in materials like $LiNbO_3$ within a Mach-Zehnder configuration [159]. These devices present several drawbacks, such as low saturation power and positive chirp in the former case and the need for high driving voltage and larger size in the latter case. Achieving a significant improvement in device performance requires a change in technological approach. Exploiting ISB transitions in QWs has been proposed as a means to reduce the driving voltage and increase the bandwidth [160–162]. Moreover, the ISB transitional oscillator strength is higher in comparison to interband transitions and should allow for enhanced miniaturization of the devices.

The first electro-absorption ISB modulation experiments on AlN/GaN QWs were based on the electrical depletion of a 5-period AlN/GaN (1.5 nm/1.5 nm) MQW structure grown on a thick GaN buffer [163]. The absorption spectrum of such a sample presents two distinct peaks related to ISB transitions in both the QWs and the 2D electron gas located at the interface of the lowest AlN barrier and the underlying GaN buffer. The ratio of these two absorption peaks can be adjusted by applying an external field, which modifies the charge distribution.

To increase the modulation depth, the interaction of light with the active medium should be enhanced, which can be achieved with a waveguide geometry [19]. Through the use of a 1-μm-thick $A_{l0.5}Ga_{0.5}N$ waveguiding layer on AlN, and with three active GaN/AlN QWs operating at $\lambda = 1.55$ μm, a modulation depth of 13.5 dB was observed for a –9 V/+7 V voltage swing (10 dB for a 5-V voltage swing).

The intrinsic speed limit can be greatly improved by emptying active QWs into a local reservoir, instead of transferring carriers over the whole active region. This is the principle of the coupled-QW modulator: The electro-modulation originates from electron tunneling between a wide well (reservoir) and a narrow well separated by an ultrathin (~1-nm) AlN barrier. Experiments on GaN QW coupling via AlN [93] or AlGaN [94] barriers have set the basis for the demonstration of room-temperature ISB electro-modulated absorption at telecommunication wavelengths in GaN/AlN-coupled QWs with AlGaN contact layers [164–166]. Such devices displayed a $BW_{-3\,\mathrm{dB}}$ cutoff frequency is limited by the resistance × capacitance (*RC*) time constant to 3 GHz for 15 × 15 μm^2 mesas, but it could be further improved by reducing the access resistance of the AlGaN contact layers. According to Hölmstrom, the high-speed performance of such modulators will ultimately be determined by the ISB absorption line width Γ, since their capacitance depends on the line width as $C \sim \Gamma^3$ [160,161].

AU: Please confirm if "*BW*" refers to bandwidth and can be made roman.

All the aforementioned electro-optical modulators rely on light amplitude modulation via ISB absorption. Based on Kramers–Kronig relations, the ISB absorption should also translate into a variation of the refractive index at wavelengths close to the transition, which can be used for phase modulation. This concept was experimentally verified at mid-IR (~10 μm) wavelengths using the Stark shift of ISB transitions in GaAs/AlGaAs step QWs [167]. The strongly nonlinear susceptibility observed in GaN/AlN QWs [156,168], which might be even enhanced in three-layer QW designs [169], has led to the first theoretical proposals of all-optical cross-phase modulators [95].

Using a depletion modulator consisting of three GaN/AlN QWs inserted in an $Al_{0.5}Ga_{0.5}N$/AlN ridge waveguide on sapphire, Lupu et al. [170] reported a variation of the refractive index around ~1.5 μm deduced from the shift of the beating interference maxima for different order modes. The change in refractive index was derived to be $\Delta n = -5 \times 10^{-3}$ as the population was changed from complete depletion to full population of the QWs. This result is in close agreement with the observation of a refractive index variation from -5×10^{-3} to 6×10^{-3} in 100-period Si-doped GaN/AlN (1.5 nm/3 nm) MQWs using a free-space Mach-Zehnder interferometer configuration [171]. The values of Δn are comparable to those obtained at the same wavelength in phase modulators based on interband transitions in InGaAsP/InP QWs using the quantum-confined Stark effect [172], and they are one order of magnitude higher than the index variation obtained in silicon [173]. These results open the way for the realization of ISB Mach-Zehnder interferometer phase modulators in the optical communication wavelength range.

8.5 INFRARED PHOTODETECTORS

8.5.1 Quantum Well/Quantum Dot Infrared Photodetectors

The main motivation for the development of III-nitride QWIPs is their potential application in optical communications, thanks to the possibility to tune ISB transitions in the 1.3- to 1.55-μm range with sub-picosecond carrier relaxation times. Photoconductive QWIPs based on hexagonal [174,175] and cubic [176] Si-doped

GaN/AlN QW superlattices have been reported; however, these devices operate at cryogenic temperatures and exhibit a non-explained photovoltaic effect. Lateral QDIPs have also been fabricated by depositing planar contacts on samples consisting of 20 periods of Si-doped GaN/AlN QDs, first operating at liquid nitrogen temperature [177] and then at room temperature [122,178]. These devices exhibit photocurrent for TM-polarized excitation in the 1.4- to 1.9-μm spectral range, which follows the intraband s–p_z selections rules. At low temperatures (T = 10 K), mid-IR photoresponse to TE-polarized light is also observed and attributed to s–$p_{x,y}$ transitions. The appearance of photocurrent due to these bound to bound transitions is attributed to conductivity via lateral hopping [122]. Further studies have shown that deep levels in the AlN barriers may also contribute to the photocurrent, giving rise to negative photoconductivity effects [179].

In spite of these early demonstrations, photoconductive devices keep presenting a low yield due to the large dark current originating from the high density of structural defects in heteroepitaxial III-nitrides, particularly in highly mismatched GaN/AlN devices targeting near-IR wavelengths. An alternative to bypass the leakage problem consists of exploiting the device's photovoltaic response, where zero-bias operation guarantees a minimum dark current. Photoconductive QWIPs have already displayed a photovoltaic response [180], which was less sensitive to defects [175], in agreement with observations in photovoltaic versus photoconductive interband detectors [181].

The photovoltaic operation of GaN/AlN QWIPs at telecommunication wavelengths and at room temperature was first studied in detail by Hofstetter et al. [29,51,182–184], as illustrated in Figure 8.12. The working principle of these photovoltaic ISB detectors is based on resonant optical rectification processes [29,185]. In a GaN/AlN superlattice, due to the asymmetric potential profile in QWs, the excitation of an electron into the upper quantized level is accompanied

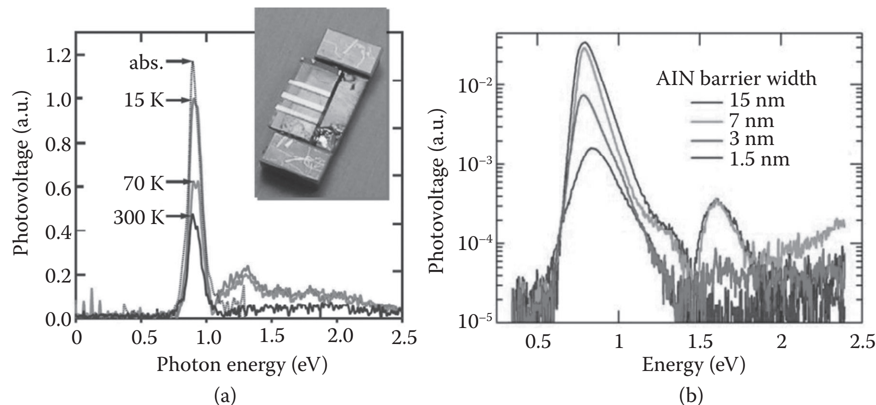

FIGURE 8.12 (a) Photovoltage measurements on a sample consisting of a 1.5-nm GaN/1.5-nm AlN superlattice with a 50-nm-thick AlN, measured in transverse-magnetic polarization at 15, 70, and 300 K. Note the good agreement with the absorbance spectra shown as a dotted line. Inset: photograph of the mounted device [182]. (b) The measured spectral photovoltage response as a function of barrier thickness. The enhancement for larger barriers is associated with the higher internal electric field in the wells. (From Hofstetter, *Appl. Phys. Lett.*, 91(13), 131115, 2007 [29].)

by a charge displacement in the growth direction, so that an electrical dipole moment is created. For a high electron density and many QWs, these microscopic dipole moments add up to a macroscopic polarization of the crystal, which can be detected as an external photovoltage. This interpretation is consistent with the enhancement of the photovoltaic response observed in structures with larger barriers, where electron tunneling is not possible (Figure 8.12b). A strong performance enhancement (responsivity increase by a factor of 60) of these detectors has been achieved by using QDs instead of QWs in the active region [186]. The improvement is attributed to the longer electron lifetime in the upper QD states and the increased lateral electron displacement.

An interesting application of GaN-based photovoltaic ISB photodetectors is the so- called multispectral detectors, which operate in various wavelength ranges. Hofstetter et al. [187] have combined optical interband and ISB transitions with a monolithic integration of a photoconductive ultraviolet (UV) interband (solar-blind) detector based on an AlGaN thin film and a photovoltaic near-IR ISB detector based on an AlN/GaN superlattice, as illustrated in Figure 8.13. The two detectors exhibit spectrally narrow responsivity curves, thus enlarging the UV to visible rejection ratio in the case of the UV device and improving the noise behavior in the case of the IR detector at room temperature.

In the far-IR spectral region, the reduction of lattice mismatch in the structure makes it more accessible to fabricate photoconductive QWIPs. The first demonstration of a nitride-based THz ISB photodetector is reported by Sudradjat et al. [188] using a bound to quasi-bound configuration following the step-QW design [87], so that the first excited subband can be positioned at any desired energy relative to the top of the barriers by changing the QW thickness (Figure 8.14a). The fabricated devices present a photocurrent spectrum centered at 23-μm wavelength (13-THz frequency), well resolved from low temperature (T = 20 K in Figure 8.14b) up to T = 50 K, with a responsivity of ~7 mA/W [188].

More recently, Pesach et al. demonstrated InGaN/(Al)GaN QWIPs fabricated on freestanding nonpolar *m*-plane GaN substrates [189]. Devices consisting of 2.5-nm $In_{0.095}Ga_{0.905}N$/56.2 nm $Al_{0.07}Ga_{0.93}N$ and 3-nm $In_{0.1}Ga_{0.9}N$/50 nm GaN superlattices displayed photocurrent peaks at 7.5 μm and 9.3 μm, respectively, when characterized at a low temperature (14 K).

8.5.2 Quantum Cascade Detectors

Quantum cascade detectors (QCDs) are photovoltaic devices consisting of several periods of an active QW coupled to a short-period superlattice, which serves as extractor [190,191]. Under illumination, electrons from the ground state, e_1, are excited to the upper state of the active QW, e_2, and then transferred to the extractor region where they experience multiple relaxations toward the next active QW. This results in a macroscopic photovoltage in an open circuit configuration. A major advantage is that their dark current is extremely low and the capacitance can be reduced by increasing the number of periods, which enables high frequency response.

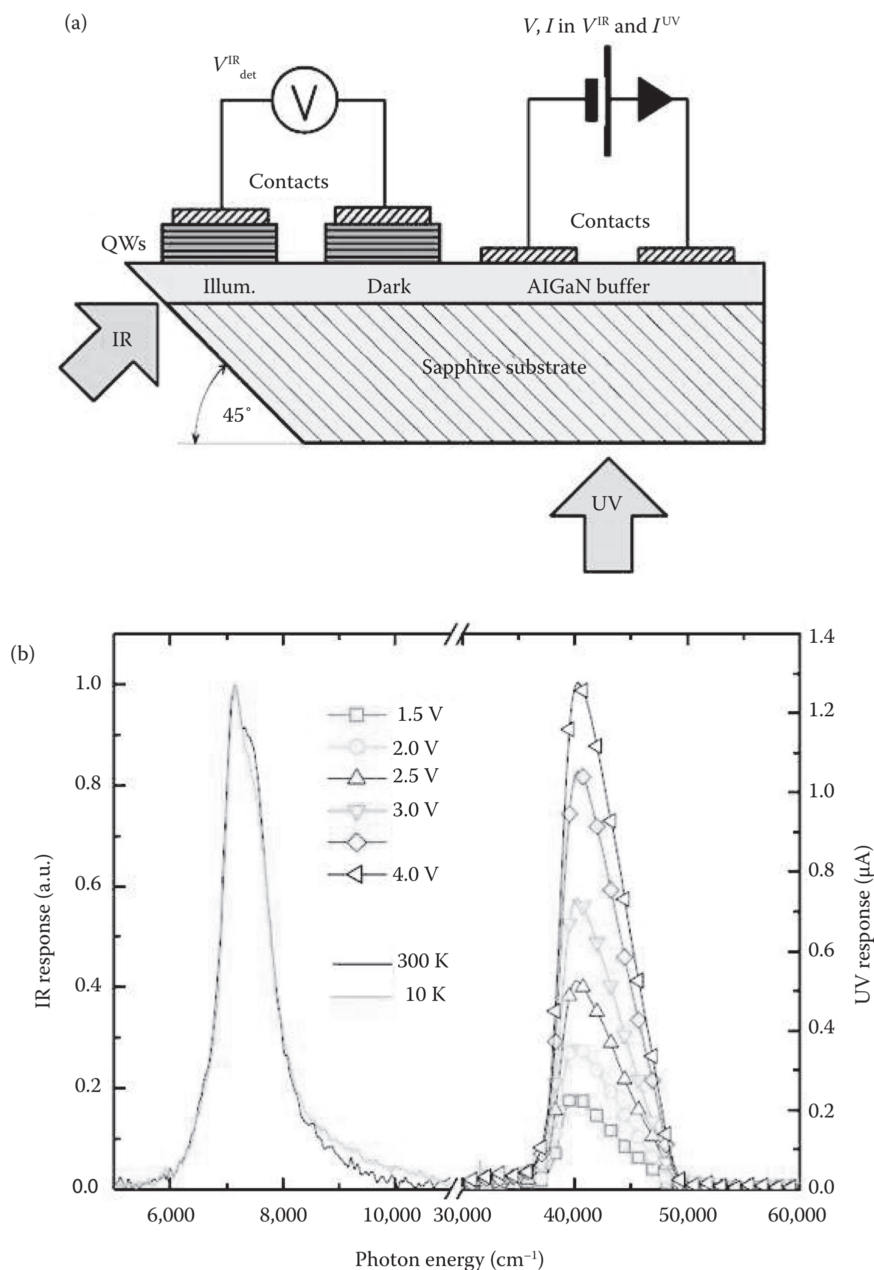

FIGURE 8.13 (a) Schematic cross section through the sample showing the relative positions of the ultraviolet (UV) and the infrared (IR) detectors. Quantum wells (QWs) are used as the detection layer for the IR, whereas AlGaN buffer is the detection layer for the UV radiation. (b) Measured spectral responsivity curves for the UV (1.5–4.0 V in steps of 0.5 V at 300 K) and the IR detector (10 and 300 K). (From Hofstetter et al., *Electron. Lett.*, 44(16), 986, 2008 [187].)

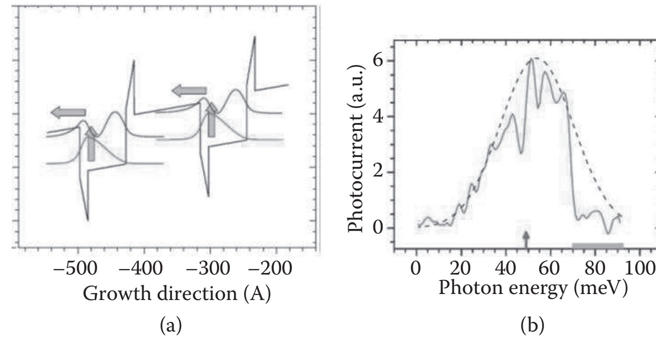

FIGURE 8.14 (a) Conduction band profile of a far-infrared (IR) quantum well infrared photodetector (QWIP) under bias. Each repeat unit consists of an $Al_{0.16}Ga_{0.84}N$/GaN/$Al_{0.08}Ga_{0.92}N$ step quantum well (QW). The squared envelope functions of the ground state and first excited state of each QW are also shown, referenced to their respective energy levels. The vertical and horizontal arrows indicate, respectively, photon absorption and photoelectron escape into the continuum of unbound states over the barriers. (b) Photocurrent spectrum of a double-step-QW AlGaN THz QWIP measured at $T = 20$ K under 0.8-V bias (solid line) and Gaussian fit (dashed line). The gray band near the horizontal axis indicates the Restrahlen band of GaN. The vertical arrow marks the calculated transition energy. (From Sudradjat et al., *Appl. Phys. Lett.*, 100(24), 241113, 2012 [188].)

GaN/AlGaN QCDs operating in the near-IR have been reported [192,193], with their structure illustrated in Figure 8.15. These devices take advantage of the polarization-induced internal electric field to design an efficient AlGaN/AlN (or GaN/AlGaN) electron extractor where the energy levels are separated by approximately the LO-phonon energy (~90 meV), forming a phonon ladder. The peak responsivity of these GaN/AlGaN QCDs at room temperature was ~10 mA/W [192,194]. Detectors containing 40 periods of active region with a size of 17 × 17 μm^2 exhibit an *RC*-limited $BW_{-3\text{ dB}}$ cutoff frequency at 19.7 GHz [195]. However, pump and probe measurements of these devices (Figure 8.15d) pointed to an ISB scattering time in the active QW of 0.1 ps and a transit time through the extractor of 1 ps [196]. With these data, the intrinsic frequency bandwidth is expected to be above 160 GHz, significantly higher than the theoretical predictions by Gryshchenko et al. [197]. Sakr et al. have shown improved performance by illuminating the side facet of the QCDs (illumination perpendicular to the growth axis), and by reducing the top contact resistance as well as the contact layer resistivity. They reached a responsivity of at least 9.5 ± 2 mA/W for 10 × 10 μm^2 devices at 1.5-μm peak detection wavelength at room temperature with a $BW_{-3\text{ dB}}$ frequency response of ~40 GHz [194].

Based on the presence of the internal field in III-nitride QWs, symmetry breaking of the potential permits ISB transitions not only between the ground electronic state and the first excited state, $e_1 \rightarrow e_2$, but also between e_1 and the second excited state e_3, a transition forbidden in symmetric QWs [16]. This feature was exploited for the fabrication of a two-color GaN-based QCD operating at 1.7 and 1 μm at room temperature [198].

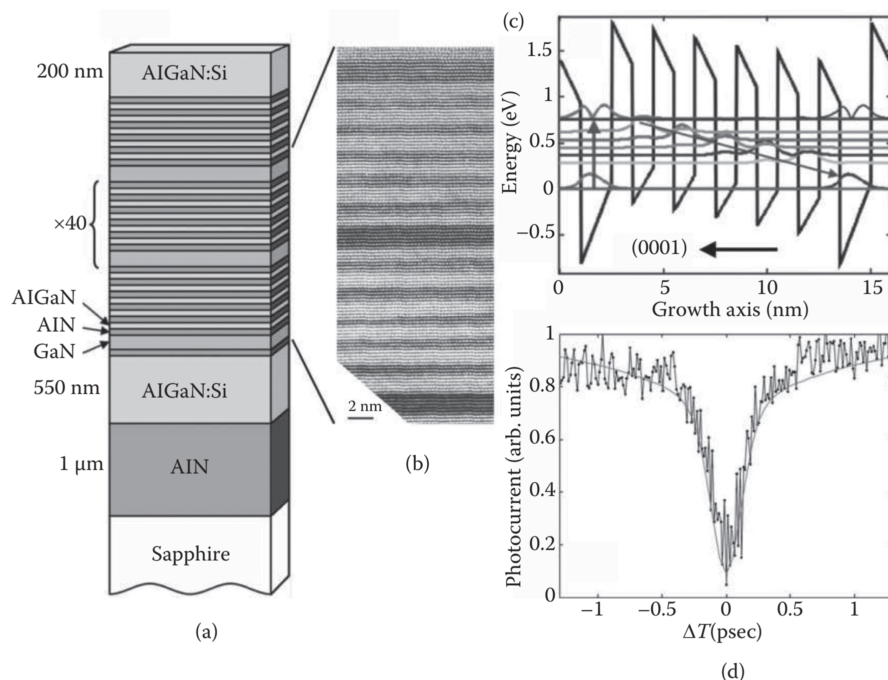

FIGURE 8.15 (a) Schematic description of a GaN/AlN/AlGaN quantum cascade detector (QCD). (b) High-resolution transmission electron microscopy image of a period of the structure (active GaN quantum well followed by 5-period AlGaN/AlN extractor), viewed along the <11-20> axis [192]. (c) Band diagram and energy levels in one stage of the structure [192]. (d) QCD photocurrent as a function of pump–probe delay at room temperature under zero bias conditions. Full line: simulation fit based on rate equations and phonon scattering theory (From Vardi et al., *Appl. Phys. Lett.*, 99(20), 202111, 2011 [196].)

Finally, a simplified QCD design replacing the extractor superlattice by an AlGaN layer has been proposed [199]. The thickness and composition of the extractor alloy is chosen so that the energy separation between the ground state of the extractor and the ground state of the active QW is close to the LO-phonon energy. An alloy-extractor device presenting peak photovoltaic response at 1.9 μm has been demonstrated [199]. The photoresponse of such detectors at normal incidence can be increased by a factor of 30 by using a 2D nanohole Ti/Au array integrated on top of the detector [200].

8.6 TOWARD THE QUANTUM CASCADE LASER

8.6.1 Light Emission in Superlattices

ISB luminescence is an inefficient process due to the competition with nonradiative electron relaxation via interactions with LO phonons (sub picosecond), or electron–electron interactions and impurity scattering (tens of picoseconds). However, this

does not hinder the realization of QCLs: In the population inversion regime, short radiative lifetime and high stimulated gain can be achieved thanks to the strong ISB transitional oscillator strength.

Despite the inefficiency of the process, room-temperature ISB luminescence in the 2- to 2.3-μm spectral range has been observed in GaN/AlN MQWs under optical pumping [201–203]. The QWs were designed to exhibit three bound states in the conduction band. The emission arises from the e_3–e_2 ISB transition. Photoluminescence excitation spectroscopy shows that the emission is only observed for TM-polarized excitation at wavelengths corresponding to the e_1–e_3 ISB transition. Further research has also provided mid-IR ISB electroluminescence measurements on chirped AlGaN/GaN MQW structures [204]. The emission line was shifted from 115 meV (FWHM = 38 meV) to 180 meV (FWHM = 58 meV) by changing the applied bias from 7 V to 14 V.

Room-temperature intraband emission has also been observed in optically pumped GaN/AlN QDs [205]. The p_z–s intraband luminescence was observed at $\lambda = 1.48$ μm under optical excitation at $\lambda = 1.34$ μm perpendicular to the [0001] growth axis.

The population of the p–z state arises from Raman scattering by GaN A_1 longitudinal optical phonons. Based on the emission spectral shape, we estimate that the homogeneous line width of the s–p_z intraband transition is less than 4 meV.

8.6.2 Quantum Cascade Laser Structures

QCLs rely on transitions between quantized conduction-band states of a suitably designed semiconductor MQW structure [11]. Due to the polarization selection rules associated with ISB transitions, these devices are in-plane emitters, with their electric-field vector perpendicular to the plane of the layers. An electron injected into the *active QWs* first undergoes an ISB lasing transition and is rapidly extracted by a fast nonradiative transition, which maintains the population inversion. Then, the electron tunnels through the *injector region* toward the upper level of the next active QWs. By using several tens or even hundreds of periods of active region + injector in a series (a cascade), higher optical gains and multiple photons per electron are obtained. These complex structures require precise structure control and excellent homogeneity of the material, both in plane and along the multiple periods that compose the active region. Due to the large lattice mismatch and defect structure of the GaN/AlN system, the fabrication of GaN-based QCLs operating in the near-IR does not appear feasible, despite several theoretical proposals [18,206,207] and promising results in terms of waveguide fabrication [208]. However, there is increasing interest and research effort in the fabrication of the first GaN QCL in the far-IR, particularly in the so-called THz domain, spectral region where the lattice mismatch of the structure is reduced and where it should be possible to exploit the large LO phonon of III-nitrides to realize devices operating at room temperature.

Since the first demonstration of a GaAs-based THz QCL in 2001 [209], rapid progress has been made in terms of device performance. To date, QCLs have been demonstrated in the 0.85- to 5-THz range [210], with pulsed operation up to 186 K [211,212] and pulsed output powers of up to 250 mW [213]. The devices have evolved

through different designs including the resonant-phonon, chirped superlattice, bound to continuum, and hybrid designs [211,214]. There are two major processes that cause the degradation of population inversion (and thus gain) in THz QCLs at high temperature: thermal backfilling and thermally activated phonon scattering. Backfilling of the lower radiative state with electrons from the heavily populated injector occurs either by thermal excitation (according to the Boltzmann distribution) or by reabsorption of nonequilibrium LO phonons (the hot-phonon effect) [215]. The other main degradation mechanism is the onset of thermally activated LO-phonon scattering, as electrons in the upper radiative state acquire sufficient in-plane kinetic energy to emit an LO phonon and relax nonradiatively to the lower radiative state. Both of these mechanisms greatly depend on the electron gas temperature, which is 50–100 K higher than the lattice temperature during device operation. The low LO-phonon energy in arsenide compounds constitutes a major bottleneck for operation at higher temperatures. Furthermore, the LO phonon of GaAs systems causes an unobtainable emission gap in lasing systems (Restrahlen band at 8 to 9 THz), which is an intrinsic property of the material system.

GaN has a LO-phonon energy of 92 meV, much higher than the ambient thermal energy. A number of designs for a GaN THz QCL have been proposed [186,216–223], all focusing on the resonant-phonon architecture first theorized in 2003 [214]. Figure 8.16 presents the basic device structure for polar III-nitrides. Later, we summarize the efforts of various groups working on this topic, who have introduced design improvements but keep the same underlying concept.

AU: Please provide section number.

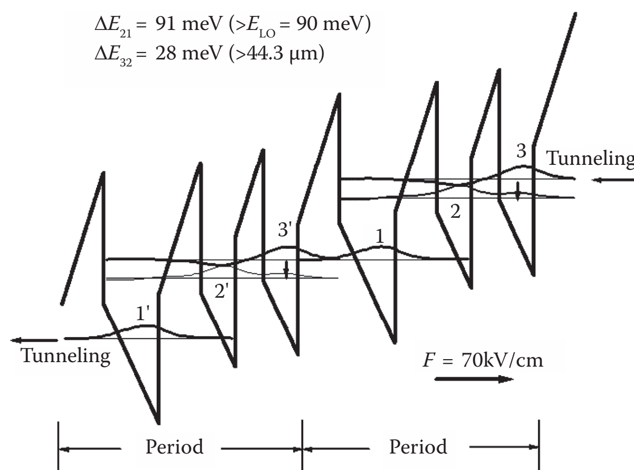

FIGURE 8.16 Band structure, subband energy separations, and envelope wave functions of the active region of the proposed AlGaN THz quantum cascade laser (QCL) structure. Two periods are shown, each with three quantum wells (QWs) with layer thicknesses (in nanometers) 3, 4, 3, 2.5, 2, and 2.5. Wells are underlined, and barriers are plain. The transition from 3-2 is engineered through a coupled QW to be 28 meV, whereas the 2-1 transition is engineered to be on the order of the longitudinal optical phonon (90 meV). With an applied bias of 70 kV/cm, tunneling between states 1 and 3 occurs for the cascade effect and carrier recycling. (From Sun et al., *Superlattice. Microst.*, 37(2), 107–113, 2005 [217].)

Researchers from the University of Leeds, United Kingdom, have engineered one of the first designs for GaN-based QCLs using a fully consistent scattering rate equation model [216] and an energy balance method [224]. Both electron–LO phonon and electron–electron scattering mechanisms are taken into account. They have created a contour plot outlining the wavelengths of emission theorized with different well and barrier thicknesses within a superlattice, after appropriate strain balancing [206]. They have also proposed a 34-μm-wavelength QCL design in both *a* and *c* planes [216].

The group of Paiella and Moustakas at Boston University has proposed a QCL design emitting at 2 THz, designed using a Schrödinger-equation solver based on the effective-mass approximation [219]. They have also performed a rigorous comparison between a GaAs/AlGaAs and GaN/AlGaN THz QCLs emitting at the same wavelength using a microscopic model of carrier dynamics in QCL gain media based on a set of Boltzmann-like equations solved with a Monte Carlo technique [219,225]. Results show that the population inversion within GaN lasers is much less dependent on temperature than conventional GaAs designs. Furthermore, they have theoretically studied methods to create lattice-matched QCL structures using quaternary InAlGaN alloys [226]. From the experimental viewpoint, they have explored tunneling effects in cascade-like superlattices, their temperature dependence, and effect of bias for multiple device architectures [227].

Sun et al. [228] have modeled a QCL structure based on a three-well design that depopulates via the LO phonon and emits at 6.77 THz and have proposed the use of a spoof surface plasmon waveguide instead of a normal surface plasmon waveguide, which should result in an order of magnitude less losses in the guiding structure.

Mirzaei et al. [223] have proposed a dual-wavelength QCL to emit at both 33 and 52 μm with similar behavior of the output optical power for both wavelengths. The design is based on the LO-phonon resonance to extract electrons from the lower radiative levels and incorporates a miniband injector, theorized via rate equation analysis to operate properly up to 265 K.

Chou et al. [222] have modeled GaN-based resonant-phonon THz lasers using a transfer matrix method, paying particular attention to the effect of the strain state [222]. They predict higher THz power in GaN/AlGaN heterostructures compared to heterostructures incorporating In [229].

Yasuda et al. have used the nonequilibrium Green's function to model GaN THz QCL devices, that is, a four-well resonant-phonon InAlGaN/GaN structure on (0001)-oriented GaN [221], and a two-well nonpolar GaN/AlGaN structure [230].

Finally, Terashima and Hirayama (RIKEN, Japan) have presented THz QCL designs based on four-well resonant-phonon GaN/AlGaN structures [220,231,232]. The structures have been synthesized by PAMBE using a "droplet elimination by thermal annealing" technique [233], and they have been processed in a single-metal plasmon waveguide geometry [220,231,234]. Electroluminescence at 1.37 THz has been reported in a first structure [231] both grown on a GaN-on-sapphire template and grown on bulk GaN, and polarization-dependent electroluminescence at 2.82 THz, slightly tunable by changing the driving voltage in the 20- to 21-V range, has been reported using a second design [234] (band diagram and emission shown in Figure 8.17) grown on an AlN-on-sapphire template. More recently, this group has

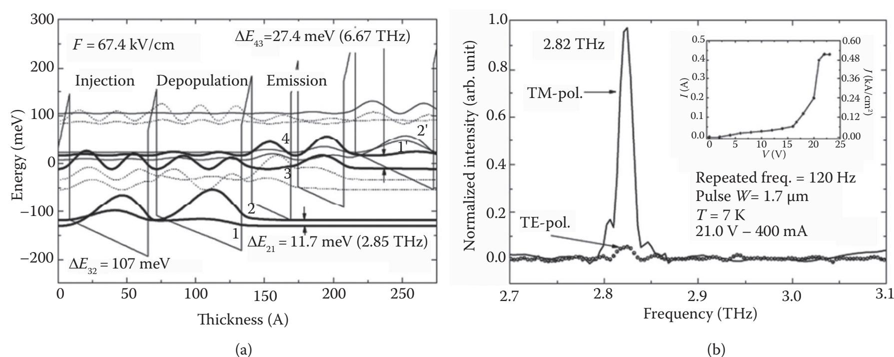

FIGURE 8.17 (a) Conduction band profile and square wave functions for a GaN/AlGaN quantum cascade laser (QCL) structure grown on an AlN template emitting at 6.67 and/or 2.85 THz under a biased external electric field of 67.4 kV/cm. (b) Electroluminescence spectra with each polarization direction for the THz QCL structure grown on an AlN template. The solid and dotted lines are spectra taken under transverse-magnetic- and transverse-electric-polarization directions, respectively. (From Hirayama, H., and Terashima, W., *Proc. SPIE*, 8993, 89930G–89930G–9, 2013 [234].)

AU: Please confirm if the insertion of journal abbreviation and volume number is correct.

reported electroluminescence at 6.97 THz in a double QW structure. In this case, the active region consisted of 200 repeats of 1.5 nm $Al_{0.15}Ga_{0.85}N$/4 nm GaN/1.5 nm $Al_{0.15}Ga_{0.85}N$/6 nm GaN grown on an AlN-on-sapphire template.

8.7 CONCLUSIONS AND PROSPECTS

In this chapter, we have reviewed recent research on III-nitride ISB optoelectronics. III-Nitride heterostructures are excellent candidates for high-speed ISB devices in the near-IR thanks to their large conduction-band offset (~1.8 eV for the GaN/AlN system) and sub-picosecond ISB scattering rates. However, bandgap engineering requires exquisite control of material growth and modeling, which is notoriously difficult in GaN/AlGaN. First prototypes of nitride-based ISB devices are room-temperature multi-Tbit/s all-optical switches operating at 1.5 μm, photovoltaic and photoconductive QWIPs, QDIPs, and ISB electro-optical modulators. Near-IR ISB luminescence from GaN/AlN QWs and QDs has been reported. The concept of quantum cascade applied to III-nitrides has been demonstrated by the development of QCDs operating in the 1.0- to 4.5-μm spectral range.

An emerging field for GaN-based ISB devices is the extension toward the far-IR spectral range, with several theoretical designs of GaN-based THz QCLs being recently reported. At far-IR wavelengths, the large GaN LO-phonon energy (92 meV) becomes a valuable property to achieve ISB operation at relatively high temperatures, and also to cover IR wavelengths that are not accessible by other III-V semiconductors due to Restrahlen absorption. Overall, many different designs of GaN-based QCLs have been presented, all focusing on the resonant-phonon architecture and predicting functionality at high temperatures. All the current research suggests that room-temperature THz QCL devices are feasible, but there are still numerous problems for device engineering, including unavailability of substrates;

K22181_C008.indd 273 6/3/15 10:53 AM

difficult band engineering; weak current transport; as well as the problems from lattice mismatch, doping, and waveguide construction. The papers summarized in this chapter provide solutions toward managing the optical/electronic design and the lattice mismatch and fabrication methodology, but the fabrication of a high-efficiency laser device still remains a challenge.

AU: Please confirm if the changes made to this sentence are correct.

ACKNOWLEDGMENTS

This chapter is supported by the European Union ERC-StG "TeraGaN" (#278428) project.

REFERENCES

1. Kamgar, A., Kneschaurek, P., Dorda, G., and Koch, J., 1974, "Resonance spectroscopy of electronic levels in a surface accumulation layer," *Physical Review Letters*, **32**(22), pp. 1251–1254.
2. Ando, T., Fowler, A. B., and Stern, F., 1982, "Electronic properties of two-dimensional systems," *Reviews of Modern Physics*, **54**(2), pp. 437–672.
3. Esaki, L., and Sakaki, H., 1977, "New photoconductor," *IBM Technical Disclosure Bulletin*, **20**, pp. 2456–2457.
4. Chiu, L. C., Smith, J. S., Margalit, S., Yariv, A., and Cho, A. Y., 1983, "Application of internal photoemission from quantum-well and heterojunction superlattices to infrared photodetectors," *Infrared Physics*, **23**(2), pp. 93–97.
5. Smith, J. S., Chiu, L. C., Margalit, S., Yariv, A., and Cho, A. Y., 1983, "A new infrared detector using electron emission from multiple quantum wells," *Journal of Vacuum Science & Technology B: Microelectronics and Nanometer Structures*, **1**(2), pp. 376–378.
6. Coon, D. D., and Karunasiri, R. P. G., 1984, "New mode of IR detection using quantum wells," *Applied Physics Letters*, **45**(6), pp. 649–651.
7. Coon, D. D., Karunasiri, R. P. G., and Liu, H. C., 1986, "Fast response quantum well photodetectors," *Journal of Applied Physics*, **60**(7), pp. 2636–2638.
8. West, L. C., and Eglash, S. J., 1985, "First observation of an extremely large- dipole infrared transition within the conduction band of a GaAs quantum well," *Applied Physics Letters*, **46**(12), pp. 1156–1158.
9. Levine, B. F., Choi, K. K., Bethea, C. G., Walker, J., and Malik, R. J., 1987, "New 10 μm infrared detector using intersubband absorption in resonant tunneling GaAlAs superlattices," *Applied Physics Letters*, **50**(16), pp. 1092–1094.
10. Levine, B. F., 1993, "Quantum-well infrared photodetectors," *Journal of Applied Physics*, **74**(8), pp. R1–R81.
11. Faist, J., Capasso, F., Sivco, D. L., Sirtori, C., Hutchinson, A. L., and Cho, A. Y., 1994, "Quantum cascade laser," *Science*, **264**(5158), pp. 553–556.
12. Bastard, G., 1988, *Wave Mechanics Applied to Semiconductor Heterostructures*, Les Editions de Physique; Halsted Press, Les Ulis, France; New York, NY.
13. Liu, H. C., and Capasso, F., 2000, *Intersubband Transitions in Quantum Wells: Physics and Device Applications I*, Academic Press, San Diego, CA.
14. Binggeli, N., Ferrara, P., and Baldereschi, A., 2001, "Band-offset trends in nitride heterojunctions," *Physical Review B*, **63**(24), p. 245306.
15. Cociorva, D., Aulbur, W. G., and Wilkins, J. W., 2002, "Quasiparticle calculations of band offsets at AlN–GaN interfaces," *Solid State Communications*, **124**(1–2), pp. 63–66.

16. Tchernycheva, M., Nevou, L., Doyennette, L., Julien, F., Warde, E., Guillot, F., Monroy, E., Bellet-Amalric, E., Remmele, T., and Albrecht, M., 2006, "Systematic experimental and theoretical investigation of intersubband absorption in GaN/AlN quantum wells," *Physical Review B*, **73**(12), p. 125347.
17. Suzuki, N., and Iizuka, N., 1997, "Feasibility study on ultrafast nonlinear optical properties of 1.55-μm intersubband transition in AlGaN/GaN quantum wells," *Japanese Journal of Applied Physics*, **36**(Part 2, No. 8A), pp. L1006–L1008.
18. Hofstetter, D., Baumann, E., Giorgetta, F. R., Théron, R., Wu, H., Schaff, W. J., Dawlaty, J., George, P. A., Eastman, L. F., Rana, F., Kandaswamy, P. K., Guillot, F., and Monroy, E., 2010, "Intersubband transition-based processes and devices in AlN/GaN-based heterostructures," *Proceedings of the IEEE*, **98**(7), pp. 1234–1248.
19. Machhadani, H., Kandaswamy, P., Sakr, S., Vardi, A., Wirtmüller, A., Nevou, L., Guillot, F., Pozzovivo, G., Tchernycheva, M., Lupu, A., Vivien, L., Crozat, P., Warde, E., Bougerol, C., Schacham, S., Strasser, G., Bahir, G., Monroy, E., and Julien, F. H., 2009, "GaN/AlGaN intersubband optoelectronic devices," *New Journal of Physics*, **11**(12), p. 125023.
20. Beeler, M., Trichas, E., and Monroy, E., 2013, "III-nitride semiconductors for intersubband optoelectronics: A review," *Semiconductor Science and Technology*, **28**(7), p. 074022.
21. Hao, M., Mahanty, S., Qhalid Fareed, R. S., Tottori, S., Nishino, K., and Sakai, S., 1999, "Infrared properties of bulk GaN," *Applied Physics Letters*, **74**(19), pp. 2788–2790.
22. Yang, J., Brown, G. J., Dutta, M., and Stroscio, M. A., 2005, "Photon absorption in the Restrahlen band of thin films of GaN and AlN: Two phonon effects," *Journal of Applied Physics*, **98**(4), p. 043517.
23. Welna, M., Kudrawiec, R., Motyka, M., Kucharski, R., Zając, M., Rudziński, M., Misiewicz, J., Doradziński, R., and Dwiliński, R., 2012, "Transparency of GaN substrates in the mid-infrared spectral range," *Crystal Research and Technology*, **47**(3), pp. 347–350.
24. Kandaswamy, P. K., Machhadani, H., Bougerol, C., Sakr, S., Tchernycheva, M., Julien, F. H., and Monroy, E., 2009, "Midinfrared intersubband absorption in GaN/AlGaN superlattices on Si (111) templates," *Applied Physics Letters*, **95**(14), p. 141911.
25. Kandaswamy, P. K., Machhadani, H., Kotsar, Y., Sakr, S., Das, A., Tchernycheva, M., Rapenne, L., Sarigiannidou, E., Julien, F. H., and Monroy, E., 2010, "Effect of doping on the mid-infrared intersubband absorption in GaN/AlGaN superlattices grown on Si (111) templates," *Applied Physics Letters*, **96**(14), p. 141903.
26. Bernardini, F., Fiorentini, V., and Vanderbilt, D., 1997, "Spontaneous polarization and piezoelectric constants of III-V nitrides," *Physical Review B*, **56**(16), pp. R10024–R10027.
27. Birner, S., Zibold, T., Andlauer, T., Kubis, T., Sabathil, M., Trellakis, A., and Vogl, P., 2007, "nextnano: General purpose 3-D simulations," *IEEE Transactions on Electron Devices*, **54**(9), pp. 2137–2142.
28. Kandaswamy, P. K., Guillot, F., Bellet-Amalric, E., Monroy, E., Nevou, L., Tchernycheva, M., Michon, A., Julien, F. H., Baumann, E., Giorgetta, F. R., Hofstetter, D., Remmele, T., Albrecht, M., Birner, S., and Dang, L. S., 2008, "GaN/AlN short-period superlattices for intersubband optoelectronics: A systematic study of their epitaxial growth, design, and performance," *Journal of Applied Physics*, **104**(9), p. 093501.
29. Hofstetter, D., Baumann, E., Giorgetta, F. R., Guillot, F., Leconte, S., and Monroy, E., 2007, "Optically nonlinear effects in intersubband transitions of GaN/AlN-based superlattice structures," *Applied Physics Letters*, **91**(13), p. 131115.
30. Nevou, L., Tchernycheva, M., Julien, F., Raybaut, M., Godard, A., Rosencher, E., Guillot, F., and Monroy, E., 2006, "Intersubband resonant enhancement of second-harmonic generation in GaN/AlN quantum wells," *Applied Physics Letters*, **89**(15), p. 151101.

31. Nevou, L., Mangeney, J., Tchernycheva, M., Julien, F. H., Guillot, F., and Monroy, E., 2009, "Ultrafast relaxation and optical saturation of intraband absorption of GaN/AlN quantum dots," *Applied Physics Letters*, **94**(13), p. 132104.
32. Sarigiannidou, E., Monroy, E., Gogneau, N., Radtke, G., Bayle-Guillemaud, P., Bellet-Amalric, E., Daudin, B., and Rouvière, J. L., 2006, "Comparison of the structural quality in Ga-face and N-face polarity GaN/AlN multiple-quantum-well structures," *Semiconductor Science and Technology*, **21**(5), pp. 612–618.
33. Gmachl, C., Ng, H. M., George Chu, S.-N., and Cho, A. Y., 2000, "Intersubband absorption at λ ~1.55μm in well- and modulation-doped GaN/AlGaN multiple quantum wells with superlattice barriers," *Applied Physics Letters*, **77**(23), pp. 3722–3724.
34. Gmachl, C., Ng, H. M., and Cho, A. Y., 2001, "Intersubband absorption in degenerately doped GaN/Al[sub x]Ga[sub 1−x]N coupled double quantum wells," *Applied Physics Letters*, **79**(11), pp. 1590–1592.
35. Kishino, K., Kikuchi, A., Kanazawa, H., and Tachibana, T., 2002, "Intersubband transition in (GaN)[sub m]/(AlN)[sub n] superlattices in the wavelength range from 1.08 to 1.61 μm," *Applied Physics Letters*, **81**(7), pp. 1234–1236.
36. Iizuka, N., Kaneko, K., and Suzuki, N., 2002, "Near-infrared intersubband absorption in GaN/AlN quantum wells grown by molecular beam epitaxy," *Applied Physics Letters*, **81**(10), pp. 1803–1805.
37. Heber, J. D., Gmachl, C., Ng, H. M., and Cho, A. Y., 2002, "Comparative study of ultrafast intersubband electron scattering times at ~1.55 μm wavelength in GaN/AlGaN heterostructures," *Applied Physics Letters*, **81**(7), pp. 1237–1239.
38. Helman, A., Tchernycheva, M., Lusson, A., Warde, E., Julien, F. H., Moumanis, K., Fishman, G., Monroy, E., Daudin, B., Le Si Dang, D., Bellet-Amalric, E., and Jalabert, D., 2003, "Intersubband spectroscopy of doped and undoped GaN/AlN quantum wells grown by molecular-beam epitaxy," *Applied Physics Letters*, **83**(25), pp. 5196–5198.
39. Zhou, Q., Chen, J., Pattada, B., Manasreh, M. O., Xiu, F., Puntigan, S., He, L., Ramaiah, K. S., and Morkoç, H., 2003, "Infrared optical absorbance of intersubband transitions in GaN/AlGaN multiple quantum well structures," *Journal of Applied Physics*, **93**(12), pp. 10140–10142.
40. Adelmann, C., Brault, J., Mula, G., Daudin, B., Lymperakis, L., and Neugebauer, J., 2003, "Gallium adsorption on (0001) GaN surfaces," *Physical Review B*, **67**(16), p. 165419.
41. Neugebauer, J., Zywietz, T., Scheffler, M., Northrup, J., Chen, H., and Feenstra, R., 2003, "Adatom kinetics on and below the surface: The existence of a new diffusion channel," *Physical Review Letters*, **90**(5), p. 056101.
42. Heying, B., Averbeck, R., Chen, L. F., Haus, E., Riechert, H., and Speck, J. S., 2000, "Control of GaN surface morphologies using plasma-assisted molecular beam epitaxy," *Journal of Applied Physics*, **88**(4), pp. 1855–1860.
43. Iliopoulos, E., and Moustakas, T. D., 2002, "Growth kinetics of AlGaN films by plasma-assisted molecular-beam epitaxy," *Applied Physics Letters*, **81**(2), pp. 295– 297.
44. Monroy, E., Daudin, B., Bellet-Amalric, E., Gogneau, N., Jalabert, D., Enjalbert, F., Brault, J., Barjon, J., and Dang, L. S., 2003, "Surfactant effect of In for AlGaN growth by plasma-assisted molecular beam epitaxy," *Journal of Applied Physics*, **93**(3), pp. 1550–1556.
45. Koblmueller, G., Averbeck, R., Geelhaar, L., Riechert, H., Hösler, W., and Pongratz, P., 2003, "Growth diagram and morphologies of AlN thin films grown by molecular beam epitaxy," *Journal of Applied Physics*, **93**(12), pp. 9591–9597.
46. Mula, G., Adelmann, C., Moehl, S., Oullier, J., and Daudin, B., 2001, "Surfactant effect of gallium during molecular-beam epitaxy of GaN on AlN (0001)," *Physical Review B*, **64**(19), p. 195406.

47. Brown, J. S., Koblmüller, G., Wu, F., Averbeck, R., Riechert, H., and Speck, J. S., 2006, "Ga adsorbate on (0001) GaN: In situ characterization with quadrupole mass spectrometry and reflection high-energy electron diffraction," *Journal of Applied Physics*, **99**(7), p. 074902.
48. Northrup, J., Neugebauer, J., Feenstra, R., and Smith, A., 2000, "Structure of GaN (0001): The laterally contracted Ga bilayer model," *Physical Review B*, **61**(15), pp. 9932–9935.
49. Koblmüller, G., Brown, J., Averbeck, R., Riechert, H., Pongratz, P., and Speck, J. S., 2005, "Continuous evolution of Ga adlayer coverages during plasma-assisted molecular-beam epitaxy of (0001) GaN," *Applied Physics Letters*, **86**(4), p. 041908.
50. Kandaswamy, P. K., Bougerol, C., Jalabert, D., Ruterana, P., and Monroy, E., 2009, "Strain relaxation in short-period polar GaN/AlN superlattices," *Journal of Applied Physics*, **106**(1), p. 013526.
51. Baumann, E., Giorgetta, F. R., Hofstetter, D., Golka, S., Schrenk, W., Strasser, G., Kirste, L., Nicolay, S., Feltin, E., Carlin, J. F., and Grandjean, N., 2006, "Near infrared absorption and room temperature photovoltaic response in AlN/GaN superlattices grown by metal-organic vapor-phase epitaxy," *Applied Physics Letters*, **89**(4), p. 041106.
52. Bayram, C., Péré-laperne, N., and Razeghi, M., 2009, "Effects of well width and growth temperature on optical and structural characteristics of AlN/GaN superlattices grown by metal-organic chemical vapor deposition," *Applied Physics Letters*, **95**(20), p. 201906.
53. Sodabanlu, H., Yang, J. -S., Sugiyama, M., Shimogaki, Y., and Nakano, Y., 2009, "Strain effects on the intersubband transitions in GaN/AlN multiple quantum wells grown by low-temperature metal organic vapor phase epitaxy with AlGaN interlayer," *Applied Physics Letters*, **95**(16), p. 161908.
54. Yang, J. -S., Sodabanlu, H., Sugiyama, M., Nakano, Y., and Shimogaki, Y., 2009, "Blueshift of intersubband transition wavelength in AlN/GaN multiple quantum wells by low temperature metal organic vapor phase epitaxy using pulse injection method," *Applied Physics Letters*, **95**(16), p. 162111.
55. Nicolay, S., Feltin, E., Carlin, J. -F., Grandjean, N., Nevou, L., Julien, F. H., Schmidbauer, M., Remmele, T., and Albrecht, M., 2007, "Strain-induced interface instability in GaN/AlN multiple quantum wells," *Applied Physics Letters*, **91**(6), p. 061927.
56. Iizuka, N., Kaneko, K., and Suzuki, N., 2006, "All-optical switch utilizing intersubband transition in GaN quantum wells," *IEEE Journal of Quantum Electronics*, **42**(8), pp. 765–771.
57. Floro, J. A., Follstaedt, D. M., Provencio, P., Hearne, S. J., and Lee, S. R., 2004, "Misfit dislocation formation in the AlGaN/GaN heterointerface," *Journal of Applied Physics*, **96**(12), pp. 7087–7094.
58. Ponce, F. A., 1997, "Detects and interfaces in GaN epitaxy," *MRS Bulletin*, **22**(2), pp. 51–57.
59. Moran, B., Wu, F., Romanov, A. E., Mishra, U. K., Denbaars, S. P., and Speck, J. S., 2004, "Structural and morphological evolution of GaN grown by metalorganic chemical vapor deposition on SiC substrates using an AlN initial layer," *Journal of Crystal Growth*, **273**(1–2), pp. 38–47.
60. Kehagias, T., Delimitis, A., Komninou, P., Iliopoulos, E., Dimakis, E., Georgakilas, A., and Nouet, G., 2005, "Misfit accommodation of compact and columnar InN epilayers grown on Ga-face GaN (0001) by molecular-beam epitaxy," *Applied Physics Letters*, **86**(15), p. 151905.
61. Hearne, S. J., Han, J., Lee, S. R., Floro, J. A., Follstaedt, D. M., Chason, E., and Tsong, I. S. T., 2000, "Brittle-ductile relaxation kinetics of strained AlGaN/GaN heterostructures," *Applied Physics Letters*, **76**(12), pp. 1534–1536.

62. Liu, R., Mei, J., Srinivasan, S., Ponce, F. A., Omiya, H., Narukawa, Y., and Mukai, T., 2006, "Generation of misfit dislocations by basal-plane slip in InGaN/GaN heterostructures," *Applied Physics Letters*, **89**(20), p. 201911.
63. Einfeldt, S., Heinke, H., Kirchner, V., and Hommel, D., 2001, "Strain relaxation in AlGaN/GaN superlattices grown on GaN," *Journal of Applied Physics*, **89**(4), pp. 2160–2167.
64. Andersson, T. G., Liu, X. Y., Aggerstam, T., Holmström, P., Lourdudoss, S., Thylen, L., Chen, Y. L., Hsieh, C. H., and Lo, I., 2009, "Macroscopic defects in GaN/AlN multiple quantum well structures grown by MBE on GaN templates," *Microelectronics Journal*, **40**(2), pp. 360–362.
65. Cherns, P. D., McAleese, C., Kappers, M. J., and Humphreys, C. J., 2007, "Strain relaxation in an AlGaN/GaN quantum well system," *Microscopy of Semiconducting Materials*, A.G. Cullis and P.A. Midgley, eds., Springer, Dordrecht, Netherlands, pp. 25–28.
66. Cantu, P., Wu, F., Waltereit, P., Keller, S., Romanov, A. E., DenBaars, S. P., and Speck, J. S., 2005, "Role of inclined threading dislocations in stress relaxation in mismatched layers," *Journal of Applied Physics*, **97**(10), p. 103534.
67. Bellet-Amalric, E., Adelmann, C., Sarigiannidou, E., Rouvière, J. L., Feuillet, G., Monroy, E., and Daudin, B., 2004, "Plastic strain relaxation of nitride heterostructures," *Journal of Applied Physics*, **95**(3), pp. 1127–1133.
68. Kotsar, Y., Doisneau, B., Bellet-Amalric, E., Das, A., Sarigiannidou, E., and Monroy, E., 2011, "Strain relaxation in GaN/AlxGa1-xN superlattices grown by plasma-assisted molecular-beam epitaxy," *Journal of Applied Physics*, **110**(3), p. 033501.
69. Yang, R., Xu, J., and Sweeny, M., 1994, "Selection rules of intersubband transitions in conduction-band quantum wells," *Physical Review B*, **50**(11), pp. 7474–7482.
70. Guillot, F., Amstatt, B., Bellet-Amalric, E., Monroy, E., Nevou, L., Doyennette, L., Julien, F. H., and Dang, L. S., 2006, "Effect of Si doping on GaN/AlN multiple-quantum-well structures for intersubband optoelectronics at telecommunication wavelengths," *Superlattices and Microstructures*, **40**(4–6), pp. 306–312.
71. Berland, K., Stattin, M., Farivar, R., Sultan, D. M. S., Hyldgaard, P., Larsson, A., Wang, S. M., and Andersson, T. G., 2010, "Temperature stability of intersubband transitions in AlN/GaN quantum wells," *Applied Physics Letters*, **97**(4), p. 043507.
72. Liu, X. Y., Holmström, P., Jänes, P., Thylén, L., and Andersson, T. G., 2007, "Intersubband absorption at 1.5–3.5 μm in GaN/AlN multiple quantum wells grown by molecular beam epitaxy on sapphire," *Physica Status Solidi (b)*, **244**(8), pp. 2892–2905.
73. Suzuki, N., and Iizuka, N., 1999, "Effect of polarization field on intersubband transition in AlGaN/GaN quantum wells," *Japanese Journal of Applied Physics*, **38**(Part 2, No. 4A), pp. L363–L365.
74. Ng, H. M., Gmachl, C., Siegrist, T., Chu, S. N. G., and Cho, A. Y., 2001, "Growth and characterization of GaN/AlGaN superlattices for near-infrared intersubband transitions," *Physica Status Solidi (a)*, **188**(2), pp. 825–831.
75. Ng, H. M., Gmachl, C., Heber, J. D., Hsu, J. W. P., Chu, S. N. G., and Cho, A. Y., 2002, "Recent progress in GaN-based superlattices for near-infrared intersubband transitions," *Physica Status Solidi (b)*, **234**(3), pp. 817–821.
76. Sherliker, B., Halsall, M., Kasalynas, I., Seliuta, D., Valusis, G., Vengris, M., Barkauskas, M., Sirutkaitis, V., Harrison, P., Jovanovic, V. D., Indjin, D., Ikonic, Z., Parbrook, P. J., Wang, T., and Buckle, P. D., 2007, "Room temperature operation of AlGaN/GaN quantum well infrared photodetectors at a 3–4 μm wavelength range," *Semiconductor Science and Technology*, **22**(11), pp. 1240–1244.
77. Péré-Laperne, N., Bayram, C., Nguyen-The, L., McClintock, R., and Razeghi, M., 2009, "Tunability of intersubband absorption from 4.5 to 5.3 μm in a GaN/Al[sub 0.2] Ga[sub 0.8]N superlattices grown by metalorganic chemical vapor deposition," *Applied Physics Letters*, **95**(13), p. 131109.

K22181_C008.indd 278 6/3/15 10:53 AM

78. Tian, W., Yan, W. Y., Hui, X., Li, S. L., Ding, Y. Y., Li, Y., Tian, Y., Dai, J. N., Fang, Y. Y., Wu, Z. H., Yu, C. H., and Chen, C. Q., 2012, "Tunability of intersubband transition wavelength in the atmospheric window in AlGaN/GaN multi-quantum wells grown on different AlGaN templates by metalorganic chemical vapor deposition," *Journal of Applied Physics*, **112**(6), p. 063526.
79. Bayram, C., 2012, "High-quality AlGaN/GaN superlattices for near- and mid- infrared intersubband transitions," *Journal of Applied Physics*, **111**(1), p. 013514.
80. Huang, C. C., Xu, F. J., Yan, X. D., Song, J., Xu, Z. Y., Cen, L. B., Wang, Y., Pan, J. H., Wang, X. Q., Yang, Z. J., Shen, B., Zhang, B. S., Chen, X. S., and Lu, W., 2011, "Intersubband transitions at atmospheric window in Al[sub x]Ga[sub 1−x]N/GaN multiple quantum wells grown on GaN/sapphire templates adopting AlN/GaN superlattices interlayer," *Applied Physics Letters*, **98**(13), p. 132105.
81. Edmunds, C., Tang, L., Li, D., Cervantes, M., Gardner, G., Paskova, T., Manfra, M. J., and Malis, O., 2012, "Near-infrared absorption in lattice-matched AlInN/GaN and strained AlGaN/GaN heterostructures grown by MBE on low- defect GaN substrates," *Journal of Electronic Materials*, **41**(5), pp. 881–886.
82. Chen, G., Li, Z. L., Wang, X. Q., Huang, C. C., Rong, X., Sang, L. W., Xu, F. J., Tang, N., Qin, Z. X., Sumiya, M., Chen, Y. H., Ge, W. K., and Shen, B., 2013, "Effect of polarization on intersubband transition in AlGaN/GaN multiple quantum wells," *Applied Physics Letters*, **102**(19), p. 192109.
83. Liu, D. -F., Jiang, J. -G., Cheng, Y., and He, J. -F., 2013, "Effect of delta doping on mid-infrared intersubband absorption in AlGaN/GaN step quantum well structures," *Physica E: Low-Dimensional Systems and Nanostructures*, **54**, pp. 253–256.
84. Edmunds, C., Tang, L., Shao, J., Li, D., Cervantes, M., Gardner, G., Zakharov, D. N., Manfra, M. J., and Malis, O., 2012, "Improvement of near-infrared absorption linewidth in AlGaN/GaN superlattices by optimization of delta-doping location," *Applied Physics Letters*, **101**(10), p. 102104.
85. Wu, T., Wei-Yi, Y., Hui, X., Jian-Nan, D., Yan-Yan, F., Zhi-Hao, W., Chen-Hui, Y., and Chang-Qin, C., 2013, "Effects of polarization on intersubband transitions of AlxGa1−xN/GaN multi-quantum wells," *Chinese Physics B*, **22**(5), p. 057302.
86. Zhuo, X., Ni, J., Li, J., Lin, W., Cai, D., Li, S., and Kang, J., 2014, "Band engineering of GaN/AlN quantum wells by Si dopants," *Journal of Applied Physics*, **115**(12), p. 124305.
87. Machhadani, H., Kotsar, Y., Sakr, S., Tchernycheva, M., Colombelli, R., Mangeney, J., Bellet-Amalric, E., Sarigiannidou, E., Monroy, E., and Julien, F. H., 2010, "Terahertz intersubband absorption in GaN/AlGaN step quantum wells," *Applied Physics Letters*, **97**(19), p. 191101.
88. Beeler, M., Bougerol, C., Bellet-Amalric, E., and Monroy, E., 2013, "Terahertz absorbing AlGaN/GaN multi-quantum-wells: Demonstration of a robust 4-layer design," *Applied Physics Letters*, **103**(9), p. 091108.
89. Beeler, M., Bougerol, C., Bellet-Amalaric, E., and Monroy, E., 2014, "THz intersubband transitions in AlGaN/GaN multi-quantum-wells: THz intersubband transitions in AlGaN/GaN MQWs," *Physica Status Solidi (a)*, **211**(4), pp. 761–764.
90. Wu, F., Tian, W., Yan, W. Y., Zhang, J., Sun, S. C., Dai, J. N., Fang, Y. Y., Wu, Z. H., and Chen, C. Q., 2013, "Terahertz intersubband transition in GaN/AlGaN step quantum well," *Journal of Applied Physics*, **113**(15), p. 154505.
91. Beeler, M., Bougerol, C., Bellet-Amalric, E., and Monroy, E., *Applied Physics Letters*, submitted.
92. Suzuki, N., Iizuka, N., and Kaneko, K., 2003, "Calculation of near-infrared intersubband absorption spectra in GaN/AlN quantum wells," *Japanese Journal of Applied Physics*, **42**(Part 1, No. 1), pp. 132–139.

AU: For reference 91, please check if article title, publishing year, volume number, and page range can be updated.

93. Tchernycheva, M., Nevou, L., Doyennette, L., Julien, F. H., Guillot, F., Monroy, E., Remmele, T., and Albrecht, M., 2006, “Electron confinement in strongly coupled GaN/AlN quantum wells,” *Applied Physics Letters*, **88**(15), p. 153113.
94. Driscoll, K., Bhattacharyya, A., Moustakas, T. D., Paiella, R., Zhou, L., and Smith, D. J., 2007, “Intersubband absorption in AlN/GaN/AlGaN coupled quantum wells,” *Applied Physics Letters*, **91**(14), p. 141104.
95. Cen, L. B., Shen, B., Qin, Z. X., and Zhang, G. Y., 2009, “Influence of polarization induced electric fields on the wavelength and the refractive index of intersubband transitions in AlN/GaN coupled double quantum wells,” *Journal of Applied Physics*, **105**(9), p. 093109.
96. Cen, L. B., Shen, B., Qin, Z. X., and Zhang, G. Y., 2009, “Near-infrared two-color intersubband transitions in AlN/GaN coupled double quantum wells,” *Journal of Applied Physics*, **105**(5), p. 053106.
97. Lupu, A., Julien, F. H., Golka, S., Pozzovivo, G., Strasser, G., Baumann, E., Giorgetta, F., Hofstetter, D., Nicolay, S., Mosca, M., Feltin, E., Carlin, J. -F., and Grandjean, N., 2008, “Lattice-Matched GaN-InAlN Waveguides at λ = 1.55 μm Grown by Metal-Organic Vapor Phase Epitaxy,” *IEEE Photonics Technology Letters*, **20**(2), pp. 102–104.
98. Nicolay, S., Carlin, J. -F., Feltin, E., Butté, R., Mosca, M., Grandjean, N., Ilegems, M., Tchernycheva, M., Nevou, L., and Julien, F. H., 2005, “Midinfrared intersubband absorption in lattice-matched AlInN/GaN multiple quantum wells,” *Applied Physics Letters*, **87**(11), p. 111106.
99. Nicolay, S., Feltin, E., Carlin, J. -F., Mosca, M., Nevou, L., Tchernycheva, M., Julien, F. H., Ilegems, M., and Grandjean, N., 2006, “Indium surfactant effect on AlN/GaN heterostructures grown by metal-organic vapor-phase epitaxy: Applications to intersubband transitions,” *Applied Physics Letters*, **88**(15), p. 151902.
100. Gonschorek, M., Carlin, J. -F., Feltin, E., Py, M. A., Grandjean, N., Darakchieva, V., Monemar, B., Lorenz, M., and Ramm, G., 2008, “Two-dimensional electron gas density in Al[sub 1−x]In[sub x]N/AlN/GaN heterostructures (0.03≤x≤0.23),” *Journal of Applied Physics*, **103**(9), p. 093714.
101. Malis, O., Edmunds, C., Manfra, M. J., and Sivco, D. L., 2009, “Near-infrared intersubband absorption in molecular-beam epitaxy-grown lattice-matched InAlN/GaN superlattices,” *Applied Physics Letters*, **94**(16), p. 161111.
102. Cywiński, G., Skierbiszewski, C., Fedunieiwcz-Żmuda, A., Siekacz, M., Nevou, L., Doyennette, L., Tchernycheva, M., Julien, F. H., Prystawko, P., Kryśko, M., Grzanka, S., Grzegory, I., Presz, A., Domagała, J. Z., Smalc, J., Albrecht, M., Remmele, T., and Porowski, S., 2006, “Growth of thin AlInN/GaInN quantum wells for applications to high-speed intersubband devices at telecommunication wavelengths,” *Journal of Vacuum Science & Technology B: Microelectronics and Nanometer Structures*, **24**(3), pp. 1505–1509.
103. Kudrawiec, R., Motyka, M., Cywin’ski, G., Siekacz, M., Skierbiszewski, C., Nevou, L., Doyennette, L., Tchernycheva, M., Julien, F. H., and Misiewicz, J., 2008, “Contactless electroreflectance spectroscopy of inter- and intersub-band transitions in AlInN/GaInN quantum wells,” *Physica Status Solidi (c)*, **5**(2), pp. 503–507.
104. Dakhlaoui, H., 2013, “Influence of doping layer concentration on the electronic transitions in symmetric Al$_x$Ga$_{(1,x)}$N/GaN double quantum wells,” *Optik—International Journal for Light and Electron Optics*, **124**(18), pp. 3726–3729.
105. Akabli, H., Almaggoussi, A., Abounadi, A., Rajira, A., Berland, K., and Andersson, T. G., 2012, “Intersubband energies in Al1−yInyN/Ga1−xInxN heterostructures with lattice constant close to aGaN,” *Superlattices and Microstructures*, **52**(1), pp. 70–77.
106. Zhu, J., Ban, S. -L., and Ha, S. -H., 2012, “Phonon-assisted intersubband transitions in wurtzite GaN/InxGa1−xN quantum wells,” *Chinese Physics B*, **21**(9), p. 097301.

AU: Please specify the correct symbol.

107. Yıldırım, H., and Aslan, B., 2014, "Intersubband transitions in InxGa1−xN/InyGa1−yN/GaN staggered quantum wells," *Journal of Applied Physics*, **115**(16), p. 164306.
108. Berryman, K. W., Lyon, S. A., and Segev, M., 1997, "Mid-infrared photoconductivity in InAs quantum dots," *Applied Physics Letters*, **70**(14), pp. 1861–1863.
109. Phillips, J., Kamath, K., and Bhattacharya, P., 1998, "Far-infrared photoconductivity in self-organized InAs quantum dots," *Applied Physics Letters*, **72**(16), pp. 2020–2022.
110. Ryzhii, V., 1996, "The theory of quantum-dot infrared phototransistors," *Semiconductor Science and Technology*, **11**(5), pp. 759–765.
111. Pan, D., Towe, E., and Kennerly, S., 1998, "Normal-incidence intersubband (In, Ga) As/GaAs quantum dot infrared photodetectors," *Applied Physics Letters*, **73**(14), pp. 1937–1939.
112. Chen, Z., Baklenov, O., Kim, E. T., Mukhametzhanov, I., Tie, J., Madhukar, A., Ye, Z., and Campbell, J. C., 2001, "Normal incidence InAs/Al[sub x]Ga[sub 1−x]As quantum dot infrared photodetectors with undoped active region," *Journal of Applied Physics*, **89**(8), pp. 4558–4563.
113. Chu, L., Zrenner, A., Bichler, M., and Abstreiter, G., 2001, "Quantum-dot infrared photodetector with lateral carrier transport," *Applied Physics Letters*, **79**(14), pp. 2249–2251.
114. Daudin, B., Widmann, F., Feuillet, G., Samson, Y., Arlery, M., and Rouvière, J., 1997, "Stranski-Krastanov growth mode during the molecular beam epitaxy of highly strained GaN," *Physical Review B*, **56**(12), pp. R7069–R7072.
115. Chamard, V., Schülli, T., Sztucki, M., Metzger, T., Sarigiannidou, E., Rouvière, J. -L., Tolan, M., and Adelmann, C., 2004, "Strain distribution in nitride quantum dot multilayers," *Physical Review B*, **69**(12), p. 125327.
116. Guillot, F., Tchernycheva, M., Nevou, L., Doyennette, L., Monroy, E., Julien, F. H., Dang, L. S., Remmele, T., Albrecht, M., Shibata, T., and Tanaka, M., 2006, "Si-doped GaN/AlN quantum dot superlattices for optoelectronics at telecommunication wavelengths," *Physica Status Solidi (a)*, **203**(7), pp. 1754–1758.
117. Andreev, A., and O'Reilly, E., 2000, "Theory of the electronic structure of GaN/AlN hexagonal quantum dots," *Physical Review B*, **62**(23), pp. 15851–15870.
118. Andreev, A. D., and O'Reilly, E. P., 2001, "Optical transitions and radiative lifetime in GaN/AlN self-organized quantum dots," *Applied Physics Letters*, **79**(4), pp. 521–523.
119. Williams, D., Andreev, A., O'Reilly, E., and Faux, D., 2005, "Derivation of built- in polarization potentials in nitride-based semiconductor quantum dots," *Physical Review B*, **72**(23), p. 235318.
120. Ranjan, V., Allan, G., Priester, C., and Delerue, C., 2003, "Self-consistent calculations of the optical properties of GaN quantum dots," *Physical Review B*, **68**(11), p. 115303.
121. Tchernycheva, M., Nevou, L., Doyennette, L., Helman, A., Colombelli, R., Julien, F. H., Guillot, F., Monroy, E., Shibata, T., and Tanaka, M., 2005, "Intraband absorption of doped GaN/AlN quantum dots at telecommunication wavelengths," *Applied Physics Letters*, **87**(10), p. 101912.
122. Vardi, A., Bahir, G., Schacham, S. E., Kandaswamy, P. K., and Monroy, E., 2009, "Photocurrent spectroscopy of bound-to-bound intraband transitions in GaN/AlN quantum dots," *Physical Review B*, **80**(15), p. 155439.
123. Nguyen, D. T., Wüster, W., Roussignol, P., Voisin, C., Cassabois, G., Tchernycheva, M., Julien, F. H., Guillot, F., and Monroy, E., 2010, "Homogeneous linewidth of the intraband transition at 1.55 µm in GaN/AlN quantum dots," *Applied Physics Letters*, **97**(6), p. 061903.
124. Himwas, C., Songmuang, R., Le Si Dang, Bleuse, J., Rapenne, L., Sarigiannidou, E., and Monroy, E., 2012, "Thermal stability of the deep ultraviolet emission from AlGaN/AlN Stranski-Krastanov quantum dots," *Applied Physics Letters*, **101**(24), p. 241914.

125. Himwas, C., den Hertog, M., Bellet-Amalric, E., Songmuang, R., Donatini, F., Si Dang, L., and Monroy, E., 2014, "Enhanced room-temperature mid-ultraviolet emission from AlGaN/AlN Stranski-Krastanov quantum dots," *Journal of Applied Physics*, **116**(2), p. 023502.
126. Beeler, M., Hille, P., Schörmann, J., Teubert, J., de la Mata, M., Arbiol, J., Eickhoff, M., and Monroy, E., 2014, "Intraband absorption in self-assembled Ge-doped GaN/AlN nanowire heterostructures," *Nano Letters*, **14**(3), pp. 1665–1673.
127. Speck, J. S., and Chichibu, S. F., 2011, "Nonpolar and semipolar group III nitride-based materials," *MRS Bulletin*, **34**(05), pp. 304–312.
128. Romanov, A. E., Baker, T. J., Nakamura, S., Speck, J. S., and ERATO/JST UCSB Group, 2006, "Strain-induced polarization in wurtzite III-nitride semipolar layers," *Journal of Applied Physics*, **100**(2), p. 023522.
129. Lahourcade, L., Bellet-Amalric, E., Monroy, E., Abouzaid, M., and Ruterana, P., 2007, "Plasma-assisted molecular-beam epitaxy of AlN (11-22) on m sapphire," *Applied Physics Letters*, **90**(13), p. 131909.
130. Lahourcade, L., Kandaswamy, P. K., Renard, J., Ruterana, P., Machhadani, H., Tchernycheva, M., Julien, F. H., Gayral, B., and Monroy, E., 2008, "Interband and intersubband optical characterization of semipolar (1122)-oriented GaN/AlN multiple-quantum-well structures," *Applied Physics Letters*, **93**(11), p. 111906.
131. Gmachl, C., and Ng, H. M., 2003, "Intersubband absorption at ~2.1 μm in A-plane GaN/AlN multiple quantum wells," *Electronics Letters*, **39**(6), pp. 567–569.
132. Edmunds, C., Shao, J., Shirazi-HD, M., Manfra, M. J., and Malis, O., 2014, "Terahertz intersubband absorption in non-polar *m*-plane AlGaN/GaN quantum wells," *Applied Physics Letters*, **105**(2), p. 021109.
133. Machhadani, H., Beeler, M., Sakr, S., Warde, E., Kotsar, Y., Tchernycheva, M., Chauvat, M. P., Ruterana, P., Nataf, G., De Mierry, P., Monroy, E., and Julien, F. H., 2013, "Systematic study of near-infrared intersubband absorption of polar and semipolar GaN/AlN quantum wells," *Journal of Applied Physics*, **113**(14), p. 143109.
134. Brazis, R., and Raguotis, R., 2006, "Monte Carlo modeling of phonon-assisted carrier transport in cubic and hexagonal gallium nitride," *Optical and Quantum Electronics*, **38**(4–6), pp. 339–347.
135. Pugh, S. K., Dugdale, D. J., Brand, S., and Abram, R. A., 1999, "Electronic structure calculations on nitride semiconductors," *Semiconductor Science and Technology*, **14**(1), pp. 23–31.
136. Suzuki, M., and Uenoyama, T., 1996, "Optical gain and crystal symmetry in III–V nitride lasers," *Applied Physics Letters*, **69**(22), pp. 3378–3380.
137. Ghasemi, F., and Razi, S., 2013, "Cuboid GaN/AlGaN quantum dot infrared photodetector; photoconductive gain and capture probability," *Optik—International Journal for Light and Electron Optics*, **124**(9), pp. 859–863.
138. DeCuir, E. A., Fred, E., Manasreh, M. O., Schörmann, J., As, D. J., and Lischka, K., 2007, "Near-infrared intersubband absorption in nonpolar cubic GaN/AlN superlattices," *Applied Physics Letters*, **91**(4), p. 041911.
139. Machhadani, H., Tchernycheva, M., Sakr, S., Rigutti, L., Colombelli, R., Warde, E., Mietze, C., As, D. J., and Julien, F. H., 2011, "Intersubband absorption of cubic GaN/Al(Ga)N quantum wells in the near-infrared to terahertz spectral range," *Physical Review B*, **83**(7), p. 075313.
140. As, D. J., and Mietze, C., 2013, "MBE growth and applications of cubic AlN/GaN quantum wells," *Physica Status Solidi A*, **210**(3), pp. 474–479.
141. Radosavljević, A., Radovanović, J., and Milanović, V., 2014, "Optimization of cubic GaN/AlGaN quantum well-based structures for intersubband absorption in the infrared spectral range," *Solid State Communications*, **182**, pp. 38–42.

142. Wada, O., 2004, "Femtosecond all-optical devices for ultrafast communication and signal processing," *New Journal of Physics*, **6**, pp. 183–183.
143. Noda, S., Yamashita, T., Ohya, M., Muromoto, Y., and Sasaki, A., 1993, "All- optical modulation for semiconductor lasers by using three energy levels in n-doped quantum wells," *IEEE Journal of Quantum Electronics*, **29**(6), pp. 1640–1647.
144. Iizuka, N., Kaneko, K., Suzuki, N., Asano, T., Noda, S., and Wada, O., 2000, "Ultrafast intersubband relaxation (≤150 fs) in AlGaN/GaN multiple quantum wells," *Applied Physics Letters*, **77**(5), pp. 648–650.
145. Gmachl, C., Frolov, S. V., Ng, H. M., Chu, S. -N. G., and Cho, A. Y., 2001, "Subpicosecond electron scattering time for ⊠ 1.55 [micro sign]m intersubband transitions in GaN/AlGaN multiple quantum wells," *Electronics Letters*, **37**(6), p. 378.
146. Rapaport, R., Chen, G., Mitrofanov, O., Gmachl, C., Ng, H. M., and Chu, S. N. G., 2003, "Resonant optical nonlinearities from intersubband transitions in GaN/AlN quantum wells," *Applied Physics Letters*, **83**(2), p. 263.
147. Iizuka, N., Kaneko, K., and Suzuki, N., 2005, "Sub-picosecond all-optical gate utilizing GaN intersubband transition," *Optics Express*, **13**(10), pp. 3835–3840.
148. Hamazaki, J., Kunugita, H., Ema, K., Kikuchi, A., and Kishino, K., 2005, "Intersubband relaxation dynamics in GaN/AlN multiple quantum wells studied by two-color pump-probe experiments," *Physical Review B*, **71**(16), p. 165334.
149. Suzuki, N., Iizuka, N., and Kaneko, K., 2000, "Intersubband transition in AlGaN-GaN quantum wells for ultrafast all-optical switching at communication wavelength," *Proceedings of SPIE*, **3940**, pp. 127–138.
150. Iizuka, N., Kaneko, K., and Suzuki, N., 2004, "Sub-picosecond modulation by intersubband transition in ridge waveguide with GaN/AlN quantum wells," *Electronics Letters*, **40**(15), p. 962963.
151. Li, Y., Bhattacharyya, A., Thomidis, C., Moustakas, T. D., and Paiella, R., 2007, "Ultrafast all-optical switching with low saturation energy via intersubband transitions in GaN/AlN quantum-well waveguides," *Optics Express*, **15**(26), pp. 17922–17927.
152. Sodabanlu, H., Yang, J. -S., Tanemura, T., Sugiyama, M., Shimogaki, Y., and Nakano, Y., 2011, "Intersubband absorption saturation in AlN-based waveguide with GaN/AlN multiple quantum wells grown by metalorganic vapor phase epitaxy," *Applied Physics Letters*, **99**(15), p. 151102.
153. Iizuka, N., Yoshida, H., Managaki, N., Shimizu, T., Hassanet, S., Cumtornkittikul, C., Sugiyama, M., and Nakano, Y., 2009, "Integration of GaN/AlN all-optical switch with SiN/AlN waveguide utilizing spot-size conversion," *Optics Express*, **17**(25), pp. 23247–23253.
154. Iizuka, N., Kaneko, K., and Suzuki, N., 2006, "Polarization dependent loss in III- nitride optical waveguides for telecommunication devices," *Journal of Applied Physics*, **99**(9), p. 093107.
155. Li, Y., and Paiella, R., 2006, "Intersubband all-optical switching based on Coulomb-induced optical nonlinearities in GaN/AlGaN coupled quantum wells," *Semiconductor Science and Technology*, **21**(8), pp. 1105–1110.
156. Valdueza-Felip, S., Naranjo, F. B., Gonzalez-Herraez, M., Fernandez, H., Solis, J., Guillot, F., Monroy, E., Nevou, L., Tchernycheva, M., and Julien, F. H., 2008, "Characterization of the resonant third-order nonlinear susceptibility of Si-doped GaN-AlN quantum wells and quantum dots at 1.5 µm," *IEEE Photonics Technology Letters*, **20**(16), pp. 1366–1368.
157. Monteagudo-Lerma, L., Valdueza-Felip, S., Naranjo, F. B., Corredera, P., Rapenne, L., Sarigiannidou, E., Strasser, G., Monroy, E., and González-Herráez, M., 2013, "Waveguide saturable absorbers at 155 µm based on intraband transitions in GaN/AlN QDs," *Optics Express*, **21**(23), p. 27578.

K22181_C008.indd 283 6/3/15 10:53 AM

158. Lewen, R., Irmscher, S., Westergren, U., Thylen, L., and Eriksson, U., 2004, "Segmented transmission-line electroabsorption modulators," *Journal of Lightwave Technology*, **22**(1), pp. 172–179.
159. Jungo Kondo, Aoki, K., Kondo, A., Ejiri, T., Iwata, Y., Hamajima, A., Mori, T., Mizuno, Y., Imaeda, M., Kozuka, Y., Mitomi, O., and Minakata, M., 2005, "High-speed and low-driving-voltage thin-sheet X-cut LiNbO/sub 3/modulator with laminated low-dielectric-constant adhesive," *IEEE Photonics Technology Letters*, **17**(10), pp. 2077–2079.
160. Holmstrom, P., 2001, "High-speed mid-IR modulator using Stark shift in step quantum wells," *IEEE Journal of Quantum Electronics*, **37**(10), pp. 1273–1282.
161. Holmstrom, P., 2006, "Electroabsorption modulator using intersubband transitions in GaN–AlGaN–AlN step quantum wells," *IEEE Journal of Quantum Electronics*, **42**(8), pp. 810–819.
162. Holmström, P., Liu, X. Y., Uchida, H., Aggerstam, T., Kikuchi, A., Kishino, K., Lourdudoss, S., Andersson, T. G., and Thylén, L., 2007, "Intersubband photonic devices by group-III nitrides," *Proceedings of SPIE*, **6782**, p. 67821N.
163. Baumann, E., Giorgetta, F. R., Hofstetter, D., Leconte, S., Guillot, F., Bellet- Amalric, E., and Monroy, E., 2006, "Electrically adjustable intersubband absorption of a GaN/AlN superlattice grown on a transistorlike structure," *Applied Physics Letters*, **89**(10), p. 101121.
164. Nevou, L., Kheirodin, N., Tchernycheva, M., Meignien, L., Crozat, P., Lupu, A., Warde, E., Julien, F. H., Pozzovivo, G., Golka, S., Strasser, G., Guillot, F., Monroy, E., Remmele, T., and Albrecht, M., 2007, "Short-wavelength intersubband electroabsorption modulation based on electron tunneling between GaN/AlN coupled quantum wells," *Applied Physics Letters*, **90**(22), p. 223511.
165. Kheirodin, N., Nevou, L., Machhadani, H., Crozat, P., Vivien, L., Tchernycheva, M., Lupu, A., Julien, F. H., Pozzovivo, G., Golka, S., Strasser, G., Guillot, F., and Monroy, E., 2008, "Electrooptical modulator at telecommunication wavelengths based on GaN/AlN coupled quantum wells," *IEEE Photonics Technology Letters*, **20**(9), pp. 724–726.
166. Dussaigne, A., Nicolay, S., Martin, D., Castiglia, A., Grandjean, N., Nevou, L., Machhadani, H., Tchernycheva, M., Vivien, L., Julien, F. H., Remmele, T., and Albrecht, M., 2010, "Growth of intersubband GaN/AlGaN heterostructures," *Proceedings of SPIE*, **7608**, p. 76080H.
167. Dupont, E. B., Delacourt, D., and Papuchon, M., 1993, "Mid-infrared phase modulation via Stark effect on intersubband transitions in GaAs/GaAlAs quantum wells," *IEEE Journal of Quantum Electronics*, **29**(8), pp. 2313–2318.
168. Li, Y., Bhattacharyya, A., Thomidis, C., Liao, Y., Moustakas, T. D., and Paiella, R., 2008, "Refractive-index nonlinearities of intersubband transitions in GaN/AlN quantum-well waveguides," *Journal of Applied Physics*, **104**(8), p. 083101.
169. Wu, F., Tian, W., Zhang, J., Wang, S., Wan, Q. X., Dai, J. N., Wu, Z. H., Xu, J. T., Li, X. Y., Fang, Y. Y., and Chen, C. Q., 2014, "Double-resonance enhanced intersubband second-order nonlinear optical susceptibilities in GaN/AlGaN step quantum wells," Optics *Express*, **22**(12), p. 14212.
170. Lupu, A., Tchernycheva, M., Kotsar, Y., Monroy, E., and Julien, F. H., 2012, "Electroabsorption and refractive index modulation induced by intersubband transitions in GaN/AlN multiple quantum wells," *Optics Express*, **20**(11), p. 12541.
171. Gross, E., Nevet, A., Pesach, A., Monroy, E., Schacham, S. E., Orenstein, M., Segev, M., and Bahir, G., 2013, "Measuring the refractive index around intersubband transition resonance in GaN/AlN multi-quantum wells," *Optics Express*, **21**(3), pp. 3800–3808.
172. Zucker, J. E., Bar-Joseph, I., Miller, B. I., Koren, U., and Chemla, D. S., 1989, "Quaternary quantum wells for electro-optic intensity and phase modulation at 1.3 and 1.55 μm," *Applied Physics Letters*, **54**(1), pp. 10–12.

173. Soref, R., and Bennett, B., 1987, "Electrooptical effects in silicon," *IEEE Journal of Quantum Electronics*, **23**(1), pp. 123–129.
174. Hofstetter, D., Schad, S. -S., Wu, H., Schaff, W. J., and Eastman, L. F., 2003, "GaN/AlN-based quantum-well infrared photodetector for 1.55 μm," *Applied Physics Letters*, **83**(3), pp. 572–574.
175. Baumann, E., Giorgetta, F. R., Hofstetter, D., Lu, H., Chen, X., Schaff, W. J., Eastman, L. F., Golka, S., Schrenk, W., and Strasser, G., 2005, "Intersubband photoconductivity at 1.6 μm using a strain-compensated AlN/GaN superlattice," *Applied Physics Letters*, **87**(19), p. 191102.
176. DeCuir, E. A., Manasreh, M. O., Tschumak, E., Schörmann, J., As, D. J., and Lischka, K., 2008, "Cubic GaN/AlN multiple quantum well photodetector," *Applied Physics Letters*, **92**(20), p. 201910.
177. Doyennette, L., Nevou, L., Tchernycheva, M., Lupu, A., Guillot, F., Monroy, E., Colombelli, R., and Julien, F. H., 2005, "GaN-based quantum dot infrared photodetector operating at 1.38 μm," *Electronics Letters*, **41**(19), pp. 1077–1078.
178. Vardi, A., Akopian, N., Bahir, G., Doyennette, L., Tchernycheva, M., Nevou, L., Julien, F. H., Guillot, F., and Monroy, E., 2006, "Room temperature demonstration of GaN/AlN quantum dot intraband infrared photodetector at fiber-optics communication wavelength," *Applied Physics Letters*, **88**(14), p. 143101.
179. Vardi, A., Bahir, G., Schacham, S. E., Kandaswamy, P. K., and Monroy, E., 2010, "Negative photoconductivity due to intraband transitions in GaN/AlN quantum dots," *Journal of Applied Physics*, **108**(10), p. 104512.
180. Baumann, E., Giorgetta, F. R., Hofstetter, D., Wu, H., Schaff, W. J., Eastman, L. F., and Kirste, L., 2005, "Tunneling effects and intersubband absorption in AlN/GaN superlattices," *Applied Physics Letters*, **86**(3), p. 032110.
181. Monroy, E., Omn s, F., and Calle, F., 2003, "Wide-bandgap semiconductor ultraviolet photodetectors," *Semiconductor Science and Technology*, **18**(4), pp. R33–R51.
182. Hofstetter, D., Baumann, E., Giorgetta, F. R., Graf, M., Maier, M., Guillot, F., Bellet-Amalric, E., and Monroy, E., 2006, "High-quality AlN/GaN-superlattice structures for the fabrication of narrow-band 1.4 μm photovoltaic intersubband detectors," *Applied Physics Letters*, **88**(12), p. 121112.
183. Giorgetta, F. R., Baumann, E., Guillot, F., Monroy, E., and Hofstetter, D., 2007, "High frequency (f = 2.37 GHz) room temperature operation of 1.55 μm AlN/GaN- based intersubband detector," *Electronics Letters*, **43**(3), pp. 185–187.
184. Hofstetter, D., Baumann, E., Giorgetta, F. R., Théron, R., Wu, H., Schaff, W. J., Dawlaty, J., George, P. A., Eastman, L. F., Rana, F., Kandaswamy, P. K., Leconte, S., and Monroy, E., 2009, "Photodetectors based on intersubband transitions using III-nitride superlattice structures," *Journal of Physics: Condensed Matter*, **21**(17), p. 174208.
185. Rosencher, E., and Bois, P., 1991, "Model system for optical nonlinearities: Asymmetric quantum wells," *Physical Review B*, **44**(20), pp. 11315–11327.
186. Hofstetter, D., Di Francesco, J., Kandaswamy, P. K., Das, A., Valdueza-Felip, S., and Monroy, E., 2010, "Performance improvement of AlN/GaN-based intersubband detectors by using quantum dots," *IEEE Photonics Technology Letters*, **22**(15), pp. 1087–1089.
187. Hofstetter, D., Theron, R., Baumann, E., Giorgetta, F. R., Golka, S., Strasser, G., Guillot, F., and Monroy, E., 2008, "Monolithically integrated AlGaN/GaN/AlN-based solar-blind ultraviolet and near-infrared detectors," *Electronics Letters*, **44**(16), p. 986.
188. Sudradjat, F. F., Zhang, W., Woodward, J., Durmaz, H., Moustakas, T. D., and Paiella, R., 2012, "Far-infrared intersubband photodetectors based on double-step III-nitride quantum wells," *Applied Physics Letters*, **100**(24), p. 241113.

189. Pesach, A., Gross, E., Huang, C. -Y., Lin, Y. -D., Vardi, A., Schacham, S. E., Nakamura, S., and Bahir, G., 2013, “Non-polar *m*-plane intersubband based InGaN/(Al)GaN quantum well infrared photodetectors,” *Applied Physics Letters*, **103**(2), p. 022110.
190. Gendron, L., Carras, M., Huynh, A., Ortiz, V., Koeniguer, C., and Berger, V., 2004, “Quantum cascade photodetector,” *Applied Physics Letters*, **85**(14), p. 2824.
191. Giorgetta, F. R., Baumann, E., Graf, M., Yang, Q., Manz, C., Kohler, K., Beere, H. E., Ritchie, D. A., Linfield, E., Davies, A. G., Fedoryshyn, Y., Jackel, H., Fischer, M., Faist, J., and Hofstetter, D., 2009, “Quantum cascade detectors,” *IEEE Journal of Quantum Electronics*, **45**(8), pp. 1039–1052.
192. Vardi, A., Bahir, G., Guillot, F., Bougerol, C., Monroy, E., Schacham, S. E., Tchernycheva, M., and Julien, F. H., 2008, “Near infrared quantum cascade detector in GaN/AlGaN/AlN heterostructures,” *Applied Physics Letters*, **92**(1), p. 011112.
193. Sakr, S., Kotsar, Y., Haddadi, S., Tchernycheva, M., Vivien, L., Sarigiannidou, I., Isac, N., Monroy, E., and Julien, F. H., 2010, “GaN-based quantum cascade photodetector with 1.5 μm peak detection wavelength,” *Electronics Letters*, **46**(25), pp. 1685–1686.
194. Sakr, S., Crozat, P., Gacemi, D., Kotsar, Y., Pesach, A., Quach, P., Isac, N., Tchernycheva, M., Vivien, L., Bahir, G., Monroy, E., and Julien, F. H., 2013, “GaN/AlGaN waveguide quantum cascade photodetectors at $\lambda \approx 1.55\,\mu m$ with enhanced responsivity and ~40 GHz frequency bandwidth,” *Applied Physics Letters*, **102**(1), p. 011135.
195. Vardi, A., Kheirodin, N., Nevou, L., Machhadani, H., Vivien, L., Crozat, P., Tchernycheva, M., Colombelli, R., Julien, F. H., Guillot, F., Bougerol, C., Monroy, E., Schacham, S., and Bahir, G., 2008, “High-speed operation of GaN/AlGaN quantum cascade detectors at $\lambda \approx 1.55$ μm,” *Applied Physics Letters*, **93**(19), p. 193509.
196. Vardi, A., Sakr, S., Mangeney, J., Kandaswamy, P. K., Monroy, E., Tchernycheva, M., Schacham, S. E., Julien, F. H., and Bahir, G., 2011, “Femto-second electron transit time characterization in GaN/AlGaN quantum cascade detector at 1.5 micron,” *Applied Physics Letters*, **99**(20), p. 202111.
197. Gryshchenko, S. V., Klymenko, M. V., Shulika, O. V., Sukhoivanov, I. A., and Lysak, V. V., 2012, “Temperature dependence of electron transport in GaN/AlGaN quantum cascade detectors,” *Superlattices and Microstructures*, **52**(4), pp. 894–900.
198. Sakr, S., Giraud, E., Dussaigne, A., Tchernycheva, M., Grandjean, N., and Julien, F. H., 2012, “Two-color GaN/AlGaN quantum cascade detector at short infrared wavelengths of 1 and 1.7 μm,” *Applied Physics Letters*, **100**(18), p. 181103.
199. Sakr, S., Giraud, E., Tchernycheva, M., Isac, N., Quach, P., Warde, E., Grandjean, N., and Julien, F. H., 2012, “A simplified GaN/AlGaN quantum cascade detector with an alloy extractor,” *Applied Physics Letters*, **101**(25), p. 251101.
200. Pesach, A., Sakr, S., Giraud, E., Sorias, O., Gal, L., Tchernycheva, M. , Orenstein, M., Grandjean, N., Julien, F. H., and Bahir, G., 2014, “First demonstration of plasmonic GaN quantum cascade detectors with enhanced efficiency at normal incidence,” *Optics Express*, **22**(17), pp. 21069–21078.
201. Nevou, L., Julien, F. H., Colombelli, R., Guillot, F., and Monroy, E., 2006, “Room-temperature intersubband emission of GaN/AlN quantum wells at λ = 2.3 μm,” *Electronics Letters*, **42**(22), pp. 1308–1309.
202. Nevou, L., Tchernycheva, M., Julien, F. H., Guillot, F., and Monroy, E., 2007, “Short wavelength (λ=2.13 μm) intersubband luminescence from GaN/AlN quantum wells at room temperature,” *Applied Physics Letters*, **90**(12), p. 121106.
203. Driscoll, K., Liao, Y., Bhattacharyya, A., Zhou, L., Smith, D. J., Moustakas, T. D., and Paiella, R., 2009, “Optically pumped intersubband emission of short-wave infrared radiation with GaN/AlN quantum wells,” *Applied Physics Letters*, **94**(8), p. 081120.
204. Hofstetter, D., Bour, D. P., and Kirste, L., 2014, “Mid-infrared electro-luminescence and absorption from AlGaN/GaN-based multi-quantum well inter-subband structures,” *Applied Physics Letters*, **104**(24), p. 241107.

205. Nevou, L., Julien, F. H., Tchernycheva, M., Guillot, F., Monroy, E., and Sarigiannidou, E., 2008, "Intraband emission at λ≈1.48 µm from GaN/AlN quantum dots at room temperature," *Applied Physics Letters*, **92**(16), p. 161105.
206. Jovanović, V. D., Ikonić, Z., Indjin, D., Harrison, P., Milanović, V., and Soref, R. A., 2003, "Designing strain-balanced GaN/AlGaN quantum well structures: Application to intersubband devices at 1.3 and 1.55 µm wavelengths," *Journal of Applied Physics*, **93**(6), pp. 3194–3197.
207. Stattin, M., Berland, K., Hyldgaard, P., Larsson, A., and Andersson, T. G., 2011, "Waveguides for nitride based quantum cascade lasers," *Physica Status Solidi (c)*, **8**(7–8), pp. 2357–2359.
208. Ive, T., Berland, K., Stattin, M., Fälth, F., Hyldgaard, P., Larsson, A., and Andersson, T. G., 2012, "Design and fabrication of AlN/GaN heterostructures for intersubband technology," *Japanese Journal of Applied Physics*, **51**(1), p. 01AG07.
209. Köhler, R., Tredicucci, A., Beltram, F., Beere, H. E., Linfield, E. H., Davies, A. G., Ritchie, D. A., Iotti, R. C., and Rossi, F., 2002, "Terahertz semiconductor- heterostructure laser," *Nature*, **417**(6885), pp. 156–159.
210. Scalari, G., Walther, C., Fischer, M., Terazzi, R., Beere, H., Ritchie, D., and Faist, J., 2009, "THz and sub-THz quantum cascade lasers," *Laser & Photonics Review*, **3**(1–2), pp. 45–66.
211. Williams, B. S., 2007, "Terahertz quantum-cascade lasers," *Nature Photonics*, **1**(9), pp. 517–525.
212. Kumar, S., Hu, Q., and Reno, J. L., 2009, "186 K operation of terahertz quantum- cascade lasers based on a diagonal design," *Applied Physics Letters*, **94**(13), p. 131105.
213. Williams, B. S., Callebaut, H., Hu, Q., and Reno, J. L., 2001, "Magnetotunneling spectroscopy of resonant anticrossing in terahertz intersubband emitters," *Applied Physics Letters*, **79**(26), p. 4444.
214. Williams, B. S., Callebaut, H., Kumar, S., Hu, Q., and Reno, J. L., 2003, "3.4-THz quantum cascade laser based on longitudinal-optical-phonon scattering for depopulation," *Applied Physics Letters*, **82**(7), pp. 1015–1017.
215. Lü, J. T., and Cao, J. C., 2006, "Monte Carlo simulation of hot phonon effects in resonant-phonon-assisted terahertz quantum-cascade lasers," *Applied Physics Letters*, **88**(6), p. 061119.
216. Jovanović, V. D., Indjin, D., Ikonić, Z., and Harrison, P., 2004, "Simulation and design of GaN/AlGaN far-infrared (λ ~ 34 µm) quantum-cascade laser," *Applied Physics Letters*, **84**(16), pp. 2995–2997.
217. Sun, G., Soref, R. A., and Khurgin, J. B., 2005, "Active region design of a terahertz GaN/Al0.15Ga0.85N quantum cascade laser," *Superlattices and Microstructures*, **37**(2), pp. 107–113.
218. Vukmirović, N., Jovanović, V. D., Indjin, D., Ikonić, Z., Harrison, P., and Milanović, V., 2005, "Optically pumped terahertz laser based on intersubband transitions in a GaN/AlGaN double quantum well," *Journal of Applied Physics*, **97**(10), p. 103106.
219. Bellotti, E., Driscoll, K., Moustakas, T. D., and Paiella, R., 2008, "Monte Carlo study of GaN versus GaAs terahertz quantum cascade structures," *Applied Physics Letters*, **92**(10), p. 101112.
220. Terashima, W., and Hirayama, H., 2009, "Design and fabrication of terahertz quantum cascade laser structure based on III-nitride semiconductors," *Physica Status Solidi (c)*, **6**(S2), pp. S615–S618.
221. Yasuda, H., Kubis, T., and Hirakawa, K., 2011, "Non-equilibrium Green's function calculation for GaN-based terahertz quantum cascade laser structures," 36th International Conference on Infrared, Millimeter and Terahertz Waves (IRMMW-THz).
222. Chou, H., Manzur, T., and Anwar, M., 2011, "Active layer design of THz GaN quantum cascade lasers," *Proceedings of SPIE*, **8023**, p. 802309.

223. Mirzaei, B., Rostami, A., and Baghban, H., 2012, "Terahertz dual-wavelength quantum cascade laser based on GaN active region," *Optics & Laser Technology*, **44**(2), pp. 378–383.
224. Harrison, P., Indjin, D., Jovanović, V. D., Mirčetić, A., Ikonić, Z., Kelsall, R. W., McTavish, J., Savić, I., Vukmirović, N., and Milanović, V., 2005, "A physical model of quantum cascade lasers: Application to GaAs, GaN and SiGe devices," *Physica Status Solidi (a)*, **202**(6), pp. 980–986.
225. Bellotti, E., Driscoll, K., Moustakas, T. D., and Paiella, R., 2009, "Monte Carlo simulation of terahertz quantum cascade laser structures based on wide-bandgap semiconductors," *Journal of Applied Physics*, **105**(11), p. 113103.
226. Shishehchi, S., Paiella, R., and Bellotti, E., 2014, "Numerical simulation of III- nitride lattice-matched structures for quantum cascade lasers," B. Witzigmann, M. Osinski, F. Henneberger, and Y. Arakawa, eds., p. 89800T.
227. Sudradjat, F., Zhang, W., Driscoll, K., Liao, Y., Bhattacharyya, A., Thomidis, C., Zhou, L., Smith, D. J., Moustakas, T. D., and Paiella, R., 2010, "Sequential tunneling transport characteristics of GaN/AlGaN coupled-quantum-well structures," *Journal of Applied Physics*, **108**(10), p. 103704.
228. Sun, G., Khurgin, J. B., and Tsai, D. P., 2013, "Spoof plasmon waveguide enabled ultrathin room temperature THz GaN quantum cascade laser: A feasibility study," *Optics Express*, **21**(23), p. 28054.
229. Chou, H., Anwar, M., and Manzur, T., 2012, "Active layer design and power calculation of nitride-based THz quantum cascade lasers," *Proceedings of SPIE*, **8268**, p. 82680O.
230. Yasuda, H., Hosako, I., and Hirakawa, K., 2012, "Designs of GaN-based terahertz quantum cascade lasers for higher temperature operations," 2012 Conference on Lasers and Electro-Optics (CLEO).
231. Terashima, W., and Hirayama, H., 2011, "Spontaneous emission from GaN/AlGaN terahertz quantum cascade laser grown on GaN substrate," *Physica Status Solidi (c)*, **8**(7–8), pp. 2302–2304.
232. Terashima, W., and Hirayama, H., 2011, "Terahertz intersubband electroluminescence from GaN/AlGaN quantum cascade laser structure on AlGaN template," 2011 36th International Conference on Infrared, Millimeter and Terahertz Waves (IRMMW-THz).
233. Terashima, W., and Hirayama, H., 2010, "The utility of droplet elimination by thermal annealing technique for fabrication of GaN/AlGaN terahertz quantum cascade structure by radio frequency molecular beam epitaxy," *Applied Physics Express*, **3**(12), p. 125501.
234. Hirayama, H., and Terashima, W., 2013, "Recent progress toward realizing GaN- based THz quantum cascade laser," *Proceedings of SPIE*, **8993**, p. 89930G–89930G–9.

AU: Book title, publisher name and publisher location are missing for reference 226. Please provide.

AU: Please confirm if the insertion of journal title and volume number is correct.

Annex 3

Phys. Status Solidi A **211**, No. 4, 761–764 (2014) / **DOI** 10.1002/pssa.201300431

physica status solidi a
www.pss-a.com
applications and materials science

THz intersubband transitions in AlGaN/GaN multi-quantum-wells

Mark Beeler*[,1], Catherine Bougerol[2], Edith Bellet-Amalaric[1], and Eva Monroy[1]

[1] CEA-CNRS Group «Nanophysique et Semiconducteurs», INAC-SP2M, CEA-Grenoble, 17 rue des Martyrs, 38054 Grenoble Cedex 9, France
[2] CEA-CNRS Group «Nanophysique et Semiconducteurs», Institut Néel-CNRS, 25 rue des Martyrs, 38042 Grenoble Cedex 9, France

Received 21 August 2013, revised 4 November 2013, accepted 24 January 2014
Published online 20 February 2014

Keywords GaN, intersubband, quantum well, terahertz

* Corresponding author: e-mail mark.beeler@cea.fr, Phone: +33(0)438782389, Fax: +33(0)438785197

Various designs of AlGaN/GaN structures displaying intersubband absorption in the THz spectral range are reported upon. Firstly, samples with 3-layer quantum wells (step-quantum-wells) displaying far-infrared intersubband absorption are presented. Theoretical analysis of the reproducibility issues associated to this architecture is done, and a more robust design based on 4-layer quantum wells is proposed. Such a structure has been fabricated by plasma-assisted molecular-beam epitaxy using two Al effusion cells to produce three AlGaN concentrations, without growth interruptions. Samples have been structurally validated by transmission electron microscopy and X-ray diffraction. Fourier transform infrared spectroscopy measurements show far-infrared absorption of TM-polarized light, which gets broader and deeper for increasing doping levels.

© 2014 WILEY-VCH Verlag GmbH & Co. KGaA, Weinheim

1 Introduction The THz spectral region is currently under intense study due to its potential applications in material characterization, security screening, medical diagnosis, or radar. The generation/detection of THz radiation using solid-state devices faces many roadblocks from a technological standpoint because of the low energy of the electronic transitions involved, and because of the ultra-high frequencies in relation to conventional microelectronics. GaAs-based quantum cascade lasers operating in this spectral range are limited by intrinsic material properties, namely the longitudinal-optical (LO) phonon, which exists at 36 meV (34 μm). This phonon has motivated research on the AlGaN system, which has a large LO-phonon energy (92 meV, 13 μm) that theoretically permits room-temperature operation of quantum cascade lasers [1–3], and the fabrication of intersubband (ISB) devices covering the 5–10 THz band, inaccessible to As-based technologies.

Using ISB optical transitions in GaN-based structures, reliable devices have been designed to operate in the near-infrared spectral range, particularly at telecommunication wavelengths [4]. Using AlGaN/GaN quantum wells (QWs) it is possible to decrease the ISB transitional energy to the outskirts of the far infrared [5–10]. This can be done by reducing the height of the quantum barriers and increasing the size of the QWs. However, in large QWs, the internal electric field associated to the spontaneous and piezoelectric polarization discontinuities in the GaN/AlGaN system become the dominating characteristic for determining the energy levels. Machhadani et al. [11] proposed a way to decrease the effect of the internal electric field by creating a 3-layer well (step-QW) with a virtually flat potential profile. This approach has been explored by Wu et al. [12], who found that the creating this flat band structure is very sensitive to small changes in aluminum concentration and well depth. Despite these deficiencies, ISB transitions in the THz region have been reported [11], and a QW infrared photodetector has been demonstrated [13].

In this work, we discuss the properties of AlGaN-based QWs designed to present ISB electronic transitions in the THz spectral range. We demonstrate ISB absorption in the THz range in samples with step-QWs, and we theoretically analyze the reproducibility issues associated to this architecture. As an improvement, we propose a more robust design based on a 4-layer QW. The structure has been realized by PAMBE, and shows distinct absorption of TM-polarized light centered around 25–30 μm.

© 2014 WILEY-VCH Verlag GmbH & Co. KGaA, Weinheim

2 Experimental Theoretical calculations of the electronic profiles were performed using the self-consistent nextnano^3 8-band $k \cdot p$ Schrödinger–Poisson solver [14] with the material parameters in Ref. [15], neglecting all the bowing parameters for AlGaN, and assuming the structure strained on GaN (unless indicated).

Samples were synthesized by PAMBE on GaN templates on float-zone Si (111) to evade problems of substrate transparency [5]. These templates incorporate a complex buffer layer to manage the thermal expansion and lattice parameters between GaN and Si. To simplify the structural characterization, identical samples were grown simultaneously on 1-μm-thick AlN-on-sapphire templates. During the deposition, the flux of active nitrogen was fixed at 0.32 monolayers per second and the growth temperature was $\sim$720 °C. All the layers were grown under self-regulated Ga-rich conditions [15].

The samples were analyzed by high-angle annular dark field scanning transmission electron microscopy (HAADF-STEM) performed in an FEI Titan 80–300 microscope working at 200 kV. An ABSF filter was used to discern the small variations of contrast between the layers, which are associated to the small alloy compositional changes. High-resolution X-ray diffraction (HRXRD) measurements were carried out in a Seifert XRD 3003 PTS-HR system, with a beam concentrator in front of the Ge(220) four-bounce monochromator, and a Ge(220) two-bounce analyzer inserted in front of the detector.

ISB absorption was probed by Fourier transform infrared spectroscopy (FTIR) with a Bruker V70v spectrometer using an Hg lamp and a Si bolometer. To account for the ISB transition selection rules, the sample facets were polished at a 60° angle to form a multi-pass waveguide with 3–4 total internal reflections.

3 Results and discussion

3.1 The step-quantum-well design Figure 1a shows the conduction band diagram of a step-QW design [in this example consisting of $Al_{0.1}Ga_{0.9}N$/GaN/$Al_{0.05}Ga_{0.95}N$ (3 nm/3 nm/13 nm)], and indicates the first and second electronic levels with their respective squared wave functions (Ψ^2). This 3-layer structure is designed around the principle of polarization equivalency. The design can be broken effectively into two portions; the first is the "barrier", which comprises of the high-Al-content $Al_xGa_{1-x}N$ layer and the GaN layer. The second portion is the "well", which is the low-Al-content $Al_xGa_{1-x}N$ layer. The design creates a semi-flat band in the "well" by having the "barrier" balanced at the same average Al percentage, i.e. the average polarization in the "barrier" is approximately equal to the average polarization in the "well". This allows the structure to have variations in conduction band edge, and therefore electron confinement, but it ensures a negligible internal electric field in the "well". However, the asymmetry of the design leads to the confinement of $\Psi^2(e_1)$ close to the GaN layer, while the bimodality of $\Psi^2(e_2)$ has the largest electron density within the middle of the "well". This forces the ISB transitions to be mainly diagonal and lowers the overall oscillator strength.

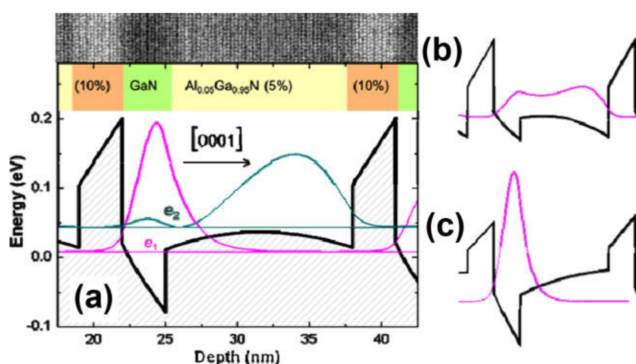

Figure 1 (a) Conduction band profile, and first (e_1) and second (e_2) electronic levels with their associated squared wave functions for an $Al_{0.1}Ga_{0.9}N$/GaN/$Al_{0.05}Ga_{0.95}N$/GaN (3 nm/3 nm/13 nm) step QW. On top, HAADF-STEM image of one period of the grown structure. (b) Shift of the wave function of the first electronic level [$\Psi^2(e_1)$] associated to a variation of the Al concentration in the "well" layer. A lower "well" Al concentration creates a secondary confinement area at the opposite side of the well. (c) A higher "well" Al concentration creates a more triangular well and increases confinement towards the GaN layer.

Starting from the base structure in Fig. 1a, minor changes in layer thickness can cause perturbations leading to the narrowing or broadening of Ψ^2, but the relative location of the electron density peak for e_2 and e_1 remains stationary. However, changing the aluminum concentration within the layers breaks the polarization balance, and causes a shift in the location of the electron density function, and in the ISB transitional energy. A decrease in the Al mole fraction of the "well" results in the formation of a secondary point of low conduction band energy at the interface between the high-Al-content barrier layer and the "well", as illustrated in Fig. 1b. This low point competes for Ψ^2 and turns e_1 into a bimodal distribution. On the other hand, with an increase in the "well" Al content, the electric field in the "well" pushes Ψ^2 towards the GaN layer and increases the confinement, as shown in Fig. 1c.

Following the step-QW design, a series of samples have been fabricated consisting of 40 periods of $Al_{0.1}Ga_{0.9}N$/GaN/$Al_{0.05}Ga_{0.95}N$ (3 nm/3 nm/13 nm) QWs. The GaN layer was either non-intentionally doped or doped with $[Si] = 3.0 \times 10^{19}$ cm^{-3}. A HAADF-STEM image of the structure on top of the band diagram in Fig. 1a illustrates the agreement of the thicknesses and chemical contrast with the nominal structure. HRXRD measurements in Fig. 2a confirm a periodicity of 18.6 ± 0.2 nm.

The samples were then tested using a Fourier transform infrared spectrometer. Measurements were performed at a temperature $T = 5$–10 K. The ISB absorption is identified as a dip in the transmission spectra for TM-polarized light, that appears centered at 22 μm in the figure. The predicted value for this structure was calculated to be 36 μm. Such a deviation can be explained considering realistic deviations in the epitaxial growth: An error bar of $\pm$10% in the aluminum

© 2014 WILEY-VCH Verlag GmbH & Co. KGaA, Weinheim

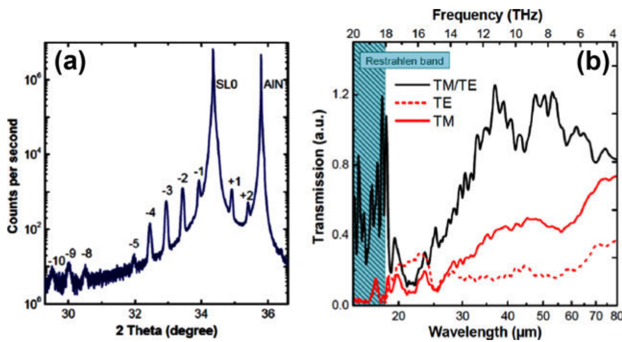

Figure 2 (a) HRXRD $\omega-2\theta$ scan of the (0002) reflection of the step-QW structure grown on an AlN-on-sapphire template. (b) Far-infrared transmission for TE- and TM-polarized light. The noise observed for wavelengths <18 µm is due to the GaN Restrahlen absorption. The TM/TE transmission ratio presents a minimum at 22 µm, which is attributed to ISB absorption.

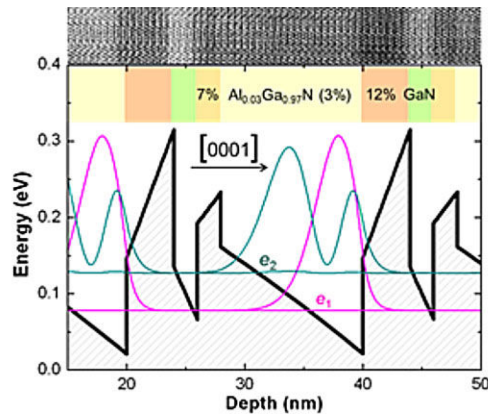

Figure 3 Conduction band profile for an $Al_{0.1}Ga_{0.9}N$/GaN/$Al_{0.07}Ga_{0.93}N$/$Al_{0.03}Ga_{0.97}N$ (4 nm/2 nm/2 nm/12 nm) 4-layer-QW design. On top, HAADF-STEM image of one period of the grown structure.

mole fraction in the $Al_xGa_{1-x}N$ well (i.e. $Al_{0.055}Ga_{0.945}N$ instead of $Al_{0.050}Ga_{0.950}N$) can induce up to 40% variance in the ISB transition energy.

3.2 The 4-layer quantum well design As discussed above, the e_2–e_1 ISB transition energy in the step-QW design is very sensitive to variations of the Al mole fraction of the layers, even within the uncertainties associated to PAMBE growth. Such a problem is due to the fact that the design is based on a very delicate polarization balance between the "barrier" and the "well". Furthermore, the effect of the GaN layer on the e_1 wave function is difficult to engineer. To surmount these limitations, we propose a modified design with an additional AlGaN layer to separate the GaN layer from the "well" [16]. This "separation layer" is designed so that there is no confined state in the GaN layer. In this architecture, the polarization is not fully compensated, which results in a triangular profile in the active well, but greatly increases the robustness of the system. The design, consisting of a 4-layer $Al_{0.1}Ga_{0.9}N$/GaN/$Al_{0.07}Ga_{0.93}N$/$Al_{0.03}Ga_{0.97}N$ (4 nm/2 nm/2 nm/12 nm) sequence, can be seen in Fig. 3. The structure can be synthesized by PAMBE through the use of two Al cells.

The robustness of this system with respect to the uncertainties associated to PAMBE growth has been analyzed in Fig. 4, and compared to the step-QW design. The figure shows the theoretical value of the ISB wavelength as the five vertices of a regular pentagon. Each vertex has a structural parameter associated to it. Such parameters were varied considering realistic deviations in the epitaxial growth: ±2 monolayers (2ML ~ 0.5 nm) as the error bar for thicknesses and ±10% as the error bar for the aluminum content in $Al_xGa_{1-x}N$. The colored area represents the minimum and maximum values of the ISB transition wavelength associated to the indicated variation of structural parameters along each radial axis. The smaller area associated to the 4-layer QW in the figure demonstrates that this design is much more robust than the step-QW structure. The ISB dependence on the thickness and composition of the "separation layer" has also been analyzed, and has been shown to exhibit the same robustness as the rest of the system [16].

The robustness of the 4-layer structure is due to the fact that the profile of Ψ^2 does not change significantly within the error bars associated to the PAMBE growth. The e_1 energy level always remains confined near the edge of the layers with 3 and 10% Al content. The e_2 energy level is also confined within the triangular quantum well, and does not drastically change in shape or position while changing the design parameters. A major benefit of this design is that there is the significant spatial overlap between the e_1 and e_2 wave functions. This translates into an increase in the

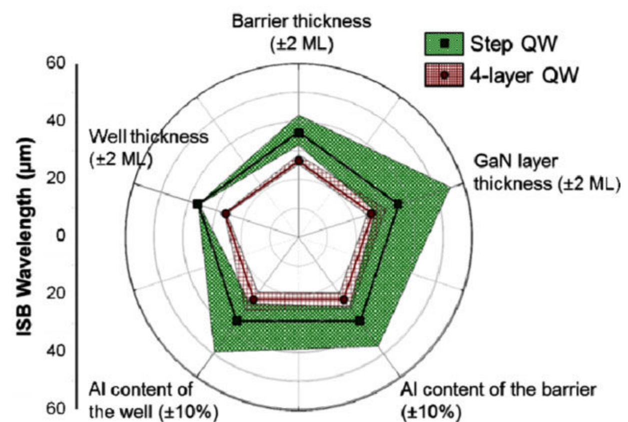

Figure 4 Illustration of the robustness of the 4-layer-QW system compared with the step-QW design. In each case, the dots indicate the nominal ISB transitional wavelength. The colored area represents the variation between the minimum and maximum values of the ISB transition wavelength associated to the indicated variation of structural parameters along each axis. The "Barrier" is $Al_{0.1}Ga_{0.9}N$, while the "Well" is the $Al_{0.03}Ga_{0.97}N$ or the $Al_{0.05}Ga_{0.95}N$ for the 4-layer and step-QW designs, respectively.

© 2014 WILEY-VCH Verlag GmbH & Co. KGaA, Weinheim

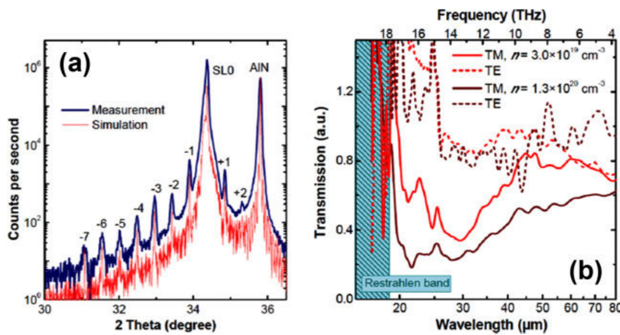

Figure 5 (a) HRXRD $\omega-2\theta$ scan of the (0002) reflection of a 4-layer-QW structure grown on an AlN-on-sapphire template. The experimental measurement is compared with simulations using the X'Pert Epitaxy software. (b) Far-infrared transmission measurement of 4-layer QWs with different doping levels for TE- and TM-polarized light. Measurements were performed at 5–10 K. The noise observed for wavelengths $<18\,\mu$m is due to GaN Restrahlen absorption. The dip in the TM-polarized transmission at 25–30 µm is assigned to the ISB absorption.

oscillator strength by a factor of three over the step-QW design.

This modified geometry has been synthesized with various doping concentrations in the GaN layer (non-intentionally doped, and $[\mathrm{Si}]=3.0\times10^{19}\,\mathrm{cm}^{-3}$, and $1.3\times10^{20}\,\mathrm{cm}^{-3}$) were synthesized, and characterized by HAADF-STEM, HRXRD, and FTIR (Figs. 3 and 5a and b, respectively). Structural characterization confirms a periodicity of 19.7 ± 0.2 nm (versus the nominal 20 nm). The transmission dip at 25–30 µm for TM-polarized light seen in Fig. 5b is assigned to ISB absorption, theoretically predicted at 26.5 µm. Consistently, this feature is not observed in an undoped reference, and it becomes broader and deeper for increasing doping levels.

The incorporation of the separation layer results in a geometry where the internal electric field is not fully compensated, i.e. the QW keeps a triangular potential profile. As a result, the tunability of this design towards longer wavelengths is partially sacrificed. Increasing the well thickness to 40 nm, for instance, should shift the absorption wavelength towards 70 µm. Extension to longer wavelengths with layer thickness below 20 nm requires drastically modified geometries.

The normalized absorption line width for the sample with a doping level $[\mathrm{Si}]=3.0\times10^{19}\,\mathrm{cm}^{-3}$ is $\Delta f/f<0.3$, which is an improvement in comparison to previous results in step QWs in Ref. [11] ($\Delta f/f\sim0.5$). Unfortunately, the results in Fig. 2b are spectrally distorted from the Restrahlen band, rendering direct comparison inutile. In the 4-layer QW sample with a higher doping level ($[\mathrm{Si}]=1.3\times10^{20}\,\mathrm{cm}^{-3}$), the enhanced broadening is associated to the higher carrier concentration.

4 Conclusions We have theoretically analyzed the reproducibility issues associated to the step-QW architecture for GaN/AlGaN ISB absorbers in the far infrared. As an improvement, we have introduced a modified design of GaN-based ISB absorber for the THz spectral range consisting of a 4-layer QW structure. Particular attention was paid to the robustness of the design regarding the uncertainties associated to the growth. The structure has been realized by PAMBE, and shows distinct absorption of TM-polarized light centred around 25–30 µm. This absorption gets deeper and broader with increasing doping levels, and is consistent with the predicted ISB transition.

Acknowledgements The authors would like to thank Y. Curé, Y. Genuist, J. Dussaud, and D. Boilot for their technical support. This work is supported by the EU ERC-StG "TeraGaN" (#278428) project.

References

[1] E. Bellotti, K. Driscoll, T. D. Moustakas, and R. Paiella, J. Appl. Phys. **105**, 113103 (2009).
[2] W. Terashima and H. Hirayama, Phys. Status Solidi C **6**, S615 (2009).
[3] B. Mirzaei, A. Rostami, and H. Baghban, Opt. Laser Technol. **44**, 378 (2012).
[4] M. Beeler, E. Trichas, and E. Monroy, Semicond. Sci. Technol. **28**, 074022 (2013).
[5] P. K. Kandaswamy, H. Machhadani, C. Bougerol, S. Sakr, M. Tchernycheva, F. H. Julien, and E. Monroy, Appl. Phys. Lett. **95**, 141911 (2009).
[6] N. Péré-Laperne, C. Bayram, L. Nguyen-The, R. McClintock, and M. Razeghi, Appl. Phys. Lett. **95**, 131109 (2009).
[7] P. K. Kandaswamy, H. Machhadani, Y. Kotsar, S. Sakr, A. Das, M. Tchernycheva, L. Rapenne, E. Sarigiannidou, F. H. Julien, and E. Monroy, Appl. Phys. Lett. **96**, 141903 (2010).
[8] C. Bayram, J. Appl. Phys. **111**, 013514 (2012).
[9] C. Edmunds, L. Tang, J. Shao, D. Li, M. Cervantes, G. Gardner, D. N. Zakharov, M. J. Manfra, and O. Malis, Appl. Phys. Lett. **101**, 102104 (2012).
[10] W. Tian, W. Y. Yan, X. Hui, S. L. Li, Y. Y. Ding, Y. Li, Y. Tian, J. N. Dai, Y. Y. Fang, Z. H. Wu, C. H. Yu, and C. Q. Chen, J. Appl. Phys. **112**, 063526 (2012).
[11] H. Machhadani, Y. Kotsar, S. Sakr, M. Tchernycheva, R. Colombelli, J. Mangeney, E. Bellet-Amalric, E. Sarigiannidou, E. Monroy, and F. H. Julien, Appl. Phys. Lett. **97**, 191101 (2010).
[12] F. Wu, W. Tian, W. Y. Yan, J. Zhang, S. C. Sun, J. N. Dai, Y. Y. Fang, Z. H. Wu, and C. Q. Chen, J. Appl. Phys. **113**, 154505 (2013).
[13] F. F. Sudradjat, W. Zhang, J. Woodward, H. Durmaz, T. D. Moustakas, and R. Paiella, Appl. Phys. Lett. **100**, 241113 (2012).
[14] S. Birner, T. Zibold, T. Andlauer, T. Kubis, M. Sabathil, A. Trellakis, and P. Vogl, IEEE Trans. Electron Dev. **54**, 2137 (2007).
[15] P. K. Kandaswamy, F. Guillot, E. Bellet-Amalric, E. Monroy, L. Nevou, M. Tchernycheva, A. Michon, F. H. Julien, E. Baumann, F. R. Giorgetta, D. Hofstetter, T. Remmele, M. Albrecht, S. Birner, and L. S. Dang, J. Appl. Phys. **104**, 093501 (2008).
[16] M. Beeler, C. Bougerol, E. Bellet-Amalric, and E. Monroy, Appl. Phys. Lett. **103**, 091108 (2013).

© 2014 WILEY-VCH Verlag GmbH & Co. KGaA, Weinheim

Annex 4

APPLIED PHYSICS LETTERS **103**, 091108 (2013)

Terahertz absorbing AlGaN/GaN multi-quantum-wells: Demonstration of a robust 4-layer design

M. Beeler,[1] C. Bougerol,[2] E. Bellet-Amalric,[1] and E. Monroy[1]
[1]*CEA-CNRS Group "Nanophysique et semiconducteurs," INAC-SP2M, CEA-Grenoble, 17 rue des Martyrs, 38054 Grenoble Cedex 9, France*
[2]*CEA-CNRS Group "Nanophysique et Semiconducteurs," Institut Néel-CNRS, 25 rue des Martyrs, 38042 Grenoble Cedex 9, France*

(Received 1 July 2013; accepted 19 August 2013; published online 29 August 2013)

We report on AlGaN/GaN multi-quantum-well structures displaying intersubband absorption in the THz spectral range. First, we theoretically analyze the weaknesses of the state-of-the-art GaN-based step-quantum-well architecture from an optoelectronic standpoint. We then propose a modified geometry with improved structural robustness considering the uncertainties associated to the growth. This later structure, consisting of 4-layer quantum wells, has been grown by plasma-assisted molecular-beam epitaxy and characterized structurally and optically. Low temperature absorption of samples with different Si doping levels confirms intersubband transitions in the far-infrared, centred at 28 μm. © *2013 AIP Publishing LLC*. [http://dx.doi.org/10.1063/1.4819950]

Wide-bandgap AlGaN/GaN heterostructures are intensively studied as a promising alternative to replace GaAs as the dominant material in solid-state THz optoelectronics. GaAs-based quantum cascade lasers operating in this spectral range are limited by intrinsic material properties, namely the LO phonon, which exists at 36 meV (34 μm). On the contrary, the large energy of GaN longitudinal-optical phonons (92 meV, 13 μm) opens prospects for GaN-based high-temperature THz quantum cascade lasers[1–5] and other intersubband (ISB) devices covering the 5–10 THz band, inaccessible to As-based technologies.

ISB transitions in GaN/AlGaN multi-quantum-wells (MQWs) can be tuned from 1.0 μm to 10 μm by reducing the Al mole fraction in the barriers and increasing the quantum well (QW) width[6–12] (see Ref. 13 for a review). This strategy faces a roadblock at longer wavelengths because of the quantum confined Stark effect (QCSE) present in these polar materials. The polarization-induced internal electric field results in QWs with a triangular profile, and the lower energy electronic levels get confined into a small fraction of the QW, so that changes in well width do not induce proportional changes in ISB energy. Therefore, to shift the absorption towards longer wavelengths, it is necessary to engineer the conduction band to reduce the internal electric field within the QWs. This has led to a 3-layer step-QW architecture aimed to flatten the band structure of the QW.[14] Following this design, ISB transitions in the THz region have been reported,[14] and a QW infrared photodetector has been demonstrated.[15] However, this design suffers from issues with reproducibility and the inability to easily predict the ISB transitional energy. To progress towards more complex and performing devices, it is therefore important to introduce a different architecture with a higher robustness with regard to the growth uncertainties.

In this work, we discuss the properties of AlGaN-based MQWs designed for ISB optoelectronics in the THz spectral range. We analyse the reproducibility issues associated to the current step-QW architecture, and we propose an alternative, robust design based on a 4-layer QW. We demonstrate that this structure, fabricated by plasma-assisted molecular-beam epitaxy (PAMBE), presents TM-polarized ISB absorption at 26 μm, with magnitude and line width that increases with the doping level.

The experimentally observed reproducibility problems associated to the step-QW geometry were analyzed theoretically using the self-consistent nextnano[3] 8-band k·p Schrödinger-Poisson solver.[16] Calculations were performed using the material parameters in Ref. 17, neglecting all the bowing parameters for AlGaN, and assuming the structure strained on GaN. Figure 1 illustrates the electronic profile of an $Al_{0.05}Ga_{0.95}N/Al_{0.1}Ga_{0.9}N/GaN$ (10 nm/3 nm/3 nm) step-QW, which presents an energy difference between the first and the second electronic levels of 35 meV (35.6 μm), a significant deviation from the measured value of 17.5 meV (70 μm).[14] The robustness of this system with respect to the uncertainties associated to PAMBE growth has been analyzed in Figure 1. There are 5 degrees of freedom within the structure, namely the thickness of each layer and the Al mole fraction in each $Al_xGa_{1-x}N$ layer. Each degree of freedom was varied considering realistic deviations in the epitaxial growth: ± 2 monolayers (ML) as the error bar for thicknesses and $\pm 10\%$ as the error bar for the aluminium mole fraction in $Al_xGa_{1-x}N$, which corresponds to a temperature difference of $\pm 4\,^{\circ}C$ for the Al effusion cells in the compositional range of this design. While some parameters evoke little variance, errors induced upon the GaN well width and the Al concentration in the step-QW induce a drastic change in ISB wavelength, which can reach up to 40% variance, from 35 μm to 50 μm.

This 3-layer structure is designed around the principle of band edge equivalency. The step-QW can be broken effectively into two portions: the first is the "barrier," which comprises of the high-Al-content $Al_xGa_{1-x}N$ layer and the GaN layer. The second portion is the well, which is the low-Al-content $Al_xGa_{1-x}N$ layer. Having the "barrier" *balanced* at the same average Al percentage as the well ensures semi-flat band conditions in the well. This configuration is associated to the minimum energy spacing between the ground

This article is copyrighted as indicated in the article. Reuse of AIP content is subject to the terms at: http://scitation.aip.org/termsconditions. Downloaded to IP: 132.168.8.249 On: Wed, 08 Apr 2015 12:42:05

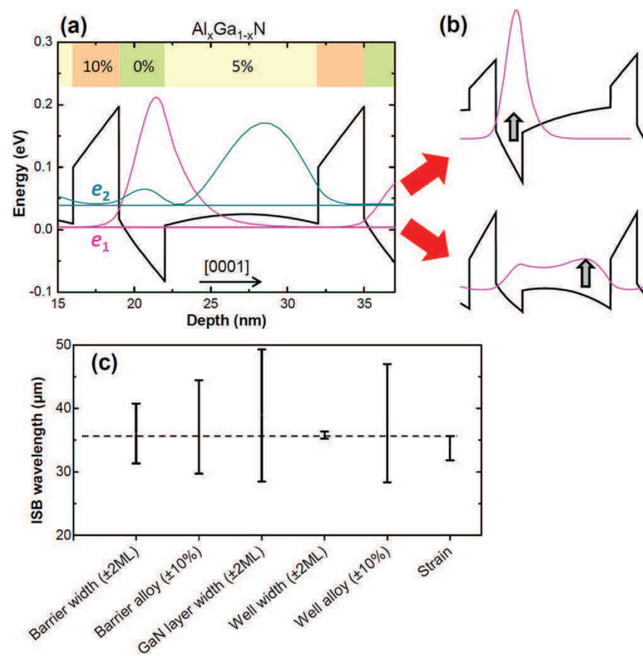

FIG. 1. (a) Conduction band profile, and first (e_1) and second (e_2) electronic levels with their associated wave functions for an $Al_{0.05}Ga_{0.95}N/Al_{0.1}Ga_{0.9}N/GaN$ (10 nm/3 nm/3 nm) step QW. (b) Shift of the wavefunction of the first electronic level associated to a variation of the Al concentration in the well layer. A higher step-well Al concentration (top) creates a more triangular well and increases confinement towards the GaN layer. A lower step-well Al concentration (down) creates a secondary confinement area at the opposite side of the well. To illustrate the effect clearly, the band profiles corresponds to $Al_{0.07}Ga_{0.93}N/Al_{0.1}Ga_{0.9}N/GaN$ (10 nm/3 nm/3 nm) (top) and $Al_{0.03}Ga_{0.97}N/Al_{0.1}Ga_{0.9}N/GaN$ (10 nm/3 nm/3 nm) (bottom). (c) Illustration of the robustness of the step-QW system. The dashed line indicates the nominal transition wavelength for an $Al_{0.05}Ga_{0.95}N/Al_{0.1}Ga_{0.9}N/GaN$ (10 nm/3 nm/3 nm) step QW. The error bars represent the minimum and maximum values attributed to the uncertainties associated to growth. The barrier and GaN well thicknesses were changed from 3 nm to 2.5 nm and 3.5 nm. The barrier Al content was changed from 10% to 11% and 9%. The step well alloy was changed from 5% to 4.5% and 5.5% (±10%). The step well thickness was changed from 10 nm to 12 nm and 8 nm. The strain error bar illustrates the variation of the ISB transition when evolving from a structure fully strained on GaN to a structure fully strained on $Al_{0.1}Ga_{0.9}N$.

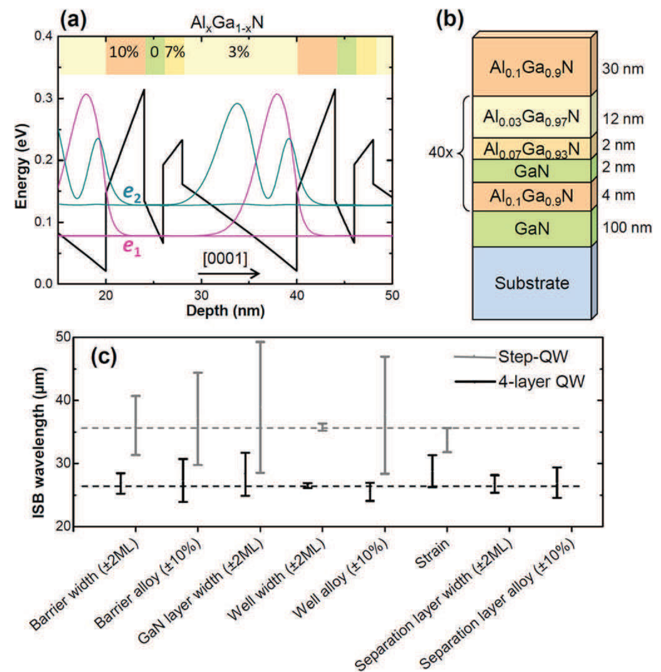

FIG. 2. (a) Conduction band profile, and first (e_1) and second (e_2) electronic levels with their associated wave functions for an $Al_{0.1}Ga_{0.9}N/GaN/Al_{0.07}Ga_{0.93}N/Al_{0.03}Ga_{0.97}N$ (4 nm/2 nm/2 nm/12 nm) 4-layer-QW design. (b) Schematic drawing of the structure synthesized by PAMBE. (c) Illustration of the robustness of the 4-layer-QW system (black) compared with the step-QW (gray). The dashed lines indicate the nominal transition wavelengths for an $Al_{0.05}Ga_{0.95}N/Al_{0.1}Ga_{0.9}N/GaN$ (10 nm/3 nm/3 nm) step QW and an $Al_{0.1}Ga_{0.9}N/GaN/Al_{0.07}Ga_{0.93}N/Al_{0.03}Ga_{0.97}N$ (4 nm/2 nm/2 nm/12 nm) 4-layer QW. The error bar represents the minimum and maximum values attributed to the uncertainties associated to growth. In the 4-layer-QW, the barrier thickness was changed from 2 nm to 1.5 nm and 2.5 nm. The barrier Al content was changed from 10% to 11% and 9%. The GaN layer thickness was changed from 2 nm to 1.5 nm and 2.5 nm. The well thickness was changed from 12 nm to 11.5 nm and 12.5 nm, and its Al content was changed from 3% to 2.7% and 3.3% (±10%). The separation layer thickness was changed from 2 nm to 1.5 nm and 2.5 nm, and its Al content was changed from 7% to 6.3% and 7.7%. The strain error bar illustrates the variation of the ISB transition when evolving from a structure fully strained on GaN to a structure fully strained on $Al_{0.1}Ga_{0.9}N$.

electronic state and the first excited state, as described in Ref. 18. The weakness of this design lies in the fact that any deviation from this balance results in an internal electric field in the well, which shifts the wavefunction associated to the first electronic level towards the GaN layer (Fig. 1(b) top, for higher Al content in the well) or towards the high-Al-content layer (Fig. 1(b) down, for lower average Al content in the well). Thus, any imbalance in the structure has a drastic effect on the ISB wavelength.

To surmount the limitations of the step-QW configuration, we propose a design which includes the insertion of an additional AlGaN layer to separate the GaN layer from the low-Al-content $Al_xGa_{1-x}N$ well. The "separation layer" is designed so that there is no confined state in the GaN layer. This architecture, described in Fig. 2(a), does not evade the quantum confined Stark effect, but the GaN layer contributes to reduce the average spontaneous polarization of the complex barrier structure ($Al_{0.1}Ga_{0.9}N/GaN/Al_{0.07}Ga_{0.93}N$), which results in a lower electric field in the QW. The robustness of this design is analyzed in Fig. 2(c) and shows much less variation of the ISB transition energy than the step-QW architecture with respect to the growth uncertainties. The "separation layer" also has an inherent robustness on the order of the rest of the structure and should not affect the overall robustness of the system.

The incorporation of separation layer results in a geometry where the internal electric field is not fully compensated, i.e., the QW keeps a triangular potential profile. As a result, this 4-layer MQW system is more sensitive to changes in strain state versus the step-QW design. The strain error bar in Fig. 2(c) illustrates the variation of the ISB transition when evolving from a structure fully strained on GaN to a structure fully strained on $Al_{0.1}Ga_{0.9}N$.[19] These error bars are comparable to those generated by uncertainties in the structural parameters. However, the MQWs are expected to evolve towards a minimum elastic energy configuration independently of the substrate,[20] so that the uncertainty in the strain state of the structure (neglecting the initial relaxation) is much smaller (<±0.025% variation of the in-plane lattice parameter) than the values simulated in Fig. 2(c) (±0.12%).

An additional effect of the internal electric field is the localization of the wave functions, which affects the oscillator strength of the ISB transitions. In the 4-layer MQW

This article is copyrighted as indicated in the article. Reuse of AIP content is subject to the terms at: http://scitation.aip.org/termsconditions. Downloaded to IP: 132.168.8.249 On: Wed, 08 Apr 2015 12:42:05

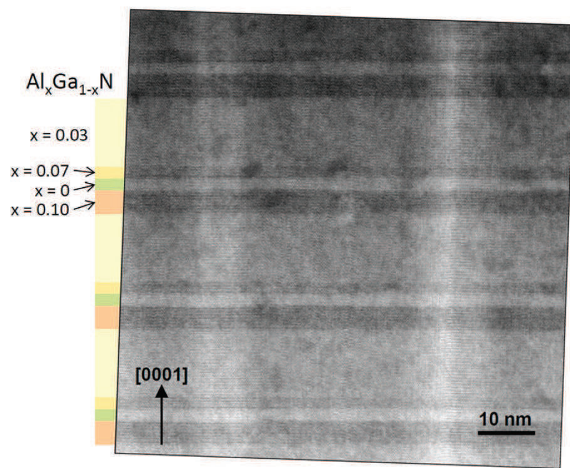

FIG. 3. HAADF-STEM image showing several 4-layer-QWs in a non-intentionally doped sample with structure described in Fig. 2(b).

design, both e1 and e2 are shifted in the [0001] direction [see Fig. 2(a)], which translates into a large oscillator strength. In contrast, the e1 of the step-QW design experiences a shift in the [000-1] direction, while e2 shifts in the [0001] direction [see Fig. 1(a)], which creates a mismatch between the first and second localized states and translates into lower oscillator strength. Simulations show that the oscillator strength of the e_1-e_2 transition within the 4-layer MQW system is about three times larger than that of the step-QW configuration.

AlGaN/GaN 40-period MQW structures following the 4-layer MQW design in Fig. 2(b) were synthesized by PAMBE on GaN templates on float-zone Si (111) to evade problems of substrate transparency.[7] These templates incorporate a complex buffer layer to manage the thermal expansion and lattice mismatch between GaN and Si. To simplify the structural characterization, identical samples were grown simultaneously on 1-μm-thick (0001)-oriented AlN-on-sapphire templates. During the deposition, the flux of active nitrogen was fixed at 0.32 ML/s, and the growth temperature was $\sim$720 °C as deduced from the Ga desorption time. The three Al concentrations were obtained using two PAMBE cells, where one flux was set to 0.03×0.32 ML/s and the second was set to 0.07×0.32 ML/s. The third Al concentration (10%) is obtained from the summation of the two fluxes. All the layers were deposited under self-regulated Ga-rich conditions[17] without growth interruptions. This growth method allows for planar growth of (Al)GaN heterostructures with interface sharpness on the atomic scale. The GaN layers were Si-doped, in order to populate the first electronic levels in the structure. Four samples with different doping concentrations (non-intentionally doped, and $[Si] = 1.5 \times 10^{19}$ cm^{-3}, 3.0×10^{19} cm^{-3}, and 1.3×10^{20} cm^{-3}) were synthesized. Figure 3 depicts four periods of the non-intentionally doped structure viewed by high-angle annular dark field scanning transmission electron microscopy (HAADF-STEM) performed in an FEI Titan 80–300 microscope working at 200 kV. An Average Background Subtraction filter was used to discern the small variations in contrast between the layers, which are associated to the alloy compositional changes. The layer thicknesses obtained from the image are 42 ML $Al_{0.03}Ga_{0.97}N$/7 ML $Al_{0.07}Ga_{0.93}N$/7 ML GaN/14 ML $Al_{0.1}Ga_{0.9}N$.

High-resolution x-ray diffraction (HRXRD) measurements were carried out in a Seifert XRD 3003 PTS-HR system, with a beam concentrator in front of the Ge(220) four-bounce monochromator and a Ge(220) two-bounce analyzer inserted in front of the detector. Figure 4 shows the ω-2θ scan of the (0002) and (0004) x-ray reflections and a reciprocal space map around the ($-$1015) reflection of the MQW structure doped with $[Si] = 3.0 \times 10^{19}$ cm^{-3} and grown on an AlN-on-sapphire template. From these measurements, we extract a superlattice period of 19.7 ± 0.2 nm. The experimental measurements in Figs. 4(a) and 4(b) are compared with a simulation using the X'Pert software, assuming an $Al_xGa_{1-x}N$/$Al_yGa_{1-y}N$/GaN/$Al_{x+y}Ga_{1-x-y}N$ (11.7 nm/2 nm/2 nm/4 nm) MQW period, where the layer thickness are proportional to

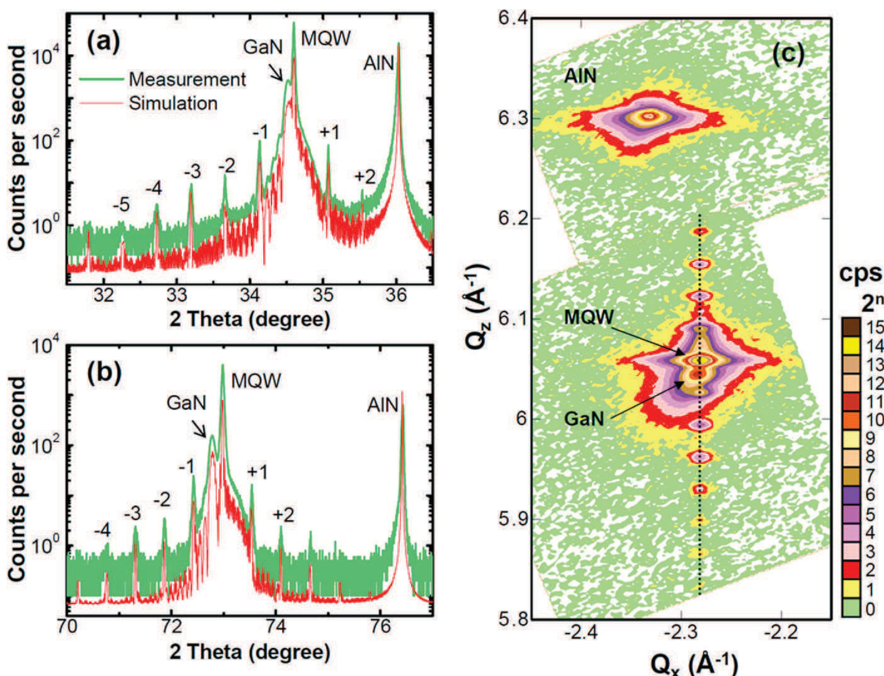

FIG. 4. HRXRD ω-2θ scans of the (a) (0002) reflection and (b) (0004) reflection of the MQW structure doped with $[Si] = 3.0 \times 10^{19}$ cm^{-3} and grown on an AlN-on-sapphire template, showing periodicity of 19.7 ± 0.2 nm. The experimental measurement is compared with simulations using the X'Pert Epitaxy software. (c) Reciprocal space map around the ($-$1015) reflection of the MQW structure.

This article is copyrighted as indicated in the article. Reuse of AIP content is subject to the terms at: http://scitation.aip.org/termsconditions. Downloaded to IP: 132.168.8.249 On: Wed, 08 Apr 2015 12:42:05

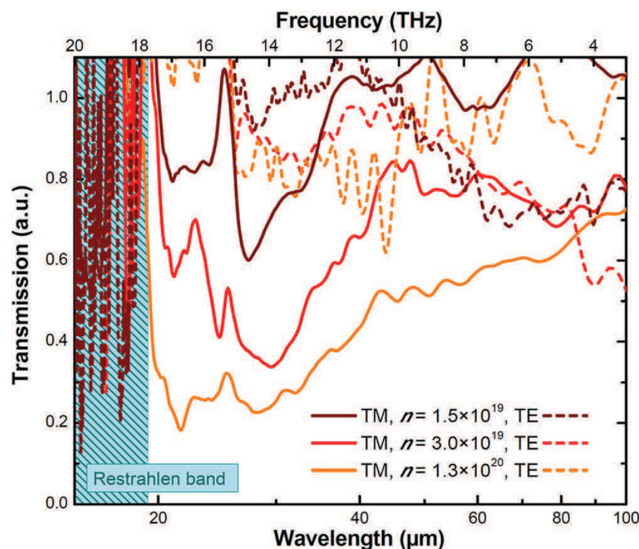

FIG. 5. Far-IR transmission measurement of 4-layer MQWs with different doping levels for TE- and TM-polarized light. The spectra have been normalized by the response of a similar undoped superlattice which exhibits no ISB activity. The noise observed for wavelengths $<10\,\mu$m is due to the GaN Restrahlen absorption. The dip in TM-polarized transmission at 27–30 μm is assigned to the transition between the first and the second electronic levels in the QWs.

the number of monolayers measured by HAADF-STEM. From the reciprocal space map in Fig. 4(c), we extracted the relaxation state of the GaN buffer (86% relaxed on the AlN substrate), and the in-plane lattice parameter of the MQWs which is almost totally strained on the GaN buffer layer. By adjusting the Al mole fractions in the MQWs to get a best fit to the (0002) and (0004) experimental diffractograms, we obtain $x = 0.025 \pm 0.005$ and $y = 0.07 \pm 0.01$. These values are in good agreement with the nominal values within the uncertainties considered above.

ISB absorption was probed by Fourier Transform Infrared spectroscopy (FTIR) with a Bruker V70v spectrometer using a Hg lamp and a Si bolometer. To account for the ISB transition selection rules, the sample facets were polished at a 60° angle to form a multi-pass waveguide with 3–4 total internal reflections. The four samples were tested in transmission mode using a far-IR polarizer to discern between TE and TM polarized light. Figure 5 shows the far-IR transmission spectra of the doped samples at low temperature ($T = 5$–10 K). In the sample with a lower doping level ($[\mathrm{Si}] = 1.5 \times 10^{19}\,\mathrm{cm}^{-3}$), we observe a TM-polarized absorption dip centred around 27–29 μm ($\sim$14 THz), which gets deeper and broader with increasing doping level. This absorption line is attributed to the transition from the first to the second electronic level in the QW, in good agreement with our theoretical calculations, which predict a transition at 26.5 μm. The normalized absorption line width for the sample with a doping level $[\mathrm{Si}] = 1.5 \times 10^{19}\,\mathrm{cm}^{-3}$ is $\Delta f/f \sim 0.25$, which is a significant improvement in comparison to results in step QWs ($\Delta f/f \sim 0.5$ in Ref. 14).

In conclusion, we have introduced a modified design of nitride-based ISB absorber for the THz spectral range consisting of a 4-layer MQW structure. Particular attention was paid to the robustness of the design with regarding the uncertainties associated to the growth. The structure has been realized by PAMBE and shows distinct absorption of TM-polarized light centred around 27–30 μm ($\sim$14 THz). This absorption gets deeper and broader with increasing doping levels and is consistent with the predicted electronic transition between the first and the second electronic levels in the QWs.

The authors would like to thank Y. Curé, Y. Genuist, J. Dussaud, and D. Boilot for their technical support. This work is supported by the EU ERC-StG "TeraGaN" (#278428) project.

[1]G. Sun, R. A. Soref, and J. B. Khurgin, Superlattices Microstruct. **37**, 107 (2005).

[2]N. Vukmirović, V. D. Jovanović, D. Indjin, Z. Ikonić, P. Harrison, and V. Milanović, J. Appl. Phys. **97**, 103106 (2005).

[3]E. Bellotti, K. Driscoll, T. D. Moustakas, and R. Paiella, J. Appl. Phys. **105**, 113103 (2009).

[4]W. Terashima and H. Hirayama, Phys. Status Solidi C **6**, S615 (2009).

[5]B. Mirzaei, A. Rostami, and H. Baghban, Opt. Laser Technol. **44**, 378 (2012).

[6]N. Suzuki and N. Iizuka, Jpn. J. Appl. Phys., Part 2 **38**, L363 (1999).

[7]P. K. Kandaswamy, H. Machhadani, C. Bougerol, S. Sakr, M. Tchernycheva, F. H. Julien, and E. Monroy, Appl. Phys. Lett. **95**(14), 141911 (2009).

[8]N. Péré-Laperne, C. Bayram, L. Nguyen-The, R. McClintock, and M. Razeghi, Appl. Phys. Lett. **95**, 131109 (2009).

[9]P. K. Kandaswamy, H. Machhadani, Y. Kotsar, S. Sakr, A. Das, M. Tchernycheva, L. Rapenne, E. Sarigiannidou, F. H. Julien, and E. Monroy, Appl. Phys. Lett. **96**, 141903 (2010).

[10]C. Bayram, J. Appl. Phys. **111**, 013514 (2012).

[11]C. Edmunds, L. Tang, J. Shao, D. Li, M. Cervantes, G. Gardner, D. N. Zakharov, M. J. Manfra, and O. Malis, Appl. Phys. Lett. **101**, 102104 (2012).

[12]W. Tian, W. Y. Yan, X. Hui, S. L. Li, Y. Y. Ding, Y. Li, Y. Tian, J. N. Dai, Y. Y. Fang, Z. H. Wu, C. H. Yu, and C. Q. Chen, J. Appl. Phys. **112**, 063526 (2012).

[13]M. Beeler, E. Trichas, and E. Monroy, Semicond. Sci. Technol. **28**, 074022 (2013).

[14]H. Machhadani, Y. Kotsar, S. Sakr, M. Tchernycheva, R. Colombelli, J. Mangeney, E. Bellet-Amalric, E. Sarigiannidou, E. Monroy, and F. H. Julien, Appl. Phys. Lett. **97**(19), 191101 (2010).

[15]F. F. Sudradjat, W. Zhang, J. Woodward, H. Durmaz, T. D. Moustakas, and R. Paiella, Appl. Phys. Lett. **100**(24), 241113 (2012).

[16]S. Birner, T. Zibold, T. Andlauer, T. Kubis, M. Sabathil, A. Trellakis, and P. Vogl, IEEE Trans. Electron Devices **54**(9), 2137 (2007).

[17]P. K. Kandaswamy, F. Guillot, E. Bellet-Amalric, E. Monroy, L. Nevou, M. Tchernycheva, A. Michon, F. H. Julien, E. Baumann, F. R. Giorgetta, D. Hofstetter, T. Remmele, M. Albrecht, S. Birner, and L. S. Dang, J. Appl. Phys. **104**(9), 093501 (2008).

[18]F. Wu, W. Tian, W. Y. Yan, J. Zhang, S. C. Sun, J. N. Dai, Y. Y. Fang, Z. H. Wu, and C. Q. Chen, J. Appl. Phys. **113**, 154505 (2013).

[19]The calculations also show that by decreasing the in-plane lattice parameter of the MQWs (compressive strain), a decrease in ISB energy is seen in the 4-layer design, which is consistent with a reduction of the internal electric field due to the smaller piezoelectric constants of GaN in comparison to AlN. In contrast, an increase of the ISB energy is seen in the step-QW design due to the tendency of the first electronic level to keep confined close to the GaN layer.

[20]Y. Kotsar, B. Doisneau, E. Bellet-Amalric, A. Das, E. Sarigiannidou, and E. Monroy, J. Appl. Phys. **110**, 033501 (2011).

This article is copyrighted as indicated in the article. Reuse of AIP content is subject to the terms at: http://scitation.aip.org/termsconditions. Downloaded to IP: 132.168.8.249 On: Wed, 08 Apr 2015 12:42:05

Annex 5

Pseudo-square AlGaN/GaN quantum wells for terahertz absorption

M. Beeler,[1,2] C. Bougerol,[1,3] E. Bellet-Amalric,[1,2] and E. Monroy[1,2]
[1]*Université Grenoble Alpes, 38000 Grenoble, France*
[2]*CEA-Grenoble, INAC/SP2M/NPSC, 17 avenue des Martyrs, 38054 Grenoble, France*
[3]*Institut Néel-CNRS, 25 avenue des Martyrs, 38042 Grenoble Cedex 9, France*

(Received 12 July 2014; accepted 17 September 2014; published online 29 September 2014)

THz intersubband transitions are reported down to 160 μm within AlGaN/GaN heterostructures following a 4-layer quantum well design. In such a geometry, the compensation of the polarization-induced internal electric field is obtained through creating a gradual increase in polarization field throughout the quantum "trough" generated by three low-Al-content layers. The intersubband transitions show tunable absorption with respect to doping level as well as geometrical variations which can be regulated from 53 to 160 μm. They also exhibit tunnel-friendly designs which can be easily integrated into existing intersubband device architectures. © *2014 AIP Publishing LLC*.
[http://dx.doi.org/10.1063/1.4896768]

Wide-bandgap AlGaN/GaN heterostructures are intensively studied as a promising alternative to replace GaAs in solid-state THz optoelectronics. GaAs-based quantum cascade lasers operating in this spectral range are limited by intrinsic material properties, namely, the longitudinal-optical (LO) phonon, which exists at 36 meV. On the contrary, the large energy of the GaN LO phonon (92 meV) opens prospects for GaN-based high-temperature THz quantum cascade lasers[1–5] and intersubband (ISB) devices covering the 5–10 THz band, inaccessible to As-based technologies.

ISB transitions in GaN/AlGaN multi-quantum-wells (MQWs) can be tuned from 1.0 μm to 10 μm by reducing the Al mole fraction in the barriers and increasing the quantum well (QW) width[6–12] (see Ref. 13 for a review). This strategy faces a roadblock at longer wavelengths because of the quantum confined Stark effect. The polarization-induced internal electric field results in QWs with a sawtooth profile and with lower electronic levels confined to a small fraction of the QW, so that changes in well width do not induce proportional changes in ISB energy. Therefore, to shift the absorption towards longer wavelengths in polar structures, it is necessary to engineer the conduction band to reduce the effect of the internal electric field within the QWs. Polarization effects can be eliminated by growing on a non-polar crystallographic plane[14] or using cubic nitride heterostructures,[15] but such approaches must face additional growth challenges. In the well-known (0001) orientation, attempts to reduce the electric field have led to 3-layer step-QW architectures, where ISB transitions in the THz region have been reported,[16] and a THz photodetector has been demonstrated around this principle.[17] However, the 3-layered design in Ref. 16 suffers from issues with reproducibility and the inability to easily predict the ISB transitional energy.[18] Alternative geometries have been proposed which increase the robustness of the ISB transition to accommodate errors in growth rate and interfacial roughness.[18] This was accomplished by introducing a complex barrier system which sacrifices tunability and does not completely compensate the internal electric field. Furthermore, the width of the complex barrier inhibits electron tunneling transport, which complicates the incorporation of such QWs in an electrically driven device structure.

In this work, we introduce an AlGaN-based pseudo-square QW design for ISB devices operating in the THz spectral range. The proposed geometry achieves THz ISB absorption thanks to the compensation of the polarization-induced internal electric fields, and the potential barriers are thin enough to facilitate tunneling at low bias. These QWs exhibit wave functions which are much more symmetric than previous designs, which translate to higher oscillator strengths. Pseudo-square QWs fabricated by plasma-assisted molecular-beam epitaxy (PAMBE) present ISB absorption at 160 μm, which blue shifts to 50 μm with increasing doping level, and can be tuned from 100 to 75 μm by changing the width of a quantum trough.

AlGaN-based pseudo-square QWs have been simulated using the self-consistent nextnano[3] 8-band k·p Schrödinger-Poisson solver.[19] Calculations were performed using the material parameters in Ref. 20, and assuming the structure strained on GaN. The proposed band structure in Fig. 1(a) consists of four compositionally different AlGaN layers with nominal Al concentrations of 12%, 0%, 5%, and 7% for the barrier, GaN, A, and B layers, respectively. The highest Al concentration (the concentration of the barrier) is chosen as the sum of the other two, so that the structure can be realized by PAMBE using two Al effusion cells. In this pseudo-square QW, the electric field is compensated by creating a gradual increase in polarization field throughout the quantum "trough" formed by the 3 low-Al-content layers. Because of this gradual increase, the electron density function is delocalized from a single layer and is quantum confined across all three layers by the effective size of the trough and not by the polarization field. Simulations show that the oscillator strength of the pseudo-square QW is the same as the 4-layered MQW system,[18] and an order of magnitude greater than that of the step-QW configuration.[16] The ISB energy of this design is nominally targeted at 25 meV, and can be tuned by changing the width of the A layer of the quantum trough. At zero bias, the second electronic level, e_2, is localized in the QW, but the tunneling probability of electrons in e_2 increases by biasing in the $\langle 0001 \rangle$ direction.

This article is copyrighted as indicated in the article. Reuse of AIP content is subject to the terms at: http://scitation.aip.org/termsconditions. Downloaded to IP: 132.168.8.249 On: Wed, 08 Apr 2015 12:42:33

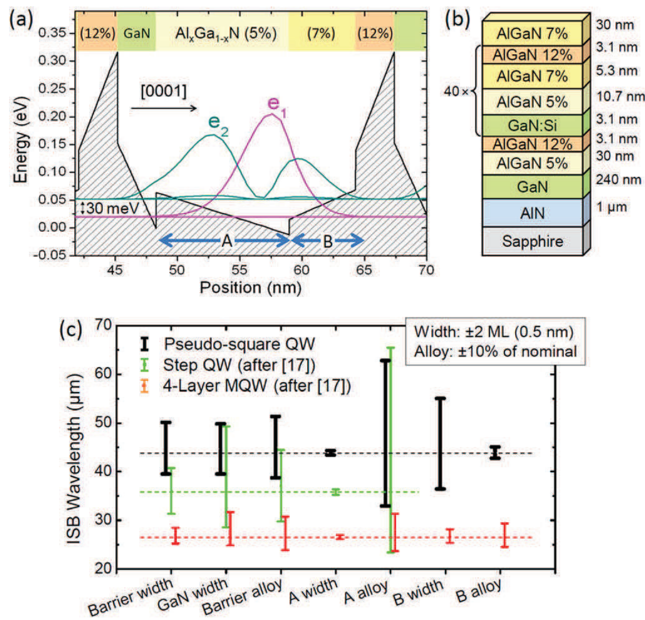

FIG. 1. (a) Band profile of a pseudo-square QW where the first and second confined electronic levels are indicated as e_1 and e_2, respectively. The nominal compositions of the layers are indicated above. (b) Schematic description of the structure which was grown on an AlN-on-sapphire substrate. (c) Illustration of the robustness of the pseudo-square QWs. The dashed lines indicate the nominal transition wavelengths. The error bars represent the minimum and maximum values attributed to the uncertainties associated to growth (geometries changed by ±0.5 nm and alloys changed by ±10%). Similar data for step-QWs and 4-layer QWs are included for comparison (after Ref. 18).

The ISB transition in this pseudo-square system has been tested against the uncertainties associated to PAMBE growth with the results described in Fig. 1(c). There are 7 degrees of freedom within the superlattice, namely, the thickness of each layer and the Al mole fraction in each $Al_xGa_{1-x}N$ layer. Each of these parameters were varied considering ±2 monolayers (ML) as the error bar for thicknesses, and ±10% of the nominal concentration as the error bar for the aluminium mole fraction in $Al_xGa_{1-x}N$. The 10% variation in alloy is roughly equivalent to a temperature difference of ±4 °C for the Al effusion cells in the compositional range of this design. Figure 1(c) shows that the variation of most of the layer thicknesses results in ISB wavelength differences of nearly 5 μm, conversely parameters such as the "B alloy" and the "A width" are almost insensitive to changes. The results of this robustness assessment are compared to the previously reported data for step QWs and 4-layer QWs,[18] also in Fig. 1(c). The ISB transition deviations in the pseudo-square design are generally smaller than those induced within the step QW, although larger than those of the 4-layer QW. For a fair comparison of the structures, it is important to consider that they are engineered to operate at different wavelengths. Defining the relative errors as $\Delta\lambda/\lambda$, the average wavelength variation that can be induced by growth uncertainties is 10%, 8.8%, and 25%, for pseudo-square QWs, 4-layer QWs, and step-QWs, respectively.

AlGaN/GaN 40-period superlattices following the pseudo-square design in Fig. 1 were synthesized by PAMBE on GaN templates deposited on float-zone Si(111).[7] These templates use a complex buffer layer to minimize the effects of the lattice mismatch between GaN and Si(111), as well as mitigate the effects of thermal expansion. Identical samples were simultaneously grown on 1-μm-thick AlN-on-sapphire templates to simplify the structural characterization. During deposition, the growth rate was 0.32 ML/s and the substrate temperature was ∼720 °C. The structure was grown uninterrupted under self-regulated Ga-rich conditions.[20,21] To populate the ground conduction band level in the quantum trough, e_1, 1.5 nm of each GaN layer was doped with Si. The structural parameters and doping level of the samples under study are summarized in Table I. A first set of samples (series I in Table I) was synthesized following the geometry in Fig. 1(b) with different doping concentrations in the GaN layer. Then, a second set of samples (series II in Table I) with a slightly modified geometry was used to determine the experimental effect of trough size, which was varied by changing the width of the $Al_{0.05}Ga_{0.95}N$ layer (layer A).

Figure 2(a) shows a high-angle annular dark field scanning transmission electron microscopy (HAADF-STEM) image of three periods of sample I.2 obtained in an FEI Titan 80–300 microscope at 200 kV. An average background subtraction filter was used to increase the atomic contrast between the layers. The interfaces appear straight and sharp, and the difference in gray scale indicates the alloy concentration, confirming the nominal chemical sequence. Furthermore, energy dispersive x-ray spectroscopy performed on a (S)TEM FEI-Osiris microscope operated at 200 kV render Al compositions very close to nominal values, namely, 11.9%, 0%, 5.6%, and 7.3% for the barrier, GaN, A, and B layers, respectively, with an estimated standard deviation of ±0.4%.

The periodicity of the samples was analyzed by high-resolution x-ray diffraction (HRXRD) using a Seifert XRD 3003 PTS-HR system with a beam concentrator before a Ge(220) four-bounce monochromator, and a Ge(220) two-bounce analyzer in front of the detector. Figure 2(b) depicts the $\omega-2\theta$ scans of the (0002) reflections of samples II.1 and II.2 grown on AlN-on-sapphire templates. From these measurements, we extracted the superlattice periods summarized in Table I. The experimental measurements in Fig. 2(b) are juxtaposed to simulated curves assuming nominal Al concentrations and a superlattice misfit compressive strain relaxation of 93.5% and 94.5%, respectively,[22] which is in accordance with previous observations of relaxation processes stating that GaN/AlGaN superlattices tend to relax towards their average aluminum concentration independent of the layer underneath.[21]

All samples grown on GaN-on-Si templates were polished at the Brewster angle of 60° to form multipass waveguides allowing 3–4 interactions with the active region. These samples were measured by Fourier Transform Infrared spectroscopy (FTIR) in transmission mode using a far-infrared polarizer to discern between the transverse-electric (TE) and transverse-magnetic (TM) polarized light. All measurements were performed at 5 K. Taking the selection rules into account, the ISB absorption peaks are identified by dividing the transmission spectra for TE polarization by the TM transmission. Figure 3(a) shows the low-temperature far-IR absorption spectra of TM-polarized light for samples

This article is copyrighted as indicated in the article. Reuse of AIP content is subject to the terms at: http://scitation.aip.org/termsconditions. Downloaded to IP: 132.168.8.249 On: Wed, 08 Apr 2015 12:42:33

TABLE I. Structural parameters, doping level in the GaN layer, superlattice period measured by HRXRD, and peak ISB absorption wavelength of the samples under study. (*) Thickness extrapolated from I-1, consistent with HAADF-STEM. (**) Thickness extrapolated from I-1.

	Sample	GaN layer (nm)	A (nm)	B (nm)	Barrier (nm)	[Si] (cm^{-3})	Period (nm)	Absorption (μm)
Series I	I-1	3.1	10.7	5.3	3.1	3.3×10^{17}	22.2 ± 0.2	160
	I-2	3.1	10.7	5.3	3.1	1.3×10^{18}	(*)	83
	I-3	3.1	10.7	5.3	3.1	1.3×10^{19}	(**)	53
Series II	II-1	3.5	6.0	6.0	3.5	4.8×10^{18}	19.5 ± 0.2	77
	II-2	3.5	8.0	6.0	3.5	4.8×10^{18}	21.2 ± 0.2	87
	II-3	3.5	10.0	6.0	3.5	4.8×10^{18}	23.4 ± 0.2	95

from series I, which displays a peak assigned to the ISB transition from the first to the second electronic levels in the QWs. Maximum interaction of light with the active layer occurred for an angle of incidence of 55°–65°. At lower angles of incidence, the ISB absorption peak decreases as illustrated in Fig. 3(c). Samples with doping level of 3.0×10^{17}, 1.3×10^{18}, and $1.3 \times 10^{19}\,cm^{-3}$ exhibit ISB absorption at 160, 83, and 53 μm, respectively, as summarized in Table I. Unintentionally doped samples, grown as a reference, do not show significant absorption across the spectrum. This blue shifting ISB absorption with higher dopant level indicates that many-body effects (depolarization shift, exchange interaction) play a large role in determining the ISB energy. The depolarization shift, estimated from,[23,24] is negligible for the architectures under study due to the small ISB transition energies under consideration. On the contrary, calculations of the exchange interaction following Bandara *et al.*,[25] assuming the wave vector $k = 0$, $k = \sqrt{2\pi\sigma}$ with σ being the two-dimensional electron density in the QW, and with a k-independent equation, give absolute values comparable to the energy of the ISB transition itself, as illustrated in Fig. 3(d). This is in accordance with Helm[24] and Guo *et al.*[26] which show that with large well widths, and small ISB energies (<20 meV), the energetic summation of the many body effects becomes as large as the ISB energy itself.

Samples with varying well width (series II) have also been measured in the fashion described above with the result

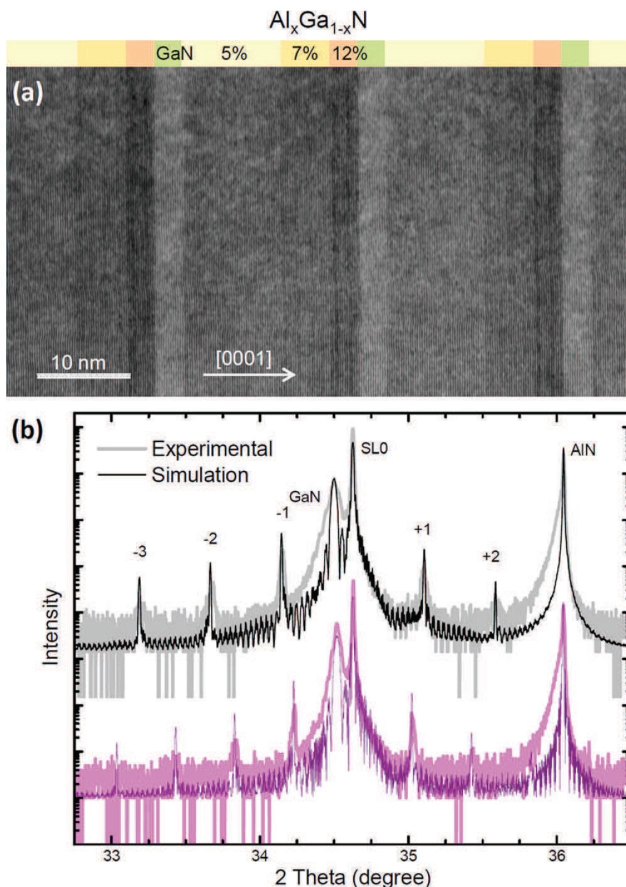

FIG. 2. HAADF-STEM image of sample I.2, which follows the architecture in Fig. 1. The nominal concentrations of each layer are shown above, where 5% represents $Al_{0.05}Ga_{0.95}N$. Layer thicknesses of 41 ML $Al_{0.05}Ga_{0.95}N$/22 ML $Al_{0.07}Ga_{0.93}N$/12 ML $Al_{0.12}Ga_{0.88}N$/12 ML GaN are seen in the image. (b) HRXRD $\omega - 2\theta$ scans around the (0002) reflection of samples II.1 (top) and II.3 (bottom). The simulations assume nominal Al concentrations and a superlattice relaxation of 93.5% and 94.5%, respectively.

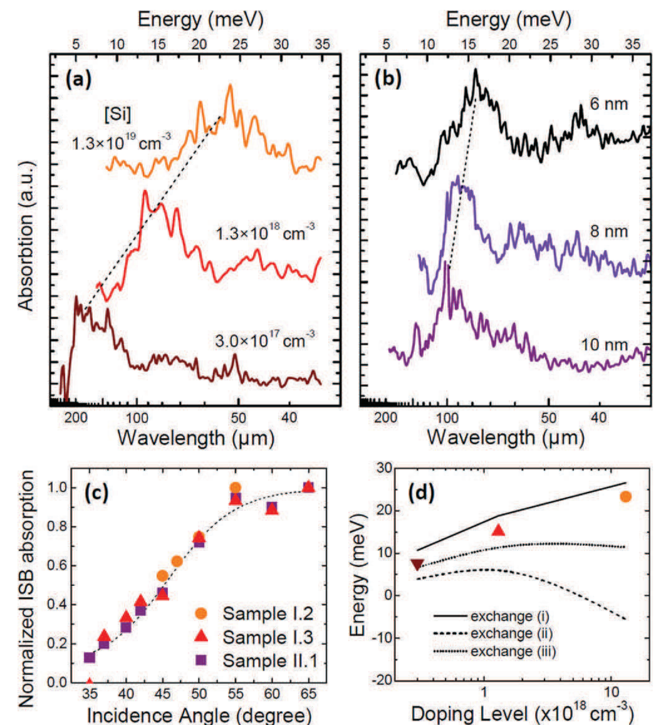

FIG. 3. (a) Spectral absorption of TM-polarized light in samples from series I with different doping levels. Spectra are found from dividing TE by TM polarized light, then normalizing this division against reference spectra not showing absorption. (b) Likewise for series II. (c) Variation of the absorption peak for TM polarized light as a function of the incidence angle, normalized to the maximum. (d) Comparison of the experimental ISB transition values with the spectral shifts associated to exchange interaction predicted by Bandara *et al.*[25] assuming (i) the wave vector $k = 0$, (ii) $k = \sqrt{2\pi\sigma}$ with σ being the two-dimensional electron density in the QW, and (iii) with a k-independent equation.

This article is copyrighted as indicated in the article. Reuse of AIP content is subject to the terms at: http://scitation.aip.org/termsconditions. Downloaded to IP: 132.168.8.249 On: Wed, 08 Apr 2015 12:42:33

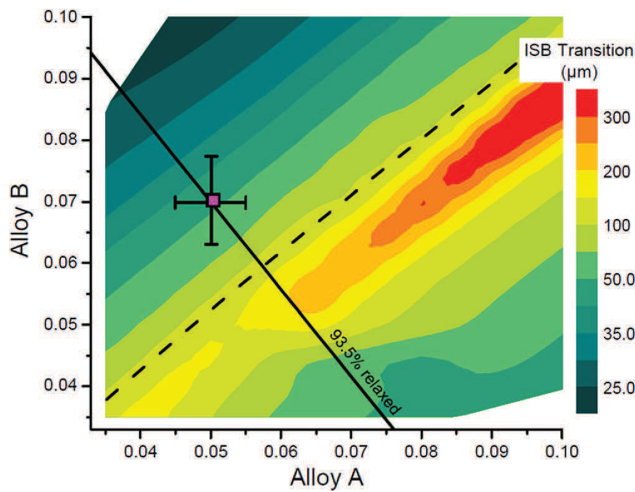

FIG. 4. Surface plots of the ISB transition wavelength for sample II-3 where the Al mole fraction in layers A and B is varied while monitoring the effect on the ISB energy, calculated with the nextnano3 software excluding the exchange interaction and depolarization shift. Nominal compositions with their error bars are marked by a square. The dashed line indicates the experimental measurement of ISB absorption. The solid line indicates the alloy configuration compatible with HRXRD measurements assuming the superlattice 93.5% relaxed.

in Fig. 3(b). Increasing well width leads to a decrease of the ISB energy. Thus, samples grown with an A layer thickness of 6, 8, and 10 nm show red-shifting ISB absorption at 77, 87, and 95 μm, respectively, as summarized in Table I. This confirms that the energies of these quantum confined levels can be modified by structurally changing the size of the quantum trough.

Figure 4 shows a simulated surface plot of the ISB transition wavelength for the structure of sample II-3 where the Al mole fraction in layers A and B are varied while monitoring the effect on the ISB energy. This is done excluding the exchange interaction and depolarization shift, while assuming the structure to be fully relaxed on GaN.[27] Nominal compositions are marked by a square with their error bars. The dashed line indicates the experimental measurement of ISB absorption. The solid line indicates the alloy configurations compatible with HRXRD measurements assuming the superlattice 93.5% relaxed and at the nominal average aluminum concentration. The intersection between these two lines occurs out of the compositional error bars, and suggests alloy values of 5.7 and 6.0 for the A and B layers, respectively. Upon the inclusion of the blue-shifting many body effects, this intersection occurs at values even further from the nominal values. We therefore conclude that further research is required to improve the convergence between theoretical calculations and experimental results.

In conclusion, we have demonstrated a tunable nitride-based ISB absorber for the THz spectral range consisting of a pseudo-square QW superlattice. The proposed architecture utilizes a quantum trough engineered with 3 AlGaN layers to confine the wave function which mitigates the effect of the internal electric field. The design is robust regarding the uncertainties associated to the PAMBE growth and can be used as the building block for further THz systems such as quantum cascade devices thanks to the use of thin AlGaN barriers which should allow tunneling transport under bias. Fabricated superlattices show ISB absorption tunable from 53 to 160 μm with respect to doping level and geometrical variations.

The authors would like to thank Y. Curé, Y. Genuist, J. Dussaud, and D. Boilot for their technical support. This work was supported by the EU ERC-StG “TeraGaN” (No. 278428) project.

[1]G. Sun, R. A. Soref, and J. B. Khurgin, Superlattices Microstruct. **37**, 107 (2005).
[2]N. Vukmirović, V. D. Jovanović, D. Indjin, Z. Ikonić, P. Harrison, and V. Milanović, J. Appl. Phys. **97**, 103106 (2005).
[3]E. Bellotti, K. Driscoll, T. D. Moustakas, and R. Paiella, J. Appl. Phys. **105**, 113103 (2009).
[4]W. Terashima and H. Hirayama, Phys. Status Solidi C **6**, S615 (2009).
[5]B. Mirzaei, A. Rostami, and H. Baghban, Opt. Laser Technol. **44**, 378 (2012).
[6]N. Suzuki and N. Iizuka, Jpn. J. Appl. Phys., Part 2 **38**, L363 (1999).
[7]P. K. Kandaswamy, H. Machhadani, C. Bougerol, S. Sakr, M. Tchernycheva, F. H. Julien, and E. Monroy, Appl. Phys. Lett. **95**(14), 141911 (2009).
[8]N. Péré-Laperne, C. Bayram, L. Nguyen-The, R. McClintock, and M. Razeghi, Appl. Phys. Lett. **95**, 131109 (2009).
[9]P. K. Kandaswamy, H. Machhadani, Y. Kotsar, S. Sakr, A. Das, M. Tchernycheva, L. Rapenne, E. Sarigiannidou, F. H. Julien, and E. Monroy, Appl. Phys. Lett. **96**, 141903 (2010).
[10]C. Bayram, J. Appl. Phys. **111**, 013514 (2012).
[11]C. Edmunds, L. Tang, J. Shao, D. Li, M. Cervantes, G. Gardner, D. N. Zakharov, M. J. Manfra, and O. Malis, Appl. Phys. Lett. **101**, 102104 (2012).
[12]W. Tian, W. Y. Yan, X. Hui, S. L. Li, Y. Y. Ding, Y. Li, Y. Tian, J. N. Dai, Y. Y. Fang, Z. H. Wu *et al.*, J. Appl. Phys. **112**, 063526 (2012).
[13]M. Beeler, E. Trichas, and E. Monroy, Semicond. Sci. Technol. **28**, 074022 (2013).
[14]C. Edmunds, J. Shao, M. Shirazi-HD, M. J. Manfra, and O. Malis, Appl. Phys. Lett. **105**, 021109 (2014).
[15]H. Machhadani, M. Tchernycheva, S. Sakr, L. Rigutti, R. Colombelli, E. Warde, C. Mietze, D. J. As, and F. H. Julien, Phys. Rev. B **83**, 075313 (2011).
[16]H. Machhadani, Y. Kotsar, S. Sakr, M. Tchernycheva, R. Colombelli, J. Mangeney, E. Bellet-Amalric, E. Sarigiannidou, E. Monroy, and F. H. Julien, Appl. Phys. Lett. **97**(19), 191101 (2010).
[17]F. F. Sudradjat, W. Zhang, J. Woodward, H. Durmaz, T. D. Moustakas, and R. Paiella, Appl. Phys. Lett. **100**, 241113 (2012).
[18]M. Beeler, C. Bougerol, E. Bellet-Amalric, and E. Monroy, Appl. Phys. Lett. **103**, 091108 (2013).
[19]S. Birner, T. Zibold, T. Andlauer, T. Kubis, M. Sabathil, A. Trellakis, and P. Vogl, IEEE Trans. Electron Devices **54**, 2137 (2007).
[20]P. K. Kandaswamy, F. Guillot, E. Bellet-Amalric, E. Monroy, L. Nevou, M. Tchernycheva, A. Michon, F. H. Julien, E. Baumann, F. R. Giorgetta *et al.*, J. Appl. Phys. **104**, 093501 (2008).
[21]Y. Kotsar, B. Doisneau, E. Bellet-Amalric, A. Das, E. Sarigiannidou, and E. Monroy, J. Appl. Phys. **110**, 033501 (2011).
[22]Relaxation is defined as $R = (c_{SL} - c_{AlN})/(c_{SL0} - c_{AlN})$, where c_{SL} is the measured average lattice parameter of the superlattice along $\langle 0001 \rangle$, c_{SL0} is the average lattice parameter of the relaxed superlattice, and c_{AlN} is the lattice parameter of the AlN substrate.
[23]S. J. Allen, D. C. Tsui, and B. Vinter, Solid State Commun. **20**, 425 (1976).
[24]M. Helm, in *Intersubband Transitions in Quantum Wells: Physics and Device Applications I*, edited by H. C. Liu and F. Capasso (Academic Press, San Diego, 2000).
[25]K. M. S. V. Bandara, D. D. Coon, O. Byungsung, Y. F. Lin, and M. H. Francombe, Appl. Phys. Lett. **53**, 1931 (1988).
[26]X. G. Guo, Z. Y. Tan, J. C. Cao, and H. C. Liu, Appl. Phys. Lett. **94**, 201101 (2009).
[27]Assuming that the superlattice relaxes to the in-plane lattice parameter corresponding to its average Al mole fraction implies a red shift of the calculated ISB transition by $\Delta\lambda/\lambda = 1.3\%$.

This article is copyrighted as indicated in the article. Reuse of AIP content is subject to the terms at: http://scitation.aip.org/termsconditions. Downloaded to IP: 132.168.8.249 On: Wed, 08 Apr 2015 12:42:33

Annex 6

Long-lived excitons in GaN/AlN nanowire heterostructures

M. Beeler,[1,2] C. B. Lim,[1,2] P. Hille,[3] J. Bleuse,[1,2] J. Schörmann,[3] M. de la Mata,[4] J. Arbiol,[4,5]
M. Eickhoff,[3] and E. Monroy[1,2]

[1] *Université Grenoble Alpes, 38000 Grenoble, France*
[2] *CEA-Grenoble, INAC, SP2M-NPSC, 17 av. des Martyrs, 38054 Grenoble, France*
[3] *I. Physikalisches Institut, Justus-Liebig-Universität Gießen, Heinrich-Buff-Ring 16, D-35392 Gießen, Germany*
[4] *Institut de Ciencia de Materials de Barcelona, ICMAB-CSIC, Campus UAB, 08193 Barcelona, Catalonia, Spain*
[5] *ICREA and Institut Català de Nanociència i Nanotecnologia (ICN2), 08193 Barcelona, Catalonia, Spain*

(Received 24 December 2014; published 27 May 2015)

GaN/AlN nanowire heterostructures can display photoluminescence (PL) decay times on the order of microseconds that persist up to room temperature. Doping the GaN nanodisk insertions with Ge can reduce these PL decay times by two orders of magnitude. These phenomena are explained by the three-dimensional electric field distribution within the GaN nanodisks, which has an axial component in the range of a few MV/cm associated to the spontaneous and piezoelectric polarization, and a radial piezoelectric contribution associated to the shear components of the lattice strain. At low dopant concentrations, a large electron-hole separation in both the axial and radial directions is present. The relatively weak radial electric fields, which are about one order of magnitude smaller than the axial fields, are rapidly screened by doping. This bidirectional screening leads to a radial and axial centralization of the hole underneath the electron, and consequently, to large decreases in PL decay times, in addition to luminescence blue shifts.

DOI: 10.1103/PhysRevB.91.205440 PACS number(s): 78.67.Uh, 62.23.Hj, 78.66.Fd, 73.21.−b

I. INTRODUCTION

Carrier lifetimes are directly related to detection, spontaneous emission, and stimulated emission efficiencies. Short radiative lifetimes in the picosecond or nanosecond range are useful in light emitters to compete with nonradiative recombination processes. On the other hand, long carrier lifetimes (microsecond) increase the collection probability of photogenerated carriers in solar cells or photodetectors, and can enhance the population inversion in lasers.

One approach to tune the band-to-band radiative time is controlling the electron-hole spatial separation. The carrier separation is achieved through the use of type II heterojunctions [1,2], or through the introduction of internal electric fields via doping or compositional gradients. In the case of polar materials, such as wurtzite III-nitride or II-oxide semiconductors [3,4], internal electric fields appear spontaneously in heterostructures due to the polarization difference between binary compounds [5]. In particular, adding up spontaneous and piezoelectric polarization, AlN/GaN quantum wells present an internal electric field on the order of 10 MV/cm [6], which leads to efficient electron-hole separation along the polar ⟨0001⟩ axis, and considerably increases the band-to-band radiative recombination time [7–13].

Further control of the carrier lifetime in typical device architectures can be achieved by confining carriers in an additional dimension, i.e., using three-dimensional (3D) nanostructures such as quantum dots. Excitons trapped in such quantum nanostructures are efficiently isolated from dislocation or surface related nonradiative recombination centers [14], which attenuates the quenching of the carrier lifetime with temperature. The synthesis of quantum dots as nanodisks inserted in nanowires (NWs) offers an exciting alternative to avoid the inherent constraints of Stranski-Krastanov growth. In NW geometries, the 3D elastic strain relaxation via the surface in the form of plane bending [15] permits a wider range of quantum dot sizes and compositions before forming misfit dislocations, i.e., plastic relaxation [15,16]. In the case of GaN/AlN quantum dots or nanodisks, the large band offsets (∼1.8 eV in the conduction band [17]) provide efficient exciton confinement, so that the observed long (microsecond) photoluminescence (PL) decay times [9,12] can persist up to room temperature [18].

Micro-PL studies of GaN nanodisks in NWs show excitonic emission lines stemming from discrete levels, as verified by photon-correlation measurements [19], which confirm their quantum-dot-like behavior. The PL spectral positions present signatures of both quantum confinement and of the polarization-induced Stark effect [16,19–23]. However, the spectral shift associated to the Stark effect is smaller in nanodisks than in quantum wells [16,19,23], which has been attributed to dislocations [16], to the surface band bending [24] and to the 3D strain configuration [19,25]. Studies of the PL decay times in GaN NWs show exponential or biexponential PL decays with subnanosecond characteristic times [26,27]. In GaN/AlN NW heterostructures, subnanosecond PL decay times have been reported in the case of small nanodisks (∼1 nm), where the emission properties are dominated by the carrier confinement and the quantum confined Stark effect is still negligible [19]. In the case of nanodisks larger than 2 nm, where the emission becomes dominated by the carrier separation due to the polarization-induced internal electric field, time-resolved PL reports are so far limited to the descreening of the polarization-induced internal electric field, in the tens of nanoseconds range [16,28], where the use of

Published by the American Physical Society under the terms of the Creative Commons Attribution 3.0 License. Further distribution of this work must maintain attribution to the author(s) and the published article's title, journal citation, and DOI.

excitations rates larger than 50 MHz (less than 20 ns between pulses) has hindered the observation of the characteristic PL decay times.

In this work, we report the observation of long-lived (microsecond) excitons in GaN/AlN NW heterostructures at room temperature, and we present a comprehensive analysis of the carrier dynamics by combining continuous-excitation and time-resolved PL measurements with 3D calculations of the electronic structure. Electric fields in the axial and radial directions translate into in-plane carrier separations that govern the carrier dynamics at low dopant concentrations, and are rapidly screened by Ge doping in the nanodisks. As a result, screening effects in nanodisks are significantly stronger than in planar structures. By varying the Ge concentration in the GaN nanodisks, the lifetime of photoinduced carriers can be varied by nearly two orders of magnitude.

II. EXPERIMENT

N-polar AlN/GaN NW heterostructures were synthesized by plasma-assisted molecular-beam epitaxy (PAMBE) on Si(111) substrates at a growth temperature of ∼790°C. At this temperature and under N-rich growth conditions, PAMBE is known to produce N-polar catalyst-free GaN NWs with a radius in the range of a few tens of nanometers [29–34]. The structures under study consist of a nonintentionally doped (NID) GaN NW base with a length of 600 nm and a radius ranging from 25–40 nm, followed by 40 periods of GaN:Ge/AlN (nominally 4 nm/4 nm) nanodisks, and a 20-nm-thick NID GaN cap layer. The GaN nanodisks were doped with Ge, using a beam equivalent pressure ranging from $0.5 - 1.5 \times 10^{-9}$ mbar. Ge was used as a dopant instead of Si as it introduces less strain in GaN being similar in size to Ga [35,36], and the change of the NW aspect ratio is negligible even for high Ge doping levels (3.3×10^{20} cm [3]) [37]. The dopant concentrations of the samples under study, estimated from secondary ion mass spectroscopy measurements in reference samples [37], are summarized in Table I.

Structural and morphological characterization of the heterostructures was performed by high-resolution transmission electron microscopy (HRTEM) and high-angle annular dark field (HAADF) scanning transmission electron microscopy (STEM) using a FEI Tecnai F20 field emission gun microscope operated at 200 kV. For microscopy studies, the NWs were directly scratched from the substrate with a holey carbon TEM grid. The periodicity of the samples was analyzed by high-resolution x-ray diffraction (HRXRD) using a PANalytical X'Pert PRO MRD system.

PL spectra were obtained by exciting with a continuous-wave frequency-doubled Ar laser ($\lambda = 244$ nm), with an excitation power around 50 μW focused on a spot with a diameter of ∼100 μm, giving a power density of about 7 $\mathrm{kW/m^2}$. The emission from the sample was collected by a Jobin Yvon HR460 monochromator equipped with an ultraviolet-enhanced charge-coupled device (CCD) camera. In the case of time-resolved PL, samples were excited using a frequency-tripled Ti:sapphire laser ($\lambda = 270$ nm) with pulse width of 200 fs. This laser was augmented with a cavity damper section with a base pulse repetition rate of 54 MHz. This allowed the period between pulses to be varied from 20 ns to 5 μs. The excitation power was about 500 μW. The luminescence was dispersed by a Jobin Yvon Triax320 monochromator and was detected by a Hamamatsu C−5680 streak camera.

III. RESULTS

Figure 1(a) shows an HAADF image of GaN NWs containing an NID GaN base, followed by the GaN/AlN heterostructure and the GaN cap. The different GaN:Ge and AlN sections can be easily distinguished by the image contrast, which scales with the atomic number of the observed material. A magnified detail of the first GaN:Ge/AlN periods near the base are displayed in temperature color in Fig. 1(b). No trace of GaN-AlN interdiffusion is appreciated in the images. Statistics performed on the nanodisks and barrier thicknesses are in good agreement with the nominal values. Figure 1(c) displays a HRTEM image of three GaN:Ge nanodisks embedded in AlN barrier material. In the HRTEM image shown, the darker contrast corresponds to the GaN:Ge insertions while the brighter lattice contrast is the AlN barrier, evidencing the presence of an AlN shell with thickness roughly equal to the size of the barriers. This shell is generated by direct deposition of the impinging Al atoms due to the low Al diffusion length at this growth temperature [16,38–41]. Furthermore, the GaN/AlN interfaces often present {1 − 102} facets close to the NW sidewalls, highlighted by a dashed line in Fig. 1(c), due to the plane bending phenomena related to the elastic strain relaxation [15,16,25].

TEM images provide a local view of selected NWs, whereas HRXRD measurements give a structural assessment of the NW ensemble. Figure 1(d) depicts the $\omega - 2\theta$ scans of the (0002) x-ray reflections of one of the samples under study. From the satellites of the GaN/AlN superlattice reflection, the superlattice periods are extracted and summarized in Table I.

TABLE I. Characteristics of the GaN/AlN NW heterostructures under study: Germanium beam equivalent pressure ($\mathrm{BEP_{Ge}}$) during the nanodisk growth, Ge concentration deduced from reference Ge-doped GaN NW samples measured by time-of-flight secondary ion mass spectroscopy, GaN/AlN period extracted from HRXRD measurements, low-temperature ($T = 5$ K) PL peak wavelength, and values of the E_a and a parameters in Eq. (3) extracted from the fits in Fig. 2(b).

Sample	$\mathrm{BEP_{Ge}}$ (mbar)	[Ge] ($\mathrm{cm^{-3}}$)	Period from HRXRD (nm)	PL peak wavelength (nm)	E_a (meV)	a
N1	0	NID	7.5 ± 0.2	454	40 ± 10	9 ± 2
N2	5.0×10^{-10}	9.0×10^{19}	7.6 ± 0.2	429	54 ± 10	31 ± 5
N3	1.0×10^{-9}	1.7×10^{20}	7.4 ± 0.2	392	53 ± 10	42 ± 11
N4	1.5×10^{-9}	3.1×10^{20}	7.4 ± 0.2	384	68 ± 10	131 ± 50

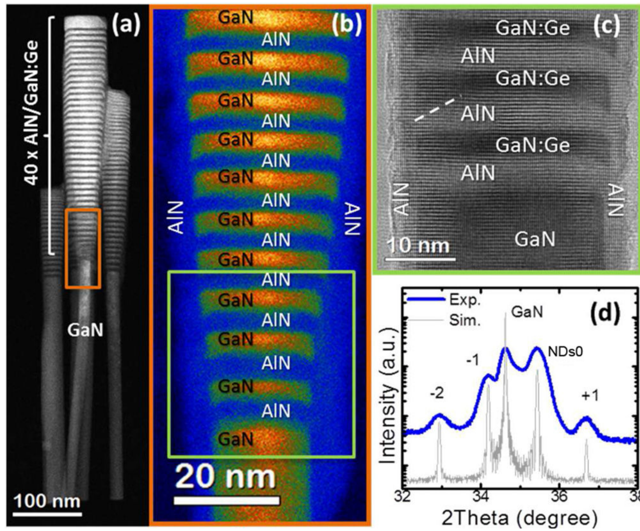

FIG. 1. (Color online) (a) HAADF STEM image of the GaN/AlN NW heterostructures. The AlN barriers (darker) and GaN disks (brighter) have nominal thicknesses of 4 nm. (b) Zoom into the squared region in (a) displayed in temperature color code. (c) HRTEM image of the first three GaN:Ge disks (near the GaN stem). (d) HRXRD $\omega - 2\theta$ scan around the (0002) reflection of sample N3, together with a simulation. The simulation is down shifted for clarity.

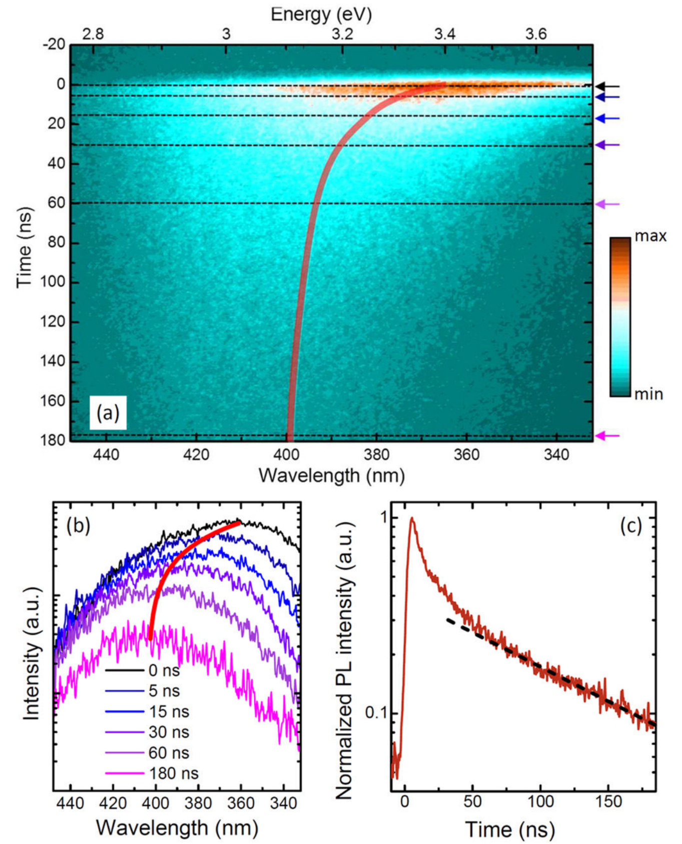

FIG. 3. (Color online) (a) Time-resolved PL spectra of sample N3. The red stripe follows the intensity maximum as a function of time. (b) Evolution of the PL spectra as a function of time. The time of maximum intensity is taken as $t = 0$. The spectra are acquired with a time integration window of 0.4 ns. (c) Evolution of the PL peak intensity as a function of time. The dashed line is an exponential fit to the PL decay for times longer than 60 ns.

These superlattice periods were in good agreement with those measured locally by means of TEM.

The optical properties of the NW heterostructures were first analyzed by continuous-wave PL spectroscopy. Figure 2(a) shows the low-temperature ($T = 5$ K) emission of the samples, displaying a blue shift with increasing dopant concentration, which is attributed to the screening of the internal electric field [25,28]. The peak PL wavelengths are summarized in Table I. Figure 2(b) shows the variation of the normalized integrated PL intensities as a function of temperature. The PL intensities remains almost constant up to about 100 K, after which, at room temperature, they drop to 20–40% of their maximum values. This behavior is characteristic of GaN/AlN nanostructures with 3D confinement [42–45], in contrast to planar structures, which generally exhibit a PL quenching of several orders of magnitude at room temperature [44].

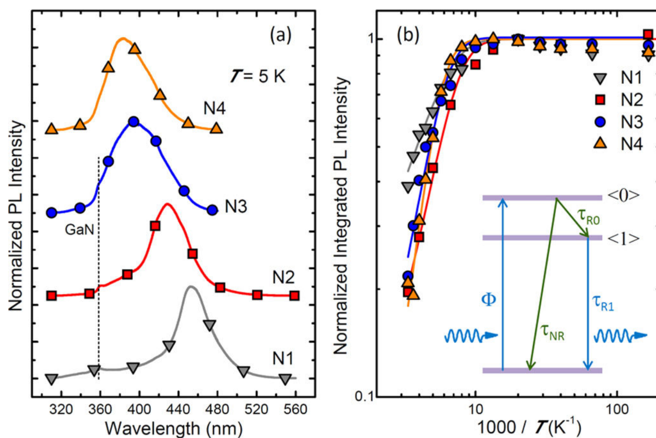

FIG. 2. (Color online) (a) Normalized PL spectra of samples N1–N4 measured at low temperature ($T = 5$ K). The spectra are normalized and vertically shifted for clarity. The dotted vertical line indicates the location of the GaN band gap. (b) Normalized integrated PL intensity of the samples shown in (a) as a function of temperature. Solid lines are fits to Eq (3). Inset: Simplified three-level model of the PL dynamics.

To probe the band-to-band carrier dynamics within this system, the decay of the PL under pulsed excitation was analyzed. As a typical example, Fig. 3(a) shows the time-resolved evolution of the PL spectra of sample N3 measured at low temperature ($T = 5$ K). The emission presents a red shift of 45 nm during the first ∼60 ns before a steady state is obtained, as illustrated in Fig. 3(b). This spectral shift is systematic through all the investigated samples and ranges from 0.1–0.3 eV, decreasing for increasing doping levels. Following the PL intensity at the maximum of the spectrum as a function of time [trajectory indicated by the red line in Figs. 3(a) and 3(b)], the intensity decay in Fig. 3(c) is obtained. Comparing Figs. 3(b) and 3(c), the initial red shift is associated to a pronounced nonexponential drop of the PL intensity during the first ∼60 ns, followed by an exponential decay. These PL dynamics are qualitatively the same for all the samples regardless of doping level.

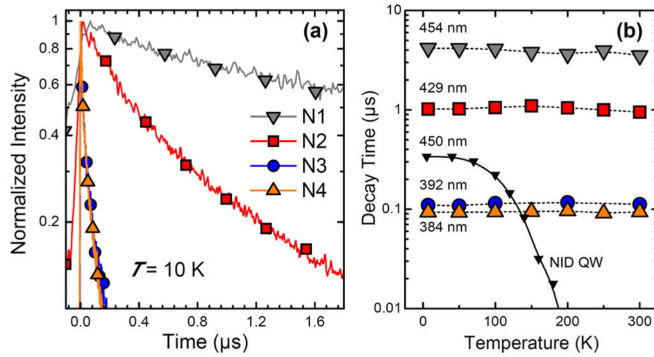

FIG. 4. (Color online) (a) PL decay for samples N1–N4 measured at low temperature ($T = 10$ K). The decays were taken following the method described in Fig. 3. (b) PL decay characteristic times extracted from the exponential part of the PL decays [similar to Fig. 1(c)], plotted as a function of temperature. The emission wavelengths are indicated in the figure. Superimposed, PL decay times of an NID GaN/AlN quantum well (labeled NID QW) emitting at approximately the same wavelength that N1.

The initial red shift and nonexponential behavior are attributed to the perturbation of the band structure induced by the excitation (screening of the polarization fields), and to band filling, as previously observed in GaN/AlGaN quantum wells [11]. Therefore, in subsequent analyses, only the time constant extracted during the exponential decay regime [dashed line in Fig. 3(c)] is addressed. This regime reflects the carrier dynamics of the original band structure, once the photoinduced perturbation from the laser is dissipated.

Figure 4(a) shows the low-temperature ($T = 5$ K) PL evolution for the NW heterostructures with different dopant concentrations. A drastic decrease of the decay time with increasing Ge concentration is observed: the NID sample displays a decay time on the order of several µs, whereas the decay times for higher dopant concentrations decrease by more than an order of magnitude (to around 100 ns). These decay times are orders of magnitude longer than shown in previous literature reports [16,28], where the PL decay times were even shorter than those of equivalent quantum well structures. This discrepancy could be explained by the measurement procedure: in Refs. [16,28], the decay times were estimated from measurements exciting with a pulse repetition rate of 78 MHz (time between pulses = 12.8 ns). Based on the data from Ref. [28], the PL from undoped (highest doped) samples would have only dropped to about 60% (14%) of the maximum value before the next laser pulse hit. From their data, a $1/e$ decay time can be extracted assuming exponential relaxation. However, our experiments prove that the initial relaxation is strongly nonexponential due to the screening of the electric field induced by the laser pulse. With the lower excitation power, after 12.8 ns none of the samples have entered the exponential regime [dashed line in Fig. 3(c)], and only the most heavily doped sample would have recovered from the initial blue shift induced by the laser. We therefore conclude that the measurements in Ref. [28] provide information mostly about the recovery of the screening of the internal fields induced by the measuring laser. This is in accordance to the decay time's (and the spectral shift's) dependency on laser power reported by Hille et al. [28].

The evolution of the characteristic PL decay time has been analyzed as a function of temperature with the results plotted in Fig. 4(b), where the relaxation times were extracted from the exponential decay profiles as indicated in Fig. 3(c). In all cases, the PL decay times remain constant (±10%) from 10 − 300 K, as previously observed in the case of Stransky-Krastanov GaN/AlN quantum dots [18]. This demonstrates that the 3D confinement in the nanodisks efficiently suppresses thermally activated nonradiative recombination channels up to room temperature. In contrast, temperature-dependent time-resolved measurements of GaN/AlN quantum well samples show a decrease in relaxation time over this temperature range by several orders of magnitude, as described in Ref. [18] and illustrated in Fig. 4(b).

The thermally stable PL decay time in Fig. 4(b) lead us to attribute the thermal quenching of the integrated PL intensity in Fig. 2(b) to carrier losses during the relaxation process of the hot photoexcited carriers to the exciton ground states. A simplified view of the process can be provided by the three-level model schematically described in the inset of Fig. 2(b). In steady-state conditions the carrier generation rate, Φ, equals the relaxation rate to the exciton emitting state ⟨1⟩ plus the nonradiative recombination rate:

$$\Phi = \frac{n_0}{\tau_{\mathrm{NR}}} + \frac{n_0}{\tau_{R0}}, \quad (1)$$

where n_0 is the optically excited population of the ⟨0⟩ level, and τ_{NR} and τ_{R0} are the characteristic times associated to the nonradiative processes and to the relaxation to the exciton emitting state, respectively. By neglecting nonradiative recombination once the excitons are trapped in the nanodisk, assumption supported by the observation of a PL decay constant with temperature, the PL intensity can be described as:

$$I = \frac{n_1}{\tau_{R1}} = \frac{n_0}{\tau_{R0}} = \frac{\Phi}{1 + \tau_{R0}/\tau_{\mathrm{NR}}}, \quad (2)$$

where n_1 is the population of the exciton emitting state in the nanodisk and τ_{R1} is the associated characteristic time.

Assuming that the photogeneration (Φ) is constant with temperature, and that nonradiative processes from state ⟨0⟩ are thermally activated, the PL intensity as a function of temperature, $I(T)$, can be described by:

$$I(T) = \frac{1(T = 0)}{1 + a\exp(-E_a/kT)}, \quad (3)$$

where E_a represents the activation energy of the nonradiative process, kT being the thermal energy, and a being a constant coefficient. Solid lines in Fig. 2(b) are fits of the experimental data to Eq. (3). The extracted values of E_a and a are summarized in Table I. An increase in both parameters with larger doping concentration is observed, which points to an enhanced probability of nonradiative processes with increasing carrier density.

IV. DISCUSSION

The strong acceleration of the PL decay with increasing Ge concentration points to a screening of the electric field in the nanodisks that drastically defines the radiative carrier lifetime. The magnitude of this effect is much larger than previously

reported for GaN quantum wells [18,46]. Comparing the low-temperature PL lifetimes of NID quantum wells and nanodisks emitting at approximately the same wavelength, i.e., with the same electron-hole separation in energy, the decay time in the case of the nanodisks is significantly longer. This juxtaposition is illustrated in Fig. 4(b) for the decay times of quantum wells emitting around 450 nm. This discrepancy points to a significantly larger electron-hole separation in space, which implies a different electric field distribution.

In order to understand the electric field distribution leading to this giant screening effect, 3D calculations of the NW strain state, band diagram and quantum confined states were performed using the NEXTNANO3 software [47] with the material parameters described in Ref. [48]. The NW was defined as a hexagonal prism consisting of a long (50 nm) GaN stem followed by a sequence of 10 AlN/GaN stacks and capped with 18 nm of GaN. The radius of the GaN base was 20 nm, the growth axis was [000−1] and the sidewall faces were {1−100} planes. The structure was defined on a GaN substrate, to provide a reference in-plane lattice parameter. The GaN stem and the AlN/GaN heterostructure were laterally surrounded by an AlN shell, and the whole structure was embedded in a rectangular prism of air, which permits the elastic deformation of misfit strain. Surface states were modeled as a surface charge density of $2 \times 10^{12}\,\mathrm{cm}^{-2}$ at the air/semiconductor interfaces [49]. The presence of {1−102} facets in the AlN sections was taken into account, as illustrated in Fig. 5(a), which shows a (1−100) cross-section view of three nanodisks in the stack.

The 3D strain distribution was calculated by minimizing the elastic energy and applying zero-stress boundary conditions at the surface. The effect of doping on the strain distribution was neglected [35,36]. Figures 5(b) and 5(c) display (1−100) cross-sectional views of the strain components along the ⟨11−20⟩ direction, ε_{xx}, and ⟨0001⟩ direction, ε_{zz}, for three nanodisks in the stack. Regarding the ε_{xx} component, the center of the disk is compressed by the AlN sections ($\varepsilon_{xx} = -1.29\%$) and there is an elastic relaxation close to the sidewalls. In contrast, the ε_{zz} strain component is almost zero ($\varepsilon_{zz} = -0.025\%$) along the center of the nanodisk, however near the sidewalls the GaN gets significantly compressed due to the presence of the AlN shell (up to $\varepsilon_{zz} = -2.2\%$). The radial inhomogeneous strain results in nonzero ε_{xz} and ε_{yz} shear strain components, as illustrated in Fig. 5(d), which in turn leads to radial piezoelectric polarization associated to the nonzero e_{15} piezoelectric constant in the wurtzite lattice. On the other hand, this particular strain distribution results also in an increase of the GaN band gap by ∼120 meV when moving from the center of the nanodisk to the sidewalls (data obtained using the deformation potentials from Ref. [50]).

The strain calculation provides a 3D map of the polarization in the heterostructure. With this input, the nonlinear Poisson equation was solved classically to obtain the 3D band structure of the complete wire. After the Poisson equation was solved in equilibrium, the eigenfunctions were calculated by solving the Schrödinger equation in a quantum region that covered one nanodisk in the center of the NW, including the AlN barriers on the top and bottom. Figures 6(a) and 6(b) show the conduction and valence band profiles along the [000−1] growth axis along the center of the NW for Fig. 6(a) undoped nanodisks and 6(b) nanodisks with an n-type dopant concentration $N_D =$

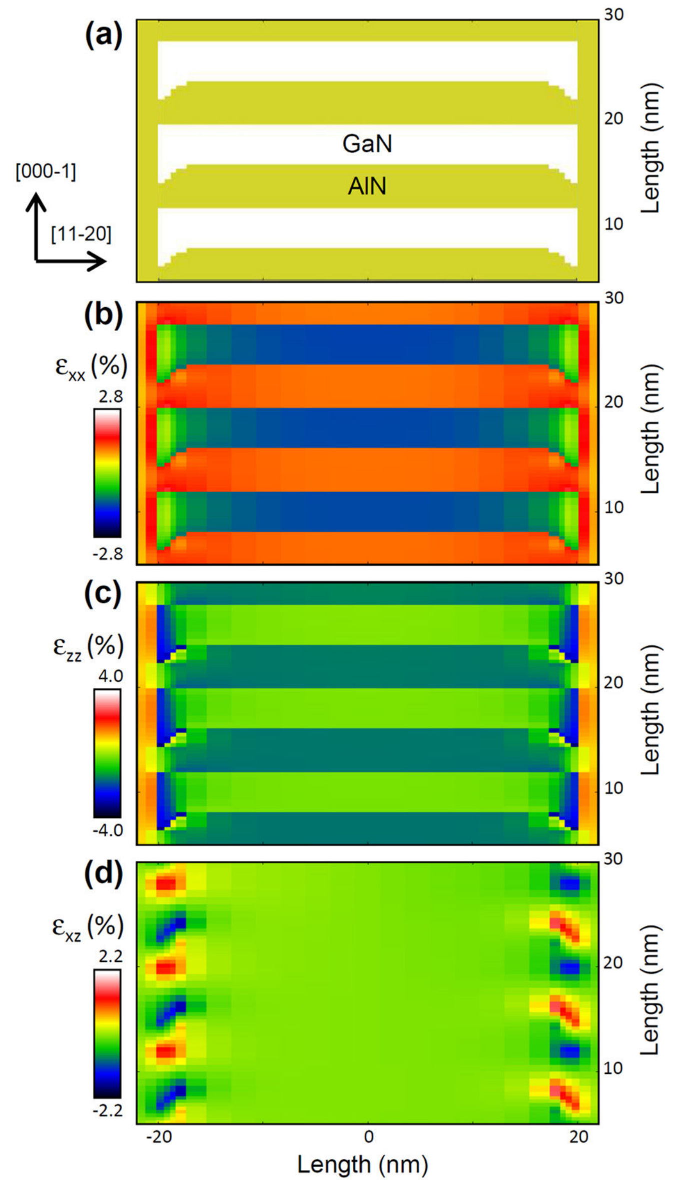

FIG. 5. (Color online) (a) Schematic representation of three GaN/AlN nanodisks in the center of the nanowire heterostructures, as they are described in the input file for NEXTNANO3. The structure is viewed along the [1−100] plane. White areas correspond to GaN and yellow areas correspond to AlN. (b) Calculation of the ε_{xx} strain component (strain along [11−20]) for these same disks. (c) Calculation of the ε_{zz} strain component (along [000–1]). (d) Calculation of the ε_{xz} shear strain component.

$1.7 \times 10^{20}\,\mathrm{cm}^{-3}$ (sample N3). In both cases, the polarization-induced internal electric fields result in a sawtooth profile with the electron level shifted towards the bottom of the nanodisk and the hole level towards the top of the nanodisk. In the doped structure, the internal electric field is reduced from 5.9 to 2.5 MV/cm due to carrier screening.

Figures 6(c) and 6(d) show the radial conduction and valence band profiles along the [11−20] axis for undoped and doped ($N_D = 1.7 \times 10^{20}\,\mathrm{cm}^{-3}$) nanodisks. In both cases, the conduction (valence) band profile was taken at the bottom (top) interface of the nanodisk. The squared wave functions of the first electron and hole levels are also represented. In

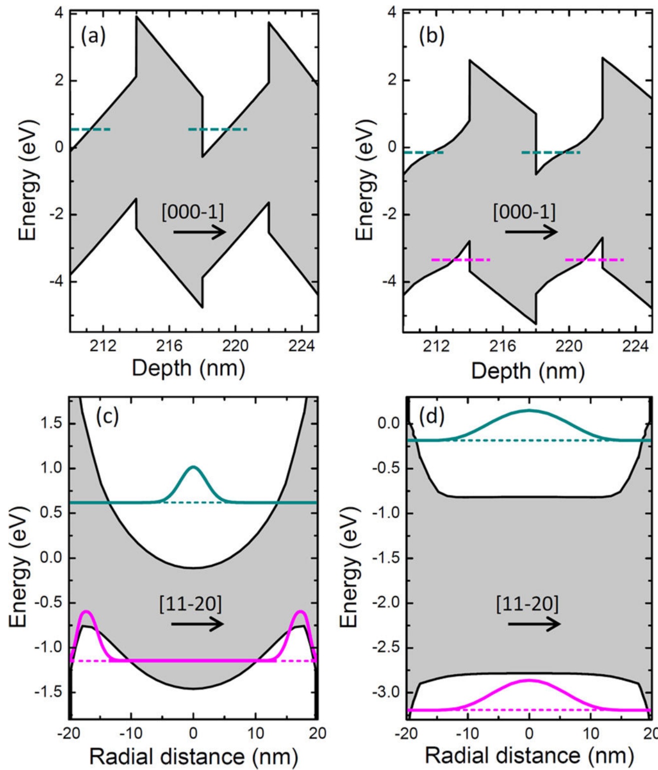

FIG. 6. (Color online) (a)–(d) Calculation of the conduction and valence band profiles and first electronic levels of electrons and holes. (a), (b) Conduction and valence band profiles along [000−1] taken at the center of the NW, for (a) undoped nanodisks and (b) Ge-doped nanodisks (sample N3). The ground electron and hole levels are indicated by dashed lines. In (a), the ground hole level is not indicated because the value of the squared wave function along the center of the NW is zero. (c), (d) Radial conduction and valence band profiles for the (c) undoped and (d) Ge-doped nanodisk in the center of the stack. Note that the conduction band was taken at the bottom of the disk, while the valence band was taken at the top of the disk. The squared wave functions of the ground electron and hole states are indicated in the figures.

the case of undoped nanodisks, the band bending induced by the AlN shell pushes the electrons towards the center of the NW, whereas the radial valence band profile has local maxima near the NW sidewalls. This result is in agreement with calculations by Rigutti *et al.* [51]. (GaN/AlGaN NW heterostructures with AlGaN shell) and Rivera *et al.* [52] (GaN/AlGaN NW heterostructures without shell), and in the same line that the calculations of Marquardt *et al.* [53] for InGaN/GaN NW heterostructures. Therefore, in addition to the polarization-induced vertical separation of electron and holes, the 3D geometry of the nanodisks leads to a radial separation of carriers, which explains the delay of the radiative recombination with respect to the quantum well case. Note that the strain-induced enlargement of the GaN band gap at the ∼5 nm closest to the nanodisk sidewalls contributes to separate the carriers, particularly the holes, from the core/shell interface. The presence of {1−102} facets at the top interface of the AlN sections, which enlarges the GaN disks close to the surface, does not have a relevant effect on the radial location of the hole. This is because the spontaneous and piezoelectric polarization shifts the hole towards the top of the GaN nanodisk. However, these facets modify the electron wave function, which results in a shift of the band-to-band transition by ∼300 meV.

At low dopant concentrations (below 10^{19} cm^3), the electric field along the [11−20] axis at the top GaN/AlN interface, depicted in Fig. 6(e), presents a maximum value of ∼0.6 MV/cm, i.e., one order of magnitude smaller than the field along [000−1]. Increasing the doping concentration leads to the screening of the lateral electric field, causing the spatial broadening of the electron wave function described in Fig. 6(d). In the valence band, the flattening of the potential profile shifts the hole wave function towards the center of the NW radially aligning them with the electron wave function. The improved electron-hole wave function overlap explains the drastic decrease of the radiative recombination lifetime. Figure 7(b) also shows the attenuation of the electric field in the radial direction as a function of the doping concentration. The transition of the hole towards the center of the NW, i.e., the inversion of the electric field sign, takes place for a doping concentration around 3.5×10^{19} cm^{-3}.

These calculations consider the presence of negatively charged surface states with a density of 2×10^{12} cm^{-2}. The negatively charged surface attracts the holes, but is not a critical

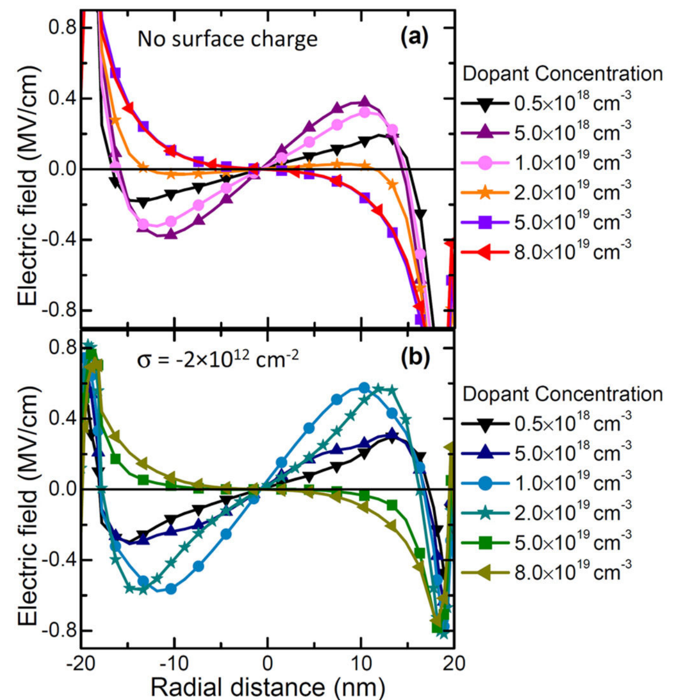

FIG. 7. (Color online) Calculation of the electric field along [11−20] at the top of the nanodisk for various doping concentrations in the nanodisks, (a) neglecting surface charges, and (b) with surface charges at a concentration of $\sigma = -2 \times 10^{12}$ cm^{-2}. With higher doping levels, the electric field in the disk is attenuated. Positive electric field implies that it points in the [11−20] direction. The sign of the electric field sees a crossover at a dopant concentration of (a) $\sim 2 \times 10^{19}$ cm^{-3}, and (b) $\sim 4 \times 10^{19}$ cm^{-3}. The magnitude of the radial electric field is (a) 0.42 MV/cm, and (b) 0.58 MV/cm. A null electric field was seen (a) 14 nm and (b) 17 nm from the center of the wire.

factor to determine the carrier distribution, since the electric field is mostly associated to the piezoelectric phenomena. Figure 7(a) describes the radial electric field in a similar structure without surface charges. A complete suppression of the surface charges lowers the required doping concentration to invert the electric field to 2.0×10^{19} cm^{-3} and results in a radial shift of the zero-field position (which corresponds to the maximum of the hole wave function) by about 3 nm towards the center of the NW for low doping levels.

The above-described calculations demonstrate that the radial misalignment of the electron and hole wave functions is a determining factor for the band-to-band dynamics in GaN/AlN nanodisks. At low dopant levels, the radial electron-hole separation leads to radiative lifetimes that are significantly longer than in GaN/AlN quantum wells emitting at the same wavelength. Upon increasing the dopant concentration, carrier screening leads to a radial centralization of the hole underneath the electron, and a large decrease in the radiative lifetime. These results are also in agreement with the radiation model shown in Fig. 2(b), which concurs that with higher centralization of the hole and electron within the nanowire, there will be a higher energetic barrier (E_a) for carriers to recombine nonradiatively at the edges of the nanowire.

V. CONCLUSIONS

The carrier dynamics in 40-period GaN/AlN (4 nm/4 nm) NW heterostructures have been explored as a function of the Ge dopant concentration in the GaN disks. Long PL decay times, on the order of microseconds, are measured in nonintentionally doped disks and persist up to room temperature. This confirms the efficiency of quantum confinement in the nanodisks to inhibit nonradiative recombination. The long relaxation times are explained as the result of internal electric fields present in the nanodisks, with an axial component in the range of a few MV/cm associated to spontaneous and piezoelectric polarization, and a radial component associated to the radial variation of lattice strain. Simulations show that at low dopant concentrations, a large electron-hole separation in both the axial and radial directions is present, with holes located axially on top of the nanodisk and radially close to the surface, and electrons located axially at the bottom of the nanodisk and radially centered. The relatively weak radial electric fields, calculated to be one order of magnitude smaller than the axial fields, are rapidly screened by doping, which leads to both a radial and axial centralization of the hole underneath the electron. This bidirectional dopant-induced giant screening leads to large decreases in radiative lifetime by about two orders of magnitude, in addition to the luminescence blue shift.

ACKNOWLEDGMENTS

This work is supported by the EU ERC-StG "TeraGaN" (#278428) project, the LOEWE program of excellence of the Federal State of Hessen (project initiative STORE-E), and by the Spanish MINECO MAT2014-51480-ERC (e-ATOM) and Generalitat de Catalunya 2014SGR1638. J.A. thanks ICN2 Severo Ochoa Excellence Program. MdlM thanks CSIC Jae-Predoc program.

[1] F. Hatami, M. Grundmann, N. N. Ledentsov, F. Heinrichsdorff, R. Heitz, J. Böhrer, D. Bimberg, S. S. Ruvimov, P. Werner, V. Ustinov, P. S. Kop'ev, and Z. I. Alferov, Phys. Rev. B **57**, 4635 (1998).
[2] Y. Zhang, Wang, and A. Mascarenhas, Nano Lett. **7**, 1264 (2007).
[3] N. Grandjean, B. Damilano, S. Dalmasso, M. Leroux, M. Laügt, and J. Massies, J. Appl. Phys. **86**, 3714 (1999).
[4] C. Morhain, T. Bretagnon, P. Lefebvre, X. Tang, P. Valvin, T. Guillet, B. Gil, T. Taliercio, M. Teisseire-Doninelli, B. Vinter, and C. Deparis, Phys. Rev. B **72**, 241305R (2005).
[5] F. Bernardini, V. Fiorentini, and D. Vanderbilt, Phys. Rev. B **56**, R10024 (1997).
[6] C. Adelmann, E. Sarigiannidou, D. Jalabert, Y. Hori, J.-L. Rouviére, B. Daudin, S. Fanget, C. Bru-Chevallier, T. Shibata, and M. Tanaka, Appl. Phys. Lett. **82**, 4154 (2003).
[7] P. Lefebvre, J. Allègre, B. Gil, H. Mathieu, N. Grandjean, M. Leroux, J. Massies, and P. Bigenwald, Phys. Rev. B **59**, 15363 (1999).
[8] R. Cingolani, A. Botchkarev, H. Tang, H. Morkoç, G. Traetta, G. Coli, M. Lomascolo, A. Di Carlo, F. Della Sala, and P. Lugli, Phys. Rev. B **61**, 2711 (2000).
[9] S. Kako, M. Miyamura, K. Tachibana, K. Hoshino, and Y. Arakawa, Appl. Phys. Lett. **83**, 984 (2003).
[10] S. Kalliakos, P. Lefebvre, and T. Taliercio, Phys. Rev. B **67**, 205307 (2003).
[11] P. Lefebvre, S. Kalliakos, T. Bretagnon, P. Valvin, T. Taliercio, B. Gil, N. Grandjean, and J. Massies, Phys. Rev. B **69**, 035307 (2004).
[12] T. Bretagnon, P. Lefebvre, P. Valvin, R. Bardoux, T. Guillet, T. Taliercio, B. Gil, N. Grandjean, F. Semond, B. Damilano, A. Dussaigne, and J. Massies, Phys. Rev. B **73**, 113304 (2006).
[13] O. Moshe, D. H. Rich, S. Birner, M. Povolotskyi, B. Damilano, and J. Massies, J. Appl. Phys. **108**, 083510 (2010).
[14] J. M. Gérard, O. Cabrol, and B. Sermage, Appl. Phys. Lett. **68**, 3123 (1996).
[15] M. de la Mata, C. Magén, P. Caroff, and J. Arbiol, Nano Lett. **14**, 6614 (2014).
[16] F. Furtmayr, J. Teubert, P. Becker, S. Conesa-Boj, J. R. Morante, A. Chernikov, S. Schäfer, S. Chatterjee, J. Arbiol, and M. Eickhoff, Phys. Rev. B **84**, 205303 (2011).
[17] M. Tchernycheva, L. Nevou, L. Doyennette, F. H. Julien, E. Warde, F. Guillot, E. Monroy, E. Bellet-Amalric, T. Remmele, and M. Albrecht, Phys. Rev. B **73**, 125347 (2006).
[18] J. Renard, P. K. Kandaswamy, E. Monroy, and B. Gayral, Appl. Phys. Lett. **95**, 131903 (2009).
[19] J. Renard, R. Songmuang, G. Tourbot, C. Bougerol, B. Daudin, and B. Gayral, Phys. Rev. B **80**, 121305 (2009).
[20] J. Ristić, E. Calleja, M. A. Sánchez-García, J. M. Ulloa, J. Sánchez-Páramo, J. M. Calleja, U. Jahn, A. Trampert, and K. H. Ploog, Phys. Rev. B **68**, 125305 (2003).

[21] J. Ristić, C. Rivera, E. Calleja, S. Fernández-Garrido, M. Povoloskyi, and A. Di Carlo, Phys. Rev. B **72**, 085330 (2005).
[22] J. Renard, R. Songmuang, C. Bougerol, B. Daudin, and B. Gayral, Nano Lett. **8**, 2092 (2008).
[23] R. Songmuang, D. Kalita, P. Sinha, M. den Hertog, R. André, T. Ben, D. González, H. Mariette, and E. Monroy, Appl. Phys. Lett. **99**, 141914 (2011).
[24] D. Camacho Mojica and Y.-M. Niquet, Phys. Rev. B **81**, 195313 (2010).
[25] M. Beeler, P. Hille, J. Schörmann, J. Teubert, M. de la Mata, J. Arbiol, M. Eickhoff, and E. Monroy, Nano Lett. **14**, 1665 (2014).
[26] J. B. Schlager, K. A. Bertness, P. T. Blanchard, L. H. Robins, A. Roshko, and N. A. Sanford, J. Appl. Phys. **103**, 124309 (2008).
[27] C. Hauswald, T. Flissikowski, T. Gotschke, R. Calarco, L. Geelhaar, H. T. Grahn, and O. Brandt, Phys. Rev. B **88**, 075312 (2013).
[28] P. Hille, J. Müßener, P. Becker, M. de la Mata, N. Rosemann, C. Magén, J. Arbiol, J. Teubert, S. Chatterjee, J. Schörmann, and M. Eickhoff, Appl. Phys. Lett. **104**, 102104 (2014).
[29] M. A. Sanchez-Garcia, E. Calleja, E. Monroy, F. J. Sanchez, F. Calle, E. Muñoz, and R. Beresford, J. Cryst. Growth **183**, 23 (1998).
[30] E. Calleja, M. A. Sánchez-García, F. J. Sánchez, F. Calle, F. B. Naranjo, E. Muñoz, U. Jahn, and K. Ploog, Phys. Rev. B **62**, 16826 (2000).
[31] R. Songmuang, O. Landré, and B. Daudin, Appl. Phys. Lett. **91**, 251902 (2007).
[32] S. Fernández-Garrido, J. Grandal, E. Calleja, M. A. Sánchez-García, and D. López-Romero, J. Appl. Phys. **106**, 126102 (2009).
[33] M. I. den Hertog, F. González-Posada, R. Songmuang, J. L. Rouviere, T. Fournier, B. Fernandez, and E. Monroy, Nano Lett. **12**, 5691 (2012).
[34] M. de la Mata, C. Magen, J. Gazquez, M. I. B. Utama, M. Heiss, S. Lopatin, F. Furtmayr, C. J. Fernández-Rojas, B. Peng, J. R. Morante, R. Rurali, M. Eickhoff, A. Fontcuberta i Morral, Q. Xiong, and J. Arbiol, Nano Lett. **12**, 2579 (2012).
[35] A. Dadgar, J. Bläsing, A. Diez, and A. Krost, Appl. Phys. Express **4**, 011001 (2011).
[36] S. Fritze, A. Dadgar, H. Witte, M. Bügler, A. Rohrbeck, J. Bläsing, A. Hoffmann, and A. Krost, Appl. Phys. Lett. **100**, 122104 (2012).
[37] J. Schörmann, P. Hille, M. Schäfer, J. Müßener, P. Becker, P. J. Klar, M. Kleine-Boymann, M. Rohnke, M. de la Mata, J. Arbiol, D. M. Hofmann, J. Teubert, and M. Eickhoff, J. Appl. Phys. **114**, 103505 (2013).
[38] R. Calarco, R. J. Meijers, R. K. Debnath, T. Stoica, E. Sutter, and H. Lüth, Nano Lett. **7**, 2248 (2007).
[39] R. Songmuang, T. Ben, B. Daudin, D. González, and E. Monroy, Nanotechnol. **21**, 295605 (2010).
[40] S. D. Carnevale, J. Yang, P. J. Phillips, M. J. Mills, and R. C. Myers, Nano Lett. **11**, 866 (2011).
[41] J. Arbiol, C. Magen, P. Becker, G. Jacopin, A. Chernikov, S. Schäfer, F. Furtmayr, M. Tchernycheva, L. Rigutti, J. Teubert, S. Chatterjee, J. R. Morante, and M. Eickhoff, Nanoscale **4**, 7517 (2012).
[42] M. Sénès, K. L. Smith, T. M. Smeeton, S. E. Hooper, and J. Heffernan, Phys. Rev. B **75**, 045314 (2007).
[43] F. Guillot, E. Bellet-Amalric, E. Monroy, M. Tchernycheva, L. Nevou, L. Doyennette, F. H. Julien, L. S. Dang, T. Remmele, M. Albrecht, T. Shibata, and M. Tanaka, J. Appl. Phys. **100**, 044326 (2006).
[44] Z. Gačević, A. Das, J. Teubert, Y. Kotsar, P. K. Kandaswamy, T. Kehagias, T. Koukoula, P. Komninou, and E. Monroy, J. Appl. Phys. **109**, 103501 (2011).
[45] C. Himwas, R. Songmuang, Le Si Dang, J. Bleuse, L. Rapenne, E. Sarigiannidou, and E. Monroy, Appl. Phys. Lett. **101**, 241914 (2012).
[46] P. K. Kandaswamy, H. Machhadani, Y. Kotsar, S. Sakr, A. Das, M. Tchernycheva, L. Rapenne, E. Sarigiannidou, F. H. Julien, and E. Monroy, Appl. Phys. Lett. **96**, 141903 (2010).
[47] S. Birner, T. Zibold, T. Andlauer, T. Kubis, M. Sabathil, A. Trellakis, and P. Vogl, IEEE Trans. Electron Devices **54**, 2137 (2007).
[48] P. K. Kandaswamy, F. Guillot, E. Bellet-Amalric, E. Monroy, L. Nevou, M. Tchernycheva, A. Michon, F. H. Julien, E. Baumann, F. R. Giorgetta, D. Hofstetter, T. Remmele, M. Albrecht, S. Birner, and L. S. Dang, J. Appl. Phys. **104**, 093501 (2008).
[49] M. Bertelli, P. Löptien, M. Wenderoth, A. Rizzi, R. G. Ulbrich, M. C. Righi, A. Ferretti, L. Martin-Samos, C. M. Bertoni, and A. Catellani, Phys. Rev. B **80**, 115324 (2009).
[50] S.-H. Park, Jpn. J. Appl. Phys. **39**, 3478 (2000).
[51] L. Rigutti, J. Teubert, G. Jacopin, F. Fortuna, M. Tchernycheva, A. De Luna Bugallo, F. H. Julien, F. Furtmayr, M. Stutzmann, and M. Eickhoff, Phys. Rev. B **82**, 235308 (2010).
[52] C. Rivera, U. Jahn, T. Flissikowski, J. L. Pau, E. Muñoz, and H. T. Grahn, Phys. Rev. B **75**, 045316 (2007).
[53] O. Marquardt, C. Hauswald, M. Wölz, L. Geelhaar, and O. Brandt, Nano Lett. **13**, 3298 (2013).

Annex 7

NANO LETTERS
Letter
pubs.acs.org/NanoLett

Intraband Absorption in Self-Assembled Ge-Doped GaN/AlN Nanowire Heterostructures

M. Beeler,[†] P. Hille,[‡] J. Schörmann,[‡] J. Teubert,[‡] M. de la Mata,[§] J. Arbiol,[§,∥] M. Eickhoff,[‡] and E. Monroy*[,†]

[†]CEA-CNRS Group Nanophysics and Semiconductors, CEA/INAC/SP2M and CNRS-Institute Néel, 17 rue des Martyrs, 38054 Grenoble cedex 9, France

[‡]I. Physikalisches Institut, Justus-Liebig-Universität Gießen, Heinrich-Buff-Ring 16, D-35392 Gießen, Germany

[§]Institut de Ciencia de Materials de Barcelona, ICMAB-CSIC, Campus de la UAB, 08193 Barcelona, Catalonia, Spain

[∥]Institucio Catalana de Recerca i Estudis Avançats (ICREA), 08010 Barcelona, Catalonia, Spain

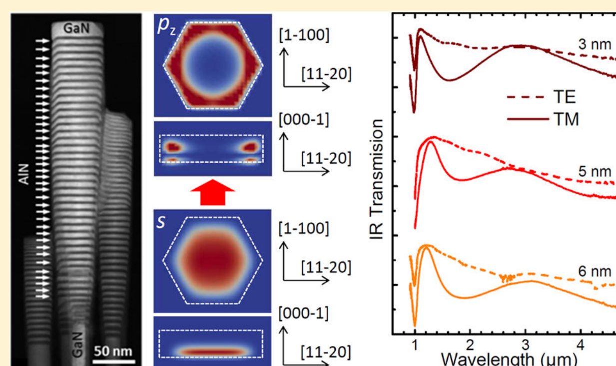

ABSTRACT: We report the observation of transverse-magnetic-polarized infrared absorption assigned to the s−p_z intraband transition in Ge-doped GaN/AlN nanodisks (NDs) in self-assembled GaN nanowires (NWs). The s−p_z absorption line experiences a blue shift with increasing ND Ge concentration and a red shift with increasing ND thickness. The experimental results in terms of interband and intraband spectroscopy are compared to theoretical calculations of the band diagram and electronic structure of GaN/AlN heterostructured NWs, accounting for their three-dimensional strain distribution and the presence of surface states. From the theoretical analysis, we conclude that the formation of an AlN shell during the heterostructure growth applies a uniaxial compressive strain which blue shifts the interband optical transitions but has little influence on the intraband transitions. The presence of surface states with density levels expected for *m*-GaN plane charge-deplete the base of the NWs but is insufficient to screen the polarization-induced internal electric field in the heterostructures. Simulations show that the free-carrier screening of the polarization-induced internal electric field in the NDs is critical to predicting the photoluminescence behavior. The intraband transitions, on the other hand, are blue-shifted due to many-body effects, namely, the exchange interaction and depolarization shift, which exceed the red shift induced by carrier screening.

KEYWORDS: *Nanowire, GaN, intraband, intersubband*

As optoelectronic devices push toward higher efficiencies, the control of carrier relaxation becomes a key aspect for device engineering, which is particularly relevant in the case of intraband/intersubband (ISB) optoelectronics (quantum well infrared photodetectors, quantum cascade detectors, quantum cascade lasers). Longer intraband lifetimes have been proven to exist in laterally confined systems, including quantum dots (QDs)[1−4] and nanowires (NWs).[5,6] In the case of NWs, their large surface-to-volume ratio allows misfit strain to be elastically released, extending the viable active region size and composition beyond the limits of planar systems or QDs. For these reasons, NWs are under study to improve the performance of THz quantum cascade lasers,[7,8] whose operating temperature is currently limited by nonradiative scattering processes which quickly depopulate the upper laser level.

Semiconductor NWs have already become a powerful kind of nanomaterial with promising applications in electronics,[9] optoelectronics,[10,11] energy conversion,[12,13] and sensorics.[14,15] However, not much information has been reported so far on NW intraband electronic transitions. From the experimental viewpoint, infrared (IR) optical absorption associated to intraband transitions between laterally confined states have been observed in bismuth NWs,[16] and intraband effects have proven relevant to understand the operation of Si-NW field effect transistors.[17] However, conduction band fluctuations associated to stacking faults and polytypism[18−20] have hindered the realization of intraband optoelectronic devices using self-assembled GaAs-based heterostructured NWs (bottom-up approach). As an alternative, intraband electroluminescence was recently obtained from nanopilars lithographically defined on a standard GaAs/AlGaAs quantum cascade laser structure (top-down approach).[21]

GaN could be a model material for the study of intraband transitions in heterostructured NWs, since the presence of

Received: January 20, 2014
Published: February 6, 2014

 © 2014 American Chemical Society

stacking faults or extended defects can be limited to the first hundred nanometers close to the substrate. III-nitrides have recently emerged as promising semiconductors for new intraband devices.[22−24] GaN is transparent over a large spectral region, notably for wavelengths longer than 360 nm, reaching into the far-IR, excluding the Restrahlen band (from 9.6 to 19 μm). Additionally, the large energy of GaN's longitudinal-optical (LO) phonons (92 meV) opens prospects for high-temperature THz quantum cascade lasers and intraband devices covering the 5−10 THz band, inaccessible to As-based technologies due to phonon absorption. Furthermore, their large conduction band offset (about 1.8 eV for GaN/AlN[25−27]) and subpicosecond intraband relaxation times[28−31] render them appealing materials for ultrafast photonic devices from the near to the far-IR.[32,33] Currently, ISB absorption in GaN/AlGaN quantum wells (QWs) can be tuned from 1.0 to 10 μm,[34−39] and in the THz range (>20 μm).[40−42] Room-temperature transverse-magnetic (TM) polarized near-IR intraband absorption in GaN/AlN QDs has also been reported.[1−4] This absorption was attributed to transitions from the ground state of the conduction band, *s*, to the first excited electronic state confined along the growth axis, p_z. The lateral confinement in the QDs gives rise to additional transitions that react to transverse-electric (TE) polarized excitation. The optical signature associated to s−$p_{x,y}$ was observed in the mid-IR by Vardi et al.[4] using in-plane electronic transport at low temperatures. However, shifting the s−p_z transition toward the mid- or far-IR is hindered by the requirement of lattice mismatch for the QD formation following the Stranski−Krastanov growth mode. Regarding GaN NWs, the only experimental result has been reported by Tanaka et al.,[43] who observed polarization-dependent near-IR absorption in a sample containing GaN/AlN (1 nm/2.7 nm) NW heterostructures. Furthermore, the feasibility of electron transport via quantized levels in the conduction band of GaN/AlN heterostructured NWs was demonstrated by the fabrication of resonant tunneling diodes.[32,33]

In this Letter, we first present a theoretical study of the intraconduction-band electronic structure of GaN/AlN heterostructured NWs, accounting for the strain distribution and the presence of surface states. Then, we report the experimental observation of TM-polarized IR absorption assigned to the s−p_z intraband transition in Ge-doped GaN/AlN nanodisks (NDs) inserted in self-assembled GaN NWs grown on Si(111) by plasma-assisted molecular-beam epitaxy (PAMBE). The s−p_z absorption line experiences a blue shift with increasing ND-doping level and a red shift with increasing ND thickness. The experimental results in terms of interband and intraband spectroscopy are compared with the theoretical calculations, and the inclusion of many-body effects is found to be critical in estimating the electronic transitions. Carrier screening of the polarization-induced internal electric field is critical for understanding the photoluminescence (PL) behavior of the NDs, and the intraband transitions are blue-shifted from the exchange interaction and depolarization shift, which overpower the red shift induced by carrier screening.

Theoretical Calculations. Three-dimensional (3D) calculations of the NW strain state, band diagram, and quantum confined states were performed using the Nextnano3 Schrödinger-Poisson equation solver.[44] The parameters used for GaN and AlN calculations are summarized in a previous paper.[45] We assumed a residual *n*-type doping $N_D = 5 \times 10^{17}$ cm^{-3}, and the dopant concentration in the GaN NDs was $N_D = 5 \times 10^{19}$ cm^{-3}. The NW was defined as a hexagonal prism consisting of a long (50 nm) GaN section followed by a sequence of 14 AlN/GaN stacks and capped with 18 nm of GaN. The growth axis was [000−1].[46,47] The NW GaN base radius was simulated to be 20 nm. The structure was defined on a GaN substrate, to provide a reference in-plane lattice parameter. The NW GaN base and the AlN/GaN heterostructures were laterally surrounded by an AlN shell,[48] and the whole structure was embedded in a rectangular prism of air, which permits elastic deformation. A schematic view of the structure excluding and including the AlN shell is presented in Figure 1a and b, respectively.

The 3D strain distribution was calculated by minimization of the elastic energy[48,49] through the application of zero-stress boundary conditions at the surface, which allowed the NW to deform in all three spatial directions. Figure 1a and b displays cross-sectional views of the strain components along the ⟨0001⟩ direction, e_{zz}, and along the <11−20> direction, e_{xx}, for a NW containing a 4 nm/4 nm GaN/AlN sequence, excluding and including a 5-nm-thick AlN shell, respectively. Figure 1c compares the e_{zz} profile in both cases. In the absence of a shell, the heterostructure evolves toward an equilibrium situation where the GaN NDs are compressively strained and the barriers are tensile strained. In the center of the NW, the relationship between $e_{zz} = -1.23\%$ and $e_{xx} = 0.66\%$ approaches the biaxial strain configuration ($e_{zz}/e_{xx} = -2c_{13}/c_{33} \approx 0.5327$, with the elastic constants $c_{13} = 106$ GPa and $c_{33} = 398$ GPa for GaN[50]). However, at the air−NW interface, the structure is almost fully relaxed. The presence of an AlN shell results in the application of a uniaxial compressive stress along ⟨0001⟩. As a result, in the center of the NDs, $e_{xx} = -1.28\%$ is still dominated by the pseudomorphic axial heterostructures, but the deformation along the growth axis is reduced to $e_{zz} = 0.006\%$.

For the calculation of the band profiles the spontaneous polarization and the piezoelectric fields resulting from the strain distribution were taken into account. The effect of surface states was simulated by introducing a two-dimensional (2D) charge density at the air/NW interface. We considered a surface charge of $\sigma = -2 \times 10^{12}$ cm^{-2}, which is a low value for a chemically clean GaN *m*-surface according to the measurements of Bertelli et al.[51] Figure 2a displays the conduction band profile at the center of the NW, comparing the cases of a NW heterostructure including and excluding the AlN shell, with and without surface states. The presence of surface charges fully depletes the GaN NW base, in agreement with previous studies and calculations.[47,52−54] The difference between the GaN polarization and the average polarization of the GaN/AlN heterostructure results in the formation of a depletion region at the base/heterostructure interface and an accumulation region at the heterostructure/cap layer interface. The GaN/AlN sequence presents the sawtooth profile characteristic of GaN/AlN superlattices, due to the spontaneous and piezoelectric polarization differences between GaN and AlN. The effect of surface charges in the heterostructure region is negligible; that is, the density of surface states considered is not enough to screen the polarization effect. Given the N polarity of the NW, the internal electric field in the NDs shifts the conduction band ground state toward the base of the NW, whereas the valence band ground state is shifted toward the top of the NW. The magnitude of the electric field is not significantly affected by the presence of the AlN shell, and it remains at 4.7 ± 0.1 MV/cm for all of the NDs, identical to the value expected for GaN/AlN (4 nm/4 nm) QWs. This is due to the fact that the change in

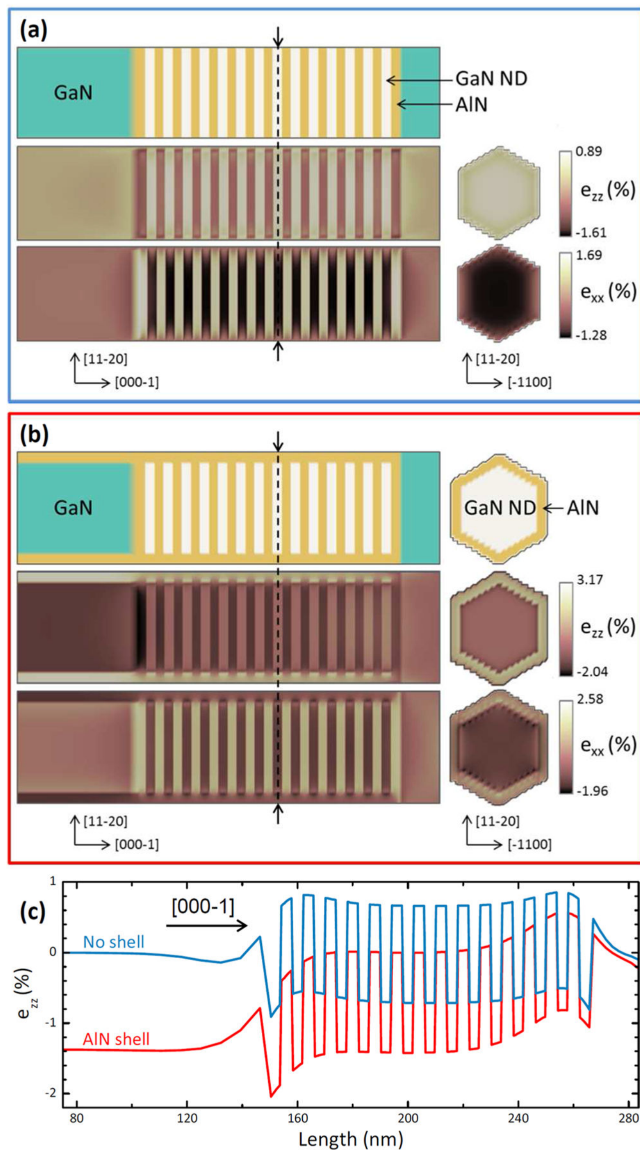

Figure 1. (a) From top to bottom, schematic material description of the simulated structure and cross-sectional views of the e_{zz} and e_{xx} strain components for a NW without AlN shell. The simulated NW incorporates 14 GaN/AlN (4 nm/4 nm) sections, and it has a radius of 20 nm in the <11−20> direction. Left: cross-sectional view along [1−100] at the center or the NW. Right: cross-sectional view along [0001] taken at the center of the eighth GaN ND (vertical dashed line on the left). (b) The same for a nanowire with a 5-nm-thick AlN shell as indicated in the schematic material description. (c) Comparison of the e_{zz} profile at along ⟨0001⟩ down the center of the NW, for a structure without shell and one with a 5-nm-thick AlN shell.

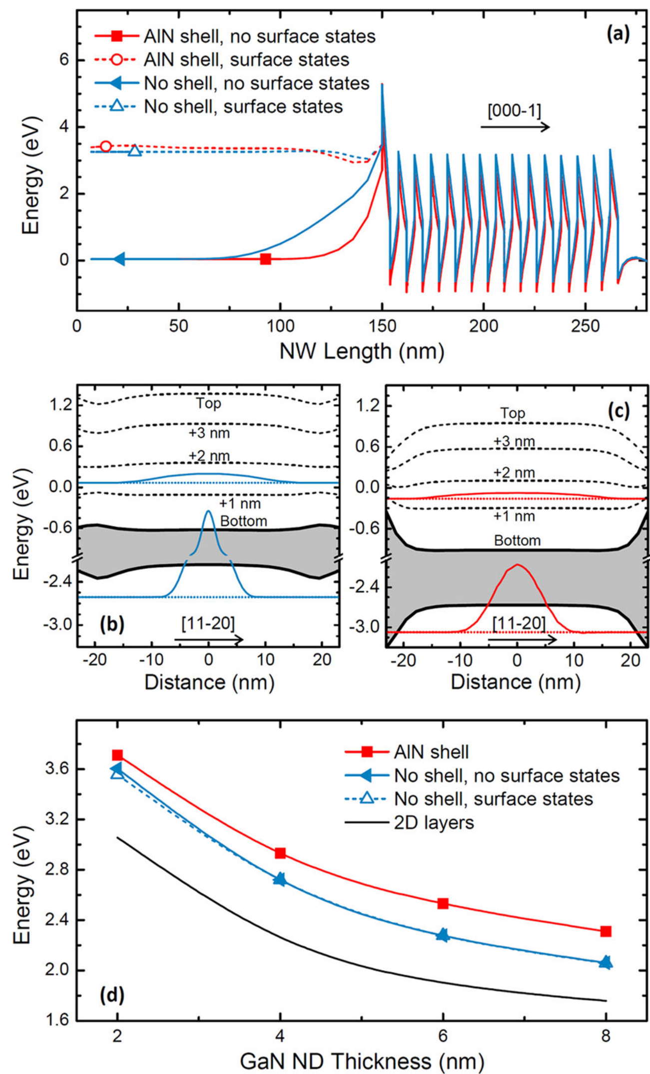

Figure 2. (a) Simulated conduction band profile along ⟨0001⟩ at the center of the NW for structures with and without shell, with and without surface states. Below, conduction (valence) band profiles obtained at the bottom (top) of the eighth GaN ND in (b) a NW without shell and (c) a NW with a 5-nm-thick AlN shell. A cross section of the probability density distribution, $|\Psi(\mathbf{r})|^2$ for the lower confined level in the conduction band and the higher confined level in the valence band is included. Dashed lines describe the variation of the conduction band profile when moving from the bottom to the top of the GaN ND; distances from the bottom of the ND are indicated. (d) Theoretical energy of the band-to-band transition energy as a function of the GaN ND thickness. Data are compared to the transition in the case of GaN/AlN QWs (2D layers).

piezoelectric polarization in the GaN NDs is compensated by the corresponding change in the AlN barriers.

The conduction (valence) band profiles along <11−20> obtained near the top (bottom) of a GaN ND are presented in Figure 2 for the cases of (b) a NW without shell and (c) a NW with a 5-nm-thick AlN shell. Results with and without surface states are indistinguishable in both cases. Cross sections of the squared wave functions, $|\Psi(\mathbf{r})|^2$, for the lower confined level in the conduction band and the higher confined level in the valence band are included. Conduction band profiles were taken at different heights within the GaN ND. Starting from the bottom of the ND, and moving upward, the conduction band profile can be seen at different points throughout the ND, as illustrated with dashed lines. At the bottom of the ND, the potential minimum is located at the center of the NW, whereas at the top of the ND, the potential minimum is located near the surface or at the ND/AlN-shell interface, that is, when migrating from the bottom to the top of the ND, the conduction band profile seems to inflate in the center. The addition of the AlN shell induces band pinning at the ND/AlN-shell interface, in conjunction with an increased rate of conduction band inflation. This band profile evolution is a direct consequence of the radial strain distribution in the ND.

Figure 2d describes the evolution of the band-to-band transition in the ND as a function of the ND thickness,

dx.doi.org/10.1021/nl5002247 | Nano Lett. 2014, 14, 1665−1673

comparing NWs including and excluding the AlN shell to GaN/AlN QWs. The lateral confinement within the NW geometry induces a blue shift of the interband transition, which cannot be justified solely by a change in the strain distribution (as explained above, the center of the NW keeps the biaxial strain configuration and the relaxation is limited to the vicinity of the surface). In the presence of the AlN shell, the uniaxial compressive strain along ⟨0001⟩ results in an increase of the GaN band gap, which further blue shifts the band-to-band transition. This uniaxial strain component is fundamental to understanding the PL from GaN/Al(Ga)N heterostructured NWs.[32,48]

Figure 3a presents cross-sectional views of the square wave function, $|\Psi(\mathbf{r})|^2$ for the three lowest electron states (s, p_x, p_y)

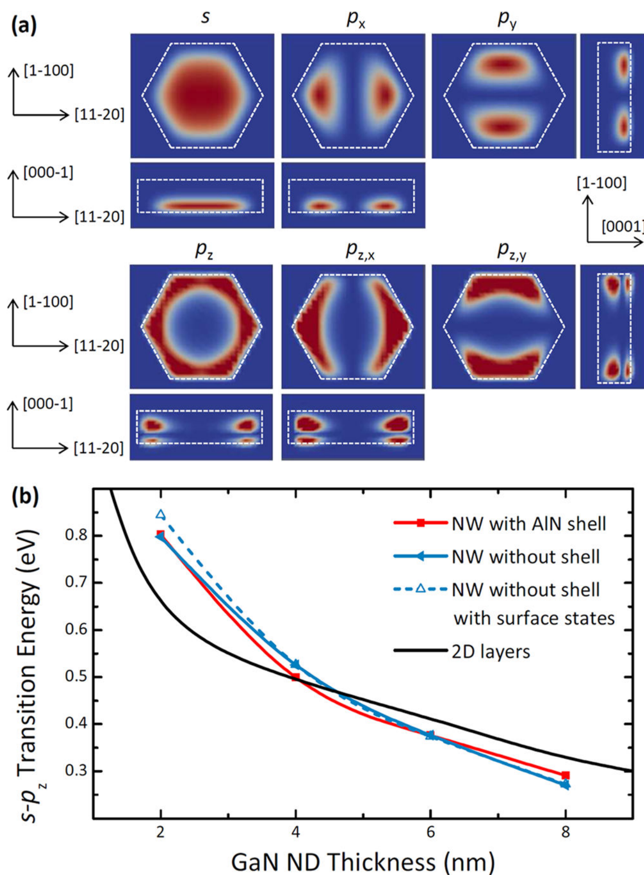

Figure 3. (a) Probability density distribution, $|\Psi(\mathbf{r})|^2$, for the three lowest electron states (s, p_x, p_y) in a GaN/AlN (4 nm/4 nm) ND in a NW with a radius of 20 nm (data correspond to a NW with a 5-nm-thick AlN shell). Below, first excited states due to confinement along the growth axis (p_z, $p_{z,x}$, $p_{z,y}$). The energies of the electron states with respect to the conduction band ground state, s, are calculated to be E_{px} = 27.6 meV, E_{py} = 28.8 meV, E_{pz} = 496 meV, E_{pzx} = 496 meV, E_{pzy} = 496 meV. (b) Variation of the s−p_z transition as a function of the GaN ND thickness in the case of a NW with an AlN shell, without shell without surface states, and without shell with a surface charge $\sigma = -2 \times 10^{12}$ cm^{-2}. Data are compared to the e_2−e_1 energy difference in the case of GaN/AlN QWs, calculated following ref 44.

in a GaN/AlN (4 nm/4 nm) ND, and the first excited states with secondary nodes along the growth axis (p_z, $p_{z,x}$, $p_{z,y}$). The data corresponds to a NW with a 5-nm-thick AlN shell, but it is qualitatively similar for NWs without a shell. As a result of the polarization-induced internal electric field, the lower electron state (s) is shifted toward the bottom of ND (maximum probability density ∼0.7 nm above the bottom of the ND). In contrast, the first excited state with a secondary node along the growth axis (p_z) presents a ring-shaped maximum probability density spatially located at the vertical center of the ND (∼2.0 nm from the bottom of the ND). This difference in location means that the wave function is distorted by the potential distribution in the center of the ND, presented in Figure 2b and c, where the potential minimum is located near the ND/AlN-shell interface, as opposed to in the center. Therefore, the s and p_z wave functions are not only vertically shifted due to the polarization-induced electric field, but also laterally due to the radial strain distribution in the ND. This lateral shift does not appear in the case of GaN/AlN QDs, where the hydrostatic compressive strain radially confines all the ground-state and excited electrons, as well as holes toward the center of the QD.[55,56] In comparison to QWs/QDs, the ND's lack of spatial overlap between the excited and ground electronic states results in a reduced oscillator strength, which should translate into slower (and nonexponential) intraband carrier relaxation, with a high dependence on the NW radius.

It is important to note that the shape of the wave functions depends on the geometry of the NDs. Current calculations are performed assuming that the NDs are hexagonal prisms. In the case of a ND stack where the radii of the disks decrease from top to bottom, the asymmetric strain distribution along ⟨0001⟩ results in a modified lateral potential profile, which shifts the conduction band potential minima toward the ND/AlN-shell interface even at the bottom of the NDs.[48] This reshapes the *s* wave function and generates a local $|\Psi(\mathbf{r})|^2$ minimum at the center of the NW and renders the wave function more ring-like.

Figure 3b displays the evolution of the s−p_z intraband transition as a function of the ND thickness, comparing various NW configurations with the e_1−e_2 transition in GaN/AlN (4 nm/4 nm) QWs. In this calculation it is assumed that the in-plane lattice parameter of the QW superlattice evolves to the minimum energy configuration, as has been experimentally observed.[57] The effect of the AlN shell is smaller for intraband transitions (∼50 meV) than for interband transitions (∼300 meV). This intraband energy shift is also smaller than the typical intraband absorption line width in GaN/AlN QWs or QDs (50−100 meV[24]).

To study the influence of the NW radius, calculations were performed for NWs containing GaN/AlN NDs with 4-nm-thick AlN barriers and different ND thicknesses (2−8 nm) as well as different NW radii (14−26 nm). The interband and s−p_z intraband transition energies were calculated, and each showed changes of less than 4% over the investigated NW radial range. On the contrary, when analyzing the s−p_x or s−p_y transitions, the radius of the NW plays a large role in the discretization. Considering a ND of height 4 nm, the s−p_x or s−p_y transition occurs around 45 meV (∼27 μm) for a NW radius of 14 nm, versus 3 meV (∼410 μm) for a NW radius of 26 nm. This is attributed to the laterally confined states whose energy levels approach at higher NW radii.

Materials and Experimental Methods. N-polar GaN/AlN heterostructured NWs were grown catalyst-free by PAMBE on floating-zone Si(111) substrates in N-rich atmosphere (III/V ≈ 0.25) at ∼790 °C.[48] The NW vertical growth rate was 390 nm/h. They consist of a nonintentionally doped (n.i.d.) GaN base with a length of 600 nm and a radius of about 25−40 nm, followed by 40 periods of GaN/AlN sections, and a 20-nm-thick n.i.d. GaN cap layer. The thickness

of the GaN sections (NDs) was varied between 3 and 8 nm, while the thickness of the AlN sections (barriers) was kept constant at 4 nm. The GaN NDs were doped with Ge, using a beam equivalent pressure (BEP_{Ge}) in the range of 0.5−1.5 × 10^{-9} mbar. Ge is known to dope *n*-type GaN NWs and to easily incorporate at large concentrations with weak impact on the NW morphology.[58] The structural details of the samples under study are summarized in Table 1.

Table 1. Description of the Samples under Study: GaN ND Thickness, BEP_{Ge} during the ND Growth, Low-Temperature (T = 5 K) PL Peak Wavelength, and Room-Temperature ISB Absorption Peak Wavelength

sample	ND thickness (nm)	BEP_{Ge} (mbar)	PL peak wavelength (nm)	ISB absorption peak wavelength (μm)
S1	4	0	454	
S2	4	5.0×10^{-10}	429	1.95
S3	4	1.0×10^{-9}	392	1.65
S4	4	1.5×10^{-9}	384	1.60
S5	3	9×10^{-10}	363	1.58
S6	4	9×10^{-10}	390	1.62
S7	6	9×10^{-10}	410	1.74
S8	7	9×10^{-10}	419	1.75
S9	8	9×10^{-10}	438	1.75

Structural and morphological characterization of the heterostructures was performed by high-resolution transmission electron microscopy (HRTEM) and annular dark field (ADF) scanning transmission electron microscopy (STEM) using a FEI Tecnai F20 field emission gun microscope operated at 200 kV. For microscopy studies, the NWs were directly scratched from the substrate with a holey carbon TEM grid.

PL spectra were obtained by exciting with a continuous-wave frequency-doubled Ar laser (λ = 244 nm), with an excitation power around 50 μW focused on a spot with a diameter of ∼100 μm. The emission from the sample was collected by a Jobin Yvon HR460 monochromator equipped with a UV-enhanced charge-coupled device (CCD) camera. Intraband absorption was probed by Fourier transform infrared spectroscopy (FTIR) performed in a Bruker V70v spectrometer using a halogen lamp, a CaF_2 beam splitter, and an HgCdTe detector. The transmission was measured at room temperature, in vacuum, with the sample tilted at the Brewster angle. The transmission spectra for TE- and TM-polarized light are corrected by the corresponding transmission of a sample containing 1-μm-long n.i.d. GaN NWs on floating zone Si(111).

Results and Discussion. For a correct interpretation of the optical studies, the geometry and dimensions of the heterostructures have been analyzed by transmission electron microscopy methods. Figure 4 shows ADF and HRTEM images of samples S6 and S9, which confirm the growth of the wires along the ⟨0001⟩ direction for both phases, GaN and AlN, with a perfect epitaxy consecutively achieved between both materials. The GaN/AlN heterostructures are enveloped by a thin (2−5 nm) AlN layer, starting from the topmost AlN barrier extending along the GaN stem. Electron energy loss spectroscopy (EELS) measurements demonstrate that there is no interdiffusion of Ga or Al, confirming sharp interfaces between the NDs and the barriers.

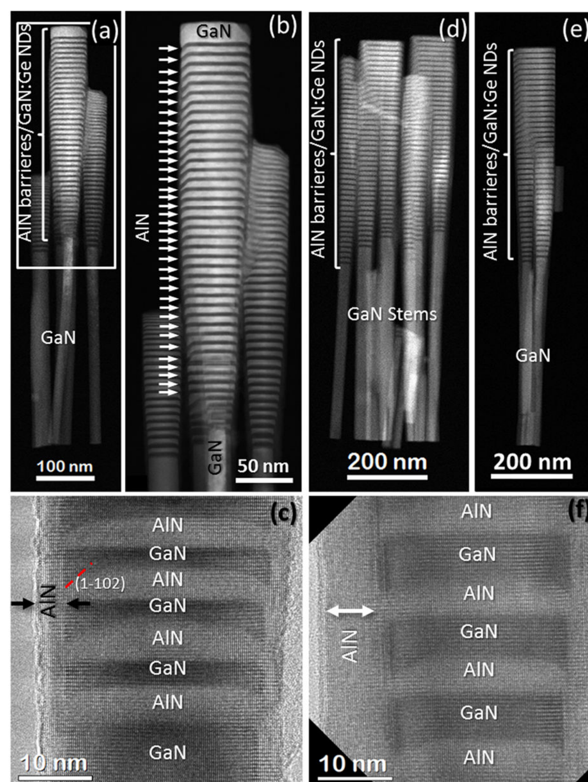

Figure 4. (a) ADF image of a set of GaN NWs from sample S6, containing 40 periods of AlN/GaN NDs. (b) Zoom-in of the squared area in (a). (c) HRTEM image of several GaN NDs and AlN barriers. (d,e) ADF images of sets of wires from sample S9. (f) HRTEM image of several GaN NDs, separated by AlN barriers.

In the HRTEM images, we observe that the AlN sections often present {1−102} facets close to the surface. To quantify the effect of this AlN {1−102} faceting on the electronic transitions, we have modeled NWs containing GaN/AlN heterostructures with a GaN ND thickness varying from 2 to 8 nm and with AlN barriers consisting of a hexagonal prism of 2 nm followed by a 2-nm-thick hexagonal truncated pyramid with {1−102} facets. Compared with the nonfaceted structures presented above, faceted structures have on average a 10% lower interband energy difference, as well as a 6% higher s−p_z intraband energy difference.

The measurement of intraband absorption requires the first electronic level of the nanostructures to be populated with electrons. Therefore, we analyzed a series of NWs containing a 40-period GaN:Ge/AlN (4 nm/4 nm) heterostructure with different Ge doping levels (samples S1−S4 in Table 1). According to time-of-flight secondary ion mass spectroscopy (ToF-SIMS) measurements,[58] the various BEP_{Ge} (5.0×10^{-10}, 1.0×10^{-9}, and 1.5×10^{-9} mbar) should produce Ge concentrations of [Ge] ∼ 9×10^{-19}, 1.7×10^{-20}, and 3.1×10^{-20} cm^{-3}, respectively. Figure 5 presents the results of (a) interband (PL) and (b) intraband (FTIR) optical characterization of this series. The low-temperature (T = 5 K) PL peak wavelength of the structures blue shifts more than 70 nm (see Table 1) and broadens for increasing doping levels, which can be assigned to the screening of the polarization-induced internal electric field in the NDs by the free carriers.[59] This further supported by the agreement between the experimental results and theoretical calculations for the band-to-band

dx.doi.org/10.1021/nl5002247 | *Nano Lett.* 2014, 14, 1665−1673

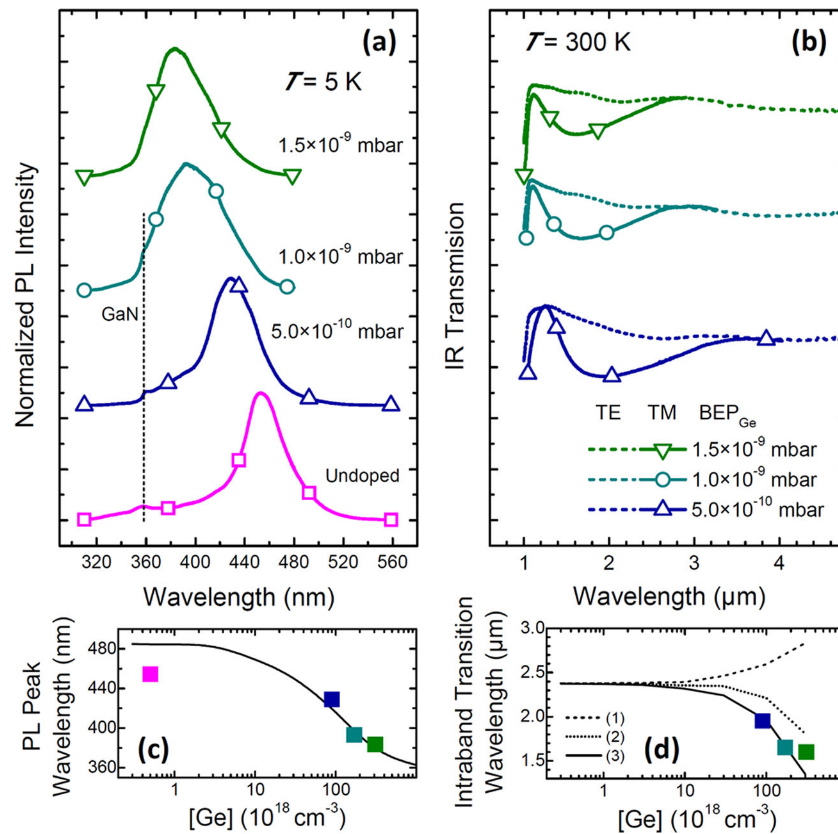

Figure 5. (a) Low-temperature PL spectra of Ge-doped GaN/AlN (4 nm/4 nm) heterostructured NWs with different doping levels in the GaN NDs (samples S1−S4 in Table 1). The spectra are normalized by their maximum and vertically shifted for clarity. The BEP_{Ge} used for Ge doping is indicated by each curve. The emission wavelength of the GaN base is indicated by a vertical dashed line. (b) Room-temperature IR transmission spectra for TE-(dashed) and TM-polarized (solid) light measured for Ge-doped GaN/AlN (4 nm/4 nm) heterostructured NWs with different doping levels in the GaN NDs. The spectra are vertically shifted for clarity. (c) Variation of the PL peak wavelength as a function of the estimated Ge concentration. Dots are experimental values from (a); the solid line is a theoretical calculation of the band-to-band transition at low temperature using a 3D model of the structure. (d) Variation of the intraband transition wavelength as a function of the estimated Ge concentration. Dots are experimental values from (b); the dashed line labeled (1) is a 1D calculation of the intraband transition accounting for the screening of the internal electric field; the dotted line (2) incorporates corrections associated to both screening and exchange interaction; the solid line (3) accounts for screening, exchange interaction, and depolarization shift.

transitions using a 3D model and including the screened internal electric fields (see Figure 5c).[60]

The intraband absorption was investigated at room temperature by measuring the IR transmission of the samples in an FTIR system, with the results depicted in Figure 5b. The dip in the IR transmission for TM-polarized light is assigned to the s−p_z transition, following the intraband polarization selection rules. This intraband absorption line shifts systematically toward shorter wavelengths with increasing dopant concentration, in contradiction to simulations considering only the screening of the polarization-induced internal electric field.[35] This discrepancy between simulations and experiments is attributed to many-body effects. We have previously shown the relevance of these many-body phenomena in the case of GaN/Al(Ga)N QWs,[61,62] where their magnitudes can be comparable to the value of the e_2−e_1 transition energy.[63]

To explain the experimental results, two kinds of many-body effects must be considered, namely, those modifying the energy levels (exchange interaction) and those modifying the intraband absorption energy (plasmon screening and excitonic shift).[64] The exchange interaction is due to the repulsion between electrons with the same spin, following the Pauli exclusion principle. We have estimated the shift induced by the exchange interaction, E_{exch}, following a one-dimensional (1D) approach, using the Hartree−Fock method with the approximation by Bandara et al.[65,66]

$$E_{exch}(k) = \frac{-e^2 k_F}{4\pi\varepsilon\varepsilon_0}\left[\frac{2}{\pi}\mathbf{E}(k/k_F) - 0.32(k_F/k_L)\right] \quad (1)$$

where e is the electron charge, ε the dielectric constant, ε_0 the vacuum permittivity, $k_F = (2\pi n_S)^{1/2}$ with n_S being the surface charge density *in* the well, $k_L = \pi/L$ with L being the QW thickness, and $\mathbf{E}(k/k_F)$ is a complete elliptical integral of the second kind.

The shift of the intraband absorption energy induced by plasmon screening (depolarization shift) and by the Coulomb interaction between the excited electron and the quasi-hole left in the ground state (excitonic or final-state interaction), was calculated as[64]

$$E_{12} = (e_2 - e_1)\sqrt{1 + \alpha - \beta} \quad (2)$$

where e_1 and e_2 are the energies of the first and second electronic levels in the well, and α and β (both >0) represent the depolarization shift and the exciton interaction, respectively. The frequency shift α was calculated by numerical methods following[64,67]

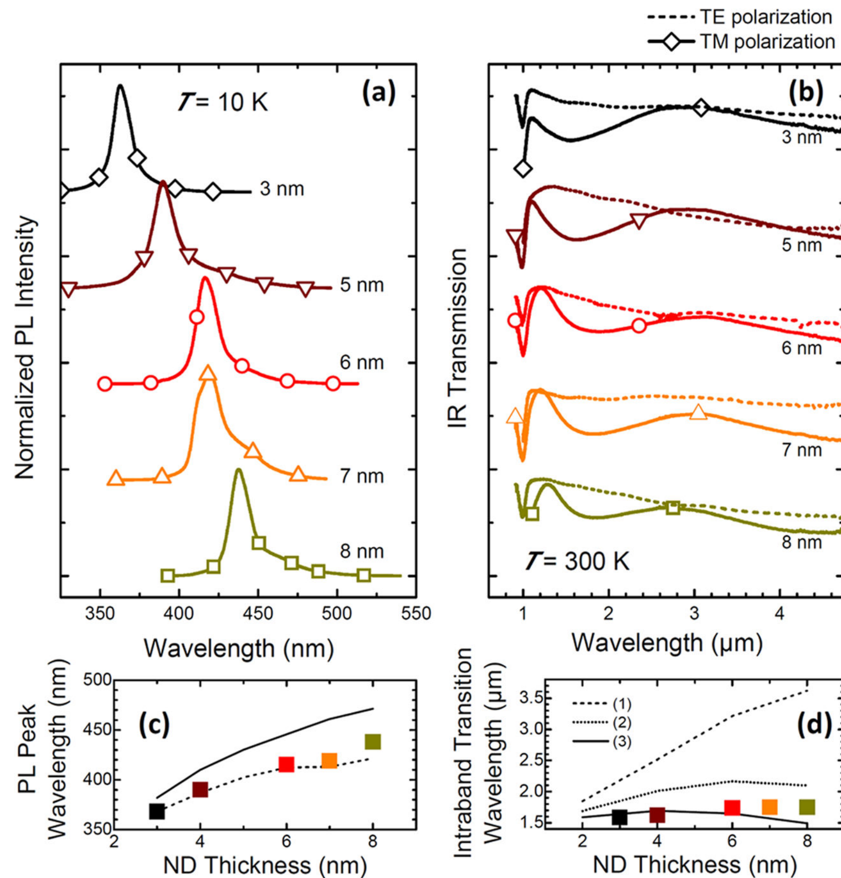

Figure 6. (a) Low-temperature PL spectra of Ge-doped GaN/AlN heterostructured NWs with 4-nm-thick AlN barriers and various GaN ND thicknesses as indicated (samples S5−S9 in Table 1). The spectra are normalized by their maximum and vertically shifted for clarity. (b) Room-temperature IR transmission spectra for TE- and TM-polarized light measured for Ge-doped GaN/AlN heterostructured NWs with different GaN ND thickness. The spectra are vertically shifted for clarity. (c) Variation of the PL peak wavelength as a function of the ND thickness. Dots are experimental values from (a); the solid line is a theoretical calculation of the band-to-band transition at low temperature using a 3D model of the structure and assuming [Ge] = 1.5 × 10^{20} cm^{-3}; the dashed line assumes [Ge] = 2.4 × 10^{20} cm^{-3}. (d) Variation of the intraband transition wavelength as a function of the ND thickness. Dots are experimental values from (b); the dashed line labeled (1) is a 1D calculation of the intraband transition accounting for the screening of the internal electric field; the dotted line (2) incorporates corrections associated to both screening and exchange interaction; the solid line (3) accounts for screening, exchange interaction, and depolarization shift.

$$\alpha = \frac{2e^2 n_S}{\varepsilon\varepsilon_0(e_2 - e_1)} \int_{-\infty}^{\infty} \mathrm{d}z\left[\int_{-\infty}^{z} \Psi_2(z')\Psi_1(z')\,\mathrm{d}z'\right]^2 \quad (3)$$

with $\Psi_1(z')$ and $\Psi_2(z')$ being the wave functions associated to e_1 and e_2, respectively. The values of $\Psi_1(z')$, $\Psi_2(z')$, e_1, and e_2 were extracted using the Nextnano3 Schrödinger−Poisson equation solver. The values of β (after eq 59 in ref 64) were found to be at least 2 orders of magnitude smaller than α (as it is also in the case of GaAs QWs) and were therefore neglected in the calculations.

Figure 5d depicts the predicted red shift of e_2−e_1 with increasing doping level, based on the Nextnano3 calculations taking the screening of the internal electric field into account (dashed line). Introducing the corrections associated to the exchange interaction (eq 1) and depolarization shift (eqs 2 and 3) translates into a blue shift of the absorption which can reach several hundreds of nanometers (solid line). The theoretical results are in good agreement with the experimental data, assuming fully ionized Ge dopants, with a density that is estimated from the BEP_{Ge} and compared to ToF-SIMS measurements in ref 58.

The s−p_x and s−p_y transitions, predicted in the far-IR around 40−50 μm and sensitive to TE-polarization, were not experimentally observed. This might be explained, by the dispersion introduced by the fluctuations in the NW radius, or by the fact that the NW geometry is expected to preferentially interact with TM coupled light and hence hinder the absorption of TE-polarized light.[54,68]

In conjunction to these experiments, we have analyzed a series of NWs containing 40-period GaN:Ge/AlN heterostructures with 4-nm-thick AlN barriers and various GaN ND thicknesses (samples S5−S9 in Table 1), all of them were doped with Ge using BEP_{Ge} = 9 × 10^{-10} mbar (estimated [Ge] ∼ 1.5 × 10^{20} cm^{-3}). The low-temperature (T = 5 K) PL peak energy from these samples, presented in Figure 6a, blue shifts for increasing ND thickness. This evolution is qualitatively described by theoretical calculations of the band-to-band transition using a 3D model which takes the screening of the internal electric field into account (see Figure 6c).[69] The blue shift of the experimental data with respect to the model could be explained by an underestimation of the effective dopant concentration (note the good agreement with the dashed-line calculations, which assume [Ge] ∼ 2.4 × 10^{20} cm^{-3}).

Room-temperature IR transmission measurements of this series are summarized in Figure 5b. As described above, the dip in the IR transmission for TM-polarized light is assigned to the

s−p_z transition, which shifts systematically toward longer wavelengths for thicker NDs. Figure 6d compares the experimental data to predictions made by Nextnano3 taking the screening of the internal electric field into account (dashed line). Introducing the corrections associated to the exchange interaction (eq 1) and depolarization shift (eqs 2 and 3) translates into a blue-shifted transition, which fits the experimental absorption data.

Limitations. It is important to keep in mind the limitations associated with the calculations of many-body effects. The models of the exchange interaction and the depolarization shift described above are approximations that consider these effects as a perturbation of the Hartree−Fock equation.[64] Equation 1 is an approximation that accounts for the deformation of the ground state assuming square QWs,[65,66] and eq 3 is extracted from a two-level model which requires that there is significant oscillator strength for transitions to only one excited state.[67] Looking at the order of magnitude of the experimental spectral shifts, comparable to the e_2-e_1 energy, the validity of these approximations is arguable. They provide a valid qualitative description, but a rigorous solution of the Hartree−Fock equation would be required, which is beyond the scope of this work.

Conclusions. From the theoretical analysis of the band diagram and electronic structure of GaN NWs containing a sequence of GaN/AlN NDs, we conclude that the formation of an AlN shell during the heterostructure growth results in a uniaxial compressive strain that blue shifts the interband optical transitions but does not have a critical influence on the intraband transitions. The presence of surface states with the density levels expected for the *m*-GaN plane causes a charge depletion of the base of the NWs, but it is not high enough to screen the polarization-induced internal electric field in the heterostructures. Variations in the NW radius do not modify significantly the interband or s−p_z intraband transitions, but they shift the intraband levels associated to the lateral confinement (p_x, p_y).

From the experimental viewpoint, we report the observation of a TM-polarized IR absorption line assigned to the s−p_z intraband transition in Ge-doped GaN/AlN NDs inserted in self-assembled GaN NWs grown on Si(111) by PAMBE. The s−p_x and s−p_y intraband transitions are not observed, most likely due to fluctuations of the NW radius and to the preferential coupling of TM light to the NW geometry. For increasing doping levels, we observe a broadening and blue shift of the PL as a result of the screening of the polarization-induced internal electric field in the NDs. Regarding intraband transitions, doping induces a blue shift of the s−p_z absorption line attributed to many-body effects, namely, the exchange interaction and depolarization shift, which dominate the red shift induced by internal electric field screening. The s−p_z transition red shifts with increasing ND thickness as theoretically expected.

AUTHOR INFORMATION

Notes

The authors declare no competing financial interest.

ACKNOWLEDGMENTS

This work was partially supported by the EU ERC-StG "TeraGaN" (#278428) project. M.d.l.M. thanks CSIC JAE-Predoc program. J.A. acknowledges the funding from the Spanish MICINN project MAT2010-15138 (COPEON) and Generalitat de Catalunya (2009 SGR770). The authors thank the TEM facilities at ICN2 (BNC-b, UAB).

REFERENCES

(1) Moumanis, K.; Helman, A.; Fossard, F.; Tchernycheva, M.; Lusson, A.; Julien, F. H.; Damilano, B.; Grandjean, N.; Massies, J. *Appl. Phys. Lett.* **2003**, *82*, 868−870.
(2) Tchernycheva, M.; Nevou, L.; Doyennette, L.; Helman, A.; Colombelli, R.; Julien, F. H.; Guillot, F.; Monroy, E.; Shibata, T.; Tanaka, M. *Appl. Phys. Lett.* **2005**, *87*, 101912.
(3) Guillot, F.; Bellet-Amalric, E.; Monroy, E.; Tchernycheva, M.; Nevou, L.; Doyennette, L.; Julien, F. H.; Dang, L. S.; Remmele, T.; Albrecht, M.; Shibata, T.; Tanaka, M. *J. Appl. Phys.* **2006**, *100*, 044326.
(4) Vardi, A.; Bahir, G.; Schacham, S. E.; Kandaswamy, P. K.; Monroy, E. *Phys. Rev. B* **2009**, *80*, 155439.
(5) Chia-Fu, H.; Jeong-Seok, O.; Zory, P.; Botez, D. *IEEE J. Sel. Top. Quantum Electron.* **2000**, *6*, 491−503.
(6) Zibik, E. A.; Grange, T.; Carpenter, B. A.; Porter, N. E.; Ferreira, R.; Bastard, G.; Stehr, D.; Winnerl, S.; Helm, M.; Liu, H. Y.; Skolnick, M. S.; Wilson, L. R. *Nat. Mater.* **2009**, *8*, 803−807.
(7) Krall, M.; Brandstetter, M.; Deutsch, C.; Detz, H.; Zederbauer, T.; Andrews, A. M.; Schrenk, W.; Strasser, G.; Unterrainer, K.; Belyanin, A. A.; Smowton, P. M. *Proc. SPIE* **2013**, *8640*, 864018−864018-7.
(8) Grange, T. *arXiv:1301.1258* **2013**.
(9) Lu, W.; Lieber, C. M. *Nat. Mater.* **2007**, *6*, 841−850.
(10) Deshpande, S.; Heo, J.; Das, A.; Bhattacharya, P. *Nat. Commun.* **2013**, *4*, 1675.
(11) Nakayama, Y.; Pauzauskie, P. J.; Radenovic, A.; Onorato, R. M.; Saykally, R. J.; Liphardt, J.; Yang, P. *Nature* **2007**, *447*, 1098−1101.
(12) Wu, W.; Wen, X.; Wang, Z. L. *Science* **2013**, *340*, 952−957.
(13) Wallentin, J.; Anttu, N.; Asoli, D.; Huffman, M.; Aberg, I.; Magnusson, M. H.; Siefer, G.; Fuss-Kailuweit, P.; Dimroth, F.; Witzigmann, B.; Xu, H. Q.; Samuelson, L.; Deppert, K.; Borgstrom, M. T. *Science* **2013**, *339*, 1057−1060.
(14) Cui, Y. *Science* **2001**, *293*, 1289−1292.
(15) Wallys, J.; Teubert, J.; Furtmayr, F.; Hofmann, D. M.; Eickhoff, M. *Nano Lett.* **2012**, *12*, 6180−6186.
(16) Black, M.; Lin, Y.-M.; Cronin, S.; Rabin, O.; Dresselhaus, M. *Phys. Rev. B* **2002**, *65*, 195417.
(17) Rustagi, S. C.; Singh, N.; Lim, Y. F.; Zhang, G.; Wang, S.; Lo, G. Q.; Balasubramanian, N.; Kwong, D.-L. *IEEE Electron Device Lett.* **2007**, *28*, 909−912.
(18) Dubrovskii, V. G.; Sibirev, N. V. *Phys. Rev. B* **2008**, *77*, 035414.
(19) Akiyama, T.; Yamashita, T.; Nakamura, K.; Ito, T. *Nano Lett.* **2010**, *10*, 4614−4618.
(20) Thelander, C.; Caroff, P.; Plissard, S.; Dey, A. W.; Dick, K. A. *Nano Lett.* **2011**, *11*, 2424−2429.
(21) Amanti, M. I.; Bismuto, A.; Beck, M.; Isa, L.; Kumar, K.; Reimhult, E.; Faist, J. *Opt. Express* **2013**, *21*, 10917.
(22) Hofstetter, D.; Baumann, E.; Giorgetta, F. R.; Théron, R.; Wu, H.; Schaff, W. J.; Dawlaty, J.; George, P. A.; Eastman, L. F.; Rana, F.; Kandaswamy, P. K.; Guillot, F.; Monroy, E. *Proc. IEEE* **2010**, *98*, 1234−1248.
(23) Machhadani, H.; Kandaswamy, P.; Sakr, S.; Vardi, A.; Wirtmüller, A.; Nevou, L.; Guillot, F.; Pozzovivo, G.; Tchernycheva, M.; Lupu, A.; Vivien, L.; Crozat, P.; Warde, E.; Bougerol, C.; Schacham, S.; Strasser, G.; Bahir, G.; Monroy, E.; Julien, F. H. *New J. Phys.* **2009**, *11*, 125023.
(24) Beeler, M.; Trichas, E.; Monroy, E. *Semicond. Sci. Technol.* **2013**, *28*, 074022.
(25) Binggeli, N.; Ferrara, P.; Baldereschi, A. *Phys. Rev. B* **2001**, *63*, 245306.
(26) Cociorva, D.; Aulbur, W. G.; Wilkins, J. W. *Solid State Commun.* **2002**, *124*, 63−66.
(27) Tchernycheva, M.; Nevou, L.; Doyennette, L.; Julien, F.; Warde, E.; Guillot, F.; Monroy, E.; Bellet-Amalric, E.; Remmele, T.; Albrecht, M. *Phys. Rev. B* **2006**, *73*, 125347.

(28) Iizuka, N.; Kaneko, K.; Suzuki, N.; Asano, T.; Noda, S.; Wada, O. *Appl. Phys. Lett.* **2000**, *77*, 648−650.
(29) Heber, J. D.; Gmachl, C.; Ng, H. M.; Cho, A. Y. *Appl. Phys. Lett.* **2002**, *81*, 1237−1239.
(30) Iizuka, N.; Kaneko, K.; Suzuki, N. *Opt. Express* **2005**, *13*, 3835−3840.
(31) Hamazaki, J.; Kunugita, H.; Ema, K.; Kikuchi, A.; Kishino, K. *Phys. Rev. B* **2005**, *71*, 165334.
(32) Songmuang, R.; Katsaros, G.; Monroy, E.; Spathis, P.; Bougerol, C.; Mongillo, M.; De Franceschi, S. *Nano Lett.* **2010**, *10*, 3545−3550.
(33) Rigutti, L.; Jacopin, G.; Bugallo, A. D. L.; Tchernycheva, M.; Warde, E.; Julien, F. H.; Songmuang, R.; Galopin, E.; Largeau, L.; Harmand, J.-C. *Nanotechnology* **2010**, *21*, 425206.
(34) Suzuki, N.; Iizuka, N. *Jpn. J. Appl. Phys.* **1999**, *38*, L363−L365.
(35) Kandaswamy, P. K.; Machhadani, H.; Bougerol, C.; Sakr, S.; Tchernycheva, M.; Julien, F. H.; Monroy, E. *Appl. Phys. Lett.* **2009**, *95*, 141911.
(36) Péré-Laperne, N.; Bayram, C.; Nguyen-The, L.; McClintock, R.; Razeghi, M. *Appl. Phys. Lett.* **2009**, *95*, 131109.
(37) Bayram, C. *J. Appl. Phys.* **2012**, *111*, 013514.
(38) Edmunds, C.; Tang, L.; Shao, J.; Li, D.; Cervantes, M.; Gardner, G.; Zakharov, D. N.; Manfra, M. J.; Malis, O. *Appl. Phys. Lett.* **2012**, *101*, 102104.
(39) Tian, W.; Yan, W. Y.; Hui, X.; Li, S. L.; Ding, Y. Y.; Li, Y.; Tian, Y.; Dai, J. N.; Fang, Y. Y.; Wu, Z. H.; Yu, C. H.; Chen, C. Q. *J. Appl. Phys.* **2012**, *112*, 063526.
(40) Machhadani, H.; Kotsar, Y.; Sakr, S.; Tchernycheva, M.; Colombelli, R.; Mangeney, J.; Bellet-Amalric, E.; Sarigiannidou, E.; Monroy, E.; Julien, F. H. *Appl. Phys. Lett.* **2010**, *97*, 191101.
(41) Sudradjat, F. F.; Zhang, W.; Woodward, J.; Durmaz, H.; Moustakas, T. D.; Paiella, R. *Appl. Phys. Lett.* **2012**, *100*, 241113.
(42) Beeler, M.; Bougerol, C.; Bellet-Amalric, E.; Monroy, E. *Appl. Phys. Lett.* **2013**, *103*, 091108.
(43) Tanaka, K.; Ikuno, K.; Kasai, Y.; Fukunaga, K.; Kunugita, H.; Ema, K.; Kikuchi, A.; Kishino, K. *J. Lumin.* **2008**, *128*, 1084−1086.
(44) Birner, S.; Zibold, T.; Andlauer, T.; Kubis, T.; Sabathil, M.; Trellakis, A.; Vogl, P. *IEEE Trans. Electron Devices* **2007**, *54*, 2137−2142.
(45) Kandaswamy, P. K.; Guillot, F.; Bellet-Amalric, E.; Monroy, E.; Nevou, L.; Tchernycheva, M.; Michon, A.; Julien, F. H.; Baumann, E.; Giorgetta, F. R.; Hofstetter, D.; Remmele, T.; Albrecht, M.; Birner, S.; Dang, L. S. *J. Appl. Phys.* **2008**, *104*, 093501.
(46) De la Mata, M.; Magen, C.; Gazquez, J.; Utama, M. I. B.; Heiss, M.; Lopatin, S.; Furtmayr, F.; Fernández-Rojas, C. J.; Peng, B.; Morante, J. R.; Rurali, R.; Eickhoff, M.; Fontcuberta i Morral, A.; Xiong, Q.; Arbiol, J. *Nano Lett.* **2012**, *12*, 2579−2586.
(47) Den Hertog, M. I.; González-Posada, F.; Songmuang, R.; Rouviere, J. L.; Fournier, T.; Fernandez, B.; Monroy, E. *Nano Lett.* **2012**, *12*, 5691−5696.
(48) Furtmayr, F.; Teubert, J.; Becker, P.; Conesa-Boj, S.; Morante, J. R.; Chernikov, A.; Schäfer, S.; Chatterjee, S.; Arbiol, J.; Eickhoff, M. *Phys. Rev. B* **2011**, *84*, 205303.
(49) Rivera, C.; Jahn, U.; Flissikowski, T.; Pau, J.; Muñoz, E.; Grahn, H. T. *Phys. Rev. B* **2007**, *75*, 045316.
(50) Polian, A.; Grimsditch, M.; Grzegory, I. *J. Appl. Phys.* **1996**, *79*, 3343−3344.
(51) Bertelli, M.; Löptien, P.; Wenderoth, M.; Rizzi, A.; Ulbrich, R.; Righi, M.; Ferretti, A.; Martin-Samos, L.; Bertoni, C.; Catellani, A. *Phys. Rev. B* **2009**, *80*, 115324.
(52) Dobrokhotov, V.; McIlroy, D. N.; Norton, M. G.; Abuzir, A.; Yeh, W. J.; Stevenson, I.; Pouy, R.; Bochenek, J.; Cartwright, M.; Wang, L.; Dawson, J.; Beaux, M.; Berven, C. *J. Appl. Phys.* **2006**, *99*, 104302.
(53) Sanford, N. A.; Blanchard, P. T.; Bertness, K. A.; Mansfield, L.; Schlager, J. B.; Sanders, A. W.; Roshko, A.; Burton, B. B.; George, S. M. *J. Appl. Phys.* **2010**, *107*, 034318.
(54) González-Posada, F.; Songmuang, R.; Den Hertog, M.; Monroy, E. *Nano Lett.* **2012**, *12*, 172−176.
(55) Andreev, A.; O'Reilly, E. *Phys. Rev. B* **2000**, *62*, 15851−15870.
(56) Ranjan, V.; Allan, G.; Priester, C.; Delerue, C. *Phys. Rev. B* **2003**, *68*, 115303.
(57) Kandaswamy, P. K.; Bougerol, C.; Jalabert, D.; Ruterana, P.; Monroy, E. *J. Appl. Phys.* **2009**, *106*, 013526.
(58) Schörmann, J.; Hille, P.; Schäfer, M.; Müßener, J.; Becker, P.; Klar, P. J.; Kleine-Boymann, M.; Rohnke, M.; de la Mata, M.; Arbiol, J.; Hofmann, D. M.; Teubert, J.; Eickhoff, M. *J. Appl. Phys.* **2013**, *114*, 103505.
(59) Hille, P.; Müßener, J.; Becker, P.; de la Mata, M.; Rosemann, N.; Magén, C.; Arbiol, J.; Teubert, J.; Chatterjee, S.; Schörmann, J.; Eickhoff, M. *arXiv:1402.3081*, **2014**.
(60) The calculations used the same 3D model as the one described in Figure 1b and tried to approach the real structure using geometrical feedback from TEM images. The GaN base radius was 20 nm, the AlN shell thickness was 2 nm, the thickness of the GaN:Ge NDs was 3.7 nm, and the AlN barriers consisted of a hexagonal prism of 2 nm followed by a 2-nm-thick hexagonal truncated pyramid with {1−102} facets. Surface charges were neglected.
(61) Helman, A.; Tchernycheva, M.; Lusson, A.; Warde, E.; Julien, F. H.; Moumanis, K.; Fishman, G.; Monroy, E.; Daudin, B.; Le Si Dang, D.; Bellet-Amalric, E.; Jalabert, D. *Appl. Phys. Lett.* **2003**, *83*, 5196−5198.
(62) Kotsar, Y.; Doisneau, B.; Bellet-Amalric, E.; Das, A.; Sarigiannidou, E.; Monroy, E. *J. Appl. Phys.* **2011**, *110*, 033501.
(63) Kandaswamy, P. K.; Machhadani, H.; Kotsar, Y.; Sakr, S.; Das, A.; Tchernycheva, M.; Rapenne, L.; Sarigiannidou, E.; Julien, F. H.; Monroy, E. *Appl. Phys. Lett.* **2010**, *96*, 141903.
(64) Helm, M. In *Intersubband Transitions in Quantum Wells: Physics and Device Applications I*; Liu, H. C., Capasso, F., Eds.; Academic Press: San Diego, 2000.
(65) Bandara, K. M. S. V.; Coon, D. D.; O, B.; Lin, Y. F.; Francombe, M. H. *Appl. Phys. Lett.* **1988**, *53*, 1931.
(66) Bandara, K. M. S. V.; Coon, D. D.; O, B.; Lin, Y. F.; Francombe, M. H. *Appl. Phys. Lett.* **1989**, *55*, 206.
(67) Allen, S. J.; Tsui, D. C.; Vinter, B. *Solid State Commun.* **1976**, *20*, 425−428.
(68) Wang, J.; Gudiksen, M. S.; Duan, X.; Cui, Y.; Lieber, C. M. *Science* **2001**, *293*, 1455−1457.
(69) Note: The calculations used the same 3D model as the one described in Figure 1b. The GaN base radius was 20 nm, the AlN shell thickness was 2 nm, and the AlN barriers consisted of a hexagonal prism of 2 nm followed by a 2-nm-thick hexagonal truncated pyramid with {1−102} facets. Surface charges were considered to be $\sigma = -2 \times 10^{12}$ cm^{-2}.

Annex 8

Intersubband transitions in nonpolar GaN/Al(Ga)N heterostructures in the short- and mid-wavelength infrared regions

C. B. Lim[1,2], M. Beeler[1,2], A. Ajay[1,2], J. Lähnemann[1,2], E. Bellet-Amalric[1,2], C. Bougerol[1,3], and E. Monroy[1,2]

[1] *University Grenoble-Alpes, 38000 Grenoble, France*

[2] *CEA, INAC-SP2M, 17 av. des Martyrs, 38000 Grenoble, France*

[3] *CNRS, Institut Néel, 25 av. des Martyrs, 38000 Grenoble, France*

ABSTRACT

This paper assesses nonpolar *m*- and *a*-plane GaN/Al(Ga)N multi-quantum-wells grown on bulk GaN for intersubband optoelectronics in the short- and mid-wavelength infrared ranges. The characterization results are compared to those for reference samples grown on the polar *c*-plane, and are verified by self-consistent Schrödinger-Poisson calculations. The best results in terms of mosaicity, surface roughness, photoluminescence linewidth and intensity, as well as intersubband absorption are obtained from *m*-plane structures, which display room-temperature intersubband absorption in the range from 1.5 to 2.9 μm. Based on these results, a series of *m*-plane GaN/AlGaN multi-quantum-wells were designed to determine the accessible spectral range in the mid-infrared. These samples exhibit tunable room-temperature intersubband absorption from 4.0 to 5.8 μm, the long-wavelength limit being set by the absorption associated with the second order of the Reststrahlen band in the GaN substrates.

I. INTRODUCTION

GaN/AlGaN nanostructures have recently emerged as promising materials for new intersubband (ISB) devices covering a large portion of the infrared spectrum.[1–3] Their large conduction band offsets and sub-picosecond ISB relaxation times make them appealing for ultrafast photonics devices operating at telecommunication wavelengths.[4,5] Additionally, the large energy of the longitudinal-optical phonon in GaN (92 meV, 13 μm) opens prospects for room temperature THz lasers.[6,7]

So far, studies on ISB transitions in group-III-nitride multi-quantum-wells (MQWs) have mostly focused on polar *c*-plane structures. However, this crystallographic orientation comes with the complicating factor of a polarization-induced internal electric field, resulting in an asymmetric triangular potential in the quantum wells (QWs). The electric field renders ISB transition energies more sensitive to the strain state of the QWs,[8] and hampers the extension of ISB transitions towards far-infrared wavelengths. This quantum-confined Stark effect is a major hurdle for device design, although it has been partially compensated by the implementation of more complex step-QW designs.[9–12] The use of nonpolar *a* or *m* crystallographic orientations allows for GaN/Al(Ga)N systems to operate without the influence of this electric field[13] and facilitates the device design while still maintaining the benefits of GaN.

Regarding nonpolar materials, ISB optical absorption at $\lambda \sim 2.1$ μm has been reported in 1.75-nm-thick *a*-plane GaN MQWs with 5.1-nm-thick AIN barriers grown by plasma-assisted molecular-beam epitaxy (PAMBE) on *r*-plane sapphire.[14] Recently, using free-standing *m*-plane GaN substrates, low-temperature ($T = 9$ K) ISB absorption has been shown at far-infrared wavelengths (47.5-79.5 μm) using *m-G*aN/AlGaN MQWs grown by PAMBE.[15] Room temperature mid-infrared (MIR) ISB absorption in the 4.20 to 4.84 μm

range has also been observed recently on *m*-plane $GaN/Al_{0.5}Ga_{0.5}N$ MQWs grown by metalorganic vapor phase epitaxy (MOVPE).[16] Finally, Pesach *et al.*[17] have demonstrated QW infrared photodetectors (QWIPs) consisting of $In_{0.095}Ga_{0.905}N/Al_{0.07}Ga_{0.93}N$ (2.5 nm / 56.2 nm) and $In_{0.1}Ga_{0.9}N/GaN$ (3 nm /50 nm) MQWs, which displayed photocurrent peaks at 7.5 µm and 9.3 µm, respectively, when characterized at 14 K.

In this paper, we compare GaN/AlN MQWs simultaneously grown on the nonpolar *a*- and *m*-planes as well as on the polar *c*-plane displaying ISB transitions in the short wavelength infrared (SWIR) region. In terms of mosaicity, surface roughness, photoluminescence (PL) linewidth and intensity, and ISB absorption, the best nonpolar results are obtained from *m*-plane structures. With respect to polar structures, the ISB transitions are redshifted, and present similar line widths. Based on these results, we designed a series of *m*-plane GaN/AlGaN MQWs to determine the accessible spectral range in the MIR. These samples show tunable room-temperature ISB absorption from 4.0 to 5.8 µm, where the long-wavelength limit is set by the absorption associated with the second order of the Reststrahlen band in the bulk GaN substrates.

II. EXPERIMENTAL

The samples were grown by PAMBE at a substrate temperature T_S = 720°C and with a nitrogen-limited growth rate of 0.4 ML/s (≈ 360 nm/h). Growth was performed under the optimum conditions for *c*-plane GaN, i.e. slightly Ga-rich conditions.[8,18,19] For *a*- and *m*-plane GaN/Al(Ga)N heterostructures, the substrates were free-standing semi-insulating GaN sliced along the respective nonpolar surfaces from (0001)-oriented GaN boules synthesized by hydride vapor phase epitaxy (resistivity $>10^6$ Ωcm, dislocation density $<5\times10^6$ cm^{-2}). For the *c*-plane GaN/Al(Ga)N heterostructures, growth was performed either on 1-µm-thick

AlN-on-sapphire templates (for SWIR structures) or on 4-µm-thick GaN-on-Si(111) templates (for MIR structures), both deposited by MOVPE. The heterostructures were simulated using the Nextnano[3] 8×8 k.p self-consistent Schrödinger-Poisson solver,[20] with the material parameters described by Kandaswamy *et al*.[8]

The surface morphology of the layers was studied by field-emission scanning electron microscopy (SEM) using a Zeiss Ultra 55 microscope, and by atomic force microscopy (AFM) in the tapping mode using a Dimension 3100 system. The periodicity and structural properties of the MQWs were studied by X-ray diffraction (XRD) using a Seifert XRD 3003 PTS-HR diffractometer with a beam concentrator in front of a Ge(220) 2- or 4-bounce monochromator and a 0.15 degree long plate collimator in front of the detector.

Photoluminescence (PL) spectra were obtained by exciting with a continuous-wave solid-state laser ($\lambda = 244$ nm), with an excitation power around 100 µW focused on a spot with a diameter of ≈100 µm. The emission from the sample was collected by a Jobin Yvon HR460 monochromator equipped with an ultraviolet-enhanced charge-coupled device camera. All PL measurements were performed at 5 K.

Fourier transform infrared spectroscopy (FTIR) was used to probe the ISB absorption using a halogen lamp and a mercury-cadmium-telluride detector incorporated into a Bruker V70v spectrometer. All samples were polished at 45° (bulk GaN or sapphire substrates) or at 30° (Si substrates) to form multipass waveguides allowing 4-5 interactions with the active region. The samples were tested in transmission mode using an MIR polarizer to discern between the transverse-electric (TE) and transverse-magnetic (TM) polarized light. Observation of ISB absorption requires a component of the electric field perpendicular to the QW plane, i.e. TE polarized light is not absorbed.[21] All FTIR measurements were performed at room temperature.

III. RESULTS

A. SWIR absorption in GaN/AlN MQWs

To compare the different crystal orientations a series of 40-period GaN/AlN MQWs was grown along the *m*-, *a*- and *c*- crystallographic directions simultaneously. This comparison was possible because each of the three crystallographic planes grows two-dimensionally under Ga-rich conditions in PAMBE.[22–24] These structures were designed to display ISB transitions in the 292-795 meV (1.4-4.2 μm) spectral range. The QWs were doped with Si at a concentration of $\approx 1\times10^{19}$ cm^{-3}. The geometry of the samples and their experimentally-obtained optical properties are summarized in Table I.

To evaluate their structural quality, the surface morphology of the samples was assessed by SEM and AFM, as illustrated in Figure 1 for samples S3a and S3m. On a large scale, the SEM images of the nonpolar samples show smooth surfaces with cracks propagating along the *c* axis (average distance between cracks ≈10 μm), resulting in $\{11\bar{2}0\}$ or $\{1\bar{1}00\}$ facets for *m*- or *a*-oriented samples, respectively. In the polar case, crack propagation occurs when GaN/AlGaN heterostructures are grown under tensile strain. In this case, cracks are isotropically distributed, and present vertical $\{1\bar{1}00\}$ facets.[25,26] Due to the anisotropy of the nonpolar lattices, relaxation along the *c* and *a/m* directions must be analyzed independently. Cracks propagating along the in-plane axis *m* have been described in *a*-AlN grown on *a*-plane 6H-SiC,[27] which was explained as due to the tensile strain along the *c* axis (−1.1% lattice mismatch) in combination with a lack of low-energy slip systems available for plastic relaxation. However, in a highly compressed configuration (with larger mismatch such as *a*-GaN on *r*-sapphire having +1.2% and +16.1% lattice mismatch along *c* and *m*, respectively), cracks are observed to propagate preferentially along the *c* axis.[28,29] In the case of *m*-AlGaN,

cracks propagating along the in-plane axis a have been reported.[30,31] For the samples in this study, it appears that these defects do not develop during the growth, but instead during the cooling process as a result of the temperature-dependent GaN/AlN lattice mismatch.[32] On the AFM scale, the root-mean-square (rms) surface roughness measured in images of an area of $5 \times 5\ \mu m^2$ was 1.1±0.2 nm, 2.0±0.6 nm, and 3.7±1.2 nm for c-, m-, and a-plane samples, respectively, i.e. m-plane growth systematically resulted in smoother surfaces than a-plane growth.

The periodicity and strain state of the samples were analyzed by XRD. Figure 2 presents the θ–2θ scans of the $(3\bar{3}00)$ reflection of samples S1m, S2m, and S3m, and the $(11\bar{2}0)$ reflection of samples S1a and S2a. Table I summarizes the MQW period extracted from the inter-satellite distance in the XRD measurements. The full width at half maximum (FWHM) of the rocking curves were measured for the substrate and the MQW zero-order reflection with $\phi = 0°$ and $\phi = 90°$ ($\Delta\omega_c$ and $\Delta\omega_a$, respectively for the m-oriented samples, and $\Delta\omega_c$ and $\Delta\omega_m$, respectively for the a-oriented sample), which provides information on the sample mosaicity in the c and a directions, respectively for the m-oriented samples, and in the c and m directions, respectively for the a-oriented samples. Comparing the values in Table I, it appears that the m-plane MQWs exhibit better crystalline quality than the a-plane structures.

To assess the MQW strain state, reciprocal space maps were measured. Figure 3 illustrates the results for sample S2m, where the $(3\bar{3}00)$, $(3\bar{3}02)$, and $(3\bar{2}\bar{1}0)$ reflections were considered. The reciprocal space is presented using the GaN substrate as a reference. The shift in q(0001) (projection of the reciprocal space vector along [0001]) of the MQW $(3\bar{3}00)$ reflection with respect to the substrate (see Fig. 3(b)) reveals a tilt of the epitaxial structure. The tilt angles towards the in-plane directions ($\delta\omega_c$ and $\delta\omega_a$ for m oriented samples, and $\delta\omega_c$ and $\delta\omega_m$ for a oriented samples) are summarized in Table I. Taking the

measured tilt into account, the strain states along the a, m and c axis can be described as $\varepsilon_p = \frac{p-p_r}{p_r}$, where ε_p is the strain along the axis p (a, m or c), p is the measured lattice parameter along this axis, and p_r is the theoretical value of p assuming that the structure is relaxed. Using the lattice parameters of Vurgaftman *et al.*[34] and Wright *et al.*[35] (a_{GaN} = 3.1891 Å; a_{AlN} = 3.112 Å; c_{GaN} = 5.1850 Å; c_{AlN} = 4.980 Å), the lattice mismatch between AlN and GaN is –2.4% in the a and m directions and –3.9% in the c direction. The larger mismatch along c explains the larger tilt towards this direction (0.05° to 0.29°). This tilt is a way to relax the in-plane lattice mismatch, and thus to reduce the number of dislocations necessary to release the strain.[33]

Figure 4 presents the values of strain extracted from the reciprocal space maps, compared with the in-plane lattice mismatch between the relaxed MQWs (considered as a relaxed AlGaN alloy with the average Al composition of the structure) and the GaN substrates. Due to the lattice mismatch, all the structures undergo in-plane tensile strain, and as a result of Hooke's law, they are compressively strained in the growth direction. In the case of m-oriented samples, all the MQWs are about 50% relaxed along the in-plane a axis, whereas almost full relaxation is observed along c.

The PL spectra of all the samples were measured at low temperature (T = 5 K), with the results in terms of emission wavelength and intensity summarized in Table I. As an illustration, Figure 5(a) shows the spectra of samples S2c, S2m and S2a. For all samples, the c- and a- orientations systematically lead to broader emission peaks than those measured for the m-orientation. In addition, the PL from m-plane samples is twice as intense as that from a-plane, and more than twenty times as intense as that from c-plane QWs.

In Figure 5(b), the PL peak emission energies are compared with theoretical calculations assuming that the in-plane lattice parameters correspond to those of an AlGaN ternary alloy

with an Al composition equal to the average Al content of the MQW. For nonpolar samples, their luminescence is systematically above the GaN band gap, supporting the absence of internal electric field. For the *c*-plane samples, the emission energy shifts below the GaN band gap when increasing the well width. In general, the emission energies are in agreement with the theoretical calculations. The deviation from the calculations observed for S1 is attributed to carrier localization in thickness fluctuations in such small QWs (the thickness of a GaN monolayer being ≈ 0.25 nm).

The ISB absorption in the SWIR range was measured at room temperature by FTIR spectroscopy. To identify the ISB transition in the samples, the TE transmission spectra were divided by the respective TM transmission spectra, and the results are presented in Figure 6(a) and Table I. As expected, the absorption is red-shifted when decreasing the QW width. In the case of nonpolar MQWs, the absence of the internal electric field results in a red shift of the ISB energy, in comparison to *c*-plane structures, where the triangular potential profile in the wells contributes to the separation of the quantized electron levels. A similar result was observed in the case of semipolar $(11\bar{2}2)$ MQWs due to the reduction of spontaneous and piezoelectric polarizations.[36] Nonpolar *m*-plane samples exhibit an absorption linewidth similar to that of polar MQWs absorbing at the same wavelengths. In contrast, the TM polarized absorption of *a*-plane sample S2a undergoes a significant broadening and deviation from the calculations, and no ISB absorption was observed for sample S3a.

In summary, ISB transitions in *m*-oriented GaN/AlN MQWs can cover the SWIR spectral range with performance comparable to polar MQWs, with the advantage of design simplicity in a geometry with square potential band profiles. Furthermore, *m*-plane structures display better results in terms of mosaicity, surface roughness, PL linewidth and intensity, and ISB absorption than those obtained when growing on the nonpolar *a* plane.

B. MIR absorption in GaN/AlGaN MQWs

In a second stage, we have analysed the possibility of covering the MIR spectral region with nonpolar QWs. Based on the previous results, only the *m* crystallographic orientation was considered. The QWs were enlarged to achieve the desired spectral shift, and the AlN barriers were replaced by the ternary alloy AlGaN with a twofold purpose: reducing the lattice mismatch in the MQW and approaching the excited level in the QW to the continuum, to mimic the band diagram of a QWIP. The barriers were chosen to be 22.6 nm thick, in order to prevent coupling between QWs even in the largest QWs. Four *m*-plane structures were designed to display ISB transitions between the ground conduction band level and the first excited level ($e_1 \rightarrow e_2$) in the 186-356 meV (3.4-6.7 µm) range, using the QW thicknesses and Al contents in the barriers summarized in Table II. Note that the use of bulk GaN as a substrate sets an additional limit for characterization. Even though the GaN Reststrahlen band spans from 9.6 µm to 19 µm, absorption in the range of 6.7 µm to 9 µm has been observed in bulk GaN substrates with carrier concentrations $<10^{16}$ cm^{-3}, and was attributed to the second harmonic of the Reststrahlen band.[37–39] Figure 7 shows the band diagrams of the *m*-plane MQWs, together with those of structures with the same dimensions but grown along the *c* direction. In the case of the *c*-oriented MQWs studied in this work, characterization of ISB absorption in the spectral range between 6.7 µm and 9 µm is possible due to the use of floating-zone silicon substrates, as previously demonstrated.[40]

A series of 50-period GaN/$Al_xGa_{1-x}N$ MQWs was grown along the *m*- and *c*-crystallographic directions simultaneously, following the designs in Table II. As a first evaluation of the structural quality, the surface morphology was assessed by AFM and SEM, as illustrated in Figure 8 for sample S4m. Similar to the SWIR samples, SEM images of the nonpolar samples reveal cracks propagating along the *c*-axis. However, the distance between cracks increased to ≈15-30 µm. At the AFM scale, all the nonpolar samples in Table II

present similar morphology: large-scale (5×5 μm² to 10×10 μm² images) roughness in the range of 7-15 nm, whereas at a smaller scale (1×1 μm² images) the surfaces are smooth, with rms roughness in the 1-2 nm range.

The periodicity, strain state and mosaicity of sample S7m were analyzed by XRD. To assess the MQW strain state, we measured various reciprocal space maps for sample S7m (the error bars of this technique were too large to extract reliable conclusions in samples containing lower Al content). The extracted strain states are $\varepsilon_m = 0.03\pm0.15\%$, $\varepsilon_a = -0.43\pm0.40\%$, and $\varepsilon_c = -0.27\pm0.40\%$. Compared to the relaxed lattice mismatch between the GaN/$Al_{0.44}Ga_{0.56}N$ MQW and the GaN substrate (–0.98% in the *a* and *m* directions and –1.6% in the *c* direction), they point to a certain relaxation in spite of the large error bars of the measurement. The FWHM of the rocking curves of the MQW reflection were $\Delta\omega_c = 0.28°$ and $\Delta\omega_a = 0.22°$, pointing to a significant improvement of the MQW crystalline quality with respect to the GaN/AlN QWs (see Table I) owing to the reduced lattice mismatch.

The PL spectra of all the samples were measured at low temperature, as illustrated by Figure 9(a). In Figure 9(b), the PL emission energies are compared with theoretical calculations as a function of the QW width. For the *c*-plane samples, the luminescence is systematically below the GaN bandgap due to the internal electric field, and it exhibits superimposed oscillations due to Fabry-Perot interferences. For nonpolar samples, the emission remains above the GaN band gap energy. In both cases, decreasing the QW width leads to a red shift of the PL energy, with emission energies in agreement with the calculations.

The ISB absorption in the MIR range was measured at room temperature by FTIR spectroscopy. To identify the ISB transition in the samples, the substrate transmission

spectrum was divided by the respective TM transmission spectra, with the results displayed in Figures 10(a) and (b). In nonpolar structures, increasing the QW width leads to a red shift of the ISB energies from 308 to 213 meV (4.0 to 5.8 µm), in agreement with calculations as shown in Figure 10(c). The deviation observed in the sample with the largest QWs (calculated transition at 186 meV) is attributed to the proximity of the second order of the Reststrahlen band at 184 meV (6.7 µm), which sets the onset of substrate absorption [shadowed area in Figures 10(a) and (c)]. For all polar samples, two absorption peaks are observed. The peak at lower energy corresponds to the ($e_1 \rightarrow e_2$) transition, whereas the higher energy peak is assigned to ISB transitions involving upper states ($e_1 \rightarrow e_3$, $e_1 \rightarrow e_4$), as previously observed in GaN/AlN QWs.[41] In symmetric structures, the $e_1 \rightarrow e_3$ transition is forbidden due to parity, whereas $e_1 \rightarrow e_4$ is allowed. However, both transitions are possible in asymmetric polar QWs, and the second peak might hence correspond to the combination of both transitions. In this series of samples, the absorption in *m*- and *c*-oriented MQWs is located in the same spectral range, both theoretically and experimentally. This coincidence is due to the choice of the Al content in the barriers, which determines the energetic location of e_2 in the *c*-plane structures. Increasing the Al content of the barriers would introduce only slight corrections to ($e_1 \rightarrow e_2$) in *m*-plane MQWs, but it would induce a major blue shift of this transition in the *c*-plane MQWs due to the internal electric field.

IV CONCLUSIONS

In summary, we have shown room temperature SWIR ISB absorption in a series of nonpolar *a*- and *m*- plane and polar *c*-plane GaN/AlN MQWs with various QW thicknesses. Comparing the two nonpolar crystallographic planes, the best results in terms of mosaicity, surface roughness, PL linewidth and intensity, and ISB absorption were obtained for *m*-

oriented samples. We have demonstrated that ISB transitions in *m*-GaN/AlN MQWs can cover the whole SWIR spectrum (1.5-2.9 µm) with performance comparable to polar MQWs and with the advantage of design simplicity. The ISB absorption is systematically red shifted with respect to polar structures with the same geometry due to the triangular potential profile induced by the internal electric field. Drawing from the experience in the SWIR range, we have designed a series of *m*-plane GaN/AlGaN MQWs with ternary barriers and with larger QWs, to shift the ($e_1 \rightarrow e_2$) ISB energy towards the MIR. We have demonstrated experimentally that the ISB absorption in these *m*-plane samples can be tuned in the range of 4.0-5.8 µm, the longer wavelength limit being set by the second order of the GaN Reststrahlen band when using bulk substrates.

ACKNOWLEDGEMENTS. This work is supported by the EU ERC-StG "TeraGaN" (#278428) project.

REFERENCES

[1] M. Beeler, E. Trichas, and E. Monroy, Semicond. Sci. Technol. **28**, 074022 (2013).
[2] D. Hofstetter, E. Baumann, F.R. Giorgetta, R. Théron, H. Wu, W.J. Schaff, J. Dawlaty, P.A. George, L.F. Eastman, F. Rana, P.K. Kandaswamy, F. Guillot, and E. Monroy, Proc. IEEE **98**, 1234 (2010).
[3] H. Machhadani, P. Kandaswamy, S. Sakr, A. Vardi, A. Wirtmüller, L. Nevou, F. Guillot, G. Pozzovivo, M. Tchernycheva, A. Lupu, L. Vivien, P. Crozat, E. Warde, C. Bougerol, S. Schacham, G. Strasser, G. Bahir, E. Monroy, and F.H. Julien, New J. Phys. **11**, 125023 (2009).
[4] N. Suzuki and N. Iizuka, Jpn. J. Appl. Phys. **36**, L1006 (1997).
[5] N. Iizuka, H. Yoshida, N. Managaki, T. Shimizu, S. Hassanet, C. Cumtornkittikul, M. Sugiyama, and Y. Nakano, Opt. Express **17**, 23247 (2009).
[6] E. Bellotti, K. Driscoll, T.D. Moustakas, and R. Paiella, J. Appl. Phys. **105**, 113103 (2009).
[7] G. Sun, J.B. Khurgin, and D.P. Tsai, Opt. Express **21**, 28054 (2013).
[8] P.K. Kandaswamy, F. Guillot, E. Bellet-Amalric, E. Monroy, L. Nevou, M. Tchernycheva, A. Michon, F.H. Julien, E. Baumann, F.R. Giorgetta, D. Hofstetter, T. Remmele, M. Albrecht, S. Birner, and L.S. Dang, J. Appl. Phys. **104**, 093501 (2008).
[9] H. Machhadani, Y. Kotsar, S. Sakr, M. Tchernycheva, R. Colombelli, J. Mangeney, E. Bellet-Amalric, E. Sarigiannidou, E. Monroy, and F.H. Julien, Appl. Phys. Lett. **97**, 191101 (2010).
[10] F.F. Sudradjat, W. Zhang, J. Woodward, H. Durmaz, T.D. Moustakas, and R. Paiella, Appl. Phys. Lett. **100**, 241113 (2012).
[11] M. Beeler, C. Bougerol, E. Bellet-Amalric, and E. Monroy, Appl. Phys. Lett. **103**, 091108 (2013).
[12] M. Beeler, C. Bougerol, E. Bellet-Amalric, and E. Monroy, Appl. Phys. Lett. **105**, 131106 (2014).
[13] J.S. Speck and S.F. Chichibu, MRS Bull. **34**, 304 (2011).
[14] C. Gmachl and H.M. Ng, Electron. Lett. **39**, 567 (2003).
[15] C. Edmunds, J. Shao, M. Shirazi-HD, M.J. Manfra, and O. Malis, Appl. Phys. Lett. **105**, 021109 (2014).
[16] T. Kotani, M. Arita, and Y. Arakawa, Appl. Phys. Lett. **105**, 261108 (2014).
[17] A. Pesach, E. Gross, C.-Y. Huang, Y.-D. Lin, A. Vardi, S.E. Schacham, S. Nakamura, and G. Bahir, Appl. Phys. Lett. **103**, 022110 (2013).
[18] B. Heying, R. Averbeck, L.F. Chen, E. Haus, H. Riechert, and J.S. Speck, J. Appl. Phys. **88**, 1855 (2000).
[19] C. Adelmann, J. Brault, G. Mula, B. Daudin, L. Lymperakis, and J. Neugebauer, Phys. Rev. B **67**, 165419 (2003).
[20] S. Birner, T. Zibold, T. Andlauer, T. Kubis, M. Sabathil, A. Trellakis, and P. Vogl, IEEE Trans. Electron Devices **54**, 2137 (2007).
[21] H.C. Liu and F. Capasso, *Intersubband Transitions in Quantum Wells : Physics and Device Applications I* (Academic Press, San Diego, CA, 2000).
[22] P. Waltereit, O. Brandt, M. Ramsteiner, R. Uecker, P. Reiche, and K.. Ploog, J. Cryst. Growth **218**, 143 (2000).
[23] R. Schuber, M.M.C. Chou, P. Vincze, T. Schimmel, and D.M. Schaadt, J. Cryst. Growth **312**, 1665 (2010).
[24] O. Brandt, Y.J. Sun, L. Däweritz, and K.H. Ploog, Phys. Rev. B **69**, (2004).
[25] S. Einfeldt, V. Kirchner, H. Heinke, M. Dießelberg, S. Figge, K. Vogeler, and D. Hommel, J. Appl. Phys. **88**, 7029 (2000).
[26] S. Einfeldt, H. Heinke, V. Kirchner, and D. Hommel, J. Appl. Phys. **89**, 2160 (2001).

[27] P. Vennegues, S. Founta, H. Mariette, and B. Daudin, Jpn. J. Appl. Phys. **49**, 040201 (2010).
[28] P. Vennéguès and Z. Bougrioua, Appl. Phys. Lett. **89**, 111915 (2006).
[29] C.H. Chiang, K.M. Chen, Y.H. Wu, Y.S. Yeh, W.I. Lee, J.F. Chen, K.L. Lin, Y.L. Hsiao, W.C. Huang, and E.Y. Chang, Appl. Surf. Sci. **257**, 2415 (2011).
[30] K. Okamoto, T. Tanaka, M. Kubota, and H. Ohta, Jpn. J. Appl. Phys. **46**, L820 (2007).
[31] E.C. Young, A.E. Romanov, C.S. Gallinat, A. Hirai, G.E. Beltz, and J.S. Speck, Appl. Phys. Lett. **96**, 041913 (2010).
[32] S. Figge, H. Kröncke, D. Hommel, and B.M. Epelbaum, Appl. Phys. Lett. **94**, (2009).
[33] J. Brault, E. Bellet-Amalric, S. Tanaka, F. Enjalbert, D. Le Si Dang, E. Sarigiannidou, J.-L. Rouviere, G. Feuillet, and B. Daudin, Phys. Status Solidi B **240**, 314 (2003).
[34] I. Vurgaftman and J.R. Meyer, J. Appl. Phys. **94**, 3675 (2003).
[35] A.F. Wright, J. Appl. Phys. **82**, 2833 (1997).
[36] H. Machhadani, M. Beeler, S. Sakr, E. Warde, Y. Kotsar, M. Tchernycheva, M.P. Chauvat, P. Ruterana, G. Nataf, P. De Mierry, E. Monroy, and F.H. Julien, J. Appl. Phys. **113**, 143109 (2013).
[37] M. Hao, S. Mahanty, R.S. Qhalid Fareed, S. Tottori, K. Nishino, and S. Sakai, Appl. Phys. Lett. **74**, 2788 (1999).
[38] J. Yang, G.J. Brown, M. Dutta, and M.A. Stroscio, J. Appl. Phys. **98**, 043517 (2005).
[39] M. Welna, R. Kudrawiec, M. Motyka, R. Kucharski, M. Zając, M. Rudziński, J. Misiewicz, R. Doradziński, and R. Dwiliński, Cryst. Res. Technol. **47**, 347 (2012).
[40] P.K. Kandaswamy, H. Machhadani, C. Bougerol, S. Sakr, M. Tchernycheva, F.H. Julien, and E. Monroy, Appl. Phys. Lett. **95**, 141911 (2009).
[41] D. Hofstetter, J. Di Francesco, P.K. Kandaswamy, and E. Monroy, Appl. Phys. Lett. **98**, 071104 (2011).

TABLES

Table I: Structural and optical characteristics of the GaN/AlN MQW samples on GaN substrates: QW thickness (t_{QW}) (barrier thickness is 3.6 nm for all samples); MQW period measured by XRD; broadening of the ω-scan of the ($3\bar{3}00$) XRD reflection in the *c* and *a* directions ($\Delta\omega_c$ and $\Delta\omega_a$, respectively) for *m*-oriented samples and substrates, and broadening of the ω-scan of the ($11\bar{2}0$) XRD reflection in the *c* and *m* directions ($\Delta\omega_c$ and $\Delta\omega_m$, respectively) for *a*-oriented samples and substrates; tilt between the MQW and the GaN substrate towards the *c* and *a* directions ($\delta\omega_c$ and $\delta\omega_a$, respectively) for *m*-oriented samples, and towards the *c* and *m* directions ($\delta\omega_c$ and $\delta\omega_m$, respectively) for *a*-oriented samples; strain state in the 3 perpendicular directions *m, a* and *c* (ε_m, ε_a, and ε_c respectively); PL peak energy and intensity normalized with respect to S1m; simulated and measured ISB transition energy.

Sample	t_{QW} (nm)	XRD Period (nm)	XRD FWHM MQW (°)	XRD FWHM GaN (°)	Tilt MQW/GaN (°)	Strain (%)	PL peak energy (eV) [normalized intensity]	Simulated / Measured ISB transition (meV)
S1m	1.5	5.1	$\Delta\omega_c = 0.33$ $\Delta\omega_a = 0.39$	$\Delta\omega_c = 0.028$ $\Delta\omega_a = 0.028$	$\delta\omega_c = 0.20$ $\delta\omega_a = 0.04$	$\varepsilon_m = 0.38\pm0.15$ $\varepsilon_a = -1.03\pm0.40$ $\varepsilon_c = -0.36\pm0.40$	3.8 [1]	712 / 799
S2m	2.3	5.9	$\Delta\omega_c = 0.44$ $\Delta\omega_a = 0.30$	$\Delta\omega_c = 0.037$ $\Delta\omega_a = 0.040$	$\delta\omega_c = 0.08$ $\delta\omega_a = 0.015$	$\varepsilon_m = 0.44\pm0.15$ $\varepsilon_a = -0.50\pm0.40$ $\varepsilon_c = -0.17\pm0.40$	3.8 [0.94]	437 / 578
S3m	3.1	6.7	$\Delta\omega_c = 0.45$ $\Delta\omega_a = 0.29$	$\Delta\omega_c = 0.026$ $\Delta\omega_a = 0.032$	$\delta\omega_c = 0.05$ $\delta\omega_a = 0.01$	$\varepsilon_m = 0.41\pm0.15$ $\varepsilon_a = -0.63\pm0.40$ $\varepsilon_c = -0.23\pm0.40$	3.7 [0.58]	296 / 425
S1a	1.5	5.1	$\Delta\omega_c = 0.28$ $\Delta\omega_m = 0.72$	$\Delta\omega_c = 0.030$ $\Delta\omega_m = 0.030$	$\delta\omega_c = 0.16$ $\delta\omega_m = 0.00$	$\varepsilon_a = 0.33\pm0.15$ $\varepsilon_m = -0.56\pm0.40$ $\varepsilon_c = -0.62\pm0.40$	3.9 [0.56]	712 / 815
S2a	2.3	5.9	$\Delta\omega_c = 0.53$ $\Delta\omega_m = 0.40$	$\Delta\omega_c = 0.019$ $\Delta\omega_m = 0.023$	$\delta\omega_c = 0.29$ $\delta\omega_m = 0.015$	$\varepsilon_a = 0.32\pm0.15$ $\varepsilon_m = -0.42\pm0.40$ $\varepsilon_c = -0.09\pm0.40$	3.7 [0.24]	431 / 755
S3a	3.1	6.7	--	--	--	--	3.7 [0.11]	296 / --
S1c	1.5	5.1	--	--	--	--	3.7 [0.014]	814 / 815
S2c	2.3	5.9	--	--	--	--	3.2 [0.008]	657 / 731
S3c	3.1	6.7	--	--	--	--	3.0 [0.003]	603 / 624

Table II: Structural and optical characteristics of the GaN/AlGaN MQW samples: QW thickness (t_{QW}) (barrier thickness is 22.6 nm for all samples); MQW period measured by XRD; Al composition in the barrier (x_B); PL peak energy; simulated and measured first ($e_1 \rightarrow e_2$), second ($e_1 \rightarrow e_3$) and third ($e_1 \rightarrow e_4$) ISB transition energies. Samples S4, S5, and S7 were Si-doped with [Si] $\approx 2\times10^{19}$ cm^{-3}. Sample S6 was doped with [Si] $\approx 8\times10^{18}$ cm^{-3}. (*) Thickness extrapolated from XRD measurements of other samples in the same series.

Sample	t_{QW} (nm)	XRD Period (nm)	x_B (%)	PL peak energy (eV)	Simul. ($e_1 \rightarrow e_2$) / Meas. ISB transition (meV)	Simul. ($e_1 \rightarrow e_3$, $e_1 \rightarrow e_4$) / Meas. ISB transition (meV)
S4m	3.1	25.7 (*)	26	3.60	186 / 222	--
S5m	2.8	25.4 (*)	31	3.64	223 / 213	--
S6m	2.5	25.1 (*)	35	3.39	261 / 251	--
S7m	2.0	24.6 (*)	44	3.40	356 / 308	--
S4c	3.1	25.7 (*)	26	3.61	162 / 188	227, 256 / 270
S5c	2.8	25.4	31	3.68	200 / 209	264, 294 / 319
S6c	2.5	25.1	35	3.41	226 / 241	292, 323 / 326
S7c	2.0	24.6	44	3.46	290 / 286	358, 387 / 378

Figure captions

Figure 1. SEM and AFM images of samples (a) S3a and (b) S3m.

Figure 2. XRD θ-2θ scans of the $(3\bar{3}00)$ reflection of samples S1m, S2m, and S3m, and the $(11\bar{2}0)$ reflection of samples S1a and S2a. The corresponding QW thicknesses are indicated at the right side of the figure.

Figure 3. Reciprocal space maps of sample S2m around asymmetric reflections (a) $(3\bar{3}02)$ with the *c*-axis in the diffraction plane and (c) $(3\bar{2}\bar{1}0)$ with the *a*-axis in the diffraction plane, and symmetric reflection (b) $(3\bar{3}00)$ oriented along *c*. (cps= counts per second)

Figure 4. Strain state of the MQWs extracted from XRD measurements. (a) In-plane lattice parameter *a* (*m* samples) or *m* (*a* samples). (b) In-plane lattice parameter *c*. (c) Out-of-plane lattice parameter. Positive (negative) values of strain correspond to compressive (tensile) strain. Dashed lines indicate the lattice mismatch between a relaxed AlGaN layer with the average Al concentration of the MQW and the GaN substrate.

Figure 5. (a) PL spectra of samples measured at low temperature ($T = 5$ K). (b) PL peak energies as a function of the QW width. Error bars correspond to the FWHM of the PL peaks. Solid lines are theoretical calculations assuming that the in-plane lattice parameters of the MQWs correspond to those of a relaxed AlGaN alloy with the average Al composition of the structure. Dashed lines mark the location of the GaN band gap.

Figure 6. (a) TM-polarized ISB absorption of the samples in Table I measured at room temperature. Data are normalized and vertically shifted for clarity. The corresponding QW thicknesses are indicated on the right side. (b) ISB energies as a function of the QW width. Solid lines correspond to theoretical simulations assuming that the in-plane lattice

parameters of the MQWs correspond to those of a relaxed AlGaN alloy with the average Al composition of the structure.

Figure 7. Conduction band diagram with first four energy levels and electron wavefunctions of a QW in the center of the active region of samples (a) S4m, (b) S7m, (c) S4c, and (d) S7c.

Figure 8. Typical (a) SEM and (b) AFM images of the GaN/AlGaN MQWs in Table II. Measurements correspond to sample S4m.

Figure 9. (a) PL spectra of the *m*- and *c*-plane GaN/AlGaN MQWs in Table II measured at low temperature. Data are normalized and vertically shifted for clarity. The corresponding QW thicknesses are indicated on the left side. (b) PL peak energies as a function of the QW width. Error bars correspond to the FWHM of the PL emission. Solid lines are theoretical calculations of the band-to-band transition assuming that the in-plane lattice parameters of the MQWs correspond to those of a relaxed AlGaN alloy with the average Al composition of the structure. Dashed lines mark the location of the GaN band gap.

Figure 10. TM-polarized ISB absorption spectra for (a) the m-plane and (b) c-plane GaN/AlGaN MQWs in Table II measured at room temperature. Data are normalized and vertically shifted for clarity. The corresponding QW thicknesses are indicated on the right side. ISB energies as a function of QW width for all (c) m-plane and (d) c-plane samples. Solid lines are theoretical calculations assuming that the in-plane lattice parameters of the MQWs correspond to those of an AlGaN alloy with the average Al composition of the structure. Shadowed areas in graphs (a) and (c) mark the second order of the Reststrahlen band of GaN.

(a)
5 µm
[0001]
[1-100]
25 nm
0
1 µm
(b)
5 µm
[0001]
[11-20]
25 nm
0
1 µm

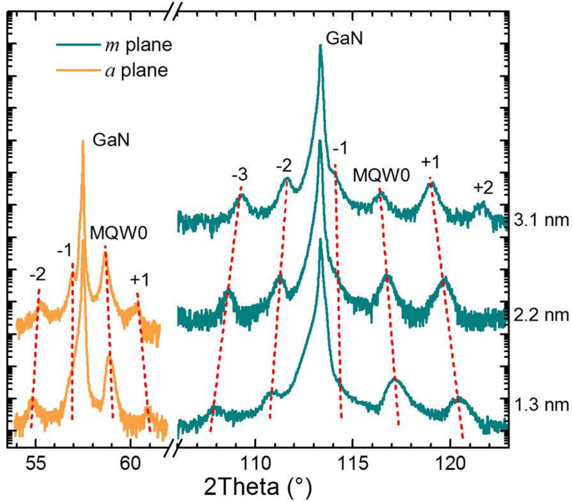

m plane
a plane
GaN
GaN
-3
-2
-1
MQW0
+1
+2
-2
-1
MQW0
+1
3.1 nm
2.2 nm
1.3 nm
Normalized Intensity (a.u.)
2Theta (°)
55
60
110
115
120

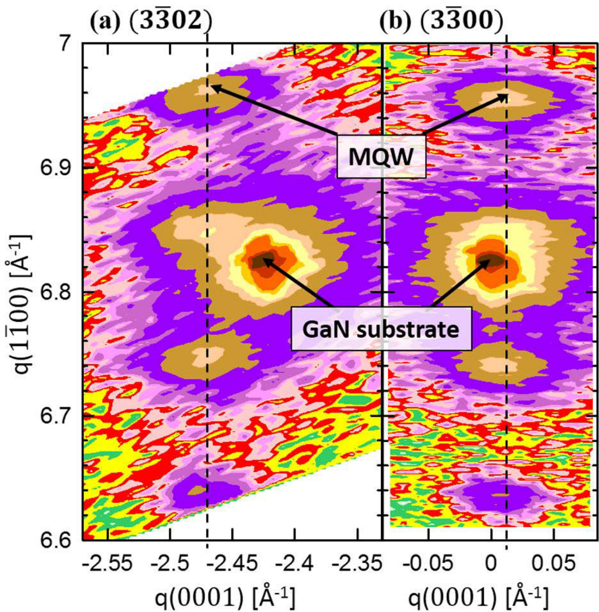
(a) $(3\bar{3}02)$
(b) $(3\bar{3}00)$
MQW
GaN substrate
7
6.9
6.8
6.7
6.6
$q(1\bar{1}00)$ [Å^{-1}]
-2.55
-2.5
-2.45
-2.4
-2.35
q(0001) [Å^{-1}]
-0.05
0
0.05
q(0001) [Å^{-1}]
(c) $(3\bar{2}\bar{1}0)$
MQW
GaN substrate
5.85
5.75
5.65
5.55
$q(1\bar{1}00)$ [Å^{-1}]
-2.1
-2.05
-2
-1.95
-1.9
$q(11\bar{2}0)$ [Å^{-1}]
cps
5000
1000
100
50
25
16
8
4
3
2.5
2
1.5
1
0.5
0.25

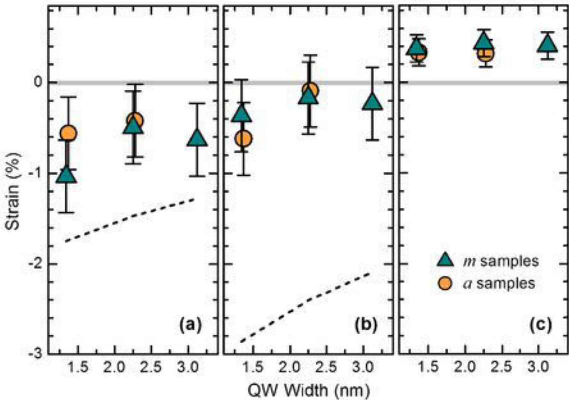

Strain (%)
0
-1
-2
-3
1.5
2.0
2.5
3.0
QW Width (nm)
(a)
(b)
(c)
m samples
a samples

Wavelength (nm)

480 440 400 360 320

m plane

a plane

c plane

(a)

T = 5 K

PL Intensity (cps)

10^6 10^5 10^4 10^3 10^2

GaN

2.5 3.0 3.5 4.0

Energy (eV)

(b)

Nonpolar

Polar

GaN

Energy (eV)

4.0 3.5 3.0

Wavelength (nm)

320 360 400 440

m plane

a plane

c plane

1.5 2.0 2.5 3.0

QW Width (nm)

(a)
Wavelength (µm)
6 4 3 2 1.5
m plane
a plane
c plane
1.3 nm
2.2 nm
3.1 nm
Normalized Absorption
0.4 0.6 0.8 1.0
Energy (eV)
(b)
T = 300 K
Polar
Nonpolar
m plane
a plane
c plane
Energy (eV)
0.2 0.4 0.6 0.8 1.0
QW Width (nm)
1.5 2.0 2.5 3.0
Wavelength (µm)
1.5 2 3 4 6 8

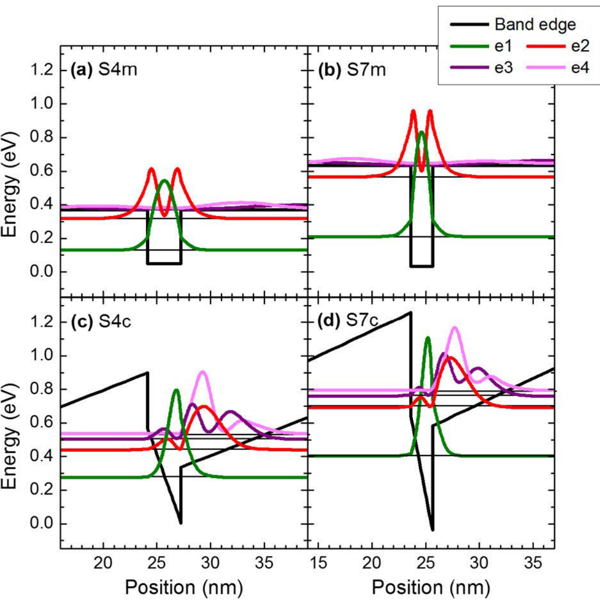

Band edge
e1
e2
e3
e4
(a) S4m
(b) S7m
(c) S4c
(d) S7c
Energy (eV)
Position (nm)
0.0
0.2
0.4
0.6
0.8
1.0
1.2
15
20
25
30
35

(a)

[0001]

[11-20]

5 µm

(b)

70 nm

0

1 µm

(a)

Wavelength (nm)

400 380 360 340 320

GaN

m plane

c plane

T = 5 K

2.0 nm

2.5 nm

2.8 nm

3.1 nm

Normalized Intensity

3.2 3.4 3.6 3.8 4.0

Energy (eV)

(b)

m plane

c plane

GaN

Energy (eV)

3.3 3.4 3.5 3.6 3.7

Wavelength (nm)

330 340 350 360 370

2.0 2.5 3.0

QW Width (nm)

Wavelength (μm)
8 7 6 5 4 3
(a) m plane
(b) c plane
T = 300 K
2.0 nm
2.5 nm
2.8 nm
3.1 nm
Normalized Absorption
0.2 0.3 0.4 0.5
Energy (eV)
(c) m plane
e2-e1
(d) c plane
e4-e1
e3-e1
e2-e1
Energy (eV)
0.40 0.35 0.30 0.25 0.20 0.15
Wavelength (μm)
3 4 5 6 7 8
2.0 2.5 3.0
QW Width (nm)

Annex 9

Systematic study of near-infrared intersubband absorption of polar and semipolar GaN/AlN quantum wells

H. Machhadani,[1,2,a)] M. Beeler,[3] S. Sakr,[1] E. Warde,[1] Y. Kotsar,[3] M. Tchernycheva,[1] M. P. Chauvat,[4] P. Ruterana,[4] G. Nataf,[5] Ph. De Mierry,[5] E. Monroy,[3] and F. H. Julien[1]
[1]*Institut d'Electronique Fondamentale, Université Paris-Sud, UMR 8622 CNRS, 91405 Orsay, France*
[2]*Semiconductor Materials, Department of Physics, Chemistry, and Biology (IFM), Linköping University, S-58183 Linköping, Sweden*
[3]*CEA-CNRS Group Nanophysique et Semiconducteurs, INAC/SP2M/NPSC, CEA-Grenoble, 17 rue des Martyrs, 38054 Grenoble Cedex 9, France*
[4]*CIMAP, UMR 6252, CNRS-ENSICAEN-CEA-UCBN, 6 Bd Maréchal Juin, 14050 Caen, France*
[5]*CRHEA, UPR 10, 1 rue Bernard Grégory, Sophia Antipolis, 06560 Valbonne, France*

(Received 23 January 2013; accepted 25 March 2013; published online 12 April 2013)

We report on the observation of intersubband absorption in GaN/AlN quantum well superlattices grown on $(11\bar{2}2)$-oriented GaN. The absorption is tuned in the 1.5–4.5 μm wavelength range by adjusting the well thickness. The semipolar samples are compared with polar samples with identical well thickness grown during the same run. The intersubband absorption of semipolar samples shows a significant red shift with respect to the polar ones due to the reduction of the internal electric field in the quantum wells. The experimental results are compared with simulations and confirm the reduction of the polarization discontinuity along the growth axis in the semipolar case. The absorption spectral shape depends on the sample growth direction: for polar quantum wells the intersubband spectrum is a sum of Lorentzian resonances, whereas a Gaussian shape is observed in the semipolar case. This dissimilarity is explained by different carrier localization in these two cases. © *2013 AIP Publishing LLC* [http://dx.doi.org/10.1063/1.4801528]

I. INTRODUCTION

Since the pioneering work of West and Eglash in 1984,[1] intersubband (ISB) transitions in semiconductor quantum wells (QWs), i.e., the transitions between the confined levels within the same band, have attracted great attention. This interest has been motivated by the development of a new kind of optoelectronic devices based on ISB transitions such as quantum cascade lasers (QCLs)[2,3] and quantum well infrared photodetectors (QWIPs).[4–6] The spectral domain accessible for ISB devices is limited on the short wavelength side by the available band offset in the heterostructure and the material transparency. To access the near-infrared spectral range, nitride heterostructures started to be intensively explored from the late 1990s.[7] Thanks to their large conduction band offset, ISB absorption in the 1.3–4 μm range has been demonstrated in GaN/AlN QWs grown along the [0001] polar direction.[8,9] Nitride heterostructures grown along the [0001] polar axis possess an intense internal electric field due to spontaneous and piezoelectric polarization.[10] The built-in field can be extremely strong up to 10 MV/cm for AlN/GaN QWs.[11] The presence of this internal field complicates the design of ISB devices[12] since it induces band bending effects and the formation of depletion/accumulation regions, while reducing the oscillator strength associated with the ISB transition. For optoelectronic applications, it is, therefore, desirable to reduce the internal electric field. This can be achieved by using III-nitride materials synthesized in the cubic phase[13–16] or by changing the growth direction to set the polarization vector at 90°.[17]

The later strategy has been implemented using nonpolar growth planes, namely, the *m*-plane $\{10\bar{1}0\}$[18] or the *a*-plane $\{11\bar{2}0\}$.[19] However, growth of nonpolar III-nitrides is challenging due to the strong anisotropy of the surface properties, resulting in layers with a high density of crystalline defects. An alternative approach is the growth along semipolar planes, such as $\{11\bar{2}2\}$. The advantage of semipolar orientations is that they allow a considerable reduction of the internal electric field[20] while presenting lower in-plane anisotropy with respect to non-polar surfaces.[21] We have previously reported the observation of ISB absorption in non-intentionally doped semipolar GaN/AlN QWs using a photoinduced absorption spectroscopic technique relying on the photogeneration of electron-hole pairs in the QWs.[22]

In this work, we present a systematic study of the photoluminescence (PL) and ISB absorption of polar and semipolar GaN/AlN QWs grown by plasma-assisted molecular beam epitaxy (PAMBE). With respect to previous studies, efficient Si doping enabled the direct observation of the ISB absorption in both polar and semipolar samples with the same well thickness, grown during the same run. The optical properties are compared with structural characterizations and simulations, confirming a strong reduction of the internal field in the case of the semipolar orientation. By increasing the well thickness from 1.2 to 3 nm, the peak ISB absorption wavelength is tuned from 1.5 to 3.3 μm for semipolar samples, and from 1.5 to 2 μm for polar samples. The spectral lineshape of the absorption is Gaussian in the case of the semipolar orientation, while it is a sum of Lorentzian functions for the polar orientation.

[a)]Electronic mail: houssaine.machhadani@gmail.com

 © 2013 AIP Publishing LLC

[This article is copyrighted as indicated in the article. Reuse of AIP content is subject to the terms at: http://scitation.aip.org/termsconditions. Downloaded to] IP: 132.168.8.249 On: Wed, 08 Apr 2015 12:48:33

II. RESULTS AND DISCUSSION

A. Sample growth and structural characterization

GaN/AlN semipolar QWs have been grown by PAMBE using the optimized growth conditions described in Ref. 22. Substrates consisted of 2-μm-thick $(11\bar{2}2)$-oriented GaN layers deposited on *m*-sapphire by MOVPE.[23] The PAMBE growth starts with a 100 nm thick GaN buffer layer. Then, a stack of 40 GaN/AlN QWs was deposited and overgrown with a 10-nm-thick AlN cap layer. The thickness of the AlN barriers and GaN QWs are summarized in Table I. To populate the ground electron state, the QWs were n-doped with Si at a nominal concentration $n_{QW} = 5 \times 10^{19} \text{cm}^{-3}$. For comparison purposes, polar samples with an identical structure were grown during the same runs on AlN on c-sapphire templates. It should be noted that these designs do not target the maximization of the ISB optical dipole, as it was done in Ref. 24 but they were chosen to evaluate the effect of the electric field in the semipolar GaN/AlN binary system.

The structural quality of the GaN/AlN semipolar MQWs has been studied by high resolution transmission electron microscopy (HRTEM).

Figure 1 displays the HRTEM images of semipolar GaN/AlN QWs viewed along the $[10\bar{1}0]$ and $[11\bar{2}3]$ zone axes. The QWs present a two-dimensional nature in both crystallographic orientations, and the interfaces are chemically sharp. The interface thickness fluctuations extend over 0.5–0.7 nm. From larger images, we estimate a density of basal stacking faults of around $3 \times 10^5 \text{cm}^{-1}$.

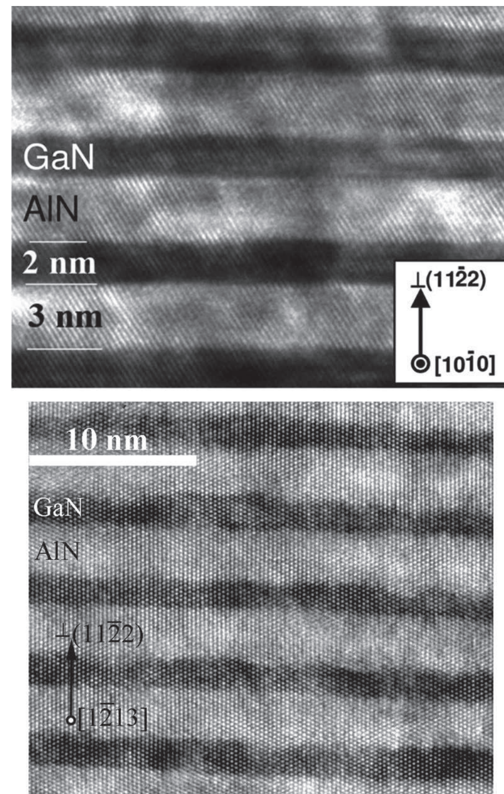

FIG. 1. Cross-section high-resolution TEM image of semipolar GaN/AlN quantum wells (sample C) viewed along the $[10\bar{1}0]$ and $[1\bar{2}13]$ zone axes.

B. Optical spectroscopic measurements

1. *Photoluminescence spectroscopy*

PL spectra were collected at liquid-helium temperature using a $f = 0.46$ m Jobin Yvon HR spectrometer equipped with a liquid-nitrogen-cooled charge-coupled device (CCD) camera. The excitation was provided by a frequency-doubled continuous-wave Ar^{++} laser at $\lambda = 244$ nm.

Figure 2 shows the PL spectra of semipolar (top) and polar (bottom) samples measured at 4 K. As expected, the PL peaks energy is red shifted when increasing the QW thickness in both polar and semipolar QWs. In polar QWs, the PL energy becomes smaller than the GaN gap energy for QW thickness larger than 1.8 nm. This is due to the quantum confined Stark effect induced by the high internal electric field in the QWs. In semipolar QWs, the PL energy peak remains systematically above the GaN gap, attesting the reduction in the internal electric field in the QWs. The full width at half maximum (FWHM) of the PL spectra of semipolar QWs increases with the PL transition energy. This is due to QW thickness fluctuations, whose effect on linewidth increases when decreasing the well thickness. The value of the FWHM in semipolar QWs is 2 to 3 times larger than that in polar QWs as a result of the larger QW thickness fluctuations and to the presence of stacking faults.

TABLE I. Structural parameters for the GaN/AlN polar and semipolar samples. L_{QW} and L_B are the well and barrier thicknesses, respectively.

Sample	L_{QW} (nm)	L_B (Nm)	n_{QW} (cm^{-3})
A	1.2	5	–
B	1.8	3	5×10^{19}
C	2.1	3	5×10^{19}
D	2.25	3	5×10^{19}
E	2.6	3	5×10^{19}
F	3	3	5×10^{19}

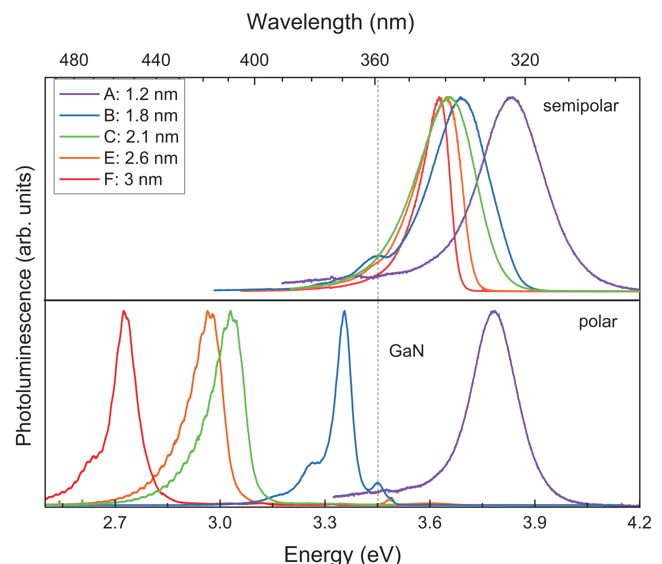

FIG. 2. Low-temperature (4 K) photoluminescence of semipolar (top) and polar (bottom) GaN/AlN QWs. The dashed line indicates the GaN band gap.

[This article is copyrighted as indicated in the article. Reuse of AIP content is subject to the terms at: http://scitation.aip.org/termsconditions. Downloaded to] IP: 132.168.8.249 On: Wed, 08 Apr 2015 12:48:33

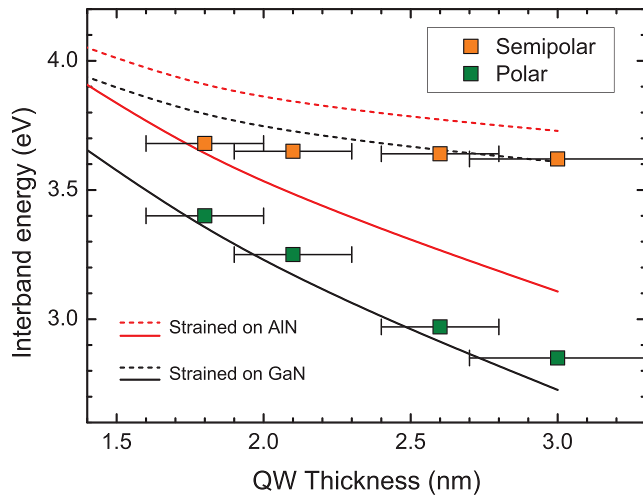

FIG. 3. Photoluminescence energy calculated as a function of QW thickness and strain state for polar and semipolar QWs.

TABLE II. ISB peak energy with corresponding broadening for polar and semipolar samples.

Sample		QWs thickness (nm)	ISB energy (eV)	FWHM (meV)
A	(0001)	1.2	0.85	123
	(11$\bar{2}$2)	**1.2**	**0.81**	**195**
B	(0001)	1.8	0.69	100
	(11$\bar{2}$2)	**1.8**	**0.59**	**153**
C	(0001)	2.1	0.66	90
	(11$\bar{2}$2)	**2.1**	**0.54**	**156**
D	(0001)	2.25	0.63	87
	(11$\bar{2}$2)	**2.25**	**0.49**	**152**
E	(0001)	2.6	0.61	100
	(11$\bar{2}$2)	**2.6**	**0.40**	**160**
F	(0001)	3	0.61	105
	(11$\bar{2}$2)	**3**	**0.38**	**100**

PL results have been interpreted by comparison with calculations of electronic structure using the NEXTNANO[3] 8-band-**k.p** Schrödinger-Poisson solver. The material parameters applied in the simulations are summarized in Ref. 25. As shown in Figure 3, the measured PL energies are in good agreement with calculations, with the experimental points from polar samples located within the band limited by the red and black solid lines, which correspond to the two extreme strain states (strained on GaN and strained on AlN). However, the emission wavelength from semipolar layers presents a certain red shift when compared with theoretical calculations, which can be attributed to carrier localization due to the presence of stacking faults and to larger thickness fluctuations than in the polar case.

2. Intersubband spectroscopy

The ISB absorption of the QWs was investigated using Fourier transform infrared spectroscopy (FTIR). The sample facets were polished at 45° angle to form a multipass waveguide. The sample transmission for *p* and *s* polarized light was measured at room temperature. Figure 4 shows the ISB absorption spectra of polar and semipolar QWs. All samples show direct absorption of *p*-polarized light except the spectrum labeled with a star, which was measured by photoinduced absorption spectroscopy. For both polar and semipolar samples, the e_1-e_2 ISB absorption red shifts when increasing the QW thickness. It covers the 1.5–3.3 μm wavelength range for semipolar QWs, compared to 1.5–2 μm for polar QWs. The ISB peak energy and the FWHM for all samples are indicated in Table II. As seen in Fig. 4, the ISB peak wavelength saturates at 2 μm for polar QWs with a well thickness larger than 2.25 nm, which is not the case for semipolar QWs.

Figure 5 compares the experimental e_1-e_2 ISB peak energy with simulations for semipolar and polar structures.

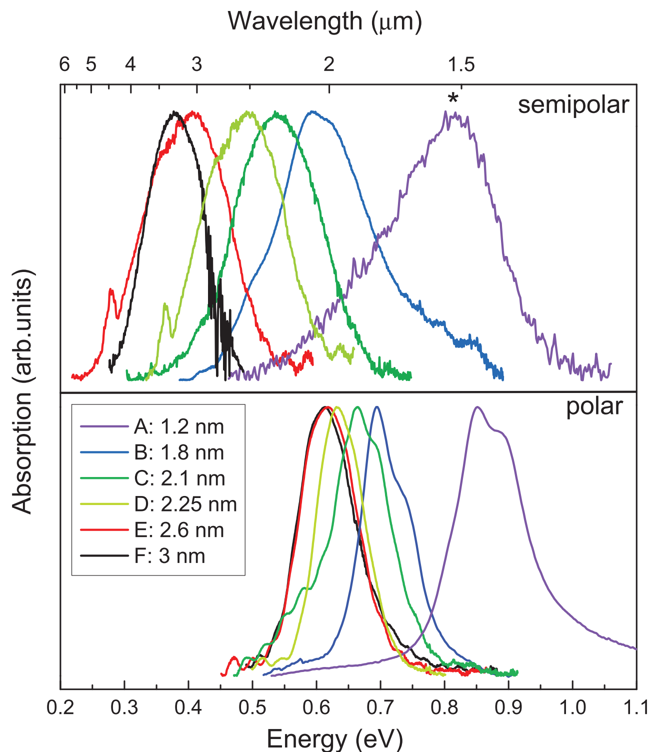

FIG. 4. Intersubband absorption spectra for semipolar (top) and polar (bottom) GaN/AlN QWs with different well thicknesses. The spectrum labeled with a star has been obtained by photoinduced absorption measurement.

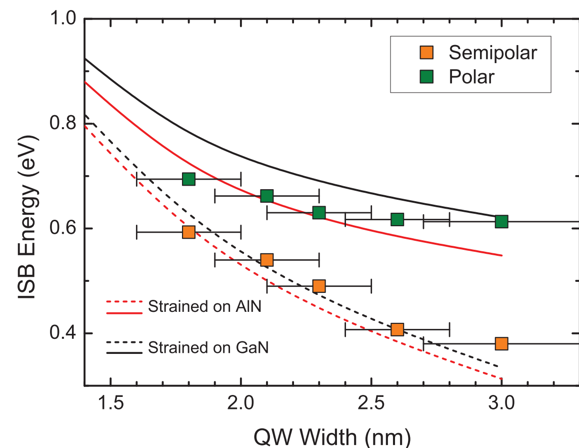

FIG. 5. Calculated and measured ISB absorption energy versus well thickness.

[This article is copyrighted as indicated in the article. Reuse of AIP content is subject to the terms at: http://scitation.aip.org/termsconditions. Downloaded to] IP: 132.168.8.249 On: Wed, 08 Apr 2015 12:48:33

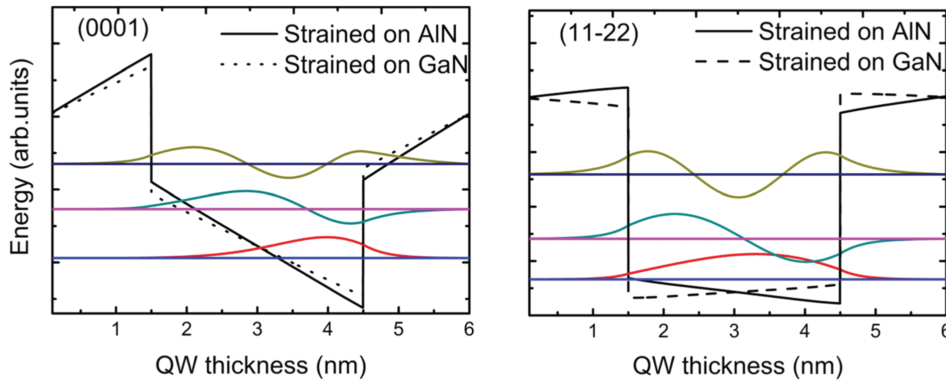

FIG. 6. Band diagram of (0001)- and (11$\bar{2}$2)-oriented GaN/AlN (3 nm/3 nm) QWs in a superlattice. Solid lines correspond to simulations assuming the superlattice strained on AlN. The conduction band in the case of the wells being strained on GaN is included as a dashed line.

The simulation confirms a significant red shift of the transition energy in large semipolar QWs with respect to the polar case due to the reduction of the electric field in the wells. The saturation of the ISB transition for large QWs is explained by the fact that both e_1 and e_2 are located in the triangular section of the polar QWs, so that they are confined by the internal electric field in at distance smaller than the total QW thickness, as illustrated in Fig. 6. It should be noted that for the chosen barrier thickness (3 nm) there is no effect of the quantum coupling between adjacent QWs.

Assuming an infinite GaN/AlN superlattice, the internal fields in the QW and in the barrier are related to the respective polarizations and layer thicknesses by

$$F_{GaN} = -\frac{\Delta P}{\varepsilon_0} \frac{L_{AlN}}{L_{AlN}\varepsilon_{GaN} + L_{GaN}\varepsilon_{AlN}}, \quad (1)$$

$$F_{AlN} = \frac{\Delta P}{\varepsilon_0} \frac{L_{GaN}}{L_{AlN}\varepsilon_{GaN} + L_{GaN}\varepsilon_{AlN}}, \quad (2)$$

where ΔP is the difference between the total polarization (piezoelectric and spontaneous) of the well and the barrier, ε_{AlN} and ε_{GaN} are the dielectric constants for AlN and GaN, respectively, while L_{AlN} and L_{GaN} are the corresponding layer thicknesses. Taking $\varepsilon_r = (\varepsilon_{GaN} + \varepsilon_{AlN})/2$, for polar GaN/AlN MQWs we calculate $\Delta P/\varepsilon_0\varepsilon_r = 10.4$ MV/cm for MQWs strained on AlN, and $\Delta P/\varepsilon_0\varepsilon_r = 12.3$ MV/cm for MQWs strained on GaN. For semipolar GaN/AlN MQWs, the value of $\Delta P/\varepsilon_0\varepsilon_r$ deduced from the simulations is 0.93 MV/cm for MQWs strained on AlN and -0.83 MV/cm for MQWs strained on GaN. The significant reduction in the polarization discontinuity is due to the fact that the spontaneous and piezoelectric polarization differences at the interfaces have opposite signs, the piezoelectric component being dominant in the MQWs strained on GaN resulting in negative ΔP.

3. Nature of ISB broadening

By analyzing the ISB absorption spectra of polar and semipolar samples, we observe that the broadening and the spectral shape are very different. In semipolar QWs, the FWHM is around 100–195 meV, which is larger than that in polar QWs (90–105 meV). In addition, in polar samples with a QW thickness below 2.1 nm (samples A, B, and C), the ISB absorption spectra present well-defined multiple structures, which are not present in semipolar spectra. The multi-structured lineshape of polar samples is well reproduced by a sum of Lorentzian curves. In contrast, for semipolar QWs, the ISB absorption resonance can be well fitted by a Gaussian function, as shown in Figure 7.

This difference is related to the sample structure and to the presence of internal electric field. In polar samples, the multistructured shape of the ISB absorption is interpreted as originating from absorption in well regions with different thickness, as discussed in Ref. 11. Due to internal electric field, for QW thickness below ≈2 nm, a variation of the thickness of the QW of ±1 atomic layer translates into an ISB energy shift comparable to the broadening factor, and therefore results in structuring of the absorption spectrum instead of an inhomogeneous broadening.

For semipolar GaN/AlN QWs, the thickness fluctuations are larger (±2–3 atomic layers, as observed in Figure 1), but the energetic shift induced by each additional atomic layer is

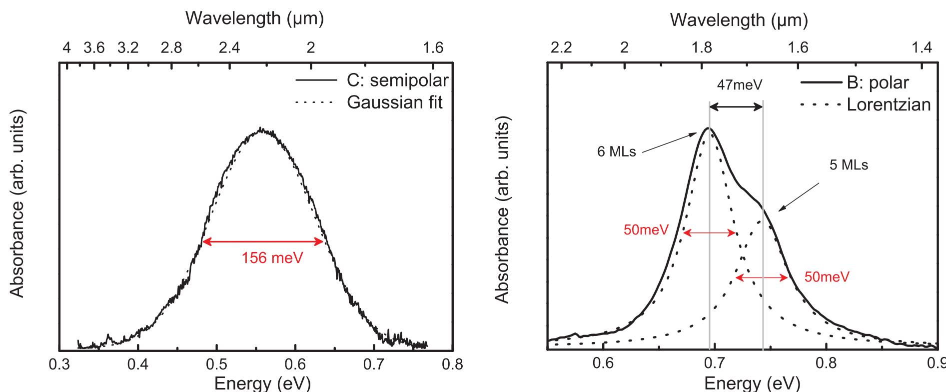

FIG. 7. (left) ISB absorbance of semipolar sample C and the corresponding Gaussian fit (dotted line). (right) ISB absorbance of polar sample B (full line), Lorentzian fitting curves (dotted lines).

[This article is copyrighted as indicated in the article. Reuse of AIP content is subject to the terms at: http://scitation.aip.org/termsconditions. Downloaded to] IP: 132.168.8.249 On: Wed, 08 Apr 2015 12:48:33

smaller, which results in an inhomogeneous broadening. Furthermore, the presence of stacking faults, as an additional perturbation of the bands, contributes to the absorption line broadening. We note that Gaussian lineshapes of the ISB absorption has also been observed in cubic GaN/Al(Ga)N QWs[16] and can be explained in the same manner.

III. CONCLUSION

In summary, we have systematically performed an experimental and theoretical study of ISB transitions in semipolar GaN/AlN quantum wells grown on $(11\bar{2}2)$ GaN. The semipolar samples are compared with the polar samples grown in the same run. The ISB transition shows a significant red shift with respect to the polar case due to the reduction of the internal electric field in the quantum wells. The absorption peak is tuned from 1.5 μm to 3.3 μm by adjusting only the well width. The ISB absorption line shape exhibits a Gaussian shape which is explained by thickness fluctuations of the QWs, and by the presence of stacking faults.

ACKNOWLEDGMENTS

The author acknowledges the support by EC FET-OPEN project Unitride under Grant Agreement #233950 and by EU ERC-StG under project TeraGaN, Grant Agreement #278428, and by the French National Research Agency under project COSNI, Grant No. ANR-08-BLAN-0298-01. The authors thank P. Lavenus for his assistance with photoluminescence measurements.

[1]L. C. West and S. J. Eglash, Appl. Phys. Lett. **46**, 1156 (1985).
[2]J. Faist, F. Capasso, D. L. Sivco, C. Sirtori, A. L. Hutchinson, and A. Y. Cho, Science **264**, 553 (1994).
[3]F. Capasso, C. Gmachl, D. L. Sivco, and A. Y. Cho, Phys. Today **55**(5), 34 (2002).
[4]S. Gunapala and S. Bandara, Semicond. Semimetals **62**, 197 (1999).
[5]B. F. Levine, S. D. Gunapala, J. M. Kuo, S. S. Pei, and S. Hui, Appl. Phys. Lett. **59**, 1864 (1991).
[6]K. L. Tsai, K. H. Chang, C. P. Lee, K. F. Huang, J. S. Tsang, and H. R. Chen, Appl. Phys. Lett. **62**, 3504 (1993).
[7]N. Iizuka, K. Kaneko, N. Suzuki, T. Asano, S. Noda, and O. Wada, Appl. Phys. Lett. **77**, 648 (2000).
[8]K. Kishino, A. Kikuchi, H. Kanazawa, and T. Tachibana, Appl. Phys. Lett. **81**, 1234 (2002).
[9]A. Helman, M. Tchernycheva, A. Lusson, E. Warde, F. H. Julien, K. Moumanis, G. Fishman, E. Monroy, B. Daudin, D. L. S. Dang, E. Bellet-Amalric, and D. Jalabert, Appl. Phys. Lett. **83**, 5196 (2003).
[10]F. Bernardini and V. Fiorentini, Phys. Rev. B **57**, R9427 (1998).
[11]M. Tchernycheva, L. Nevou, L. Doyennette, F. H. Julien, E. Warde, F. Guillot, E. Monroy, E. Bellet-Amalric, T. Remmele, and M. Albrecht, Phys. Rev. B **73**, 125347 (2006).
[12]H. Machhadani, P. Kandaswamy, S. Sakr, A. Vardi, A. Wirtmüller, L. Nevou, F. Guillot, G. Pozzovivo, M. Tchernycheva, and A. Lupu, New J. Phys. **11**, 125023 (2009).
[13]D. As, Microelectron. J. **40**, 204 (2009).
[14]E. DeCuir, Jr., M. Manasreh, J. Schörmann, D. As, and K. Lischka, Appl. Phys. Lett. **91**, 041911 (2007).
[15]E. DeCuir, Jr., M. Manasreh, E. Tschumak, J. Schörmann, D. As, and K. Lischka, Appl. Phys. Lett. **92**, 201910 (2008).
[16]H. Machhadani, M. Tchernycheva, S. Sakr, L. Rigutti, R. Colombelli, E. Warde, C. Mietze, D. As, and F. Julien, Phys. Rev. B **83**, 075313 (2011).
[17]J. Speck and S. Chichibu, MRS Bull. **34**, 304 (2009).
[18]P. Waltereit, O. Brandt, A. Trampert, H. Grahn, J. Menniger, M. Ramsteiner, M. Reiche, and K. Ploog, Nature **406**, 865 (2000).
[19]M. D. Craven, S. H. Lim, F. Wu, J. S. Speck, and S. P. DenBaars, Appl. Phys. Lett. **81**, 1201 (2002).
[20]A. Romanov, T. Baker, S. Nakamura, and J. Speck, J. Appl. Phys. **100**, 023522 (2006).
[21]L. Lahourcade, E. Bellet-Amalric, E. Monroy, M. Abouzaid, and P. Ruterana, Appl. Phys. Lett. **90**, 131909 (2007).
[22]L. Lahourcade, P. K. Kandaswamy, J. Renard, P. Ruterana, H. Machhadani, M. Tchernycheva, F. H. Julien, B. Gayral, and E. Monroy, Appl. Phys. Lett. **93**, 111906 (2008).
[23]P. D. Mierry, T. Guehne, M. Nemoz, S. Chenot, E. Beraudo, and G. Nataf, Jpn. J. Appl. Phys., Part 1 **48**, 031002 (2009).
[24]V. Jovanović, D. Indjin, Z. Ikonić, V. Milanović, and J. Radovanović, Solid state Commun. **121**, 619 (2002).
[25]P. Kandaswamy, F. Guillot, E. Bellet-Amalric, E. Monroy, L. Nevou, M. Tchernycheva, A. Michon, F. Julien, E. Baumann, and F. Giorgetta, J. Appl. Phys. **104**, 093501 (2008).

[This article is copyrighted as indicated in the article. Reuse of AIP content is subject to the terms at: http://scitation.aip.org/termsconditions. Downloaded to] IP: 132.168.8.249 On: Wed, 08 Apr 2015 12:48:33

GaN/Al(Ga)N nanostructures have emerged during the last decade as promising materials for new intersubband (ISB) optoelectronics devices, with the potential to cover the whole infrared (IR) spectrum. These technologies rely on electron transitions between quantum-confined states in the conduction band of nanostructures –quantum wells (QWs), quantum dots (QDs), nanowires (NWs). A variety of GaN-based ISB optoelectronic devices have recently been demonstrated, including photodetectors, switches and electro-optical modulators. However, a number of issues remain open, particularly concerning the extension towards longer wavelengths and the improvement of electrically pumped devices performance.

One of the main challenges to extend the GaN-ISB technology towards the far-IR comes from the polarization-induced internal electric field, which imposes an additional confinement that increases the energetic distance between the electronic levels in the QWs. In order to surmount this constraint, I propose alternative multi-layer QW designs that create a pseudo-square potential profile. The robustness of the designs in terms of variations due to growth uncertainties, and the feasibility of their integration in devices architectures requiring resonant tunneling transport are discussed. Experimental realizations by molecular-beam epitaxy displaying TM-polarized THz absorption are presented. A quantum cascade laser design incorporating pseudo-square QWs is introduced.

An alternative approach to obtain square potential profiles is the use of nonpolar orientations. Room-temperature ISB absorption in the range of 1.5–5.8 µm is demonstrated.

Longer intraband lifetimes have been proven to exist in laterally confined systems, which motivates studies to incorporate NWs as active elements in ISB devices. In this thesis, I report the experimental observation of TM-polarized IR absorption assigned to the s-p_z intraband transition in Ge-doped GaN/AlN nanodisks inserted in self-assembled GaN NWs. Results are compared with theoretical calculations accounting for the 3D strain distribution, surface charges and many-body effects.

Keywords: Quantum engineering, nitrides, thin films, nanowires, intersubband, infrared

---

Ces dix dernières années ont vu l'essor des nanostructures GaN/Al(Ga)N en raison de leur potentiel pour le développement de technologies intersousbandes (ISB) en optoélectronique, et ce dans le spectre infrarouge (IR) complet. Ces technologies sont basées sur des transitions électroniques entre des états confinés de la bande de conduction de nanostructures, telles que les puits quantiques (PQ), les boîtes quantiques (BQ) et les nanofils (NF). Récemment, plusieurs technologies optoélectroniques ISB basées sur le GaN ont été développées, comprenant des photodétecteurs, des switchs, et des modulateurs électro-optiques. Cependant, plusieurs défis restent à relever, en particulier concernant l'extension vers les grandes longueurs d'ondes et l'amélioration des performances des appareils pompés électriquement.

Une des difficultés principales opposées à l'extension des technologies GaN ISB vers le lointain infrarouge résulte de la présence d'un champ électrique interne. Pour pallier à ce problème, on propose une structure de PQs alternative, dont les multiples couches créent un potentiel pseudo-carré. On discute la robustesse de ce design quant aux variations causées par les incertitudes de croissance, et la possibilité de l'intégrer dans des structures nécessitant un transport électronique par effet tunnel résonnant. On décrit également les structures fabriquées par épitaxie par jets moléculaires et présentant de l'absorption de lumière polarisée TM dans la gamme THz. Enfin on propose un design de laser à cascade quantique basé sur ces PQs pseudo-carrés.

L'utilisation d'orientations non-polaires est une autre façon possible d'obtenir des potentiels carrés. On démontre des absorptions ISB à température ambiante dans la fenêtre 1.5-5.8 µm.

L'existence de temps de vie plus longs dans les systèmes confinés latéralement a été démontrée et motive l'intégration des NFs en tant qu'élément actif dans les technologies ISB. Dans ce manuscrit, on décrit l'observation expérimentale d'absorption de lumière IR polarisée TM attribuée à la transition intrabande s-p_z dans des nanodisques GaN/AlN dopés avec du Ge et insérés dans des NFs de GaN. On compare les résultats obtenus avec les calculs théoriques, qui prennent en compte la distribution en trois dimensions de la tension, les charges de surface et les effets à corps multiples.

Mots clés : Ingénierie quantique, nitrures, puits quantiques, nanofils, inter-sous-bande, infrarouge